

Roberto Weigert *Editor*

---

# Advances in Intravital Microscopy

From Basic to Clinical Research

 Springer

[www.ebook777.com](http://www.ebook777.com)

## Advances in Intravital Microscopy



Roberto Weigert  
Editor

# Advances in Intravital Microscopy

From Basic to Clinical Research



Springer



*Editor*

Roberto Weigert  
National Institute of Dental  
and Craniofacial Research,  
National Institutes of Health  
Bethesda, MD  
USA

ISBN 978-94-017-9360-5      ISBN 978-94-017-9361-2 (eBook)  
DOI 10.1007/978-94-017-9361-2  
Springer Dordrecht Heidelberg New York London

Library of Congress Control Number: 2014953598

© Springer Science+Business Media Dordrecht 2014

This work is subject to copyright. All rights are reserved by the Publisher, whether the whole or part of the material is concerned, specifically the rights of translation, reprinting, reuse of illustrations, recitation, broadcasting, reproduction on microfilms or in any other physical way, and transmission or information storage and retrieval, electronic adaptation, computer software, or by similar or dissimilar methodology now known or hereafter developed. Exempted from this legal reservation are brief excerpts in connection with reviews or scholarly analysis or material supplied specifically for the purpose of being entered and executed on a computer system, for exclusive use by the purchaser of the work. Duplication of this publication or parts thereof is permitted only under the provisions of the Copyright Law of the Publisher's location, in its current version, and permission for use must always be obtained from Springer. Permissions for use may be obtained through RightsLink at the Copyright Clearance Center. Violations are liable to prosecution under the respective Copyright Law.

The use of general descriptive names, registered names, trademarks, service marks, etc. in this publication does not imply, even in the absence of a specific statement, that such names are exempt from the relevant protective laws and regulations and therefore free for general use.

While the advice and information in this book are believed to be true and accurate at the date of publication, neither the authors nor the editors nor the publisher can accept any legal responsibility for any errors or omissions that may be made. The publisher makes no warranty, express or implied, with respect to the material contained herein.

Printed on acid-free paper

Springer is part of Springer Science+Business Media ([www.springer.com](http://www.springer.com))

## Preface

Intravital microscopy (IVM) has come a long way from the time of Rudolph Wagner, who imaged the rollover of leukocytes in the leg of a live frog for the very first time (Wagner 1839). Indeed, the last two decades have witnessed a series of major technological breakthroughs that have transformed IVM from an “exotic” imaging technique into a powerful approach that has enabled biologists to dissect several processes in living animals at a molecular level and to extract accurate quantitative information. IVM has become a fundamental tool in basic and preclinical research, and it has moved forward several fields, which include neurobiology, tumor biology, immunology, physiology, and cell biology (Weigert et al. 2013). Moreover, IVM is now rapidly transitioning to clinical applications as a high-resolution diagnostic tool.

This book collects some of the most recent technological developments in IVM and provides a broad view of its applications to various areas of the biomedical field. The first three chapters focus on the use of IVM in the neurosciences that have been the first area benefiting from the development of two-photon microscopy, which has made it possible to perform deep tissue imaging (Denk et al. 1990). Chapter 1 provides a general overview of the state-of-the-art techniques used to monitor neuronal activity in the brain of live mice (Gonçalves and Mostany), whereas Chap. 2 introduces the most recent developments in imaging the cerebral vasculature in awake mice (Summers et al.). Chapter 3 deals with the use of IVM in neurodegenerative disease and provides a comparison with other well-established brain imaging techniques (Wang et al.) Chapter 3. One of the most productive applications of IVM has been the ability to follow individual cells in vivo. This has shed new light on (1) the complexity of the interactions among the cells of immune systems (Chap. 4 – Mathieu et al.), (2) the development of tumors and their interaction with the surrounding environment (Chap. 5 – Fein et al., Chap. 6 – Tozer et al.), and (3) the biology of the stem cells in their niche (Chap. 7 – Mortensen et al.). The most recent advancements in subcellular IVM have contributed to extend this approach to cell biology and in particular to membrane trafficking (Chap. 8 – Cao and Abe, Chap. 9 – Masedunskas et al.) and to finally provide the unique opportunity to bridge basic biology to organ physiology in vivo, as highlighted for the kidney in Chap. 10 (Sandoval and Molitoris) and the lungs in Chap. 11 (Presson et al.).

The development of IVM has been tightly linked to the tools developed to facilitate imaging. In particular, new generations of fluorescent probes optimized for deep tissue imaging have been instrumental to study the bio-distribution of various molecules under both physiological and pathological conditions, as illustrated in Chap. 12 (Yu and Gambhir) and Chap. 13 (Giedt et al.).

Finally, the last three chapters of this book highlight the ongoing transition of IVM to clinical studies. IVM has the potential to provide invaluable insights on the status of the tissue by revealing changes in either the cellular architecture by using miniaturized probes and endoscopes (Chap. 14 – Hall et al., Chap. 15 – Huland et al.) or the chemical composition of the microenvironment in situ by using fluorescence lifetime imaging, FLIM (Chap. 16 – Washington et al.).

Bethesda, MD, USA

Roberto Weigert

## References

- Denk W, Strickler JH, Webb WW (1990) Two-photon laser scanning fluorescence microscopy. *Science* 248:73–76
- Wagner R (1839) *Erläuterungstaflen zur Physiologie und Entwicklungsgeschichte*. Leopold Voss, Leipzig
- Weigert R, Porat-Shliom N, Amornphimoltham P (2013) Imaging cell biology in live animals: ready for prime time. *J Cell Biol* 201(7):969–979

Contents

<b>1</b>	<b>Intravital Two-Photon Excitation Microscopy in Neuroscience: General Concepts and Applications . . . . .</b>	<b>1</b>
	J. Tiago Gonçalves and Ricardo Mostany	
<b>2</b>	<b>Two-Photon Imaging of Cerebral Vasodynamics in Awake Mice During Health and Disease . . . . .</b>	<b>25</b>
	Philipp M. Summers, Zachary J. Taylor, and Andy Y. Shih	
<b>3</b>	<b>In Vivo Imaging in Neurodegenerative Diseases . . . . .</b>	<b>45</b>
	Xueying Wang, Michal Arbel-Ornath, Susanne K. Wegmann, Ksenia V. Kastanenko, and Brian J. Bacskai	
<b>4</b>	<b>Intravital Imaging of the Immune System. . . . .</b>	<b>81</b>
	Melanie P. Matheu, Michael D. Cahalan, and Ian Parker	
<b>5</b>	<b>Cancer in the Spotlight: Using Intravital Imaging in Cancer Research . . . . .</b>	<b>105</b>
	Miriam R. Fein, Robert W. Wysocki, and Mikala Egeblad	
<b>6</b>	<b>Haemodynamics and Oxygenation of the Tumour Microcirculation. . . . .</b>	<b>125</b>
	Gillian M. Tozer, Rachel Daniel, Sarah Jane Lunt, Constantino C. Reyes-Aldasoro, and Vincent J. Cunningham	
<b>7</b>	<b>In Vivo Imaging of Bone Marrow Stem Cells . . . . .</b>	<b>143</b>
	Luke J. Mortensen, Walid Zaher, Cristina Lo Celso, and Charles P. Lin	
<b>8</b>	<b>Live Imaging of Subcellular Structures and Cellular Processes in Mouse Intraperitoneal Organs . . . . .</b>	<b>163</b>
	Liqin Cao and Kuniya Abe	
<b>9</b>	<b>Intravital Imaging of the Lactating Mammary Gland in Transgenic Mice Expressing Fluorescent Proteins . . . . .</b>	<b>187</b>
	Andrius Masedunskas, Roberto Weigert, and Ian H. Mather	

**10    Fluorescent Dextrans in Intravital Multi-Photon Microscopy . . . . .**    205  
      Ruben M. Sandoval and Bruce A. Molitoris

**11    Intravital Microscopy of the Lung . . . . .**    221  
      Robert G. Presson, Irina Petrache, and Mary Beth Brown

**12    Intravital Microscopy for Molecular Imaging  
      in Cancer Research . . . . .**    233  
      Hongmei Yu and Sanjiv Sam Gambhir

**13    Imaging Drug Distribution and Effects at the Single  
      Cell Level In Vivo . . . . .**    263  
      Randy Giedt, Katy Yang, and Ralph Weissleder

**14    Nonlinear Endomicroscopy Imaging Technology  
      for Translational Applications. . . . .**    281  
      Gunnsteinn Hall, Wenxuan Liang, and Xingde Li

**15    Intravital Multiphoton Endoscopy . . . . .**    305  
      David M. Huland, Dimitre G. Ouzounov, David R. Rivera,  
      Chris M. Brown, and Chris Xu

**16    Fluorescence Lifetime Imaging for Diagnostic  
      and Therapeutic Intravital Microscopy . . . . .**    371  
      Washington Y. Sanchez, Zhen Song, Wolfgang Becker,  
      Karsten Koenig, and Michael S. Roberts

**Index . . . . .**    419

# Chapter 1

## Intravital Two-Photon Excitation Microscopy in Neuroscience: General Concepts and Applications

J. Tiago Gonçalves and Ricardo Mostany

**Abstract** Multiphoton excitation microscopy has revolutionized biomedical research during the last two decades by enabling high resolution fluorescent microscopy in intact tissues. This feature makes two-photon excitation (2PE) microscopy ideal for intravital imaging of neural tissue, permitting the observation of structural and functional neuronal dynamics in undisrupted neural circuits. Here we review the fundamental concepts of intravital 2PE microscopy, describe methods and techniques associated with it, and highlight the most significant findings reported on neuron and glia structure dynamics as well as on neuronal activity using this *in vivo* imaging technique.

**Keywords** Chronic in vivo imaging • Calcium imaging • Dendritic spine • Axonal bouton • Fluorophore • GECI • Cranial window • Thinned-skull • Pyramidal neuron • Glia • Deep tissue imaging • Optogenetics

### 1.1 From Cajal to Two-Photon Excitation Microscopy

Microscopy has been one of the most important allies in the history of neuroscience. It was the main tool for Santiago Ramón y Cajal when he produced his vast contribution to neuroscience more than 100 years ago. Since then microscopy has evolved enormously due to the introduction of new light sources, the invention of more sensitive light detectors, computerization of microscopes as well as the development of more specific and sensitive stains and brighter fluorescent dyes. All of these progressing technologies have contributed to the unstoppable advance of microscopy,

---

J.T. Gonçalves

Laboratory of Genetics, Salk Institute for Biological Studies, La Jolla, CA 92037, USA

R. Mostany (✉)

Department of Pharmacology, Tulane University School of Medicine,  
1430 Tulane Ave. SL-83, New Orleans, LA 70112, USA

e-mail: [rmostany@tulane.edu](mailto:rmostany@tulane.edu)

© Springer Science+Business Media Dordrecht 2014

R. Weigert (ed.), *Advances in Intravital Microscopy*:

*From Basic to Clinical Research*, DOI 10.1007/978-94-017-9361-2\_1

1

and in turn, to many other fields of science, particularly neuroscience. Among all the technological innovations involved in the evolution of microscopy, one in particular changed the way we understand the study of biological systems today: the introduction of fluorescent molecules. Although the use of fluorophores in biological investigations began in the 1940's (Ghiran 2011), the utilization of these compounds took several years to achieve wide recognition (Weller and Coons 1954). Later, the use of fluorescence microscopy spread and it is now considered one of the most powerful tools in cell biology. The success of this technique has been closely associated with the development of other new technologies which have revolutionized how we know microscopy nowadays. In this sense, we will highlight two technological advances that per se already have had an enormous impact on biological research, but their combined use is expanding our knowledge further and faster every day: the development in the last two decades of genetically encoded fluorescent molecules and the application of the two-photon excitation (2PE) principle to biomedical research.

The importance of the discovery of the green fluorescent protein (GFP) by Shimomura et al. (1962), its incorporation into the DNA of eukaryotic cells (Chalfie et al. 1994), and the subsequent development of multiple versions of its structure (Tsien 1998) were recognized with the awarding of the shared 2008 Nobel Prize in Chemistry to Drs. Osamu Shimomura, Martin Chalfie, and Roger Tsien. Previously in 1931, Maria Goeppert-Mayer described the 2PE principle, but her theoretical work was far ahead of the ability of the scientific community to empirically demonstrate the concept and it took another three decades to experimentally verify this photon absorption modality. She was awarded the Nobel Prize in Physics in 1963, not for this achievement, but for her work on the mathematical model for the structure of the nuclear shell. Almost six decades after the 2PE principle was enunciated, Winfried Denk, in the laboratory of Watt W. Webb, reported the application of 2PE of fluorescence to laser scanning microscopy (Denk et al. 1990). Since then a plethora of applications, techniques, genetic approaches, and most importantly, brilliant ideas based on this particular microscopy modality have generated new knowledge about the structure and function of the central nervous system.

## 1.2 Single vs. Multiphoton Excitation

A fluorophore (also known as fluorochrome) is a molecule capable of emitting light upon the absorption of energy transferred as electromagnetic radiation such as visible light. Most of the energy absorbed by electrons transitioning to a higher energy level is subsequently released as photons: the fluorescence emission (Lakowicz 2010). In single photon excitation, electrons in a low energy state, i.e., ground state, absorb energy from individual photons (usually in the ultraviolet or blue/green range) with sufficient and appropriate energy to transit to an electronically excited state (Fig. 1.1). The principle of multiphoton excitation is based on the concept that more than one photon of low energy can excite a fluorophore if the

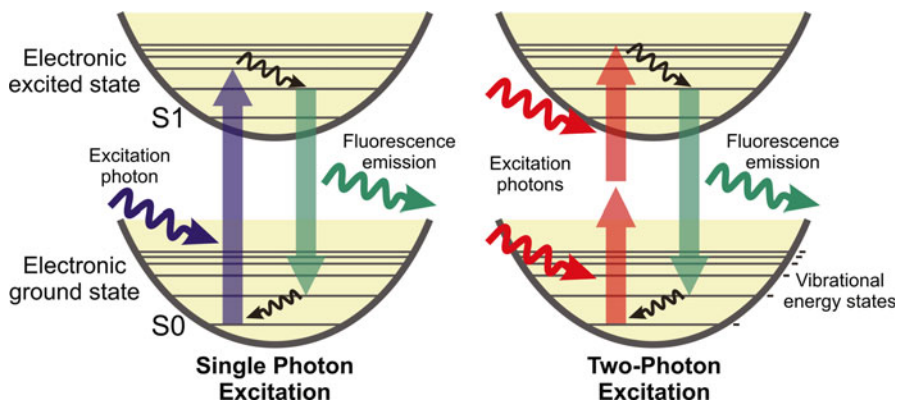


**Fig. 1.1** Simplified Jablonski energy diagram showing single-photon and two-photon excitation processes. Single-photon excitation requires the absorption of one photon with the appropriate energy level to excite a ground orbital electron of a fluorophore to its electronically excited state (*left*). After internal conversion (in internal conversion energy is transferred to vibrational and rotational energies of the fluorescent molecule) this electron relaxes to its ground state, emitting a photon of lower energy (longer wavelength) than the excitation photon. In 2PE (*right*), the internal conversion and emission transitions are similar: one photon excites one orbital electron of the fluorophore to an intermediate state while a second photon, reaching the electron within femtoseconds from the first one, further excites the fluorophore to the excited state. In this case the emitted photon is of shorter wavelength than that the photons used for the excitation process

sum of their energies is higher than the energy required to excite the molecule. In non-linear 2PE the same excitation mechanism is achieved by the absorption of two lower-energy consecutive photons, with the second photon being absorbed only a few femtoseconds after the first. Given that the energy of a photon is inversely proportional to its wavelength, the two photons must be of a longer wavelength (in the near infrared spectrum), which is approximately double that required for single-photon excitation. The comparatively lower energy of the photons used for 2PE significantly reduces tissue photodamage, resulting in increased viability of the samples. This allows experiments requiring either time lapse imaging (multiple time points of imaging of the same region of interest) or extended exposure of the sample to the laser while continuously recording (e.g., neuronal activity using calcium imaging). Furthermore, the longer wavelengths required for 2PE are less absorbed and scattered in biological samples than UV or blue-green light and therefore are able to penetrate deeper into the tissue to allow the excitation of fluorophores at a depth of several hundreds of microns inside the specimen. Due to the intrinsic properties of this modality of non-linear excitation, the requirements for 2PE are only fulfilled at the focal point, with estimated volumes of excited sample in the sub-femtolitre range, so that every single emitted photon collected is a useful signal. As a consequence of these properties, three dimensional contrast and resolution is enhanced without the need for physical filters, such as a confocal pinhole.



In summary, the intrinsic properties of 2PE microscopy provide this technique with several advantages compared with conventional fluorescence or confocal microscopy: it enables the observation of fluorescent structures deep in the brain because the long wavelengths used for 2PE travel better through highly scattering tissue, the photodamage of the sample is minimized because lower energy photons are used, and the excitation of the fluorophore is confined to the focal point of the laser and does not affect the tissue above or below the focal plane. These properties make 2PE ideal for *in vivo* imaging, allowing researchers to examine the same cellular structure or activity multiple times with exceptional resolution.

### 1.3 *In Vivo* 2PE Setup

2PE microscopy setups are commercially available from all of the major microscopy companies. However, most of these systems are optimized for studies using *ex vivo* preparations or tissue and cell cultures and have limited physical space to accommodate larger specimens such as mice or rats. During the last several years the number of companies offering *in vivo* systems has increased, although many laboratories still opt for a custom-built system (Tsai and Kleinfeld 2009) or for a modified conventional commercial system (Denk 1994; Majewska et al. 2000; Potter 2000; Nikolenko et al. 2003).

The main components of an *in vivo* 2PE microscope are the light source, the scanning system, and the emitted light detectors. Ultrafast lasers, with pulse duration in the femtosecond range and with high repetition rates of around 80–100 MHz, such as mode-locked titanium-sapphire (Ti:S) oscillators (Fig. 1.2), are the most commonly used light sources for 2PE microscopy. Tunable Ti:S lasers are the preferred choice because they allow the use of a wide variety of fluorophores since they cover a tuning wavelength range of 350–400 nm, depending on the make and model.

The choice of scanning system will depend on the requirements of the imaging application and mostly upon the speed of image acquisition. The rule of thumb is that the image quality is inversely related to the speed of scanning: the faster the rate of scanning, the lower the quality of the image because the lower exposure time leads to fewer photons captured and, consequently, a decrease in the signal-to-noise ratio. The most common scanners are galvanometer mirrors. These scanners offer great performance for applications where scanning speed is not a limiting factor and they allow for the rotation and zooming of the imaged sample. When an application requires higher scanning speeds, for example to record calcium transients with millisecond-range temporal resolution, the use of resonant galvanometers is recommended. The use of acousto-optic deflectors (AOD) is another alternative but usually the quality of the image is sacrificed for faster speeds even when using random-access scanning of dispersed areas of interest.

The detection of the emitted light is achieved using photomultiplier tubes (PMTs). PMTs are widely used because of their high sensitivity, low noise, large photosensitive area, and their spectral properties. These devices are able to multiply the current

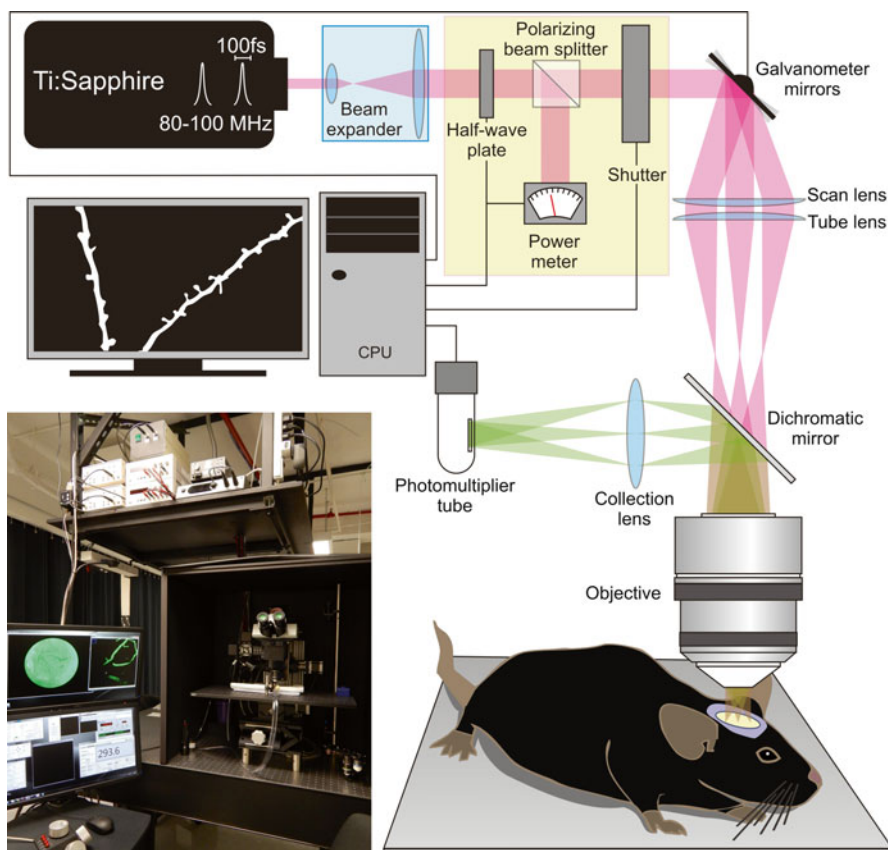


**Fig. 1.2** Setup for intravital 2PE microscopy. A two-photon excitation imaging system for intravital microscopy consists of several mechanical, optical and electronic components. This diagram shows the fundamental components of an *in vivo* 2PE microscope: a two-photon light source (mode-locked Ti:Sapphire Ultrafast Laser), a set of scanning mirrors (x and y galvanometers), and the emitted light detector (photomultiplier tube that receives the emitted photons from the sample and converts them into electrical currents). In addition, a series of components intended to: increase the diameter of the collimated laser beam (beam expander, blue box); control the laser intensity (half-wave plate, polarizing beam splitter, and power meter; yellow box); control the laser exposure (shutter); focus the laser beam onto the sample (scan and tube lenses, and objective); collect the emitted light (dichromatic mirror plus collection lens); and a computer that controls the image acquisition, are other components that constitute an *in vivo* imaging setup. Some of these components can be identified in the picture on the bottom left

originated by the emitted light photons by several million times using a consecutive dynode cascade that sequentially increases the number of photoelectrons. An alternative to commonly used PMTs are the hybrid photodetectors which utilize a photoelectron multiplication based on the electron bombardment of an avalanche diode.

In addition to these elements, a series of optical, electronic, and mechanical components complete the *in vivo* setup as observed in Fig. 1.2.

## 1.4 Optical Preparations for Intravital 2PE Microscopy in Neuroscience

In neuroscience most of the preparations for intravital 2PE microscopy require obtaining optical access to the surface of the brain or the spinal cord. Intravital imaging of the spinal cord requires the removal of one or several laminae covering this structure. After imaging, the spinal cord can be covered with dural substitute, the laminectomy closed, and the wound sutured until the next imaging time point (Kerschensteiner et al. 2005). An alternative method consists of imaging through the intervertebral space and thinned vertebrae without surgical removal of the vertebral laminae (Kim et al. 2010), but this method only allows a restricted area for imaging. Recently, both Farrar et al. (2012) and Fenrich et al. (2012) described the utilization of custom-made implanted imaging chambers for chronic spinal cord imaging.

To obtain optical access to the brain, researchers have conceived several preparations which can be reduced to two types: the cranial window preparation and the thinned-skull preparation. There is a third modality, the polished and reinforced thinned skull preparation (PoRTS), that combines the two preparations mentioned previously (Fig. 1.3).

The cranial window preparation consists of replacing a piece of skull with a thin cover glass. Depending on the requirements of the experiment, the researcher may choose to cover the whole extension of the craniotomy with the cover glass and seal the preparation (closed cranial window, Mostany and Portera-Cailliau 2008a; Holtmaat et al. 2009), or use an open cranial window where part of the brain surface is accessible and the rest is under the cover glass (Svoboda et al. 1997; Golshani and Portera-Cailliau 2008; Gonçalves et al. 2013). The closed cranial window is intended for chronic experiments with multiple data collection time points several days or weeks apart and for acute experiments where the heart beat motion artifact needs to be reduced by applying a light pressure using a cover glass. This preparation allows for chronic imaging of large cortical areas (>3 mm diameter) without the need for additional surgeries and for performing cortical injections of fluorescent dyes, viral vectors, or drugs before the craniotomy is covered. On the other hand, the open cranial window preparation is ideal for acute experiments where the injection of a dye or the recording of electrical activity is required.

The thinned-skull preparation requires the removal of the superficial layers of the skull bone with a small drill first and then with a surgical blade until the skull is thin enough to allow for the imaging of the brain structures underneath (Yang et al. 2010; Kelly and Majewska 2010). This technique allows for several (4–5 maximum) time points of imaging of small brain areas (<0.3 mm<sup>2</sup>).

The PoRTS preparation is a combination of the closed cranial window and the thinned-skull preparation. The cranial bone (up to 3 mm diameter) is thinned with a drill, polished, and covered with cover glass glued to the thinned skull with cyanoacrylate cement (Drew et al. 2010; Shih et al. 2012b).

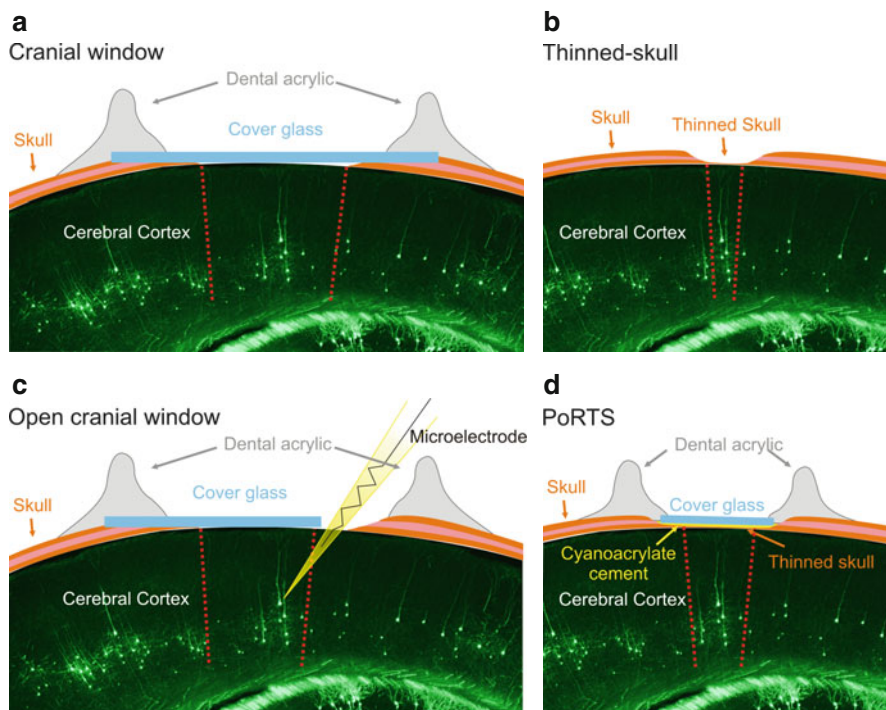


**Fig. 1.3** Optical preparations for intravital 2PE microscopy of the brain. Several preparations have been developed to obtain optical access to the brain for intravital 2PE imaging. The cranial window preparation (**a**) consists in the removal of a piece of skull and replacing it with a thin cover glass. The thinned-skull preparation (**b**) requires the removal of the superficial layers of the skull bone until its thinness allows for the imaging of the brain structures beneath it. The researcher may opt for an open cranial window (**c**) where areas of the brain surface are accessible while others are under the cover glass. For the PoRTS preparation (**d**) the cranial bone is thinned, polished, and covered with cover glass. The relative sizes of the brain areas that can be imaged using each preparation are depicted as the areas between the red dotted lines

These preparations allow for the intravital imaging of cellular activity, cells, or cellular structures which have been labeled or tagged with fluorescent molecules in the spinal cord or the brain. In many cases the use of transgenic mice expressing fluorescent proteins in specific cell types or cell populations facilitates the process of labeling the structures of interest (Feng et al. 2000; Livet et al. 2007; Cai et al. 2013) and permits imaging of cellular dynamics and functionality (Chen et al. 2012). Some available genetic strategies allow the conditional expression of a reporter gene in a specific cell type (e.g., Cre-loxP recombination system; (Zariwala et al. 2012)) or the inducible expression or repression of a fluorophore by exposure to tetracycline or doxycycline (e.g., Tet-expression systems; (Sato et al. 2013)). However, there are many other instances in which transgenic animals are not available, and the injection of the fluorophore or a genetic vector encoding for a fluorescent protein to be expressed in the transfected neurons is needed. Several techniques

have been developed to circumvent this problem: bulk loading of fluorophores conjugated with acetoxymethyl (AM) ester groups (e.g., Fura-2 AM, OGB-1 AM) are taken by large numbers of cells which remove the AM group using cellular esterases, trapping the fluorophore and rendering it incapable of crossing the cellular membrane (Stosiek et al. 2003; Golshani et al. 2009; Gonçalves et al. 2013). Injections of recombinant adeno-associated virus (rAAV; (Stettler et al. 2006)) as well as lentiviral vectors (Dittgen et al. 2004) are also commonly used to transfect neurons with the fluorescent protein gene. Direct cellular injection of fluorescent dyes using patch pipettes (Svoboda et al. 1997; Majewska et al. 2000) as well as single cell electroporation of dextran-conjugated indicators (Grienberger and Konnerth 2012) or of plasmid DNA encoding for fluorescent dyes (Judkewitz et al. 2009) allow the targeted labeling of individual neurons in the cortex. Other electroporation modalities such as *in utero* or *in vivo* electroporation allow the incorporation of DNA plasmids into the brain cells of living mice by applying electrical fields that increase the conductivity and permeability of the cells surrounding the injection site (Saito and Nakatsuji 2001; Dixit et al. 2011).

## 1.5 Intravital Structural Imaging of Brain Cells

Intravital 2PE microscopy provides the possibility of examining the intact brain with exceptional resolution, preserving the structural anatomy of the brain cells and the circuitry of the different cortical and subcortical areas. Additionally, it allows access to another dimension to the study of the living brain: the temporal dimension. For many decades, the main experimental tools for the study of synaptic and large-scale structural plasticity have been Golgi's method and other staining techniques which have yielded much of our current knowledge. The results obtained from these type of fixed tissue techniques, however, allowed mere snapshots of what was occurring in a piece of tissue at the moment the sample was collected. 2PE microscopy allows multiple observations of the same neuron (or glial cell) over periods of time ranging from minutes (Cruz-Martin et al. 2010) to years (Mostany et al. 2013) (Fig. 1.4), enabling the study of the dynamics of dendritic spines and axonal boutons, the main players of excitatory cortical synapses.

The large-scale structure of layer (L) 2/3 (Chow et al. 2009) and L5 (Trachtenberg et al. 2002; Mostany and Portera-Cailliau 2011) pyramidal neurons in the cerebral cortex as well as of mitral and tufted cells within the olfactory bulb (Mizrahi and Katz 2003) is preserved in the healthy brain over periods of months. Only minimal changes in the length of both the apical dendritic tips and the overall apical dendritic tree have been reported for L2/3 (Chow et al. 2009) and L5 (Chow et al. 2009; Mostany and Portera-Cailliau 2011) pyramidal neurons, whereas inhibitory neurons seem to be more dynamic (Chen et al. 2011; Chen and Nedivi 2013). In contrast with the structural stability of neurons under normal conditions, microglia, the primary immune effector cells in the nervous system, have been reported to be relatively active, with very motile protrusions and processes even during the resting

state (Nimmerjahn et al. 2005). The extraordinary optical resolution of 2PE, however, has enabled the observation of the formation of *de novo* dendritic spines and axonal boutons, as well as their elimination, in the absence of large-scale changes in the arborization of the dendritic or axonal tree. This technique has demonstrated that some dendritic spines and filopodia are very motile and are able to change shape, appear, and disappear over a span of minutes (Lendvai et al. 2000; Cruz-Martin et al. 2010), whereas others are very persistent and are detectable on the surface of the dendritic shaft for more than a year (Grutzendler et al. 2002; Mostany et al. 2013) (Fig. 1.4). The densities of these protrusions, dendritic spines and axonal boutons, change during the life span. After an intensive process of synaptogenesis during the first weeks of life (Holtmaat et al. 2005; Cruz-Martin et al. 2010), there is a period of elimination of supernumerary, meaningless cortical synaptic contacts (Holtmaat et al. 2005; Zuo et al. 2005; Mostany et al. 2013) continuing until the brain reaches adulthood. New data from normally aging mice suggests that as the brain ages, the density of dendritic spines increases until reaching a steady density late in life (Mostany et al. 2013) (Fig. 1.4).

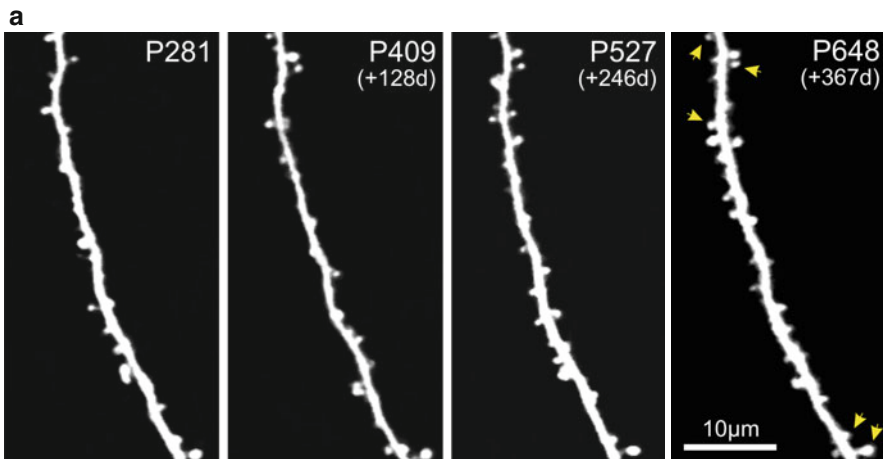


**Fig. 1.4** Intravital 2PE structural imaging of the cerebral cortex. **(a)** Time lapse imaging of long term spine dynamics of an apical dendritic segment of a L5 pyramidal neuron in the somatosensory cortex of a mouse. Note that some dendritic spines persist (yellow arrows) for the whole imaging period, from postnatal day (P) 281 to P648=367 days apart. **(b)** Dendritic spine density from L5 pyramidal neurons in somatosensory cortex in juvenile (<1 month), young (3–5 months), mature (8–15 months), and old (>20 month) mice. **(c)** Time lapse imaging of cortical axonal segments showing the dynamics of *en passant* boutons in an old mouse. Yellow arrows point to stable axonal boutons. **(d)** Intravital 2PE imaging also allows the *in vivo* study of the brain vasculature structure (left) as well as *in vivo* measurements of blood flow dynamics (right) as red blood cell (RBC) speed ( $Dx/Dt$ ) and RBC linear density (RBC/sec). **(e)**, Chronic imaging of dendritic structure of an apical dendritic segment from a L5 pyramidal neuron in peri-infarct cortex before (day 0) and up to 90 days after middle cerebral artery occlusion in a mouse. Yellow arrows indicate a few examples of always-present spines and blue asterisks at day +4 denote transient dendritic swelling after stroke (Panels **(a)**, **(b)** and **(c)** adapted from Mostany et al. (2013). Panels **(d)** and **(e)** adapted from Mostany et al. (2010))



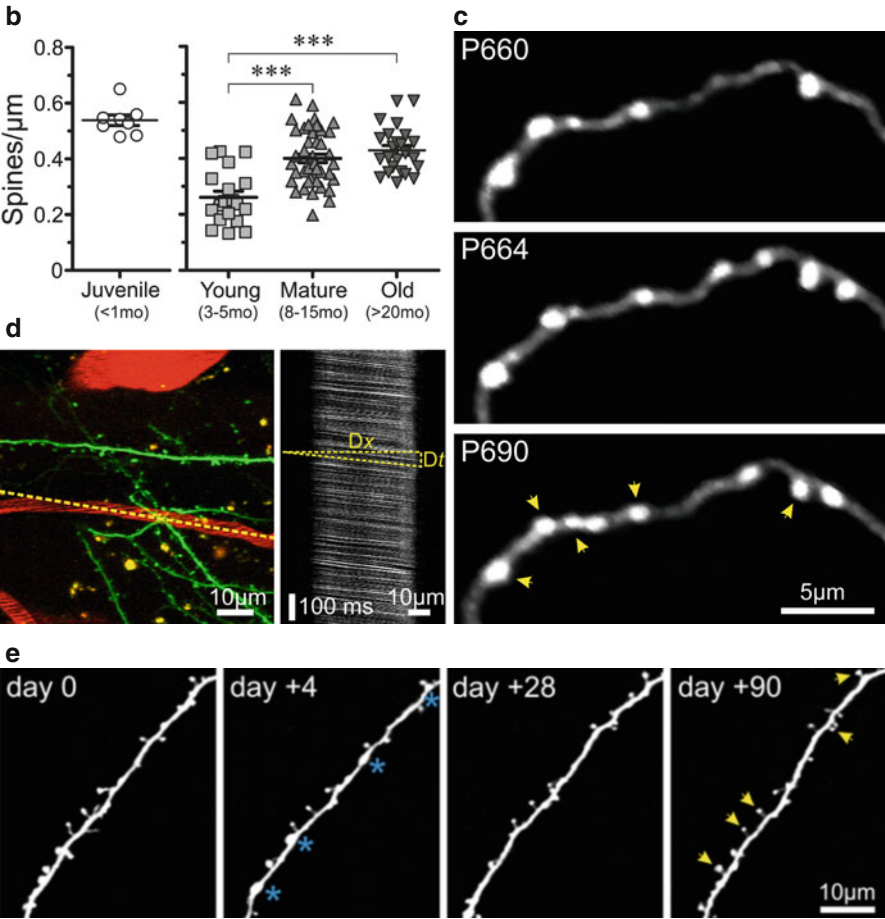


Fig. 1.4 (continued)

An important aspect of intravital 2PE microscopy is the ability to image the same neuronal structures multiple times, which allows the analysis of the dynamic changes of dendritic spines and axonal boutons. Different studies have shown that in mice the dynamics of these structures change throughout the life span. Thus, increased numbers of gained and lost dendritic spines have been reported to occur during the first weeks of life (Lendvai et al. 2000; Cruz-Martin et al. 2010; Mostany et al. 2013) during brain development, whereas cortical circuits stabilize later in life and the dynamic nature of these protrusions is reduced, but not eliminated (Holtmaat et al. 2005; Mostany et al. 2013). The fraction of dendritic spines with shorter lifespans that appear and disappear is probably the substrate for newly formed synaptic contacts (Holtmaat and Svoboda 2009). If the axon-spine interaction is successful, the synapse is stabilized by long term potentiation (Nimchinsky et al. 2002; Harvey

and Svoboda 2007; De Roo et al. 2008) and the synaptic contact can participate in and modulate the response of the postsynaptic neuron. This then, lays the foundation for experience-dependent synaptic plasticity as well as for learning and memory (Holtmaat et al. 2006; Xu et al. 2009; Fu et al. 2012; Lai et al. 2012). On the other hand, cortical axonal boutons seem to be more stable, exhibiting lower turnover rates than observed for dendritic spines (Majewska et al. 2006; Mostany et al. 2013) (Fig. 1.4). Most of the intravital 2PE imaging studies in the cortex have focused on the apical tufts of two types of pyramidal neurons, L2/3 and L5, which show differences in the density and turnover rates of dendritic spines (Holtmaat et al. 2005) suggesting that synaptic dynamics in different neuronal types are differentially regulated. Further analyses of the density and dynamics of these protrusions are needed, not only in additional neuronal subtypes, but also in different brain areas since the dynamics of dendritic spines might be function-specific and the structure of the cortical circuits in different cortical areas might require different rates of formation and elimination of synaptic elements to achieve optimal tuning and efficiency. The differences in spine turnover between the somatosensory and visual cortex have been described (Holtmaat et al. 2005) as well as the differences among the motility of these protrusions in the visual, auditory, and somatosensory cortex (Majewska et al. 2006).

Because intravital 2PE allows us to observe changes in the synaptic network associated with new experiences or while learning a new task, it has provided valuable knowledge about the mechanisms that the cortex uses to store information. Studies where animals were deprived of sensory stimulation have shown that these manipulations induce changes in the formation and elimination of dendritic spines in the visual (Keck et al. 2008) and somatosensory cortex (Holtmaat et al. 2006), suggesting that newly-formed synaptic contacts play an important role in the experience-dependent mechanisms of learning and memory. This increase in the dynamics of dendritic spines is also evident in the motor cortex when mice are forced to learn new motor skills suggesting that the formation and stabilization of new spines are the foundation for long-term motor memory (Xu et al. 2009; Fu et al. 2012).

In the last several years, the application of 2PE microscopy to *in vivo* imaging has produced a large number of studies examining alterations in normal cortical plasticity, for example, after an epileptic episode (Rensing et al. 2005; Guo et al. 2012), stroke (Brown et al. 2007; Mostany et al. 2010; Mostany and Portera-Cailliau 2011), in animal models of traumatic brain injury (Sword et al. 2013), spinal cord injury (Fenrich et al. 2012), and Alzheimer's disease (Spires-Jones et al. 2007; Dong et al. 2010).

In addition to the studies on structural plasticity of neurons, neuroglia dynamics have also been studied using intravital 2PE microscopy in normal and in pathophysiological conditions. Hughes et al. (Hughes et al. 2013) recently described the elevated motility of oligodendrocytes, including dynamic filopodia with fast responses to CNS. Microglia have also been reported to be highly active in their resting state, but can transition from patrolling behavior to shielding of injured sites when a blood vessel is damaged (Nimmerjahn et al. 2005). Similarly, initial studies



on the role of astrocytes after brain injury have described the existence of a heterogeneous population of astrocytes, probably with different functionalities during inflammation and healing processes (Bardehle et al. 2013).

The interplay between the vascular and neuronal components of the brain has been studied in the cortex showing how the activity of a particular set of neurons is followed by changes in the volume and flow of blood to that brain area (Drew et al. 2011; Shih et al. 2012a). Fluorescent dextrans injected intravenously, in combination with intravital 2PE microscopy, enable the viewer to image the cortical vasculature, determine the speed of the red blood cells, and ultimately to allow the measurement of blood flow (Kleinfeld et al. 1998; Mostany and Portera-Cailliau 2008b) (Fig. 1.4). This approach has provided valuable information about blood flow dynamics under normal and pathophysiological conditions (Blinder et al. 2010, 2013; Shih et al. 2012a) such as those leading to stroke (Nishimura et al. 2006; Schaffer et al. 2006; Shih et al. 2009; Mostany et al. 2010) (Fig. 1.4).

## 1.6 Monitoring Neuronal Activity with *in Vivo* Two-Photon Microscopy

Applications of two-photon imaging methods to record neuronal activity can be divided into two broad categories: potentiometric and calcium imaging (and to a lesser degree other ionic imaging, e.g., chloride).

### 1.6.1 Potentiometric Imaging

Potentiometric dyes (Cohen and Salzberg 1978) can be used to measure neuronal membrane potentials including sub-threshold depolarizations both *in vitro* and *in vivo* (Orbach and Cohen 1983; Kleinfeld and Delaney 1996). For example, Petersen et al. (2003) imaged the propagation of sub-threshold depolarizations in the barrel cortex of rats in response to whisker deflections. Compared with calcium dyes, the most common method of imaging neuronal activity, potentiometric dyes are more sensitive to subthreshold activity and are faster. They can capture inhibitory events and do not change the intrinsic calcium buffering capacity of the cell (Peterka et al. 2011). However, potentiometric measurements are usually done with single-photon excitation wide-field imaging which, although having the speed to image the propagation of depolarizations, lack single cell resolution and the ability to record activity in deeper layers. Using 2PE excitation to image potentiometric dyes addresses the latter shortcoming and the 2PE absorption cross-sections of several voltage-sensitive dyes have been measured (Fisher et al. 2005). Kuhn et al. (2008) demonstrated that it is possible to monitor voltage changes in different cortical layers *in vivo* using

2PE. Additionally, single-cell resolution has also been achieved by combining genetically encoded voltage sensitive dyes with 2PE imaging (Akemann et al. 2013).

### 1.6.2 Calcium Imaging

Calcium imaging has emerged as a widely used method to monitor neuronal activity *in vivo* (Grienberger and Konnerth 2012). This is partially due to the ubiquitous role of calcium in intracellular signaling, but also because of the availability of very sensitive calcium dyes (Tsien 1980; Spence and Johnson 2010). These can easily be loaded into neurons either through intracellular injection or, in the case of membrane permeable dyes, by adding them to the extracellular space. More recently, the introduction of genetically-encoded calcium indicators (GECIs) (Miyawaki et al. 1997; Tian et al. 2012) combined with virus-based gene expression systems has enabled long-term recording of activity with cell-type specificity. Although initially inferior at detecting action potentials, when compared to small-molecule sensors, GECIs have come of age and currently perform equally well, or better than, their small-molecule counterparts (Chen et al. 2013).

Whereas excitation-light ratiometric dyes such as Fura-2 allow measurements of absolute calcium concentrations, generally this approach is not compatible with *in vivo* 2PE microscopy due to the broader spectrum of the excitation light pulses that 2PE microscopy uses. An alternative to measuring absolute calcium concentrations is to use the different fluorescence lifetimes of  $\text{Ca}^{2+}$ -bound and  $\text{Ca}^{2+}$ -unbound dyes (Lattarulo et al. 2011).

Although calcium imaging does not record signals from inhibitory synapses, these can be monitored with chloride imaging modalities, and several genetically encoded and small-molecule chloride sensors have been developed for this purpose. For a review and protocol see (Kovalchuk and Garaschuk 2012).

The first approaches to recording calcium transients using *in vivo* 2PE microscopy resorted to glass microelectrodes to inject indicator dyes intracellularly (Svoboda et al. 1997). This technique has some advantages, especially when used in conjunction with *in vivo* whole-cell recordings. The targeted staining of single neurons allows for efficient and sparse labeling. Single-cell loading approaches are useful for studying the spatio-temporal dynamics of intracellular calcium particularly single synapse activation patterns. In a remarkable series of experiments, Jia et al. (2010) used single cell loading to show that individual synapses in the visual cortex respond selectively and can be responsive to single visual stimulus orientation and that neighboring synapses can have different orientation selectivities.

One of the greatest advantages of optical recording techniques over electrode recordings is the ability to simultaneously record the activity of large numbers of cells. This is particularly important since understanding networks is essential for understanding brain function. Bulk loading of cells with calcium dyes *in vivo*

(Stosiek et al. 2003) allows for the staining of hundreds of cell bodies as well as neuropil. Somatic calcium imaging can detect action potentials with high reliability, whereas neuropil calcium signals are strongly correlated with incoming pre-synaptic activity and are highly correlated with local field potentials (Kerr et al. 2005). Therefore, given the current shortcomings of potentiometric dyes, somatic calcium signals are commonly used as a surrogate for action potential detection. Nevertheless, monitoring neuronal firing through calcium is technically challenging, mostly because the sampling rates of imaging techniques are generally much slower than the time-course of action potentials. Most laser scanning 2PE microscopes designed for *in vivo* imaging use a set of two galvanometric mirrors that usually scan a line no faster than 1 ms. A typical field of view containing ~100–120 cells at 20× magnification, results in a frame scanning rate of ~4 Hz. At this sampling rate, and depending on the imaging system used, ~40 % of single and ~80 % of doublet spikes are detected, as measured by simultaneous cell-attached recordings and calcium imaging (Kerr et al. 2005; Golshani et al. 2009). Not surprisingly, over the last few years much effort has focused on improving *in vivo* imaging techniques toward better spike detection, primarily through increasing sampling rates (Grewe and Helmchen 2009; Grienberger and Konnerth 2012).

## 1.7 Improving the Temporal Resolution of Two-Photon Intravital Imaging in the Brain

Some of the earliest approaches toward improving imaging speeds involved the optimization of scanning paths. For example, a simple approach is to scan a single one-dimensional line, instead of a 2-dimensional frame. Typically this allows recording from few cells (usually <10 at 20× magnification) with a ~1 kHz sampling rate. Extending this principle, an optimized scanning trajectory can be created which crosses several cells instead of scanning the whole field-view. When used in conjunction with piezo-electric focusing actuator, this approach has been used to scan 300+ cells in 3-D volumes of ~250 μm side length at 10 Hz sampling rate (Gobel et al. 2007). Scan-path optimization approaches limit data collection to the structures of interest by sampling only a few pixels per cell, but comes with a remarkable increase in sampling rate while conserving the same pixel dwell-time of full-frame approaches.

Other approaches to scanning large volumes in 3-D involve the use of electrically tunable lenses which enable rapid shift of focus and can be combined with most 2-D scanning methods (Grewe et al. 2011), or beam multiplexing, i.e. scanning the sample with several beams simultaneously. The latter approach has been applied to both single- and multi-plane imaging (Cheng et al. 2011), effectively enabling the recording of activity from different cortical layers simultaneously. Using a resonant scanning mirror and 4-beam multiplexing, single-frame rates of up to 250 Hz are achievable.

Finally, approaches that eliminate mechanical scanners are being used to improve scanning speeds. AODs are inertia-less, and therefore excel at random-access scanning, while also achieving much faster sequential scanning speeds. High speed calcium imaging with AOD-based systems has been reported to detect action potential timing with near millisecond precision (Grewe et al. 2010), which comes close to the performance of single-unit electrode recordings as a method to record neuronal firing.

New developments in imaging technologies have, therefore, dramatically increased acquisition speeds, with frame rates of more than 250 Hz becoming possible. However, due to the brightness and kinetics of calcium dyes, these high sampling rates usually result in oversampling and signal averaging is routinely performed. Whereas not all of the increases in speed directly translate to improvements in action potential detection, newer action potential detection algorithms are capable of determining spike timing and seem to perform optimally when signals are downsampled to 20–30 Hz (Grewe et al. 2010; Cheng et al. 2011).

## 1.8 Deep Tissue Imaging

Although multiphoton microscopy enables deep tissue imaging, in practice, *in vivo* microscopy within the brain has been mostly limited to the first ~600  $\mu\text{m}$  closest to the surface, which in the mouse brain does not span the entire depth of the cortex. This limit exists primarily because emitted fluorescence light, and to a lesser extent excitation light, is heavily scattered in deep tissue. Moreover, auto-fluorescence from more superficial layers eventually further degrades the signal-to-noise ratio (Oheim et al. 2001; Helmchen and Denk 2005). Several approaches have been used to image deeper structures, the simplest of which is removing superficial tissue surgically to expose and image deep lying features. This has been successfully demonstrated in the mouse hippocampus (Mizrahi et al. 2004) and thalamus (Marshall et al. 2012). A variation on this technique consists of implanting a gradient-index (GRIN) microlens into the brain (Jung and Schnitzer 2003). Combined with a miniaturized, head-mounted microscope/endoscope (Flusberg et al. 2008), this approach allows chronic imaging of deep-lying structures in freely moving mice.

Ideally however, one should be able to image deep brain areas with minimal tissue disruption. This is becoming possible through a combination of improvements in imaging technology. The first of these is the use of longer wavelength excitation which reduces the attenuation of excitation light and minimizes tissue absorption, thereby reducing background fluorescence. Optical Parametric Oscillators (OPO) can be combined with Ti:S lasers to extend tuning ranges to 1,300+ nm. Longer wavelength laser sources can then be used to excite red and far-red emitting fluorophores that have reduced scattering in the brain. Recently, as reviewed in Shcherbakova et al. (2012), several far-red fluorescent proteins have been developed specifically for deep tissue imaging. Using an OPO tuned to 1,280 nm, Kobat

et al. (2011) were able to image brain vasculature to a depth of 1.6 mm. A different approach by the same group used three-photon excitation to image hippocampal red fluorescent protein-labeled neurons at depths exceeding 1 mm (Horton et al. 2013). Yet another recent development in deep-tissue imaging involved using a picosecond pulsed 1,030 nm laser to image enhanced yellow fluorescent protein (EYFP)-labeled neurons in the mouse hippocampus at depths of up to 1.4 mm (Kawakami et al. 2013). In this case, the longer wavelength reduced the excitation light scattering while the longer pulse width made it less prone to group velocity dispersion. Finally, new advances in adaptive optics promise to improve both the resolution and signal-to-noise ratio of deep-tissue two-photon images. Using a new method for *in-vivo* wavefront-imaging, Ji et al. (2012) demonstrated that it is possible to compensate for optical aberrations with adaptive optics and obtain diffraction-limited images up to a depth of 450  $\mu\text{m}$  in the intact mouse brain. This approach resulted in a threefold increase in axial resolution and improved signals in calcium imaging experiments.

## 1.9 Optogenetics and Intravital 2PE Microscopy

The introduction of optogenetics into the field of neuroscience during the last decade is changing the way cortical circuits are studied now. This technology allows for the control of specific sets of excitable cells within complex tissues by using a combined genetic and optical approach that leaves the other cells in the tissue unaltered (Deisseroth 2011; Fenno et al. 2011; Yizhar et al. 2011). The introduction of microbial opsin (light-gated protein that acts as ion channels) genes into hippocampal neurons in culture and the subsequent control of neuronal spiking properties by high speed optical stimulation (Boyden et al. 2005) was the first demonstration of this technique in neurons. Since then multiple variations of these opsins with different functional and excitation properties were developed, being channelrhodopsin-2 (ChR2), halorhodopsin (HR), and archaerhodopsin-3 (Arch), the most commonly used (see Yizhar et al. 2011 for review). ChR2 is a cation channel with excitatory effects on the cells that express it when illuminated with blue light (Boyden et al. 2005); HR is a chloride pump that hyperpolarizes the cell upon 490 nm light activation (Zhang et al. 2007); Arch is a proton pump with inhibitory effects on the cell upon 566 nm light illumination. These optogenetic tools have been used extensively to map motor (Harrison et al. 2012; Silasi et al. 2013), somatosensory (Petreanu et al. 2007; Huber et al. 2008), and many more cortical and subcortical (Desai et al. 2011; Poulet et al. 2012) brain areas. However, simultaneous intravital 2PE imaging of neuronal activity and optogenetic stimulation is still a work in progress, and more suitable calcium indicators with excitation spectra which do not overlap the action spectra of ChR2, HR, and Arch are desirable. In this sense, RCaMP, a red-shifted GECI (based on the fluorescent protein mRuby) has been engineered recently which allows simultaneous optogenetic stimulation of ChR2 and imaging of calcium transients *in vivo* in *Caenorhabditis elegans* (Fig. 1.5) (Akerboom et al. 2013).

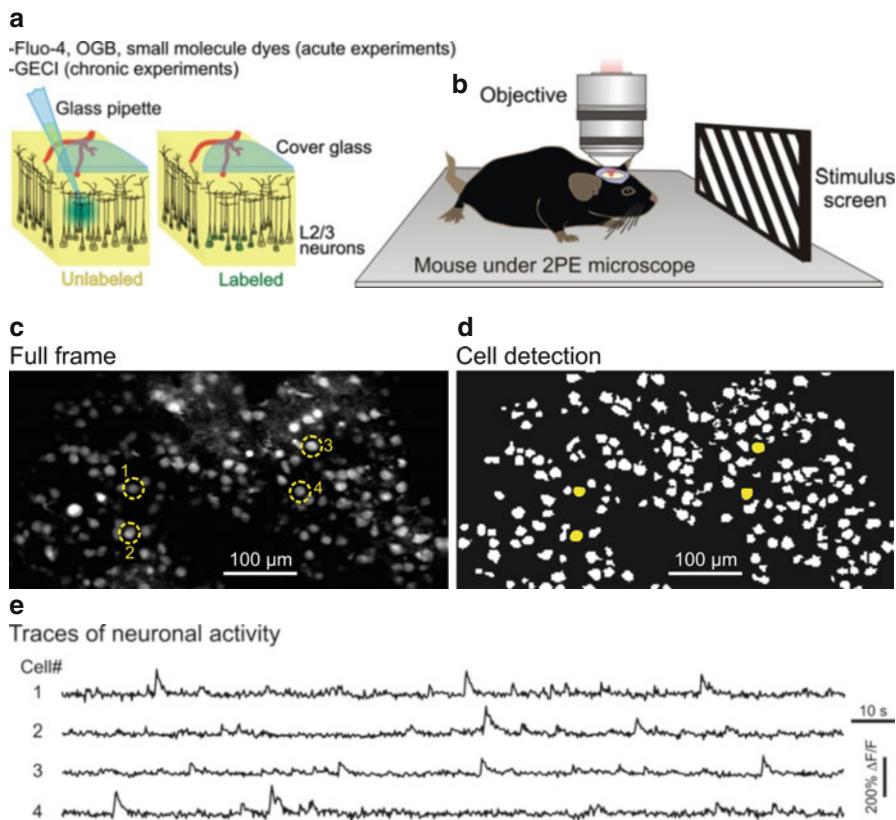


**Fig. 1.5** Intravital 2PE imaging of neuronal activity in the cerebral cortex in mice. (a) Neurons are labeled with a calcium indicator dye through a craniotomy. Small molecule dyes or viral vectors encoding GECIs can be injected with a glass micropipette through a craniotomy, which is then covered with a glass “window”. (b) The mouse is transferred to a 2PE microscope and imaged either under anesthesia or awake conditions. For the latter, treadmills are commonly used and can be combined with virtual-reality environments and head-fixed behavioral tasks. Another common modality is imaging sensory stimulus-evoked activity, for example, a visual stimulus displayed on a screen. (c–e) Typical field of view of OGB1 stained cortical layer 2/3 neurons. Analysis software can segment the image into several regions of interest (circles in c and yellow dots in d, and e) extract fluorescence changes ( $\Delta F/F$ ) of cells 1–4 in (e)

## References

- Akemmann W, Sasaki M, Mutoh H, Imamura T, Honkura N, Knopfel T (2013) Two-photon voltage imaging using a genetically encoded voltage indicator. *Sci Rep* 3:2231. doi:[10.1038/srep02231](https://doi.org/10.1038/srep02231)
- Akerboom J, Carreras Calderón N, Tian L, Wabnig S, Prigge M, Toló J, Gordus A, Orger M, Severi K, Macklin J, Patel R, Pulver S, Wardill T, Fischer E, Schüller C, Chen T-W, Sarkisyan K, Marvin J, Bargmann C, Kim D, Kügler S, Lagnado L, Hegemann P, Gottschalk A, Schreiter E, Looger L (2013) Genetically encoded calcium indicators for multi-color neural activity imaging and combination with optogenetics. *Front Mol Neurosci* 6:2. doi:[10.3389/fnmol.2013.00002](https://doi.org/10.3389/fnmol.2013.00002)



- Bardehle S, Krüger M, Buggenthin F, Schwausch J, Ninkovic J, Clevers H, Snippert H, Theis F, Meyer-Luehmann M, Bechmann I, Dimou L, Götz M (2013) Live imaging of astrocyte responses to acute injury reveals selective juxtavascular proliferation. *Nat Neurosci* 16(5):580–586. doi:[10.1038/nn.3371](https://doi.org/10.1038/nn.3371)
- Blinder P, Shih A, Rafie C, Kleinfeld D (2010) Topological basis for the robust distribution of blood to rodent neocortex. *Proc Natl Acad Sci U S A* 107(28):12670–12675. doi:[10.1073/pnas.1007239107](https://doi.org/10.1073/pnas.1007239107)
- Blinder P, Tsai P, Kaufhold J, Knutsen P, Suhl H, Kleinfeld D (2013) The cortical angiome: an interconnected vascular network with noncolumnar patterns of blood flow. *Nat Neurosci* 16(7):889–897. doi:[10.1038/nn.3426](https://doi.org/10.1038/nn.3426)
- Boyden E, Zhang F, Bamberg E, Nagel G, Deisseroth K (2005) Millisecond-timescale, genetically targeted optical control of neural activity. *Nat Neurosci* 8(9):1263–1268. doi:[10.1038/nn1525](https://doi.org/10.1038/nn1525)
- Brown C, Li P, Boyd J, Delaney K, Murphy T (2007) Extensive turnover of dendritic spines and vascular remodeling in cortical tissues recovering from stroke. *J Neurosci* 27(15):4101–4110. doi:[10.1523/jneurosci.4295-06.2007](https://doi.org/10.1523/jneurosci.4295-06.2007)
- Cai D, Cohen K, Luo T, Lichtman J, Sanes J (2013) Improved tools for the Brainbow toolbox. *Nat Methods* 10(6):540–547. doi:[10.1038/nmeth.2450](https://doi.org/10.1038/nmeth.2450)
- Chalfie M, Tu Y, Euskirchen G, Ward W, Prasher D (1994) Green fluorescent protein as a marker for gene expression. *Science (New York, NY)* 263(5148):802–805. doi:[10.1126/science.8303295](https://doi.org/10.1126/science.8303295)
- Chen J, Nedivi E (2013) Highly specific structural plasticity of inhibitory circuits in the adult neocortex. *Neuroscientist* 19(4):384–393. doi:[10.1177/1073858413479824](https://doi.org/10.1177/1073858413479824)
- Chen J, Flanders G, Lee W-CA, Lin W, Nedivi E (2011) Inhibitory dendrite dynamics as a general feature of the adult cortical microcircuit. *J Neurosci* 31(35):12437–12443. doi:[10.1523/JNEUROSCI.0420-11.2011](https://doi.org/10.1523/JNEUROSCI.0420-11.2011)
- Chen Q, Cichon J, Wang W, Qiu L, Lee S-JR, Campbell N, Destefino N, Goard M, Fu Z, Yasuda R, Looger L, Arenkiel B, Gan W-B, Feng G (2012) Imaging neural activity using Thy1-GCaMP transgenic mice. *Neuron* 76(2):297–308. doi:[10.1016/j.neuron.2012.07.011](https://doi.org/10.1016/j.neuron.2012.07.011)
- Chen TW, Wardill TJ, Sun Y, Pulver SR, Renninger SL, Baohan A, Schreier ER, Kerr RA, Orger MB, Jayaraman V, Looger LL, Svoboda K, Kim DS (2013) Ultrasensitive fluorescent proteins for imaging neuronal activity. *Nature* 499(7458):295–300. doi:[10.1038/nature12354](https://doi.org/10.1038/nature12354)
- Cheng A, Gonçalves JT, Golshani P, Arisaka K, Portera-Cailliau C (2011) Simultaneous two-photon calcium imaging at different depths with spatiotemporal multiplexing. *Nat Methods* 8(2):139–142. doi:[10.1038/nmeth.1552](https://doi.org/10.1038/nmeth.1552)
- Chow D, Groszer M, Pribadi M, Machnicki M, Carmichael S, Liu X, Trachtenberg J (2009) Laminar and compartmental regulation of dendritic growth in mature cortex. *Nat Neurosci* 12(2):116–124. doi:[10.1038/nn.2255](https://doi.org/10.1038/nn.2255)
- Cohen LB, Salzberg BM (1978) Optical measurement of membrane potential. *Rev Physiol Biochem Pharmacol* 83:35–88
- Cruz-Martin A, Crespo M, Portera-Cailliau C (2010) Delayed stabilization of dendritic spines in fragile X mice. *J Neurosci* 30(23):7793–8596. doi:[10.1523/jneurosci.0577-10.2010](https://doi.org/10.1523/jneurosci.0577-10.2010)
- De Roo M, Klausner P, Muller D (2008) LTP promotes a selective long-term stabilization and clustering of dendritic spines. *PLoS Biol* 6(9):e219. doi:[10.1371/journal.pbio.0060219](https://doi.org/10.1371/journal.pbio.0060219)
- Deisseroth K (2011) Optogenetics. *Nat Methods* 8(1):26–29. doi:[10.1038/nmeth.f.324](https://doi.org/10.1038/nmeth.f.324)
- Denk W (1994) Two-photon scanning photochemical microscopy: mapping ligand-gated ion channel distributions. *Proc Natl Acad Sci U S A* 91(14):6629–6633. doi:[10.1073/pnas.91.14.6629](https://doi.org/10.1073/pnas.91.14.6629)
- Denk W, Strickler J, Webb W (1990) Two-photon laser scanning fluorescence microscopy. *Science (New York, NY)* 248(4951):73–76. doi:[10.1126/science.2321027](https://doi.org/10.1126/science.2321027)
- Desai M, Kahn I, Knoblich U, Bernstein J, Atallah H, Yang A, Kopell N, Buckner R, Graybiel A, Moore C, Boyden E (2011) Mapping brain networks in awake mice using combined optical neural control and fMRI. *J Neurophysiol* 105(3):1393–1405. doi:[10.1152/jn.00828.2010](https://doi.org/10.1152/jn.00828.2010)
- Dittgen T, Nimmerjahn A, Komai S, Licznarski P, Waters J, Margrie T, Helmchen F, Denk W, Brecht M, Osten P (2004) Lentivirus-based genetic manipulations of cortical neurons and their optical and electrophysiological monitoring in vivo. *Proc Natl Acad Sci U S A* 101(52):18206–18211. doi:[10.1073/pnas.0407976101](https://doi.org/10.1073/pnas.0407976101)

- Dixit R, Lu F, Cantrup R, Gruenig N, Langevin L, Kurrasch D, Schuurmans C (2011) Efficient gene delivery into multiple CNS territories using in utero electroporation. *J Vis Exp* (52). doi:[10.3791/2957](https://doi.org/10.3791/2957)
- Dong J, Revilla-Sanchez R, Moss S, Haydon P (2010) Multiphoton in vivo imaging of amyloid in animal models of Alzheimer's disease. *Neuropharmacology* 59(4–5):268–275. doi:[10.1016/j.neuropharm.2010.04.007](https://doi.org/10.1016/j.neuropharm.2010.04.007)
- Drew P, Shih A, Driscoll J, Knutsen P, Blinder P, Davalos D, Akassoglou K, Tsai P, Kleinfeld D (2010) Chronic optical access through a polished and reinforced thinned skull. *Nat Methods* 7(12):981–984. doi:[10.1038/nmeth.1530](https://doi.org/10.1038/nmeth.1530)
- Drew P, Shih A, Kleinfeld D (2011) Fluctuating and sensory-induced vasodynamics in rodent cortex extend arteriole capacity. *Proc Natl Acad Sci U S A* 108(20):8473–8478. doi:[10.1073/pnas.1100428108](https://doi.org/10.1073/pnas.1100428108)
- Farrar M, Bernstein I, Schlafer D, Cleland T, Fetcho J, Schaffer C (2012) Chronic in vivo imaging in the mouse spinal cord using an implanted chamber. *Nat Methods* 9(3):297–302. doi:[10.1038/nmeth.1856](https://doi.org/10.1038/nmeth.1856)
- Feng G, Mellor R, Bernstein M, Keller-Peck C, Nguyen Q, Wallace M, Nerbonne J, Lichtman J, Sanes J (2000) Imaging neuronal subsets in transgenic mice expressing multiple spectral variants of GFP. *Neuron* 28(1):41–92
- Fenno L, Yizhar O, Deisseroth K (2011) The development and application of optogenetics. *Annu Rev Neurosci* 34:389–412. doi:[10.1146/annurev-neuro-061010-113817](https://doi.org/10.1146/annurev-neuro-061010-113817)
- Fenrich K, Weber P, Hocine M, Zalc M, Rougon G, Debarbieux F (2012) Long-term in vivo imaging of normal and pathological mouse spinal cord with subcellular resolution using implanted glass windows. *J Physiol* 590(Pt 16):3665–3675. doi:[10.1113/jphysiol.2012.230532](https://doi.org/10.1113/jphysiol.2012.230532)
- Fisher JA, Salzberg BM, Yodh AG (2005) Near infrared two-photon excitation cross-sections of voltage-sensitive dyes. *J Neurosci Methods* 148(1):94–102. doi:[10.1016/j.jneumeth.2005.06.027](https://doi.org/10.1016/j.jneumeth.2005.06.027)
- Flusberg B, Nimmerjahn A, Cocker E, Mukamel E, Barretto R, Ko T, Burns L, Jung J, Schnitzer M (2008) High-speed, miniaturized fluorescence microscopy in freely moving mice. *Nat Methods* 5(11):935–943. doi:[10.1038/nmeth.1256](https://doi.org/10.1038/nmeth.1256)
- Fu M, Yu X, Lu J, Zuo Y (2012) Repetitive motor learning induces coordinated formation of clustered dendritic spines in vivo. *Nature* 483(7387):92–97. doi:[10.1038/nature10844](https://doi.org/10.1038/nature10844)
- Ghiran I (2011) Introduction to fluorescence microscopy. *Methods Mol Biol* (Clifton, NJ) 689:93–136. doi:[10.1007/978-1-60761-950-5\\_7](https://doi.org/10.1007/978-1-60761-950-5_7)
- Gobel W, Kampa BM, Helmchen F (2007) Imaging cellular network dynamics in three dimensions using fast 3D laser scanning. *Nat Methods* 4(1):73–79. doi:[10.1038/nmeth989](https://doi.org/10.1038/nmeth989)
- Golshani P, Portera-Cailliau C (2008) In vivo 2-photon calcium imaging in layer 2/3 of mice. *J Vis Exp* (13). doi:[10.3791/681](https://doi.org/10.3791/681)
- Golshani P, Gonçalves J, Khoshkhoo S, Mostany R, Smirnakis S, Portera-Cailliau C (2009) Internally mediated developmental desynchronization of neocortical network activity. *J Neurosci* 29(35):10890–10899. doi:[10.1523/jneurosci.2012-09.2009](https://doi.org/10.1523/jneurosci.2012-09.2009)
- Gonçalves J, Anstey J, Golshani P, Portera-Cailliau C (2013) Circuit level defects in the developing neocortex of Fragile X mice. *Nat Neurosci* 16(7):903–909. doi:[10.1038/nn.3415](https://doi.org/10.1038/nn.3415)
- Grewe BF, Helmchen F (2009) Optical probing of neuronal ensemble activity. *Curr Opin Neurobiol* 19(5):520–529. doi:[10.1016/j.conb.2009.09.003](https://doi.org/10.1016/j.conb.2009.09.003)
- Grewe BF, Langer D, Kasper H, Kampa BM, Helmchen F (2010) High-speed in vivo calcium imaging reveals neuronal network activity with near-millisecond precision. *Nat Methods* 7(5):399–405
- Grewe BF, Voigt FF, Van't Hoff M, Helmchen F (2011) Fast two-layer two-photon imaging of neuronal cell populations using an electrically tunable lens. *Biomed Opt Express* 2(7):2035–2046
- Grienberger C, Konnerth A (2012) Imaging calcium in neurons. *Neuron* 73(5):862–885. doi:[10.1016/j.neuron.2012.02.011](https://doi.org/10.1016/j.neuron.2012.02.011)
- Grutzendler J, Kasthuri N, Gan W-B (2002) Long-term dendritic spine stability in the adult cortex. *Nature* 420(6917):812–818. doi:[10.1038/nature01276](https://doi.org/10.1038/nature01276)
- Guo D, Arnsperger S, Rensing N, Wong M (2012) Brief seizures cause dendritic injury. *Neurobiol Dis* 45(1):348–355. doi:[10.1016/j.nbd.2011.08.020](https://doi.org/10.1016/j.nbd.2011.08.020)



- Harrison T, Ayling O, Murphy T (2012) Distinct cortical circuit mechanisms for complex fore-limb movement and motor map topography. *Neuron* 74(2):397–409. doi:[10.1016/j.neuron.2012.02.028](https://doi.org/10.1016/j.neuron.2012.02.028)
- Harvey C, Svoboda K (2007) Locally dynamic synaptic learning rules in pyramidal neuron dendrites. *Nature* 450(7173):1195–1200. doi:[10.1038/nature06416](https://doi.org/10.1038/nature06416)
- Helmchen F, Denk W (2005) Deep tissue two-photon microscopy. *Nat Methods* 2(12):932–972. doi:[10.1038/nmeth818](https://doi.org/10.1038/nmeth818)
- Holtmaat A, Svoboda K (2009) Experience-dependent structural synaptic plasticity in the mammalian brain. *Nat Rev Neurosci* 10(9):647–705. doi:[10.1038/nrn2699](https://doi.org/10.1038/nrn2699)
- Holtmaat A, Trachtenberg J, Wilbrecht L, Shepherd G, Zhang X, Knott G, Svoboda K (2005) Transient and persistent dendritic spines in the neocortex in vivo. *Neuron* 45(2):279–370. doi:[10.1016/j.neuron.2005.01.003](https://doi.org/10.1016/j.neuron.2005.01.003)
- Holtmaat A, Wilbrecht L, Knott G, Welker E, Svoboda K (2006) Experience-dependent and cell-type-specific spine growth in the neocortex. *Nature* 441(7096):979–1062. doi:[10.1038/nature04783](https://doi.org/10.1038/nature04783)
- Holtmaat A, Bonhoeffer T, Chow D, Chuckowree J, De Paola V, Hofer S, Hübener M, Keck T, Knott G, Lee W-CA, Mostany R, Mrsic-Flogel T, Nedivi E, Portera-Cailliau C, Svoboda K, Trachtenberg J, Wilbrecht L (2009) Long-term, high-resolution imaging in the mouse neocortex through a chronic cranial window. *Nat Protoc* 4(8):1128–1172. doi:[10.1038/nprot.2009.89](https://doi.org/10.1038/nprot.2009.89)
- Horton NG, Wang K, Kobat D, Clark CG, Wise FW, Schaffer CB, Xu C (2013) In vivo three-photon microscopy of subcortical structures within an intact mouse brain. *Nat Photonics* 7(3):205–209. doi:[10.1038/Nphoton.2012.336](https://doi.org/10.1038/Nphoton.2012.336)
- Huber D, Petreanu L, Ghitani N, Ranade S, Hromádka T, Mainen Z, Svoboda K (2008) Sparse optical microstimulation in barrel cortex drives learned behaviour in freely moving mice. *Nature* 451(7174):61–64. doi:[10.1038/nature06445](https://doi.org/10.1038/nature06445)
- Hughes E, Kang S, Fukaya M, Bergles D (2013) Oligodendrocyte progenitors balance growth with self-repulsion to achieve homeostasis in the adult brain. *Nat Neurosci* 16(6):668–676. doi:[10.1038/nn.3390](https://doi.org/10.1038/nn.3390)
- Ji N, Sato TR, Betzig E (2012) Characterization and adaptive optical correction of aberrations during in vivo imaging in the mouse cortex. *Proc Natl Acad Sci U S A* 109(1):22–27. doi:[10.1073/pnas.1109202108](https://doi.org/10.1073/pnas.1109202108)
- Jia H, Rochefort NL, Chen X, Konnerth A (2010) Dendritic organization of sensory input to cortical neurons in vivo. *Nature* 464(7293):1307–1312. doi:[10.1038/nature08947](https://doi.org/10.1038/nature08947)
- Judkewitz B, Rizzi M, Kitamura K, Häusser M (2009) Targeted single-cell electroporation of mammalian neurons in vivo. *Nat Protoc* 4(6):862–869. doi:[10.1038/nprot.2009.56](https://doi.org/10.1038/nprot.2009.56)
- Jung JC, Schnitzer MJ (2003) Multiphoton endoscopy. *Opt Lett* 28(11):902–904
- Kawakami R, Sawada K, Sato A, Hibi T, Kozawa Y, Sato S, Yokoyama H, Nemoto T (2013) Visualizing hippocampal neurons with in vivo two-photon microscopy using a 1030 nm picosecond pulse laser. *Sci Rep* 3:1014. doi:[10.1038/Srep01014](https://doi.org/10.1038/Srep01014)
- Keck T, Mrsic-Flogel T, Vaz Afonso M, Eysel U, Bonhoeffer T, Hübener M (2008) Massive restructuring of neuronal circuits during functional reorganization of adult visual cortex. *Nat Neurosci* 11(10):1162–1169. doi:[10.1038/nn.2181](https://doi.org/10.1038/nn.2181)
- Kelly E, Majewska A (2010) Chronic imaging of mouse visual cortex using a thinned-skull preparation. *Journal of visualized experiments*. *J Vis Exp* (44). doi:[10.3791/2060](https://doi.org/10.3791/2060)
- Kerr JN, Greenberg D, Helmchen F (2005) Imaging input and output of neocortical networks in vivo. *Proc Natl Acad Sci U S A* 102(39):14063–14068. doi:[10.1073/pnas.0506029102](https://doi.org/10.1073/pnas.0506029102)
- Kerschensteiner M, Schwab M, Lichtman J, Misgeld T (2005) In vivo imaging of axonal degeneration and regeneration in the injured spinal cord. *Nat Med* 11(5):572–577. doi:[10.1038/nm1229](https://doi.org/10.1038/nm1229)
- Kim J, Jiang N, Tadokoro C, Liu L, Ransohoff R, Lafaille J, Dustin M (2010) Two-photon laser scanning microscopy imaging of intact spinal cord and cerebral cortex reveals requirement for CXCR6 and neuroinflammation in immune cell infiltration of cortical injury sites. *J Immunol Methods* 352(1–2):89–100. doi:[10.1016/j.jim.2009.09.007](https://doi.org/10.1016/j.jim.2009.09.007)

- Kleinfeld D, Delaney KR (1996) Distributed representation of vibrissa movement in the upper layers of somatosensory cortex revealed with voltage-sensitive dyes. *J Comp Neurol* 375(1): 89–108. doi:[10.1002/\(SICI\)1096-9861\(19961104\)375:1<89::AID-CNE6>3.0.CO;2-K](https://doi.org/10.1002/(SICI)1096-9861(19961104)375:1<89::AID-CNE6>3.0.CO;2-K)
- Kleinfeld D, Mitra P, Helmchen F, Denk W (1998) Fluctuations and stimulus-induced changes in blood flow observed in individual capillaries in layers 2 through 4 of rat neocortex. *Proc Natl Acad Sci U S A* 95(26):15741–15747
- Kobat D, Horton N, Xu C (2011) In vivo two-photon microscopy to 1.6-mm depth in mouse cortex. *J Biomed Opt* 16(10):106014
- Kovalchuk Y, Garaschuk O (2012) Two-photon chloride imaging using MQAE in vitro and in vivo. *Cold Spring Harb Protoc* 2012(7):778–785. doi:[10.1101/pdb.prot070037](https://doi.org/10.1101/pdb.prot070037)
- Kuhn B, Denk W, Bruno RM (2008) In vivo two-photon voltage-sensitive dye imaging reveals top-down control of cortical layers 1 and 2 during wakefulness. *Proc Natl Acad Sci U S A* 105(21):7588–7593. doi:[10.1073/pnas.0802462105](https://doi.org/10.1073/pnas.0802462105)
- Lai C, Franke T, Gan W-B (2012) Opposite effects of fear conditioning and extinction on dendritic spine remodelling. *Nature* 483(7387):87–91. doi:[10.1038/nature10792](https://doi.org/10.1038/nature10792)
- Lakowicz JR (2010) Principles of fluorescence spectroscopy, 3rd edn. Springer, New York
- Lattarulo C, Thyssen D, Kuchibholta K, Hyman B, Bacskai B (2011) Microscopic imaging of intracellular calcium in live cells using lifetime-based ratiometric measurements of Oregon Green BAPTA-1. *Methods Mol Biol* (Clifton, NJ) 793:377–389. doi:[10.1007/978-1-61779-328-8\\_25](https://doi.org/10.1007/978-1-61779-328-8_25)
- Lendvai B, Stern E, Chen B, Svoboda K (2000) Experience-dependent plasticity of dendritic spines in the developing rat barrel cortex in vivo. *Nature* 404(6780):876–881. doi:[10.1038/35009107](https://doi.org/10.1038/35009107)
- Livet J, Weissman T, Kang H, Draft R, Lu J, Bennis R, Sanes J, Lichtman J (2007) Transgenic strategies for combinatorial expression of fluorescent proteins in the nervous system. *Nature* 450(7166):56–62. doi:[10.1038/nature06293](https://doi.org/10.1038/nature06293)
- Majewska A, Yiu G, Yuste R (2000) A custom-made two-photon microscope and deconvolution system. *Pflugers Arch* 441(2–3):398–408. doi:[10.1007/s004240000435](https://doi.org/10.1007/s004240000435)
- Majewska A, Newton J, Sur M (2006) Remodeling of synaptic structure in sensory cortical areas in vivo. *J Neurosci* 26(11):3021–3029. doi:[10.1523/JNEUROSCI.4454-05.2006](https://doi.org/10.1523/JNEUROSCI.4454-05.2006)
- Marshall JH, Kaye AP, Nauhaus I, Callaway EM (2012) Anterior-posterior direction opponency in the superficial mouse lateral geniculate nucleus. *Neuron* 76(4):713–720. doi:[10.1016/J.Neuron.2012.09.021](https://doi.org/10.1016/J.Neuron.2012.09.021)
- Miyawaki A, Llopis J, Heim R, McCaffery JM, Adams JA, Ikura M, Tsien RY (1997) Fluorescent indicators for Ca<sup>2+</sup> based on green fluorescent proteins and calmodulin. *Nature* 388(6645):882–887. doi:[10.1038/42264](https://doi.org/10.1038/42264)
- Mizrahi A, Katz L (2003) Dendritic stability in the adult olfactory bulb. *Nat Neurosci* 6(11):1201–1207. doi:[10.1038/nn1133](https://doi.org/10.1038/nn1133)
- Mizrahi A, Crowley JC, Shtoyerman E, Katz LC (2004) High-resolution in vivo imaging of hippocampal dendrites and spines. *J Neurosci* 24(13):3147–3151. doi:[10.1523/Jneurosci.5218-03.2004](https://doi.org/10.1523/Jneurosci.5218-03.2004)
- Mostany R, Portera-Cailliau C (2008a) A craniotomy surgery procedure for chronic brain imaging. *Journal of visualized experiments. J Vis Exp* (12). doi:[10.3791/680](https://doi.org/10.3791/680)
- Mostany R, Portera-Cailliau C (2008b) A method for 2-photon imaging of blood flow in the neocortex through a cranial window. *Journal of visualized experiments. J Vis Exp* (12). doi:[10.3791/678](https://doi.org/10.3791/678)
- Mostany R, Portera-Cailliau C (2011) Absence of large-scale dendritic plasticity of layer 5 pyramidal neurons in peri-infarct cortex. *J Neurosci* 31(5):1734–1742. doi:[10.1523/jneurosci.4386-10.2011](https://doi.org/10.1523/jneurosci.4386-10.2011)
- Mostany R, Chowdhury T, Johnston D, Portonovo S, Carmichael S, Portera-Cailliau C (2010) Local hemodynamics dictate long-term dendritic plasticity in peri-infarct cortex. *J Neurosci* 30(42):14116–14142. doi:[10.1523/jneurosci.3908-10.2010](https://doi.org/10.1523/jneurosci.3908-10.2010)
- Mostany R, Anstey J, Crump K, Maco B, Knott G, Portera-Cailliau C (2013) Altered synaptic dynamics during normal brain aging. *J Neurosci* 33(9):4094–4104. doi:[10.1523/JNEUROSCI.4825-12.2013](https://doi.org/10.1523/JNEUROSCI.4825-12.2013)

- Nikolenko V, Nemet B, Yuste R (2003) A two-photon and second-harmonic microscope. *Methods* (San Diego, Calif) 30(1):3–18
- Nimchinsky E, Sabatini B, Svoboda K (2002) Structure and function of dendritic spines. *Annu Rev Physiol* 64:313–353. doi:[10.1146/annurev.physiol.64.081501.160008](https://doi.org/10.1146/annurev.physiol.64.081501.160008)
- Nimmerjahn A, Kirchhoff F, Helmchen F (2005) Resting microglial cells are highly dynamic surveillants of brain parenchyma in vivo. *Science* (New York, NY) 308(5726):1314–1318. doi:[10.1126/science.1110647](https://doi.org/10.1126/science.1110647)
- Nishimura N, Schaffer C, Friedman B, Tsai P, Lyden P, Kleinfeld D (2006) Targeted insult to sub-surface cortical blood vessels using ultrashort laser pulses: three models of stroke. *Nat Methods* 3(2):99–207. doi:[10.1038/nmeth844](https://doi.org/10.1038/nmeth844)
- Oheim M, Beaupaire E, Chaigneau E, Mertz J, Charpak S (2001) Two-photon microscopy in brain tissue: parameters influencing the imaging depth. *J Neurosci Methods* 111(1):29–37
- Orbach HS, Cohen LB (1983) Optical monitoring of activity from many areas of the in vitro and in vivo salamander olfactory bulb: a new method for studying functional organization in the vertebrate central nervous system. *J Neurosci* 3(11):2251–2262
- Peterka DS, Takahashi H, Yuste R (2011) Imaging voltage in neurons. *Neuron* 69(1):9–21. doi:[10.1016/j.neuron.2010.12.010](https://doi.org/10.1016/j.neuron.2010.12.010)
- Petersen C, Grinvald A, Sakmann B (2003) Spatiotemporal dynamics of sensory responses in layer 2/3 of rat barrel cortex measured in vivo by voltage-sensitive dye imaging combined with whole-cell voltage recordings and neuron reconstructions. *J Neurosci* 23(4):1298–1607
- Petreaun L, Huber D, Sobczyk A, Svoboda K (2007) Channelrhodopsin-2-assisted circuit mapping of long-range callosal projections. *Nat Neurosci* 10(5):663–668. doi:[10.1038/nn1891](https://doi.org/10.1038/nn1891)
- Potter SM (2000) Two-photon microscopy for 4D imaging of living neurons. In: Yuste R, Lanni F, Konnerth A (eds) *Imaging neurons: a laboratory manual*, 1st edn. Cold Spring Harbor Laboratory Press, Cold Spring Harbor, pp 20.21–20.16
- Poulet J, Fernandez L, Crochet S, Petersen C (2012) Thalamic control of cortical states. *Nat Neurosci* 15(3):370–372. doi:[10.1038/nn.3035](https://doi.org/10.1038/nn.3035)
- Rensing N, Ouyang Y, Yang X-F, Yamada K, Rothman S, Wong M (2005) In vivo imaging of dendritic spines during electrographic seizures. *Ann Neurol* 58(6):888–898. doi:[10.1002/ana.20658](https://doi.org/10.1002/ana.20658)
- Saito T, Nakatsuji N (2001) Efficient gene transfer into the embryonic mouse brain using in vivo electroporation. *Dev Biol* 240(1):237–246. doi:[10.1006/dbio.2001.0439](https://doi.org/10.1006/dbio.2001.0439)
- Sato T, Muroyama Y, Saito T (2013) Inducible gene expression in postmitotic neurons by an in vivo electroporation-based tetracycline system. *J Neurosci* 214(2):170–176. doi:[10.1016/j.jneumeth.2013.01.014](https://doi.org/10.1016/j.jneumeth.2013.01.014)
- Schaffer C, Friedman B, Nishimura N, Schroeder L, Tsai P, Ebner F, Lyden P, Kleinfeld D (2006) Two-photon imaging of cortical surface microvessels reveals a robust redistribution in blood flow after vascular occlusion. *PLoS Biol* 4(2):e22. doi:[10.1371/journal.pbio.0040022](https://doi.org/10.1371/journal.pbio.0040022)
- Shcherbakova DM, Subach OM, Verkhusa VV (2012) Red fluorescent proteins: advanced imaging applications and future design. *Angew Chem Int Ed Engl* 51(43):10724–10738. doi:[10.1002/anie.201200408](https://doi.org/10.1002/anie.201200408)
- Shih A, Friedman B, Drew P, Tsai P, Lyden P, Kleinfeld D (2009) Active dilation of penetrating arterioles restores red blood cell flux to penumbral neocortex after focal stroke. *J Cereb Blood Flow Metab* 29(4):738–789. doi:[10.1038/jcbfm.2008.166](https://doi.org/10.1038/jcbfm.2008.166)
- Shih A, Driscoll J, Drew P, Nishimura N, Schaffer C, Kleinfeld D (2012a) Two-photon microscopy as a tool to study blood flow and neurovascular coupling in the rodent brain. *J Cereb Blood Flow Metab* 32(7):1277–1309. doi:[10.1038/jcbfm.2011.196](https://doi.org/10.1038/jcbfm.2011.196)
- Shih A, Mateo C, Drew P, Tsai P, Kleinfeld D (2012b) A polished and reinforced thinned-skull window for long-term imaging of the mouse brain. *J Vis Exp* (61). doi:[10.3791/3742](https://doi.org/10.3791/3742)
- Shimomura O, Johnson F, Saiga Y (1962) Extraction, purification and properties of aequorin, a bioluminescent protein from the luminous hydromedusa, Aequorea. *J Cell Comp Physiol* 59:223–239. doi:[10.1002/jcp.1030590302](https://doi.org/10.1002/jcp.1030590302)
- Silasi G, Boyd J, Ledue J, Murphy T (2013) Improved methods for chronic light-based motor mapping in mice: automated movement tracking with accelerometers, and chronic EEG recording in a bilateral thin-skull preparation. *Front Neural Circuits* 7:123. doi:[10.3389/fncir.2013.00123](https://doi.org/10.3389/fncir.2013.00123)

- Spence MTZ, Johnson ID (2010) The molecular probes handbook: a guide to fluorescent probes and labeling technologies, 11th edn. Live Technologies Corporation, Carlsbad
- Spires-Jones T, Meyer-Luehmann M, Osetek J, Jones P, Stern E, Bacskai B, Hyman B (2007) Impaired spine stability underlies plaque-related spine loss in an Alzheimer's disease mouse model. *Am J Pathol* 171(4):1304–1315. doi:[10.2353/ajpath.2007.070055](https://doi.org/10.2353/ajpath.2007.070055)
- Stettler D, Yamahachi H, Li W, Denk W, Gilbert C (2006) Axons and synaptic boutons are highly dynamic in adult visual cortex. *Neuron* 49(6):877–887. doi:[10.1016/j.neuron.2006.02.018](https://doi.org/10.1016/j.neuron.2006.02.018)
- Stosiek C, Garaschuk O, Holthoff K, Konnerth A (2003) In vivo two-photon calcium imaging of neuronal networks. *Proc Natl Acad Sci U S A* 100(12):7319–7343. doi:[10.1073/pnas.1232232100](https://doi.org/10.1073/pnas.1232232100)
- Svoboda K, Denk W, Kleinfeld D, Tank D (1997) In vivo dendritic calcium dynamics in neocortical pyramidal neurons. *Nature* 385(6612):161–165. doi:[10.1038/385161a0](https://doi.org/10.1038/385161a0)
- Sword J, Masuda T, Croom D, Kirov S (2013) Evolution of neuronal and astroglial disruption in the peri-contusional cortex of mice revealed by in vivo two-photon imaging. *Brain* 136(Pt 5):1446–1461. doi:[10.1093/brain/awt026](https://doi.org/10.1093/brain/awt026)
- Tian L, Hires SA, Looger LL (2012) Imaging neuronal activity with genetically encoded calcium indicators. *Cold Spring Harb Protoc* 2012(6):647–656. doi:[10.1101/pdb.top069609](https://doi.org/10.1101/pdb.top069609)
- Trachtenberg J, Chen B, Knott G, Feng G, Sanes J, Welker E, Svoboda K (2002) Long-term in vivo imaging of experience-dependent synaptic plasticity in adult cortex. *Nature* 420(6917):788–882. doi:[10.1038/nature01273](https://doi.org/10.1038/nature01273)
- Tsai PS, Kleinfeld D (2009) In vivo two-photon laser scanning microscopy with concurrent plasma-mediated ablation: principles and hardware realization. In: Frostig RD (ed) *In vivo optical imaging of brain function*, 2nd edn. CRC Press, Boca Raton, pp 59–115
- Tsien RY (1980) New calcium indicators and buffers with high selectivity against magnesium and protons: design, synthesis, and properties of prototype structures. *Biochemistry* 19(11):2396–2404
- Tsien R (1998) The green fluorescent protein. *Annu Rev Biochem* 67:509–544. doi:[10.1146/annurev.biochem.67.1.509](https://doi.org/10.1146/annurev.biochem.67.1.509)
- Weller T, Coons A (1954) Fluorescent antibody studies with agents of varicella and herpes zoster propagated in vitro. *Proc Soc Exp Biol Med* 86(4):789–794. doi:[10.3181/00379727-86-21235](https://doi.org/10.3181/00379727-86-21235)
- Xu T, Yu X, Perlik A, Tobin W, Zweig J, Tennant K, Jones T, Zuo Y (2009) Rapid formation and selective stabilization of synapses for enduring motor memories. *Nature* 462(7275):915–924. doi:[10.1038/nature08389](https://doi.org/10.1038/nature08389)
- Yang G, Pan F, Parkhurst C, Grutzendler J, Gan W-B (2010) Thinned-skull cranial window technique for long-term imaging of the cortex in live mice. *Nat Protoc* 5(2):201–208. doi:[10.1038/nprot.2009.222](https://doi.org/10.1038/nprot.2009.222)
- Yizhar O, Fenno L, Davidson T, Mogri M, Deisseroth K (2011) Optogenetics in neural systems. *Neuron* 71(1):9–34. doi:[10.1016/j.neuron.2011.06.004](https://doi.org/10.1016/j.neuron.2011.06.004)
- Zariwala H, Borghuis B, Hoogland T, Madisen L, Tian L, De Zeeuw C, Zeng H, Looger L, Svoboda K, Chen T-W (2012) A Cre-dependent GCaMP3 reporter mouse for neuronal imaging in vivo. *J Neurosci* 32(9):3131–3141. doi:[10.1523/JNEUROSCI.4469-11.2012](https://doi.org/10.1523/JNEUROSCI.4469-11.2012)
- Zhang F, Wang L-P, Brauner M, Liewald J, Kay K, Watzke N, Wood P, Bamberg E, Nagel G, Gottschalk A, Deisseroth K (2007) Multimodal fast optical interrogation of neural circuitry. *Nature* 446(7136):633–639. doi:[10.1038/nature05744](https://doi.org/10.1038/nature05744)
- Zuo Y, Yang G, Kwon E, Gan W-B (2005) Long-term sensory deprivation prevents dendritic spine loss in primary somatosensory cortex. *Nature* 436(7048):261–266. doi:[10.1038/nature03715](https://doi.org/10.1038/nature03715)

## Chapter 2

# Two-Photon Imaging of Cerebral Vasodynamics in Awake Mice During Health and Disease

Philipp M. Summers, Zachary J. Taylor, and Andy Y. Shih

**Abstract** The energy demands of the brain are supplied by a dynamic and topologically organized vascular system. *In vivo* two-photon laser-scanning microscopy has become an essential tool for studying several aspects of cerebrovascular function, including neurovascular coupling, collateral arterial flow, and vasculopathies associated with stroke and neurodegeneration. Recently there has been a strong effort to perform imaging studies on mice in the awake state. This is to avoid the dampening effect that anesthetics have on neurovascular dynamics, and also to enable studies on trained behaviors. Studying awake mice has revealed a rich dynamism of cerebral blood flow control, but also raised a number of challenges in the collection of rigorous and meaningful datasets. In this chapter, we describe techniques routinely used for two-photon blood flow imaging in awake mice. This includes chronic window implantations and head fixation techniques to reduce movement during imaging, as well as blood flow data processing techniques that are robust to movement artifacts. Finally, we describe a non-invasive photothrombotic stroke model that can be performed on awake mice for imaging of ischemic pathology.

**Keywords** In vivo imaging • Awake mice • Two-photon laser scanning microscopy • Red blood cell velocity • Vasodynamics • Vasculopathies • Stroke • Neurodegeneration • Cortical vessels

## Abbreviations

ACSF	Artificial cerebral spinal fluid
BOLD fMRI	Blood oxygen level dependent functional magnetic resonance imaging
PoRTS	Polished and reinforced thinned skull
RBC	Red blood cell
TPLSM	Two-photon laser scanning microscopy

---

P.M. Summers • Z.J. Taylor • A.Y. Shih (✉)

Department of Neurosciences, Medical University of South Carolina, Charleston, SC, USA

e-mail: [shiha@musc.edu](mailto:shiha@musc.edu)

© Springer Science+Business Media Dordrecht 2014

R. Weigert (ed.), *Advances in Intravital Microscopy*:

*From Basic to Clinical Research*, DOI 10.1007/978-94-017-9361-2\_2

25

## 2.1 Overview

The constant energy demands of brain function are supplied by a reliable and dynamic cerebrovascular system (Attwell and Laughlin 2001). In the cerebral cortex, this system begins with the great cerebral arteries that emanate from the Circle of Willis and source a planar network of highly interconnected pial arterioles on the brain surface (Mchedlishvili 1963). Blood flow in this network is relatively insensitive to blockages (Schaffer et al. 2006; Blinder et al. 2010), but also allows the dynamic redistribution of blood toward regions of heightened electrical activity (Devor et al. 2007; Derdikman et al. 2003) (Fig. 2.1). Pial vessels are in turn connected to an underlying, three-dimensional network of microvessels by radially directed penetrating arterioles, which form bottlenecks in flow to columns of cortical microvasculature (Blinder et al. 2013). Blood is then drained from the microvasculature back to the cortical surface through penetrating venules and emptied into the central sinus to complete the supply chain. While the topology of the cortical vasculature is well established, the cellular and molecular mechanisms underlying moment-to-moment regulation of flow are a topic of considerable debate (Attwell et al. 2010). As we begin to unravel these mechanisms *in vivo* using animal models, it is important to consider not only how the use of anesthetics impacts coupling of neuronal activity to blood flow in the normal brain, but also its impact on the progression of pathology in disease models.

*In vivo* two-photon laser-scanning microscopy (TPLSM) is an established method to visualize cerebrovascular topology and quantify blood flow at the level of single

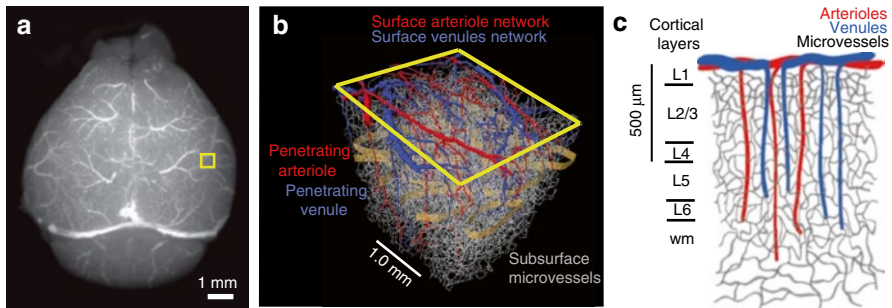


**Fig. 2.1** The vasculature of the mouse cortex. **(a)** Dorsal surface of the whole mouse brain. The vasculature was filled with a fluorescein-gelatin cast and the brain was removed from the cranium to obtain a whole brain image. **(b)** Three-tiered topology of vasculature in mouse cortex, showing highly interconnected surface pial networks (tier 1) and subsurface microvascular networks (tier 3) bridged by bottleneck penetrating vessels (tier 2). Arterioles are colored *red* and venules in *blue*. This piece of tissue was removed from the barrel field of the primary somatosensory cortex (demarcated by a *yellow square*, inset of panel **a**). A golden band denotes the border of each vibrissa barrel column (Adapted from Blinder et al. (2013)). **(c)** A schematic diagram illustrating penetrating vessels as they project radially from the pial surface into deeper layers of cortex. The density of microvasculature across different layers of cortex is generally uniform until the white matter where the density decreases (Tsai et al. 2009) (Adapted from Shih et al. (2012b))



vessels in the rodent cortex (Kleinfeld et al. 1998; Shih et al. 2012b). In this respect, TPLSM has become a key tool to understand the basis of neurovascular coupling in health and disease (Helmchen and Kleinfeld 2008; Mischak and Kerschensteiner 2006). While a rich body of data has resulted from studies on anesthetized animals, there remains a striking paucity of studies on vasodynamics in the awake state. Anesthetics greatly dampen the activity of neurons (Franks 2008) and astrocytes (Thrane et al. 2012), and alter vascular dynamics in basal and stimulated states (Drew et al. 2011). Anesthetics further preclude the study of vascular function during voluntary sensorimotor function. To image brain vasculature in the awake state, only minor enhancements upon routine *in vivo* imaging techniques are necessary. First, chronically implanted cranial windows are required to allow imaging well after recovery from initial surgeries. Second, a rigid head mount and gradual habituation to head restraint is needed to minimize movement during imaging. Here, we describe methods to visualize and quantify blood flow at the level of individual vessels in the cerebral cortex of awake, head-restrained mice. We further provide an example of how this technique can be used to study the effects of sensory-evoked neuronal activity on vascular responses. Finally we consider how non-invasive stroke models might be useful to study the trajectory of stroke injury on vascular function in the awake mouse.

## 2.2 Visualizing the Cerebral Vasculature

To gain optical access to the mouse cortex, a portion of the overlying skull must be thinned to translucency or removed entirely. This window is contained within a larger head-piece that is constructed, typically from dental acrylic, directly on the cleaned skull surface (Fig. 2.2a). Detailed methods have been described for chronic bone-removed cranial windows (Holtmaat et al. 2009; Mostany and Portera-Cailliau 2008) and semi-chronic thinned skull windows, which can provide excellent imaging quality for months (Yang et al. 2010) (See Chap. 1, by Mostany et al.). Recent work, however, indicates that complete bone removal can lead to cortical inflammation and gliosis that might affect the phenomenon under study (Xu et al. 2007). For this reason, chronically-implanted polished and reinforced thinned-skull windows (PoRTs), which avoid exposure of the cortex to air and compression of the brain with an overlying coverslip, may be preferred for awake imaging experiments (Fig. 2.2b) (Drew et al. 2010b; Shih et al. 2012a). PoRTs windows are stable for several weeks of imaging and provide optical access to the upper 250  $\mu\text{m}$  of cortex with conventional TPLSM imaging systems. To study deeper cortical layers, however, one must use bone-removed cranial window, which can provide access to cortical structures as deep as 600–800  $\mu\text{m}$ , or even the full 1 mm depth of cortex with special techniques (Kobayashi et al. 2009). Thus, the type of window used depends largely upon the goal of the experiment, and the factors to consider are imaging depth and potential effects of surgically-induced inflammation (Shih et al. 2012b). Both chronic bone-removed and PoRTs window types are suitable to awake two-photon imaging.

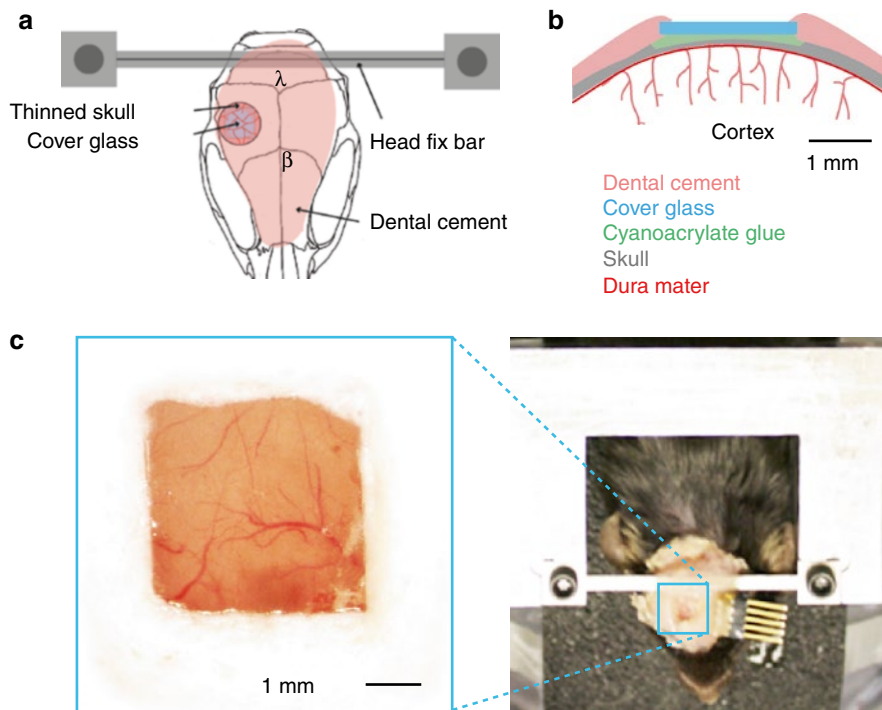


**Fig. 2.2** Polished and reinforced thinned-skull transcranial window for imaging mouse cortex. (a) Schematic diagram showing dorsal view of the head mount and position of various components. A cross bar mount is added for stability when imaging awake preparations.  $\beta$  bregma and  $\lambda$  lambda. (b) Schematic diagram showing cross section of a PoRTS window and the components involved in its construction. (c) Magnified view of PoRTs window generated over the somatosensory cortex. The cross bar is affixed to a custom mounting apparatus. Two attachment points greatly reduces degrees of freedom for repeated imaging of the same location within the window. In this example, a connector was also implanted to organize electrodes for repeated electrocorticogram recordings (Adapted from Shih et al. (2012b))

## 2.3 Habituation to Head Restraint for Imaging

Artifacts caused by animal movement account for the majority of the noise during imaging of animals in the awake state. Movements caused by struggling can be greatly reduced through a gradual process of habituation to the head restraint apparatus designed to hold the head of the animal steady during imaging sessions. One to two days following surgery, animals can begin the process of habituation to head restraint. The animal's head-piece must include a metal flange to hold the head steady during imaging (Fig. 2.2c). The apparatus for holding the flange typically consists of an optical breadboard with miniature optomechanical components commercially available from Newport or ThorLabs, and a custom-machined component designed to couple to the flange (Shih et al. 2012b). While the design of the head



restraint apparatus differs widely between labs, stability is key. Thus, having at least two anchoring points for the custom flange holder, and as few degrees of freedom as possible will help minimize movement artifacts.

A new animal can be gradually accustomed to head restraint over a period of 3–7 days, starting with 15 min sessions without imaging and working up to several hours (Drew et al. 2011). Head-restrained mice tend to struggle less when their bodies are enclosed within a loose-fitting plastic or cardboard tube. The first two-photon imaging session should be at least 3 days after the initiation of habituation when the animal has become more accustomed to the apparatus. For each imaging session, restraining the animal for 2 h at a time is reasonable, but times can differ for each animal. Discomfort should be gauged by the extent of struggling and vocalizations emitted, and the restraint time adjusted accordingly. For imaging sessions lasting hours, drinking water should be supplied with a pipette. In our experience, approximately 10 % of mice never become habituated to head-fixation and cannot be used for awake imaging.

In practice, a properly habituated animal will provide movement-free data for several minutes at a time even during sensory stimulation. While, intermittent periods of animal movement are unavoidable, it is important to identify significant movement artifacts such that the data can be omitted from analysis. Typically, several trials are collected for each stimulus paradigm and trials with excessive movement will be discarded. As a quality control measure, data acquisition can be tested on capillaries, which are only 3–5  $\mu\text{m}$  in diameter and thus most sensitive to motion. Similarly, a surface arteriole, which may move due to dilations/constriction, can be scanned simultaneously with a neighboring venule that should exhibit little or no change in lumen diameter. A movement in both vessels would indicate movement of the animal. Finally, low-cost piezoelectric sensors and accelerometers can be used to identify movement alongside vasodynamic measurements, allowing data sets with excessive movement to be removed (Drew et al. 2011).

## 2.4 Measurement of Blood Flow Dynamics in Single Cortical Vessels

Prior to imaging, the mouse must be briefly anesthetized with isoflurane for an intravenous injection of fluorescent dextran dye. Typically, 25–50  $\mu\text{L}$  of 5 % (w/v) fluorescent-dextran dye, fluorescein-dextran (FD2000S; Sigma) or Texas red-dextran (D1830; Invitrogen), is dissolved in saline and injected either through the tail vein or infraorbital vein to label the blood serum. The dye will remain in circulation for approximately 3–4 h, and supplements can be given as necessary if the animal is re-anesthetized.

When the vasculature is labeled with an intravenous bolus of fluorescent-conjugated dextran, red blood cells (RBCs) exclude the high molecular weight dextran dye and will appear as dark shadows moving against a bright fluorescent background of serum within the vascular lumen. This differential staining is the

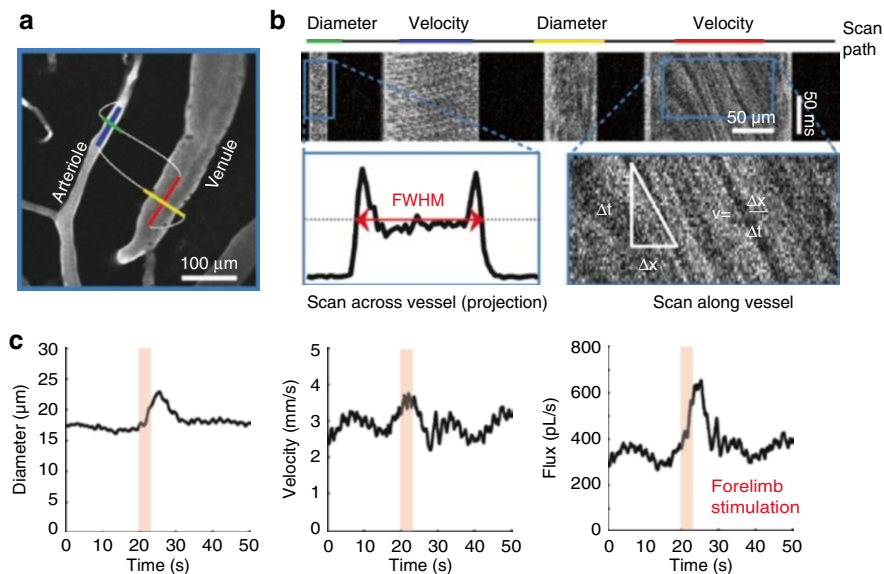


**Fig. 2.3** Single vessel vasodynamics measured with spatially optimized line-scans in somatosensory cortex of an anesthetized Sprague Dawley rat. (a) Planar image of pial arteriole and venule labeled by intravenous injection of 2 MDa fluorescein-dextran. This animal was anesthetized with continuous intravenous delivery of alpha-chloralose. These vessels were located in the forelimb region of somatosensory cortex. The line-scan path is overlaid on the image, with the colored segments corresponding to scan regions when the mirrors moved at constant velocity and interconnecting white lines as regions when the mirrors were accelerated to reduce total scan time. (b) The line-scans generated from the path are stacked sequentially as a function of time to produce a space-time plot. Bottom left, the diameter is calculated as the full-width half-maximum of a time-average of several scans across the width of a vessel. Bottom right, red blood cell velocity is calculated from the angle of the RBC streaks from portions of the scan that traverse the centerline of the vessel. (c) Data traces of diameter, RBC velocity, and flux for the arteriole before, during, and after electrical stimulation of the forelimb, processed to remove heart rate and smoothed with a running window. The arteriole shows an increase in flux in response to stimulation attributed to an increase in both lumen diameter and RBC speed (Adapted from Driscoll et al. (2011))

basis for measuring RBC velocity using laser-scanning microscopy (Villringer et al. 1989; Kleinfeld et al. 1998). Conventionally, single line-scans have been used to sample the RBC velocity and diameter of a vessel separately (Schaffer et al. 2006; Shih et al. 2009). However, blood flow is dynamic and could change within the time between each scan. In order to collect more samples simultaneously and with varying trajectories within the imaging plane, we use custom software to direct the imaging laser beam in a user-defined path (Figs. 2.3a, 2.4b, and 2.5c) (Valmianski et al. 2010; Driscoll et al. 2011), following earlier work (Göbel et al. 2007; Göbel and Helmchen 2007; Lillis et al. 2008). Linear segments of constant scan speed traverse along the length of the center of the vessel and across the width of the vessel to measure RBC speed and lumen diameter, respectively (Fig. 2.3a). These

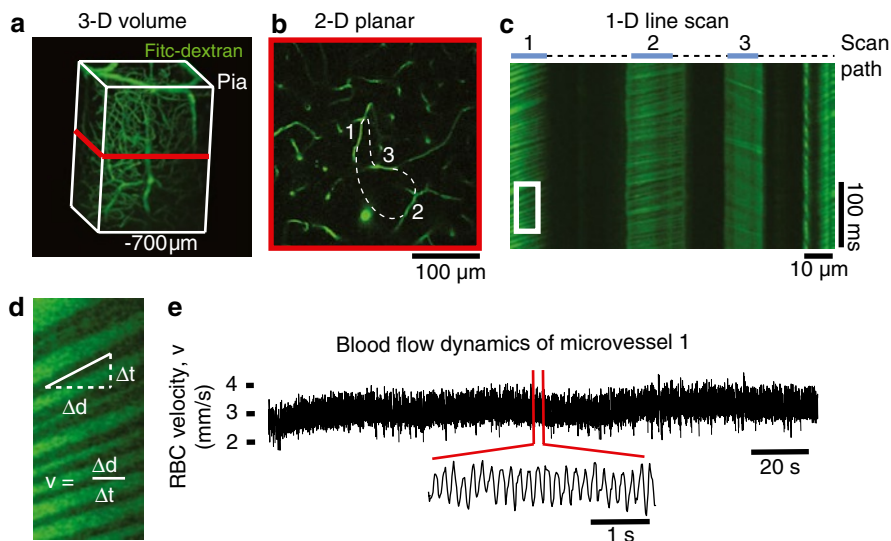


**Fig. 2.4** Simultaneous measurement of red blood cell velocity from multiple subsurface capillaries in the cortex of an anesthetized mouse. **(a)** Three dimensional reconstruction of image stack collected *in vivo* through a bone-removed cranial window of an isoflurane-anesthetized mouse. Note, that imaging depths of up to 700 µm below the pia can be achieved after complete removal of the overlying skull. **(b)** A single plane from the reconstruction shown in panel (a), taken from the depth of the *red box* (325 µm below the pia). Three microvessels are scanned simultaneously with an optimized line-scan path. **(c)** The resulting space-time plot from the line-scan shows streaks generated by flowing RBCs in each microvessel. **(d)** The speed of RBC flow is extracted from the slope of the streaks generated by RBC movement. **(e)** Data traces of RBC speed collected over several minutes from microvessel 1. Heart-beat frequencies are present in the data, providing a check for data quality

linear scan segments are connected by polynomial splines, where connecting portions of the scan are accelerated to allow for rapid data collection across multiple vessels (Driscoll et al. 2011). The resulting line-scan is a space-time plot, typically displayed with the individual scan lines stacked on top of each other (Figs. 2.3b, 2.4c, and 2.5d).

### 2.4.1 Calculating Red Blood Cell Velocity

Portions of the scan path along the centerline of the vessel lumen reveal angled streaks within the space-time plot (Figs. 2.3b, bottom right, and 2.4d). Moving RBCs in flowing vessels sampled at a sufficient rate will appear as diagonal streaks. Stalls in flow will result in vertical streaks with distance as the abscissa and time as the ordinate. This is a common occurrence when measuring from capillaries, and may also occur in pial arteriolar and venous anastomoses (Shih et al. 2009; Nguyen

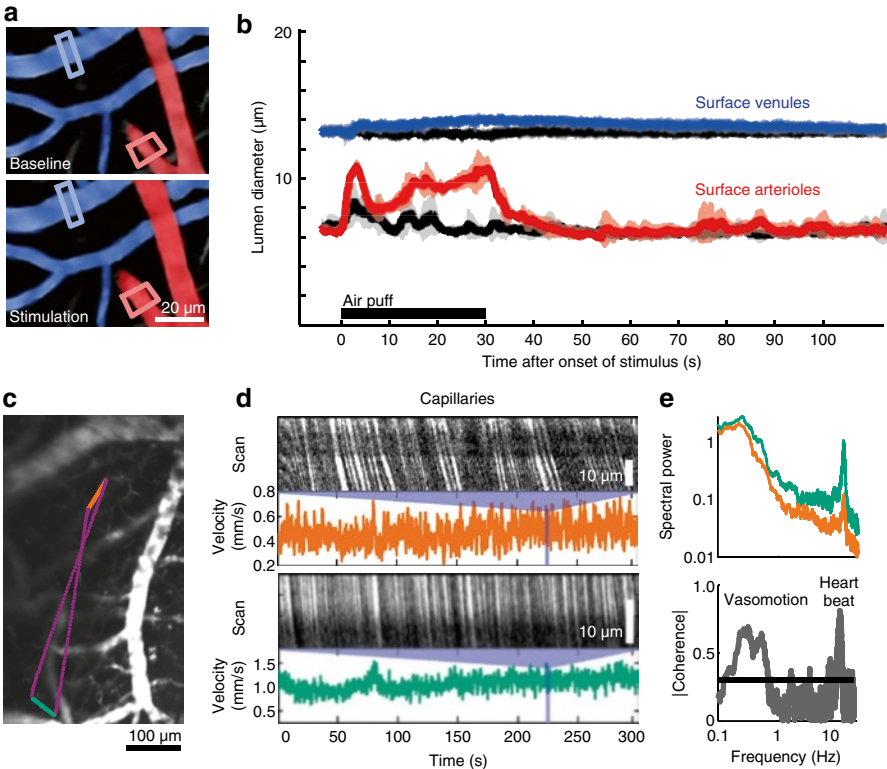


**Fig. 2.5** Spontaneous and stimulus-induced vascular dynamics in the somatosensory cortex of an awake mouse. (a) Two-photon images of pial surface vessels taken from an awake mouse. Arterioles are shown in *red*, while venules are shown in *blue*. (b) Averaged time-series of the diameter of an arteriole and venule in response to a 30 s period of contralateral vibrissal stimulation using focused 8 Hz air puffs. The response of the arteriole during control air puffs to the tail provides a control for general arousal (*black traces*). Data are mean  $\pm$  standard deviation. (c) Maximal z-dimension projection over 90  $\mu$ m of images of fluorescein dextran-labeled vasculature collected through a PoRTs window. The line-scan trajectory used to sample from two distinctly separated capillaries is overlaid on the image; *green* and *orange lines* are constant velocity segments along capillaries and *purple* are minimum time segments between capillaries. (d) Space-time plots of one segment of line-scan data from each of two capillaries sampled. The calculated instantaneous RBC speed for the entire 300 s period of scanning is shown below each space-time plot. (e) Power spectra for the two RBC velocity traces in panel (d) (0.083 Hz bandwidth; *top*) and magnitude of the spectral coherence between the velocities of the two capillaries as a function of frequency (0.1 Hz bandwidth; *bottom*). Panels (a, b) are adapted from Drew et al. (2011). Panels (c–e) are adapted from Drew et al. (2010b)

et al. 2007). In the limiting case of extremely fast flowing vessels, the streaks will become horizontal and velocity data cannot be extracted unless faster scanning methods are used (see Future Directions). The centerline velocity is proportional to the slope of the RBC streaks. This slope can be efficiently determined with a Radon

transform of windowed portions of the data (Drew et al. 2010a), which is available in the MATLAB™ Image Processing Toolbox (Mathworks). The direction of flow can be ascertained from the sign of the slope and the direction of the line-scan sweep.

A velocity time series is calculated by taking successive time-windowed portions of the line-scan (Figs. 2.3c center, 2.4e, and 2.5d). The size of the window must be sufficiently short to resolve the highest velocity modulation frequency, the heart rate, which is 8–10 Hz for awake mice (Drew et al. 2011). In addition, the window size must be large enough to capture a sufficient portion of the streak lines for the Radon transform to calculate an accurate slope, but small enough to prevent smoothing out the higher frequencies of the velocity data. When sampling with line-scan rates of ~1 kHz, we find that a window size of 40 ms is a good compromise, which yields a Nyquist frequency of 12.5 Hz. We further use a window spacing of 10 ms. Oscillating physiological rhythms within the RBC velocity are a first indicator of good data quality. In addition to heart rate (Figs. 2.4e and 2.5e), other physiological signals detected in the RBC velocity may include breathing at ~1–2 Hz, and vasomotion at ~0.1–1 Hz (Kleinfeld and Mitra 2011; Mayhew et al. 1996) (Fig. 2.5e). Breathing rate, however, is not always detectable in the flow data collected from awake mice (Drew et al. 2011).

Measurement of RBC velocity is the limiting factor for the measurement of flow in larger arterioles on the cortical surface. In practice, conventional galvanometric mirrors are sufficiently fast to simultaneously capture RBC velocity and diameter from one penetrating arteriole at a time in the anesthetized state (Shih et al. 2013). However, in the awake state RBC velocity tends to increase, and thus atypical fast scanning and/or special analysis techniques (Kim et al. 2012) may be necessary or smaller pial vessels should be sampled. Venules and deep microvessels exhibit slower RBC velocity and thus three to four vessels can be measured simultaneously with spatially-optimized line-scans (Figs. 2.4 and 2.5c–e). Greater distances traversed by the laser will reduce the sampling frequency and a 1–2 kHz line-scan rate is recommended for accurate sampling of the movement of RBCs in pial arterioles (Driscoll et al. 2011).

### 2.4.2 Calculating Lumen Diameter

As with RBC velocity, the diameter calculations are also taken from time-windowed portions of the line-scan data. The same window size and spacing used for velocity is typically used for diameter so that both parameters can be calculated on the same time scale. Vessel diameter is calculated as full-width at half-max of the vessel profile for each window (Fig. 2.3b, bottom left, and c, left). Note the intensity profile tends to increase near the edges due to the exclusion of RBCs from the glycocalyx, which generates two peaks. The two outermost half-max points of these peaks are used to calculate the vessel boundary. Linear interpolation adds sub-pixel accuracy to the diameter measurement.

### 2.4.3 *Estimating the Flux of Red Blood Cells*

There are two limiting cases for the flux. When the diameter of the vessel allows the passage of RBCs only in single file, as in the case of capillaries, the flux of RBCs is just the number of RBCs that pass per second (Kleinfeld et al. 1998; Chuquet et al. 2007). In this limit, the blood plasma has an essentially constant velocity profile as a function of distance from the center of the vessel, then the velocity falls rapidly to zero near the walls. The thin layer of plasma near the walls acts as a lubricating layer that, together with the glycocalyx, minimizes friction (Secomb et al. 1998).

When the diameter of the vessel is much greater than that of the RBC, as is the case for all pial surface vessels, the flow is laminar and nearly parabolic as RBCs flow in parallel streams (Schaffer et al. 2006; Rovainen et al. 1993). The two vascular parameters, RBC velocity and lumen diameter, are combined to calculate the volume flux, *i.e.*, RBCs and plasma, for each vessel (Fig. 2.3c, right panel). Flux is a more complete description of blood flow in single vessels, as RBC velocity and lumen diameter can change independently of each other (Shih et al. 2009; Kontos 1989). The volume flux through the vessel is given by

$$\bar{F} = \langle \bar{v} \rangle A = \frac{\pi}{8} \bar{v}(0) d^2$$

where  $\langle v \rangle$  is the average RBC velocity over  $A$ , the cross-sectional area of the vessel lumen,  $\bar{v}(0)$ , is the time-averaged RBC velocity at the center line of the vessel, and  $d$  is the lumen diameter. Note that this formula underestimates the flux as the nonzero spatial extent of the RBC flattens the parabola of Poiseuille flow; empirical corrections have been discussed (Nishimura et al. 2010).

### 2.4.4 *Measurement of Vessel Diameter from 2-D Planar Images*

If the goal is to examine only changes in vascular diameter, the collection of 2-dimensional planar images may be more desirable than line-scans. Arteriolar dilations occur on the order of seconds and do not require fast acquisition rates. Thus, movies collected at 5 Hz, for example, would be adequate to capture diameter changes associated with sensory-evoked hemodynamic responses and vasomotion (Drew et al. 2011). Heart-beat and breathing rates do not typically result in appreciable diameter changes. A further advantage of planar scans is that conduction of dilatory or constrictive changes may be easily observed along a length of vasculature. As with line-scan data, the full-width of half maximum of a segment of



vasculature is calculated from each image using custom-written software to generate a diameter time-series from the movie.

### 2.4.5 *Vasodynamics in Awake Mice*

We show an example study of pial surface and capillary vasodynamics measured under normal conditions (Fig. 2.5). A mouse was habituated to head fixation and blood flow was measured using planar movies through a chronically implanted PoRTS window (Fig. 2.5a). Consistent with hemodynamic coupling of blood flow to neural activity, robust arteriole dilations could be evoked by prolonged contralateral whisker stimulation with puffs of air (Fig. 2.5b). Dilatory events consisted of an early peak followed by a secondary slowly-rising plateau, in averaged data, during sustained stimulation. The dilatory affect returned to baseline over 10 s following cessation of stimulation. Pial venules, typically thought to be static in terms of diameter, show a weak dilation in the awake state (Fig. 2.5b). These data suggest that functional hyperemia detected by blood oxygen level dependent functional magnetic resonance imaging (BOLD fMRI) may be dominated by large changes in arteriole volume, in agreement with recent studies (Kim and Kim 2011), rather than in venules as predicted by the “balloon” model (Buxton et al. 1998).

The speed of RBCs within arterioles is high during the awake state and thus fast line-scanning frequencies are required to capture this data in a smaller pial arteriole. However, RBC velocity can be routinely measured within the full range of capillaries for awake mice at 1 kHz scanning frequency (Drew et al. 2010b, 2011). While the basal vasomotor activity manifest as spontaneous arteriole dilations on the cortical surface, this translates into changes in microvascular RBC velocity as the blood flows into the brain tissue. These oscillations range from 0.1 to 1 Hz in frequency and are commonly observed in the awake state but may be dampened or non-existent during anesthesia. Vasomotor blood flow changes are more globally spread over the cortical mantle, compared to relatively local sensory-driven hemodynamic responses. Consistent with this idea, spontaneous oscillations in capillaries are strongly correlated across distant sites within the cranial window (Fig. 2.5c–e).

Both basal and stimulated responses of arterioles and venules are strongly suppressed by the use of urethane, a common anesthetic (Drew et al. 2011), that can attenuate the magnitude of the overall dilatory response by up to 75 % in the anesthetized state. Other commonly used anesthetics, including isoflurane (Takuwaa et al. 2012),  $\alpha$ -chloralose (Dudley et al. 1982), and propofol (Alkire et al. 1995), similarly suppress the neurovascular response. In addition to the direct neural effects, anesthetics exert strong depressing effects on cardiovascular function (Janssen et al. 2004). Consistent with the depressive effects of anesthetics on neural and cardiovascular system, optical imaging studies of neurovascular coupling have



found differences between the awake and anesthetized animal (Nakao et al. 2001; Jones et al. 2008; Martin et al. 2006).

## 2.5 Awake Imaging and Disease Models

The awake imaging methods we describe are also amenable to the study of cerebrovascular pathology in any mouse disease model. Here we focus here on pathology associated with ischemia. Anesthesia alters key mechanisms of stroke injury and repair and will therefore affect the trajectory of the disease. In the acute stage of ischemic injury, this can occur by suppression of neuronal activity or by engaging collateral blood flow sources. Common anesthetics, such as isoflurane, reduce the cerebral metabolic rate for oxygen consumption and likely the extent of excitotoxic neuronal toxicity (Scheller et al. 1988). Ketamine, in particular, is an antagonist of the NMDA receptor and attenuates production of the potent vasomediator, nitric oxide, during stroke (Olney et al. 1991; Lin et al. 1996). Cortical spreading depression (CSD), a wave of hyperactivity followed by a wave of depression (Siesjö and Bengtsson 1989), contributes to the expansion of tissue infarction (Lauritzen et al. 2011). The frequency of CSD events has been shown to be attenuated or modulated by numerous anesthetics, including ketamine (Hernández-Cáceres et al. 1987; Verhaegen et al. 1992), volatile anesthetics halothane, isoflurane and sevoflurane (Kudo et al. 2008; Kitahara et al. 2001), and urethane-chloralose (Guedes and Barreto 1992). Thus, many anesthetics mediate an overall protective effect in stroke by attenuating excitotoxic injury (Kawaguchi et al. 2005).

Anesthesia can also affect cerebral blood flow, which may have opposing effects on stroke outcome. Pentobarbital and isoflurane, in particular, cause global cerebral vasodilation that lead to a hypoperfusion, which can further decrease perfusion in the stroke penumbra and exacerbate injury (Hendrich et al. 2001). Conversely, the dilation of cerebral arterioles can conceivably promote tissue survival by engaging collateral blood supply through leptomeningeal anastomoses. Another important consideration is that hemodynamic responses measured by BOLD fMRI are widely used to infer tissue recovery after stroke (Cramer et al. 1997). Given the suppressive effects of anesthetics on arterial and neuronal reactivity, it is unclear when models using anesthesia fail to mimic the human condition (Austin et al. 2005; Antognini et al. 1997). Studies on awake preparations will be important to establish whether changes in arterial reactivity during stroke are masked or altered by the anesthetics used.

The effects of anesthetics can extend beyond the acute phase of stroke when the infarct stabilizes and the peri-infarct zone begins to recover. Longitudinal *in vivo* imaging studies typically involve repeated periods of anesthesia that could affect repair/recovery processes. Anesthetics impact the activity of microglia directly by altering the expression of inflammatory mediators and also indirectly by reducing CSD, which promotes microglial activation (Gehrmann et al. 1993). The effect varies with the type of anesthetic used, as isoflurane appears to promote cytokine

expression (Ye et al. 2013; Wu et al. 2012), while ketamine has an inhibitory effect (Chang et al. 2009). Further, the activity of microglia is tightly linked to post-stroke repair process through release of matrix metalloproteinases (MMPs). MMPs are associated with the breakdown of tight junction proteins in acute stroke (Patel et al. 2013), but also appear to be involved in remodeling of neuronal connectivity (Wake et al. 2009) and possibly nascent blood vessel formation, which involves MMP activity (Arai et al. 2009). In summary, awake imaging preparations are expected to reveal the natural evolution of stroke injury, and will therefore provide more clinically relevant data on (i) the spatiotemporal features of tissue injury and repair processes, (ii) the timing of interventional therapies, and (iii) the metrics used to gauge brain recovery, such as hemodynamic responses.

One limitation in current preclinical stroke studies is that the models are often invasive, necessitating deep and prolonged anesthesia. This precludes the visualization of early changes in stroke, which can in turn dictate the extent and long-term trajectory of the injury. We suggest that photothrombosis, a technique to non-invasively occlude blood vessels by light-mediated focal activation of the intravenous photosensitizer Rose Bengal, can be easily applied to awake preparations (Shih et al. 2011, 2013; Nishimura et al. 2007). An animal previously habituated to awake imaging would only need to be briefly anesthetized, (<1 min) for intravenous injection of a photosensitizer, minimizing the exposure time and allowing the stroke to develop more naturally during the period of the study. Photothrombotic stroke also provides the advantage of targeting the location of ischemia within the imaging window. Collimated laser beams, ranging in areas between 0.16 and 2 mm<sup>2</sup>, have been used to ablate specific areas of cortex in sophisticated studies of functional remapping after stroke (Winship and Murphy 2008; Brown et al. 2009). While such lesions are spatially specific, they possess a limited ischemic penumbra (Zhang et al. 2005). A second approach using focused laser beams to irradiate single cortical penetrating vessels leads to similar areas of damage, depending upon the RBC flux of the vessel, but generates a more gradual degradation of tissue due to a substantial penumbra (Shih et al. 2011, 2013). This allows for imaging of mechanisms involved in tissue death at the evolving core-penumbra interface (Fig. 2.6).

## 2.6 Future Directions

We show that methods to transition from anesthetized to awake imaging preparations are straight-forward and will be an important step to truly understand mechanisms of vascular control in the normal brain state. Since anesthesia has clear effects on the trajectory of stroke injury, it is also critical to understand how vascular degradation during acute stroke and repair in chronic stroke differ between anesthetized and awake preparations.

Two-photon imaging fills an important gap in the existing range of tools for blood flow quantification and enables the study of vasodynamics in awake mice. While intrinsic optical imaging, laser speckle, and BOLD fMRI enable measurement

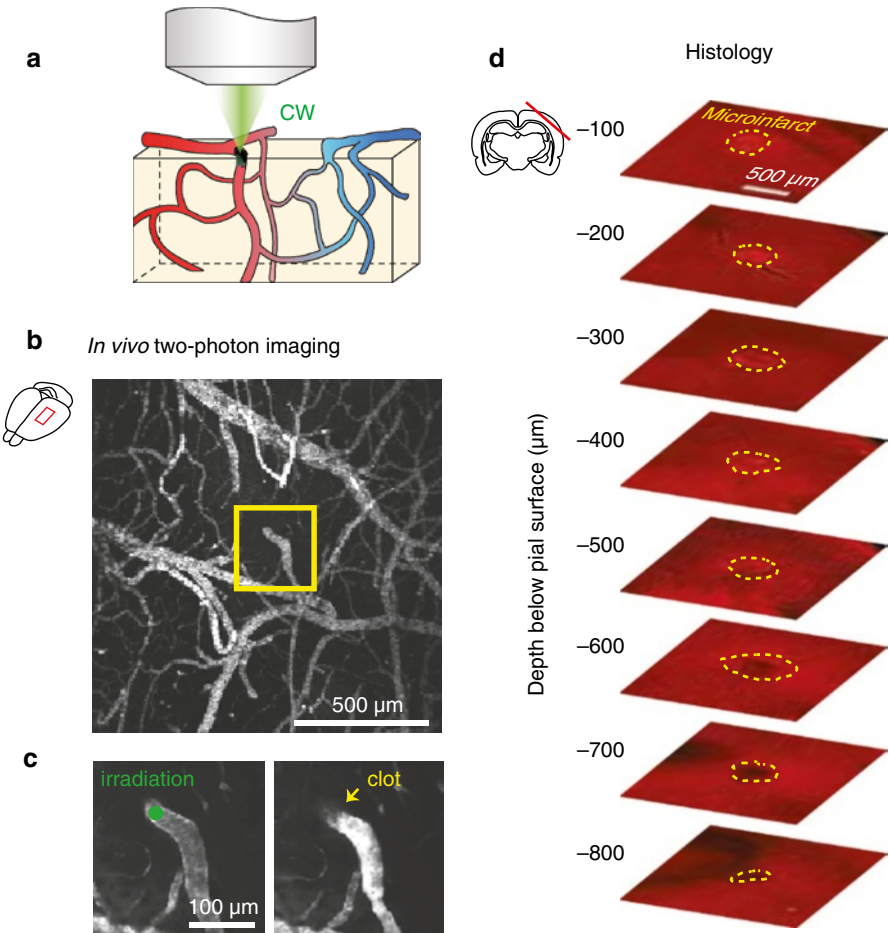


**Fig. 2.6** Generation of a localized ischemic stroke by targeted photothrombosis of single penetrating vessels in mouse cortex. **(a)** Schematic showing focused *green* laser irradiation of a penetrating arteriole to generate a focal occlusion, following intravenous injection of Rose Bengal. Targeted photothrombosis can be performed through the thinned skull (Drew et al. 2010b). **(b)** Low magnification, maximally Z-dimension projected image of fluorescein dextran-labeled pial vasculature visualized through a thinned skull PoRTS window. A single penetrating arteriole within the window is identified for photothrombosis (yellow box). **(c)** Green laser irradiation of a single penetrating arteriole (left panel) immediately following intravenous administration of Rose Bengal leads to localized clotting (right panel). After successful photothrombosis, a dark clot is seen at the site of irradiation and the vessel becomes brighter upstream due to stagnation of RBC flow. **(d)** Post-mortem immunohistochemistry with the pan-neuronal marker NeuN demarcating the boundaries of the resulting infarct (yellow-dotted line), as observed 48 h following occlusion

of flow over broader areas of brain, two-photon microscopy complements these techniques and provides a view of dynamics at the resolution of individual small cortical vessels. Further, TPLSM can be concurrently used to examine activity of surrounding cells that could be driving vascular activity (Takano et al. 2006; Nizar

et al. 2013). Recent advances in hardware and optics now allow TPLSM images to be collected over entire cranial windows several millimeters in size, potentially enabling the spatiotemporal features of broader hemodynamic responses to be studied at capillary resolution.

Some further advances will be necessary to fully capitalize on awake imaging experiments. First, faster laser-scanning is necessary to capture RBC velocity within larger cortical arterioles. Acousto-optic modulators (Lechleiter et al. 2002) can in principle scan vessels with faster flow as well as sample from larger populations of vessels simultaneously. Recent advances in processing of line-scan data using particle image velocimetry will also be useful to assess RBC velocity in larger vessels (Kim and Kim 2011). Additionally, application of filtering techniques to line-scan data may provide more robust measurements in the face of small movement artifacts caused by animal movement (Chhatbar and Kara 2013). Second, physiological parameters most relevant to blood flow including blood pressure and blood gas remain difficult to measure in awake mice. In particular, even when these parameters are measured invasively from catheters in peripheral vessels, they may not reflect conditions in the cerebral vessel being examined. Novel imaging probes need to be developed to assess real-time changes in blood pressure, gas, and pH at the vessel being examined. Finally, new tools to manipulate cell-specific vasoactive signaling cascades will be an important step in dissecting the chemical basis of neurovascular coupling (Kleinfeld et al. 2011).

**Acknowledgements** Our work is generously supported by grants to A.Y.S. from the National Institutes of Health for generous support (1R21NS085402-01), Dana Foundation (David Mahoney Neuroimaging Program) and South Carolina Clinical and Translational Institute (UL1TR000062).

## References

- Alkire MT, Haier RJ, Barker SJ, Shah NK, Wu JC, Kao YJ (1995) Cerebral metabolism during propofol anesthesia in humans studied with positron emission tomography. *Anesthesiology* 82(2):393–403
- Antognini JF, Buonocore MH, Disbrow EA, Carstens E (1997) Isoflurane anesthesia blunts cerebral responses to noxious and innocuous stimuli: a fMRI study. *Life Sci* 61(24):349–354
- Arai K, Jin G, Navaratna D, Lo EH (2009) Brain angiogenesis in developmental and pathological processes: neurovascular injury and angiogenic recovery after stroke. *FEBS J* 276(17):4644–4652
- Attwell D, Laughlin SB (2001) An energy budget for signaling in the grey matter of the brain. *J Cereb Blood Flow Metab* 21:1133–1145
- Attwell D, Buchan AM, Charpak S, Lauritzen M, MacVicar BA, Newman EA (2010) Glial and neuronal control of brain blood flow. *Nature* 468(7321):232–243
- Austin VC, Blamire AM, Allers KA, Sharp T, Styles P, Matthews PM, Sibson NR (2005) Confounding effects of anesthesia on functional activation in rodent brain: a study of halothane and alpha-chloralose anesthesia. *Neuroimage* 24(1):92–100
- Blinger P, Shih AY, Rafie CA, Kleinfeld D (2010) Topological basis for the robust distribution of blood to rodent neocortex. *Proc Natl Acad Sci U S A* 107:12670–12675
- Blinger P, Tsai PS, Kaufhold JP, Knutsen PM, Suhl H, Kleinfeld D (2013) The cortical angiome: an interconnected vascular network with noncolumnar patterns of blood flow. *Nat Neurosci* 16:889–897

- Brown CE, Aminoltejari K, Erb H, Winship IR, Murphy TH (2009) In vivo voltage-sensitive dye imaging in adult mice reveals that somatosensory maps lost to stroke are replaced over weeks by new structural and functional circuits with prolonged modes of activation within both the peri-infarct zone and distance sites. *J Neurosci* 29:1719–1734
- Buxton RB, Wong EC, Frank LR (1998) Dynamics of blood flow and oxygenation changes during brain activation: the balloon model. *Magn Reson Med* 39:855–864
- Chang YLJ, Hsieh CY, Hsiao G, Chou DS, Sheu JR (2009) Inhibitory effects of ketamine on lipopolysaccharide-induced microglial activation. *Mediators Inflamm* 2009:705379
- Chhatbar PY, Kara P (2013) Improved blood velocity measurements with a hybrid image filtering and iterative Radon transform algorithm. *Front Neurosci* 7:106
- Chuquet J, Hollender L, Nimchinsky EA (2007) High-resolution *in vivo* imaging of the neurovascular unit during spreading depression. *J Neurosci* 27:4036–4044
- Cramer SC, Nelles G, Benson RR, Kaplan JD, Parker RA, Kwong KK, Kennedy DN, Finklestein SP, Rosen BR (1997) A functional MRI study of subjects recovered from hemiparetic stroke. *Stroke* 28(12):2518–2527
- Derdikman D, Hildesheim R, Ahissar E, Arieli A, Grinvald A (2003) Imaging spatiotemporal dynamics of surround inhibition in the barrels somatosensory cortex. *J Neurosci* 23:3100–3105
- Devor A, Tian P, Nishimura N, Teng IC, Hillman EM, Narayanan SN, Ulbert I, Boas DA, Kleinfeld D, Dale AM (2007) Suppressed neuronal activity and concurrent arteriolar vasoconstriction may explain negative blood oxygenation level-dependent signaling. *J Neurosci* 27:4452–4459
- Drew PJ, Blinder P, Cauwenberghs G, Shih AY, Kleinfeld D (2010a) Rapid determination of particle velocity from space-time images using the Radon transform. *J Comput Neurosci* 29:5–11
- Drew PJ, Shih AY, Driscoll JD, Knutsen PM, Davalos D, Blinder P, Akassoglou K, Tsai PS, Kleinfeld D (2010b) Chronic optical access through a polished and reinforced thinned skull. *Nat Methods* 7:981–984
- Drew PJ, Shih AY, Kleinfeld D (2011) Fluctuating and sensory-induced vasodynamics in rodent cortex extends arteriole capacity. *Proc Natl Acad Sci U S A* 108:8473–8478
- Driscoll JD, Shih AY, Drew PJ, Cauwenberghs G, Kleinfeld D (2011) Two-photon imaging of blood flow in cortex. In: Helmchen F, Konnerth A, Yuste R (eds) *Imaging in neuroscience: a laboratory manual*, vol 2. Cold Spring Harbor Laboratory Press, New York, pp 927–938
- Dudley RE, Nelson SR, Samson F (1982) Influence of chloralose on brain regional glucose utilization. *Brain Res* 233:173–180
- Franks NP (2008) General anaesthesia: from molecular targets to neuronal pathways of sleep and arousal. *Nat Rev Neurosci* 5:370–386
- Gehrmann J, Mies G, Bonnekoh P, Banati R, Iijima T, Kreutzberg GW, Hossmann KA (1993) Microglial reaction in the rat cerebral cortex induced by cortical spreading depression. *Brain Pathol* 3(1):11–17
- Göbel W, Helmchen F (2007) New angles on neuronal dendrites *in vivo*. *J Neurophysiol* 98:3770–3779
- Göbel W, Kampa BM, Helmchen F (2007) Imaging cellular network dynamics in three dimensions using fast 3D laser scanning. *Nat Methods* 4:73–79
- Guedes RC, Barreto JM (1992) Effect of anesthesia on the propagation of cortical spreading depression in rats. *Braz J Med Biol Res* 25(4):393–397
- Helmchen F, Kleinfeld D (2008) *In vivo* measurements of blood flow and glial cell function with two-photon laser scanning microscopy. *Methods Enzymol* 444:231–254
- Hendrich KS, Kochanek PM, Melick JA, Schiding JK, Statler KD, Williams DS, Marion DW, Ho C (2001) Cerebral perfusion during anesthesia with fentanyl, isoflurane, or pentobarbital in normal rats studied by arterial spin-labeled MRI. *Magn Reson Med* 46(1):202–206
- Hernández-Cáceres J, Macías-González R, Brozek G, Bures J (1987) Systemic ketamine blocks cortical spreading depression but does not delay the onset of terminal anoxic depolarization in rats. *Brain Res* 437(2):360–364
- Holtmaat A, Bonhoeffer T, Chow DK, Chuckowree J, De Paola V, Hofer SB, Hübener M, Keck T, Knott G, Lee WC, Mostany R, Mrcic-Flogel TD, Nedivi E, Portera-Cailliau C, Svoboda K, Trachtenberg JT, Wilbrecht L (2009) Long-term, high-resolution imaging in the mouse neocortex through a chronic cranial window. *Nat Protoc* 4:1128–1144

- Janssen BJ, De Celle T, Debets JJ, Brouns AE, Callahan MF, Smith TL (2004) Effects of anesthetics on systemic hemodynamics in mice. *Am J Physiol Heart Circ Physiol* 287(4):H1618–H1624
- Jones M, Devonshire IM, Berwick J, Martin C, Redgrave P, Mayhew J (2008) Altered neurovascular coupling during information-processing states. *Eur J Neurosci* 27:2758–2772
- Kawaguchi M, Furuya H, Patel PM (2005) Neuroprotective effects of anesthetic agents. *J Anesth* 19(2):150–156
- Kim T, Kim SG (2011) Temporal dynamics and spatial specificity of arterial and venous blood volume changes during visual stimulation: implication for BOLD quantification. *J Cereb Blood Flow Metab* 31:1211–1222
- Kim TN, Goodwill PW, Chen Y, Conolly SM, Schaffer CB, Liepmann D, Wang RA (2012) Line-scanning particle image velocimetry: an optical approach for quantifying a wide range of blood flow speeds in live animals. *PLoS One* 7(6):e38590
- Kitahara Y, Taga K, Abe H, Shimoji K (2001) The effects of anesthetics on cortical spreading depression elicitation and c-fos expression in rats. *J Neurosurg Anesthesiol* 13(1):26–32
- Kleinfeld D, Mitra PP (2011) Applications of spectral methods in functional brain imaging. In: Yuste R (ed) *Imaging: a laboratory manual*, vol 1. Cold Spring Harbor Laboratory Press, New York, pp 12.11–12.17
- Kleinfeld D, Mitra PP, Helmchen F, Denk W (1998) Fluctuations and stimulus-induced changes in blood flow observed in individual capillaries in layers 2 through 4 of rat neocortex. *Proc Natl Acad Sci U S A* 95:15741–15746
- Kleinfeld D, Blinder P, Drew PJ, Driscoll JD, Muller A, Tsai PS, Shih AY (2011) A guide to delineate the logic of neurovascular signaling in the brain. *Front Neuroenergetics* 1:1–9
- Kobat D, Durst ME, Nishimura N, Wong AW, Schaffer CB, Xu C (2009) Deep tissue multiphoton microscopy using longer wavelength excitation. *Opt Express* 17:13354–13364
- Kontos HA (1989) Validity of cerebral arterial blood flow calculations from velocity measurements. *Stroke* 20:1–3
- Kudo C, Nozari A, Moskowitz MA, Ayata C (2008) The impact of anesthetics and hyperoxia on cortical spreading depression. *Exp Neurol* 212(1):201–206
- Lauritzen M, Dreier JP, Fabricius M, Hartings JA, Graf R, Strong AJ (2011) Clinical relevance of cortical spreading depression in neurological disorders: migraine, malignant stroke, subarachnoid and intracranial hemorrhage, and traumatic brain injury. *J Cereb Blood Flow Metab* 31(1):17–35
- Lechleiter JD, Lin DT, Sieneart I (2002) Multi-photon laser scanning microscopy using an acoustic optical deflector. *Biophys J* 83:2292–2299
- Lillis KP, Eng A, White JA, Mertz J (2008) Two-photon imaging of spatially extended neuronal network dynamics with high temporal resolution. *J Neurosci Methods* 172:178–184
- Lin SZ, Chiou AL, Wang Y (1996) Ketamine antagonizes nitric oxide release from cerebral cortex after middle cerebral artery ligation in rats. *Stroke* 27(4):747–752
- Martin C, Martindale J, Berwick J, Mayhew J (2006) Investigating neural-hemodynamic coupling and the hemodynamic response function in the awake rat. *Neuroimage* 32:33–48
- Mayhew JEW, Askew S, Zeng Y, Porcill J, Westby GWM, Redgrave P, Rector DM, Harper RM (1996) Cerebral vasomotion: 0.1 Hz oscillation in reflectance imaging of neural activity. *Neuroimage* 4:183–193
- Mchedlishvili G (1963) *Arterial behavior and blood circulation in the brain*. Consultants Bureau, New York
- Misgeld T, Kerschensteiner M (2006) *In vivo* imaging of the diseased nervous system. *Nat Rev Neurosci* 7:449–463
- Mostany R, Portera-Cailliau C (2008) A method for 2-photon imaging of blood flow in the neocortex through a cranial window. *J Vis Exp* 12:678
- Nakao Y, Itoh Y, Kuang TY, Cook M, Jehle J, Sokoloff L (2001) Effects of anesthesia on functional activation of cerebral blood flow and metabolism. *Proc Natl Acad Sci* 98(13):7593–7598
- Nguyen J, Nishimura N, Iadecola C, Schaffer CB (2007) Single venule occlusions induced by photodisruption using femtosecond laser pulses cause decreased blood flow in rat cortex. In: Society for Neuroscience (ed) *Society for Neuroscience, San Diego, Society for Neuroscience*
- Nishimura N, Schaffer CB, Friedman B, Lyden PD, Kleinfeld D (2007) Penetrating arterioles are a bottleneck in the perfusion of neocortex. *Proc Natl Acad Sci U S A* 104:365–370



- Nishimura N, Rosidi NL, Iadecola C, Schaffer CB (2010) Limitations of collateral flow after occlusion of a single cortical penetrating arteriole. *J Cereb Blood Flow Metab* 30:1914–1927
- Nizar K, Uhlirova H, Tian P, Saisan PA, Cheng Q, Reznichenko L, Weldy KL, Steed TC, Sridhar VB, MacDonald CL, Cui J, Gratiy SL, Sakadzic S, Boas DA, Beka TI, Einevoll GT, Chen J, Masliah E, Dale AM, Silva GA, Devor A (2013) In vivo stimulus-induced vasodilation occurs without IP3 receptor activation and may precede astrocytic calcium increase. *J Neurosci* 19:8411–8422
- Olney JW, Labruyere J, Wang G, Wozniak DF, Price MT, Sesma MA (1991) NMDA antagonist neurotoxicity: mechanism and prevention. *Science* 254(5037):1515–1518
- Patel AR, Ritzel R, McCullough LD, Liu F (2013) Microglia and ischemic stroke: a double-edged sword. *Int J Physiol Pathophysiol Pharmacol* 5(2):73–90
- Rovainen CM, Woolsey TA, Blocher NC, Wang D-B, Robinson OF (1993) Blood flow in single surface arterioles and venules on the mouse somatosensory cortex measured with videomicroscopy, fluorescent dextrans, nonoccluding fluorescent beads, and computer-assisted image analysis. *J Cereb Blood Flow Metab* 13:359–371
- Schaffer CB, Friedman B, Nishimura N, Schroeder LF, Tsai PS, Ebner FF, Lyden PD, Kleinfeld D (2006) Two-photon imaging of cortical surface microvessels reveals a robust redistribution in blood flow after vascular occlusion. *PLoS Biol* 4:258–270
- Scheller MS, Tateishi A, Drummond JC, Zornow MH (1988) The effects of sevoflurane on cerebral blood flow, cerebral metabolic rate for oxygen, intracranial pressure, and the electroencephalogram are similar to those of isoflurane in the rabbit. *Anesthesiology* 68(4):548–551
- Secomb TW, Hsu R, Pries AR (1998) A model for red blood cell motion in glycocalyx-lined capillaries. *Am J Physiol Heart Circ Physiol* 274:H1016–H1022
- Shih AY, Friedman B, Drew PJ, Tsai PS, Lyden PD, Kleinfeld D (2009) Active dilation of penetrating arterioles restores red blood cell flux to penumbral neocortex after focal stroke. *J Cereb Blood Flow Metab* 29:738–751
- Shih AY, Nishimura N, Nguyen J, Friedman B, Lyden PD, Schaffer CB, Kleinfeld D (2011) Optically induced occlusion of single blood vessels in neocortex. In: Konnerth A, Yuste R, Helmchen F (eds) *Imaging in neuroscience: a laboratory manual*. Cold Spring Harbor Laboratory Press, New York, pp 939–948
- Shih AY, Drew PJ, Mateo C, Tsai PS, Kleinfeld D (2012a) A polished and reinforced thinned skull window for long-term imaging and optical manipulation of the mouse cortex. *J Vis Exp* 7(61)
- Shih AY, Driscoll JD, Drew PJ, Nishimura N, Schaffer CB, Kleinfeld D (2012b) Two-photon microscopy as a tool to study blood flow and neurovascular coupling in the rodent brain. *J Cereb Blood Flow Metab* 32(7):1277–1309
- Shih AY, Blinder P, Stanley G, Tsai PS, Friedman B, Lyden PD, Kleinfeld D (2013) The smallest stroke: occlusion of one penetrating vessel leads to infarction and a cognitive deficit. *Nat Neurosci* 6(1):55–63
- Siesjo BK, Bengtsson F (1989) Calcium fluxes, calcium antagonists, and calcium-related pathology in brain ischemia, hypoglycemia, and spreading depression: a unifying hypothesis. *J Cereb Blood Flow Metab* 9:127–140
- Takano T, Tian GF, Peng W, Lou N, Libionka W, Han X, Nedergaard M (2006) Astrocyte-mediated control of cerebral blood flow. *Nat Neurosci* 9:260–267
- Takuwaa H, Matsuura T, Obataa T, Kawaguchia H, Kannoa I, Ito H (2012) Hemodynamic changes during somatosensory stimulation in awake and isoflurane-anesthetized mice measured by laser-Doppler flowmetry. *Brain Res* 1472:107–112
- Thrane AS, Thranea VR, Zeppenfeld D, Loua N, Xua Q, Nagelhus EA, Nedergaard M (2012) General anesthesia selectively disrupts astrocyte calcium signaling in the awake mouse cortex. *Proc Natl Acad Sci* 109(46):18974–18979
- Tsai PS, Kaufhold J, Blinder P, Friedman B, Drew P, Karten HJ, Lyden PD, Kleinfeld D (2009) Correlations of neuronal and microvascular densities in murine cortex revealed by direct counting and colocalization of cell nuclei and microvessels. *J Neurosci* 18:14553–14570



- Valmianski I, Shih AY, Driscoll J, Matthews DM, Freund Y, Kleinfeld D (2010) Automatic identification of fluorescently labeled brain cells for rapid functional imaging. *J Neurophysiol* 104:1803–1811
- Verhaegen M, Todd MM, Warner DS (1992) The influence of different concentrations of volatile anesthetics on the threshold for cortical spreading depression in rats. *Brain Res* 581(1):153–155
- Villringer A, Haberl RL, Dirnagl U, Anneser F, Verst M, Einhaupl KM (1989) Confocal laser microscopy to study microcirculation on the rat brain surface *in vivo*. *Brain Res* 504:159–160
- Wake H, Moorhouse AJ, Jinno S, Kohsaka S, Nabekura J (2009) Resting microglia directly monitor the functional state of synapses *in vivo* and determine the fate of ischemic terminals. *J Neurosci* 29(13):3974–3980
- Winship IR, Murphy TH (2008) Calcium imaging reveals functional rewiring of single somatosensory neurons after stroke. *J Neurosci* 28(26):6592–6606
- Wu X, Lu Y, Dong Y, Zhang G, Zhang Y, Xu Z, Culley DJ, Crosby G, Marcantonio ER, Tanzi RE, Xie Z (2012) The inhalation anesthetic isoflurane increases levels of proinflammatory TNF- $\alpha$ , IL-6, and IL-1 $\beta$ . *Neurobiol Aging* 33(7):1364–1378
- Xu HT, Pan F, Yang G, Gan WB (2007) Choice of cranial window type for *in vivo* imaging affects dendritic spine turnover in the cortex. *Nat Neurosci* 10:549–551
- Yang G, Pan F, Parkhurst CN, Grutzendler J, Gan WB (2010) Thinned-skull cranial window technique for long-term imaging of the cortex in live mice. *Nat Protoc* 5:201–208
- Ye X, Lian Q, Eckenhoff MF, Eckenhoff RG, Pan JZ (2013) Differential general anesthetic effects on microglial cytokine expression. *PLoS One* 8(1):e52887
- Zhang S, Boyd J, Delaney KR, Murphy TH (2005) Rapid reversible changes in dendritic spine structure *in vivo* gated by the degree of ischemia. *J Neurosci* 25:5333–5338

## Chapter 3

# In Vivo Imaging in Neurodegenerative Diseases

Xueying Wang, Michal Arbel-Ornath, Susanne K. Wegmann,  
Ksenia V. Kastanenka, and Brian J. Bacsikai

**Abstract** *In vivo* neuroimaging techniques provide a fundamental approach for neurological discovery. Popular tools such as magnetic resonance imaging (MRI), positron emission tomography (PET), single photon emission computed tomography (SPECT) and multiphoton microscopy (MPM), are widely used to discover and assess the physiological and pathological changes in the central nervous system (CNS). This chapter reviews the recent progress in advanced brain imaging modalities in neurodegenerative disease studies, as well as their utility in clinical diagnosis and treatment follow-ups. Furthermore, development of high-resolution imaging tools for small animal systems is highlighted given the potential to uncover the underlying mechanisms of neurodegeneration, which will ultimately lead to future therapeutic treatment strategies.

**Keywords** *In vivo* imaging • MRI • PET • SPECT • Multiphoton • Alzheimer's disease • Parkinson's disease

### 3.1 Introduction

Seeing is believing. From the establishment of the basic concept of the nature of light to the development of sophisticated imaging systems, visualization of the human condition with imaging has progressed enormously. Neuroimaging, in particular, has advanced our understanding of brain morphology and physiology in normal and disease states. The development of *in vivo* neuroimaging technologies is now aiming to serve as a reliable and accurate diagnostic tool, as well as a critical readout of pharmacological treatment and drug delivery. In parallel, small-animal imaging approaches have proven to be quite informative for describing the progression of neurological diseases and allowing the design and testing of novel therapeutic strategies.

---

X. Wang • M. Arbel-Ornath • S.K. Wegmann • K.V. Kastanenka • B.J. Bacsikai, PhD (✉)  
Department of Neurology, MassGeneral Institute for Neurodegenerative Diseases,  
Massachusetts General Hospital, 114 16th Street, Charlestown, MA 02129, USA  
e-mail: [bbacsikai@mgm.harvard.edu](mailto:bbacsikai@mgm.harvard.edu)

With the advantage of being non-invasive, magnetic resonance imaging (MRI), positron emission tomography (PET) and single photon emission computed tomography (SPECT) are the most desirable imaging techniques for brain structural and functional studies, and these methods have already been broadly used in clinical and preclinical research for decades. Given the versatility and relatively high spatial and temporal resolutions, MRI enables longitudinal and three-dimensional detection of anatomical and functional changes in the brain associated with neurological disorders, allowing multiparametric assessment of pathology, recovery mechanisms, and treatments in human and/or experimental animal models of stroke, brain tumors, traumatic brain injury, mental disorders, and neurodegenerative diseases. Quantitative emission tomographic methods such as PET and SPECT for *in vivo* measurements of regional rates of cerebral blood flow, glucose metabolism, and protein synthesis have significantly contributed to our knowledge of physiological processes of the brain. With increasing spatial resolution and ultra high sensitivity, PET and SPECT are now carried out to study brain function in animal models. Like MRI, PET and SPECT allow repeated studies of the same animal, i.e., studying the same animal under different conditions or longitudinally. Furthermore, a notable trend in medical imaging is now receiving great attention – the combination of different imaging tools as multimodal imaging modalities, e.g. PET/SPECT (Ono and Saji 2012; Orbay et al. 2013) and PET/MRI (Judenhofer and Cherry 2013), as integrated imaging systems built in combination of PET and SPECT, and PET and MRI, respectively. These hybrids provide complementary information, and therefore, this type of dual-modality assessment of brain function is extremely powerful.

A complementary approach – multiphoton microscopy (MPM), is a powerful *in vivo* tool for brain imaging with subcellular resolution in superficial brain tissues (Bacskai et al. 2001; Zipfel et al. 2003b; Chklovskii et al. 2004; Levene et al. 2004; Svoboda and Yasuda 2006). MPM results in exceptionally high spatial resolution ( $\sim 1\ \mu\text{m}$ ) and high sensitivity in intact neural tissues, and its applications have contributed to our understanding of a broad array of neurological phenomena, including the dynamics of individual protein channels, the functional organization of cortical maps and the pathological changes in disease nervous systems (Lippincott-Schwartz et al. 2001; Bacskai et al. 2003b; Zipfel et al. 2003b; Chklovskii et al. 2004). Even though MPM is fast in image acquisition and offers superior resolution about two orders of magnitude higher than MRI, the major disadvantages are the semi-invasive nature of the approach and the limited detection volume.

### 3.2 Characteristics of Brain Imaging Methods

Ideally, neuroimaging techniques used for diagnosis and treatment follow-up would offer high sensitivity and high spatial and temporal resolution. In the real world, there is often a trade-off between these attributes. When using exogenous contrast agents or radioactive tracers, there are additional constraints as these probes must be validated for specificity, sensitivity, and low toxicity. Additionally, the probes must

be designed to cross the blood-brain barrier (BBB), thus the physicochemical characteristics of the compounds need to be optimized to allow entry into the CNS. Another concern in the use of radioactive probes is that the half-life of the probes should be sufficiently long in order to allow the quantification of specific binding. Furthermore, a good probe/tracer should always prove a high signal-to-noise ratio during detection.

We will be discussing these features and characteristics in the pages below to review the principles of the methods and their applications in either clinical studies or experimental animal models. More critical discussion will be focusing on neurodegenerative diseases such as Alzheimer's Disease (AD), Amyotrophic Lateral Sclerosis (ALS), Huntington's Disease (HD) and Parkinson's Disease (PD).

### 3.3 Magnetic Resonance Imaging

MRI is a conventional medical imaging technique used primarily to visualize internal structures of the body and produce high quality images based on the principles of nuclear magnetic resonance (NMR). Atomic nuclei with an odd number of protons and/or neutrons such as  $^1\text{H}$ ,  $^{13}\text{C}$ ,  $^{15}\text{N}$ ,  $^{19}\text{F}$  or  $^{31}\text{P}$ , possess intrinsic quantum properties that allow the observation of NMR phenomena are theoretically potential candidates for MRI. The two key factors that influence the MRI signal are the natural and biological abundances of the nuclei. Since hydrogen is the most abundant natural element in biological systems and the proton is the most sensitive nucleus to NMR, the MRI signal in most clinical diagnostic tests is based on the spatial detection of the distribution of  $^1\text{H}$ .

A typical MRI machine requires an applied, uniform and powerful magnetic field ( $B_0$ ) to align the nuclear spins in the samples along with the direction of  $B_0$ . Then a radio frequency (RF) pulse is briefly turned on to produce a varying electromagnetic field for induction of NMR to perturb the original spin alignment. Accordingly, lower energy protons absorb the energy from the RF pulse and transit to higher energy states (flipping the spin of the proton in the magnetic field) to bring on NMR. When the electromagnetic field is turned off, a relaxation process occurs, i.e. protons return to thermodynamic equilibrium and get realigned with  $B_0$ . The MRI signal is generated during the relaxation and involves two relatively independent phases: spin-lattice relaxation time ( $T_1$ ) and spin-spin relaxation time ( $T_2$ ).  $T_1$  characterizes the rate at which longitudinal magnetization of the nuclei recovers exponentially towards its equilibrium state by passing the energy obtained previously from the RF pulse (higher energy state) on to the surrounding tissues (the "lattice", i.e. lower energy state), thereby providing the information of local energy exchange and distribution of the atomic nuclei held within a lattice structure. Because different tissues have different  $T_1$  values,  $T_1$  weighted images are used to significantly differentiate between areas such as grey matter and white matter in brain scans (Paus et al. 2001).  $T_2$  represents the time it takes for the transverse magnetization of the nuclei to exponentially decay towards its equilibrium. When the net magnetization

starts to dephase, nuclei experience slightly different magnetic fields due to local molecular interactions and rotate at their own Larmor frequencies resulting from the variations of  $B_0$ . Thus, different samples and different tissues have different  $T_2$  values as well. In comparison to  $T_1$  weighted images,  $T_2$  weighted images are often considered more as “pathology scans” because detection of abnormal tissues is usually at higher contrast than that of normal tissues (Kono et al. 2001).

The principle feature of MRI is its capability of taking high spatial resolution 2D or 3D images of the body. The spatial resolution of MRI achieved in human brain depends on imaging time and magnet strength with resolutions as fine as 0.25 mm at 3 T (van Wijk et al. 2013), although 1 mm is more common. For applications in ultra high-field MRI, the spatial resolution can be obtained up to 0.05 mm in animal studies (Marzola et al. 2003). Given that MRI is a non-invasive imaging tool allowing longitudinal and three-dimensional assessment of brain structure, physiology and function, the clinical as well as preclinical research findings based on various established MRI approaches are of particular interest for neurological disease and/or disorder studies. Diffusion-weighted MRI (DWI) has shown great sensitivity to several cellular changes and tissue abnormalities and the potential for detecting disease at an earlier stage than conventional MRI (Dijkhuizen and Nicolay 2003). Diffusion tensor imaging (DTI) has become one of the most popular forms of diffusion MRI in brain research and clinical studies. DTI maps the diffusion process of molecules (mainly water molecules) in the tissue in three-dimensions, which therefore reveals microscopic details about tissue microstructure in normal or diseased states (Le Bihan et al. 2001). Perfusion MRI techniques are able to measure brain hemodynamics typically coupled with the use of paramagnetic contrast agents. In the last 10 years, functional MRI (fMRI) has proven to be a powerful imaging tool for studying human brain functions in both health and disease. Blood oxygenation level-dependent (BOLD) MRI is the primary form of fMRI pertaining to the magnetic property of blood, which is based on the oxygenation state of hemoglobin (Ogawa et al. 1990). Detecting local changes in blood flow and oxygenation related to active brain regions, BOLD MRI can localize brain activity and allow mapping of function to location. More importantly, fMRI methods also allow the study of the underlying networks within the brain (Guye et al. 2010).

In this review section, we will provide an overview of the present clinical and preclinical applications of MRI particularly in neurodegenerative disease studies and discuss the current promising developments in the field and their potential for future clinical applications.

### 3.3.1 MRI in Alzheimer’s Disease

Imaging as a widely accepted and well-established *in vivo* biomarker has been playing a significant role in clinical diagnostic use for specific pathologies. Alzheimer’s disease is a complex progressive condition that involves sequentially interacting pathological cascades, which are associated with accumulation of abnormal

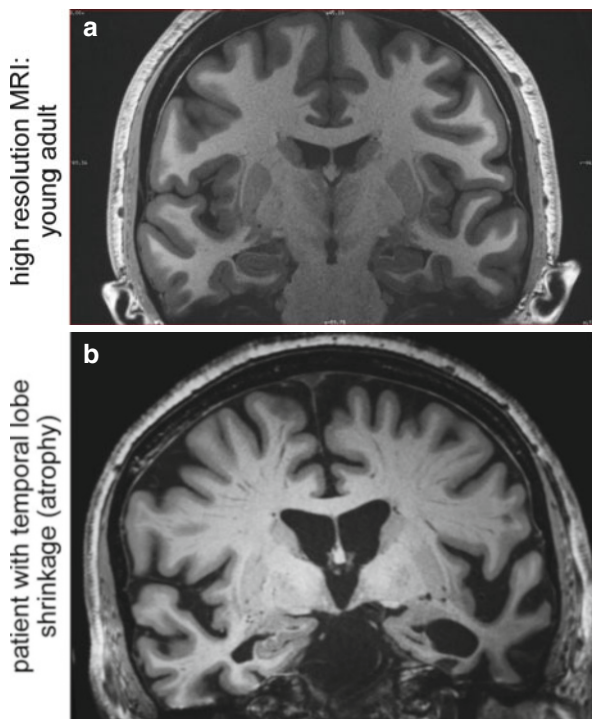
proteins (amyloid- $\beta$  and hyperphosphorylated tau) and activated microglia in the brain that lead to synaptic, neuronal and axonal damage (Davies et al. 1987; Hardy and Higgins 1992; Barger and Harmon 1997; Phinney et al. 1999; Small et al. 2001; Selkoe 2002). One big challenge for AD diagnosis on MRI is that neurological changes (e.g. substantial neuronal loss) occur years before detectable cognitive symptoms appear (Gomez-Isla et al. 1996). In recent years, measures of brain atrophy on MRI have been reliable markers of AD pathology (Bobinski et al. 2000; Jack et al. 2002; Silbert et al. 2003; Jagust et al. 2008) in human clinical studies. For thorough introduction and summary of neuroimaging in AD, see Johnson et al. 2012 for review.

Structural MRI in clinically affected AD patients has demonstrated significant tissue damage or loss in characteristically vulnerable brain regions, such as the hippocampus, entorhinal cortex, amygdala and supramarginal gyrus (Desikan et al. 2009; Dickerson et al. 2009). In longitudinal studies, MRI can serve as a potential marker to distinguish between disease-modifying drug effects and purely symptomatic treatment effects by monitoring the rate of atrophy of certain brain areas (Frisoni et al. 2010; Hampel et al. 2010). Moreover, the clinical application of structural MRI in differentiating AD from other brain pathologies, such as vascular or non-AD neurodegeneration, has been fairly established as well (Frisoni et al. 2010). Meanwhile, fMRI studies of memory in patients with AD have revealed a pattern of altered activation in the medial temporal lobes and parietal lobes, wherein recent single-center studies in AD, have exhibited the discovery of particular treatment effects on regional brain activation (Bokde et al. 2009). Multicenter and longitudinal studies using fMRI in AD patients seem to be a more feasible approach given the successful demonstrations using classic static biomarkers (e.g. hippocampal volume). The current state of fMRI as a tool in providing informative dynamic diagnostic biomarkers in AD is promising, however, further rigorous validation is needed (Hampel et al. 2010, 2011; Prvulovic et al. 2011).

Additionally, studies using transgenic animal models of AD have been focusing on the detection of the well-known AD pathological hallmark – amyloid- $\beta$  (A $\beta$ ) plaques by magnetic resonance microimaging (MRMI) with or without paramagnetic contrast agents (Poduslo et al. 2002; Wadghiri et al. 2003; Jack et al. 2004; Falangola et al. 2005). In studies pursuing non-invasive MRMI with intrinsic imaging contrast (i.e., without administration of an exogenous labeling agent), the spatial resolution of the detection is not capable of resolving individual plaques (Jack et al. 2004; Falangola et al. 2005). On the contrary, plaque-labeling contrast media has been used in MRMI with success (Poduslo et al. 2002; Wadghiri et al. 2003). Gadolinium (Gd) tagged A $\beta$  fragments have been used to identify senile plaques *in vivo*, but require manipulations of the blood-brain barrier and only recognize a subset of plaques with relatively low sensitivity (Poduslo et al. 2002; Wadghiri et al. 2003). Other contrast agents have also been assessed by exploiting the negligible background of  $^{19}\text{F}$  (Higuchi et al. 2005) or with the use of superparamagnetic iron oxide (USPIO) nanoparticles that have a limiting capability of entering brain (Wadghiri et al. 2013). In brief, MRMI in transgenic animals has the potential for *in vivo* imaging but suffers from the same limitations of sensitivity (Fig. 3.1) (Jack et al. 2007).



**Fig. 3.1** Ultrahigh-resolution (380  $\mu\text{m}$  in-plane voxel size) structural MRI images of the human brain in (a) a 24 year-old neurologically intact individual and in (b) a 72 year-old patient with mild Alzheimer's disease. In the young individual, a variety of brain regions can be clearly seen at a level of resolution not typically visible in most routine MRI scans, demonstrating the potential value of advanced image acquisition techniques; in the patient with neurodegenerative disease, atrophy (shrinkage) of numerous structures particularly within the temporal lobe is obvious (Images courtesy of Dr. Brad Dickerson, Massachusetts General Hospital)



### 3.3.2 MRI in Amyotrophic Lateral Sclerosis

Amyotrophic Lateral Sclerosis (ALS) is a progressive degeneration of the motor system, comprised of upper motor neurons of the primary motor cortex and corticospinal tract, medullary brainstem nuclei, and the lower motor neurons arising from the anterior horns of the spinal cord (Kiernan et al. 2011). Other extra-motor cerebral neuronal populations in the frontal and temporal lobes are also involved in ALS (Smith 1960). Thus, the core feature of ALS pathology is the involvement of the CNS and therefore, discovery of biomarkers in ALS has been prioritized due to the remarkable clinical heterogeneity, frequent diagnostic delay and reliance of therapeutic trials on survival (Turner et al. 2009). Automated and unbiased whole-brain analysis techniques established based on  $T_1$ -weighted images include voxel-based morphometry (VBM) that measures relative grey and white matter volumes in specific brain regions (Ashburner and Friston 2000) and surface-based morphometry (SBM) that measures cortical thickness (Fischl and Dale 2000; Das et al. 2009). Studies implementing VBM in ALS patients have found grey matter atrophy in the motor cortex (Chang 2005; Kassubek 2005; Grosskreutz 2006; Agosta 2007; Turner 2007) and two longitudinal studies have demonstrated progressive atrophy in extra-motor as well as motor regions (Agosta 2009a; Senda 2011), but this method has constantly shown poor consistency and low sensitivity (Turner et al. 2012). SBM studies have consistently found reductions in cortical thickness in the ALS motor cortex (Roccatagliata et al. 2009; Agosta 2012; Libon 2012; Verstraete 2012) and



longitudinal studies have also reported progressive cortical thinning over 9 months (Agosta 2009a). SBM seems more advantageous over VBM as it not only provides higher reliability and sensitivity, but also allows decomposition of cortical volumes into both thickness and surface area (Pereira et al. 2012; Turner et al. 2012).

Diffusion tensor imaging is highly sensitive to cerebral white matter pathology and has increasing potential in the spinal cord (Basser et al. 1994; Pierpaoli and Basser 1996), thus it has been widely used in ALS studies. Two main scalar measures in DTI are fractional anisotropy (FA) that examines the degree of a preferred axis of water diffusion and mean diffusion (MD) that averages water diffusivity properties from all three axes (Foerster et al. 2013), and both measurements should be interpreted with care (Alexander et al. 2007). DTI studies have consistently reported decreased FA and increased MD (Turner et al. 2012; Foerster et al. 2013) within the corticospinal tract (Ellis 1999; Abe 2004; Graham 2004; Cosottini 2005; Ciccarelli et al. 2006; Sage et al. 2007; Iwata 2008; Roccatagliata et al. 2009; Senda 2009; Agosta 2010; Filippini et al. 2010), corpus callosum (Sach 2004; Agosta 2007; Sage et al. 2007; Ciccarelli 2009; Senda 2009; Filippini et al. 2010; Verstraete et al. 2010; Zhang 2011; Rose et al. 2012), frontal lobe (Abe 2004; Sach 2004; Sage et al. 2007; Prell et al. 2013), deep grey nuclei (Sach 2004; Thivard 2007; Sharma et al. 2012), and brainstem (Toosy 2003; Iwata 2008; Lombardo 2009). DTI has also been applied to differentiate clinical phenotypes (Rajagopalan et al. 2013) and quantify white matter changes in patients with a slowly progressive familial form of ALS (Turner et al. 2012). For longitudinal studies, DTI has been employed to track white matter changes in ALS though such investigations are challenging as accumulated disability, particularly orthopnea resulting from diaphragm weakness, may preclude MRI implementation (Blain 2007; Mitsumoto 2007; Sage et al. 2007; Agosta 2009b; van der Graaff et al. 2011). In this regard, DTI is currently unrivaled as an exceptional neuroimaging biomarker of upper motor neuron involvement in ALS, although its sensitivity to longitudinal changes may be limited.

Resting-state functional connectivity MRI (rs-fcMRI) offers a unique opportunity to access and study ALS pathology through its indirect visualization of inter-related cerebral networks (Turner et al. 2012; Foerster et al. 2013). Previous rs-fcMRI studies have shown decreased motor network connectivity (Mohammadi 2009; Jelsone-Swain 2010; Tedeschi 2012), or a trend towards decreased motor network connectivity (Verstraete 2010). Interestingly, a combination of rs-fcMRI and DTI modalities has proven the increased connectivity of motor network in ALS patients with greater disease burden (Douaud et al. 2011). These findings may offer critical insights when applied to presymptomatic ALS cases, and with patient enrollment at earlier stages of the disease, longitudinal studies of changes in intrinsic connectivity in ALS are highly demanded for further investigation.

### 3.3.3 MRI in Huntington's Disease

Huntington's disease is an inherited neurodegenerative disease characterized by progressive dementia and chorea, starting around 30–40 years of age in humans. HD is caused by a dominantly inherited CAG repeat expansion mutation (in the

gene *IT15* of chromosome 4) that generates lengthening of the protein huntingtin with size-dependent neurotoxicity, and the length of this CAG repeat correlates with the age of onset of HD and the extent of neuropathology at death (Group THsDCR 1993; Furtado et al. 1996). Given that the CAG repeat expansion is an excellent biomarker for identifying the mutant gene carriers, the development of genetic screens has been very successful in diagnosis and prognosis of the disease and thereby somewhat lowered the need of using brain-imaging techniques in the past. Nevertheless, the symptoms and progression of HD are highly variable that in turn leads to the variability in clinical measures. In that regard, HD clinical trials of neuroprotective treatments are subject to large numbers of participants and long trial durations (Rosas et al. 2004). Newer neuroimaging methods as a sensitive and reliable surrogate biomarker have indicated huge potential in testing neuroprotective agents in clinical trials and monitoring the overall progression of the disease. Furthermore, the combination of genetic screening with imaging modalities also promotes the study of the phenotype-genotype relationship in HD (Mascalchi et al. 2004).

Early structural MRI studies concentrated on striatal atrophy (the caudate nucleus and putamen) and reported a pattern of fast and linear loss of striatal tissue over time in individuals between 20 and 5 years from predicted disease onset (Paulsen et al. 2008). Substantial loss of diffuse white matter, correlating with the decline in cognitive and motor performance, has been described in HD patients as well (Hobbs et al. 2010). In addition, observed cortical volume loss may suggest a possible role of individual variability in regional cortical volume loss, which in turn provides an interpretation of phenotypic variability (Rosas et al. 2008). Furthermore, powerful longitudinal effect sizes for varied brain regions in patients with premanifest disease and early HD have been detected by structural MRI (Aylward et al. 2011; Tabrizi et al. 2011) and other research has demonstrated that the presence of neurodevelopmental anomalies can be identified by the very early structural changes in premanifest disease (Nopoulos et al. 2011).

By providing information on neuronal fiber orientation and white matter connectivity, DTI has been utilized in HD studies to distinguish premanifest individuals from controls and measure white matter degeneration longitudinally. One recent study has shown altered white matter connections of the sensorimotor cortex in both manifest and premanifest HD (Dumas et al. 2012). On the other hand, T<sub>2</sub>-weighted imaging has been applied to patients with premanifest disease and linking the number of hypointensities (indicators of iron deposition in the basal ganglia that has been identified in HD) to motor dysfunction, CAG repeat length and a greater probability of developing symptoms within 5 years (Jurgens et al. 2010).

Data from fMRI studies have identified both reduced and enhanced cortical activations in HD patients during cognitive tasks and the inconsistencies between studies are consequent upon the differences in examined brain regions, cognitive task types and task complexity (Georgiou-Karistianis 2009). Most have shown impaired task performance as well as significantly reduced task-related activations in several subcortical and cortical regions (Kim et al. 2004; Wolf et al. 2008a, b), whereas findings of enhanced activation in various cortical areas are also widely

demonstrated (Dierks et al. 1999; Clark et al. 2002; Georgiou-Karistianis et al. 2007) that has often been interpreted as cortical recruitment – a compensatory mechanism for task performances typically activated by dysfunctional brain regions. Recent cortical activation studies have also provided evidence of neuronal dysfunction preceding even the earliest phenotypes of HD (Georgiou-Karistianis 2009) and led to the suggestion that premanifest disease could even be divided into different stages (Weir et al. 2011).

### 3.3.4 MRI in Parkinson's Disease

Parkinson's disease (PD) is a chronic and progressive degenerative neurological disorder characterized by bradykinesia, resting tremor, rigidity and postural instability. A disturbed  $\alpha$ -synuclein protein forming so-called Lewy bodies seems to play a causal role, which led to the designation of PD as a  $\alpha$ -synucleinopathy. The main pathophysiological changes result from degeneration of dopaminergic neurons in the substantia nigra, but degradations in serotonergic, cholinergic, noradrenergic, opioid and other central neurotransmitter systems are also involved (Jellinger 1991; Braak et al. 2003). Therefore, PD is now considered a multisystem degenerative process given the complex and widespread atrophy events during development (Brooks and Pavese 2011).

Early conventional MRI showed brain structural changes as reductions in volume (atrophy) and alterations in  $T_1$ - and  $T_2$ -weighted MRI signals but it failed in diagnosis of idiopathic PD and detection of reduced nigral volume in PD (O'Neill et al. 2002; Geng et al. 2006), thus was performed in a restricted manner in PD studies (Brooks and Pavese 2011). Recently, diffusion weighted (DWI) or diffusion tensor (DTI) magnetic resonance imaging has been used to quantify loss of anisotropy or demonstrate disruption of neural tracts. DWI has been reported to be highly sensitive to changes in striatal structure (Schocke et al. 2002; Seppi et al. 2003; Nicoletti et al. 2006; Paviour et al. 2007) and could be evaluated for use in early stage diagnostic imaging (Brooks and Pavese 2011). By detecting the regional fractional anisotropy (FA) within the nigra, high-resolution DTI has also revealed great potential in increasing the sensitivity of MRI detection of structural changes. A recent study has reported reduced nigral FA in patients with established PD in comparison to a control group (Vaillancourt et al. 2009), which may suggest DTI to be a meaningful tool in support of PD diagnosis.

Meanwhile, functional MRI has been increasingly used to study PD (Nandhagopal et al. 2008). Changes in the BOLD signal determined by fMRI during different tasks or behavioral conditions can provide important information for assessment of the dynamic effects of motor tasks, behavioral and sensory modulation, pharmacologic manipulations and surgical intervention. Functional MRI has been applied to infer modulation of cortical motor activation where impaired activation of the pre-supplementary motor area (SMA) and dorsolateral prefrontal area (DLPFC) leads to abnormal pallidal outflow during both motor imagery and actual movement

(Cunnington et al. 2001; Thobois et al. 2002). Moreover, clinical studies that emphasize the pattern of deactivation of regional cerebral blood flow (rCBF) during transition from baseline (usually the resting state) to more cognitively demanding conditions, have shown inconsistent responses to treatment. One study revealed that ventromedial prefrontal cortex (vmPFC) was the only brain region in which deactivation correlated with task complexity during treatment with the dopamine receptor agonist apomorphine (Nagano-Saito et al. 2009). Another study, on the contrary, showed impaired posterior midline deactivation during a facial emotion recognizing task in unmedicated PD patients, which can be restored by levodopa (Delaveau et al. 2010). These different observations may be the result of differences in baseline cognitive condition, cognitive task and imaging modality. Despite these controversies, fMRI has been exploring PD as a model of dopamine deficiency and serving as a platform to appreciate the role of dopaminergic transmission in neurobehavioral processes.

### 3.4 Positron Emission Tomography and Single Photon Emission Computed Tomography

Positron emission tomography (PET) and single photon emission computed tomography (SPECT, or less commonly, SPET) are two leading nuclear medicine imaging techniques of emission tomography (ET) – a branch of medical imaging that uses radioactive probes to image properties of the body's physiology. PET and SPECT are constructed on the basis of two principles: imaging through the use of gamma-ray emission (called the *tracer principle*) and volumetric imaging of the body's interior (called *tomography*) (Wernick and Aarsvold 2004). Tracer principle requires the introduction (usually by intravenous injection) of biologically active molecules labeled with positron emitting radionuclides as representative markers, or tracers, which is the foundation of present-day PET and SPECT imaging. Development of artificial radiopharmaceuticals has provided valuable diagnostic information revealing the natural and pathological processes of the body. On the other hand, the magic of tomography is that three-dimensional information of tracer concentration within the body can be reconstructed by computer analysis to generate tomographic images. Thus, the basic working theory of PET and SPECT is that they use the energy (gamma photon) emitted during the radioactive decay of unstable isotopes to produce three-dimensional tomographic images that characterize functional processes in the body. In this way, both PET and SPECT have been used extensively in either clinical or research fields for diagnosis of cancer or certain brain diseases such as various types of dementias, mapping normal human brain and heart function, measurement of metabolic processes, protein synthesis, receptor binding, receptor gene expression, and drug development (Phelps 2000; Sharma et al. 2002; Herholz 2003; Wagner et al. 2006; Chen 2007; Dobrucki and Sinusas 2010; Benadiba et al. 2012).

PET and SPECT are non-invasive and exceptionally sensitive imaging tools with the capability of detecting concentrations of neuroreceptors, transporters, as well as neurotransmitters in the picomolar range with high signal-to-noise ratio (SNR),

which is extremely helpful for defining and diagnosing pathological status and changes when structural neuroimaging is unable to fully elucidate the symptoms. More importantly, PET and SPECT allow the same subject (human or animal) to be studied repeatedly over a period of time (weeks or months), which is extremely useful for monitoring the effects of a wide range of interventional strategies or animal models of chronic disease (Jacobs and Cherry 2001). However, one classic weakness of PET systems is the physical limits of spatial resolution due to detector size, photon noncollinearity and positron range (i.e., the distance between the positron emission and the point of annihilation). For human PET imaging, spatial resolution could be achieved up to 3–5 mm in the whole body scanners and 2 mm in the head scanners. Although SPECT scanners have theoretically “unlimited” intrinsic resolutions, the loss of sensitivity precludes the realization and the achievable spatial resolution for SPECT at present is 10 mm (Khalil et al. 2011). In recent years, PET imaging systems that have been developed for small animal model imaging ( $\leq 20$  cm diameter), now open up a number of new investigative possibilities. High-resolution PET studies have shown spatial resolutions ranges from  $\sim 0.6$  mm for PET isotope  $^{18}\text{F}$  to  $\sim 1.6$  mm for  $^{15}\text{O}$  (Schmidt and Smith 2005; Smith et al. 2005). Even though these improved numbers are still comparably insufficient to detect and identify sub-cellular structures or small microlesions, small-animal PET scanners are still actively being constructed with the hope of bringing the cameras to higher sensitivity and resolution for future studies.

In current PET applications, frequently used positron emitters are  $^{11}\text{C}$ ,  $^{13}\text{N}$ ,  $^{15}\text{O}$  and  $^{18}\text{F}$ , which are nuclides with short-half lives ranging from 2.05 min ( $^{15}\text{O}$ ) to 109.8 min ( $^{18}\text{F}$ ) (Otte and Halsband 2006). Compounds labeled with longer half-life radionuclides such as  $^{123}\text{I}$  and  $^{99\text{m}}\text{Tc}$  are more commonly used in SPECT imaging (Benadiba et al. 2012). These positron emitters can then be labeled to molecules such as glucose in the form of  $^{18}\text{F}$ -labeled 2-deoxy-2-fluoro-D-glucose (FDG) for PET (Otte and Halsband 2006) or  $^{99\text{m}}\text{Tc}$ -labeled FDG for SPECT (Stoll et al. 1994; Sandler et al. 1998). Although these radioprobes have been developed for decades, the designs are still mainly based on glucose metabolism for present studies. Therefore, an emerging major challenge for PET or SPECT imaging is to further develop its currently limited availability of radiotracers. Given that PET and SPECT imaging offer superior sensitivity, this continues to be a promising field with advances in the development of PET and SPECT techniques.

Research studies of functional brain activity generally image changes in blood flow or metabolic processes using  $^{18}\text{F}$ -FDG. This approach has been used extensively in cancer studies to localize primary tumors and their metastases and AD cases to provide a sensitive indirect surrogate marker with proven diagnostic accuracy (Silverman et al. 2001). Moreover,  $^{18}\text{F}$ -FDG PET studies also show a detectable preferential reduction in posterior cingulate activity before primary cognitive symptoms are observed (Mankoff and Bellon 2001; Weber 2009). For SPECT studies of regional cerebral blood flow,  $^{99\text{m}}\text{Tc}$ -d,l-hexamethylpropyleneamine oxime (HMPAO) is widely used as either a diagnostic tool or an assessment of drug therapies when chronic treatments are needed. By this means, blood flow and metabolism have been evaluated in depression (Kowatch et al. 1999; Fountoulakis et al. 2004),

schizophrenia (Catafau et al. 1994; Gonul et al. 2003; Wake et al. 2010), AD and dementia (Holman et al. 1992; Kemp et al. 2005; Nobili et al. 2007; Papma et al. 2013; Yeo et al. 2013), and HD (von Horsten et al. 2003; Pimlott and Sutherland 2011). In this section, we focus on the implementation of PET and SPECT techniques in current studies of neurodegenerative disease and discuss the potential applications for future development.

### 3.4.1 PET and SPECT in Alzheimer's Disease

PET enables a broad range of *in vivo* assessments of functional processes in the AD brain and provides quantitative regional brain data that can be used to objectively evaluate diagnostic accuracy and treatment effects (for review, see Nordberg et al. 2010). Radiotracer  $^{18}\text{F}$ -FDG has been widely used to monitor brain glucose metabolism and thus has been employed in AD PET imaging in both research and clinical studies (Herholz et al. 2007; Small et al. 2008). Progressive reduction in glucose metabolism measured by  $^{18}\text{F}$ -FDG shows great potential in early-stage diagnosis (Mosconi et al. 2009; Chew and Silverman 2013) and has been demonstrated to correlate with severity of dementia (Mosconi 2005; Engler et al. 2006) although its ability of differentiating AD from frontotemporal dementia is rather low (Mosconi 2005; Jagust et al. 2007). Functional changes in the brain can be detected by  $^{18}\text{F}$ -FDG in healthy individuals who are at risk with familial AD-causing mutations (Small et al. 1995; Reiman et al. 2004; Mosconi 2005; Schöll et al. 2011). Given that  $^{18}\text{F}$ -FDG is a marker of clinical measures in AD (Matthews et al. 2003; Dickerson and Sperling 2005; Foster et al. 2008), it might also be useful for characterizing the longitudinal changes in function resulting from drug treatment in patients with AD (Drzezga et al. 2003; Diehl-Schmid et al. 2006, 2007).

Amyloid binding PET ligands, such as  $^{18}\text{F}$ -FDDNP (Shoghi-Jadid et al. 2002),  $^{11}\text{C}$ -PIB (Klunk et al. 2004),  $^{11}\text{C}$ -SB-13 (Verhoeff et al. 2004),  $^{18}\text{F}$ -BAY94-9172 (Rowe et al. 2008),  $^{18}\text{F}$ -AV-45 (Choi et al. 2009),  $^{18}\text{F}$ -flumetamol (Nelissen et al. 2009), and  $^{11}\text{C}$ -AZD2184 (Nyberg et al. 2009) have been developed to enable *in vivo* imaging of brain amyloid. Among these tracers,  $^{11}\text{C}$ -PIB is perhaps the best-characterized compound (Klunk et al. 2004; Rowe et al. 2007).  $^{11}\text{C}$ -PIB retention is increased in cortical and subcortical brain regions in AD patients compared with similar regions in healthy controls (Klunk et al. 2004) and correlated very well with levels of amyloid in AD brain tissue taken at autopsy (Ikonomovic et al. 2008; Leinonen et al. 2008; Svedberg et al. 2009).  $^{11}\text{C}$ -PIB has high affinity (within nanomolar range) for binding fibrillar A $\beta$  and crosses the BBB readily, making itself a popular and effective radioligand for PET imaging in AD. Other amyloid tracers have also been developed for clinical PET imaging (Rowe and Villemagne 2013) that have overcome the issues related to binding affinity, lipophilicity and sensitivity. Ultimately, an  $^{18}\text{F}$ -labeled tracer has advantages over  $^{11}\text{C}$ -labeled compounds for clinical studies because of the longer half-life (110 min vs. 20 min, respectively). Great success has been achieved with florbetapir, and a number of other ligands



(Vandenberghe et al. 2013). Furthermore, it would be of great interest in developing PET tracers to detect and visualize oligomeric A $\beta$  instead of its fibrillar form in the brain (Nordberg et al. 2010).

Inflammation has been known to be associated with AD, and is characterized by the upregulation of activated microglia. The radiotracer  $^{11}\text{C}$ -(R)-PK11195, a peripheral benzodiazepine receptor ligand, has been used to visualize inflammatory lesions (Cagnin 2001; Debruyne et al. 2003). This compound was applied in a study of AD patients and exhibited an increased binding of  $^{11}\text{C}$ -(R)-PK11195 in the temporal cortex, hippocampus and parietal cortex compared with healthy controls (Cagnin 2001). However, this measurement is an indirect and non-specific approach for assessing the mechanisms underlying AD, and requires further validation.

Two technetium ( $^{99\text{m}}\text{Tc}$ ) and rhenium (Re) labeled ligands have been recently synthesized for amyloid imaging with SPECT. However, these compounds show low affinity for fibrillar A $\beta$  and require further refinements in order to improve their diffusibility through BBB (Cui et al. 2011). Given that SPECT is less sensitive with lower spatial resolution compared with PET, the detection accuracy of SPECT may show differences from current PET amyloid imaging (Benadiba et al. 2012). SPECT tracers for inflammation have shown promising results, for instance,  $^{123}\text{I}$ -PK11195 has recently been used in a pilot SPECT study with AD patients (Versijpt et al. 2003). In addition, the  $^{123}\text{I}$ -radiolabeled compound  $^{123}\text{I}$ -CLINDE has also been successfully tested in preclinical studies. Using different animal models of neuroinflammation,  $^{123}\text{I}$ -CLINDE demonstrates its capability of assessing both astroglial and microglial activations by targeting the activation-related 18 kDa translocator protein (Fig. 3.2) (Arlicot et al. 2008; Mattner et al. 2011).

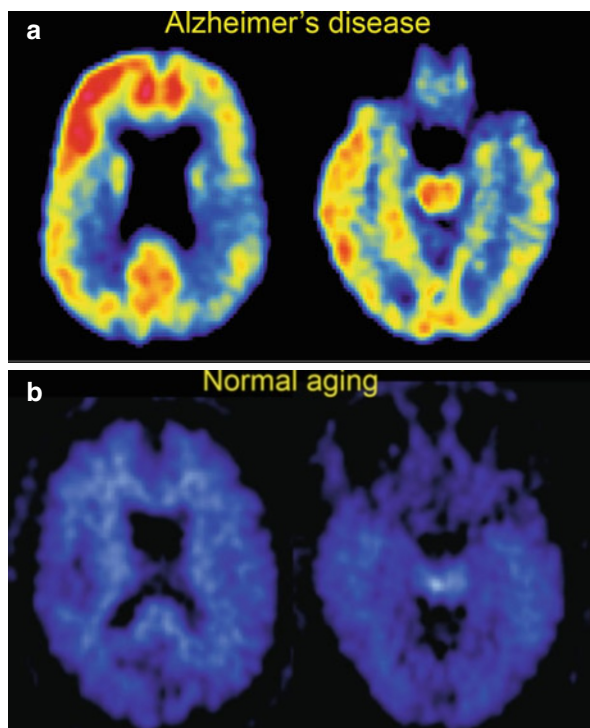
### 3.4.2 PET and SPECT in Amyotrophic Lateral Sclerosis

Early studies with PET in ALS using  $^{18}\text{F}$ -FDG has revealed widespread and progressive reductions in cortical glucose metabolism in ALS patients in parallel with clinical deterioration (Dalakas et al. 1987). Another report confirmed this measure and linked it to neuropsychological deficits in verbal fluency (Ludolph et al. 1992). Alternative tracers  $\text{H}_2^{15}\text{O}$  and  $\text{C}^{15}\text{O}_2$  were used to demonstrate similar reductions in regional cerebral blood flow in ALS patients with dementia (Tanaka et al. 1993) as well as abnormalities of verbal fluency in ALS patients without overt dementia (Kew et al. 1993a). The shift in the boundary of the upper limb output zone through cortical activation in response to a free selection task supplied early evidence for a potential loss of inhibitory cortical influence (Kew et al. 1993b).

Given that radiotracers can be developed to selectively bind to receptors on specific neuronal populations, various PET ligands have been designed to illustrate different aspects of the pathogenesis in ALS. In keeping with the emerging theme of a multisystem cerebral degeneration, an early PET study using the radiotracer  $^{18}\text{F}$ -6-fluoradopa that was originally developed for studies in PD, provided striking evidence for loss of nigral dopaminergic cells in ALS (Takahashi et al. 1993). More



**Fig. 3.2** Trans-axial amyloid PET images acquired with  $^{11}\text{C}$  Pittsburgh Compound B ( $^{11}\text{C}$ -PIB) from (a) a 72 year-old man with mild AD dementia (*top row*) show extensive fibrillar  $\text{A}\beta$  deposition throughout the cortex (*red and yellow areas*), compared to (b) a 78 year-old cognitively normal woman (*bottom row*) in whom only low, non-specific binding can be seen (*light blue*) (Images courtesy of Dr. Keith Johnson, Massachusetts General Hospital)



interestingly, the use of GABA<sub>A</sub> receptor ligand  $^{11}\text{C}$ -flumazenil has paved the way for pivotal PET ligand studies with respect to the widespread extra-motor cortical changes. The extensive decreases in cortical binding suggest the potential impact on loss of GABAergic interneurons (Lloyd et al. 2000), backing up an established mechanism of excitotoxicity in ALS through glutamate dysregulation (Turner and Kiernan 2012). Subsequent  $^{11}\text{C}$ -flumazenil PET studies in patients with a mutant superoxide dismutase 1 (*SOD1*) gene that causes both sporadic ALS and familial-type ALS, have shown relative preservation of binding in motor cortex and motor associated regions in sporadic ALS only, demonstrating the increased cortical excitability in sporadic ALS patients and supporting the idea that preservation of inhibitory influence may have prognostic significance (Turner et al. 2005a). Furthermore, neuroinflammatory mechanisms in the pathogenesis of ALS are now of great interest in the function of microglia in the disease (Philips and Robberecht 2011). The PET ligand  $^{11}\text{C}$ -PK11195 has provided the *in vivo* evidence of widespread cortico-spinal tract and extra motor microglial activation in ALD patients (Turner et al. 2004). Meanwhile, the serotonin 5-HT<sub>1A</sub> receptor PET ligand  $^{11}\text{C}$ -WAY100635 has also revealed significant loss of binding mainly in frontotemporal regions in a group of non-depressed ALS patients (Turner et al. 2005b). In order to identify novel therapeutic targets, development of new PET ligands is challenged to create pharmacodynamic markers for drug discovery, providing proof of mechanism in the early stages of drug development.

As previously mentioned, the commonly used tracer  $^{99}\text{Tc}$ -HMPAO serves as a probe of regional cerebral metabolism for SPECT disease studies. However, the earliest SPECT studies in ALS adopted an alternative tracer *N*-isopropyl-p- $^{123}\text{I}$ -iodoamphetamine ( $^{123}\text{I}$ -IMP), indicating more pronounced global cortical reductions in patients with longer disease periods (Ludolph et al. 1989). Subsequent SPECT studies in ALS demonstrated the frontotemporal changes in ALS cases with dementia (Neary et al. 1990), and later elegantly proved the now established theory of a continuum between ALS and frontotemporal dementia (FTD) (Talbot et al. 1995).

### 3.4.3 PET and SPECT in Huntington's Disease

PET and SPECT imaging techniques have been used to monitor the progression of striatal and cortical functions implicated in HD since reduced striatal glucose metabolism and dopamine receptor binding, together with reduced striatal and cortical opioid receptor binding are evident in all symptomatic HD patients and in ~50 % of asymptomatic adult mutation carriers (Andrews and Brooks 1998). In this regard, various radioligands have been developed to investigate changes in brain biochemistry in HD patients, such as  $^{11}\text{C}$ -SCH 23390 (Andrews et al. 1999) for targeting dopamine receptor D1,  $^{11}\text{C}$ -raclopride (Pavese et al. 2003),  $^{125}\text{I}$ -epidepride (Pirker et al. 1997) and  $^{123}\text{I}$ -IBZM (Toyama et al. 1993) for targeting dopamine receptor D2,  $^{11}\text{C}$ -flumazenil (Holthoff et al. 1993) for binding benzodiazepine receptors, and  $^{11}\text{C}$ -diprenorphine (Weeks et al. 1997) for binding opioid receptors. Studies based on these approaches have provided quantitative assessments of the status of neurotransmitter systems in order to track the progressive decline of individuals with the mutated HD gene. Furthermore, a recent study showed for the first time that microglia activation is correlated with striatal neuronal dysfunction and could be an early indicator of the pathogenic processes in HD. As a marker of microglia activation,  $^{11}\text{C}$ -(R)-PK11195 may also be a potentially useful tracer of active subclinical disease and a tool for evaluating the efficacy of neuroprotection strategies (Tai et al. 2007).

Besides the approaches discussed above, functional  $^{18}\text{F}$ -FDG-PET imaging is of particular interest in HD studies (Teune et al. 2013). Early studies have shown hypometabolism in the caudate nucleus, both in symptomatic and asymptomatic mutation carriers (Grafton et al. 1992; Antonini et al. 1996) and more interestingly, metabolic decreases in asymptomatic carriers were significantly associated with the CAG repeat number (Antonini et al. 1996). In addition to the mutation size,  $^{18}\text{F}$ -FDG uptake in the caudate nucleus has been demonstrated to provide a predictive measure for time-to-onset of the disease (Ciarmiello et al. 2012). Another study using network analysis of  $^{18}\text{F}$ -FDG-PET scans in presymptomatic mutation carriers reports HD related metabolic covariance patterns (HDRP) characterized by caudate and putamenal hypometabolism, that includes mediotemporal reductions as well as relative increases in occipital regions (Feigin et al. 2001). Therefore, the presence of

these discrete patterns of metabolic abnormalities may project to the psychiatric and cognitive deteriorations that occur in the earliest stages of HD, before the onset of motor signs (Cummings 1995). In the mean time, an  $^{18}\text{F}$ -FDG-PET imaging study in an animal HD model showed reductions in brain metabolism that resembled the human condition (von Horsten et al. 2003). Just like PET imaging in other neurological disease studies, high-resolution small animal PET is experimentally advantageous for *in vivo* longitudinal research to monitor long-term treatment effects or assess the efficacy of putative neuroprotective agents in future HD investigations.

### 3.4.4 PET and SPECT in Parkinson's Disease

PET and SPECT imaging have been the most successful approaches employed extensively for early diagnosis of PD and demonstration of dopamine terminal dysfunction (Brooks and Pavese 2011). Dopaminergic deficiency has been linked to PD associated dementia, which results from presynaptic dopaminergic loss largely indicated by reduced 6- $^{18}\text{F}$ -fluorodopa ( $^{18}\text{F}$ -DOPA) uptake in ventral striatum, anterior cingulate and in the right caudate nucleus (Ito et al. 2002).  $^{18}\text{F}$ -DOPA in PD striatum was reported to reflect the number of remaining nigral dopaminergic cells in human (Snow et al. 1993) as well as in monkey (Pate et al. 1993), and most surprisingly, putamen uptake of  $^{18}\text{F}$ -DOPA is reduced by 50 % in PD at the onset of motor symptoms (Morrish et al. 1998). Decreased  $^{18}\text{F}$ -DOPA uptake also associated with poor attention, problems in working memory and verbal fluency (Rinne et al. 2000). Moreover,  $^{18}\text{F}$ -DOPA PET has been serving as an *in vivo* biomarker of PD progression where loss of striatal  $^{18}\text{F}$ -DOPA uptake occurs more rapidly in PD patients than in age-matched controls (Vingerhoets et al. 1994; Morrish et al. 1996, 1998; Nurmi et al. 2001, 2003; Benadiba et al. 2012) while putaminal  $^{18}\text{F}$ -DOPA uptake declined annually by ~10 % of the baseline level in early PD (Morrish et al. 1996; Nurmi et al. 2000). Alternative PET radiotracers for assessment of dopaminergic dysfunction in PD include  $^{11}\text{C}$ - and  $^{18}\text{F}$ -dihydrotetrabenazine (DTBZ),  $^{11}\text{C}$ -CFT,  $^{18}\text{F}$ -FP-CIT, and  $^{11}\text{C}$ -RTI-32 or with  $^{11}\text{C}$ -methylphenidate. Available SPECT ligands include  $^{123}\text{I}$ - $\beta$ -CIT,  $^{123}\text{I}$ -FP-CIT,  $^{123}\text{I}$ -IPT,  $^{123}\text{I}$ -altropine, and  $^{99\text{m}}\text{Tc}$ -TRODAT-1 (Brooks 2006; Brooks and Pavese 2011). For more details of these radioligands, see Brooks and Pavese 2011 for review.

Given that cognitive impairment in PD is not defined by a single mechanism, other factors should be addressed. Cholinergic impairment in PD plays a crucial role in the development of dementia. Acetylcholine analogue radiotracers, such as N- $^{11}\text{C}$ -methylpiperidin-4-yl acetate ( $^{11}\text{C}$ -MP4A) and N- $^{11}\text{C}$ -methylpiperidin-4-yl propionate ( $^{11}\text{C}$ -MP4P or  $^{11}\text{C}$ -PMP) have been designed to map the acetylcholinesterase (AChE) activity in the brain (Irie et al. 1996). AChE-PET demonstrated that posterior brain regions are related to cognitive deficits in PD patients (Shimada et al. 2009). With amyloid neuroimaging, the popular amyloid radiotracer  $^{11}\text{C}$ -PIB has been applied to PD studies and showed that PD patients with severe cognitive impairments are associated with high amyloid burden in the cerebral cortex (Hirano et al. 2012). Studies in regional glucose metabolism assessed by  $^{18}\text{F}$ -FDG PET

imaging have revealed global cortical hypometabolism in PD patients with dementia (Klein et al. 2010), and other studies have demonstrated abnormal metabolic patterns that can specifically and effectively distinguish between PD and non-PD subjects and monitor cognitive function of individual PD patients longitudinally (Tang et al. 2010).

### 3.5 Multi-Photon Imaging

MPM has been an exciting tool for imaging brain structure and physiology in intact animals for over a decade (Bacsikai et al. 2001, 2003a; Zipfel et al. 2003a, b; Levene et al. 2004; Misgeld and Kerschensteiner 2006; Svoboda and Yasuda 2006; Kerr and Denk 2008) since its first introduction (Denk et al. 1990). The principle of MPM is based on a nonlinear process – two-photon excitation (2PE), where two low-energy photons cooperate almost simultaneously to cause a higher energy electronic transition in a fluorescent molecule, and the excited fluorophore can then emit a single photon of fluorescence (Denk et al. 1990; Svoboda and Yasuda 2006). The properties of MPM provide many advantages for microscopy in scattering specimens and thereby make it particularly well suited to deep-tissue imaging (Denk et al. 1994; Denk 1996; Denk and Svoboda 1997; Helmchen and Denk 2005). One of the key features of MPM is the excitation wavelengths used in 2PE (deep red and near infrared) are capable of penetrating much deeper in live tissue than visible light because of the reduced scattering and absorption by endogenous chromophores (Svoboda and Block 1994; Oheim et al. 2001; Yaroslavsky et al. 2002). The nature of nonlinear excitation also ensures that even deep in the tissue, excitation is still mostly limited to a tiny focal volume (Svoboda and Yasuda 2006). More importantly, a great variety of fluorophores are available for both structural and functional imaging (Xu et al. 1996; Spiess et al. 2005) and the fact that different fluorophores can be excited simultaneously by a single laser, increasing the applications of multicolor imaging measurements (Xu et al. 1996; Yasuda et al. 2004).

With these features in principle, MPM is probably the most popular method used for acquisition of *in vivo* imaging data at the subcellular level. This minimally invasive tool can provide extremely high spatial resolution as fine as  $\sim 1\ \mu\text{m}$ . More importantly, MPM offers accessibility to thick tissue samples with imaging depths achievable up to 1 mm (Theer et al. 2003), despite a decrease in image quality at greater depths. Though this approach is impressive compared to other high-resolution imaging methods, the limitation in depth has restricted MPM's ability of imaging larger volumes of the mammalian brain. Fiber-like (e.g. gradient index) lenses provide opportunities to reach deeper structures with excellent resolution (Levene et al. 2004; Flusberg et al. 2005), however, this solution is balanced by concerns for damage to tissues or induced immune responses.

In experimental animal models, MPM imaging is mostly applied through a cranial window (Trachtenberg et al. 2002; Bacsikai et al. 2003a; McLellan et al. 2003) but a thinned skull approach can be an alternative (Christie et al. 2001b; Grutzendler

et al. 2002). Both methods enable *in vivo* longitudinal imaging of the neural structures and brain circuits, which is of great value in basic research or disease studies. However, current protocols for MPM imaging are unlikely to be applied to clinical studies as a consequence of the invasiveness of the procedure, extremely high spatial resolution, limited depth resolution and limited field of view.

### 3.5.1 MPM in Alzheimer's Disease

Multiphoton imaging has been extensively used in transgenic animal models of AD to study the dynamic processes and the underlying mechanisms of A $\beta$  deposition and tau pathology in living brain (Bacskai et al. 2001, 2002, 2003a; Christie et al. 2001a, b; Kuchibhotla et al. 2008, 2009, 2014). High spatial resolution and high signal-to-noise ratio of MPM allow imaging of the neuropathological features of AD, which are too small to be observed by conventional imaging methods. Demonstration of plaque imaging *in vivo* has exploited the amyloid binding ligands such as thioflavin-T, thioflavin-S, Congo red, methoxy-XO<sub>4</sub> (Klunk et al. 2002) and PIB (Mathis et al. 2002) to decorate the dense core of amyloid plaques in AD mouse brains. The development of BBB-permeable probes (e.g. methoxy-XO<sub>4</sub> and PIB) further enables live imaging of plaques after a single peripheral administration of the ligand (Klunk et al. 2002). Longitudinal studies exploring the temporal correlation between plaque formation and changes in brain microstructure have shown that new plaques do not change in size after formation that are stable for up to 5-months regardless of their initial size (Christie et al. 2001c; Meyer-Luehmann et al. 2008). Brain microstructures including neuronal soma, neurites and dendritic spines have been followed in a variety of transgenic mice including double-transgenic mice that express both mutated APP and YFP in neurons, or APP mice injected with adeno-associated virus (AAV) encoding for GFP to study the neuritic or synaptic pathology related to plaque physiology (Tsai et al. 2004; Spires et al. 2005; Spires-Jones et al. 2007). In addition, longitudinal imaging can readily evaluate the efficacy of therapeutic approaches designed to interfere with the amyloid cascade since regions of interest could be imaged before and after treatments in living mice (Bacskai et al. 2001; Garcia-Alloza et al. 2009; Spires-Jones et al. 2009). More interestingly, the effect of antioxidants like curcumin were also evaluated through longitudinal imaging of individual plaques, and revealed that curcumin disrupts and clears existing plaques with a limited ability of reversing the abnormal curvature of distorted neurites and size of neuritic dystrophies, (Garcia-Alloza et al. 2007).

More recently, functional calcium imaging based on MPM has served as a powerful tool for studies of neuronal activity and neural signaling pathways in neurodegeneration (for reviews, see Bezprozvanny and Mattson 2008; Arbel-Ornath et al. 2011). In the mean time, development of molecular imaging indicators has also paved the way for *in vivo* measurement of cellular functions and physiological processes (Tsien 1989; Miyawaki et al. 1999; Stosiek et al. 2003; Kuchibhotla et al. 2008). In recent AD studies, *in vivo* calcium imaging has been used to quantitatively measure intracellular calcium changes in both neuronal processes (Kuchibhotla et al. 2008) and

astrocytes (Kuchibhotla et al. 2009). APP transgenic mice were injected with AAV encoding the YC3.6 ratiometric calcium indicator, which had been calibrated to allow quantitative imaging of resting calcium levels. Transgenic mice with plaques were compared with age-matched controls to detect calcium overload in neurites and dendritic spines in areas near the senile plaques as well as areas far from the plaques. Changes in calcium concentration were also observed to correlate with altered morphologies of individual neurites. Focusing on astrocyte signaling (Kuchibhotla et al. 2009), the calcium indicator OGB-1 AM was used in combination with lifetime imaging microscopy to quantitatively assess astrocytic calcium levels in AD transgenic mice (Kuchibhotla et al. 2009). Interestingly, observations from this study showed that resting calcium levels in astrocytes were higher in AD transgenic mice compared with age-matched control, regardless of the proximity to plaques. Moreover, calcium transients were seen more frequently in astrocytes, and synchronously coordinated across long distances without coupling with neuronal activity. These results suggest emerging roles in astrocytic calcium dysregulation and synaptic plasticity in AD (Bezprozvanny 2009; Vincent et al. 2010). Another new discovery in AD employing calcium imaging has focused on the emerging role of intracellular accumulation of tau into neurofibrillary tangles (NFTs) in both resting calcium homeostasis (Kopeikina et al. 2013) and neural network responses to sensory stimulation (Kuchibhotla et al. 2014). This recent evidence demonstrates that the presence of NFTs does not lead to gross physiological alterations in cortical circuits, and suggests that soluble forms of tau may be more relevant targets for therapeutics.

In addition to calcium imaging, other *in vivo* functional imaging methods were also developed for AD studies. Fluorogenic oxidation reporter Amplex Red has been used to quantitatively emphasize oxidative stress in AD (Garcia-Alloza et al. 2006) and numerous fluorescent caspase indicators have been developed to monitor apoptotic activity (Hanson and Hanson 2008; Spires-Jones et al. 2008). Most recently, development of redox-sensitive variants of the green fluorescent protein (roGFP) has elegantly demonstrated that the local oxidative stress surrounding A $\beta$  plaques initiates caspase-dependent apoptosis in neurons and precedes rapid cell death in living AD animals (Xie et al. 2013b). Recent *in vivo* imaging of neuronal mitochondria has provided strong evidence for the first time that revealed severe mitochondrial impairments induced in the immediate vicinity of A $\beta$  plaques, suggesting the role of senile plaques as focal sources of toxicity in AD (Fig. 3.3) (Xie et al. 2013a).

### 3.6 Near-Infrared Imaging

Near-infrared spectroscopy (NIRS) is known for its capability of providing non-invasive measurement of blood-flow and metabolism based on the intrinsic differential absorption of oxy- versus deoxyhemoglobin (Pouratian et al. 2002, 2003; Strangman et al. 2002). Near-infrared fluorescence (NIRF) tomography is a relatively new approach that relies on the deep transmission of near-infrared light through thick scattering tissue and allows optical imaging with PET-like resolution in intact animals and humans. NIRF requires targeted molecular imaging probes



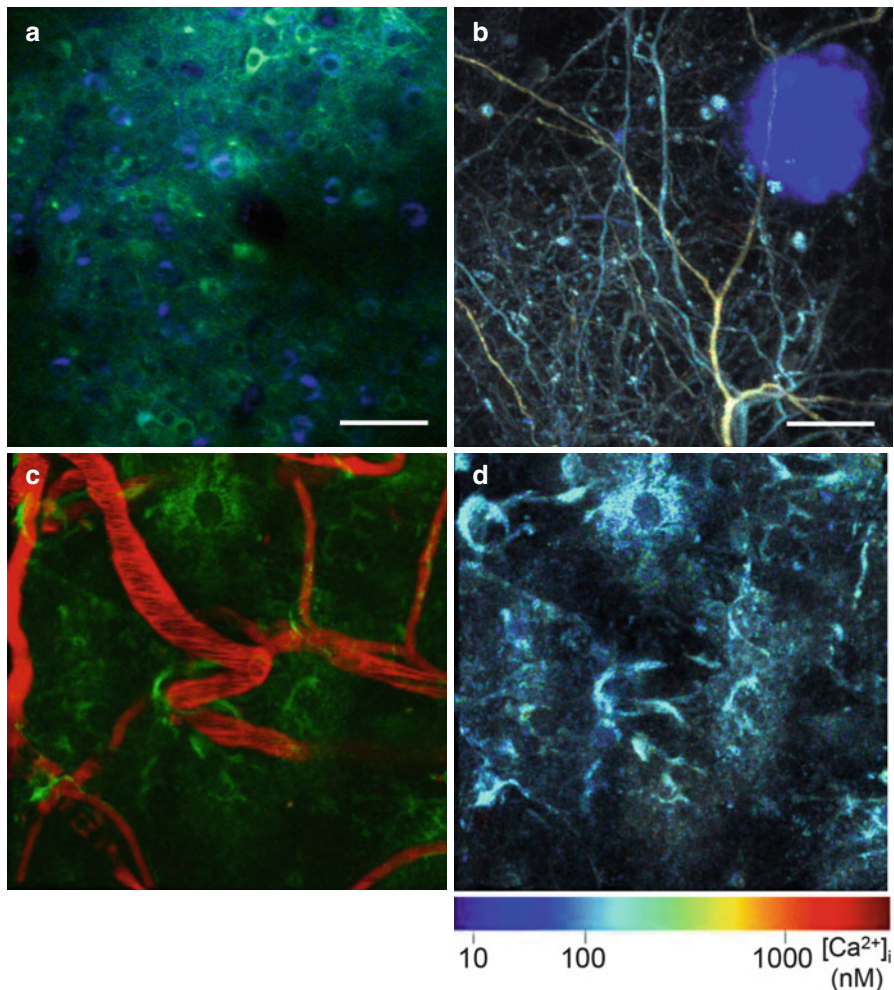


**Fig. 3.3** Live calcium imaging in AD. **(a)** *In vivo* multi-photon imaging of neurons in layers 2/3 of primary visual cortex in adult rTg4510 transgenic mice. Animals were transduced with the adeno-associated virus (AAV) encoding the ratiometric calcium indicator Yellow Cameleon 3.6 (Green, single channel intensity image) to monitor calcium levels. To identify a subpopulation of tangle-bearing neurons in rTg4510 mice, cortical neurofibrillary tangles were labeled with systemic administration of Methoxy-XO<sub>4</sub> (blue) and imaged 30 min later with laser excitation at 800 nm. Scale bar, 100  $\mu$ m. **(b)** *In vivo* multi-photon imaging deep in the neocortex of 18-month Tg2576 transgenic mice previously injected with YC3.6 AAV. The image is pseudocolored according to resting calcium levels (indicated by color bar) converted from YFP and CFP intensity ratios. YC3.6-filled dendrites and axons are shown near an amyloid plaque (blue). Scale bar applies to **b**, **c** and **d**, 20  $\mu$ m. **(c, d)** YC3.6 expression led robust labeling of astrocytes. pAAV-gfa2-YC3.6 was injected into cortical layers 2/3 of adult C57 wildtype mice and imaged using multi-photon microscopy 4 weeks after injection. *Left panel* (**c**) show the max intensity projection of an 80  $\mu$ m depth (YC3.6 in green; vasculature, labeled with texas red-dextran, in red) and the *right panel* (**d**) shows the same image pseudocolored to calcium concentration, indicated by the color bar



that are fluorescent and have excitation and emission spectra within the range of 650–950 nm. The spatial resolution of NIRF can range from 1 mm to several centimeters in brain tissue varying with depth. An advantage of using optical probes is that changes in fluorescence quantum yield, lifetime, and emission spectra would allow quantitative imaging of bound versus unbound probe and thus increase the sensitivity of detection (Hintersteiner et al. 2005; Raymond et al. 2008; Schmidt and Pahnke 2012). Recently, studies using fluorescence lifetime-based separation of spectrally overlapping fluorophores demonstrated NIRF's ability of localizing distinct organs in full-body imaging in mice (Raymond et al. 2010), which promises interest in future investigations using multiple fluorophores with NIRF. Integration of NIRF probes for imaging has shown remarkable advantages over conventional imaging methods such as PET and SPECT, and more attractively, this technique does not involve radioactive tracers and the equipment is less expensive. On the other hand, while the depth penetration of NIR wavelengths is high, it does not compare to the volumes achievable with PET or SPECT imaging.

### 3.7 Conclusion

Neuroimaging techniques result in attractive biomarkers that offer various possibilities for investigating the physiology and pathology underlying neurodegenerative disease. These approaches have shown remarkable sensitivity for detecting altered structure and physiology within the brains of individuals with neurodegenerative disease, sometimes many years before the disease onset. This has great potential for early diagnosis and treatment strategies. Neuroimaging methods are also appealing for their generally non-invasive nature and reproducibility. In recent years, neuroimaging has been playing a key role in basic research and clinical studies addressing the mechanisms of neurodegenerative diseases and the development of therapeutic interventions. It is foreseeable that brain-imaging techniques in the future will serve as increasingly promising and powerful tools for more thorough investigations into neuropathological processes that will eventually help to realize our ultimate goal – curing people suffering from these debilitating diseases.

**Acknowledgements** This work supported by NIH grant EB000768.

### References

- Abe O (2004) Amyotrophic lateral sclerosis: diffusion tensor tractography and voxel-based analysis. *NMR Biomed* 17:411–416
- Agosta F (2007) Voxel-based morphometry study of brain volumetry and diffusivity in amyotrophic lateral sclerosis patients with mild disability. *Hum Brain Mapp* 28:1430–1438
- Agosta F (2009a) Longitudinal assessment of grey matter contraction in amyotrophic lateral sclerosis: a tensor based morphometry study. *Amyotroph Lateral Scler* 10:168–174

- Agosta F (2009b) A longitudinal diffusion tensor MRI study of the cervical cord and brain in amyotrophic lateral sclerosis patients. *J Neurol Neurosurg Psychiatry* 80:53–55
- Agosta F (2010) Assessment of white matter tract damage in patients with amyotrophic lateral sclerosis: a diffusion tensor MR imaging tractography study. *AJNR Am J Neuroradiol* 31:1457–1461
- Agosta F (2012) The cortical signature of amyotrophic lateral sclerosis. *PLoS One* 7:e42816
- Alexander AL, Lee JE, Lazar M, Field AS (2007) Diffusion tensor imaging of the brain. *Neurotherapeutics* 4:316–329
- Andrews TC, Brooks DJ (1998) Advances in the understanding of early Huntington's disease using the functional imaging techniques of PET and SPET. *Mol Med Today* 4:532–539
- Andrews TC, Weeks RA, Turjanski N, Gunn RN, Watkins LH, Sahakian B, Hodges JR, Rosser AE, Wood NW, Brooks DJ (1999) Huntington's disease progression. PET and clinical observations. *Brain* 122(Pt 12):2353–2363
- Antonini A, Leenders KL, Spiegel R, Meier D, Vontobel P, Weigell-Weber M, Sanchez-Pernaute R, de Yebenez JG, Boesiger P, Weindl A, Maguire RP (1996) Striatal glucose metabolism and dopamine D2 receptor binding in asymptomatic gene carriers and patients with Huntington's disease. *Brain* 119(Pt 6):2085–2095
- Arbel-Ornath M, Garcia-Alloza M, Kuchibhotla KV, Spires-Jones T, Bacskai BJ (2011) Two-photon imaging of structure and function in Alzheimer's disease. Cold Spring Harbor, NY
- Arlicot N, Katsifis A, Garreau L, Mattner F, Vergote J, Duval S, Kousignian I, Bodard S, Guilloteau D, Chalons S (2008) Evaluation of CLINDE as potent translocator protein (18 kDa) SPECT radiotracer reflecting the degree of neuroinflammation in a rat model of microglial activation. *Eur J Nucl Med Mol Imaging* 35:2203–2211
- Ashburner J, Friston KJ (2000) Voxel-based morphometry—the methods. *Neuroimage* 11:805–821
- Aylward EH, Nopoulos PC, Ross CA, Langbehn DR, Pierson RK, Mills JA, Johnson HJ, Magnotta VA, Juhl AR, Paulsen JS (2011) Longitudinal change in regional brain volumes in prodromal Huntington disease. *J Neurol Neurosurg Psychiatry* 82:405–410
- Bacskai BJ, Kajdasz ST, Christie RH, Carter C, Games D, Seubert P, Schenk D, Hyman BT (2001) Imaging of amyloid-beta deposits in brains of living mice permits direct observation of clearance of plaques with immunotherapy. *Nat Med* 7:369–372
- Bacskai BJ, Klunk WE, Mathis CA, Hyman BT (2002) Imaging amyloid-beta deposits in vivo. *J Cereb Blood Flow Metab* 22:1035–1041
- Bacskai BJ, Hickey GA, Skoch J, Kajdasz ST, Wang Y, Huang GF, Mathis CA, Klunk WE, Hyman BT (2003a) Four-dimensional multiphoton imaging of brain entry, amyloid binding, and clearance of an amyloid-beta ligand in transgenic mice. *Proc Natl Acad Sci U S A* 100:12462–12467
- Bacskai BJ, Skoch J, Hickey GA, Allen R, Hyman BT (2003b) Fluorescence resonance energy transfer determinations using multiphoton fluorescence lifetime imaging microscopy to characterize amyloid-beta plaques. *J Biomed Opt* 8:368–375
- Barger SW, Harmon AD (1997) Microglial activation by Alzheimer amyloid precursor protein and modulation by apolipoprotein E. *Nature* 388:878–881
- Basser PJ, Mattiello J, LeBihan D (1994) Estimation of the effective self-diffusion tensor from the NMR spin echo. *J Magn Reson B* 103:247–254
- Benadiba M, Luurtsema G, Wichert-Ana L, Buchpiguel CA, Busatto Filho G (2012) New molecular targets for PET and SPECT imaging in neurodegenerative diseases. *Rev Bras Psiquiatr* 34(Suppl 2):S125–S136
- Bezprozvanny I (2009) Amyloid goes global. *Sci Signal* 2:pe16
- Bezprozvanny I, Mattson MP (2008) Neuronal calcium mishandling and the pathogenesis of Alzheimer's disease. *Trends Neurosci* 31:454–463
- Blain CR (2007) A longitudinal study of diffusion tensor MRI in ALS. *Amyotroph Lateral Scler* 8:348–355

- Bobinski M, de Leon MJ, Wegiel J, Desanti S, Convit A, Saint Louis LA, Rusinek H, Wisniewski HM (2000) The histological validation of post mortem magnetic resonance imaging-determined hippocampal volume in Alzheimer's disease. *Neuroscience* 95:721–725
- Bokde AL, Karmann M, Teipel SJ, Born C, Lieb M, Reiser MF, Moller HJ, Hampel H (2009) Decreased activation along the dorsal visual pathway after a 3-month treatment with galantamine in mild Alzheimer disease: a functional magnetic resonance imaging study. *J Clin Psychopharmacol* 29:147–156
- Braak H, Del Tredici K, Rub U, de Vos RA, Jansen Steur EN, Braak E (2003) Staging of brain pathology related to sporadic Parkinson's disease. *Neurobiol Aging* 24:197–211
- Brooks DJ (2006) Imaging the role of dopamine in health and disease Parkinson's disease as a lesion model. *Wien Klin Wochenschr* 118:570–572
- Brooks DJ, Pavese N (2011) Imaging biomarkers in Parkinson's disease. *Prog Neurobiol* 95:614–628
- Cagnin A (2001) In-vivo measurement of activated microglia in dementia. *Lancet* 358:461–467
- Catafau AM, Parellada E, Lomena FJ, Bernardo M, Pavia J, Ros D, Setoain J, Gonzalez-Monclus E (1994) Prefrontal and temporal blood flow in schizophrenia: resting and activation technetium-99m-HMPAO SPECT patterns in young neuroleptic-naive patients with acute disease. *J Nucl Med* 35:935–941
- Chang JL (2005) A voxel-based morphometry study of patterns of brain atrophy in ALS and ALS/FTLD. *Neurology* 65:75–80
- Chen W (2007) Clinical applications of PET in brain tumors. *J Nucl Med* 48:1468–1481
- Chew J, Silverman DH (2013) FDG-PET in early AD diagnosis. *Med Clin North Am* 97:485–494
- Chklovskii DB, Mel BW, Svoboda K (2004) Cortical rewiring and information storage. *Nature* 431:782–788
- Choi SR, Golding G, Zhuang Z, Zhang W, Lim N, Hefti F, Benedum TE, Kilbourn MR, Skovronsky D, Kung HF (2009) Preclinical properties of 18F-AV-45: a PET agent for Abeta plaques in the brain. *J Nucl Med* 50:1887–1894
- Christie R, Kimchi E, Kajdasz S, Bacskai B, Hyman BT (2001a) Multiphoton microscopy and amyloid angiopathy. *Amyloid* 8(Suppl 1):48–50
- Christie R, Yamada M, Moskowitz M, Hyman B (2001b) Structural and functional disruption of vascular smooth muscle cells in a transgenic mouse model of amyloid angiopathy. *Am J Pathol* 158:1065–1071
- Christie RH, Bacskai BJ, Zipfel WR, Williams RM, Kajdasz ST, Webb WW, Hyman BT (2001c) Growth arrest of individual senile plaques in a model of Alzheimer's disease observed by in vivo multiphoton microscopy. *J Neurosci* 21:858–864
- Ciarmiello A, Giovacchini G, Orobello S, Bruselli L, Elifani F, Squitieri F (2012) 18F-FDG PET uptake in the pre-Huntington disease caudate affects the time-to-onset independently of CAG expansion size. *Eur J Nucl Med Mol Imaging* 39:1030–1036
- Ciccarelli O (2009) Investigation of white matter pathology in ALS and PLS using tract-based spatial statistics. *Hum Brain Mapp* 30:615–624
- Ciccarelli O, Behrens TE, Altmann DR, Orrell RW, Howard RS, Johansen-Berg H, Miller DH, Matthews PM, Thompson AJ (2006) Probabilistic diffusion tractography: a potential tool to assess the rate of disease progression in amyotrophic lateral sclerosis. *Brain* 129:1859–1871
- Clark VP, Lai S, Deckel AW (2002) Altered functional MRI responses in Huntington's disease. *Neuroreport* 13:703–706
- Cosottini M (2005) Diffusion-tensor MR imaging of corticospinal tract in amyotrophic lateral sclerosis and progressive muscular atrophy. *Radiology* 237:258–264
- Cui M, Tang R, Li Z, Ren H, Liu B (2011) 99mTc- and re-labeled 6-dialkylamino-2-naphthylethylidene derivatives as imaging probes for beta-amyloid plaques. *Bioorg Med Chem Lett* 21:1064–1068
- Cummings JL (1995) Behavioral and psychiatric symptoms associated with Huntington's disease. *Adv Neurol* 65:179–186

- Cunnington R, Egan GF, O'Sullivan JD, Hughes AJ, Bradshaw JL, Colebatch JG (2001) Motor imagery in Parkinson's disease: a PET study. *Mov Disord* 16:849–857
- Dalakas MC, Hatazawa J, Brooks RA, Di Chiro G (1987) Lowered cerebral glucose utilization in amyotrophic lateral sclerosis. *Ann Neurol* 22:580–586
- Das SR, Avants BB, Grossman M, Gee JC (2009) Registration based cortical thickness measurement. *Neuroimage* 45:867–879
- Davies CA, Mann DM, Sumpter PQ, Yates PO (1987) A quantitative morphometric analysis of the neuronal and synaptic content of the frontal and temporal cortex in patients with Alzheimer's disease. *J Neurol Sci* 78:151–164
- Debruyne JC, Versijpt J, Van Laere KJ, De Vos F, Keppens J, Strijckmans K, Achten E, Slegers G, Dierckx RA, Korf J, De Reuck JL (2003) PET visualization of microglia in multiple sclerosis patients using [<sup>11</sup>C]PK11195. *Eur J Neurol* 10:257–264
- Delaveau P, Salgado-Pineda P, Fossati P, Witjas T, Azulay JP, Blin O (2010) Dopaminergic modulation of the default mode network in Parkinson's disease. *Eur Neuropsychopharmacol* 20:784–792
- Denk W (1996) Two-photon excitation in functional biological imaging. *J Biomed Opt* 1:296–304
- Denk W, Svoboda K (1997) Photon upmanship: why multiphoton imaging is more than a gimmick. *Neuron* 18:351–357
- Denk W, Strickler JH, Webb WW (1990) Two-photon laser scanning fluorescence microscopy. *Science* 248:73–76
- Denk W, Delaney KR, Gelperin A, Kleinfeld D, Strowbridge BW, Tank DW, Yuste R (1994) Anatomical and functional imaging of neurons using 2-photon laser scanning microscopy. *J Neurosci Methods* 54:151–162
- Desikan RS, Cabral HJ, Hess CP, Dillon WP, Glastonbury CM, Weiner MW, Schmansky NJ, Greve DN, Salat DH, Buckner RL, Fischl B (2009) Automated MRI measures identify individuals with mild cognitive impairment and Alzheimer's disease. *Brain* 132:2048–2057
- Dickerson BC, Sperling RA (2005) Neuroimaging biomarkers for clinical trials of disease-modifying therapies in Alzheimer's disease. *NeuroRx* 2:348–360
- Dickerson BC, Bakkour A, Salat DH, Feczko E, Pacheco J, Greve DN, Grodstein F, Wright CI, Blacker D, Rosas HD, Sperling RA, Atri A, Growdon JH, Hyman BT, Morris JC, Fischl B, Buckner RL (2009) The cortical signature of Alzheimer's disease: regionally specific cortical thinning relates to symptom severity in very mild to mild AD dementia and is detectable in asymptomatic amyloid-positive individuals. *Cereb Cortex* 19:497–510
- Diehl-Schmid J, Grimmer T, Drzezga A, Bornschein S, Perneczky R, Forstl H, Schwaiger M, Kurz A (2006) Longitudinal changes of cerebral glucose metabolism in semantic dementia. *Dement Geriatr Cogn Disord* 22:346–351
- Diehl-Schmid J, Grimmer T, Drzezga A, Bornschein S, Riemenschneider M, Forstl H, Schwaiger M, Kurz A (2007) Decline of cerebral glucose metabolism in frontotemporal dementia: a longitudinal 18F-FDG-PET-study. *Neurobiol Aging* 28:42–50
- Dierks T, Linden DE, Hertel A, Gunther T, Lanfermann H, Niesen A, Frolich L, Zanella FE, Hor G, Goebel R, Maurer K (1999) Multimodal imaging of residual function and compensatory resource allocation in cortical atrophy: a case study of parietal lobe function in a patient with Huntington's disease. *Psychiatry Res* 90:67–75
- Dijkhuizen RM, Nicolay K (2003) Magnetic resonance imaging in experimental models of brain disorders. *J Cereb Blood Flow Metab* 23:1383–1402
- Dobrucki LW, Sinusas AJ (2010) PET and SPECT in cardiovascular molecular imaging. *Nat Rev Cardiol* 7:38–47
- Douaud G, Filippini N, Knight S, Talbot K, Turner MR (2011) Integration of structural and functional magnetic resonance imaging in amyotrophic lateral sclerosis. *Brain* 134:3470–3479
- Drzezga A, Lautenschlager N, Siebner H, Riemenschneider M, Willeoch F, Minoshima S, Schwaiger M, Kurz A (2003) Cerebral metabolic changes accompanying conversion of mild cognitive impairment into Alzheimer's disease: a PET follow-up study. *Eur J Nucl Med Mol Imaging* 30:1104–1113
- Dumas EM, van den Bogaard SJ, Ruber ME, Reilman RR, Stout JC, Craufurd D, Hicks SL, Kennard C, Tabrizi SJ, van Buchem MA, van der Grond J, Roos RA (2012) Early changes in

- white matter pathways of the sensorimotor cortex in premanifest Huntington's disease. *Hum Brain Mapp* 33:203–212
- Ellis CM (1999) Diffusion tensor MRI assesses corticospinal tract damage in ALS. *Neurology* 53:1051–1058
- Engler H, Forsberg A, Almkvist O, Blomquist G, Larsson E, Savitcheva I, Wall A, Ringheim A, Langstrom B, Nordberg A (2006) Two-year follow-up of amyloid deposition in patients with Alzheimer's disease. *Brain* 129:2856–2866
- Falangola MF, Lee SP, Nixon RA, Duff K, Helpert JA (2005) Histological co-localization of iron in Abeta plaques of PS/APP transgenic mice. *Neurochem Res* 30:201–205
- Feigin A, Leenders KL, Moeller JR, Missimer J, Kuenig G, Spetsieris P, Antonini A, Eidelberg D (2001) Metabolic network abnormalities in early Huntington's disease: an [(18)F]FDG PET study. *J Nucl Med* 42:1591–1595
- Filippini N, Douaud G, Mackay CE, Knight S, Talbot K, Turner MR (2010) Corpus callosum involvement is a consistent feature of amyotrophic lateral sclerosis. *Neurology* 75:1645–1652
- Fischl B, Dale AM (2000) Measuring the thickness of the human cerebral cortex from magnetic resonance images. *Proc Natl Acad Sci U S A* 97:11050–11055
- Flusberg BA, Cocker ED, Piyawattanametha W, Jung JC, Cheung EL, Schnitzer MJ (2005) Fiber-optic fluorescence imaging. *Nat Methods* 2:941–950
- Foerster BR, Welsh RC, Feldman EL (2013) 25 years of neuroimaging in amyotrophic lateral sclerosis. *Nat Rev Neurol* 9:513–524
- Foster NL, Wang AY, Tasdizen T, Fletcher PT, Hoffman JM, Koeppe RA (2008) Realizing the potential of positron emission tomography with 18F-fluorodeoxyglucose to improve the treatment of Alzheimer's disease. *Alzheimers Dement* 4:S29–S36
- Fountoulakis KN, Iacovides A, Gerasimou G, Fotiou F, Ioannidou C, Basciella F, Grammaticos P, Kaprinis G (2004) The relationship of regional cerebral blood flow with subtypes of major depression. *Prog Neuropsychopharmacol Biol Psychiatry* 28:537–546
- Frisoni GB, Fox NC, Jack CR Jr, Scheltens P, Thompson PM (2010) The clinical use of structural MRI in Alzheimer disease. *Nat Rev Neurol* 6:67–77
- Furtado S, Suchowersky O, Rewcastle B, Graham L, Klimek ML, Garber A (1996) Relationship between trinucleotide repeats and neuropathological changes in Huntington's disease. *Ann Neurol* 39:132–136
- Garcia-Alloza M, Dodwell SA, Meyer-Luehmann M, Hyman BT, Bacskai BJ (2006) Plaque-derived oxidative stress mediates distorted neurite trajectories in the Alzheimer mouse model. *J Neuropathol Exp Neurol* 65:1082–1089
- Garcia-Alloza M, Borrelli LA, Rozkalne A, Hyman BT, Bacskai BJ (2007) Curcumin labels amyloid pathology in vivo, disrupts existing plaques, and partially restores distorted neurites in an Alzheimer mouse model. *J Neurochem* 102:1095–1104
- Garcia-Alloza M, Subramanian M, Thyssen D, Borrelli LA, Fauq A, Das P, Golde TE, Hyman BT, Bacskai BJ (2009) Existing plaques and neuritic abnormalities in APP:PS1 mice are not affected by administration of the gamma-secretase inhibitor LY-411575. *Mol Neurodegener* 4:19
- Geng DY, Li YX, Zee CS (2006) Magnetic resonance imaging-based volumetric analysis of basal ganglia nuclei and substantia nigra in patients with Parkinson's disease. *Neurosurgery* 58:256–262; discussion 256–262
- Georgiou-Karistianis N (2009) A peek inside the Huntington's brain: will functional imaging take us one step closer in solving the puzzle? *Exp Neurol* 220:5–8
- Georgiou-Karistianis N, Sritharan A, Farrow M, Cunningham R, Stout J, Bradshaw J, Churchyard A, Brawn TL, Chua P, Chiu E, Thiruvady D, Egan G (2007) Increased cortical recruitment in Huntington's disease using a Simon task. *Neuropsychologia* 45:1791–1800
- Gomez-Isla T, Price JL, McKeel DW Jr, Morris JC, Growdon JH, Hyman BT (1996) Profound loss of layer II entorhinal cortex neurons occurs in very mild Alzheimer's disease. *J Neurosci* 16:4491–4500
- Gonul AS, Kula M, Esel E, Tutus A, Sofuoglu S (2003) A Tc-99m HMPAO SPECT study of regional cerebral blood flow in drug-free schizophrenic patients with deficit and non-deficit syndrome. *Psychiatry Res* 123:199–205

- Grafton ST, Mazziotta JC, Pahl JJ, St George-Hyslop P, Haines JL, Gusella J, Hoffman JM, Baxter LR, Phelps ME (1992) Serial changes of cerebral glucose metabolism and caudate size in persons at risk for Huntington's disease. *Arch Neurol* 49:1161–1167
- Graham JM (2004) Diffusion tensor imaging for the assessment of upper motor neuron integrity in ALS. *Neurology* 63:2111–2119
- Grosskreutz J (2006) Widespread sensorimotor and frontal cortical atrophy in amyotrophic lateral sclerosis. *BMC Neurol* 6:17
- Group THsDCR (1993) A novel gene containing a trinucleotide repeat that is expanded and unstable on Huntington's disease chromosomes. The Huntington's Disease Collaborative Research Group. *Cell* 72:971–983
- Grutzendler J, Kasthuri N, Gan WB (2002) Long-term dendritic spine stability in the adult cortex. *Nature* 420:812–816
- Guye M, Bettus G, Bartolomei F, Cozzone PJ (2010) Graph theoretical analysis of structural and functional connectivity MRI in normal and pathological brain networks. *MAGMA* 23:409–421
- Hampel H, Frank R, Broich K, Teipel SJ, Katz RG, Hardy J, Herholz K, Bokde AL, Jessen F, Hoessler YC, Sanhai WR, Zetterberg H, Woodcock J, Blennow K (2010) Biomarkers for Alzheimer's disease: academic, industry and regulatory perspectives. *Nat Rev Drug Discov* 9:560–574
- Hampel H, Prvulovic D, Teipel SJ, Bokde AL (2011) Recent developments of functional magnetic resonance imaging research for drug development in Alzheimer's disease. *Prog Neurobiol* 95:570–578
- Hanson GT, Hanson BJ (2008) Fluorescent probes for cellular assays. *Comb Chem High Throughput Screen* 11:505–513
- Hardy JA, Higgins GA (1992) Alzheimer's disease: the amyloid cascade hypothesis. *Science* 256:184–185
- Helmchen F, Denk W (2005) Deep tissue two-photon microscopy. *Nat Methods* 2:932–940
- Herholz K (2003) PET studies in dementia. *Ann Nucl Med* 17:79–89
- Herholz K, Carter SF, Jones M (2007) Positron emission tomography imaging in dementia. *Br J Radiol* 80 Spec No 2:S160–S167
- Higuchi M, Iwata N, Matsuba Y, Sato K, Sasamoto K, Saido TC (2005) 19F and 1H MRI detection of amyloid beta plaques in vivo. *Nat Neurosci* 8:527–533
- Hintersteiner M, Enz A, Frey P, Jatón AL, Kinzy W, Kneuer R, Neumann U, Rudin M, Staufenbiel M, Stoeckli M, Wiederhold KH, Gremlich HU (2005) In vivo detection of amyloid-beta deposits by near-infrared imaging using an oxazine-derivative probe. *Nat Biotechnol* 23:577–583
- Hirano S, Shinotoh H, Eidelberg D (2012) Functional brain imaging of cognitive dysfunction in Parkinson's disease. *J Neurol Neurosurg Psychiatry* 83:963–969
- Hobbs NZ, Henley SM, Ridgway GR, Wild EJ, Barker RA, Scahill RI, Barnes J, Fox NC, Tabrizi SJ (2010) The progression of regional atrophy in premanifest and early Huntington's disease: a longitudinal voxel-based morphometry study. *J Neurol Neurosurg Psychiatry* 81:756–763
- Holman BL, Johnson KA, Gerada B, Carvalho PA, Satlin A (1992) The scintigraphic appearance of Alzheimer's disease: a prospective study using technetium-99m-HMPAO SPECT. *J Nucl Med* 33:181–185
- Holthoff VA, Koeppe RA, Frey KA, Penney JB, Markel DS, Kuhl DE, Young AB (1993) Positron emission tomography measures of benzodiazepine receptors in Huntington's disease. *Ann Neurol* 34:76–81
- Ikonomovic MD, Klunk WE, Abrahamson EE, Mathis CA, Price JC, Tsopelas ND, Lopresti BJ, Ziolk S, Bi W, Paljug WR, Debnath ML, Hope CE, Isanski BA, Hamilton RL, DeKosky ST (2008) Post-mortem correlates of in vivo PiB-PET amyloid imaging in a typical case of Alzheimer's disease. *Brain* 131:1630–1645
- Irie T, Fukushi K, Namba H, Iyo M, Tamagami H, Nagatsuka S, Ikota N (1996) Brain acetylcholinesterase activity: validation of a PET tracer in a rat model of Alzheimer's disease. *J Nucl Med* 37:649–655



- Ito K, Nagano-Saito A, Kato T, Arahata Y, Nakamura A, Kawasumi Y, Hatano K, Abe Y, Yamada T, Kachi T, Brooks DJ (2002) Striatal and extrastriatal dysfunction in Parkinson's disease with dementia: a 6-[18F]fluoro-L-dopa PET study. *Brain* 125:1358–1365
- Iwata NK (2008) Evaluation of corticospinal tracts in ALS with diffusion tensor MRI and brain-stem stimulation. *Neurology* 70:528–532
- Jack CR Jr, Dickson DW, Parisi JE, Xu YC, Cha RH, O'Brien PC, Edland SD, Smith GE, Boeve BF, Tangalos EG, Kokmen E, Petersen RC (2002) Antemortem MRI findings correlate with hippocampal neuropathology in typical aging and dementia. *Neurology* 58:750–757
- Jack CR Jr, Garwood M, Wengenack TM, Borowski B, Curran GL, Lin J, Adrian G, Grohn OH, Grimm R, Poduslo JF (2004) In vivo visualization of Alzheimer's amyloid plaques by magnetic resonance imaging in transgenic mice without a contrast agent. *Magn Reson Med* 52:1263–1271
- Jack CR Jr, Marjanska M, Wengenack TM, Reyes DA, Curran GL, Lin J, Preboske GM, Poduslo JF, Garwood M (2007) Magnetic resonance imaging of Alzheimer's pathology in the brains of living transgenic mice: a new tool in Alzheimer's disease research. *Neuroscientist* 13:38–48
- Jacobs RE, Cherry SR (2001) Complementary emerging techniques: high-resolution PET and MRI. *Curr Opin Neurobiol* 11:621–629
- Jagust W, Reed B, Mungas D, Ellis W, Decarli C (2007) What does fluorodeoxyglucose PET imaging add to a clinical diagnosis of dementia? *Neurology* 69:871–877
- Jagust WJ, Zheng L, Harvey DJ, Mack WJ, Vinters HV, Weiner MW, Ellis WG, Zarow C, Mungas D, Reed BR, Kramer JH, Schuff N, DeCarli C, Chui HC (2008) Neuropathological basis of magnetic resonance images in aging and dementia. *Ann Neurol* 63:72–80
- Jellinger KA (1991) Pathology of Parkinson's disease. Changes other than the nigrostriatal pathway. *Mol Chem Neuropathol* 14:153–197
- Jelson-Swain LM (2010) Reduced interhemispheric functional connectivity in the motor cortex during rest in limb-onset amyotrophic lateral sclerosis. *Front Syst Neurosci* 4:158
- Johnson KA, Fox NC, Sperling RA, Klunk WE (2012) Brain imaging in Alzheimer disease. *Cold Spring Harb Perspect Med* 2:a006213
- Judenhofer MS, Cherry SR (2013) Applications for preclinical PET/MRI. *Semin Nucl Med* 43:19–29
- Jurgens CK, Jasinschi R, Ekin A, Witjes-Ane MN, Middelkoop H, van der Grond J, Roos RA (2010) MRI T2 hypointensities in basal ganglia of premanifest Huntington's disease. *PLoS Curr* 2:52
- Kassubek J (2005) Global brain atrophy and corticospinal tract alterations in ALS, as investigated by voxel-based morphometry of 3-D MRI. *Amyotroph Lateral Scler Other Motor Neuron Disord* 6:213–220
- Kemp PM, Hoffmann SA, Holmes C, Bolt L, Ward T, Holmes RB, Fleming JS (2005) The contribution of statistical parametric mapping in the assessment of precuneal and medial temporal lobe perfusion by 99mTc-HMPAO SPECT in mild Alzheimer's and Lewy body dementia. *Nucl Med Commun* 26:1099–1106
- Kerr JN, Denk W (2008) Imaging in vivo: watching the brain in action. *Nat Rev Neurosci* 9:195–205
- Kew JJ, Goldstein LH, Leigh PN, Abrahams S, Cosgrave N, Passingham RE, Frackowiak RS, Brooks DJ (1993a) The relationship between abnormalities of cognitive function and cerebral activation in amyotrophic lateral sclerosis. A neuropsychological and positron emission tomography study. *Brain* 116(Pt 6):1399–1423
- Kew JJ, Leigh PN, Playford ED, Passingham RE, Goldstein LH, Frackowiak RS, Brooks DJ (1993b) Cortical function in amyotrophic lateral sclerosis. A positron emission tomography study. *Brain* 116(Pt 3):655–680
- Khalil MM, Tremoleda JL, Bayomy TB, Gsell W (2011) Molecular SPECT imaging: an overview. *Int J Mol Imaging* 2011:796025
- Kiernan MC, Vucic S, Cheah BC, Turner MR, Eisen A, Hardiman O, Burrell JR, Zoing MC (2011) Amyotrophic lateral sclerosis. *Lancet* 377:942–955



- Kim JS, Reading SA, Brashers-Krug T, Calhoun VD, Ross CA, Pearlson GD (2004) Functional MRI study of a serial reaction time task in Huntington's disease. *Psychiatry Res* 131:23–30
- Klein JC, Eggers C, Kalbe E, Weisenbach S, Hohmann C, Vollmar S, Baudrexel S, Diederich NJ, Heiss WD, Hilker R (2010) Neurotransmitter changes in dementia with Lewy bodies and Parkinson disease dementia in vivo. *Neurology* 74:885–892
- Klunk WE, Bacskai BJ, Mathis CA, Kajdasz ST, McLellan ME, Frosch MP, Debnath ML, Holt DP, Wang Y, Hyman BT (2002) Imaging Abeta plaques in living transgenic mice with multiphoton microscopy and methoxy-X04, a systemically administered Congo red derivative. *J Neuropathol Exp Neurol* 61:797–805
- Klunk WE, Engler H, Nordberg A, Wang Y, Blomqvist G, Holt DP, Bergstrom M, Savitcheva I, Huang GF, Estrada S, Aussen B, Debnath ML, Barletta J, Price JC, Sandell J, Lopresti BJ, Wall A, Koivisto P, Antoni G, Mathis CA, Langstrom B (2004) Imaging brain amyloid in Alzheimer's disease with Pittsburgh Compound-B. *Ann Neurol* 55:306–319
- Kono K, Inoue Y, Nakayama K, Shakudo M, Morino M, Ohata K, Wakasa K, Yamada R (2001) The role of diffusion-weighted imaging in patients with brain tumors. *AJNR Am J Neuroradiol* 22:1081–1088
- Kopeikina KJ, Wegmann S, Pitstick R, Carlson GA, Bacskai BJ, Betensky RA, Hyman BT, Spire-Jones TL (2013) Tau causes synapse loss without disrupting calcium homeostasis in the rTg4510 model of tauopathy. *PLoS One* 8:e80834
- Kowatch RA, Devous MD Sr, Harvey DC, Mayes TL, Trivedi MH, Emslie GJ, Weinberg WA (1999) A SPECT HMPAO study of regional cerebral blood flow in depressed adolescents and normal controls. *Prog Neuropsychopharmacol Biol Psychiatry* 23:643–656
- Kuchibhotla KV, Goldman ST, Lattarulo CR, Wu HY, Hyman BT, Bacskai BJ (2008) Abeta plaques lead to aberrant regulation of calcium homeostasis in vivo resulting in structural and functional disruption of neuronal networks. *Neuron* 59:214–225
- Kuchibhotla KV, Lattarulo CR, Hyman BT, Bacskai BJ (2009) Synchronous hyperactivity and intercellular calcium waves in astrocytes in Alzheimer mice. *Science* 323:1211–1215
- Kuchibhotla KV, Wegmann S, Kopeikina KJ, Hawkes J, Rudinskiy N, Andermann ML, Spire-Jones TL, Bacskai BJ, Hyman BT (2014) Neurofibrillary tangle-bearing neurons are functionally integrated in cortical circuits in vivo. *Proc Natl Acad Sci U S A* 111:510–514
- Le Bihan D, Mangin JF, Poupon C, Clark CA, Pappata S, Molko N, Chabriat H (2001) Diffusion tensor imaging: concepts and applications. *J Magn Reson Imaging* 13:534–546
- Leinonen V, Alafuzoff I, Aalto S, Suotunen T, Savolainen S, Nagren K, Tapiola T, Rinne J, Jaaskelainen JE, Soininen H, Rinne JO (2008) Assessment of beta-amyloid in a frontal cortical brain biopsy specimen and by positron emission tomography with carbon 11-labeled Pittsburgh Compound B. *Arch Neurol* 65:1304–1309
- Levene MJ, Dombeck DA, Kasischke KA, Molloy RP, Webb WW (2004) In vivo multiphoton microscopy of deep brain tissue. *J Neurophysiol* 91:1908–1912
- Libon DJ (2012) Deficits in concept formation in amyotrophic lateral sclerosis. *Neuropsychology* 26:422–429
- Lippincott-Schwartz J, Snapp E, Kenworthy A (2001) Studying protein dynamics in living cells. *Nat Rev Mol Cell Biol* 2:444–456
- Lloyd CM, Richardson MP, Brooks DJ, Al-Chalabi A, Leigh PN (2000) Extramotor involvement in ALS: PET studies with the GABA(A) ligand [(11)C]flumazenil. *Brain* 123(Pt 11):2289–2296
- Lombardo F (2009) Diffusion tensor MRI and MR spectroscopy in long lasting upper motor neuron involvement in amyotrophic lateral sclerosis. *Arch Ital Biol* 147:69–82
- Ludolph AC, Elger CE, Bottger IW, Kuttig AG, Lottes G, Brune GG (1989) N-isopropyl-p-123I-amphetamine single photon emission computer tomography in motor neuron disease. *Eur Neurol* 29:255–260
- Ludolph AC, Langen KJ, Regard M, Herzog H, Kemper B, Kuwert T, Bottger IG, Feinendegen L (1992) Frontal lobe function in amyotrophic lateral sclerosis: a neuropsychologic and positron emission tomography study. *Acta Neurol Scand* 85:81–89

- Mankoff DA, Bellon JR (2001) Positron-emission tomographic imaging of cancer: glucose metabolism and beyond. *Semin Radiat Oncol* 11:16–27
- Marzola P, Osculati F, Sbarbati A (2003) High field MRI in preclinical research. *Eur J Radiol* 48:165–170
- Mascalchi M, Lolli F, Della Nave R, Tessa C, Petralli R, Gavazzi C, Politi LS, Macucci M, Filippi M, Piacentini S (2004) Huntington disease: volumetric, diffusion-weighted, and magnetization transfer MR imaging of brain. *Radiology* 232:867–873
- Mathis CA, Bacskai BJ, Kajdasz ST, McLellan ME, Frosch MP, Hyman BT, Holt DP, Wang Y, Huang GF, Debnath ML, Klunk WE (2002) A lipophilic thioflavin-T derivative for positron emission tomography (PET) imaging of amyloid in brain. *Bioorg Med Chem Lett* 12:295–298
- Matthews B, Siemers ER, Mozley PD (2003) Imaging-based measures of disease progression in clinical trials of disease-modifying drugs for Alzheimer disease. *Am J Geriatr Psychiatry* 11:146–159
- Mattner F, Bandin DL, Staykova M, Berghofer P, Gregoire MC, Ballantyne P, Quinlivan M, Fordham S, Pham T, Willenborg DO, Katsifis A (2011) Evaluation of [(1)(2)(3)I]-CLINDE as a potent SPECT radiotracer to assess the degree of astroglia activation in cuprizone-induced neuroinflammation. *Eur J Nucl Med Mol Imaging* 38:1516–1528
- McLellan ME, Kajdasz ST, Hyman BT, Bacskai BJ (2003) In vivo imaging of reactive oxygen species specifically associated with thioflavine S-positive amyloid plaques by multiphoton microscopy. *J Neurosci* 23:2212–2217
- Meyer-Luehmann M, Spiess-Jones TL, Prada C, Garcia-Alloza M, de Calignon A, Rozkalne A, Koenigsknecht-Talboo J, Holtzman DM, Bacskai BJ, Hyman BT (2008) Rapid appearance and local toxicity of amyloid-beta plaques in a mouse model of Alzheimer's disease. *Nature* 451:720–724
- Misgeld T, Kerschensteiner M (2006) In vivo imaging of the diseased nervous system. *Nat Rev Neurosci* 7:449–463
- Mitsumoto H (2007) Quantitative objective markers for upper and lower motor neuron dysfunction in ALS. *Neurology* 68:1402–1410
- Miyawaki A, Griesbeck O, Heim R, Tsien RY (1999) Dynamic and quantitative Ca<sup>2+</sup> measurements using improved cameleons. *Proc Natl Acad Sci U S A* 96:2135–2140
- Mohammadi B (2009) Changes of resting state brain networks in amyotrophic lateral sclerosis. *Exp Neurol* 217:147–153
- Morrish PK, Sawle GV, Brooks DJ (1996) An [18F]dopa-PET and clinical study of the rate of progression in Parkinson's disease. *Brain* 119(Pt 2):585–591
- Morrish PK, Rakshi JS, Bailey DL, Sawle GV, Brooks DJ (1998) Measuring the rate of progression and estimating the preclinical period of Parkinson's disease with [18F]dopa PET. *J Neurol Neurosurg Psychiatry* 64:314–319
- Mosconi L (2005) Brain glucose metabolism in the early and specific diagnosis of Alzheimer's disease. FDG-PET studies in MCI and AD. *Eur J Nucl Med Mol Imaging* 32:486–510
- Mosconi L, Mistur R, Switalski R, Tsui WH, Glodzik L, Li Y, Pirraglia E, De Santi S, Reisberg B, Wisniewski T, de Leon MJ (2009) FDG-PET changes in brain glucose metabolism from normal cognition to pathologically verified Alzheimer's disease. *Eur J Nucl Med Mol Imaging* 36:811–822
- Nagano-Saito A, Liu J, Doyon J, Dagher A (2009) Dopamine modulates default mode network deactivation in elderly individuals during the Tower of London task. *Neurosci Lett* 458:1–5
- Nandhagopal R, McKeown MJ, Stoessl AJ (2008) Functional imaging in Parkinson disease. *Neurology* 70:1478–1488
- Neary D, Snowden JS, Mann DM, Northen B, Goulding PJ, Macdermott N (1990) Frontal lobe dementia and motor neuron disease. *J Neurol Neurosurg Psychiatry* 53:23–32
- Nelissen N, Van Laere K, Thurfjell L, Owenius R, Vandenbulcke M, Koole M, Bormans G, Brooks DJ, Vandenberghe R (2009) Phase 1 study of the Pittsburgh compound B derivative 18F-flutemetamol in healthy volunteers and patients with probable Alzheimer disease. *J Nucl Med* 50:1251–1259

- Nicoletti G, Lodi R, Condino F, Tonon C, Fera F, Malucelli E, Manners D, Zappia M, Morgante L, Barone P, Barbiroli B, Quattrone A (2006) Apparent diffusion coefficient measurements of the middle cerebellar peduncle differentiate the Parkinson variant of MSA from Parkinson's disease and progressive supranuclear palsy. *Brain* 129:2679–2687
- Nobili F, Koulibaly PM, Rodriguez G, Benoit M, Girtler N, Robert PH, Brugnolo A, Darcourt J (2007) 99mTc-HMPAO and 99mTc-ECD brain uptake correlates of verbal memory in Alzheimer's disease. *Q J Nucl Med Mol Imaging* 51:357–363
- Nopoulos PC, Aylward EH, Ross CA, Mills JA, Langbehn DR, Johnson HJ, Magnotta VA, Pierson RK, Beglinger LJ, Nance MA, Barker RA, Paulsen JS (2011) Smaller intracranial volume in prodromal Huntington's disease: evidence for abnormal neurodevelopment. *Brain* 134:137–142
- Nordberg A, Rinne JO, Kadir A, Langstrom B (2010) The use of PET in Alzheimer disease. *Nat Rev Neurol* 6:78–87
- Nurmi E, Ruottinen HM, Kaasinen V, Bergman J, Haaparanta M, Solin O, Rinne JO (2000) Progression in Parkinson's disease: a positron emission tomography study with a dopamine transporter ligand [18F]CFT. *Ann Neurol* 47:804–808
- Nurmi E, Ruottinen HM, Bergman J, Haaparanta M, Solin O, Sonninen P, Rinne JO (2001) Rate of progression in Parkinson's disease: a 6-[18F]fluoro-L-dopa PET study. *Mov Disord* 16:608–615
- Nurmi E, Bergman J, Eskola O, Solin O, Vahlberg T, Sonninen P, Rinne JO (2003) Progression of dopaminergic hypofunction in striatal subregions in Parkinson's disease using [18F]CFT PET. *Synapse* 48:109–115
- Nyberg S, Jonhagen ME, Cselenyi Z, Halldin C, Julin P, Olsson H, Freund-Levi Y, Andersson J, Varnas K, Svensson S, Farde L (2009) Detection of amyloid in Alzheimer's disease with positron emission tomography using [11C]AZD2184. *Eur J Nucl Med Mol Imaging* 36:1859–1863
- O'Neill J, Schuff N, Marks WJ Jr, Feiwell R, Aminoff MJ, Weiner MW (2002) Quantitative 1H magnetic resonance spectroscopy and MRI of Parkinson's disease. *Mov Disord* 17:917–927
- Ogawa S, Lee TM, Kay AR, Tank DW (1990) Brain magnetic resonance imaging with contrast dependent on blood oxygenation. *Proc Natl Acad Sci U S A* 87:9868–9872
- Oheim M, Beaupaire E, Chaigneau E, Mertz J, Charpak S (2001) Two-photon microscopy in brain tissue: parameters influencing the imaging depth. *J Neurosci Methods* 111:29–37
- Ono M, Saji H (2012) Molecular approaches to the treatment, prophylaxis, and diagnosis of Alzheimer's disease: novel PET/SPECT imaging probes for diagnosis of Alzheimer's disease. *J Pharmacol Sci* 118:338–344
- Orbay H, Hong H, Zhang Y, Cai W (2013) PET/SPECT imaging of hindlimb ischemia: focusing on angiogenesis and blood flow. *Angiogenesis* 16:279–287
- Otte A, Halsband U (2006) Brain imaging tools in neurosciences. *J Physiol Paris* 99:281–292
- Papma JM, Seelaar H, de Koning I, Hasan D, Reijds A, Valkema R, Prins ND, van Swieten JC (2013) Episodic memory impairment in frontotemporal dementia; a (9)(9mTc- HMPAO SPECT study. *Curr Alzheimer Res* 10:332–339
- Pate BD, Kawamata T, Yamada T, McGeer EG, Hewitt KA, Snow BJ, Ruth TJ, Calne DB (1993) Correlation of striatal fluorodopa uptake in the MPTP monkey with dopaminergic indices. *Ann Neurol* 34:331–338
- Paulsen JS, Langbehn DR, Stout JC, Aylward E, Ross CA, Nance M, Guttman M, Johnson S, MacDonald M, Beglinger LJ, Duff K, Kayson E, Biglan K, Shoulson I, Oakes D, Hayden M (2008) Detection of Huntington's disease decades before diagnosis: the Predict-HD study. *J Neurol Neurosurg Psychiatry* 79:874–880
- Paus T, Collins DL, Evans AC, Leonard G, Pike B, Zijdenbos A (2001) Maturation of white matter in the human brain: a review of magnetic resonance studies. *Brain Res Bull* 54:255–266
- Pavese N, Andrews TC, Brooks DJ, Ho AK, Rosser AE, Barker RA, Robbins TW, Sahakian BJ, Dunnett SB, Piccini P (2003) Progressive striatal and cortical dopamine receptor dysfunction in Huntington's disease: a PET study. *Brain* 126:1127–1135
- Paviour DC, Thornton JS, Lees AJ, Jager HR (2007) Diffusion-weighted magnetic resonance imaging differentiates Parkinsonian variant of multiple-system atrophy from progressive supranuclear palsy. *Mov Disord* 22:68–74

- Pereira JB, Ibarretxe-Bilbao N, Marti MJ, Compta Y, Junque C, Bargallo N, Tolosa E (2012) Assessment of cortical degeneration in patients with Parkinson's disease by voxel-based morphometry, cortical folding, and cortical thickness. *Hum Brain Mapp* 33:2521–2534
- Phelps ME (2000) PET: the merging of biology and imaging into molecular imaging. *J Nucl Med* 41:661–681
- Philips T, Robberecht W (2011) Neuroinflammation in amyotrophic lateral sclerosis: role of glial activation in motor neuron disease. *Lancet Neurol* 10:253–263
- Phinney AL, Deller T, Stalder M, Calhoun ME, Frotscher M, Sommer B, Staufenbiel M, Jucker M (1999) Cerebral amyloid induces aberrant axonal sprouting and ectopic terminal formation in amyloid precursor protein transgenic mice. *J Neurosci* 19:8552–8559
- Pierpaoli C, Basser PJ (1996) Toward a quantitative assessment of diffusion anisotropy. *Magn Reson Med* 36:893–906
- Pimlott SL, Sutherland A (2011) Molecular tracers for the PET and SPECT imaging of disease. *Chem Soc Rev* 40:149–162
- Pirker W, Asenbaum S, Wenger S, Kornhuber J, Angelberger P, Deecke L, Podreka I, Brucke T (1997) Iodine-123-epidepride-SPECT: studies in Parkinson's disease, multiple system atrophy and Huntington's disease. *J Nucl Med* 38:1711–1717
- Poduslo JF, Wengenack TM, Curran GL, Wisniewski T, Sigurdsson EM, Macura SI, Borowski BJ, Jack CR Jr (2002) Molecular targeting of Alzheimer's amyloid plaques for contrast-enhanced magnetic resonance imaging. *Neurobiol Dis* 11:315–329
- Pouratian N, Sicotte N, Rex D, Martin NA, Becker D, Cannestra AF, Toga AW (2002) Spatial/temporal correlation of BOLD and optical intrinsic signals in humans. *Magn Reson Med* 47:766–776
- Pouratian N, Sheth SA, Martin NA, Toga AW (2003) Shedding light on brain mapping: advances in human optical imaging. *Trends Neurosci* 26:277–282
- Prell T, Peschel T, Hartung V, Kaufmann J, Klauschies R, Bodammer N, Kollwe K, Dengler R, Grosskreutz J (2013) Diffusion tensor imaging patterns differ in bulbar and limb onset amyotrophic lateral sclerosis. *Clin Neurol Neurosurg* 115:1281–1287
- Prvulovic D, Bokde AL, Faltraco F, Hampel H (2011) Functional magnetic resonance imaging as a dynamic candidate biomarker for Alzheimer's disease. *Prog Neurobiol* 95:557–569
- Rajagopalan V, Yue GH, Pioro EP (2013) Brain white matter diffusion tensor metrics from clinical 1.5T MRI distinguish between ALS phenotypes. *J Neurol* 260:2532–2540
- Raymond SB, Skoch J, Hills ID, Nesterov EE, Swager TM, Bacskaï BJ (2008) Smart optical probes for near-infrared fluorescence imaging of Alzheimer's disease pathology. *Eur J Nucl Med Mol Imaging* 35(Suppl 1):S93–S98
- Raymond SB, Boas DA, Bacskaï BJ, Kumar AT (2010) Lifetime-based tomographic multiplexing. *J Biomed Opt* 15:046011
- Reiman EM, Chen K, Alexander GE, Caselli RJ, Bandy D, Osborne D, Saunders AM, Hardy J (2004) Functional brain abnormalities in young adults at genetic risk for late-onset Alzheimer's dementia. *Proc Natl Acad Sci U S A* 101:284–289
- Rinne JO, Portin R, Ruottinen H, Nurmi E, Bergman J, Haaparanta M, Solin O (2000) Cognitive impairment and the brain dopaminergic system in Parkinson disease: [18F]fluorodopa positron emission tomographic study. *Arch Neurol* 57:470–475
- Roccatagliata L, Bonzano L, Mancardi G, Canepa C, Caponnetto C (2009) Detection of motor cortex thinning and corticospinal tract involvement by quantitative MRI in amyotrophic lateral sclerosis. *Amyotroph Lateral Scler* 10:47–52
- Rosas HD, Feigin AS, Hersch SM (2004) Using advances in neuroimaging to detect, understand, and monitor disease progression in Huntington's disease. *NeuroRx* 1:263–272
- Rosas HD, Salat DH, Lee SY, Zaleta AK, Pappu V, Fischl B, Greve D, Hevelone N, Hersch SM (2008) Cerebral cortex and the clinical expression of Huntington's disease: complexity and heterogeneity. *Brain* 131:1057–1068
- Rose S, Pannek K, Bell C, Baumann F, Hutchinson N, Coulthard A, McCombe P, Henderson R (2012) Direct evidence of intra- and interhemispheric corticomotor network degeneration in amyotrophic lateral sclerosis: an automated MRI structural connectivity study. *Neuroimage* 59:2661–2669

- Rowe CC, Villemagne VL (2013) Amyloid imaging with PET in early Alzheimer disease diagnosis. *Med Clin North Am* 97:377–398
- Rowe CC, Ng S, Ackermann U, Gong SJ, Pike K, Savage G, Cowie TF, Dickinson KL, Maruff P, Darby D, Smith C, Woodward M, Merory J, Tochon-Danguy H, O’Keefe G, Klunk WE, Mathis CA, Price JC, Masters CL, Villemagne VL (2007) Imaging beta-amyloid burden in aging and dementia. *Neurology* 68:1718–1725
- Rowe CC, Ackerman U, Browne W, Mulligan R, Pike KL, O’Keefe G, Tochon-Danguy H, Chan G, Berlangieri SU, Jones G, Dickinson-Rowe KL, Kung HP, Zhang W, Kung MP, Skovronsky D, Dyrks T, Holl G, Krause S, Friebe M, Lehman L, Lindemann S, Dinkelborg LM, Masters CL, Villemagne VL (2008) Imaging of amyloid beta in Alzheimer’s disease with 18F-BAY94-9172, a novel PET tracer: proof of mechanism. *Lancet Neurol* 7:129–135
- Sach M (2004) Diffusion tensor MRI of early upper motor neuron involvement in amyotrophic lateral sclerosis. *Brain* 127:340–350
- Sage CA, Peeters RR, Gorner A, Robberecht W, Sunaert S (2007) Quantitative diffusion tensor imaging in amyotrophic lateral sclerosis. *Neuroimage* 34:486–499
- Sandler MP, Bax JJ, Patton JA, Visser FC, Martin WH, Wijns W (1998) Fluorine-18-fluorodeoxyglucose cardiac imaging using a modified scintillation camera. *J Nucl Med* 39:2035–2043
- Schmidt A, Pahnke J (2012) Efficient near-infrared in vivo imaging of amyloid-beta deposits in Alzheimer’s disease mouse models. *J Alzheimers Dis* 30:651–664
- Schmidt KC, Smith CB (2005) Resolution, sensitivity and precision with autoradiography and small animal positron emission tomography: implications for functional brain imaging in animal research. *Nucl Med Biol* 32:719–725
- Schocke MF, Seppi K, Esterhammer R, Kremser C, Jaschke W, Poewe W, Wenning GK (2002) Diffusion-weighted MRI differentiates the Parkinson variant of multiple system atrophy from PD. *Neurology* 58:575–580
- Schöll M, Almkvist O, Axelman K, Stefanova E, Wall A, Westman E, Langstrom B, Lannfelt L, Graff C, Nordberg A (2011) Glucose metabolism and PIB binding in carriers of a His163Tyr presenilin 1 mutation. *Neurobiol Aging* 32:1388–1399
- Selkoe DJ (2002) Alzheimer’s disease is a synaptic failure. *Science* 298:789–791
- Senda J (2009) Correlation between pyramidal tract degeneration and widespread white matter involvement in amyotrophic lateral sclerosis: a study with tractography and diffusion-tensor imaging. *Amyotroph Lateral Scler* 10:288–294
- Senda J (2011) Progressive and widespread brain damage in ALS: MRI voxel-based morphometry and diffusion tensor imaging study. *Amyotroph Lateral Scler* 12:59–69
- Seppi K, Schocke MF, Esterhammer R, Kremser C, Brenneis C, Mueller J, Boesch S, Jaschke W, Poewe W, Wenning GK (2003) Diffusion-weighted imaging discriminates progressive supranuclear palsy from PD, but not from the parkinson variant of multiple system atrophy. *Neurology* 60:922–927
- Sharma V, Luker GD, Piwnica-Worms D (2002) Molecular imaging of gene expression and protein function in vivo with PET and SPECT. *J Magn Reson Imaging* 16:336–351
- Sharma KR, Sheriff S, Maudsley A, Govind V (2012) Diffusion tensor imaging of basal ganglia and thalamus in amyotrophic lateral sclerosis. *J Neuroimaging* 23:368–374
- Shimada H, Hirano S, Shinotoh H, Aotsuka A, Sato K, Tanaka N, Ota T, Asahina M, Fukushi K, Kuwabara S, Hattori T, Suhara T, Irie T (2009) Mapping of brain acetylcholinesterase alterations in Lewy body disease by PET. *Neurology* 73:273–278
- Shoghi-Jadid K, Small GW, Agdeppa ED, Kepe V, Ercoli LM, Siddarth P, Read S, Satyamurthy N, Petric A, Huang SC, Barrio JR (2002) Localization of neurofibrillary tangles and beta-amyloid plaques in the brains of living patients with Alzheimer disease. *Am J Geriatr Psychiatry* 10:24–35
- Silbert LC, Quinn JF, Moore MM, Corbridge E, Ball MJ, Murdoch G, Sexton G, Kaye JA (2003) Changes in premorbid brain volume predict Alzheimer’s disease pathology. *Neurology* 61:487–492



- Silverman DH, Small GW, Chang CY, Lu CS, Kung De Aburto MA, Chen W, Czernin J, Rapoport SI, Pietrini P, Alexander GE, Schapiro MB, Jagust WJ, Hoffman JM, Welsh-Bohmer KA, Alavi A, Clark CM, Salmon E, de Leon MJ, Mielke R, Cummings JL, Kowell AP, Gambhir SS, Hoh CK, Phelps ME (2001) Positron emission tomography in evaluation of dementia: regional brain metabolism and long-term outcome. *JAMA* 286:2120–2127
- Small GW, Mazziotta JC, Collins MT, Baxter LR, Phelps ME, Mandelkern MA, Kaplan A, La Rue A, Adamson CF, Chang L et al (1995) Apolipoprotein E type 4 allele and cerebral glucose metabolism in relatives at risk for familial Alzheimer disease. *JAMA* 273:942–947
- Small DH, Mok SS, Bornstein JC (2001) Alzheimer's disease and Abeta toxicity: from top to bottom. *Nat Rev Neurosci* 2:595–598
- Small GW, Bookheimer SY, Thompson PM, Cole GM, Huang SC, Kepe V, Barrio JR (2008) Current and future uses of neuroimaging for cognitively impaired patients. *Lancet Neurol* 7:161–172
- Smith MC (1960) Nerve fibre degeneration in the brain in amyotrophic lateral sclerosis. *J Neurol Neurosurg Psychiatry* 23:269–282
- Smith CB, Schmidt KC, Qin M, Burlin TV, Cook MP, Kang J, Saunders RC, Bacher JD, Carson RE, Channing MA, Eckelman WC, Herscovitch P, Laverman P, Vuong BK (2005) Measurement of regional rates of cerebral protein synthesis with L-[1-11C]leucine and PET with correction for recycling of tissue amino acids: II. Validation in rhesus monkeys. *J Cereb Blood Flow Metab* 25:629–640
- Snow BJ, Tooyama I, McGeer EG, Yamada T, Calne DB, Takahashi H, Kimura H (1993) Human positron emission tomographic [18F]fluorodopa studies correlate with dopamine cell counts and levels. *Ann Neurol* 34:324–330
- Spies E, Bestvater F, Heckel-Pompey A, Toth K, Hacker M, Stobrawa G, Feurer T, Wotzlaw C, Berchner-Pfannschmidt U, Porwol T, Acker H (2005) Two-photon excitation and emission spectra of the green fluorescent protein variants ECFP, EGFP and EYFP. *J Microsc* 217:200–204
- Spires TL, Meyer-Luehmann M, Stern EA, McLean PJ, Skoch J, Nguyen PT, Bacskai BJ, Hyman BT (2005) Dendritic spine abnormalities in amyloid precursor protein transgenic mice demonstrated by gene transfer and intravital multiphoton microscopy. *J Neurosci* 25:7278–7287
- Spires-Jones TL, Meyer-Luehmann M, Osetek JD, Jones PB, Stern EA, Bacskai BJ, Hyman BT (2007) Impaired spine stability underlies plaque-related spine loss in an Alzheimer's disease mouse model. *Am J Pathol* 171:1304–1311
- Spires-Jones TL, de Calignon A, Matsui T, Zehr C, Pitstick R, Wu HY, Osetek JD, Jones PB, Bacskai BJ, Feany MB, Carlson GA, Ashe KH, Lewis J, Hyman BT (2008) In vivo imaging reveals dissociation between caspase activation and acute neuronal death in tangle-bearing neurons. *J Neurosci* 28:862–867
- Spires-Jones TL, Mielke ML, Rozkalne A, Meyer-Luehmann M, de Calignon A, Bacskai BJ, Schenk D, Hyman BT (2009) Passive immunotherapy rapidly increases structural plasticity in a mouse model of Alzheimer disease. *Neurobiol Dis* 33:213–220
- Stoll HP, Hellwig N, Alexander C, Ozbek C, Schieffer H, Oberhausen E (1994) Myocardial metabolic imaging by means of fluorine-18 deoxyglucose/technetium-99m sestamibi dual-isotope single-photon emission tomography. *Eur J Nucl Med* 21:1085–1093
- Stosiek C, Garaschuk O, Holthoff K, Konnerth A (2003) In vivo two-photon calcium imaging of neuronal networks. *Proc Natl Acad Sci U S A* 100:7319–7324
- Strangman G, Culver JP, Thompson JH, Boas DA (2002) A quantitative comparison of simultaneous BOLD fMRI and NIRS recordings during functional brain activation. *Neuroimage* 17:719–731
- Svedberg MM, Hall H, Hellstrom-Lindahl E, Estrada S, Guan Z, Nordberg A, Langstrom B (2009) [(11)C]PIB-amyloid binding and levels of Abeta40 and Abeta42 in postmortem brain tissue from Alzheimer patients. *Neurochem Int* 54:347–357
- Svoboda K, Block SM (1994) Biological applications of optical forces. *Annu Rev Biophys Biomol Struct* 23:247–285

- Svoboda K, Yasuda R (2006) Principles of two-photon excitation microscopy and its applications to neuroscience. *Neuron* 50:823–839
- Tabrizi SJ, Scahill RI, Durr A, Roos RA, Leavitt BR, Jones R, Landwehrmeyer GB, Fox NC, Johnson H, Hicks SL, Kennard C, Craufurd D, Frost C, Langbehn DR, Reilmann R, Stout JC (2011) Biological and clinical changes in premanifest and early stage Huntington's disease in the TRACK-HD study: the 12-month longitudinal analysis. *Lancet Neurol* 10:31–42
- Tai YF, Pavese N, Gerhard A, Tabrizi SJ, Barker RA, Brooks DJ, Piccini P (2007) Microglial activation in presymptomatic Huntington's disease gene carriers. *Brain* 130:1759–1766
- Takahashi H, Snow BJ, Bhatt MH, Peppard R, Eisen A, Calne DB (1993) Evidence for a dopaminergic deficit in sporadic amyotrophic lateral sclerosis on positron emission scanning. *Lancet* 342:1016–1018
- Talbot PR, Goulding PJ, Lloyd JJ, Snowden JS, Neary D, Testa HJ (1995) Inter-relation between "classic" motor neuron disease and frontotemporal dementia: neuropsychological and single photon emission computed tomography study. *J Neurol Neurosurg Psychiatry* 58:541–547
- Tanaka M, Kondo S, Hirai S, Sun X, Yamagishi T, Okamoto K (1993) Cerebral blood flow and oxygen metabolism in progressive dementia associated with amyotrophic lateral sclerosis. *J Neurol Sci* 120:22–28
- Tang CC, Poston KL, Eckert T, Feigin A, Frucht S, Gudesblatt M, Dhawan V, Lesser M, Vonsattel JP, Fahn S, Eidelberg D (2010) Differential diagnosis of parkinsonism: a metabolic imaging study using pattern analysis. *Lancet Neurol* 9:149–158
- Tedeschi G (2012) Interaction between aging and neurodegeneration in amyotrophic lateral sclerosis. *Neurobiol Aging* 33:886–898
- Teune LK, Bartels AL, Leenders KL (2013) FDG-PET imaging in neurodegenerative brain diseases. In: Signorelli DF (ed) *Functional brain mapping and the endeavor to understand the working brain*. InTech, Rijeka, Croatia
- Theer P, Hasan MT, Denk W (2003) Two-photon imaging to a depth of 1000 microm in living brains by use of a Ti:Al<sub>2</sub>O<sub>3</sub> regenerative amplifier. *Opt Lett* 28:1022–1024
- Thivard L (2007) Diffusion tensor imaging and voxel based morphometry study in amyotrophic lateral sclerosis: relationships with motor disability. *J Neurol Neurosurg Psychiatry* 78:889–892
- Thobois S, Dominey P, Fraix V, Mertens P, Guenot M, Zimmer L, Pollak P, Benabid AL, Broussolle E (2002) Effects of subthalamic nucleus stimulation on actual and imagined movement in Parkinson's disease: a PET study. *J Neurol* 249:1689–1698
- Toosy AT (2003) Diffusion tensor imaging detects corticospinal tract involvement at multiple levels in amyotrophic lateral sclerosis. *J Neurol Neurosurg Psychiatry* 74:1250–1257
- Toyama H, Ichise M, Ballinger JR, Fornazzari L, Kirsh JC (1993) Dopamine D2 receptor SPECT imaging: basic in vivo characteristics and clinical applications of 123I-IBZM in humans. *Ann Nucl Med* 7:29–38
- Trachtenberg JT, Chen BE, Knott GW, Feng G, Sanes JR, Welker E, Svoboda K (2002) Long-term in vivo imaging of experience-dependent synaptic plasticity in adult cortex. *Nature* 420:788–794
- Tsai J, Grutzendler J, Duff K, Gan WB (2004) Fibrillar amyloid deposition leads to local synaptic abnormalities and breakage of neuronal branches. *Nat Neurosci* 7:1181–1183
- Tsien RY (1989) Fluorescent probes of cell signaling. *Annu Rev Neurosci* 12:227–253
- Turner MR (2007) Volumetric cortical loss in sporadic and familial amyotrophic lateral sclerosis. *Amyotroph Lateral Scler* 8:343–347
- Turner MR, Kiernan MC (2012) Does interneuronal dysfunction contribute to neurodegeneration in amyotrophic lateral sclerosis? *Amyotroph Lateral Scler* 13:245–250
- Turner MR, Cagnin A, Turkheimer FE, Miller CC, Shaw CE, Brooks DJ, Leigh PN, Banati RB (2004) Evidence of widespread cerebral microglial activation in amyotrophic lateral sclerosis: an [11C](R)-PK11195 positron emission tomography study. *Neurobiol Dis* 15:601–609
- Turner MR, Hammers A, Al-Chalabi A, Shaw CE, Andersen PM, Brooks DJ, Leigh PN (2005a) Distinct cerebral lesions in sporadic and 'D90A' SOD1 ALS: studies with [11C]flumazenil PET. *Brain* 128:1323–1329



- Turner MR, Rabiner EA, Hammers A, Al-Chalabi A, Grasby PM, Shaw CE, Brooks DJ, Leigh PN (2005b) [11C]-WAY100635 PET demonstrates marked 5-HT1A receptor changes in sporadic ALS. *Brain* 128:896–905
- Turner MR, Kiernan MC, Leigh PN, Talbot K (2009) Biomarkers in amyotrophic lateral sclerosis. *Lancet Neurol* 8:94–109
- Turner MR, Agosta F, Bede P, Govind V, Lule D, Verstraete E (2012) Neuroimaging in amyotrophic lateral sclerosis. *Biomark Med* 6:319–337
- Vaillancourt DE, Spraker MB, Prodoehl J, Abraham I, Corcos DM, Zhou XJ, Comella CL, Little DM (2009) High-resolution diffusion tensor imaging in the substantia nigra of de novo Parkinson disease. *Neurology* 72:1378–1384
- van der Graaff MM, Sage CA, Caan MW, Akkerman EM, Lavini C, Majoie CB, Nederveen AJ, Zwinderman AH, Vos F, Brugman F, van den Berg LH, de Rijk MC, van Doorn PA, Van Hecke W, Peeters RR, Robberecht W, Sunaert S, de Visser M (2011) Upper and extra-motoneuron involvement in early motoneuron disease: a diffusion tensor imaging study. *Brain* 134:1211–1228
- van Wijk DF, Strang AC, Duivenvoorden R, Enklaar DJ, van der Geest RJ, Kastelein JJ, de Groot E, Stroes ES, Nederveen AJ (2014) Increasing spatial resolution of 3T MRI scanning improves reproducibility of carotid arterial wall dimension measurements. *MAGMA* 27(3):219–226
- Vandenberghe R, Adamczuk K, Dupont P, Laere KV, Chetelat G (2013) Amyloid PET in clinical practice: its place in the multidimensional space of Alzheimer's disease. *Neuroimage Clin* 2:497–511
- Verhoeff NP, Wilson AA, Takeshita S, Trop L, Hussey D, Singh K, Kung HF, Kung MP, Houle S (2004) In-vivo imaging of Alzheimer disease beta-amyloid with [11C]SB-13 PET. *Am J Geriatr Psychiatry* 12:584–595
- Verstijpt JJ, Dumont F, Van Laere KJ, Decoo D, Santens P, Audenaert K, Achten E, Slegers G, Dierckx RA, Korf J (2003) Assessment of neuroinflammation and microglial activation in Alzheimer's disease with radiolabelled PK11195 and single photon emission computed tomography. A pilot study. *Eur Neurol* 50:39–47
- Verstraete E (2010) Motor network degeneration in amyotrophic lateral sclerosis: a structural and functional connectivity study. *PLoS One* 2012:e13664
- Verstraete E (2012) Structural MRI reveals cortical thinning in amyotrophic lateral sclerosis. *J Neurol Neurosurg Psychiatry* 83:383–388
- Verstraete E, van den Heuvel MP, Veldink JH, Blanken N, Mandl RC, Hulshoff Pol HE, van den Berg LH (2010) Motor network degeneration in amyotrophic lateral sclerosis: a structural and functional connectivity study. *PLoS One* 5:e13664
- Vincent AJ, Gasperini R, Foa L, Small DH (2010) Astrocytes in Alzheimer's disease: emerging roles in calcium dysregulation and synaptic plasticity. *J Alzheimers Dis* 22:699–714
- Vingerhoets FJ, Snow BJ, Lee CS, Schulzer M, Mak E, Calne DB (1994) Longitudinal fluorodopa positron emission tomographic studies of the evolution of idiopathic parkinsonism. *Ann Neurol* 36:759–764
- von Horsten S, Schmitt I, Nguyen HP, Holzmann C, Schmidt T, Walther T, Bader M, Pabst R, Kobbe P, Krotova J, Stiller D, Kask A, Vaarmann A, Rathke-Hartlieb S, Schulz JB, Grasshoff U, Bauer I, Vieira-Saecker AM, Paul M, Jones L, Lindenberg KS, Landwehrmeyer B, Bauer A, Li XJ, Riess O (2003) Transgenic rat model of Huntington's disease. *Hum Mol Genet* 12:617–624
- Wadghiri YZ, Sigurdsson EM, Sadowski M, Elliott JJ, Li Y, Scholtzova H, Tang CY, Aguinaldo G, Pappolla M, Duff K, Wisniewski T, Turnbull DH (2003) Detection of Alzheimer's amyloid in transgenic mice using magnetic resonance microimaging. *Magn Reson Med* 50:293–302
- Wadghiri YZ, Li J, Wang J, Hoang DM, Sun Y, Xu H, Tsui W, Li Y, Boutajangout A, Wang A, de Leon M, Wisniewski T (2013) Detection of amyloid plaques targeted by bifunctional USPIO in Alzheimer's disease transgenic mice using magnetic resonance microimaging. *PLoS One* 8:e57097
- Wagner S, Breyholz HJ, Faust A, Holtke C, Levkau B, Schober O, Schafers M, Kopka K (2006) Molecular imaging of matrix metalloproteinases in vivo using small molecule inhibitors for SPECT and PET. *Curr Med Chem* 13:2819–2838

- Wake R, Miyaoka T, Kawakami K, Tsuchie K, Inagaki T, Horiguchi J, Yamamoto Y, Hayashi T, Kitagaki H (2010) Characteristic brain hypoperfusion by 99mTc-ECD single photon emission computed tomography (SPECT) in patients with the first-episode schizophrenia. *Eur Psychiatry* 25:361–365
- Weber WA (2009) Assessing tumor response to therapy. *J Nucl Med* 50(Suppl 1):1S–10S
- Weeks RA, Cunningham VJ, Piccini P, Waters S, Harding AE, Brooks DJ (1997) 11C-diprenorphine binding in Huntington's disease: a comparison of region of interest analysis with statistical parametric mapping. *J Cereb Blood Flow Metab* 17:943–949
- Weir DW, Sturrock A, Leavitt BR (2011) Development of biomarkers for Huntington's disease. *Lancet Neurol* 10:573–590
- Wernick MN, Aarsvold JN (2004) Emission tomography: the fundamentals of PET and SPECT. Elsevier, San Diego, CA, Access Online via Elsevier
- Wolf RC, Sambataro F, Vasic N, Schonfeldt-Lecuona C, Ecker D, Landwehrmeyer B (2008a) Aberrant connectivity of lateral prefrontal networks in presymptomatic Huntington's disease. *Exp Neurol* 213:137–144
- Wolf RC, Vasic N, Schonfeldt-Lecuona C, Ecker D, Landwehrmeyer GB (2008b) Functional imaging of cognitive processes in Huntington's disease and its presymptomatic mutation carriers. *Nervenarzt* 79:408–420
- Xie H, Guan J, Borrelli LA, Xu J, Serrano-Pozo A, Bacskai BJ (2013a) Mitochondrial alterations near amyloid plaques in an Alzheimer's disease mouse model. *J Neurosci* 33:17042–17051
- Xie H, Hou S, Jiang J, Sekutowicz M, Kelly J, Bacskai BJ (2013b) Rapid cell death is preceded by amyloid plaque-mediated oxidative stress. *Proc Natl Acad Sci U S A* 110:7904–7909
- Xu C, Zipfel W, Shear JB, Williams RM, Webb WW (1996) Multiphoton fluorescence excitation: new spectral windows for biological nonlinear microscopy. *Proc Natl Acad Sci U S A* 93:10763–10768
- Yaroslavsky AN, Schulze PC, Yaroslavsky IV, Schober R, Ulrich F, Schwarzmaier HJ (2002) Optical properties of selected native and coagulated human brain tissues in vitro in the visible and near infrared spectral range. *Phys Med Biol* 47:2059–2073
- Yasuda R, Nimchinsky EA, Scheuss V, Pologruto TA, Oertner TG, Sabatini BL, Svoboda K (2004) Imaging calcium concentration dynamics in small neuronal compartments. *Sci STKE* 2004:pl5
- Yeo JM, Lim X, Khan Z, Pal S (2013) Systematic review of the diagnostic utility of SPECT imaging in dementia. *Eur Arch Psychiatry Clin Neurosci* 263:539–552
- Zhang Y (2011) Progression of white matter degeneration in amyotrophic lateral sclerosis: a diffusion tensor imaging study. *Amyotroph Lateral Scler* 12:421–429
- Zipfel WR, Williams RM, Christie R, Nikitin AY, Hyman BT, Webb WW (2003a) Live tissue intrinsic emission microscopy using multiphoton-excited native fluorescence and second harmonic generation. *Proc Natl Acad Sci U S A* 100:7075–7080
- Zipfel WR, Williams RM, Webb WW (2003b) Nonlinear magic: multiphoton microscopy in the biosciences. *Nat Biotechnol* 21:1369–1377

## Chapter 4

# Intravital Imaging of the Immune System

Melanie P. Matheu, Michael D. Cahalan, and Ian Parker

**Abstract** Two-photon imaging of the immune system has revealed an active world of in vivo intercellular dynamics. Rather than static bystanders, immune cells have been re-cast as active participants in the local orchestration of immune responses. Their active motility and probing lead to new questions regarding how localization, motility, and cell-cell interactions contribute to immune responses. In combination with imaging, the use of fluorescent proteins and genetic approaches is also helping to define a role for endogenous receptor-ligand interactions and structural elements in supporting communication between the highly specialized hematopoietic cells that comprise the immune system. Although explanted tissue and organ systems are convenient for several applications, and can be established with minimal perturbation of cellular behavior or tissue environment many disease models and questions surrounding lymphocyte function require the development of stable imaging preparations that allow for long-term access to often difficult-to-reach tissues in the living animal. Here, we review emerging and established techniques for in vivo peripheral tissue imaging by two-photon microscopy.

**Keywords** Multiphoton microscopy • Lymphocyte dynamics • Antigen presentation • Lymph node

---

M.P. Matheu (✉)  
Bluestone Laboratory, UCSF Diabetes Center,  
513 Parnassus Ave HSW 1102, San Francisco, CA 94143, USA  
e-mail: [mpmatheu@gmail.com](mailto:mpmatheu@gmail.com)

M.D. Cahalan  
Department of Physiology and Biophysics and the Center for Immunology,  
University of California, Irvine, Irvine, CA 92697-4561, USA  
e-mail: [mcahalan@uci.edu](mailto:mcahalan@uci.edu)

I. Parker  
Department of Neurobiology and Behavior, University of California, Irvine,  
Irvine, CA 92697-4561, USA  
e-mail: [iparker@uci.edu](mailto:iparker@uci.edu)

## 4.1 Introduction

The advent of two-photon (2P) microscopy has revolutionized studies of cellular immunology by enabling high-resolution imaging deep into intact tissues and organs with minimal photo-damage to living cells. Two-photon excitation occurs when a fluorophore is excited by the near-simultaneous absorption of energy from two infra-red photons, each of which contributes one half of the energy required to induce fluorescence. Because there is a quadratic dependence on excitation intensity, fluorescence is constrained to the focal spot formed by the microscope objective, thereby providing an inherent ‘optical sectioning’ effect (Cahalan et al. 2002). In order to achieve practicable fluorescence signals, the photon density in the focal spot must be incredibly high to achieve the excited state through near-simultaneous absorption of low-energy photons, while avoiding photo-toxicity. This is achieved by use of femtosecond pulsed lasers, which concentrate photon output into brief (sub-picosecond) bursts with enormous instantaneous power interspersed by much longer dark periods (Cahalan et al. 2002). The quadratic dependence of excitation constrains fluorescence to the focal spot formed by the microscope objective, thereby providing an inherent ‘optical sectioning’ effect. To form an image plane, the single point of excitation is rapidly raster-scanned in the x, y dimensions by a system of computer-controlled galvanometer mirrors, creating a size-adjustable imaging plane. Images are often compiled in the axial (z) dimension as well, creating a 3-dimensional stack of images taken over time, hence 4-dimensional imaging. If we consider multiple fluorescent probes emitting at different wavelengths, often yielding real-time intercellular information in, for example examination of calcium signaling or NFAT relocation to the nucleus, *in vivo* imaging becomes 5 dimensional (Marangoni et al. 2013; Wei et al. 2007). One major advantage of 2P microscopy is that light scattering by particles in biological tissue decreases with increasing wavelength, and absorption by hemoglobin and other proteins is minimized at long wavelengths. Thus, the infra-red wavelengths (750–1,200 nm) used for two-photon imaging allow at least a five-fold deeper tissue penetration than confocal imaging. This is of crucial importance for imaging into intact, complex tissues such as the lymph node, where cells and cell interactions may be localized hundreds of micrometers below the tissue surface. Moreover, infrared wavelengths cause minimal phototoxicity, thereby facilitating long-term imaging because tissue damage is largely confined to the focal plane where 2-photon absorption occurs. For the same reason, photobleaching of fluorescent probes is confined to the focal plane which, during time-lapse z-stack imaging illuminates only a fraction of the imaged volume at any given time. Finally, the two-photon excitation spectra of most fluorophores and fluorescent proteins are generally broader than their single-photon excitation spectra. Therefore, a single excitation wavelength can be used to efficiently and simultaneously excite multiple probes with distinct emission wavelengths. It should be noted that the quantum efficiency of many fluorescent proteins is often enhanced or diminished by two-photon excitation relative to single photon fluorescence yields and cannot be predicted but is determined empirically (Drobizhev et al. 2011).

In summary, the inherent properties of 2-P excitation allow for greater preservation of native cell behavior in living tissue than other imaging techniques. Single cell resolution enables researchers to directly examine the dynamics of cell behavior and interactions in the immune system. Within 24 h, antigen-specific naïve cells that represent less than 0.00001 % of the lymphocytes in the body must correctly locate, communicate, proliferate, secrete cytokines and initiate a highly specific immune response. Imaging these processes in real-time has shed light on a previously unknown choreography of cell-cell interactions that support and contribute to immune system dynamics. Several articles comprehensively describe the use of 2-P microscopy for live cell immunoimaging (Zinselmeyer et al. 2009; Cahalan and Parker 2008; Matheu et al. 2011a; Dzhagalov et al. 2012). Here, we focus specifically on the preparation and implementation of intravital 2-P imaging techniques in living animals.

## 4.2 General Considerations for Intravital Preparation of Tissues for Two-Photon Imaging

In comparison with imaging of explanted tissues, intravital imaging is laborious and often requires prolonged (several hours) anesthesia and surgical procedures that may lead to a higher experimental failure rate. Nevertheless, intravital imaging yields imaging information under more truly physiological conditions, and enables study of processes such as lymphocyte homing, egress, and extravasation that cannot otherwise be investigated. Therefore, careful experimental design, identification of pertinent questions that can only be elucidated by live tissue imaging, and selection of the most relevant time-points are essential components to address before embarking on an intravital two-photon imaging experiment. It is often helpful to initially undertake *in situ* imaging of explant preparations to troubleshoot and identify critical time-points in preparation for subsequent intravital experiments. A generalized experimental workflow for development and implementation of an intravital imaging experiment is presented in Table 4.1. A list of common equipment that will be needed in most, if not every intravital imaging preparation is provided in Table 4.2.

## 4.3 Cell and Tissue Labeling

Immune cell imaging typically necessitates that more than one specific cell population be fluorescently labeled. This may be accomplished by staining cells with vital fluorescent dyes; by adoptively transferring cells expressing genetically encoded fluorescent proteins (FPs); or by imaging in transgenic animals expressing fluorescent proteins under a specific promoter.

**Table 4.1** Work flow for the design and development of an intravital imaging protocol

1. Identify model, relevant question, and tissue (s) of interest
2. Determine how relevant cell types will be labeled and check that all PMT filters and excitation wavelengths are compatible
Endogenously expressed FPs are best for longitudinal studies of cell behavior
Many fluorophores with differing emission spectra can be excited at a single femtosecond laser wavelength. However this is not universally true. For example, eCFP and tdTomato do not have compatible excitation spectra. Dual laser excitation will eliminate this issue
3. Are cells of interest $\leq 400$ $\mu$ m deep?
Imaging into tissues to depths $>300\text{--}400$ $\mu$ m may require additional microsurgery, or tissue slicing to expose the area of interest
4. Is the tissue of interest adjacent to vital organs or large blood supply?
Special surgical stabilization equipment such as retractors, clamps, and additional dissection practice may be necessary
5. Is the imaged tissue subject to pulse or respiratory movement (lung, heart)?
A suction window preparation may be necessary (Table 4.4)
Timing z-stack acquisition in synchrony with controlled tissue movement, as with ventilated lung makes imaging possible without the use of a suction window
6. Is the tissue easily separated from the animal body without significant damage to the organ? (e.g. ear, skin flap, spleen, pancreas)
Securing the tissue to a simple warmed platform with warmed media above or perfused over the tissue may be sufficient
If the tissue is not easily separated from the thorax of the animal consider a suction window design
7. Identify the relevant time-points for imaging by FACS assessment of tissues for cells of interest, or by in situ 2-photon experiments
Intra vital imaging and surgery are time consuming and have a high failure rate relative to in situ imaging
Determination of relevant time points should be performed in a more high-throughput, less time consuming manner
8. Design, have animal care committee approved, and practice anesthesia, surgical procedures and tissue stabilization prior to running a full experiment

The first 2P immune-imaging experiments visualized highly motile T cells that were labeled with cell-permeable amine-reactive or thiol-reactive fluorescent dyes (CFSE and CMTMR, respectively) and were then adoptively transferred into recipient animals (Miller et al. 2002). This technique has several advantages, including bright fluorescence of the cell tracker dyes that can be modulated by changing the labeling time of the cells; the availability of dyes with widely differing emission spectra enabling simultaneous imaging of multiple, discrete cell types; and the capacity to monitor cell division in vivo by sequential dilution of the dye. Beyond these dyes which are used to simply mark specific cell types, functional fluorescent probes can be used to monitor various cellular processes; for example, the use of fluorescent calcium indicator dyes to image calcium flux in vivo. Such assays provide information regarding cell activation and behavior relative to the local environment (Wei et al. 2007). Furthermore, real-time information about antigen

**Table 4.2** General list of equipment and reagents for intravital 2P microscopy

Equipment/reagents	Purpose
Waterproof imaging stage	To stabilize the animal under the objective and protect imaging equipment from media leakage or spills
Anesthetic (see Table 4.3)	Necessary for surgery and for maintenance during imaging
Warming pad/stage	Anesthesia may cause a drop in animal body temperature, and exposed tissues cool easily
O-ring or sealable imaging well	To hold the organ of interest in liquid for imaging with a water dipping objective
Suture string	To maintain animal positioning, secure trachea in lung imaging
First aid or sports tape	To restrain animal limbs, or secure animal position
Fine surgical tools	Surgery as necessary
Electric shaver	Fur near surgical site should be removed prior to surgery
Temperature sensor	To measure the temperature of media and or local tissue near imaging site
70 % Ethanol	To ‘wet’ the incision area prior to surgery
Gauze, cotton swabs	To control bleeding during surgery and positioning of animal
Vetbond or similar	For adhering imaging apparatus or o-ring to the animal tissue
Bio-compatible glue	
Vacuum grease or Gel Seal	Additional sealing around imaging wells
RPMI1640 with or without Glucose	For perfusion over tissue or to fill an imaging well created around the imaging site. Glucose helps minimize local swelling
PBS	For hydration via ip injection in recovery studies; and to keep the surgical site moist
Ointment/antibiotics	To protect eyes/ensure recovery in longitudinal studies

presentation can be inferred from peptide-associated dye labels that become activated when cleaved, such as DQ-Ovalbumin. Thus, adoptive transfer of cells remains a convenient and powerful tool for in-vivo imaging of a variety of lymphocyte behaviors.

Despite the power and convenience of exogenous cell labeling and adoptive transfer, endogenous expression of a variety of cell-lineage specific fluorescent protein circumvents potential artifacts due to label toxicity or a high number of adoptively transferred cells. Numerous transgenic mice have been generated that express a wide range of fluorescent proteins (including eCFP, eYFP, eGFP, RFP, tdTomato). FP expression may be controlled by under specific promoters for proteins of interest (Reinhardt et al. 2009), or by a general promoter such as Rosa,  $\beta$ -actin, or ubiquitin. It should be noted, however, that the half-life of FPs may vary in vivo, especially when tagged to a protein of interest. Therefore, measurements of fluorescence intensity as a read-out of gene expression should be interpreted with caution. Once characterized, genetically-encoded fluorescent proteins can be employed to provide gene expression information, in addition to merely tracking cell movements. Linking of FP expression to genetic output allows analysis of subpopulations and



potential changes in behavior as a result of either gene expression or activation status in the living tissue. Finally, fluorescent proteins can be incorporated into probes for cellular signaling; for example to monitor cytosolic calcium levels, TCR signaling via Nur77 expression, or NFAT translocation (Marangoni et al. 2013; Moran et al. 2011; Wei et al. 2007).

When selecting an FP-expressing animal strain for an imaging project, a critical consideration is the expression level and brightness of the fluorescent protein. As a general guideline, if the fluorescence intensity in the cells of interest is  $>2.5$  log units over background by flow cytometry, cells will likely be bright enough to be detected by 2P microscopy. Increased laser excitation or longer scan times may be used to detect dim cells. However, controls for tissue damage and cell death should be used in such situations as laser toxicity can develop cumulatively over the course of an imaging experiment. Transgenic mice expressing free cytosolic FPs under the actin promoter are useful in cases where the cells of interest can be isolated and adoptively transferred, and have the advantage that the fluorescence signal does not become diluted by successive rounds of cell division.

Fluorescently labeled and / or blocking antibodies have been used to identify structural elements and cells *in vivo*, presenting a convenient way to quickly examine structures of interest or particular cell populations. Using labeled antibodies and deconvolution analysis allows for tremendous flexibility and improved information (Gerner et al. 2012), however, results of such studies that depend on the analysis of motile cells must be carefully interpreted and controlled as an antibody may significantly alter cell-cell, cell-substrate interactions or elicit aberrant signaling that may affect cell behavior. Vascular architecture may be highlighted by injection of label conjugated dextran, non-targeted quantum dots or microspheres into the blood stream.

2P microscopy of fluorescent labels can be readily combined with second-harmonic imaging of tissue substructure. Proteins with non-centrosymmetric, molecular structures, such as collagen and myosin, generate a second harmonic signal that is half the wavelength of the 2-photon excitation wavelength (Rivard et al. 2013; Gauderon et al. 2001; Zoumi et al. 2002); for example, an excitation wavelength of 900 nm yields a violet-blue signal at  $\sim 450$  nm. The second-harmonic generation propagates in the direction of the excitation light, but there is typically sufficient back-scattered light to provide enough signal to be detected by a typical 2P epifluorescence imaging system.

Various methods for *in vivo* and *in situ* labeling of cells for two-photon imaging and their associated advantages and caveats are summarized in Table 4.3.

## 4.4 Anesthesia and General Surgical Considerations

Several combinations of anesthetics and analgesics can be used to achieve and maintain a surgical plane of anesthesia for *in vivo* imaging. Injectable drugs such as ketamine/xylene combinations do not require additional equipment in the

**Table 4.3** Fluorescent labeling of immune cells for in vivo 2P imaging

Method	Advantages	Caveats
<b>Exogenous label and adoptive transfer</b>	Bright	Cells lost during staining
Purify cells of interest from naive, KO or transgenic donor. Label with cell-tracker dyes. Adoptively transfer into recipient animal either directly or after culture	Multiple colors	High purity necessary
	Rapid labeling	5–7 days maximum detection
	Any cell of interest	Multiple labels must have balanced brightness
	Cell division tracked	Transfer of excessive numbers of cells may lead to artifactual responses
	Ca <sup>2+</sup> imaging	
	Cell arrival can be synchronized	
	Cell death can be tracked	
<b>Transgenic animals expressing fluorescent proteins in specific cell types, tagged to specific proteins, or as functional probes</b>	Unperturbed endogenous population	Many FP labels are dim
Image directly without need for further labeling	Long-term studies possible	High cell density may limit single-cell resolution
	FP tagged transcription factors and cytokines yield real-time information	Some FPs rapidly photo-bleach
	Compatible with adoptively transferred dye-labeled cells	Several backcrosses may be necessary to specifically label cells of interest
	Natural second harmonic signal highlights collagen and myosin	In Cre reporter animals variable expression may alter identifiable populations
	Interactions via FRET can be monitored	
	Photo-convertible proteins can be used to study trafficking	
<b>Dye-conjugated antibodies and other fluorescent reagents</b>	Antibodies are available for a myriad of relevant targets	Antibodies may alter endogenous cell function and behavior
	Several choices of fluorescent label	Tissue injection or soaking of the LN must ensure antibody distribution
	Deconvolution of multiple signals is possible using commercially available software	Many conjugates are highly photo sensitive
	Lymphatics and blood vessels are easily labeled by local subcutaneous or iv injection, respectively with Q-dots or fluorescently conjugated dextrans (>70 KDa)	Antibody staining in vivo require controls to ensure specificity

microscopy room. However, monitoring and maintaining the surgical plane when using injectable anesthetics for extended period of time is challenging, particularly as 2P imaging is generally done in near-darkness due to wide-field detector (PMT) sensitivity to stray light. In contrast, inhaled anesthetics have a higher margin of safety due to administration of a constant dose that produces a stable plane of surgical anesthesia, when used with a calibrated vaporizer. Accidental animal recovery or overdose is less likely to occur. Therefore, inhalant anesthesia systems such as isoflurane are often the better choice for dedicated high-use 2-P *in vivo* imaging systems. Although there are several approved anesthetics and analgesics, different institutions often have different recommendations. As with any anesthesia, labored, agonal breathing is a sign of overdose with both inhalant and injectable anesthesia and the animal should be further monitored for partial recovery prior to proceeding with the experiment. Here we provide summary of widely available, commonly used and approved anesthetics for both terminal and recovery procedures is provided in Table 4.4 (Fish et al. 2008).

In general, surgical procedures should be minimally invasive, maintain circulation in the tissue of interest, and should be developed in collaboration with veterinarians and approved by animal care and use committees. Surgical sites surrounding the imaging area should be kept moist with a phosphate-buffered saline solution or hydrating gel, and the imaged tissue should be maintained at physiologic temperatures. Prior to initiating surgery, a surgical plane of anesthesia marked by unconsciousness, muscular relaxation, and lack of pain response/reflex must be established. Animal vital signs must be monitored throughout the entirety of the procedure.

Although survival surgery is possible with antibiotic treatment, local inflammation, and tissue scarring may significantly alter the results of an immunological based study of local cell behavior (Davalos and Akassoglou 2012). A semi-permanent 'window' into the tissue, as developed for brain imaging studies (Isshiki and Okabe 2014), is ideal as the tissue of interest is kept intact and protected from inflammation at the surgical site. However, repeated survival surgery in a short period of time (a few days) may confound results by introducing additional swelling, local tissue damage, and introduction of exogenous pathogens. Other essential considerations are maintenance of blood and lymphatic flow, animal respiration under anesthesia (avoiding hypoxia), and tissue integrity. Additionally, careful dissection under a microscope to remove fat layers covering a tissue of interest while preserving blood flow will improve the label signal, imaging depth, and image quality. Intra-vital imaging also requires minimization of movement of the imaging site owing to respiration and heartbeat. Surgical sites that are the most easily exposed and imaged are those that are in the periphery and do not involve the abdominal cavity, head or neck. Organs that can be externalized (from the abdominal cavity) and stabilized such that movement from heart beat and breathing do not interfere with image stability may be achieved through a small incision in the abdominal wall. The most advanced intravital imaging involves practice, surgical skill, and the creative development of techniques to stabilize moving or fragile organs such as lung or pancreas. Many tissues have been successfully imaged intravitaly and several key tissues and general procedures are summarized in Table 4.5.

**Table 4.4** Anesthesia methods

Anesthetic	Dosage	Use	Route/dosing	Notes
Isoflurane or Sevoflurane	2–3 % inhalant to effect (up to 4 % for induction)	Especially useful for lung imaging during which ventilation is necessary	Inhalation	Survival surgery requires additional pain management (analgesia)
	Sevoflurane may require a higher dosage			
Ketamine	K: 60–100 mg/kg	Convenient when a dedicated ventilator is not available	IP	Precision vaporizer and gas scavenger required to avoid venting into room air
Xylazine	X: 5–10 mg/kg			If re-dosing, use Ketamine alone – additional Xylazine will suppress respiration
or				Acepromazine provides sedative effects and can be included in additional dosages
Ketamine	K: 50–100 mg/kg			
Xylazine	X: 10–20 mg/kg			
Acepromazine	A: 2–3 mg/kg			
	Single syringe mixture		Monitor vital signs and re-dose as necessary (e.g. every 30–45 min)	

**Table 4.5** Surgical procedures for different intravital imaging preparations

Tissue	General procedure (s)	Imaging stage(s)	Selected references
Lymph node	Expose and stabilize Inguinal or popliteal LN	Inguinal: o-ring holder to isolate LN and contain media Popliteal: media well around joint	Miller et al. (2003), Liou et al. (2012), Matheu et al. (2011b), Mempel et al. (2004)
Spleen	Small incision on left side, elevate organ away from body	Suction window or moveable platform that secures organ above the animal	Ferrer et al. (2012)
Lung	Incision large enough to remove three ribs on left or right side below forearm. Ventilation system required	Suction window to stabilize local lung movement and reduce imaging artifact	Thornton et al. (2012), Kreisel et al. (2010), Looney et al. (2011)
Pancreas	Small incision on left side to expose spleen, gently pull spleen followed by pancreas away from the body	Platform with warmed media circulation or an adapted suction window as used with the lung procedure	Coppieters K et al. (2010)
Intestine	Small midline incision. Either pull from the mouse or rat body or leave secured in place with coverslip glued above. Paralytic (atropine at 1 mg/kg may be necessary)	Intestine may be pulled away from the core of the animal and secured to a small warmed imaging platform or directly imaged in the core of the animal by gluing a coverslip at the bottom of an imaging chamber to the intestine	McDole et al. (2012), Chieppa et al. (2006)
Footpad	Restrain of limb of interest with the footpad facing the microscope objective	On a warming platform mold a water-tight well or place a fitted imaging well around the leg of the animal	Sen et al. (2010), Zinselmeyer et al. (2008)
Ear	Secure ear to a warmed platform and place an o-ring over the site of interest for imaging	Simple platform that will easily accommodate a mouse or rat ear with warming capabilities	Sen et al. (2010), Peters et al. (2008)
Skin	Shave the area of interest	Using tissue-safe glue place an o-ring over the area of interest, fill the o-ring with tissue culture media or 1× PBS	Kim et al. (2010), Odoardi et al. (2007)
Spinal cord	Basic laminectomy of 3–5 vertebrae, using caution to avoid disrupting the spinal cord	Platform to support the head and tail with the mouse or rat in the prone position. Mounted small-animal tissue retractors expose the laminectomy site	Llewellyn et al. (2008), Rothstein et al. (2005)

**Table 4.5** (continued)

Tissue	General procedure (s)	Imaging stage(s)	Selected references
Muscle	Restrain the animal and expose the muscle of interest	General use warming platform. Place an o-ring over the area to be imaged or build a media well around the area using inert tack	McGavern and Kang (2011), Dombeck et al. (2007), Pai et al. (2012)
Brain	Create a skin flap above the area of interest. Thin the skull	A small o-ring may be glued around the imaging area to help retain media. Or imaging may be performed directly with a few drops of media	Ishii et al. (2009), Kohler et al. (2011)
Heart	Ectopic transplant and engraftment for ease of exposure. Acquisition timed with ventilation to minimize movement	Adjustable upper and lower plates with an o-ring holder built in the middle to stabilize the imaging well	Li et al. (2013), Li et al. (2012)

4.5 Construction of In Vivo Imaging Stages

In general, an imaging stage should be constructed such that it is easily moved and compact but can be stably secured under the microscope. This may require tapping new screw holes in the microscope stage. The stage should be large enough in the x, y dimensions to support and position the animal while allowing for securing of perfusion tubes, additional stage parts, and suture string by taping. Finally, the imaging stage should be designed to prevent fluid leaks/spill-over into the microscope housing, stage, air-table or other equipment. Building a stage with raised edges is one way to protect from media leakage or spills. For some procedures, such as ear imaging, a block or platform secured to the stage is used to further support the tissue. Stage modifications may be achieved temporarily with waterproof tape, or by permanent attachment via waterproof epoxy glue or by stage-specific screws.

Several materials are suitable for the construction of an imaging stage. Plexiglass or Lexan are inexpensive, easily cut or milled, heat resistant, durable, and easy to clean. However, metal stages have the advantage of being less easily stripped by screw-in modular parts and represent a viable alternative for a high-use stage. 3D printing technology now allows for easy creation of small custom parts, including head restraints, nose cones, custom o-ring holders and vacuum-suction imaging windows. Several free 3D rendering programs designed to work with 3D printers are available online (e.g. Autodesk 123D, Blender, Wings3D). and commercial programs such as AutoCAD and Solidworks offer student and academic program versions.

A warming plate attachment is necessary to maintain constant temperature at the site of imaging. Often the animal can be warmed with a simple heating pad



placed under the whole animal. Additional local warming of the imaged tissue is necessary in the case of tissues isolated from the core of the animal, such as in skin-flap or spleen imaging, or with use of liquid on a peripheral tissue (ear and footpad). A simple warming device is easily created by attaching a resistor with thermal compound to a copper or aluminum platform. Small square resistors ( $\sim 10\text{--}40\ \Omega$ ) that are designed to be attached to a heat-sink will provide enough power to warm an imaging stage to  $37\text{--}38\ ^\circ\text{C}$  when attached to a variable 12 V power supply. The resistor should be placed at least an inch or two away from the imaging site to avoid getting wet or interfering with animal positioning. The warming plate may be covered with a layer of heat-resistant Vinyl tape which will allow for easy cleaning while protecting the warming device from repeated contact with tissue and liquid. A small thermocouple or thermistor probe is used to monitor the temperature of the tissue close to the imaging site, which can be regulated either by manual adjustment of the power to the heater, or by a feedback circuit.

## 4.6 Intravital Imaging Preparations

### 4.6.1 Skin

Imaging the ear pinna or footpad of the mouse or rat is a convenient way to examine the behavior of cells in the skin. Because the footpad is hairless, auto-fluorescent hair follicles do not interfere with the imaging signal. Also, the ear pinna has little hair, particularly the lateral surface, or inside of the pinna leading to the ear canal. The skin is perfused by blood vessels near the surface, and local injections are easily carried out in the footpad or pinna allowing for straightforward design of lymphocyte homing or infection/pathogen invasion studies. No surgery is necessary to visualize lymphocytes, facilitating longitudinal imaging studies in the footpad and ear pinna. Intravital imaging in the footpad and ear pinna has been used to successfully monitor several immune reactions and cell types that are native to the skin, including delayed-type hypersensitivity (DTH), parasite infections, T cell, ILC2 (type 2 innate lymphoid cells), adjuvant mobilization of dermal dendritic cells and Langerhans cells, and neutrophil behavior (Matheu et al. 2008; Peters et al. 2008; Chtanova et al. 2008; Zinselmeyer et al. 2008; Roediger et al. 2013; Kreisel et al. 2010). In comparison to the mouse, we find that deeper imaging in the ear pinna of the rat requires some surgery to remove the thicker epidermal layers, particularly under conditions of inflammation and local tissue edema. The ear and footpad are collagen-rich tissues, and the second harmonic signal from the collagen provides useful structural markers during two-photon imaging. Injection of a high molecular weight (70 kDa or higher) fluorescent dextran, or unconjugated quantum dots can be used to mark blood vessels. Here, we describe methods for preparing the footpad and ear pinna for 2P imaging.

#### 4.6.1.1 Footpad Imaging

Once the surgical plane of anesthesia is achieved, place the animal in a prone position with the hind leg of interest extended behind the animal and over a warming plate pre-warmed and stable between 35 and 37 °C. Note that the ear and footpad are naturally slightly cooler than mouse core body temperature. Using breathable medical tape, secure the fore-paws of the animal to the stage. If a nose-cone is being used to administer isoflurane or medical oxygen, tape the nose cone and tubing securely to the imaging stage. Gently tie suture string around 2–3 toes, carefully pull the string taught, wrap it around the edge of the stage and secure it to the underside using waterproof tape. At this point the circulation to the toes of the animal should be checked by looking for swelling or significant color change. This is especially important for survival imaging and longitudinal imaging studies. The footpad and suture strings should be as flat as possible against the imaging stage. Tape the hind leg in place close to the body and the tail off to the side, away from the footpad that will be imaged. Once the animal is secure, build a well of sticky poster-tack around the footpad large enough to allow free access by the microscope objective. To ensure a water-tight seal, a layer of vacuum grease may be applied, and the leg may be shaved if fur interferes with the integrity of the well. Mold the tack around suture strings and above the foot-pad of the animal. If footpad imaging will be high-use or high-throughput a plastic well shaped to accommodate the leg of the animal may be built and placed over a thin layer of sticky-tack adhered to the animal to maintain a seal.

#### 4.6.1.2 Ear Pinna Imaging

Ear imaging is facilitated by raising the pinna on a small plastic block or platform that is secured next to the head of the animal, and is fitted on its upper surface with a small warming plate. This will allow the animal to be placed in a natural supine or prone position rather than placing the animal laterally to lay the ear flat, which introduces more movement artifact. Place the anesthetized animal in the prone or supine position to expose the side of the ear to be imaged. The ventral side (interior) of the ear pinna is preferred for imaging due to a lower number of autofluorescent hair follicles. Secure the animal in this position using medical tape and, if necessary, gauze bundles to provide additional support. Cover the warming pad with medical tape to which the animal ear may be glued directly with cyanoacrylate (VetBond 3M™) adhesive; alternatively, the tip of the ear may be taped down to the imaging stage. For longitudinal studies the tape and animal can be removed from the imaging stage and the tape removed from the ear with gentle washing with 70 % ethanol. Once the ear is secured, either of two imaging chambers can be employed. First, for imaging of a small area an o-ring may be glued directly to the ear tissue and filled with media. If leakage near the base of the ear occurs, more glue may be applied to the outside of the o-ring and thin layer of vacuum grease

will maintain the seal. Alternatively, a moldable imaging chamber may be constructed with Sticky Tack (Poster Tack), which has the advantage of allowing for imaging closer to the animal head as the tack can be molded around the ear to create a sealed well.

The ear and footpad are collagen-rich tissues, thus a robust second harmonic signal within these tissues provides useful structural markers during 2-P imaging. Injection of a high molecular weight (70 kDa or higher) fluorescent dextran, or unconjugated quantum dots can further be used to mark blood vessels.

The use of depilatory cream or similar products is contra-indicated for imaging of immune responses, because a locally induced inflammatory response may alter endogenous cell behavior, progression or outcome of the immune response; although dendritic cell migration is reported to be unaffected careful controls for induced inflammation should be considered (Roediger et al. 2008).

### 4.6.2 *Lymph Node Imaging*

Imaging lymphocyte behavior is essential for understanding the underlying choreography and orchestration of an immune response. The development of an immune response and native behavior of lymphocytes under multiple conditions including thymic selection has been studied intensely within the last decade (Germain et al. 2012; Jacobelli et al. 2013; Tang et al. 2013), however, the nature of many cell-cell interactions, and underlying molecular forces that support cell-cell communication during various immune responses remain undefined.

The lymphatic system is comprised of a network of dedicated vessels that, starting from the extreme periphery, ferry lymphatic fluid, antigens, infectious particles and lymphocytes through sequentially arranged peripheral lymph nodes, eventually returning lymph to the circulation via the thoracic duct. Lymph nodes filter and collect pathogens as well as peripheral antigen bearing APCs, creating a contained local environment to facilitate rapid response upon local injury and infection (Girard et al. 2012). They are highly organized structures wherein cell-cell contacts and antigen delivery by DCs or lymph node-resident macrophages are tightly controlled by local chemokines to orchestrate the development of a pathogen relevant immune response (Phan et al. 2009; Gray et al. 2012; Germain et al. 2012).

The inguinal lymph node is a large, accessible lymph node that is easily prepared for intravital imaging. The popliteal lymph node is another popular choice for imaging, but is more challenging to achieve a stable preparation. Here we describe the original preparation of the mouse inguinal lymph node for 2-P imaging and present two designs for tissue stabilization during imaging. Additional equipment required for the imaging of peripheral lymph nodes using these methods is provided in Table 4.6.

**Table 4.6** Procedure-specific equipment

Lymph node imaging	Dissecting microscope
	Necessary for the removal of fat above lymph node
	O-ring holder
	Static chamber over warming platform
	Superfusion chamber attached to stage (warmed media)
	12 mm ID rubber O-ring
	Small bundles of gauze to help position the animal
Lung imaging	PBS to keep surrounding tissue moist
	1–1.5 inch long 18–22 gauge intubation tube
	Y connector for intubation tubes
	50 mL conical tube
	Rubber stopper that fits 50 mL conical tube
	Small animal ventilator (mouse/rat)
	Vacuum pressure regulator (20–25 mmHg)
	Vacuum imaging window and stabilizing/attachment arm
	12 mm circular glass or unbreakable plastic coverslip
Spinal cord imaging	Compressed room air
	Mounted small animal retractors for laminectomy
	Laminectomy forceps
	Artificial cerebrospinal fluid (ACSF)
	Small animal holder/ restraint
	Stereotactic holder for the head and support of hind limbs may be useful to keep the spine straight during imaging

**4.6.2.1 Inguinal Lymph Node Imaging Procedures**

Once the animal is properly anesthetized, begin by shaving the lower abdomen and stomach with electric clippers, wet any remaining fur with 70 % ethanol, and make a mid-line incision from the lower abdomen to the base of the lungs without cutting into the peritoneum. On the side of the lymph node to be imaged, make a second cut starting from the lower abdomen midline incision along the inside of the leg down to the top of the knee forming a skin flap. Gently separate the skin-flap from the body of the animal, exposing the region of the inguinal lymph node. Ensure that the skin flap is separated enough to comfortably place the o-ring holder over the area of the lymph node without pressing against the body of the animal. Hold a rubber o-ring (12 mm ID) in a pair of forceps and apply a thin film of VetBond 3M™ to the bottom surface, wiping off superfluous glue such that only a thin layer is left. Gently place the o-ring onto the skin flap, centered over the exposed lymph node. To cure the glue from the inside of the o-ring, fill the o-ring with ~1 mL of PBS and wipe away excess cured glue that will float to surface. Excess glue can adhere to the exposed lymph node and obscure the two-photon signal. Flush the area around the outside of the o-ring with PBS to cure the glue around the outer edges of the o-ring

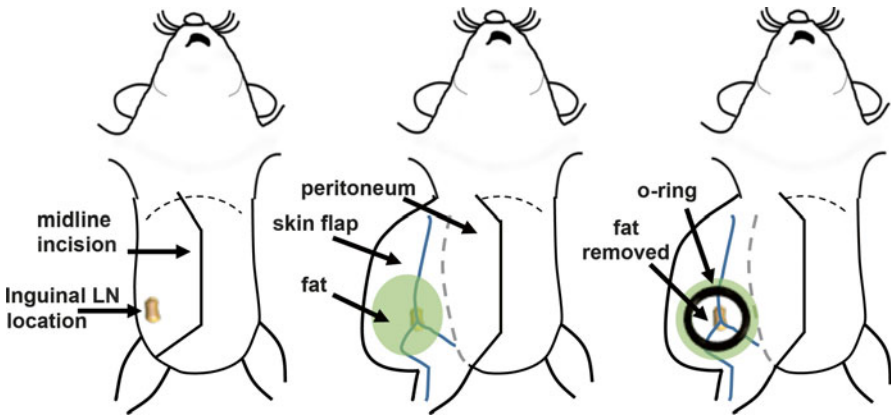


**Fig. 4.1** Preparation of inguinal lymph node for in vivo 2P imaging

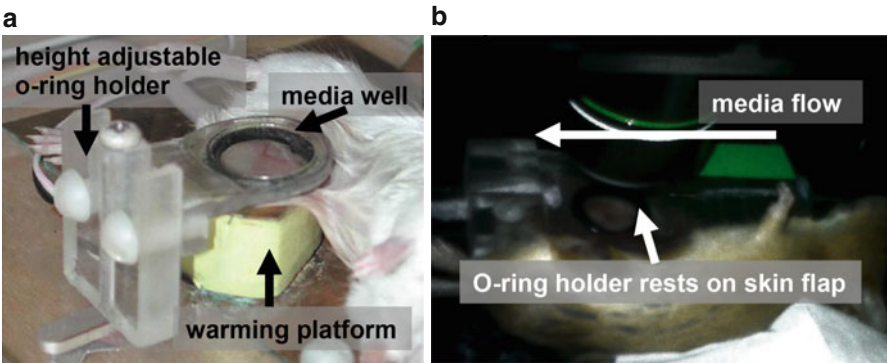


**Fig. 4.2** O-ring based chambers for inguinal lymph node imaging. (a) Static well on warming platform (b) Superfusion chamber

to cure any remaining glue and ensure that the skin flap is hydrated. Soak 2 or 3 gauze strips in PBS and place them on the exposed areas of the animal to keep them moist while leaving the skin flap free. Fill the o-ring with media and place the animal under a dissecting microscope. Using fine-tipped forceps carefully remove fat around the organ while maintaining blood vessel integrity. Fat removal will be facilitated by the liquid in the o-ring which will allow it to float to the top. Replace the media in the o-ring if too much fat is present and cannot be wicked away. A schematic illustrating the o-ring preparation of the inguinal lymph node is presented in Fig. 4.1.

Figure 4.2a shows a simple design of an o-ring holder to stabilize the node and maintain physiological conditions for imaging. Once the lymph node is exposed, line the inside of the o-ring holder with a thin layer of vacuum grease, position the animal such that the o-ring is directly under the holder and gently press upwards such that the o-ring is secure in the holder. At this point the animal should be

supported by a small warming platform such that the o-ring is level with the animal and no tension is placed on the tissue. The warming platform should extend under the imaged lymph node and skin flap. Check the o-ring system for leaks and proceed with two-photon imaging.

An alternative o-ring holding system may be used conjunction with a warmed media superfusion system as seen in Fig. 4.2b, which enables improved temperature control and minimizes leakage or drying of the imaging well. A perfusion-coupled o-ring holder should be the length of the animal, fitting under the foreleg and over the leg, with a carved-out region on the underside such that the lower leg can be positioned and taped in place. In the center of the block a hole for the o-ring should be made with an inlet for media perfusion on one side and suction on the other. The underside of the o-ring holder should be thinned in the area of the skin flap such that it can be placed directly over the tissue without pressing on the skin flap and impairing circulation, while still holding the o-ring in place. Using this system, media warmed by an in-line heater may be superfused over the tissue during imaging, yielding improved temperature and imaging stability.

### 4.6.3 *Imaging Organs of the Abdominal Cavity*

When imaging organs in the abdominal cavity they must be stabilized such that breathing and heartbeat do not cause tissue movement during imaging. Several abdominal organs including lung, liver, pancreas, and intestine have been successfully imaged (McDole et al. 2012; Thornton et al. 2012; Coppieters et al. 2010; Chieppa et al. 2006; Egen et al. 2008). Here we describe a simple preparation for spleen imaging; and a suction window preparation for use in lung imaging (Thornton et al. 2012; Looney et al. 2011). The latter system is readily adapted to imaging of multiple tissues that require stabilization. We also present unpublished methods for the stable imaging of a spinal cord preparation.

#### 4.6.3.1 **Lung Imaging**

Live imaging of the lung enables the behavior of lymphocytes to be visualized during a myriad of disease responses in this delicate tissue. However imaging depth is typically limited to less than 100  $\mu\text{m}$  by the difference in refractive index between air in the alveoli and tissue which is closer to that of water. To image deep in the lung, a slice preparation is a useful way to examine cellular behavior (Thornton et al. 2012; Matheu et al. 2013). Additional equipment and materials for lung imaging can be found in Table 4.6.

A diagram of the ventilation system and intubation is provided in Fig. 4.3a. Imaging the inflated lung requires a custom vacuum window as shown in Fig. 4.3b, stable intubation, a mechanical ventilation system (e.g. Harvard Apparatus or Kent Scientific), an isofluorane vaporizer, and a positive end-expiratory pressure



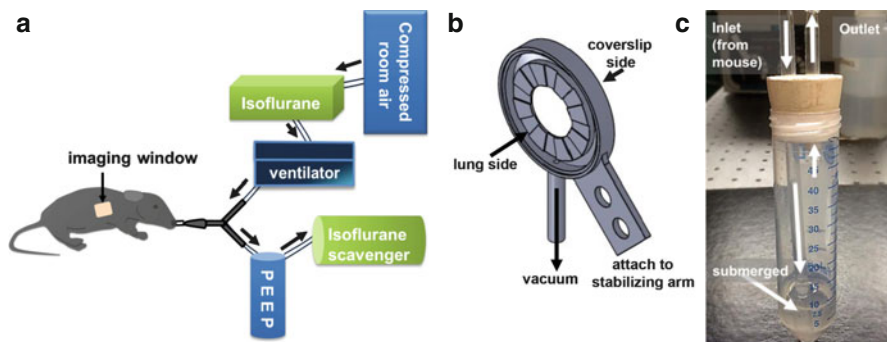


**Fig. 4.3** Vacuum window system for in vivo lung imaging. (a) Ventilation system and mouse intubation. (b) Custom vacuum window. (c) Custom-made positive end-expiratory pressure ventilation system (PEEP). (Images courtesy of the Biological Imaging development Center, UCSF)

ventilation system (PEEP) that may be constructed in-house. The imaging window system described here was developed and designed in the Krummel laboratory at UCSF. For anesthesia, isoflurane-perfused room air is best used due to acid build-up associated with pure oxygen usage over an extended period of time. A PEEP is easily created by submerging the outflow from the intubated animal under  $\sim 3$  cm of water in the bottom of a stoppered conical tube (Fig. 4.3c). Outflow from the conical tube should be collected via a second tube (not submerged) and fed into an isoflurane scavenging system.

Full-sized mice (20–25 g) are best used for lung imaging to improve the success rate of surgery. First set up the vacuum window system with a small round coverslip secured to the flat part of the window with a thin line of vacuum grease, taking care not to have any grease enter the grooves that will allow for suction. The conical side of the window should be facing down and will make contact with the lung itself. The window arm should be secured using a compact right-angle clamp holder (Bosshead style) which will allow it to be secured to a vertical support rod screwed into the microscope stage. This will allow for easy positioning in the x, y and z-direction relative to the lung. The animal may be anesthetized with either injectable anesthetic or isoflurane. Shave the area of the animal where lung imaging will be performed (typically left or right side, just under the foreleg), also shave the underside of the throat for the intubation surgery. If isoflurane is being used, intubation surgery must be performed quickly (within 1 min) such that the animal does not regain consciousness. Extensive practice of this procedure is recommended prior to live animal use. The general procedure for intubation requires that an incision of 2–3 cm is made from just even with the jaw, down to the collar bone of the animal. Next, gently pull aside the skin, then the muscle covering the trachea to expose at least  $\frac{1}{2}$  cm of the trachea. Thread a suture string under the exposed trachea, partially transect the trachea above the string and immediately intubate the animal. Tie the suture string around the trachea and intubation tube making an air-tight seal.

Once the tracheal intubation is complete and the animal is stability ventilated, turn and position the animal on its side exposing the shaved area for surgery. Folded

gauze is placed under the animal to support the thorax and improve lung exposure. Tape the animal in place on the heated stage. Make a small incision on the side of the animal under the forearm or on the chest and cut away the skin above at least three ribs. Carefully cut three ribs by gently cutting them at either side of the incision and removing them, cauterizing as necessary. This will expose the outside of the lung. The exposed lung should be inflated and moving in time with the respirator. Move the animal and stage under the microscope and lower the vacuum window with mounted coverslip onto the exposed lung tissue. Once the vacuum pressure is stable (between 20 and 25 mmHg; 0.02–0.03 bar) and the lung is secure against the coverslip, place a drop or two of media on top of the coverslip, lower the microscope objective and focus on the tissue. During imaging, monitor the vacuum pressure and replace evaporated media as necessary to maintain the image.

#### 4.6.3.2 Spinal Cord Imaging

Spinal cord imaging methods have been reported by several groups, utilizing similar preparations to expose the dorsal side of the spinal cord for imaging of axons and infiltrating lymphocytes (Johannssen and Helmchen 2013; Davalos et al. 2008; Davalos and Akassoglou 2012; Steffens et al. 2012). It should be noted that the ventral side of the spinal cord is not readily accessible to intravital imaging, and the high lipid content of the spinal cord precludes imaging through the thickness of the cord. Therefore, if the cells of interest are located on the ventral side, an ex-vivo preparation may yield better imaging results.

For intravital imaging, place the anesthetized animal in a prone position on a warmed imaging stage. To keep the back as straight as possible, it is necessary to support the tail and head of the animal. Support can be achieved with a folded and secured piece of gauze or fixed platform that will allow for the nose cone to remain on the animal. Shave the back of the animal around the site where surgery will be performed and clean the surgical site with ethanol to remove any remaining stray fur. Make a 1½–2 cm longitudinal incision in the skin, centered above the imaging site. Carefully retract the skin and the underlying muscle by pulling them to the side and placing small retractor clamps or small spinal cord clamps on either side to keep the spine exposed. Choose an area in the center where the lamina will be removed. Carefully cut the lamina free by lifting the spine with forceps and sliding small, very sharp surgical scissors under the lamina and cutting the bone on both sides. The lamina should be removed in one piece with no further tugging or pulling on the spinal cord. Any bleeding may be controlled by using a small vessel cauterizer, or by gently placing pressure on the area with a small piece of gauze, kimwipe, or gel-foam. Rinse the surgical site with warmed artificial cerebro-spinal fluid (ACSF) and fill the well created by the skin and muscle retractors with ACSF. If a larger imaging site is desired remove 1–2 more lamina exposing a length of spinal cord that can be scanned for cells of interest. Add ACSF to the incision site and proceed with imaging. If additional depth around the imaging site is needed Gelseal™ (Vascutek) or similar biologically inert gel may be used to form a deeper well. Because it is

difficult to directly warm the spinal cord, the fluid well above the cord may be superfused with warmed media, or the animal may be placed in a warming chamber kept at 37 °C. Animals may be recovered from the laminectomy and re-imaged several weeks or days later, however due to the open-air nature of 2-photon imaging recovery will necessitate antibiotics, analgesics, and further animal monitoring.

Additional equipment and materials for spinal cord imaging can be found in Table 4.6.

## 4.7 Summary

For in vivo examination of cell behavior, video-rate two-photon imaging is unparalleled by any other imaging technology. Two-photon imaging allows cells to be visualized deep inside living tissues for long periods of time with minimal photo-toxicity. Although in situ preparations are often more convenient and can yield more data per animal, intravital imaging remains a necessary technique for any imaging that requires intact blood and lymphatic flow. With continued development of multi-color reporters and novel analysis methods, two photon imaging both in situ and in vivo will contribute novel insight to our understanding of immune response orchestration.

## References

- Cahalan MD, Parker I (2008) Choreography of cell motility and interaction dynamics imaged by two-photon microscopy in lymphoid organs. *Annu Rev Immunol* 26:585–626. doi:10.1146/annurev.immunol.24.021605.090620
- Cahalan MD, Parker I, Wei SH, Miller MJ (2002) Two-photon tissue imaging: seeing the immune system in a fresh light. *Nat Rev Immunol* 2(11):872–880. doi:10.1038/nri935
- Chieppa M, Rescigno M, Huang AY, Germain RN (2006) Dynamic imaging of dendritic cell extension into the small bowel lumen in response to epithelial cell TLR engagement. *J Exp Med* 203(13):2841–2852. doi:jem.20061884 [pii]
- Chtanova T, Schaeffer M, Han SJ, van Dooren GG, Nollmann M, Herzmark P, Chan SW, Satija H, Camfield K, Aaron H, Striepen B, Robey EA (2008) Dynamics of neutrophil migration in lymph nodes during infection. *Immunity* 29(3):487–496. doi:10.1016/j.immuni.2008.07.012
- Coppieters K, Martinic MM, Kiessens WB, Amirian N, von Herrath M (2010) A novel technique for the in vivo imaging of autoimmune diabetes development in the pancreas by two-photon microscopy. *PLoS One* 5(12):e15732. doi:10.1371/journal.pone.0015732, nmeth.1543 [pii]
- Davalos D, Akassoglou K (2012) In vivo imaging of the mouse spinal cord using two-photon microscopy. *J Vis Exp* 59:e2760. doi:10.3791/2760
- Davalos D, Lee JK, Smith WB, Brinkman B, Ellisman MH, Zheng B, Akassoglou K (2008) Stable in vivo imaging of densely populated glia, axons and blood vessels in the mouse spinal cord using two-photon microscopy. *J Neurosci Methods* 169(1):1–7. doi:10.1016/j.jneumeth.2007.11.011
- Dombeck DA, Khabbazi AN, Collman F, Adelman TL, Tank DW (2007) Imaging large-scale neural activity with cellular resolution in awake, mobile mice. *Neuron* 56(1):43–57. doi:S0896-6273(07)00614-9

- Drobizhev M, Makarov NS, Tillo SE, Hughes TE, Rebane A (2011) Two-photon absorption properties of fluorescent proteins. *Nat Methods* 8(5):393–399. doi:[10.1038/nmeth.1596](https://doi.org/10.1038/nmeth.1596)
- Dzhagalov IL, Melichar HJ, Ross JO, Herzmark P, Robey EA (2012) Two-photon imaging of the immune system. *Curr Protoc Cytom Chapter 12:Unit 12 26*. doi:[10.1002/0471142956.cy1226s60](https://doi.org/10.1002/0471142956.cy1226s60)
- Egen JG, Rothfuchs AG, Feng CG, Winter N, Sher A, Germain RN (2008) Macrophage and T cell dynamics during the development and disintegration of mycobacterial granulomas. *Immunity* 28(2):271–284. doi:[10.1016/j.immuni.2007.12.010](https://doi.org/10.1016/j.immuni.2007.12.010)
- Ferrer M, Martin-Jaular L, Calvo M, del Portillo HA (2012) Intravital microscopy of the spleen: quantitative analysis of parasite mobility and blood flow. *J Vis Exp* (59). doi:[10.3791/3609](https://doi.org/10.3791/3609)
- Fish R, PJDE, Brown M, Karas A, (eds) (2008) Anesthesia and analgesia in laboratory animals, 2nd edn. (American College of Laboratory Animal Medicine). Elsevier, London, UK
- Gauderon R, Lukins PB, Sheppard CJ (2001) Simultaneous multichannel nonlinear imaging: combined two-photon excited fluorescence and second-harmonic generation microscopy. *Micron* 32(7):685–689
- Germain RN, Robey EA, Cahalan MD (2012) A decade of imaging cellular motility and interaction dynamics in the immune system. *Science* 336(6089):1676–1681. doi:[10.1126/science.1221063](https://doi.org/10.1126/science.1221063)
- Gerner MY, Kastenmuller W, Ifrim I, Kabat J, Germain RN (2012) Histo-cytometry: a method for highly multiplex quantitative tissue imaging analysis applied to dendritic cell subset micro-anatomy in lymph nodes. *Immunity* 37(2):364–376. doi:[10.1016/j.immuni.2012.07.011](https://doi.org/10.1016/j.immuni.2012.07.011)
- Girard JP, Moussion C, Forster R (2012) HEVs, lymphatics and homeostatic immune cell trafficking in lymph nodes. *Nat Rev Immunol* 12(11):762–773. doi:[10.1038/nri3298](https://doi.org/10.1038/nri3298)
- Gray EE, Friend S, Suzuki K, Phan TG, Cyster JG (2012) Subcapsular sinus macrophage fragmentation and CD169+ bleb acquisition by closely associated IL-17-committed innate-like lymphocytes. *PLoS One* 7(6):e38258. doi:[10.1371/journal.pone.0038258](https://doi.org/10.1371/journal.pone.0038258)
- Ishii M, Egen JG, Klauschen F, Meier-Schellersheim M, Saeki Y, Vacher J, Proia RL, Germain RN (2009) Sphingosine-1-phosphate mobilizes osteoclast precursors and regulates bone homeostasis. *Nature* 458(7237):524–528. doi:[10.1038/nature07713](https://doi.org/10.1038/nature07713)
- Isshiki M, Okabe S (2014) Evaluation of cranial window types for in vivo two-photon imaging of brain microstructures. *Microscopy (Oxf)* 63(1):53–63. doi:[10.1093/jmicro/dfi043](https://doi.org/10.1093/jmicro/dfi043)
- Jacobelli J, Lindsay RS, Friedman RS (2013) Peripheral tolerance and autoimmunity: lessons from in vivo imaging. *Immunol Res* 55(1–3):146–154. doi:[10.1007/s12026-012-8358-7](https://doi.org/10.1007/s12026-012-8358-7)
- Johannssen HC, Helmchen F (2013) Two-photon imaging of spinal cord cellular networks. *Exp Neurol* 242:18–26. doi:[10.1016/j.expneurol.2012.07.014](https://doi.org/10.1016/j.expneurol.2012.07.014)
- Kim JV, Jiang N, Tadokoro CE, Liu L, Ransohoff RM, Lafaille JJ, Dustin ML (2010) Two-photon laser scanning microscopy imaging of intact spinal cord and cerebral cortex reveals requirement for CXCR6 and neuroinflammation in immune cell infiltration of cortical injury sites. *J Immunol Methods* 352(1–2):89–100. doi:[10.1016/j.jim.2009.09.007](https://doi.org/10.1016/j.jim.2009.09.007)
- Kohler A, Geiger H, Gunzer M (2011) Imaging hematopoietic stem cells in the marrow of long bones in vivo. *Methods Mol Biol* 750:215–224. doi:[10.1007/978-1-61779-145-1\\_15](https://doi.org/10.1007/978-1-61779-145-1_15)
- Kreisel D, Nava RG, Li W, Zinselmeyer BH, Wang B, Lai J, Pless R, Gelman AE, Krupnick AS, Miller MJ (2010) In vivo two-photon imaging reveals monocyte-dependent neutrophil extravasation during pulmonary inflammation. *Proc Natl Acad Sci U S A* 107(42):18073–18078. doi:[10.1073/pnas.1008737107](https://doi.org/10.1073/pnas.1008737107)
- Li W, Nava RG, Bribiesco AC, Zinselmeyer BH, Spahn JH, Gelman AE, Krupnick AS, Miller MJ, Kreisel D (2012) Intravital 2-photon imaging of leukocyte trafficking in beating heart. *J Clin Invest* 122(7):2499–2508. doi:[10.1172/JCI62970](https://doi.org/10.1172/JCI62970)
- Li W, Goldstein DR, Kreisel D (2013) Intravital 2-photon imaging, leukocyte trafficking, and the beating heart. *Trends Cardiovasc Med* 23(8):287–293. doi:[10.1016/j.tcm.2013.04.002](https://doi.org/10.1016/j.tcm.2013.04.002)
- Liou HL, Myers JT, Barkauskas DS, Huang AY (2012) Intravital imaging of the mouse popliteal lymph node. *J Vis Exp* (60). doi:[10.3791/3720](https://doi.org/10.3791/3720)

- Llewellyn ME, Barretto RP, Delp SL, Schnitzer MJ (2008) Minimally invasive high-speed imaging of sarcomere contractile dynamics in mice and humans. *Nature* 454(7205):784–788. doi:[10.1038/nature07104](https://doi.org/10.1038/nature07104)
- Looney MR, Thornton EE, Sen D, Lamm WJ, Glenn RW, Krummel MF (2011) Stabilized imaging of immune surveillance in the mouse lung. *Nat Methods* 8(1):91–96. doi:[10.1038/nmeth.1543](https://doi.org/10.1038/nmeth.1543)
- Marangoni F, Murooka TT, Manzo T, Kim EY, Carrizosa E, Elpek NM, Mempel TR (2013) The transcription factor NFAT exhibits signal memory during serial T cell interactions with antigen-presenting cells. *Immunity* 38(2):237–249. doi:[10.1016/j.immuni.2012.09.012](https://doi.org/10.1016/j.immuni.2012.09.012)
- Matheu MP, Beeton C, Garcia A, Chi V, Rangaraju S, Safrina O, Monaghan K, Uemura MI, Li D, Pal S, de la Maza LM, Monuki E, Flugel A, Pennington MW, Parker I, Chandy KG, Cahalan MD (2008) Imaging of effector memory T cells during a delayed-type hypersensitivity reaction and suppression by Kv1.3 channel block. *Immunity* 29(4):602–614. doi:[10.1016/j.immuni.2008.07.015](https://doi.org/10.1016/j.immuni.2008.07.015)
- Matheu MP, Cahalan MD, Parker I (2011a) Immunoimaging: studying immune system dynamics using two-photon microscopy. *Cold Spring Harb Protoc* 2011(2):pdb top99. doi:[10.1101/pdb.top99](https://doi.org/10.1101/pdb.top99)
- Matheu MP, Cahalan MD, Parker I (2011b) In vivo lymph node imaging. *Cold Spring Harb Protoc* 2011(2):pdb prot5568. doi:[10.1101/pdb.prot5568](https://doi.org/10.1101/pdb.prot5568)
- Matheu MP, Teijaro JR, Walsh KB, Greenberg ML, Marsolais D, Parker I, Rosen H, Oldstone MB, Cahalan MD (2013) Three phases of CD8 T cell response in the lung following H1N1 influenza infection and sphingosine 1 phosphate agonist therapy. *PLoS One* 8(3):e58033. doi:[10.1371/journal.pone.0058033](https://doi.org/10.1371/journal.pone.0058033)
- McDole JR, Wheeler LW, McDonald KG, Wang B, Konjufca V, Knoop KA, Newberry RD, Miller MJ (2012) Goblet cells deliver luminal antigen to CD103+ dendritic cells in the small intestine. *Nature* 483(7389):345–349. doi:[10.1038/nature10863](https://doi.org/10.1038/nature10863)
- McGavern DB, Kang SS (2011) Illuminating viral infections in the nervous system. *Nat Rev Immunol* 11(5):318–329. doi:[10.1038/nri2971](https://doi.org/10.1038/nri2971)
- Mempel TR, Henrickson SE, Von Andrian UH (2004) T-cell priming by dendritic cells in lymph nodes occurs in three distinct phases. *Nature* 427(6970):154–159. doi:[10.1038/nature02238](https://doi.org/10.1038/nature02238)
- Miller MJ, Wei SH, Parker I, Cahalan MD (2002) Two-photon imaging of lymphocyte motility and antigen response in intact lymph node. *Science* 296(5574):1869–1873. doi:[10.1126/science.1070051](https://doi.org/10.1126/science.1070051)
- Miller MJ, Wei SH, Cahalan MD, Parker I (2003) Autonomous T cell trafficking examined in vivo with intravital two-photon microscopy. *Proc Natl Acad Sci U S A* 100(5):2604–2609. doi:[10.1073/pnas.2628040100](https://doi.org/10.1073/pnas.2628040100)
- Moran AE, Holzapfel KL, Xing Y, Cunningham NR, Maltzman JS, Punt J, Hogquist KA (2011) T cell receptor signal strength in Treg and iNKT cell development demonstrated by a novel fluorescent reporter mouse. *J Exp Med* 208(6):1279–1289. doi:[10.1084/jem.20110308](https://doi.org/10.1084/jem.20110308)
- Odoardi F, Kawakami N, Klinkert WE, Wekerle H, Flugel A (2007) Blood-borne soluble protein antigen intensifies T cell activation in autoimmune CNS lesions and exacerbates clinical disease. *Proc Natl Acad Sci U S A* 104(47):18625–18630. doi:[10.1073/pnas.0705033104](https://doi.org/10.1073/pnas.0705033104) [pii]
- Pai S, Danne KJ, Qin J, Cavanagh LL, Smith A, Hickey MJ, Weninger W (2012) Visualizing leukocyte trafficking in the living brain with 2-photon intravital microscopy. *Front Cell Neurosci* 6:67. doi:[10.3389/fncel.2012.00067](https://doi.org/10.3389/fncel.2012.00067)
- Peters NC, Egen JG, Secundino N, Debrabant A, Kimblin N, Kamhawi S, Lawyer P, Fay MP, Germain RN, Sacks D (2008) In vivo imaging reveals an essential role for neutrophils in leishmaniasis transmitted by sand flies. *Science* 321(5891):970–974. doi:[10.1126/science.1159194](https://doi.org/10.1126/science.1159194)
- Phan TG, Green JA, Gray EE, Xu Y, Cyster JG (2009) Immune complex relay by subcapsular sinus macrophages and noncognate B cells drives antibody affinity maturation. *Nat Immunol* 10(7):786–793. doi:[10.1038/ni.1745](https://doi.org/10.1038/ni.1745)
- Reinhardt RL, Liang HE, Locksley RM (2009) Cytokine-secreting follicular T cells shape the antibody repertoire. *Nat Immunol* 10(4):385–393. doi:[10.1038/ni.1715](https://doi.org/10.1038/ni.1715)

- Rivard M, Popov K, Couture CA, Laliberte M, Bertrand-Grenier A, Martin F, Pepin H, Pfeffer CP, Brown C, Ramunno L, Legare F (2013) Imaging the noncentrosymmetric structural organization of tendon with Interferometric Second Harmonic Generation microscopy. *J Biophotonics*. doi:[10.1002/jbio.201300036](https://doi.org/10.1002/jbio.201300036)
- Roediger B, Ng LG, Smith AL, Fazekas de St Groth B, Weninger W (2008) Visualizing dendritic cell migration within the skin. *Histochem Cell Biol* 130(6):1131–1146. doi:[10.1007/s00418-008-0531-7](https://doi.org/10.1007/s00418-008-0531-7)
- Roediger B, Kyle R, Yip KH, Sumaria N, Guy TV, Kim BS, Mitchell AJ, Tay SS, Jain R, Forbes-Blom E, Chen X, Tong PL, Bolton HA, Artis D, Paul WE, Fazekas de St Groth B, Grimbaldston MA, Le Gros G, Weninger W (2013) Cutaneous immunosurveillance and regulation of inflammation by group 2 innate lymphoid cells. *Nat Immunol* 14(6):564–573. doi:[10.1038/ni.2584](https://doi.org/10.1038/ni.2584)
- Rothstein EC, Carroll S, Combs CA, Jobsis PD, Balaban RS (2005) Skeletal muscle NAD(P)H two-photon fluorescence microscopy in vivo: topology and optical inner filters. *Biophys J* 88(3):2165–2176. doi:[S0006-3495\(05\)73278-1](https://doi.org/S0006-3495(05)73278-1) [pii]
- Sen D, Forrest L, Kepler TB, Parker I, Cahalan MD (2010) Selective and site-specific mobilization of dermal dendritic cells and Langerhans cells by Th1- and Th2-polarizing adjuvants. *Proc Natl Acad Sci U S A* 107(18):8334–8339. doi:[10.1073/pnas.0912817107](https://doi.org/10.1073/pnas.0912817107)
- Steffens H, Nadrigny F, Kirchhoff F (2012) In vivo two-photon imaging of neurons and glia in the mouse spinal cord. *Cold Spring Harb Protoc* 2012(12):1290–1294. doi:[10.1101/pdb.prot072264](https://doi.org/10.1101/pdb.prot072264)
- Tang J, van Panhuys N, Kastennuller W, Germain RN (2013) The future of immunoimaging—deeper, bigger, more precise, and definitively more colorful. *Eur J Immunol* 43(6):1407–1412. doi:[10.1002/eji.201243119](https://doi.org/10.1002/eji.201243119)
- Thornton EE, Krummel MF, Looney MR (2012) Live imaging of the lung. *Curr Protoc Cytom* Chapter 12:Unit12 28. doi:[10.1002/0471142956.cy1228s60](https://doi.org/10.1002/0471142956.cy1228s60)
- Wei SH, Safrina O, Yu Y, Garrod KR, Cahalan MD, Parker I (2007) Ca<sup>2+</sup> signals in CD4<sup>+</sup> T cells during early contacts with antigen-bearing dendritic cells in lymph node. *J Immunol* 179(3):1586–1594. doi:[179/3/1586](https://doi.org/10.1002/0471142956.cy1228s60) [pii]
- Zinselmeyer BH, Lynch JN, Zhang X, Aoshi T, Miller MJ (2008) Video-rate two-photon imaging of mouse footpad – a promising model for studying leukocyte recruitment dynamics during inflammation. *Inflamm Res* 57(3):93–96. doi:[10.1007/s00011-007-7195-y](https://doi.org/10.1007/s00011-007-7195-y)
- Zinselmeyer BH, Dempster J, Wokosin DL, Cannon JJ, Pless R, Parker I, Miller MJ (2009) Chapter 16. Two-photon microscopy and multidimensional analysis of cell dynamics. *Methods Enzymol* 461:349–378. doi:[10.1016/S0076-6879\(09\)05416-0](https://doi.org/10.1016/S0076-6879(09)05416-0)
- Zoumi A, Yeh A, Tromberg BJ (2002) Imaging cells and extracellular matrix in vivo by using second-harmonic generation and two-photon excited fluorescence. *Proc Natl Acad Sci U S A* 99(17):11014–11019



## Chapter 5

# Cancer in the Spotlight: Using Intravital Imaging in Cancer Research

Miriam R. Fein, Robert W. Wysocki, and Mikala Egeblad

**Abstract** Intravital imaging can provide unique insights into cancer biology and has been particularly useful for research into therapy responses, metastasis, and immune responses. Here, we discuss the protocols that we routinely use for intravital imaging of mammary tumors to follow drug responses and for imaging of lungs to study metastatic seeding. These methods include: (1) the skin-flap technique used to image mammary tumors in a single, long experiment; (2) the use of an implantable imaging window for long-term serial imaging of mammary glands; and (3) the use of a thoracic window for intravital imaging of lungs to study the processes involved in the metastatic spread to lungs. We discuss common technical issues encountered when using each of these methods and provide our solutions for overcoming them. Finally, we discuss some of the exciting, new techniques on the horizon for intravital imaging in cancer biology.

**Keywords** Tumor biology • Mammary imaging • Lung imaging • Angiogenesis • Pre-clinical imaging • Skin flap • Tumor blood supply

---

M.R. Fein  
Cold Spring Harbor Laboratory, 1 Bungtown Road,  
Cold Spring Harbor, NY 11724, USA

Graduate Program in Genetics, Stony Brook University,  
Stony Brook, NY 11794, USA  
e-mail: [mfein@cshl.edu](mailto:mfein@cshl.edu)

R.W. Wysocki  
Cold Spring Harbor Laboratory, 1 Bungtown Road,  
Cold Spring Harbor, NY 11724, USA

Medical Scientist Training Program, School of Medicine, Stony Brook University,  
Stony Brook, NY 11794, USA

Graduate Program in Genetics, Stony Brook University,  
Stony Brook, NY 11794, USA  
e-mail: [rwyssocki@cshl.edu](mailto:rwyssocki@cshl.edu)

M. Egeblad (✉)  
Cold Spring Harbor Laboratory, 1 Bungtown Road,  
Cold Spring Harbor, NY 11724, USA  
e-mail: [egeblad@cshl.edu](mailto:egeblad@cshl.edu)

## 5.1 Introduction

Tumors are complex tissues which contain many other cells types besides cancer cells, such as fibroblasts, immune cells, and vascular cells (Egeblad et al. 2010). Determining how communications between non-cancerous cell types influence tumor initiation growth, metastatic spread, and response to therapy requires multiple, complementary approaches, such as genetic manipulation, immunohistochemistry, DNA sequencing, and transcriptional profiling. Intravital microscopy is an additional technique that can provide unique insights into issues such as tumor heterogeneity, cell motility, cell-cell interactions, tumor cell proliferation and survival.

Techniques in the field are improving steadily, including new injectable fluorescent probes for measuring specific enzyme activities and new fluorescent proteins with excitation in the near infrared spectra (Shcherbakova and Verkhusha 2013). In addition, new approaches are being developed allowing imaging in tissues that had been impossible to image previously, as well as procedures allowing for long-term studies over weeks or even months within the same animal (Looney and Bhattacharya 2013; Looney et al. 2011; Ritsma et al. 2012, 2013). As these advances continue, intravital imaging will become even better at probing the inner workings of tumors, from drug responses to reactivity of immune cells, and the metastatic process.

The earliest imaging windows were developed in the 1920's, and were implanted into rabbit ears to study angiogenesis and growth of an epithelioma implant (Clark and Clark 1932; Ide et al. 1939). These studies relied on light microscopy and a rabbit trained to lie still during imaging. Intravital imaging has come a long way since then, but the goal is still the same: to understand and view complex biology as it occurs in a living organism. Most other techniques in biology, such as DNA or RNA sequencing, or immunohistochemical staining of a fixed tissue, give only a snapshot of gene activity. With intravital microscopy, we are able to examine the consequences of gene activity acutely and over time, almost as though we are taking a living biopsy continuously from the same mouse for hours, days, or even weeks. This makes the technique invaluable for examining dynamic changes such as drug delivery, behaviors of cancer or stromal cells, including cell death and proliferation, or cancer cell intra- or extravasation during metastasis (Nakasone et al. 2012; Condeelis and Segall 2003; Stoletov et al. 2010). The latter is one example of a process that been extremely difficult to study otherwise, but through microscopy, we can view how cancer cells enter and leave the vasculature: a process no other technique can allow us to view.

## 5.2 Examples of Uses of Imaging in Preclinical Cancer Research

We have found intravital imaging to be particularly useful for gaining insights into the heterogeneous delivery and response to drugs, and in turn, how to improve drug responses. Certain drugs, such as doxorubicin, are naturally fluorescent and their

distribution from the bloodstream into the tumor tissue and their subsequent effects on cancer and stromal cells can therefore be determined relatively easily. In a recent paper, our laboratory used the skin-flap technique to image murine mammary tumors and showed that doxorubicin delivery to tumor tissue was increased in areas where the vasculature was most leaky (Nakasone et al. 2012). Other compounds, such as therapeutic antibodies, can be labeled with fluorophores so they can be monitored by intravital microscopy (Egeblad et al. 2008; Tremoleda et al. 2012). For example, we are currently studying the delivery and angiogenic response to the anti-vascular endothelial growth factor (VEGF) antibody, bevacizumab, in mouse models of breast cancer. To determine how cell death is induced by anti-cancer drugs, we use cell-impermeable DNA labeling drugs (such as propidium iodide or To-Pro3), which can only enter cells after the plasma membrane has been disrupted, such as in cases of cellular necrosis or apoptosis. This has allowed us to specifically label cells that are undergoing cell death and quantify cell death rates under various conditions and in different tumor regions (Nakasone et al. 2012).

Metastasis is still the foremost problem facing cancer patients, as the vast majority of cancer-related mortality is in patients with metastatic disease (American Cancer Society 2011). Unfortunately, there are no cures for most types of metastatic disease. How the metastatic process is regulated also largely remains a mystery. Intravital imaging provides a unique way of examining the metastatic process and may ultimately help us understand how it can be blocked.

Traditionally, studies on metastasis have relied on measurements made at the end-point of the process, the establishment of micro- or macrometastasis, *e.g.*, by histology. However, such methods do not address the dynamic aspect of the metastatic process: cancer cells exit the primary tumor, invade the local tissue, intravasate into blood or lymphatic vessels, then are transported to and extravasate into tissue at a secondary site. To gain insight into the dynamics of metastasis, intravital imaging has been applied with great success (Fein and Egeblad 2013). Live microscopy with expression of fluorescent proteins (*e.g.*, green and red fluorescent proteins [GFP and RFP]) by cancer and stromal cells has provided insights into what types of behaviors and cell-cell interactions differentiate metastatic and non-metastatic cancer cells. Important biological insights into the process of metastasis gained through different types of imaging technologies demonstrate how interactions between the cancer cells and components of the microenvironment, such as the extracellular matrix (ECM), the vasculature, fibroblasts, and immune cells contribute to the metastatic process (Condeelis and Segall 2003; Friedl and Alexander 2011; Wolf and Friedl 2011). Studies using confocal or two-photon microscopy have for example shown that during metastasis, cancer cells migrate towards chemoattractants (Wang et al. 2003, 2005); cancer cells can migrate as single cells, in single-cell files or collectively (Giampieri et al. 2010); both protease-dependent and -independent cancer cell migration can lead to dissemination (Sahai 2007; Wolf and Friedl 2011); the vasculature undergoes dynamic changes (Fukumura et al. 2010; Vakoc et al. 2009); macrophages and invadopodia promote intravasation (Kessenbrock et al. 2010; Wyckoff et al. 2004; Gligorijevic et al. 2012); extravasation of cancer cells is related to expression of epithelial-to-mesenchymal (EMT)

regulating transcription factors (Wells et al. 2011); and specific microenvironmental factors are necessary for homing of cancer cells (Joyce and Pollard 2009).

Cell culture-based methods can model aspects of the metastatic process (such as invasion), but they cannot model the full, complex context cancer cells encounter in the tissue, making intravital microscopy an essential technique in studying metastasis. Two major themes have emerged from imaging experiments: they have pointed to the critical role of the tumor microenvironment (*e.g.*, ECM, vasculature, macrophages, fibroblasts, and neutrophils) in the metastatic process, and they have helped to visualize dynamics of cellular movements as well as the signaling pathways involved in these processes (Fein and Egeblad 2013). The dynamics of tumor-stroma interactions and the behavior that cells exhibit at the various stages of metastasis could not have been revealed by any other means. Thus, insights from live imaging may ultimately shed light on how to effectively treat cancer metastasis.

### 5.3 Specific Protocols for Surgical Preparation of Tissues for Intravital Imaging in Preclinical Cancer Research

Intravital imaging techniques to probe drug responses and the process of metastasis require great technical skills. For example, poor surgical techniques can lead to infection and result in an acute infiltration of the area by immune cells, lead to excessive bleeding, or stop the blood supply in the area being imaged. Similarly, it is pivotal to maintain the animal at as close to physiological conditions as possible, for example, maintaining proper temperature, hydration, and oxygenation, otherwise the data gathered may not be biologically significant. Here, we discuss solutions that we have found to mitigate these problems.

The first major requirement for successful intravital imaging is appropriate preparation and access to tissues for imaging. In this section, we describe three specific protocols used to achieve this for intravital imaging in preclinical cancer research. In addition to these techniques currently used in our laboratory, an implanted abdominal imaging window was designed, which can be used for repeated imaging for up to 1 month of an abdominal organ, such as the spleen, kidney, small intestine, pancreas or liver. This window has been used to monitor liver metastases in a transplant model from the extravasation of single cancer cells in the liver in the to the establishment of micro-metastases (Ritsma et al. 2012). A complete protocol for this technique was recently published and is not described here (Ritsma et al. 2013).

#### 5.3.1 Mammary Skin Flap

We use a skin flap technique to expose and image the inguinal mammary gland in order to study such processes as drug distribution, cancer cell death after chemotherapy, and the reactive infiltration of myeloid cells after chemotherapy (Egeblad

et al. 2008; Ewald et al. 2011b; Nakasone et al. 2012). The skin flap technique is relatively easy to learn (usually mastered after ten experiments) and allows for continuous imaging for up to 40 h (Nakasone et al. 2013). Our protocol is optimized to reduce surgical trauma, foreign bodies, or bacterial contamination, which can result in tissue damage and an acute inflammatory response.

- 3.1.1. Anesthetize the mouse in an induction chamber with 4 % isoflurane with 21 % oxygen and balance nitrogen (flow rate set to 1.0 L/min) as the carrier gas.

**Note:** Gas anesthesia is easier to regulate over long time intervals than injectable anesthesia, though injectable anesthesia does not require any special consideration of ventilation or the collection of the anesthetic gas (Nakasone et al. 2013). We have found that starting the experiments with 21 % oxygen, rather than 100 %, results in longer survival times. It enables the operator to increase oxygen levels if an animal's blood oxygen levels fall below 95 % saturation, as occasionally happens during longer imaging procedures.

- 3.1.2. Move the mouse to a clean surgical area, and reduce the concentration of isoflurane from 4 to 2.5 %.
- 3.1.3. Remove hair from the ventral surface of the animal using an electronic shaver or a chemical hair depilatory cream (*e.g.*, Nair). Stray hairs in the imaging site not only autofluoresce but they also rapidly induce a strong infiltration of innate immune cells into the region.

**Note:** We prefer removing hair with an electric shaver 12–48 h before the procedure as freshly shaved fur often results in small stray hairs in the imaging field, while mice, when allowed to self-groom, mostly remove any remaining cut hair. Depilatory creams do not result in stray hair, but may result in undesired inflammation of the skin.

- 3.1.4. Disinfect the ventral surface of the animal with topical antiseptic bactericide, such as betadine (Povidone-iodine, 5 %) and 70 % isopropanol wipes.
- 3.1.5. Expose the tumor on the inguinal mammary gland by making a ventral midline incision through the skin from approximately 3 mm above the urethra to the xiphoid process, while avoiding puncturing or cutting through the peritoneum.

**Note:** Tumors are ideal for imaging using the skin flap technique when they are 6–8 mm in diameter as measured by a caliper. Tumors larger than that are more difficult to position on the microscope stage as they are often not as flat as the smaller tumors.

- 3.1.6. Peel back the skin from the peritoneum to expose the tumor using sterile forceps and scissors. If done carefully, there will be minimal tissue damage or disruption of microvasculature.

**Note:** Care should be taken not to damage the vasculature of the tumor. This may occur if the skin is not peeled away gently.

- 3.1.7. Position a glass microscope slide on the outside of the skin, such that the tumor will sit flat once it is exposed. Use superglue (*e.g.*, Krazy Glue) to attach the skin to the slide.

- 3.1.8. Quickly transfer the mouse to the microscope stage for imaging. Be sure to properly place the tumor to be imaged over the imaging port on the stage (using an inverted microscope).

**Note:** Excessive repositioning of the mammary tumor on the imaging platform can result in microvessel damage, induce an immune response, and result in the death of the outer layers of cells. We use customized stage inserts (see (Ewald et al. 2011a) for our design).

- 3.1.9. Reduce the isoflurane to 1.5 % once the mouse is stable on the microscope stage. Maintain the isoflurane concentration between 0.8 and 1.5 % during the imaging session.

- 3.1.10. Insert an indwelling intraperitoneal line, attached to a syringe, to provide 50–100  $\mu$ l/h of 0.9 % saline (or PBS) during imaging. This line may also be used for administration of medications (*e.g.*, chemotherapeutics) and imaging dyes or probes (Nakasone et al. 2013).

**Note:** Loss of fluid volume during long imaging sessions may impact blood volume and thereby the physiology of the mouse.

- 3.1.11. Maintain a rectal temperature of 37 °C (we use TH-5 Thermalert Monitoring Thermometer, Physitemp Instruments Inc.) using a water-filled heating blanket (T-pump, Gaymar), a heated box, a heated stage, or heating lamp (the latter may require that the image field is shielded from the light of the lamp).

**Note:** Even minor decreases in the temperature of the tissue may affect the migratory properties of lymphocytes (Germain et al. 2006). We have found that the combination of a heating pad and heat lamp give good temperature control.

- 3.1.12. Maintain proper levels of anesthesia throughout imaging by monitoring vital signs – pulse, blood oxygen levels and breath rates – with an oximeter probe (*e.g.*, the MouseOx system by Starr Life Sciences, Inc.).

**Note:** Under optimal anesthesia, the heart rate is steady and between 300 beats per minute (bpm) and 450 bpm, oxygen saturation stays at 95–98 %, and breath rate is 55–65 breaths per minute. Under too deep anesthesia, the heart rate falls below 300 bpm and may become erratic, oxygen saturation drops below 95 %, and the breath rate slows to <50 breaths per minute. Under too light anesthesia, the heart rate increases to >450 bpm, and the breath rate increases to above 70 breaths per minute. For additional details, see (Nakasone et al. 2013; Ewald et al. 2011b). The isoflurane concentration is dependent on mouse background and age, and the optimal concentration often changes during long imaging sessions. For example, we have found that the optimal level of isoflurane for 3- to 5-month-old mice on the FVB/n background is almost always 0.9–1.1 %. The required levels often become lower as time under anesthesia progresses.



### 5.3.2 Mammary Imaging Window

The mammary skin flap imaging method is a terminal procedure, allowing a single mouse to be imaged continuously in one single setting. To follow changes in a tumor over days to weeks, a mammary imaging window allowing repeated imaging of the same tumor has been developed (Kedrin et al. 2008). We have also started implementing similar windows to follow *e.g.*, vascular changes and immune response over time, as tumors grow or are treated with chemotherapeutic drugs. However, the insertion of mammary windows is considerably more difficult than the skin flap technique, with a greater risk of causing inflammation and infection to the surgical site and the imaging field. We use custom-made titanium windows implanted either over existing tumors (spontaneous or transplanted) in the inguinal mammary gland, or sometimes we inject cancer cells immediately after surgery (Figs. 5.1 and 5.2). Others have published protocols for generating plastic windows from sterile petri dishes (Kedrin et al. 2008).

- 3.2.1. Three days prior to surgery, start the animals on water supplemented with antibiotics (TMP-SMX: Trimethoprim 0.12 mg/ml; Sulfamethoxazole 0.6 mg/ml).
- 3.2.2. One to 2 days prior to surgery, remove hair over the mammary gland with depilatory cream (*e.g.*, Nair). A large depilated area creates the best surgical field.
- 3.2.3. Prepare the mammary window for surgery by gluing an 8 mm round coverslip into the insert with superglue (*e.g.*, Krazy Glue), gently applying pressure on the glass for 1 min with a cotton swab. Apply superglue along the edges of the coverslip and the window to make a watertight seal, and allow the glue to dry completely. Remove excess glue from the coverslip with a cotton swab soaked in acetone and remove acetone with a cotton swab soaked in 70 % (vol/vol) ethanol.  
**Note:** Be careful to not remove too much glue as the watertight seal might be compromised. After the experiment is completed, the glue can be dissolved with acetone and the titanium frame reused.
- 3.2.4. Once the glue is dry, check that the window is watertight by placing the window glass side-down a tissue and filling it with water. The tissue should remain dry after 5 min.
- 3.2.5. Sterilize the windows by autoclaving, or alternatively, either placing them in 70 % (vol/vol) ethanol for at least 30 min, or in a flow cabinet underneath a UV lamp for approximately 120 min on each side.
- 3.2.6. On the day of surgery, prepare a sterile area for surgery inside a flow hood. Place all surgical instruments and mammary imaging windows nearby,

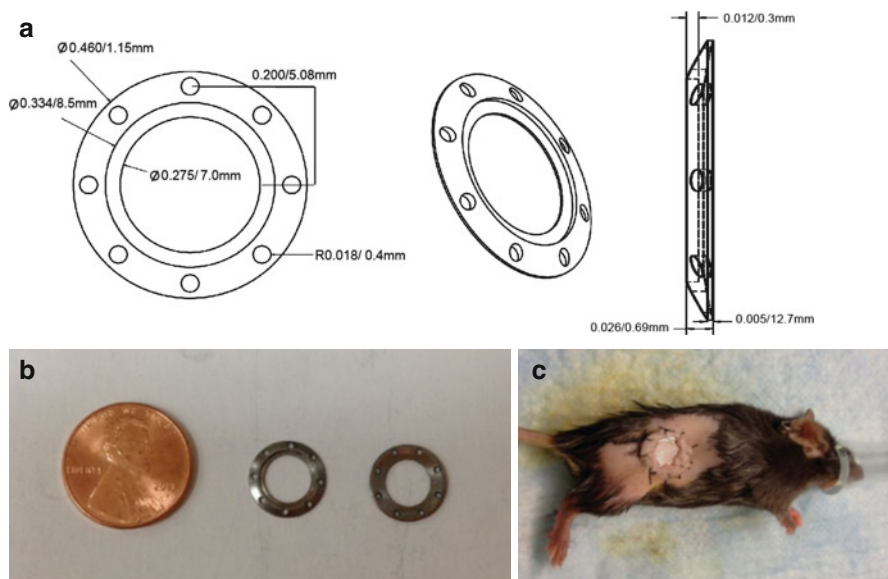


**Fig. 5.1** (a) Specifications for mammary imaging window, designed using AutoCad Software. Measurements are first listed in imperial units (inch), followed by millimeter measurements. ‘R’ refers to radius and  $\varnothing$  refers to diameter. The window holds an 8 mm coverslip, which is glued into the inset. There are eight holes around the perimeter used for suturing the window in place. Illustration on the right-hand side shows the dimensions through the cross-section of the window. (b) Front (*middle image*) and rear view (*right-hand image*) of a model of the finished mammary imaging window compared to the size of a penny (*left*). The imaging window is made of titanium. (c) Photo of an anesthetized mouse with a window placed over the dorsal side of its fourth inguinal mammary gland

including sterile Q-tips, a bottle of 70 % (vol/vol) ethanol, betadine, ophthalmic ointment, and sterile gloves.

**Note:** We strongly recommend using sterile drapes to cover the surgical area as well as sterile gloves to minimize infection.

- 3.2.7. Anesthetize the mouse in the sterile hood using 4 % isoflurane in an induction chamber.
- 3.2.8. Transfer the mouse to the surgical area, reduce the isoflurane concentration to 2.5 %, and apply ophthalmic ointment to both eyes to keep them from drying out and to prevent infection.
- 3.2.9. Place the mouse on its ventral side so that the incision can be made along the dorsal side near its hind limb.

**Note:** We have found that placing the window on the dorsal side of the mouse is preferable: a large portion of the inguinal mammary gland is easily accessible and the placement of the window does not inhibit the animal’s movement after surgery as much as does placement on the ventral side.

- 3.2.10. Clean the skin with betadine and wipe clean with 70 % (vol/vol) ethanol.

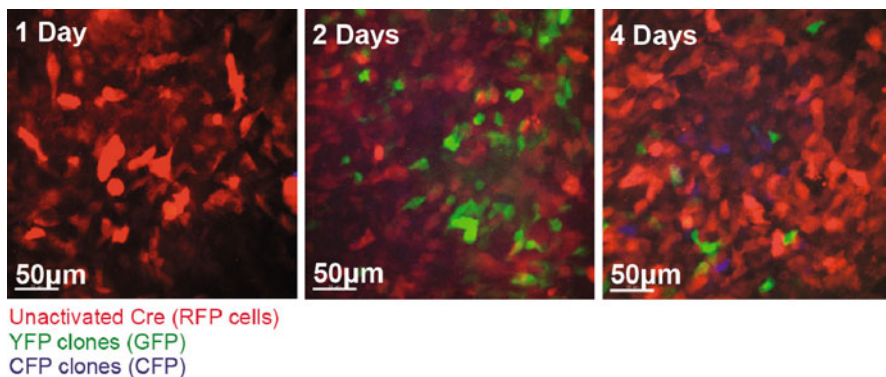


**Fig. 5.2** To trace the clonal evolution of cells *in vivo*, 4T1 mammary breast cancer cells were stably expressed with the multi-fluorescent construct Brainbow (originally developed for *in vivo* labeling of individual neuron cells), which produces color switching in response to Cre activity (Livet et al. 2007). This plasmid contains multiple Lox sites and three coding genes driving expression of either red, yellow, or cyan fluorescent proteins (RFP, YFP, or CFP, respectively). The expression of a specific fluorescent protein by any given cell clone was achieved by random Cre-LoxP DNA recombination. These cells were injected beneath a mammary imaging window and tracked for several days following implantation to determine outgrowth of specific clones. Images shown were collected on days 1, 2, and 4. Cells began to switch from RFP to YFP (cells appear as *green*) or CFP within 48 h. Scale bar represents 50 µm

3.2.11. Locate the inguinal mammary gland, and make a small incision with sterile scissors in the outer skin layer, taking care to avoid puncturing or cutting through the peritoneum. The incision should be about 2 mm in diameter.

3.2.12. Separate the underlying mammary fat pad from the skin. The separation should cover an area large enough to accommodate insertion of the mammary imaging window between the skin and the mammary gland.

**Note:** If a vessel is accidentally hit during surgery, a sterile Q-tip or cautery can be used to stop the bleeding. Notice that this step is very different from protocol steps 3.1.5 and 3.1.6, for the skin-flap technique, where the mammary gland is kept attached to the skin and loosened from the peritoneum, while the mammary gland here is detached from the skin and kept attached to the peritoneum.

3.2.13. Insert the window such that there is skin on top of the window base, and suture it in place using non-absorbable thread. Apply Vetbond (or another tissue adhesive) over the suture knots.

**Note:** Vetbond helps prevent the animals from removing the sutures.

3.2.14. Cover the window and wound with a bandage to prevent the mice from chewing out the sutures. We have found that the Band-Aid brand Active-Flex (or any similar type), that can stretch around the animal's body and adhere strongly to itself is very difficult for the mouse to remove, and prevents the mouse from chewing its sutures for the first several days.

**Note:** Be sure to place sterile gauze with antibiotic ointment beneath the bandage, or the bandage will adhere directly to the window.

- 3.2.15. Inject analgesic (buprenorphine 0.1 mg/kg) subcutaneously immediately post-surgery, and again daily for up to 3 days after surgery.
- 3.2.16. Allow the animal to recover under a heat lamp, and monitor closely over the next several days. Administration of antibiotics (Trimethoprim and Sulfamethoxazole) in water should be continued for 3 days after surgery to prevent infection.
- 3.2.17. Imaging can begin as soon as 24 h after surgery, for 1–2 h a day. We typically image on alternate days, for 1–3 weeks.

### 5.3.3 Lung Imaging Window

Our most challenging imaging technique is imaging of the lung using a protocol adapted from (Thornton et al. 2012). A thoracic suction window, made from stainless steel, is used to gently stabilize the lung so it presses against a glass coverslip during respiration (Fig. 5.3). Ventilation is preserved during imaging by putting the mouse on a ventilator. Lung imaging has previously been used to visualize inflammation and injury-induced neutrophil dynamics in physiologically-intact lungs (Looney et al. 2011). Using this protocol, we image for approximately 3–5 h after surgery, which is sufficient to provide information on tumor-host interactions during extravasation of metastatic breast cancer cells into the lung tissue.

- 3.3.1. Prepare the thoracic suction window prior to imaging by carefully gluing a coverslip onto the etched inset of the window with Krazy Glue and gently applying pressure for 1 min with a cotton swab.
- 3.3.2. Apply glue along the edges of the coverslip and the window to make a watertight seal, and allow glue to dry completely. This will only take 30 s to 1 min. Remove excess glue from coverslip with a cotton swab soaked in acetone. Be careful not to remove too much glue, or the watertight seal might be compromised. Remove acetone with a cotton swab soaked in 70 % (vol/vol) ethanol.
- 3.3.3. Check that the window is tightly sealed by attaching tubing to the metal pin coming out of the window directly to a house vacuum, and placing the window on a piece of tissue paper. If the tissue is sucked to the window, it is sealed properly.
- 3.3.4. Disinfect the window by either placing it in 70 % (vol/vol) ethanol for at least 30 min or by placing the window in a flow cabinet underneath a UV lamp for approximately 120 min on each side.
- 3.3.5. On the day of imaging, anesthetize the animal with an intraperitoneal injection of ketamine (100 mg/kg) and dexdomitor (0.5 mg/kg).  
**Note:** There is a large variation in response to injectable anesthetics between different mouse strains, and the dose may need to be adjusted accordingly (Tremoleda et al. 2012).
- 3.3.6. Use small sterile scissors and forceps to expose the trachea. Make a small horizontal incision with fine scissors in the anterior trachea. Carefully insert PE-90 tubing that is cut at an angle, and secure the tubing with a silk suture, size 4-0.

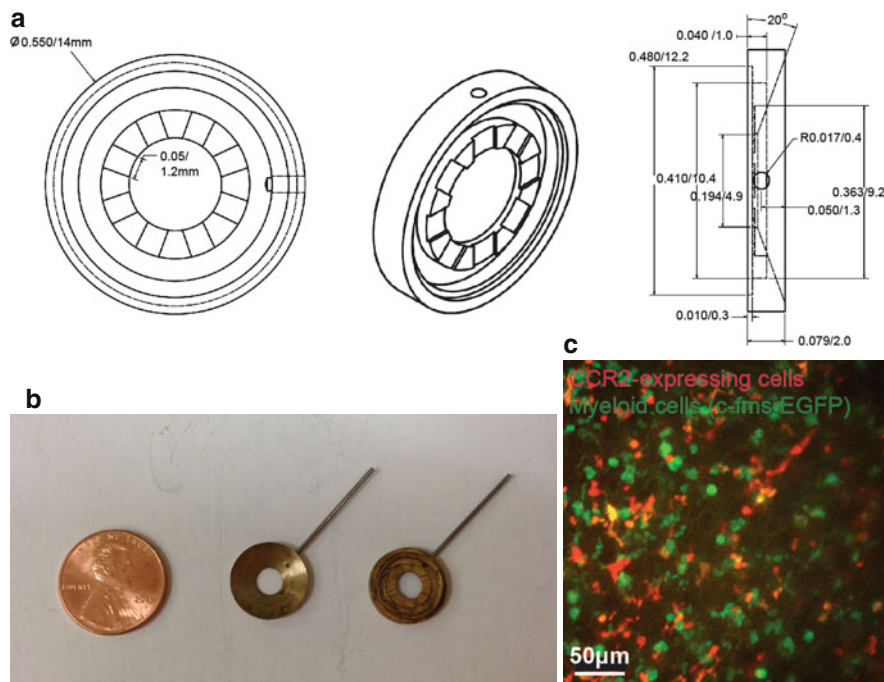


**Fig. 5.3** (a) Specifications for the thoracic suction imaging window, designed using AutoCad Software. Measurements are first listed in imperial units (inch) followed by millimeter measurements. 'R' refers to radius and  $\phi$  refers to diameter. The window holds a 12 mm coverslip that is glued into the inset. The window must be attached to a vacuum source through a metal connector that fits into the small hole on the side of window. Illustration on the right-hand side shows the dimensions through a cross-section of the window. (b) Front (*middle image*) and rear view (*right-hand image*) of the thoracic imaging window compared to the size of a penny (*left*). The window is made of stainless steel. The metal piece protruding from the window is the connector that will be attached to the vacuum source. (c) An image obtained through a thoracic window of the lung of a CCR2 knock-in RFP mouse crossed to a c-fms-GFP mouse. CCR2-expressing cells and myeloid cells are indicated. Scale bar represents 50  $\mu$ m

- 3.3.7. Turn on the mechanical ventilator (MiniVent Ventilator for Mice, Harvard Apparatus) and continue anesthesia through the tracheotomy tube with approximately 1.5 % isoflurane and a mixture of oxygen (21 % or higher fractions of oxygen) and nitrogen as a carrier gas. For volume-regulated ventilators, use tidal volumes of 8–10  $\mu$ l/g body weight and respiratory rates of approximately 60–120 breaths per minute. Apply positive-end expiratory pressure (PEEP) (approximately 3 cm H<sub>2</sub>O) to the exhalation circuit before exhaled gases are scavenged.
- 3.3.8. Place mouse on a heated microscope stage and insert rectal thermometer probe (TH-5 Thermalert Monitoring Thermometer, Physitemp Instruments Inc.). Maintain the mouse core temperature at 37 °C through the imaging session.  
**Note:** A heated pad can be taped to the stage to provide heat if the microscope stage is not heated. We combine the heated pad with a heat-lamp.

- 3.3.9. Remove hair from the ventral and left lateral surfaces of the animal using chemical hair depilatory cream (*e.g.*, Nair).
- 3.3.10. Position the mouse on its right side for thoracotomy. The left lung lobe is preferred since the lobe is larger.  
**Note:** Placing an empty syringe under the mouse works well to obtain the best position for surgery and imaging.
- 3.3.11. Inject 0.5–1.0 ml PBS intraperitoneally to provide additional fluids to the mouse prior to surgery. A repeat injection of 0.3 ml PBS can be given at 2 h, and every hour thereafter (these volumes are larger than for the mammary skin flap protocol, as mice lose more fluids during surgery for lung imaging).
- 3.3.12. Use an alcohol swab to wipe down the skin over the left thoracic cavity. Remove skin, subcutaneous tissue, and muscle layers overlying the left side of the thoracic cavity. Delicately dissect until the ribs are visualized. Remove all tissue overlying approximately four ribs at the anterior side. If bleeding begins, apply pressure with a Q-tip or cauterize the vessel.
- 3.3.13. Remove parts of three ribs overlying the left lung lobe. Remove an area smaller than the suction window, or ventilation will be compromised. Take care not to touch the surface of the lung with the surgical instruments or ribs.
- 3.3.14. Attach the thoracic suction window to a micromanipulator (*e.g.*, Thorlabs) so that its positioning can be fine adjusted later, and place the suction window right above the hole in the chest cavity.
- 3.3.15. Apply 10–30 mmHg of vacuum pressure to the tubing connecting the thoracic window and lower the window until it is covering the hole in the chest cavity; the lung underneath will be sucked towards the cover glass and thus stabilized for imaging. The exact value of the vacuum pressure may change between different systems, but the lowest possible pressure should be used to avoid tissue damage.

## 5.4 Considerations When Imaging Tumors of Living Mice

Intravital microscopy allows for visualization of cell and gene activities over time in its most physiological setting. In addition to the specific challenges addressed under each of the surgical techniques discussed above, intravital imaging has other major, common challenges as addressed below.

### 5.4.1 Fluorophore Choices

The choice of fluorophores is a very important factor in imaging and depends on the availability of probes or proteins and on the microscope. In our setup, we have five lasers, with excitations at 405, 488, 514, 560, and 647 nm. We use various emission filters controlled by a fast (20–30 ms) and very robust filter wheel (Applied Scientific Instrumentation [ASI] FW-1000) (Ewald et al. 2011a). We essentially get an



additional channel when we use quantum dots (*e.g.*, conjugated to antibodies or to label vasculature), as these can be excited at 405 nm and emit in the far-red spectra, and therefore are distinguishable from most other fluorophores. To maximize fluorescence selectivity and avoid bleed-through, we use single color images and an acousto-optic tunable filter (AOTF) to enable fast switching between individual excitation laser lines. Nevertheless, spectral bleed-through of fluorescence emission often occurs due to the asymmetrical or broad spectral profiles exhibited by many fluorophores, and this can be misinterpreted as co-localization of signals. Proper controls, for example performing imaging to detect background signal in all channels before injection of each new probe, are therefore essential. Absorption spectra are generally skewed towards shorter wavelengths, whereas emission spectra are skewed towards longer wavelengths. Therefore, cross-talk can be reduced by imaging the fluorophore with the longest wavelength first (red) using excitation wavelengths that are only minimally absorbed by the spectral tails of the bluer dyes with shorter wavelengths.

### ***5.4.2 Imaging Depth***

One of the limitations of intravital imaging is that it is not possible to image deep into a tumor mass, and this must be considered when interpreting data. Spinning disk microscopy can image 50–100  $\mu\text{m}$  into tissues, while multi-photon microscopy can image two to four-fold deeper, depending on the fluorophore and the specific type of tissue.

### ***5.4.3 Phototoxicity and Tissue Damage***

Phototoxicity, the damage or death of cells caused by illumination of the fluorophores due to energy transfer, or damage to the tissue is a problem, particularly if high laser power is used to get a stronger signal from weakly labeled cells or probes (Germain et al. 2006). Of particular consideration is using lasers at lower wavelength, such as 405 nm, when combined with DNA intercalating dyes, such as 4',6-diamidino-2-phenylindole (DAPI). Therefore, exposure times and laser power should always be kept to a minimum; we minimize cell damage by using an intensified charge-coupled device (CCD) camera (Stanford Photonics XR/Mega-10EX S30), which allows us to image at low laser power, although with a fair amount of noise.

### ***5.4.4 Motion Artifacts and Image Acquisition Speed***

Image acquisition speed is an important consideration during intravital imaging due to motion artifacts resulting from breathing. This is particularly a problem when imaging in the abdominal cavity (pancreas and liver) or in the lungs of breathing

animals. We custom-configured a spinning-disk confocal microscope with the assistance of a microscope integration company (Solamere Technology Group), and many components were selected specifically to increase image acquisition speed. We use a relatively fast spinning-disk confocal scan head (30 Hz; Yokogawa CSU-X1), combined with a fast camera, AOTF, and filter wheel. Currently, the rate limiting issue for speed is the computer-controlled switch between lasers and excitation filters. After acquisition, analysis software, such as Imaris (Bitplane) and ImageJ, can use its built-in algorithms to correct for minor motion artifacts (Egeblad et al. 2008; Soulet et al. 2013). It is also possible to trigger imaging to follow the respiratory cycle, so that *e.g.*, a series of z-stacks are taken between breaths (Presson et al. 2011). However, not all motion artifacts can be avoided or corrected by these combined approaches, as these images are acquired in living tissues.

### 5.4.5 *Mouse Physiology During Imaging*

It is critical to maintain the mouse's physiology during imaging. Of particular concern is maintaining body temperature and normal fluid levels. It must also be recognized that all anesthetic agents influence the physiology of the animal and it is therefore important to monitor vital signs throughout imaging. Anesthesia can result in reduced cardiac output, blood pressure, altered blood flow, respiratory depression, and hypothermia. Additionally, because rodents have a high body/surface ratio and high metabolic rate, this can compromise pharmacological efficiency of injectable agents and body temperature regulation.

Most anesthetic agents depress thermoregulation, so both hypo- and hyperthermia should be avoided. Care should be taken to minimize heat loss during surgery, and extremities, especially the tail, should be covered whenever possible. The core body temperature should be measured throughout imaging as described above. In the situation of extensive long-term anesthesia (over 24 h, as we often do using the mammary skin-flap protocol), there is risk of oxygen toxicity (Tremoleda et al. 2012). This is one of the reasons we keep inhaled oxygen as close to 21 % as possible (using the lowest levels that result in a blood oxygen saturation of >95 %). In addition, we have found it critical for long-term survival of mice under anesthesia to humidify the inhaled gas mixture to minimize airway drying and irritation. This is easily done by connecting a humidifier to the gas tubing so that the air that the mouse inhales is humidified (Nakasone et al. 2013).

If the animal is mechanically ventilated, it receives intermittent positive pressure to its airways, which provides the tidal volume and physiologically relevant respiratory rates. During mechanical ventilation, the ventilator applies a positive pressure to the anesthetic gases to overcome airway resistance and elastic recoil of the chest, and flow occurs into the lungs. It is important to set the right parameters on the ventilator for the mouse, taking into account the breath rate, and inhalation vs. exhalation ratio. However, one must keep in mind that mechanical ventilation reverses the normal process of ventilation. During spontaneous ventilation, the negative pressure

inside the thoracic cavity draws in air, and maintains normal blood homeostasis, as opposed to the positive pressure from mechanical ventilation. The ventilation should also be adjusted to maintain physiological levels of  $O_2/CO_2$  (Tremoleda et al. 2012).

## 5.5 Outlook

Many of these recent advances have facilitated imaging in difficult-to-image regions of the body, such as lungs and abdominal internal organs, enabling the interrogation of questions that otherwise have been difficult to address. Imaging the interactions between cancer cells and immune cells, and the resulting signaling activities during the metastatic process could be a critical step to determine whether there are opportunities to block pro-metastatic effects while leaving anti-metastatic effects of the immune system intact. The pro-metastatic effects of immune cells of the macrophage lineage are well-established (Pollard 2004; Lin et al. 2001). In mice that were transplanted with MDA-MB-231 human breast cancer cells, blocking the recruitment of the macrophage precursor, monocytes, by a CCL2 (chemokine [C-C motif] ligand 2) neutralizing antibody resulted in a reduction of cancer cell extravasation into lung tissue. When the lungs were imaged (ex vivo) in an intact-lung imaging chamber, monocytes expressing CCR2 (chemokine [C-C motif] receptor 2), a receptor for CCL2, were shown to directly interact with cancer cells during extravasation (Qian et al. 2011). A different study, however, showed that lung metastasis instead is *inhibited* in a CCL2-dependent manner by another type of immune cell, the neutrophil (Granot et al. 2011). Resolving this discrepancy might be possible by imaging lungs during metastatic seeding and simultaneously following cancer cells, monocytes, and neutrophils.

Intravital imaging has already been combined with technologies for genome-level analysis, providing clues as to the molecular mechanisms driving cellular behaviors. Genes involved in invasive behavior were identified first by live imaging of cells migrating towards a microneedle containing chemoattractants (such as epidermal growth factor [EGF]) followed by analysis of gene expression profiles of cells collected in the needles (Wang et al. 2003; Wyckoff et al. 2000). Combining live imaging with methods to trace cancer cell lineage through fluorescent-based lineage-tracking techniques (Schepers et al. 2012) or single-cell sequencing techniques (Navin et al. 2011) might enable a deeper understanding of how heterogeneity in cancer cell pheno- and genotypes contributes to metastasis and therapy resistance.

The use of imaging techniques to determine signaling activities within single cells is well established in the cell culture setting, for example, labeling individual proteins within a signaling cascade, *e.g.*, E-cadherin, and tracking how their location changes with activation (Canel et al. 2010; Serrels et al. 2009). Adapting these techniques for in vivo use has so far been challenging due to a reduced signal-to-noise ratio in the live tissue from scattering and absorption of light (Cuccia et al. 2009). Nevertheless, fluorescence recovery after photobleaching (FRAP) has been used to show how activation of specific signaling pathways influences cell migration both in vitro and in vivo. With this technique, fluorescently tagged fusion

proteins can be used to track changes in protein mobility after photobleaching. In vivo, FRAP was used to show that the mobility of E-cadherin in cell membranes is lower in migratory cells than in stationary cells, and that inhibition of migration, through inhibition of Src, FAK or  $\beta$ 1-integrin, reduces collective cell movement and increases E-cadherin membrane mobility (Canel et al. 2010; Serrels et al. 2009).

Fluorescence resonance energy transfer (FRET) has been useful for monitoring the activation stage of signaling molecules in real-time, including the activation of Rho-family GTPases. FRET is the transfer of emission energy from one fluorophore to another, resulting in excitation of the latter. FRET only occurs when the two molecules are in close proximity and it is therefore useful for studying molecular interactions in live cells (Timpson et al. 2009). Many FRET biosensors have been developed recently, including those that label protein conformational changes, post-translational modifications, and second messengers (Sabouri-Ghomi et al. 2008), and we foresee that soon, some of these will be successfully exploited in vivo to understand signaling in individual cancer cells.

Finally, manipulation of signaling pathways through light – so-called optogenetics – is possible by constructing molecules that change conformation in response to specific wavelengths of light (Williams and Deisseroth 2013). So far, optogenetics has been used primarily by neuroscientists, but the approach is now making its way into the cancer field. Some of the classical oncogenic pathways, *e.g.*, the MAP-kinase pathway, can now be activated by short, localized pulses of light (Toettcher et al. 2013). When oncogenic signaling activation is applied to a single cell within the context of its normal tissue organization, and is combined with long-term window imaging techniques, we foresee that new insights can be gained into the initiating events in cancer and the role of the microenvironment in restraining cancer.

## 5.6 Conclusion

Studying cancer biology is a very challenging undertaking; many dynamic processes are occurring simultaneously within tumors and these processes are difficult to analyze. Intravital imaging creates a platform on which to study these dynamic events as they occur in a live animal, something that static analytical techniques, *e.g.*, histology or genomics, cannot fully explore. Intravital imaging allows for the testing of hypotheses that focus on the dynamics of the cellular interactions that occur within tumors. Even co-culture assays that address the role of tumor-stroma interactions in therapy response and metastasis fail to take into account the complexity of the many components present in a tumor. However, by observing these processes in a live mouse, we can account for all these components. As further improvements are made in microscopy and imaging probes, intravital imaging will become more powerful and will allow much more information to be gathered. Just as importantly, new imaging methodologies will allow us to view new organs, and to image these organs over longer time periods. One of the current limitations of some imaging modalities, such as the mammary skin flap method, is that they are

terminal procedures with a finite imaging time. Perfection and expansion of imaging windows will allow imaging of the same mouse for weeks or even months, allowing for long-term study of the tumor microenvironment. Combining these with other cutting-edge techniques in optogenetics, tracking of signaling activities, and single cell genomics, will make intravital imaging increasingly important for advancing the field of cancer biology.

**Acknowledgements** This work was supported by funds from the National Cancer Institute (U01 CA141451), the Hope Foundation, the Long Island 2-Day Walk to Fight Breast Cancer, the Joni Gladowsky Breast Cancer Foundation, Manhasset Women's Coalition Against Breast Cancer, and the Islip Breast Cancer Coalition to M.E and through funds from NIHGM MSTP Training Award T32-GM008444 to R.W. W. The protocols described were developed with assistance from the Cold Spring Harbor Laboratory Animal and Instrumentation Shared Resources, which are supported by the Cancer Center Support Grant (5P30CA045508).

## References

- American Cancer Society (2011) Cancer facts & figures 2011. American Cancer Society, Atlanta
- Canel M, Serrels A, Miller D, Timpson P, Serrels B, Frame MC, Brunton VG (2010) Quantitative in vivo imaging of the effects of inhibiting integrin signaling via Src and FAK on cancer cell movement: effects on E-cadherin dynamics. *Cancer Res* 70(22):9413–9422. doi:[10.1158/0008-5472.CAN-10-1454](https://doi.org/10.1158/0008-5472.CAN-10-1454), 0008–5472.CAN-10-1454 [pii]
- Clark ER, Clark EL (1932) Observations on living preformed blood vessels as seen in a transparent chamber inserted into the rabbit ear. *Am J Anat* 49:441–447
- Condeelis J, Segall JE (2003) Intravital imaging of cell movement in tumours. *Nat Rev Cancer* 3(12):921–930. doi:[10.1038/nrc1231](https://doi.org/10.1038/nrc1231), nrc1231 [pii]
- Cuccia DJ, Bevilacqua F, Durkin AJ, Ayers FR, Tromberg BJ (2009) Quantitation and mapping of tissue optical properties using modulated imaging. *J Biomed Opt* 14(2):024012. doi:[10.1117/1.3088140](https://doi.org/10.1117/1.3088140)
- Egeblad M, Ewald AJ, Askautrud HA, Truitt ML, Welm BE, Bainbridge E, Peeters G, Krummel MF, Werb Z (2008) Visualizing stromal cell dynamics in different tumor microenvironments by spinning disk confocal microscopy. *Dis Model Mech* 1(2–3):155–167. doi:[10.1242/dmm.000596](https://doi.org/10.1242/dmm.000596); discussion 165
- Egeblad M, Nakasone ES, Werb Z (2010) Tumors as organs: complex tissues that interface with the entire organism. *Dev Cell* 18(6):884–901. doi:[10.1016/j.devcel.2010.05.012](https://doi.org/10.1016/j.devcel.2010.05.012)
- Ewald AJ, Werb Z, Egeblad M (2011a) Dynamic, long-term in vivo imaging of tumor-stroma interactions in mouse models of breast cancer using spinning-disk confocal microscopy. *Cold Spring Harb Protoc* 2011(2):pdb top97. doi:[10.1101/pdb.top97](https://doi.org/10.1101/pdb.top97)
- Ewald AJ, Werb Z, Egeblad M (2011b) Monitoring of vital signs for long-term survival of mice under anesthesia. *Cold Spring Harb Protoc* 2011(2):pdb prot5563. doi:[10.1101/pdb.prot5563](https://doi.org/10.1101/pdb.prot5563)
- Fein MR, Egeblad M (2013) Caught in the act: revealing the metastatic process by live imaging. *Dis Model Mech* 6(3):580–593. doi:[10.1242/dmm.009282](https://doi.org/10.1242/dmm.009282)
- Friedl P, Alexander S (2011) Cancer invasion and the microenvironment: plasticity and reciprocity. *Cell* 147(5):992–1009. doi:[10.1016/j.cell.2011.11.016](https://doi.org/10.1016/j.cell.2011.11.016)
- Fukumura D, Duda DG, Munn LL, Jain RK (2010) Tumor microvasculature and microenvironment: novel insights through intravital imaging in pre-clinical models. *Microcirculation* 17(3):206–225. doi:[10.1111/j.1549-8719.2010.00029.x](https://doi.org/10.1111/j.1549-8719.2010.00029.x)
- Germain RN, Miller MJ, Dustin ML, Nussenzweig MC (2006) Dynamic imaging of the immune system: progress, pitfalls and promise. *Nat Rev Immunol* 6(7):497–507. doi:[10.1038/nri1884](https://doi.org/10.1038/nri1884)

- Giampieri S, Pinner S, Sahai E (2010) Intravital imaging illuminates transforming growth factor beta signaling switches during metastasis. *Cancer Res* 70(9):3435–3439. doi:[10.1158/0008-5472.CAN-10-0466](https://doi.org/10.1158/0008-5472.CAN-10-0466)
- Gligorijevic B, Wyckoff J, Yamaguchi H, Wang Y, Roussos ET, Condeelis J (2012) N-WASP-mediated invadopodium formation is involved in intravasation and lung metastasis of mammary tumors. *J Cell Sci* 125(Pt 3):724–734. doi:[10.1242/jcs.092726](https://doi.org/10.1242/jcs.092726)
- Granot Z, Henke E, Comen EA, King TA, Norton L, Benezra R (2011) Tumor entrained neutrophils inhibit seeding in the premetastatic lung. *Cancer Cell* 20(3):300–314. doi:[10.1016/j.ccr.2011.08.012](https://doi.org/10.1016/j.ccr.2011.08.012)
- Ide AG, Baker NH, Warren SL (1939) Vascularization of the Brown Pearce rabbit epithelioma transplant as seen in the transparent ear chamber. *Am J Roentgenol* 42:891–899
- Joyce JA, Pollard JW (2009) Microenvironmental regulation of metastasis. *Nat Rev Cancer* 9(4):239–252. doi:[10.1038/nrc2618](https://doi.org/10.1038/nrc2618)
- Kedrin D, Gligorijevic B, Wyckoff J, Verkhusha VV, Condeelis J, Segall JE, van Rheenen J (2008) Intravital imaging of metastatic behavior through a mammary imaging window. *Nat Methods* 5(12):1019–1021. doi:[10.1038/nmeth.1269](https://doi.org/10.1038/nmeth.1269)
- Kessenbrock K, Plaks V, Werb Z (2010) Matrix metalloproteinases: regulators of the tumor microenvironment. *Cell* 141(1):52–67. doi:[10.1016/j.cell.2010.03.015](https://doi.org/10.1016/j.cell.2010.03.015)
- Lin EY, Nguyen AV, Russell RG, Pollard JW (2001) Colony-stimulating factor 1 promotes progression of mammary tumors to malignancy. *J Exp Med* 193(6):727–740
- Livet J, Weissman TA, Kang H, Draft RW, Lu J, Bennis RA, Sanes JR, Lichtman JW (2007) Transgenic strategies for combinatorial expression of fluorescent proteins in the nervous system. *Nature* 450(7166):56–62. doi:[10.1038/nature06293](https://doi.org/10.1038/nature06293)
- Looney MR, Bhattacharya J (2013) Live imaging of the lung. *Annu Rev Physiol*. doi:[10.1146/annurev-physiol-021113-170331](https://doi.org/10.1146/annurev-physiol-021113-170331)
- Looney MR, Thornton EE, Sen D, Lamm WJ, Glenny RW, Krummel MF (2011) Stabilized imaging of immune surveillance in the mouse lung. *Nat Methods* 8(1):91–96. doi:[10.1038/nmeth.1543](https://doi.org/10.1038/nmeth.1543)
- Nakasone ES, Askautrud HA, Kees T, Park JH, Plaks V, Ewald AJ, Fein M, Rasch MG, Tan YX, Qiu J, Park J, Sinha P, Bissell MJ, Frengen E, Werb Z, Egeblad M (2012) Imaging tumor-stroma interactions during chemotherapy reveals contributions of the microenvironment to resistance. *Cancer Cell* 21(4):488–503. doi:[10.1016/j.ccr.2012.02.017](https://doi.org/10.1016/j.ccr.2012.02.017)
- Nakasone ES, Askautrud HA, Egeblad M (2013) Live imaging of drug responses in the tumor microenvironment in mouse models of breast cancer. *J Vis Exp* 73:e50088. doi:[10.3791/50088](https://doi.org/10.3791/50088)
- Navin N, Kendall J, Troge J, Andrews P, Rodgers L, McIndoo J, Cook K, Stepansky A, Levy D, Esposito D, Muthuswamy L, Krasnitz A, McCombie WR, Hicks J, Wigler M (2011) Tumour evolution inferred by single-cell sequencing. *Nature* 472(7341):90–94. doi:[10.1038/nature09807](https://doi.org/10.1038/nature09807)
- Pollard JW (2004) Tumour-educated macrophages promote tumour progression and metastasis. *Nat Rev Cancer* 4(1):71–78. doi:[10.1038/nrc1256](https://doi.org/10.1038/nrc1256)
- Presson RG Jr, Brown MB, Fisher AJ, Sandoval RM, Dunn KW, Lorenz KS, Delp EJ, Salama P, Molitoris BA, Petrache I (2011) Two-photon imaging within the murine thorax without respiratory and cardiac motion artifact. *Am J Pathol* 179(1):75–82. doi:[10.1016/j.ajpath.2011.03.048](https://doi.org/10.1016/j.ajpath.2011.03.048)
- Qian BZ, Li J, Zhang H, Kitamura T, Zhang J, Campion LR, Kaiser EA, Snyder LA, Pollard JW (2011) CCL2 recruits inflammatory monocytes to facilitate breast-tumour metastasis. *Nature* 475(7355):222–225. doi:[10.1038/nature10138](https://doi.org/10.1038/nature10138)
- Ritsma L, Steller EJ, Beerling E, Loomans CJ, Zomer A, Gerlach C, Vriskoop N, Seinstra D, van Gurp L, Schafer R, Raats DA, de Graaff A, Schumacher TN, de Koning EJ, Rinkes IH, Kranenburg O, Rheenen J (2012) Intravital microscopy through an abdominal imaging window reveals a pre-micrometastasis stage during liver metastasis. *Sci Transl Med* 4(158):158ra145. doi:[10.1126/scitranslmed.3004394](https://doi.org/10.1126/scitranslmed.3004394)
- Ritsma L, Steller EJ, Ellenbroek SI, Kranenburg O, Borel Rinkes IH, van Rheenen J (2013) Surgical implantation of an abdominal imaging window for intravital microscopy. *Nat Protoc* 8(3):583–594. doi:[10.1038/nprot.2013.026](https://doi.org/10.1038/nprot.2013.026)



- Sabouri-Ghomi M, Wu Y, Hahn K, Danuser G (2008) Visualizing and quantifying adhesive signals. *Curr Opin Cell Biol* 20(5):541–550. doi:[10.1016/j.ceb.2008.05.004](https://doi.org/10.1016/j.ceb.2008.05.004)
- Sahai E (2007) Illuminating the metastatic process. *Nat Rev Cancer* 7(10):737–749. doi:[10.1038/nrc2229](https://doi.org/10.1038/nrc2229)
- Schepers AG, Snippert HJ, Stange DE, van den Born M, van Es JH, van de Wetering M, Clevers H (2012) Lineage tracing reveals Lgr5+ stem cell activity in mouse intestinal adenomas. *Science* 337(6095):730–735. doi:[10.1126/science.1224676](https://doi.org/10.1126/science.1224676)
- Serrels A, Timpson P, Canel M, Schwarz JP, Carragher NO, Frame MC, Brunton VG, Anderson KI (2009) Real-time study of E-cadherin and membrane dynamics in living animals: implications for disease modeling and drug development. *Cancer Res* 69(7):2714–2719. doi:[10.1158/0008-5472.CAN-08-4308](https://doi.org/10.1158/0008-5472.CAN-08-4308)
- Shcherbakova DM, Verkhusha VV (2013) Near-infrared fluorescent proteins for multicolor in vivo imaging. *Nat Methods* 10(8):751–754. doi:[10.1038/nmeth.2521](https://doi.org/10.1038/nmeth.2521)
- Soulet D, Pare A, Coste J, Lacroix S (2013) Automated filtering of intrinsic movement artifacts during two-photon intravital microscopy. *PLoS One* 8(1):e53942. doi:[10.1371/journal.pone.0053942](https://doi.org/10.1371/journal.pone.0053942)
- Stoletov K, Kato H, Zardouzian E, Kelber J, Yang J, Shattil S, Klemke R (2010) Visualizing extravasation dynamics of metastatic tumor cells. *J Cell Sci* 123(Pt 13):2332–2341. doi:[10.1242/jcs.069443](https://doi.org/10.1242/jcs.069443)
- Thornton EE, Krummel MF, Looney MR (2012) Live imaging of the lung. *Curr Protoc Cytom* Chapter 12:Unit12.28. doi:[10.1002/0471142956.cy1228s60](https://doi.org/10.1002/0471142956.cy1228s60)
- Timpson P, Serrels A, Canel M, Frame MC, Brunton VG, Anderson KI (2009) Quantitative real-time imaging of molecular dynamics during cancer cell invasion and metastasis in vivo. *Cell Adh Migr* 3(4):351–354
- Toettcher JE, Weiner OD, Lim WA (2013) Using optogenetics to interrogate the dynamic control of signal transmission by the ras/erk module. *Cell* 155(6):1422–1434. doi:[10.1016/j.cell.2013.11.004](https://doi.org/10.1016/j.cell.2013.11.004)
- Tremoleda JL, Kerton A, Gsell W (2012) Anaesthesia and physiological monitoring during in vivo imaging of laboratory rodents: considerations on experimental outcomes and animal welfare. *EJNMMI Res* 2(1):44. doi:[10.1186/2191-219X-2-44](https://doi.org/10.1186/2191-219X-2-44)
- Vakoc BJ, Lanning RM, Tyrrell JA, Padera TP, Bartlett LA, Stylianopoulos T, Munn LL, Tearney GJ, Fukumura D, Jain RK, Bouma BE (2009) Three-dimensional microscopy of the tumor microenvironment in vivo using optical frequency domain imaging. *Nat Med* 15(10):1219–1223. doi:[10.1038/nm.1971](https://doi.org/10.1038/nm.1971)
- Wang W, Wyckoff JB, Wang Y, Bottinger EP, Segall JE, Condeelis JS (2003) Gene expression analysis on small numbers of invasive cells collected by chemotaxis from primary mammary tumors of the mouse. *BMC Biotechnol* 3:13. doi:[10.1186/1472-6750-3-13](https://doi.org/10.1186/1472-6750-3-13)
- Wang W, Goswami S, Sahai E, Wyckoff JB, Segall JE, Condeelis JS (2005) Tumor cells caught in the act of invading: their strategy for enhanced cell motility. *Trends Cell Biol* 15(3):138–145. doi:[10.1016/j.tcb.2005.01.003](https://doi.org/10.1016/j.tcb.2005.01.003)
- Wells A, Chao YL, Grahovac J, Wu Q, Lauffenburger DA (2011) Epithelial and mesenchymal phenotypic switchings modulate cell motility in metastasis. *Front Biosci* 16:815–837
- Williams SC, Deisseroth K (2013) Optogenetics. *Proc Natl Acad Sci U S A* 110(41):16287. doi:[10.1073/pnas.1317033110](https://doi.org/10.1073/pnas.1317033110)
- Wolf K, Friedl P (2011) Extracellular matrix determinants of proteolytic and non-proteolytic cell migration. *Trends Cell Biol* 21(12):736–744. doi:[10.1016/j.tcb.2011.09.006](https://doi.org/10.1016/j.tcb.2011.09.006)
- Wyckoff JB, Segall JE, Condeelis JS (2000) The collection of the motile population of cells from a living tumor. *Cancer Res* 60(19):5401–5404
- Wyckoff J, Wang W, Lin EY, Wang Y, Pixley F, Stanley ER, Graf T, Pollard JW, Segall J, Condeelis J (2004) A paracrine loop between tumor cells and macrophages is required for tumor cell migration in mammary tumors. *Cancer Res* 64(19):7022–7029. doi:[10.1158/0008-5472.CAN-04-1449](https://doi.org/10.1158/0008-5472.CAN-04-1449)

## Chapter 6

# Haemodynamics and Oxygenation of the Tumour Microcirculation

Gillian M. Tozer, Rachel Daniel, Sarah Jane Lunt,  
Constantino C. Reyes-Aldasoro, and Vincent J. Cunningham

**Abstract** Abnormalities of the tumour vasculature and their consequences on the microenvironment of tumour cells impact on tumour progression and response to both blood-borne anti-cancer agents and radio-therapy, as well as making tumour blood vessels a target for therapy in their own right. Intravital microscopy of experimental tumours, most commonly grown in ‘window’ chambers, such as the dorsal skin fold chamber in mice and rats, enables investigations of tumour microcirculatory function. This is needed both to understand the molecular control of tumour vascular function and to measure the response of the vasculature to treatment. In particular, intravital microscopy enables parameters associated with blood supply, vascular permeability and oxygenation to be estimated, at high spatial and temporal resolution. In this chapter, methods used for measuring a range of these parameters, specific examples of their applications, the significance of findings and some of the limitations of the techniques are described.

**Keywords** In vivo imaging • Tumor-mediated angiogenesis • Vascular permeability • Oxygenation • Dorsal skin chamber

---

G.M. Tozer (✉) • R. Daniel • S.J. Lunt  
Department of Oncology, Tumour Microcirculation Group,  
CR-UK/YCR Sheffield Cancer Research Centre,  
The University of Sheffield, Sheffield, UK

Department of Oncology, F Floor, School of Medicine,  
Beech Hill Road, Sheffield S10 2RX, UK  
e-mail: [g.tozer@sheffield.ac.uk](mailto:g.tozer@sheffield.ac.uk)

C.C. Reyes-Aldasoro  
Information Engineering and Medical Imaging Group, School of Engineering  
and Mathematical Sciences, City University,  
London EC1V OHB, UK

V.J. Cunningham  
Division of Applied Medicine, School of Medicine and Dentistry,  
Aberdeen Biomedical Imaging Centre, Institute of Medical Sciences,  
University of Aberdeen, Forester Hill, Aberdeen AB25 2ZD, UK

## 6.1 Introduction

Intravital microscopy is one of the few research techniques available to study functional aspects of the tumour microcirculation. Reliance of tumour growth and metastasis on tumour vascular function makes the tumour vasculature a sought after therapeutic target. Furthermore, abnormalities of the tumour vasculature and their microenvironmental consequences, such as hypoxia and raised interstitial fluid pressure, also impact on tumour progression and therapeutic response to various treatment modalities. Optimum progression on exploiting these targets requires an understanding of the processes involved in tumour vascularization, the functional abnormalities of the tumour vasculature and analysis of response to therapy. A large part of what is known to date in these areas has been revealed from studies using intravital microscopy, which has been a mainstay of tumour microcirculation research since the first demonstration, in 1924, of a surgically implanted transparent ‘window’ chamber for studies of growing tissue (Sandison 1924).

The dorsal skin fold chamber (DSFC), in mice or rats, is currently the most commonly used surgical preparation for studying the tumour microcirculation because it allows for both transmitted and epi-fluorescence microscopy of developing tumour vasculature for periods up to several weeks. Its construction has changed little from the late 1970s (Papenfuss et al. 1979) and consists of a metal chamber (usually aluminium or titanium) supporting a skin flap, in which dermal layers from one or both sides of the flap are removed for optical clarity. A tumour fragment or cell suspension is implanted onto the exposed striated muscle layer (panniculus carnosus) and protected by a glass coverslip (Koehl et al. 2009). Developments of this model include the cranial chamber (Monsky et al. 2002), mammary gland chamber (Shan et al. 2003), lung observation chamber (Hatakawa et al. 2002) and ‘body wall’ chamber that allow access to tissues for orthotopic tumour transplantation (Tsuzuki et al. 2001; Ritsma et al. 2013). Uses for the DSFC and other chamber techniques in the field of tumour angiogenesis and microcirculation are continuously evolving, as developments are made for both 2- and 3-dimensional imaging in fluorescent/bioluminescent probe design, microscopy, camera systems and image acquisition/analysis technology. Thus, intravital microscopy is set to continue playing an important role in this field for many years to come. Potential limitations associated with use of the DSFC are highlighted in Box 6.1.

### Box 6.1

It is important to recognize some fundamental limitations of intravital microscopy techniques for tumour studies, which are not overcome by modern technology. Specifically referring to the DSFC, tumours are essentially sub-cutaneous and tumour size is limited by the dimensions of the chamber, which exerts considerable tissue pressure. The surgery is relatively time-consuming and can induce bleeding, inflammation and growth of

granulation tissue. Over-stretching of the skin and over- or under-tightening of retaining screws can cause problems and chambers may sag with time after surgery. As with other animal experiments, general anaesthesia can cause major haemodynamic changes. In order to avoid these, conscious mice can be restrained in specially designed jigs for microscopy, noting that the restraint itself will also impact on the animal's physiology. Consideration also needs to be given to temperature control, toxicity of contrast agents and photo-toxicity.

In this chapter, we discuss some of the methods used for functional studies of the tumour microcirculation that relate to *tumour blood supply*, *vascular permeability* and *oxygenation*.

## 6.2 Tumour Blood Supply

### 6.2.1 Significance

The tumour blood supply plays a critical role in cancer therapy, knowledge of which is central to understanding the angiogenic process, by which most tumours vascularise. Blood flow is a major determinant of the delivery rate of oxygen and nutrients to tissue and so is intimately related to tumour growth and progression. In cancer therapy, blood flow to a tumour determines drug delivery. Tumour oxygenation levels, which are critically dependent on oxygen delivery, classically impact on radio-sensitivity and response to certain chemotherapeutic drugs. Therefore, quantitative measures of a tumour's blood supply are essential for understanding the role of the tumour microcirculation in tumour progression and treatment outcome. In addition, the tumour microcirculation is a direct target for anti-angiogenic and vascular disrupting cancer therapy, for which quantitative measures of tumour blood supply are required for relevant and sensitive pharmacodynamic end-points.

### 6.2.2 Functional Measures of Tumour Blood Supply

#### 6.2.2.1 Definitions

The most definitive measure of a tissue's blood supply is *blood flow rate*. This is defined as the rate of delivery of arterial blood to the capillary beds within a particular mass of tissue. The units are mls of blood per unit mass of tissue per minute ( $\text{ml.g}^{-1}.\text{min}^{-1}$ ) or per unit volume of tissue per minute ( $\text{ml.ml}^{-1}.\text{min}^{-1}$ ). Small, lipid-soluble, metabolically inert molecules, which rapidly cross the vascular wall and diffuse through the extra-vascular space, are useful as blood

flow markers. In this case, the fraction of marker crossing the capillary vascular wall from the blood in a single pass through the tissue (extraction fraction,  $E$ ) is close to 1.0 and for fully perfused tissue the accessible volume fraction ( $\alpha$ ) of the tissue is also close to 1.0. For a short period after intra-venous injection, net uptake rate of this type of marker into tissue is determined primarily by blood flow rate. Use of this type of marker has normally employed radioactive isotope labeling for ease of detection and sensitivity, which enables concentration of the marker to be used at true tracer levels. Quantitative estimation of tissue blood flow rate can be made from measurement of an arterial input function and a tissue response function (Tozer et al. 2009). If suitable radioactive isotopes such as  $^{14}\text{C}$  or  $^{125}\text{I}$  are used to label the tracer, high spatial resolution maps of blood flow rate can be obtained by measuring tissue radioactivity with autoradiography or phosphor imaging, at the end of the experiment. Similar computational methods are commonly applied in clinical positron emission tomography (PET) (Lammertsma et al. 1990) and, using markers at non-tracer concentrations, in dynamic contrast-enhanced magnetic resonance imaging (DCE-MRI) (Tofts et al. 1999). These methods are more difficult to apply to intravital microscopy, especially when using conventional 2-D fluorescence microscopy, mainly because of the difficulty in relating measured fluorescence intensity to true marker concentration (Waters 2009). In order to investigate blood supply to tumours growing in the DSFC, two parameters that are related to blood flow rate have been measured instead, namely *red blood cell velocity* (RBC velocity) and the so-called *blood supply time* (BST). It should be noted that there is no direct relationship between either RBC velocity or BST and blood flow rate, as defined above. This is most easily seen from the classical relationship known as the *central volume principle* (Stewart 1894) that relates tissue blood flow rate ( $F$  in  $\text{ml.g}^{-1}.\text{min}^{-1}$ ) to fractional blood volume of the tissue ( $V$  in  $\text{ml.g}^{-1}$ ):

$$\tau = V / F \quad (6.1)$$

where  $\tau$  is the capillary mean transit time (the average time taken for blood to pass through a particular capillary bed). From this equation, it can be seen that  $\tau$  is only indirectly proportional to  $F$ , if  $V$  is constant and  $\tau$  can only provide a quantitative measure of  $F$  if  $V$  can be measured simultaneously. Notwithstanding this caveat, measurements of both *RBC velocity* and *BST* have revealed important insights into the tumour microcirculation.

### 6.2.2.2 Red Blood Cell Velocity (RBC Velocity)

*RBC velocity* can be measured relatively easily by intravital microscopy using either commercially or freely available tracking algorithms (Reyes-Aldasoro et al. 2008a, 2011) (Fig. 6.1). Tracking techniques require fast camera frame rates and fluorescence labeling of a fraction of circulating red blood cells, which normally entails injecting a small volume of red blood cells that have been labeled *ex vivo* with a

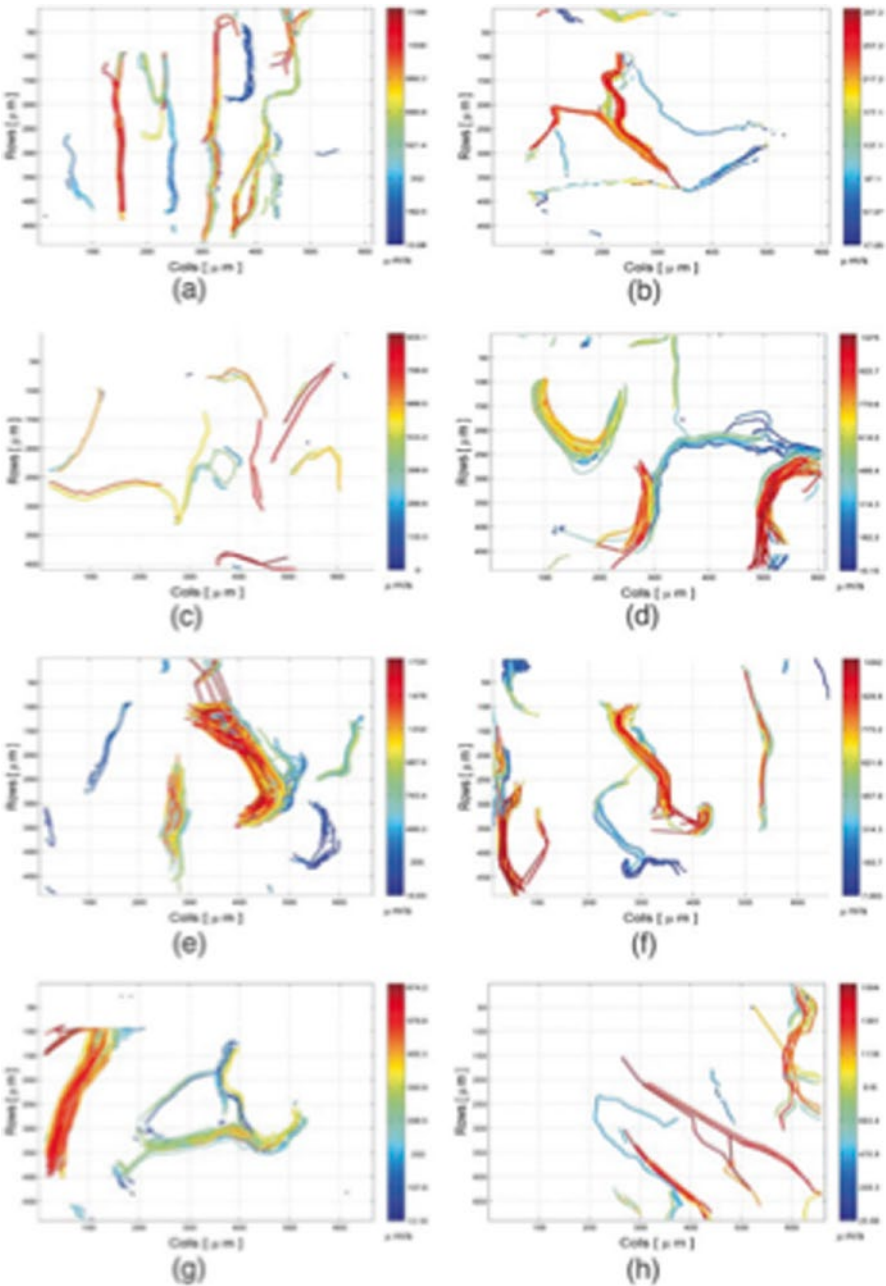


**Fig. 6.1** Examples of tracks made by red blood cells (RBC) as they flow through the tumour microcirculation. Tracks were obtained from eight different mouse fibrosarcomas, (a–h). Each RBC track is represented by a *line*, where the direction and colour represent RBC velocity (This figure is reproduced, with permission, from Reyes-Aldasoro et al. 2008a, p. 163–173)



membrane-binding dye<sup>1</sup> into the animal's circulation and tracking their passage through individual vessel segments over time. Alternatively, if the passage of red cells along a particular vessel segment is relatively sparse, slit devices can be used to monitor the interference pattern of light reaching the camera, caused by the traversing red cells. A fluorescent plasma marker, such as a FITC-labelled dextran is usually employed, so that red cells appear dark on a bright background. By matching the interference patterns recorded via the individual slits, which record at known distances along a vessel segment, RBC velocity can be calculated (Jain et al. 2013). This technique, known as temporal correlation velocimetry, was developed by Intaglietta and colleagues and has been used for many decades (Intaglietta and Tompkins 1973). Similar principles have recently been applied on a pixel-by-pixel basis, where optical signals at each spatial location are compared with neighbouring locations over time, so that a series of cross-correlations are used to calculate both speed and direction of blood flow in the form of 2-dimensional maps. When used with conventional single photon microscopy, the true *RBC velocity* is approximated by the measured *RBC velocity in the plane of the image*. Measurement of *RBC velocity* has been used primarily to monitor effects of treatment such as anti-angiogenic agents (Strieth et al. 2006), vascular disrupting agents (Tozer et al. 2001), photodynamic therapy and liposomes encapsulating chemotherapeutics (Chen et al. 2004; Strieth et al. 2004). In addition, *RBC velocity* has been used to monitor the process of vascular normalization (Akerman et al. 2013) that can occur after various cancer treatments, most notably following anti-angiogenic therapy, where vascular pruning and/or a reduction in vascular permeability can lead to improved tumour perfusion and delivery of low molecular weight chemotherapeutic drugs (Carmeliet and Jain 2011).

Measurements of *RBC velocity* have also been combined with measurements of red blood cell flux (number of red blood cells traversing a vessel segment per unit time) to calculate tumour microvascular haematocrit (Brizel et al. 1993). Red cell flux is highly variable in the tumour microcirculation and intravital microscopy studies have shown that large temporal changes in red cell flux can occur over short time-scales (tens of minutes). These acute fluctuations were shown to temporally co-ordinate with measured changes in oxygen partial pressure in the nearby tumour parenchyma, especially in poorly vascularized tumour regions, demonstrating that acute periods of severe tumour hypoxia, which could impact on tumour progression and therapy, can occur quite commonly (Kimura et al. 1996).

Measurements of *RBC velocity* (*RBCv*) have also been combined with morphological measurements of blood vessel segments to calculate each segment's *volume blood flow rate* ( $F_{seg}$ ), assuming that the RBCs are traveling with the bulk plasma flow and using the formula:

$$F_{seg} = RBCv \times \pi / 4 \times d \wedge 2 \quad (6.2)$$

where  $d$  is vessel segment diameter

<sup>1</sup> A membrane marker commonly used is DiI (1,1'-dioctadecyl-3,3,3',3'-tetramethylindocarbocyanine perchlorate), an indocarbocyanine dye retained in lipid bi-layers.

This should not be confused with *blood flow rate* ( $F$ ) as defined above, which refers to the delivery rate of blood per mass or volume of tissue.

*RBC velocity* can also be used as an approximation for *vessel wall shear rate*. This parameter is particularly important for understanding the angiogenic process, which is influenced by endothelial cell transduction of mechanical signals from flowing cells across their luminal surface (Egginton 2011).

Recently, a method for estimating *RBC velocity* and related parameters in 3-dimensional intravital images, utilizing multi-photon fluorescence microscopy (MPFM) imaging, has been developed (Kamoun et al. 2010). This method involves a fluorescent plasma marker, as above, and scanning the central axes of blood vessels at high frequency. The angle of the resulting streaked signals in the space-time plot provides a measure of RBC velocity.

### 6.2.2.3 Blood Supply Time (BST)

The blood supply time (BST), although related to RBC velocity, is calculated from the dynamics of plasma, rather than red blood cell, flow. Developed by Oye and colleagues (2008), intravital microscopy is used to rapidly image the first-pass of a high molecular weight contrast agent (e.g. 155 kDa TRITC-dextran) through the tumour microcirculation, following intravenous injection. Typical images used for this type of analysis are shown in Fig. 6.2. BST is defined, for each pixel within the vascular image, as the time difference between the frame showing maximum fluorescence intensity in the pixel and the frame showing maximum fluorescence intensity in the tumour-supplying artery. This enables pixel-by-pixel maps of BST to be constructed for regional analysis of spatial blood flow heterogeneity. Repetition of this process over 20 min time intervals within the same tumours also demonstrated substantial temporal heterogeneity in BST in A-07 human melanoma tumours (Brurberg et al. 2008). The same group has used this technique to investigate the effects of chronic cycling hypoxia (Gaustad et al. 2013), differing angiogenesis-related gene profiles (Simonsen et al. 2013) and anti-angiogenic treatment (Gaustad et al. 2012) on blood flow in xenografted human melanomas.

## 6.3 Tumour Vascular Permeability

### 6.3.1 Significance

The tumour blood vessel wall constitutes an obvious barrier between tumour tissue and blood-borne anti-cancer agents and controls protein transport between blood and tissue. However, high vascular permeability to macromolecules is a characteristic feature of the tumour vasculature, with established links to tumour angiogenesis, progression and poor treatment outcome (McDonald and Baluk 2002; Lunt et al. 2009). Changes in barrier function may provide an early pharmacodynamic end-point for treatment with anti-angiogenic or vascular disrupting drugs (Tozer et al. 2005). Therefore, methods for estimating tumour vascular permeability parameters are of great interest.

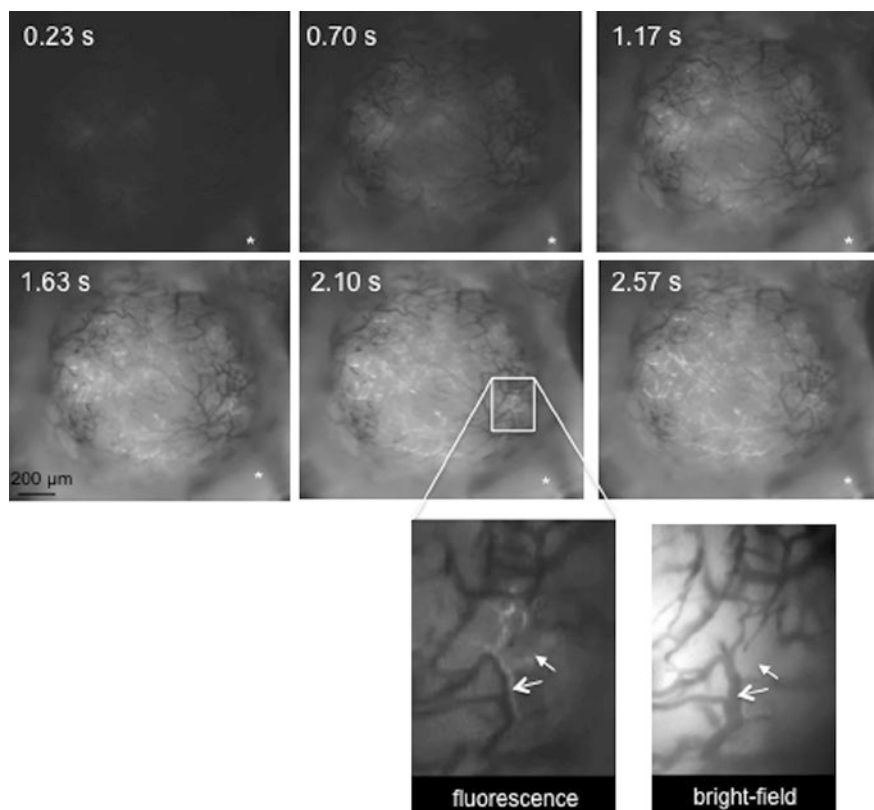


**Fig. 6.2** *Top panels* show a time-series of epi-fluorescence images taken of a mouse fibrosarcoma (fs188) growing in a mouse DSFC, following the intravenous injection of 80 mg/kg FITC-dextran. Times shown are relative to the appearance above background of fluorescence in a tumour supplying arteriole, indicated by \* in each image. Similar images have been used to estimate the blood supply time (BST) – see main text for details. An expanded epifluorescence image and the corresponding transmitted light image are shown in the lower panels. The arrows in the epifluorescence image indicate vessel segments that have filled very rapidly with FITC-dextran, indicating that they are close to the arterial side of the micro-circulatory network. The vessel segment indicated by the open arrow lies immediately adjacent to an unfilled vessel segment. It is impossible to discriminate between these two segments in the corresponding bright-field image, where the vessel pairing appears as a single vessel (*open arrow*). The *closed arrow* indicates a rapidly filled vessel, which is hardly distinguishable in the bright-field image

### 6.3.2 Estimation of Vascular Permeability

#### 6.3.2.1 Definitions

Vascular permeability of tumour blood vessels can be studied using intravital microscopy. Typically, this involves monitoring the clearance kinetics of a fluorescently labeled molecule (usually an albumin or dextran) from the blood vessels to

the interstitium, following intra-venous injection. However, a simple qualitative assessment of leakage rate, as is commonly carried out, can be misleading because of the influence of blood flow rate on the time-course of the fluorescence concentration in the capillary ( $C_{vess}$ ) and hence the amount of leakage. The high spatial resolution of intravital microscopy is a major advantage over other imaging methods, allowing a direct estimation of the vascular permeability-surface area product (*PS-product*) in ml plasma per unit mass or volume of tissue per min ( $\text{ml.g}^{-1}.\text{min}^{-1}$  or  $\text{ml.ml}^{-1}.\text{min}^{-1}$ ), where  $P$  is permeability and  $S$  is the vascular surface area per volume of tissue.

### 6.3.2.2 Application in Intravital Microscopy

Analysis of intravital microscopy data can conveniently be carried out using a so-called 'Patlak plot' (Patlak et al. 1983) to obtain the *PS-product*. Here, the time-course of the ratio of the extra-vascular tissue image intensity to  $C_{vess}$  ( $C_i/C_{vess}$ ) is plotted against the time-course of the ratio  $\int C_{vess}/C_{vess}$ , such that the curve produced tends to linearity, as it would have done had  $C_{vess}$  been constant over the whole time-course of the measurements. The slope of the line provides an estimate of *PS-product*, as illustrated in Fig. 6.3. Furthermore, intravital microscopy provides images of vascular and tumour morphology that can be used to estimate  $S$ , from which  $P$  can be readily calculated (Reyes-Aldasoro et al. 2008b).

It is only correct to use the Patlak plot when extravasation is effectively irreversible (uni-directional) over the time-course of the experiment but this condition is usually met by using a high molecular weight contrast agent, for which  $P$  is relatively low. Estimation of *PS-product* using intravital microscopy *does* suffer from the same difficulties associated with obtaining accurate quantification of fluorescence intensity, as mentioned for blood flow rate,  $F$ , above (Yuan et al. 1993). 3D imaging of fluorescence, especially using multi-photon fluorescence techniques, have alleviated some of these problems (Reyes-Aldasoro et al. 2008b). Studies of tumour vascular permeability using this and other analytical methods within intravital microscopy have revealed specific features of the tumour vasculature. Early studies established that tumour vascular permeability is elevated compared with most normal tissues (Gerlowski and Jain 1986), although there is an inherent variability between different tumour models (Yuan et al. 1994). Use of different molecular size markers, allowed estimation of pore sizes in the tumour vascular wall (Hobbs et al. 1998). The effect of a blocking antibody against vascular endothelial growth factor (VEGF) on vascular permeability to albumin was investigated in tumours growing in both cranial windows and the DSFC (Yuan et al. 1996) and a high molecular weight fluorescent dextran was used to establish that the vascular disrupting agent, combretastatin A4 phosphate (CA4P), rapidly compromised the barrier function of micro-vessels in a rat sarcoma model (Fig. 6.3 and Reyes-Aldasoro et al. 2008b).

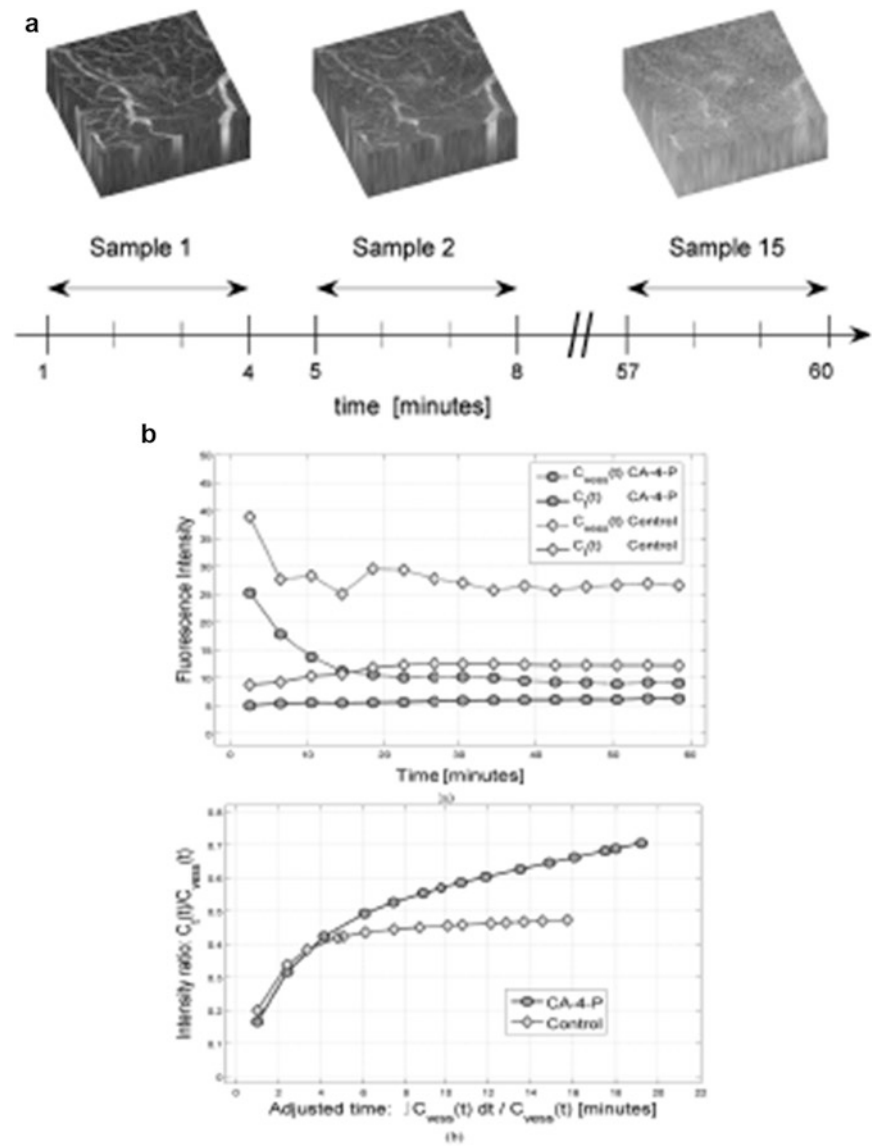


**Fig. 6.3** Panel **a** shows examples of a 3-D tumour volume ( $512 \times 512 \times 11$  voxels corresponding to  $1331.2 \times 1331.2 \times 50 \mu\text{m}^3$ ) of fluorescence intensity images acquired using multiphoton fluorescence microscopy, at various times following intravenous injection of 40 kDa FITC-dextran to a tumour-bearing rat. A total of 15 volumes were acquired in a 60-min time-frame, from a subcutaneously transplanted rat P22 sarcoma. Panel **b** (a) shows example time-activity curves of the fluorescence intensities of intravascular tissues ( $C_{\text{vess}}(t)$ ) and extravascular tissue ( $C_e(t)$ ) versus time for two data sets, similar to those shown in A. Data were acquired following image segmentation into the intravascular and extravascular tissue regions. Data from one animal treated with the vascular disrupting agent, combretastatin A4 phosphate (CA-4-P), and from one control, untreated animal are shown. Panel **b** (b) shows the same data, as in (a), transformed, as described by Patlak et al. (1983) and in the main text. The slope of the linear portion of the curve provides the estimate of the *PS-product*. (Figs. **a** and **b** are reproduced, with permission, from Reyes-Aldasoro et al. 2008b)

## 6.4 Tumour Oxygenation

### 6.4.1 Significance

Hypoxia was definitively recognized as a common feature of human tumours in the 1990s, although its existence had been predicted several decades earlier (Thomlinson and Gray 1955). The ability of oxygen to radiosensitise cells was also discovered at this time (Alper and Howard-Flanders 1956), leading to a major interest in hypoxia and its influence on tumour progression and treatment outcome, which continues to this day. Research effort into developing methods to overcome hypoxia in tumours for therapeutic benefit has gradually evolved into one where the major focus is on targeting specific points in the oxygen-sensing pathway, many of which involve the hypoxia inducible transcription factors, HIF-1 and 2 (Semenza 2012). HIF-1, in particular, is known to induce transcription of an expanding cohort of genes (>70) in response to hypoxia, via binding to hypoxia response elements (HREs) in the promoter regions of the genes. The hypoxia-responsive genes, such as the genes for vascular endothelial growth factor (VEGF) and glucose transporter 1 (GLUT1), are generally associated with tumour progression. Despite stimulation of angiogenesis in response to hypoxia, the neo-vasculature fails to overcome this condition and regions of both chronic (diffusion-limited) and acute (perfusion-limited) hypoxia persist. Indeed, as tumours grow they tend to become more hypoxic. There is considerable interest in understanding more about the hypoxic condition in tumours, in order to optimize therapeutic approaches.

### 6.4.2 Functional Measures of Tumour Oxygenation

#### 6.4.2.1 Definitions

At normal haemoglobin concentrations (150 g per l blood) and under normal conditions, the oxygen concentration in blood is approximately 9 mM. Tissue oxygen concentration is dependent on the balance between oxygen consumption and delivery. Oxygen delivery (concentration per unit time) depends on blood flow rate, haemoglobin concentration in RBCs, haemoglobin oxygen saturation ( $sO_2$ ), haematocrit, distance from the nearest capillaries and the oxygen diffusion coefficient in tissue. The oxygen partial pressure ( $pO_2$ ) in arterial blood is approximately 13 kPa (99 mmHg). The oxygen partial pressure ( $pO_2$ ) in mixed venous blood is approximately 5 kPa (38 mmHg). Cells become significantly radioresistant when oxygen levels drop below approximately 0.5 kPa (4 mmHg). HIF-1- $\alpha$  (HIF-1- $\alpha$ ) is activated when oxygen levels drop below approximately 1.0 kPa (8 mmHg).



#### 6.4.2.2 Haemoglobin Oxygen Saturation

Oxy- and deoxy-haemoglobin absorb light differently across the visible and near-infra-red spectrum, such that spectra obtained from intravital microscopy of tissue microvessels can be deconstructed to estimate the oxygen saturation of haemoglobin ( $sO_2$ ) at distinct spatial locations within the vasculature (Shonat et al. 1997; Nighswander-Rempel et al. 2002; Gillies et al. 2003). The availability of sophisticated optical filtering systems, such as acousto-optic or liquid crystal tunable filters, has significantly advanced this method, known as hyperspectral imaging. Both visual and near-infra-red light can be used in either absorbance or reflection mode. Hyperspectral intravital imaging has been pioneered for tumour biology by Sorg, Dewhirst and colleagues, initially to investigate the spatial relationship between microvascular  $sO_2$  and tumour response to hypoxia, using tumour cells engineered to express green fluorescent protein (GFP) under the control of a HRE (Sorg et al. 2005). Other basic studies have investigated the relationship between fluctuations in tumour micro-vascular oxygenation and the location of arterio-venous shunts (Sorg et al. 2008), macrophage infiltration (Choe et al. 2010) and blood flow using the BST method described above (Lee et al. 2013). Studies of therapy have demonstrated reoxygenation of tumours following radiation treatment, which correlated with an increase in glycolysis (Zhong et al. 2013) and hypoxia-induction followed by re-oxygenation induced by the vascular disrupting agent, Oxi4503 (Wankhede et al. 2010). Examples of tumour microvascular  $sO_2$  values are shown in Fig. 6.4.

#### 6.4.2.3 Phosphorescence Life-Time Imaging

The phosphorescence induced by light excitation of porphyrin derivatives is rapidly quenched by oxygen, providing a method for estimating  $pO_2$  in tumours. Helmlinger et al. (1997) applied this technique to intravital microscopy of LS174T human colon adenocarcinoma xenografts and compared measurements with regional measurements of  $pH$ , using the pH-sensitive fluorochrome 2', 7' -bis-(2-carboxyethyl)-5,6-carboxyfluorescein (BCECF). Phosphorescence life-time imaging provided  $pO_2$  measurements in intra- and extra-vascular tumour regions at 10  $\mu m$  spatial resolution. They found a complex relationship between  $pH$  and  $pO_2$  at a local level, although there was a strong correlation between mean  $pH$  and  $pO_2$  profiles.  $pO_2$  gradients away from blood vessels were highly variable but consistently low in avascular areas and at distances greater than 150  $\mu m$  from the supporting vasculature. Phosphorescence life-time imaging of a porphyrin derivative confined to the tumour vasculature also revealed the existence of longitudinal vascular gradients of  $pO_2$  from the arterial to the venous side of the tumour microcirculation, in the rat mammary adenocarcinoma (R3230AC) model (Dewhirst et al. 1999). This study neatly exploited two different excitation wavelengths to excite the porphyrin through different tissue depths away from the tumour-supplying arterioles in the fascial plane (approximately 50 and 200  $\mu m$  for blue and green light respectively). Oxyphor G2 was used in a subsequent study to compare oxygenation levels in three

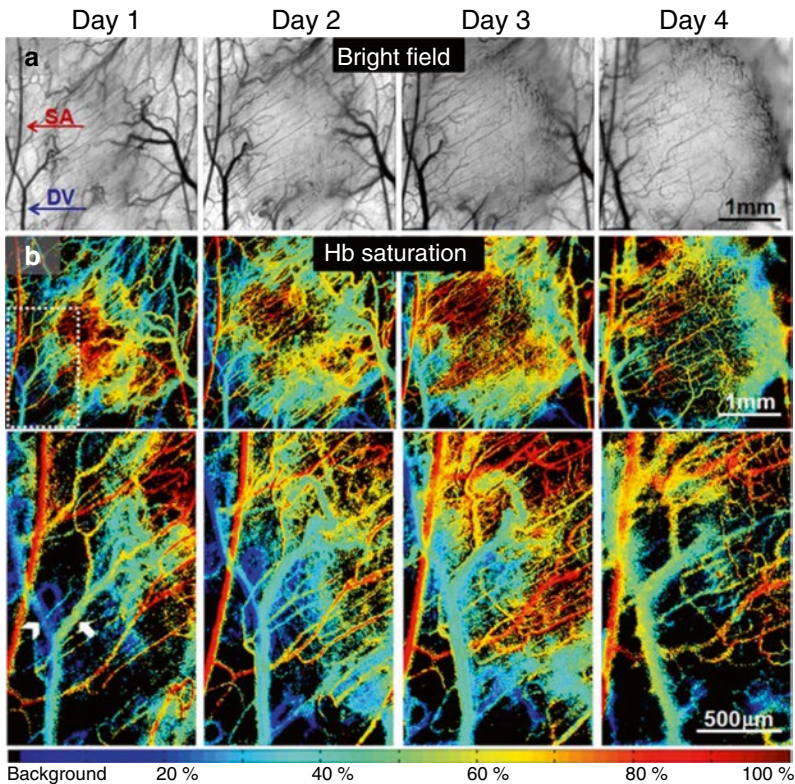


**Fig. 6.4** Examples of tumor hemoglobin oxygen saturation ( $sO_2$ ) with tumor growth, estimated from hyperspectral imaging. (a) Brightfield images of the Caki-2 human renal carcinoma growing the DSFC, showing a tumor supplying artery (SA) and draining vein (DV). (b)  $sO_2$  maps corresponding to images in (a). Arrow-head indicates a venous branch from non-tumor tissue. Arrow indicates a vessel carrying shunted blood (Figs. a and b are reproduced, with permission, from Lee et al. 2013, p. 332–334)

murine tumour models; K1735 malignant melanoma, RENCA renal cell carcinoma and Lewis lung carcinoma (Ziemer et al. 2005). The different patterns of oxygenation across the tumour types correlated well with the spatial distributions of oxygenation revealed by the oxygen-sensitive tissue binding of the nitroimidazole, EF5.

Other phosphorescent markers have been developed more recently for *in vivo* application. A polymer-based nano-particle with both fluorescence and phosphorescence properties enabled a technique to be used for measuring the ratio of oxygen-sensitive phosphorescence against a fluorescence standard, thus negating the need for specialized equipment for phosphorescence life-time imaging (Palmer et al. 2010). In this case, the nano-particle solution was suffused over the surface of the tumour, beneath the cover-slip of the DSFC, to provide an oxygen-sensitive overlay. The tissue  $pO_2$  values obtained were found to correlate significantly with estimates

of haemoglobin oxygen saturation, using the hyperspectral imaging technique described above, and to associate with HIF-1 activity assayed using a GFP-based reporter system. Other developments include a platinum(II)-octaethyl-porphyrin in a transparent thin film format. This has been tested in a hamster model, using the amelanotic melanoma A-Mel-3 growing in the DSFC (Babilas et al. 2005). The thin film was applied directly to the coverslip, so that it was in contact with both tumour and surrounding normal tissue and could be excited by a LED array. Following suitable calibration, tumour  $pO_2$  values were recorded, which were in good agreement with previous surface oxygen electrode measurements.

## 6.5 Concluding Remarks

Intravital microscopy has played, and continues to play, a vital role in studies designed to develop an understanding of the functional aspects of the tumour micro-circulation and its response to therapy. It is still a challenge to obtain fully quantifiable data on vascular function routinely and with sufficient spatial and numerical accuracy to allow detection of subtle changes with therapy. However, innovative technical developments continue apace and developments in micro-endoscopy, for instance, hold the promise of translating quantitative intravital microscopy studies of tumour vascular function to deep-seated human tumours for therapeutic benefit. Simultaneous application of intravital microscopy with other imaging modalities in clinical use, such as MRI and PET, provides an opportunity to maximise the advantages and overcome the disadvantages of each modality.

**Acknowledgements** The authors' research was funded by a Programme Grant from Cancer Research UK.

## References

- Akerman S, Fisher M, Daniel RA, Lefley D, Reyes-Aldasoro CC, Lunt SJ, Harris S, Bjorndahl M, Williams LJ, Evans H, Barber PR, Prise VE, Vojnovic B, Kanthou C, Tozer GM (2013) Influence of soluble or matrix-bound isoforms of vascular endothelial growth factor-A on tumor response to vascular-targeted strategies. *Int J Cancer* 133(11):2563–2576. doi:[10.1002/ijc.28281](https://doi.org/10.1002/ijc.28281). Epub 2013 Jul 10
- Alper T, Howard-Flanders P (1956) Role of oxygen in modifying the radiosensitivity of *E. coli* B. *Nature* 178:978–979
- Babilas P, Liebsch G, Schacht V, Klimant I, Wolfbeis OS, Szeimies RM, Abels C (2005) In vivo phosphorescence imaging of  $pO_2$  using planar oxygen sensors. *Microcirculation* 12:477–487
- Brizel DM, Klitzman B, Cook JM, Edwards J, Rosner G, Dewhirst MW (1993) A comparison of tumor and normal tissue microvascular hematocrits and red cell fluxes in a rat window chamber model. *Int J Radiat Oncol Biol Phys* 25:269–276
- Brurberg KG, Gaustad JV, Mollatt CS, Rofstad EK (2008) Temporal heterogeneity in blood supply in human tumor xenografts. *Neoplasia* 10:727–735

- Carmeliet P, Jain RK (2011) Principles and mechanisms of vessel normalization for cancer and other angiogenic diseases. *Nat Rev Drug Discov* 10:417–427
- Chen Q, Tong S, Dewhirst MW, Yuan F (2004) Targeting tumor microvessels using doxorubicin encapsulated in a novel thermosensitive liposome. *Mol Cancer Ther* 3:1311–1317
- Choe SW, Acharya AP, Keselowsky BG, Sorg BS (2010) Intravital microscopy imaging of macrophage localization to immunogenic particles and co-localized tissue oxygen saturation. *Acta Biomater* 6:3491–3498
- Dewhirst M, Ong E, Braun R, Smith B, Klitzman B, Evans S, Wilson D (1999) Quantification of longitudinal tissue  $pO_2$  gradients in window chamber tumors: impact on tumor hypoxia. *Br J Cancer* 79:1717–1722
- Egginton S (2011) In vivo shear stress response. *Biochem Soc Trans* 39:1633–1638
- Gaustad JV, Simonsen TG, Leinaas MN, Rofstad EK (2012) Sunitinib treatment does not improve blood supply but induces hypoxia in human melanoma xenografts. *BMC Cancer* 12:388
- Gaustad JV, Simonsen TG, Roa AM, Rofstad EK (2013) Tumors exposed to acute cyclic hypoxia show increased vessel density and delayed blood supply. *Microvasc Res* 85:10–15
- Gerlowski LE, Jain RK (1986) Microvascular permeability of normal and neoplastic tissues. *Microvasc Res* 31:288–305
- Gillies R, Freeman JE, Cancio LC, Brand D, Hopmeier M, Mansfield JR (2003) Systemic effects of shock and resuscitation monitored by visible hyperspectral imaging. *Diabetes Technol Ther* 5:847–855
- Hatakawa H, Funakoshi N, Onizuka M, Yanagi K, Ohshima N, Satoh Y, Yamamoto T, Ishikawa S (2002) Blood flow does not correlate with the size of metastasis in our new intravital observation model of Lewis lung cancer. *Microvasc Res* 64:32–37
- Helmlinger G, Yuan F, Dellian M, Jain RK (1997) Interstitial pH and  $pO_2$  gradients in solid tumors in vivo: high-resolution measurements reveal a lack of correlation. *Nat Med* 3:177–182
- Hobbs SK, Monsky WL, Yuan F, Roberts WG, Griffith L, Torchilin VP, Jain RK (1998) Regulation of transport pathways in tumor vessels: role of tumor type and microenvironment. *Proc Natl Acad Sci U S A* 95:4607–4612
- Intaglietta M, Tompkins WR (1973) Microvascular measurements by video image shearing and splitting. *Microvasc Res* 5:309–312
- Jain RK, Munn LL, Fukumura D (2013) Measuring angiogenesis and hemodynamics in mice. *Cold Spring Harb Protoc* 2013:354–358
- Kamoun WS, Chae SS, Lacorre DA, Tyrrell JA, Mitre M, Gillissen MA, Fukumura D, Jain RK, Munn LL (2010) Simultaneous measurement of RBC velocity, flux, hematocrit and shear rate in vascular networks. *Nat Methods* 7:655–660
- Kimura K, Braun RD, Ong ET, Hsu R, Secomb TW, Papahadjopoulos D, Hong K, Dewhirst MW (1996) Fluctuations in red cell flux in tumor microvessels can lead to transient hypoxia and reoxygenation in tumor parenchyma. *Cancer Res* 56:5522–5528
- Koehl GE, Gaumann A, Geissler EK (2009) Intravital microscopy of tumor angiogenesis and regression in the dorsal skin fold chamber: mechanistic insights and preclinical testing of therapeutic strategies. *Clin Exp Metastasis* 26:329–344
- Lammertsma AA, Cunningham VJ, Deiber MP, Heather JD, Bloomfield P, Nutt J, Frackowiak RSJ, Jones T (1990) Combination of dynamic and integral methods for generating reproducible functional CBF images. *J Cereb Blood Flow Metab* 10:675–686
- Lee JA, Kozikowski RT, Sorg BS (2013) Combination of spectral and fluorescence imaging microscopy for wide-field in vivo analysis of microvessel blood supply and oxygenation. *Opt Lett* 38:332–334
- Lunt SJ, Chaudary N, Hill RP (2009) The tumor microenvironment and metastatic disease. *Clin Exp Metastasis* 26:19–34
- Mcdonald DM, Baluk P (2002) Significance of blood vessel leakiness in cancer. *Cancer Res* 62:5381–5385
- Monsky WL, Mouta Carreira C, Tsuzuki Y, Gohongi T, Fukumura d, Jain RK (2002) Role of host microenvironment in angiogenesis and microvascular functions in human breast cancer xenografts: mammary fat pad versus cranial tumors. *Clin Cancer Res* 8:1008–1013

- Nighswander-Rempel SP, Anthony Shaw R, Mansfield JR, Hewko M, Kupriyanov VV, Mantsch HH (2002) Regional variations in myocardial tissue oxygenation mapped by near-infrared spectroscopic imaging. *J Mol Cell Cardiol* 34:1195–1203
- Oye KS, Gulati G, Graff BA, Gaustad JV, Brurberg KG, Rofstad EK (2008) A novel method for mapping the heterogeneity in blood supply to normal and malignant tissues in the mouse dorsal window chamber. *Microvasc Res* 75:179–187
- Palmer GM, Fontanella AN, Zhang G, Hanna G, Fraser CL, Dewhirst MW (2010) Optical imaging of tumor hypoxia dynamics. *J Biomed Opt* 15:066021
- Papenfuss HD, Gross JF, Intaglietta M, Treese FA (1979) A transparent access chamber for the rat dorsal skin fold. *Microvasc Res* 18:311–318
- Patlak CS, Blasberg RG, Fenstermacher JD (1983) Graphical evaluation of blood-to-brain transfer constants from multiple-time uptake data. *J Cereb Blood Flow Metab* 3:1–7
- Reyes-Aldasoro CC, Akerman S, Tozer GM (2008a) Measuring the velocity of fluorescently labelled red blood cells with a keyhole tracking algorithm. *J Microsc* 229:162–173
- Reyes-Aldasoro CC, Wilson I, Prise VE, Barber PR, Ameer-Beg SM, Vojnovic B, Cunningham VJ, Tozer GM (2008b) Estimation of apparent tumor vascular permeability from multiphoton fluorescence microscopic images of P22 rat sarcomas in vivo. *Microcirculation* 15:65–79
- Reyes-Aldasoro CC, Griffiths MK, Savas D, Tozer GM (2011) CAIMAN: an online algorithm repository for Cancer Image Analysis. *Comput Methods Programs Biomed* 103:97–103
- Ritsma L, Steller EJ, Ellenbroek SI, Kranenburg O, Borel Rinkes IH, Van Rheenen J (2013) Surgical implantation of an abdominal imaging window for intravital microscopy. *Nat Protoc* 8:583–594
- Sandison JC (1924) A new method for the microscopic study of living growing tissues by the introduction of a transparent chamber in the rabbit's ear. *Anat Rec* 28:281–287
- Semenza GL (2012) Hypoxia-inducible factors: mediators of cancer progression and targets for cancer therapy. *Trends Pharmacol Sci* 33:207–214
- Shan S, Sorg B, Dewhirst MW (2003) A novel rodent mammary window of orthotopic breast cancer for intravital microscopy. *Microvasc Res* 65:109–117
- Shonat RD, Wachman ES, Niu W, Koretsky AP, Farkas DL (1997) Near-simultaneous hemoglobin saturation and oxygen tension maps in mouse brain using an AOTF microscope. *Biophys J* 73:1223–1231
- Simonsen TG, Gaustad JV, Leinaas MN, Rofstad EK (2013) Tumor-line specific causes of intertumor heterogeneity in blood supply in human melanoma xenografts. *Microvasc Res* 85:16–23
- Sorg BS, Moeller BJ, Donovan O, Cao Y, Dewhirst MW (2005) Hyperspectral imaging of hemoglobin saturation in tumor microvasculature and tumor hypoxia development. *J Biomed Opt* 10:44004
- Sorg BS, Hardee ME, Agarwal N, Moeller BJ, Dewhirst MW (2008) Spectral imaging facilitates visualization and measurements of unstable and abnormal microvascular oxygen transport in tumors. *J Biomed Opt* 13:014026
- Stewart GN (1894) Researches on the circulation time in organs and on the influences which affect it. *J Physiol (Lond)* 15(Parts I-III):1–89
- Strieth S, Eichhorn ME, Sauer B, Schulze B, Teifel M, Michaelis U, Dellian M (2004) Neovascular targeting chemotherapy: encapsulation of paclitaxel in cationic liposomes impairs functional tumor microvasculature. *Int J Cancer* 110:117–124
- Strieth S, Eichhorn ME, Sutter A, Jonczyk A, Berghaus A, Dellian M (2006) Antiangiogenic combination tumor therapy blocking  $\alpha(v)$ -integrins and VEGF-receptor-2 increases therapeutic effects in vivo. *Int J Cancer* 119:423–431
- Thomlinson RH, Gray LH (1955) The histological structure of some human lung cancers and the possible implications for radiotherapy. *Br J Cancer* 9:539–549
- Tofts PS, Brix G, Buckley DL, Evelhoch JL, Henderson E, Knopp MV, Larsson HB, Lee TY, Mayr NA, Parker GJ, Port RE, Taylor J, Weisskoff RM (1999) Estimating kinetic parameters from dynamic contrast-enhanced T(1)- weighted MRI of a diffusable tracer: standardized quantities and symbols. *J Magn Reson Imaging* 10:223–232



- Tozer GM, Prise VE, Wilson J, Cemazar M, Shan S, Dewhirst MW, Barber PR, Vojnovic B, Chaplin DJ (2001) Mechanisms associated with tumor vascular shut-down induced by combretastatin A-4 phosphate: intravital microscopy and measurement of vascular permeability. *Cancer Res* 61:6413–6422
- Tozer GM, Kanthou C, Baguley BC (2005) Disrupting tumour blood vessels. *Nat Rev Cancer* 5:423–435
- Tozer GM, Prise VE, Cunningham VJ (2009) Quantitative estimation of tissue blood flow rate. *Methods Mol Biol* 467:271–286
- Tsuzuki Y, Mouta Carreira C, Bockhorn M, Xu L, Jain RK, Fukumura D (2001) Pancreas micro-environment promotes VEGF expression and tumor growth: novel window models for pancreatic tumor angiogenesis and microcirculation. *Lab Invest* 81:1439–1451
- Wankhede M, Dedeugd C, Siemann DW, Sorg BS (2010) In vivo functional differences in micro-vascular response of 4T1 and Caki-1 tumors after treatment with OXi4503. *Oncol Rep* 23:685–692
- Waters JC (2009) Accuracy and precision in quantitative fluorescence microscopy. *J Cell Biol* 185:1135–1148
- Yuan F, Leunig M, Berk DA, Jain RK (1993) Microvascular permeability of albumin, vascular surface area, and vascular volume measured in human adenocarcinoma LS174T using dorsal chamber in SCID mice. *Microvasc Res* 45:269–289
- Yuan F, Salehi HA, Boucher Y, Vasthare US, Tuma RF, Jain RK (1994) Vascular permeability and microcirculation of gliomas and mammary carcinomas transplanted in rat and mouse cranial windows. *Cancer Res* 54:4564–4568
- Yuan F, Chen Y, Dellian M, Safabakhsh N, Ferrara N, Jain RK (1996) Time-dependent vascular regression and permeability changes in established human tumor xenografts induced by an anti-vascular endothelial growth factor/vascular permeability factor antibody. *Proc Natl Acad Sci U S A* 93:14765–14770
- Zhong J, Rajaram N, Brizel DM, Frees AE, Ramanujam N, Batinic-Haberle I, Dewhirst MW (2013) Radiation induces aerobic glycolysis through reactive oxygen species. *Radiother Oncol* 106:390–396
- Ziemer LS, Lee WM, Vinogradov SA, Sehgal C, Wilson DF (2005) Oxygen distribution in murine tumors: characterization using oxygen-dependent quenching of phosphorescence. *J Appl Physiol* 98:1503–1510



## Chapter 7

# In Vivo Imaging of Bone Marrow Stem Cells

Luke J. Mortensen, Walid Zaher, Cristina Lo Celso, and Charles P. Lin

**Abstract** Stem cells are defined by their ability to self-renew and differentiate into mature cells (Keller 2005). They are responsible for tissue maintenance during homeostatic conditions and are able to respond to injury by adapting their ability to generate differentiated progeny according to the organism's need. Knowing the biology of multiple tissue stem cells will allow treatment of diseases characterized by tissue failure. For example, novel approaches are needed for the treatment of degenerative diseases such as Parkinson's disease, liver failure, leukemia, diabetes, osteoarthritis, and osteoporosis, for which there is currently no effective therapy. An emerging therapeutic approach for the management of these conditions is cell therapy or cellular therapeutics where organ functions are restored through transplanting healthy and functional cells. Administration of factors that stimulate regeneration by endogenous stem cells and transplantation of exogenous stem cells or engineered tissue derived from stem cells are the main approaches that regenerative medicine aims to develop. Moreover, gene therapy approaches are becoming a concrete possibility if stem cells are targeted.

---

L.J. Mortensen

Advanced Microscopy Program, Center for Systems Biology and Wellman  
Center for Photomedicine, Massachusetts General Hospital, Harvard Medical School,  
CPZN 8238, 185 Cambridge Street, Boston, MA 02114, USA

W. Zaher

Advanced Microscopy Program, Center for Systems Biology and Wellman  
Center for Photomedicine, Massachusetts General Hospital, Harvard Medical School,  
CPZN 8238, 185 Cambridge Street, Boston, MA 02114, USA

Department of Endocrinology and Metabolism, Endocrine Research Laboratory (KMEB),  
Odense University Hospital and University of Southern Denmark, Odense, Denmark

Stem Cell Unit, Department of Anatomy, College of Medicine, King Saudi University,  
Riyadh, Saudi Arabia

C.L. Celso

Department of Life Sciences, Imperial College London, London, UK

C.P. Lin (✉)

Advanced Microscopy Program, Center for Systems Biology and Wellman  
Center for Photomedicine, Massachusetts General Hospital, Harvard Medical School,  
CPZN 8238, 185 Cambridge Street, Boston, MA 02114, USA

Harvard Stem Cell Institute, Cambridge, MA 02138, USA

**Keywords** Haematopoietic Stem Cells • Mesenchymal Stem Cells • Bone Marrow • Cell Labeling • Cell Tracking • Molecular Imaging • Intravital Microscopy

## 7.1 Stem Cells and the Bone Marrow Microenvironment

Stem cells are defined by their ability to self-renew and differentiate into mature cells (Keller 2005). They are responsible for tissue maintenance during homeostatic conditions and are able to respond to injury by adapting their ability to generate differentiated progeny according to the organism's need. Knowing the biology of multiple tissue stem cells will allow treatment of diseases characterized by tissue failure. For example, novel approaches are needed for the treatment of degenerative diseases such as Parkinson's disease, liver failure, leukemia, diabetes, osteoarthritis, and osteoporosis, for which there is currently no effective therapy. An emerging therapeutic approach for the management of these conditions is cell therapy or cellular therapeutics where organ functions are restored through transplanting healthy and functional cells. Administration of factors that stimulate regeneration by endogenous stem cells and transplantation of exogenous stem cells or engineered tissue derived from stem cells are the main approaches that regenerative medicine aims to develop. Moreover, gene therapy approaches are becoming a concrete possibility if stem cells are targeted.

### 7.1.1 Bone Marrow Stem Cells

The adult bone marrow houses two distinct subsets of stem cells: hematopoietic stem cells (HSCs) that give rise to blood components, and mesenchymal stem cells (MSCs) that give rise to stromal components of the bone marrow.

HSCs are the immature, multipotent cells from which all blood cells are derived. HSCs are capable of both self-renewal and differentiation into mature progeny (myeloid and lymphoid cell types). Remarkably, transplantation of a single HSC into a lethally irradiated mouse is sufficient to regenerate all blood cells and rescue the mouse from the otherwise lethal effect of radiation (Osawa et al. 1996; Matsuzaki et al. 2004; Camargo et al. 2006). Therapeutic applications of HSCs include their routine use in stem cell transplantation to treat hematopoietic malignancies or bone marrow failure. Research and clinical experience have provided tools for the immunophenotypic identification and functional analysis of HSCs, and have provided increasing evidence suggesting that HSC regulation is greatly influenced by signals from their niches in the bone marrow. Although they represent one of the most rigorously studied stem cell types, still more remains to be learned about how HSCs are regulated and their response to stress conditions.

MSCs are multipotent cells that were first identified by Friedenstein as bone marrow osteogenic stem cells (Friedenstein et al. 1987). MSCs originate from the mesodermal germ layer and are defined in vitro as non-hematopoietic, plastic adherent multipotent stem cells that are present among the bone marrow stroma. They are

capable of differentiating into cells of mesodermal lineage including osteoblasts (Kassem et al. 1993), adipocytes (Abdallah et al. 2005) and chondrocytes (Johnstone et al. 1998) in vitro, and to form bone and bone marrow organ that supports hematopoiesis upon implantation in an open system (ectopic bone formation). They express a number of non-specific CD markers: CD90, CD73, CD140b, CD166 but they are negative for certain CD markers: CD31, CD45, CD34 or MHC class II (Dominici et al. 2006).

In addition to their presence in bone marrow, MSC-like cell populations have been isolated from the stromal component of adipose tissue, umbilical cord, dental pulp, skeletal muscle, synovium, and periodontal ligament (Asakura et al. 2001; Bianco et al. 2001; De Bari et al. 2001; Zuk et al. 2001; Seo et al. 2004; Kermani et al. 2008; Akiyama et al. 2012) but these cells exhibit differences in molecular signature and differentiation potential from the bone marrow stromal cells (Al-Nbaheen et al. 2013). A number of different cell types of the osteoblast lineage are present in bone and bone marrow including MSCs, osteoprogenitor cells, osteoblasts and osteocytes.

Clinical transplantation of MSCs has been explored for multiple conditions such as skeletal bone injury (Quarto et al. 2001; Gangji and Hauzeur 2005; Le Blanc et al. 2005), type I diabetes mellitus (Estrada et al. 2008; Bhansali et al. 2009), Crohn's disease (Duijvestein et al. 2010; Liang et al. 2012), myocardial infarction (Chen et al. 2004; Hare et al. 2009) and graft versus host disease (Le et al. 2008). Initial results of these Phase I or Phase I-II trials are encouraging (Aldahmash et al. 2012). However, a growing number of experiments and pre-clinical studies have demonstrated that MSCs possess a limited homing potential (Bentzon et al. 2005) and poor ability to contribute to tissue regeneration, but rather function via an immunomodulatory role, which contributes to reducing inflammation and inducing regeneration (Le et al. 2003).

### 7.1.2 *The Stem Cell Niche*

Stem cells reside in a specialized microenvironment that helps to maintain and regulate these cells. Adult HSC niches are located in the bone marrow and are thought to comprise a multi-cellular complex with possible involvement of osteolineage cells, vascular endothelial cells, perivascular cells along with other stromal components (Méndez-Ferrer et al. 2010) and cells of the hematopoietic lineage itself, such as macrophages (Winkler et al. 2010) and regulatory T cells (Fujisaki et al. 2011). Osteoblasts are an important component of the niche and are found in a layer along the endosteum at the interface between bone and bone marrow (Fig. 7.1). Support for osteoblastic cells as main components of the endosteal HSC niche came from murine models in which increased osteoblast number and activity would lead to an increase in HSC number (Calvi et al. 2003) while induced ablation of osteoblasts would lead to hematopoietic failure (Visnjic et al. 2004). Recently, it was shown through in vivo imaging of ex vivo labeled, transplanted hematopoietic stem and progenitor cell (HSPC) populations, that HSPCs localize to different locations according to their stage of differentiation, that when challenges drove their engraftment or expansion, HSCs assumed positions in close proximity to bone and osteoblasts (Lo Celso et al. 2009a), while

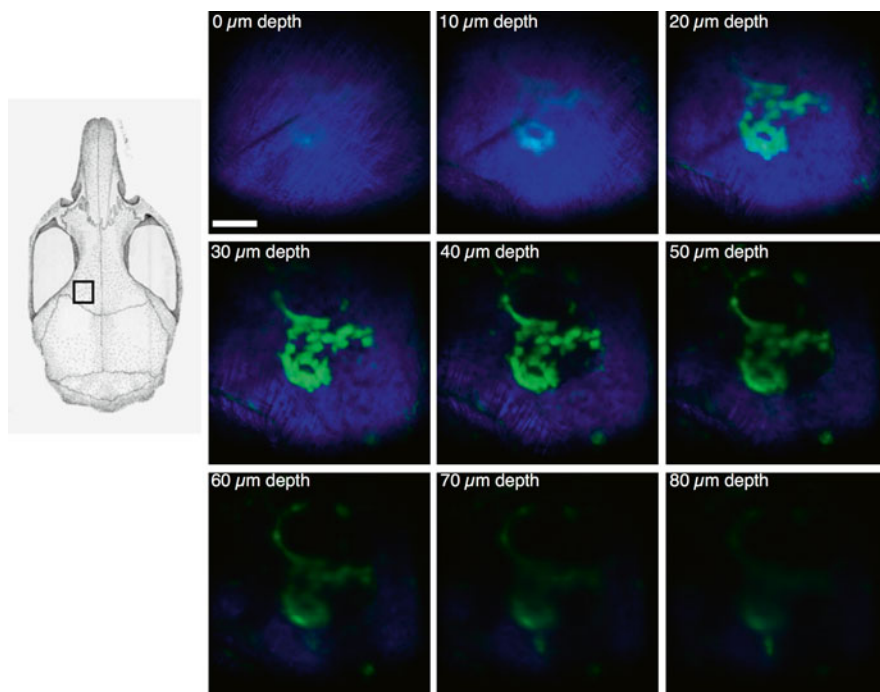


**Fig. 7.1** Osteoblasts in the bone marrow and bone structure. In vivo imaging of mouse calvarium bone marrow cavity. Second harmonic signal (blue) is used to visualize the bone (rich in type-1 collagen). GFP fluorescence (green) signal from osteolineage specific expression in a transgenic Col2.3-GFP mouse is used to visualize osteoblasts lining the inner surface of the bone cavity (endosteum). Unlabeled cells in the bone marrow cavity are not visualized in these images. Scale bar = 100  $\mu$ m

when injected into recipients carrying non-supportive niches, HSCs localized at least some cell diameters away from osteoblasts (Lane et al. 2011).

On the other hand, some studies have shown that HSCs are associated with the sinusoidal endothelium (the vascular niche) during homeostasis (Calvi et al. 2003; Zhang et al. 2003; Kiel et al. 2005) or that they are osteoblast independent (Kiel et al. 2007). However, recent studies based on femur bone immunolabeling pointed at small, highly vascularized, bone invaginations as sites of HSPC expansion (Wang et al. 2013). In summary, the characteristics and precise microanatomic organization of the HSC niche remain an enigma. Moreover, HSCs are known to leave the niche, mobilize to the vasculature, and enter the circulation where they (or their progeny) exert most of their functions. Later on, they home back to the bone marrow niche through trans-endothelial migration from the peripheral circulation (Lapidot et al. 2005). Through this process, the HSCs can encounter a dynamic, changing microenvironment rather than remaining confined to a static niche.

The niche is believed also to be under the influence of a plethora of chemokines and adhesion molecules. For example, the stromal cell derived factor-1 alpha (SDF-1 $\alpha$ , CXCL12) and its cognate chemokine receptor CXCR4 (chemokine receptor type 4, fusin or CD184) have been assumed to play an important role in HSC homing to bone marrow (Lapidot and Kollet 2002) and MSC homing to injured

tissues (Wynn et al. 2004; Granero-Molto et al. 2009). Based on deletion of CXCL12 in endothelial cells, Ding and Morrison et al. have recently suggested that HSCs may occupy a perivascular niche while early lymphoid progenitors occupy an endosteal niche (Ding and Morrison 2013).

The in vivo location of MSCs has been suggested to be in a perivascular niche and in close association with pericytes and endothelial cells (Crisan et al. 2008). The possibility that MSCs form a supportive niche for HSCs in the bone marrow (Méndez-Ferrer et al. 2010) is a particularly intriguing observation that might shed light on the complex microenvironment of bone marrow niche structure and the mechanisms that govern homing of HSC to specific locations within the bone marrow space.

## 7.2 Imaging the Bone Marrow: Technical Considerations

Reliable imaging modalities to track the fate of stem cells in vivo are highly desirable as they can provide crucial information on stem cell survival, distribution, proliferation, and homing mechanisms, all of which are dynamic events and are best studied in vivo over time. Furthermore, imaging of transplanted cells in living subjects is a powerful tool in pre-clinical research that can be used for optimization of regenerative therapy as it provides a better understanding on the interaction between transplanted stem cells and the host microenvironment. Using cell-labeling methods such as direct labeling or marker gene transfection in combination with various imaging modalities have allowed scientists to examine the mechanisms governing cell trafficking. Cell labeling followed by cell tracking allows monitoring of their homing patterns as well as accurate quantification of their functions in vivo.

The bone marrow hematopoietic stem cell niche is a complex microenvironment that provides a protected sanctuary for HSCs and quickly responds to biological need to rapidly generate blood cells. Despite the ease with which our bodies perform this task, it has not yet been possible to duplicate the process outside of the body. By directly imaging the stem cell niche in vivo, much could be gained to evaluate the location where stem cells reside, their proximity and interaction with other cell types, and their interactions with the bone marrow microenvironment. Already, the ability to visualize bone marrow stem cells has provided important insight into addressing biological controls of stem cell maintenance and proliferation, but much remains to be learned about the dynamics of HSC-niche interactions during homeostasis and in response to stress, and about anatomical and functional patterns of HSC niches within large areas of bone marrow.

Stem cells in culture are typically examined by standard microscopy techniques such as phase contrast, differential interference contrast, and immunofluorescence microscopy. Raman microscopy is a label-free technique that can provide information on cellular biochemistry (through vibrational analysis of biomolecules) and has shown promise in monitoring stem cell differentiation in culture (Downes et al. 2011). On the other hand, whole-body imaging modalities such as bioluminescence imaging (BLI) and magnetic resonance imaging (MRI) are powerful tools for tracking populations of stem cells and their progeny in vivo (Cao et al. 2004;

Daldrup-Link et al. 2005; Downes et al. 2011). However, both BLI and MRI lack the sensitivity or spatial resolution for single cell tracking in vivo. Intravital microscopy is a rapidly developing field that aims to extend the high resolution of optical microscopy to live imaging of single cells in whole animals. Rapid advancement in the field is driven by several converging trends, including improvements in laser technology, particularly for nonlinear microscopy (Horton et al. 2013), cell labeling techniques (Progatzy et al. 2013), and image processing/analysis methods. In addition to cell tracking (Runnels et al. 2006; Sackstein et al. 2008; Lo Celso et al. 2009a; Sanchez-Aguilera et al. 2011; Sarkar et al. 2011), intravital microscopy has also been used to image molecular expression (e.g. adhesion molecules and chemokines) on vascular endothelial cells (Sipkins et al. 2005; Runnels et al. 2006; Sarkar et al. 2011).

### 7.2.1 Instrumentation

To image stem cells in the bone marrow microenvironment, 3D optical sectioning (by confocal or multiphoton microscopy) is essential to visualize the marrow space beneath the bone surface. In our laboratory we developed a custom video rate scanning confocal and multiphoton hybrid platform that is specifically designed for live animal imaging (Fig. 7.2). While fast scanning (30 frames per second in our system) is not a prerequisite, it is very useful for scanning large tissue volume which helps to provide a broad view of the tissue landscape and also helps to find rare stem cells that may be distributed throughout tissue. In addition, fast scanning helps to minimize motion artifacts due to animal heartbeat and breathing.

Our scanning engine consists of a rotating polygon for the fast scanning (x) axis and a galvanometer for the slow (y) axis to generate a 2D image. The animal is mounted on a computer-controlled stage that can be stepped in the third dimension (z) with submicron precision to obtain a 3D stack. A femtosecond laser source (e.g. a Ti:Sapphire laser, tunable from ~700 to >1,000 nm) is used to generate two-photon excited fluorescence. Simultaneously, second harmonic generation of the type I bone collagen provides useful morphological information about the bone architecture. A continuous wave laser at 633 nm is used to provide single-photon excitation of DiD- or DiR-stained stem cells, which are detected using confocal detection. These longer wavelength dyes have 2-photon excitation spectra that are outside the range of commonly used Ti:Sapphire lasers and suffer from relatively low 2-photon absorption cross-sections. Additional continuous-wave lasers (blue, 491 nm, green, 532 nm, and yellow, 561 nm) are provided for excitation of shorter-wavelength dyes such as DiI and DiO, if needed. Each laser beam has individually adjusted collimation telescopes to minimize chromatic aberration and attain parfocality. In our system GFP can be excited interchangeably by two-photon excitation (920–980 nm) or by single-photon excitation (491 nm) and confocal detection. Two-photon excitation is usually preferred due to its intrinsic optical sectioning capability, deeper tissue penetration depth, and reduced out-of-focus photobleaching and photodamage. However, when the GFP signal is weak, confocal detection using a large pinhole size can increase detection sensitivity at the expense of spatial resolution.



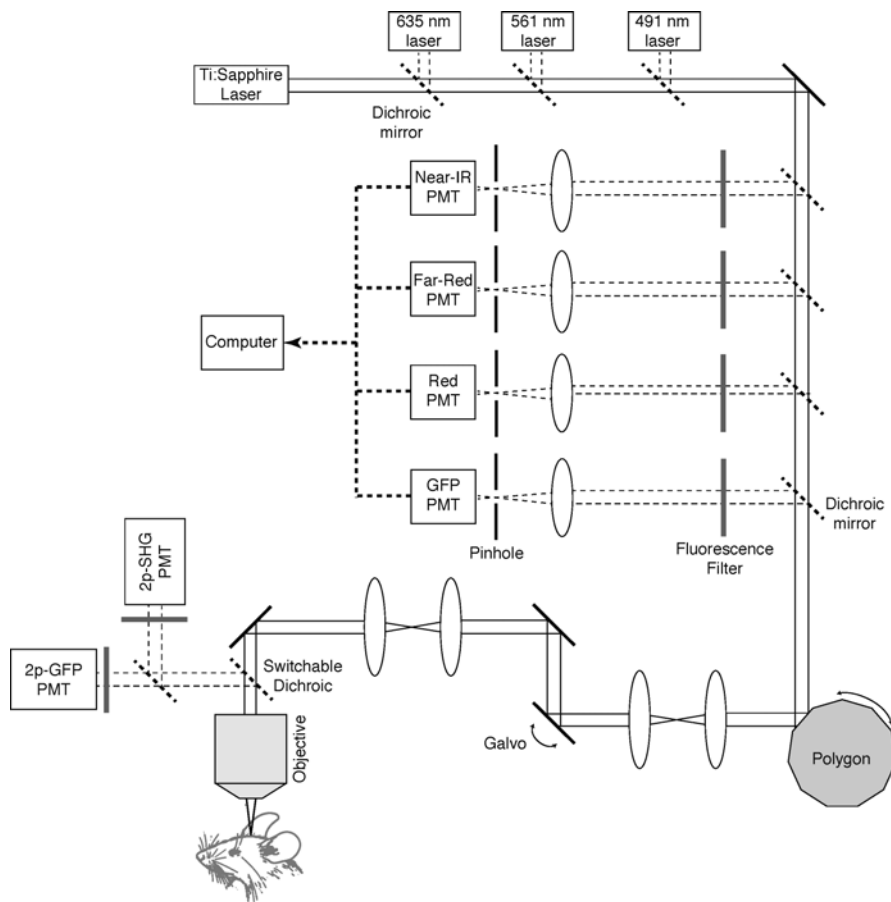


**Fig. 7.2** System diagram. Video-rate laser scanning two-photon and confocal microscope with multi-channel detection. Excitation sources include a femtosecond Ti:Sapphire pulsed laser and three diode lasers (491, 561, 635 nm). During imaging, the anesthetized mouse, with its scalp open and skull intact, is placed on a pre-warmed (37 °C) stage with automated and precise X-Y-Z translation control. Collected fluorescence signal is divided by wavelength between multiple confocal PMTs with filters to acquire NIR, Far Red, Red and green fluorescence signal and 2-photon PMTs to acquire second harmonic generation (SHG) of type I bone collagen and 2-photon GFP fluorescent signal (switchable from confocal detection) simultaneously at video-rate. *PMT* photo multiplier tube, *NIR* near infra-red, *GFP* green fluorescence protein, *SHG* second harmonic generation

Much of the imaging presented in this chapter uses one of several primary channels (Fig. 7.2). The blue signal is usually assigned to second harmonic generation in bone (type I collagen), the green signal is usually assigned to GFP-expressing cells (such as a transgenic mouse strain with Col2.3-GFP marking the osteoblasts (Kalajzic et al. 2005)), red signal is most commonly blood vessels (stained by non-targeted Qtracker quantum dots or rhodamine-dextran intravenously injected at the start of imaging), and white is normally transplanted stem cells (stained with DiD). In addition to the primary imaging channels, an

autofluorescence channel (not normally displayed in our images) must be monitored to separate putative stem cells from the autofluorescent cells that are abundant in the bone marrow. Imaging stem cells in the live animal requires one of several strategies to allow the explicit identification of the stem cell and the ability to distinguish it from the surrounding tissue.

### 7.2.2 *Imaging Locations*

Intravital imaging of stem cells in the bone marrow requires optical access to the bone marrow space. One approach involves surgical removal of muscle and connective tissue to access long bones such as the femur or tibia, followed by mechanical thinning of the bone surface (Askenasy and Farkas 2002). Stem cells preferentially localize to the trabecular region of the long bone, where they are found throughout the spongy region. Although this approach has been demonstrated to allow stem cell imaging in vivo, the procedure is complex, highly invasive, and most commonly is terminal.

An alternative approach is to image the skull (calvarial) bone marrow, which was first described by Mazo, von Andrian, and coworkers (Mazo et al. 1998). The calvarial bone resides just underneath the skin of the scalp, and the outer layer of hard bone is thin enough to allow intravital imaging of the marrow compartment without a need for mechanical bone thinning. The HSC rich calvarial bone marrow is organized primarily in a few hundred micron diameter region around the central vein, where there are highly vascularized areas.

The accessibility and ease of longitudinal imaging in the calvarial bone marrow have enabled studies of hematopoietic stem cell (Adams et al. 2009; Ferraro et al. 2011; Alt et al. 2012), mesenchymal stem cells (Méndez-Ferrer et al. 2010), immune cells and dendritic cells (Luster et al. 2005; Mazo et al. 2005), and malignancies (Sipkins et al. 2005; Colmone et al. 2008; Azab et al. 2009; Lane et al. 2011).

## 7.3 Cell Labeling Strategies

One way to image stem cells specifically without causing any change to cell function or the microenvironment is via an endogenous spectral signature such as Raman spectral fingerprinting. However, there is currently no known method to spectrally distinguish stem cells from their surrounding cells without exogenous labels. Raman spectroscopy has not yet been demonstrated for stem cell identification in a complex cellular environment such as the bone marrow. Therefore the search is on for stem cell labels that have high brightness, are highly specific, and do not alter the cell function or the cellular microenvironment. However, current technologies have limitations in one or more of these areas.

### 7.3.1 *Fluorescent Proteins*

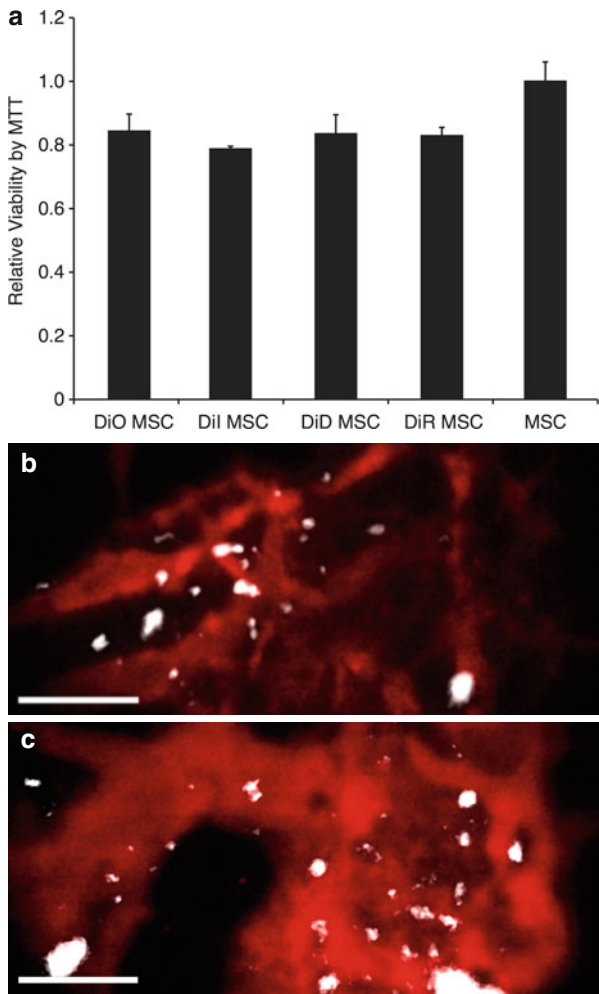
A method that could generate high specificity and contrast would be the expression of a fluorescent protein tagged to a particular stem cell marker. For MSCs, several markers have been suggested including nestin, Mx-1, leptin receptor, alpha-smooth muscle actin, and prx1 (Cai et al. 2009; Méndez-Ferrer et al. 2010; Ding et al. 2012; Park et al. 2012; Greenbaum et al. 2013). However, for HSCs no single genes driving fluorescent protein expression have yet been found. The lack of a single cell surface marker for HSCs has also limited the potential use of exogenous antibodies. The combination of multiple positive and negative markers required for identification of stem cells in vitro (Shizuru et al. 2004) has deterred the use of such strategies for in vivo imaging. To overcome the problem of marker specificity for stem cells, researchers have adopted the method of stem cell transplantation. To do so, bone marrow is harvested from healthy mouse donors, the stem cells are purified by flow cytometry using a panel of accepted markers for HSCs (Ema et al. 2006) or MSCs (Dominici et al. 2006; Morikawa et al. 2009), and the cells are transplanted into recipients.

An important component of the success of therapies such as HSC transplantation is the ability of HSCs to find their way from the blood back to the bone marrow where they can repopulate blood derived cells after intravenous infusion. This homing ability allows the successful use of intravital microscopy to study HSC biology following transplantation of labeled cells. Isolation and transplantation of HSCs from universal GFP or DsRed expressing mice allows the monitoring of homing events in the bone marrow and can even potentially allow tracking of bone marrow reconstitution progress. For the study of HSC biology, the universality of the expression reduces usefulness to soon after transplantation since all blood lineage progeny will also express the fluorescent protein. For the study of exogenous MSC biology, where minimal proliferation is expected after transplantation, fluorescent protein expression may also prove to be useful.

### 7.3.2 *Tracker Dyes*

The use of lipophilic membrane dyes represents an alternative and reliable method for tracking stem cells in vivo. These dyes are bright, available with emission wavelengths in the green (DiO), red (DiI), far-red (DiD), and near-IR (DiR), and most importantly, have minimal impact on cell viability and do not interfere with homing for MSCs (Fig. 7.3). For HSCs, staining with a tracker dye does not significantly reduce their blood reconstitution ability (Lo Celso et al. 2009a). Due to an optimal combination of long wavelength (low tissue scattering) and high staining efficiency, the DiD dye is most often used. This dye can be excited by helium-neon or diode lasers in the 630–650 nm wavelength range, and has a peak emission of 665 nm. The other dye members of this series, in particular DiI and DiR, have also been used

**Fig. 7.3** MSC homing to bone marrow and viability after staining. **(a)** Relative percent of viable cells after staining human MSCs with different tracker dyes, viability was measured with using MTT, and error bars indicate standard deviation of three independent experiments. **(b)** Representative z-projected image from a 3D stack of mouse calvarium bone marrow after intravenous injection of  $10^5$  DiD Labeled MSCs (white) in a C57BL/6 mouse with vasculature shown in red. When mice are subjected to gamma irradiation, the vasculature has less well-defined borders **(c)** and MSCs are still found in high numbers. Scale bar = 100  $\mu$ m



extensively for bone marrow imaging. DiI has a shorter peak excitation (549 nm) and emission (565 nm), with a commensurate increase in tissue scattering that may reduce the detection efficiency of deeper cells relative to DiD. DiR is of particular interest due to its near-IR emission at 780 nm. At this wavelength range, diminished tissue scattering and autofluorescence could potentially contribute to improved cell detection. DiR is also a photo-convertible dye that changes its color upon illumination at a proper wavelength (Carlson et al. 2013), making it particularly useful for optically highlighting a single cell or a group of cells for subsequent tracking. In practice, commonly used detectors such as photomultiplier tubes often have reduced quantum efficiency by 780 nm, which somewhat mitigates the potential advantages of DiR.

## 7.4 Imaging and Analysis

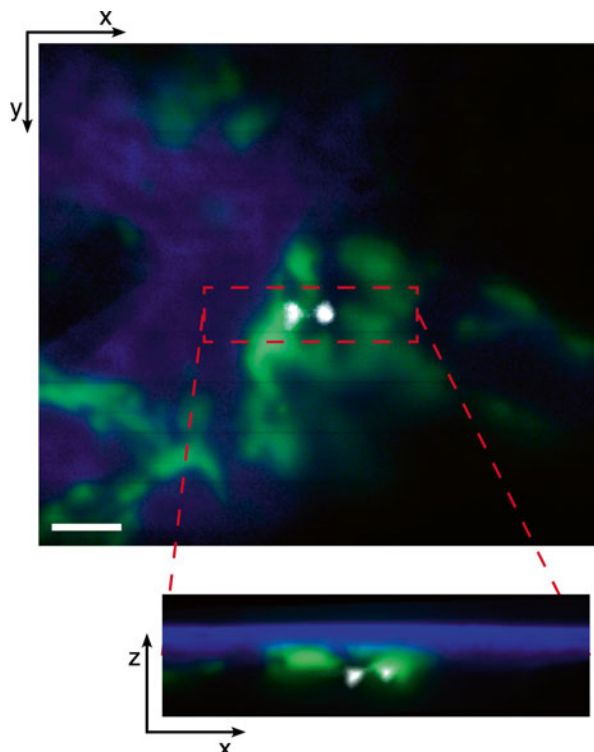
### 7.4.1 *Longitudinal Bone Marrow Stem Cell Tracking*

A primary motivation for the use of intravital microscopy is the ability to perform dynamic longitudinal analysis in single animals, which can provide new knowledge about dynamic cellular processes. For example, live longitudinal imaging has led to such important biological discoveries as elements in the multicomponent inflammatory homing cascade (von Andrian et al. 1991) and other stem cell regenerative processes (Schroeder 2008). In the bone marrow, stem cell engraftment and division in the first several hours to days after transplantation can be followed in a single animal. Intravital imaging of the bone marrow is most commonly performed over a 1–2 h time frame, with a maximum time attainable of roughly 4–6 h. Use of isoflurane gas anesthesia allows long imaging sessions, but long imaging times increases the risk of complications. During the time course of a standard imaging session, it is possible to observe the migration of moving cells with typical velocities of a few micrometers per minute (Fujisaki et al. 2011). However, to observe more rare events such as HSC cell division it is necessary to perform multiple imaging sessions on subsequent days. After each imaging session, the skin incision above the scalp is sutured and the animal is allowed to recover from anesthesia. Imaging sessions on subsequent days are possible, but generally image degradation due to scar tissue build up precludes any more than 3–4 total imaging sessions. To ensure that the same cell(s) are imaged in successive imaging session, the technique of photoconversion can be used to highlight the specific cell of interest (Carlson et al. 2013).

### 7.4.2 *Stem Cell Transplantation Dosing*

A consideration in the intravital imaging of stem cells in the bone marrow microenvironment is the infused number of cells. HSCs exhibit high efficiency of homing to the bone marrow, and it is important to limit the number of injected cells to prevent saturation, i.e. to ensure that HSC homing locations only occupy sites that would be filled by HSCs under normal circumstances. Practically speaking, systemic infusion of  $10^4$  HSCs yields 5–10 HSCs in the calvarial bone marrow detected by scanning a  $4 \times 6$  mm region (Lo Celso et al. 2009b). For exogenously administered MSCs, doses commonly used in therapeutic trials are on the order of  $10^6$  cells/mouse. However, for imaging purposes this dose yields very high numbers of MSCs in the bone marrow. With approximately  $10^5$  MSCs infused intravenously, a high but still manageable number of MSCs can be detected in healthy and irradiated calvarial bone marrow (Fig. 7.4).

**Fig. 7.4** HSCs in the endosteal niche. In vivo imaging of DiD labeled HSCs (*white*), bone second harmonic signal (*blue*), and Col2.3 osteoblasts (*green*) in close proximity to the HSC 24 h after systemic infusion into an irradiated recipient. Scale bar= 100  $\mu$ m



### 7.4.3 Image Processing and Quantification

Several key parameters in stem cell biology can be evaluated with the assistance of intravital microscopy of bone marrow stem cells. First is the number of cells localized as a function of time after infusion. With adequate signal to noise ratio, cell number can be quantified in a specific location over time. Elimination of autofluorescent events is critical because autofluorescence is the primary source of experimental error while imaging (Lo Celso et al. 2011). To avoid sampling bias due to the small field of view, multiple adjacent images (or 3D stacks) should be acquired and stitched together to provide a more reliable readout. Quantification of stem cell homing or delivery to the bone marrow after exogenous administration (HSCs and MSCs) and proliferation in the niche (mostly HSCs) is important for improving stem cell-based therapy.

The next important parameter is the location of endogenous or transplanted stem cells relative to other cells or structures in the bone marrow, such as the endosteal surface or blood vessels. The ability to measure objects in 3-dimensions using intravital microscopy provides an advantage in accuracy over the predominately 2-dimensional measurements available with histological sectioning. With the help of ImageJ, basic image processing and thresholding techniques described in detail



elsewhere (Lo Celso et al. 2009b) allow the analysis of distances between object edges in the bone marrow compartment, which can yield useful insight into bone marrow stem cell localization and interaction. Although automated segmentation and quantification algorithms can be used for such measurements, generally evaluation of nearest neighbor distances is more easily and reliably performed manually in the highly heterogeneous medium of the bone marrow (Lo Celso et al. 2011).

Another interesting parameter that can be quantified is cell motility in the bone marrow. This can be quantified by capturing an image or 3-D stack at set time intervals, and evaluating the movement velocity of cells from the assembled time-lapse movie. The addition of the third dimension by capturing sequential stacks improves the accuracy of movement measurements, but the complexities of stack registration often limit movement acquisition to two dimensions.

## 7.5 What Have We Learned

### 7.5.1 *Intravital Microscopy of Hematopoietic Stem Cells*

One of the most significant findings of bone marrow visualization is that the bone marrow, as a whole and including the endosteal surface, is highly vascularized. The observation that the endosteal niche is perivascular (Lo Celso et al. 2009a) has important implications since the two commonly referenced bone marrow niches (the endosteal niche and the vascular niche) may not be distinct and may in fact share common characteristics. In addition, it has been estimated that greater than 90 % of the bone marrow is within 20  $\mu\text{m}$  of a blood vessel (Dr. Juwell W. Wu, private communication), raising the question how the stem niche can be hypoxic, as is widely assumed. In a recent elegant paper, a comparison of HSC niches in the calvaria, long bones epiphyses, and diaphyses was achieved using a combination of whole body imaging and intravital microscopy. The authors reported a considerable heterogeneity between different BM compartments in terms of bone hypoxia state, remodeling activity and blood volume fraction (Lassailly et al. 2013).

A low but consistent number of HSCs can be reliably found in the bone marrow niche with similar numbers of injected cells. Without gamma irradiation, these cells can be observed for up to 30 days with DiD staining (Fujisaki et al. 2011). With gamma irradiation, the location and division of HSCs to begin repopulation can be clearly visualized, with cell division and formation of small clusters of 2–4 cells by imaging on consecutive days (Lo Celso et al. 2009a, b, 2011). Although this occurrence is unlikely to be due to additional migratory events, conclusive evidence of HSC proliferation came from DiR photoconversion experiments (such that only one cell in the entire animal has the correct photoconverted color). The appearance of two or more cells with the same color supports that HSC accumulation at a specified location in the bone marrow is in fact due to proliferation (Carlson et al. 2013).

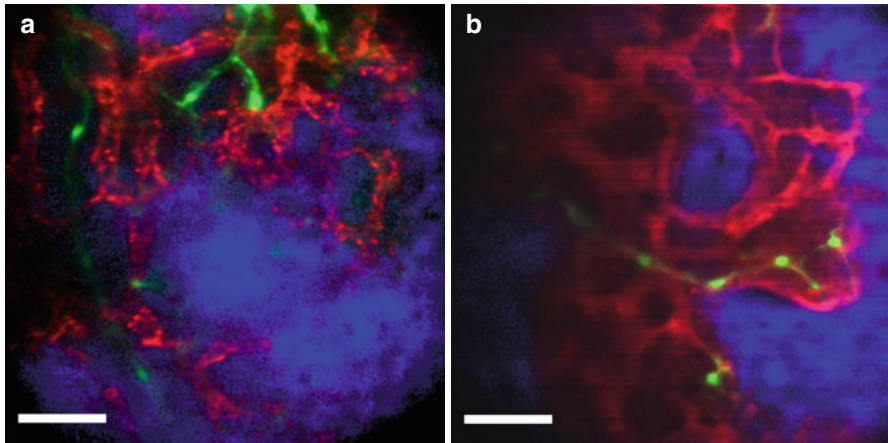


**Fig. 7.5** In vivo imaging using putative MSC markers. (a) Skull imaging of Nestin GFP MSC in a transgenic mouse with second harmonic signal (blue) to visualize the bone. The vasculature is visualized (red) by injecting CD31 into the circulation, (green) signal from nestin specific expression of the green-fluorescent protein showing nestin positive cells near the vasculature and the endosteal surface. (b) Skull imaging showing signal from alpha-SMA-GFP perivascular cells (green), bone second harmonic generation (blue), and vasculature (red) in a transgenic mouse

### 7.5.2 Intravital Microscopy of Mesenchymal Stem Cells

Recently, the role of nestin-expressing bone marrow cells (Fig. 7.5a) in the homing of HSCs to bone marrow was demonstrated where purified HSCs were injected into the circulation of lethally irradiated nestin+ mice. Using intravital microscopy, analyses of distance between nestin+ cells and the homing HSCs cells have shown that HSC home near nestin+ cells in the irradiated bone marrow (Méndez-Ferrer et al. 2010). The alpha smooth muscle actin ( $\alpha$ -SMA) marker (Kalajzic et al. 2008) was also used to observe cell proliferation, migration, and homing during bone regeneration in transgenic mice (Fig. 7.5b).

Kinetics of MSCs within the circulation is another field where intravital microscopy has been used. MSCs were tracked after injection into mouse arterial vasculature and it was noticed that 1 min after human MSC injection, arterial blood velocity declined by 60 % and such decrease was attributed to the human MSCs being entrapped in the mouse capillaries after arterial injection (Furlani et al. 2009). In a similar study, it was shown that upon intra-arterial injection of in vitro expanded MSCs, they become entrapped in precapillary vessels, leading in interruption of blood flow in the corresponding artery (Toma et al. 2009).

Combining tracker dyes and intravital microscopy has proven to be very useful for stem cell in vivo monitoring as well. In order to improve the homing of MSC to bone marrow, Sackstein et al. converted the native CD44 glycoform on MSCs into

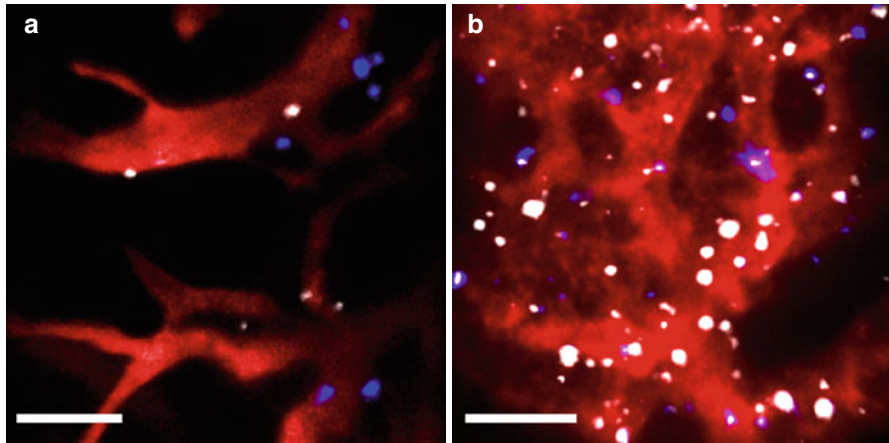


**Fig. 7.6** Delivery of modified MSC to the bone marrow. (a) Representative image of MSC localization in the bone marrow after injection of PSGL-1 and FUT-7 overexpressing MSCs (blue) and unmodified MSCs (white). Most cells extravasated through the vessel walls (red, visualized by rhodamine-dextran). (b) Representative image of MSCs (white) carrying a fluorescent microparticle cargo (blue) to the bone marrow (vessels in red, visualized by rhodamine-dextran) after systemic infusion. Scale bar = 100  $\mu\text{m}$

hematopoietic cell E-selectin/L-selectin ligand (HCELL) 6, which possessed potent E-selectin binding without affecting cell viability or multipotency. Real-time intravital microscopy in immunocompromised (NOD/SCID) mice showed that intravenously infused DiD labeled HCELL+ MSCs home efficiently to the bone marrow, with endosteal localization and generation of new human bone tissue (Sackstein et al. 2008). In another attempt to improve homing of MSCs, their surface was modified with sialyl Lewis<sub>x</sub> (SLe<sub>x</sub>) that is found on the surface of leukocytes and mediates its rolling. Labeling the MSCs with DiD and DiR dyes allowed the observation of an enhanced rolling response on inflamed endothelium in vivo and homing to inflamed tissue with higher efficiency compared to native MSCs (Sarkar et al. 2011).

In a recent study, mRNA transfection was utilized to generate MSCs that simultaneously express P-selectin glycoprotein ligand-1 (PSGL-1), Sialyl-Lewis<sub>x</sub> (SLe<sub>x</sub>), and interleukin-10 (IL-10). Using membrane dyes, the cells were tracked in vivo following systemic injection, and a rapid homing of MSCs to the inflamed site was observed with a higher anti-inflammatory effect that decreased local inflammation (Levy et al. 2013). These modified cells also exhibited enhanced homing to the calvarial bone marrow (Fig. 7.6a). It has been suggested that MSCs can act as vehicles for gene and drug delivery (Fig. 7.6b) because of their low immune response, easy expansion and immunomodulatory properties (Porada and Almeida-Porada 2010; Sarkar et al. 2010) which holds a great promise of targeting specific locations with desired genes or therapeutics in the future.

### 7.5.3 *Intravital Microscopy of Stem Cell Interactions in the Bone Marrow*

Although much has been learned so far by intravital microscopy of the bone marrow, clearly the next frontier is the dynamic evaluation and modification of cellular interaction in the stem cell niche. Although a body of work has demonstrated interplay between HSCs, MSCs, and a multiplicity of other cells, proportionally less has leveraged the direct evidence available with intravital microscopy. In perhaps the earliest reported bone marrow intravital imaging, Mazo, von Andrian, and others visualized hematopoietic progenitor cells rolling on the endothelium of bone marrow vasculature (Mazo et al. 1998). More recent work in the bone marrow stem cell niche found that HSCs transplanted into irradiated mice home near the endosteal surface and are in close proximity to osteoblasts, supporting the notion of an osteoblast HSC niche (Lo Celso et al. 2009a). Further examining the relationship between HSCs and their niche, Mendez-Ferrer et al. found that HSCs home near nestin+ MSCs by intravital microscopy, and that the nestin+ MSCs are required for the homing process (Méndez-Ferrer et al. 2010). After homing to the bone marrow niche in non-irradiated mice, allogeneic HSCs are found by intravital microscopy to persist in immune competent host without being rejected. The allograft survival is dependent on the presence of bone marrow regulatory T cells (visualized by their FOXP3-GFP expression), which provide immune privilege to transplanted HSCs in vivo (Fujisaki et al. 2011).

## 7.6 Conclusions and Closing Remarks

The bone marrow is an important source of stem cells that form blood, skeleton, and connective tissue. In the malignant setting the bone marrow can also harbor cancer stem cells that either originate there (such as leukemia) or metastasize to this site (from solid tumors). Detailed characterization how normal stem cells are maintained in the bone marrow will help advance cell-based therapies as well as help to uncover how cancer stem cells can survive in this location even after chemo- or radiation therapy. Intravital microscopy will be particularly useful for visualizing the changing microenvironment and the dynamics of cellular interactions after therapeutic manipulation.

Thus far, we have only touched on the major components in the bone marrow microenvironment- the HSCs, MSCs, and some of their supporting cells. The next frontier will be a systems approach to identification of the complex cellular network involved in niche maintenance. Intravital microscopy will no doubt have a vital role in helping to advance this next frontier.

**Acknowledgements** We would like to acknowledge David Rowe for providing the Col2.3 transgenic mice, Grigori N. Enikolopov for the nestin-gfp transgenic mice, Peter Hauschka for the alpha-SMA transgenic mice, and Joseph Phillips for acquiring the alpha-SMA picture. This work was funded in part by NIH R01 EB017274, R01 HL 097748, R01 HL97794, and U01HL 100402 (to CPL), the Kay Kendall Leukaemia Fund, BBSRC, HFSP, and CRUK (to CLC)

## References

- Abdallah BM, Haack-Sorensen M et al (2005) Maintenance of differentiation potential of human bone marrow mesenchymal stem cells immortalized by human telomerase reverse transcriptase gene despite [corrected] extensive proliferation. *Biochem Biophys Res Commun* 326(3):527–538
- Adams GB, Alley IR et al (2009) Haematopoietic stem cells depend on Galpha(s)-mediated signaling to engraft bone marrow. *Nature* 459(7243):103–107
- Akiyama K, Chen C et al (2012) Lineage differentiation of mesenchymal stem cells from dental pulp, apical papilla, and periodontal ligament. *Methods Mol Biol* 887:111–121
- Aldahmash A, Zaher W et al (2012) Human stromal (mesenchymal) stem cells: basic biology and current clinical use for tissue regeneration. *Ann Saudi Med* 32(1):68–77
- Al-Nbaheen M, Vishnubalaji R et al (2013) Human stromal (mesenchymal) stem cells from bone marrow, adipose tissue and skin exhibit differences in molecular phenotype and differentiation potential. *Stem Cell Rev* 9(1):32–43
- Alt C, Runnels JM et al (2012) In vivo tracking of hematopoietic cells in the retina of chimeric mice with a scanning laser ophthalmoscope. *IntraVital* 1(2):132–140
- Asakura A, Komaki M et al (2001) Muscle satellite cells are multipotential stem cells that exhibit myogenic, osteogenic, and adipogenic differentiation. *Differentiation* 68(4–5):245–253
- Askenasy N, Farkas DL (2002) Optical imaging of PKH-labeled hematopoietic cells in recipient bone marrow in vivo. *Stem Cells* 20(6):501–513
- Azab AK, Runnels JM et al (2009) CXCR4 inhibitor AMD3100 disrupts the interaction of multiple myeloma cells with the bone marrow microenvironment and enhances their sensitivity to therapy. *Blood* 113(18):4341–4351
- Bentzon JF, Stenderup K et al (2005) Tissue distribution and engraftment of human mesenchymal stem cells immortalized by human telomerase reverse transcriptase gene. *Biochem Biophys Res Commun* 330(3):633–640
- Bhansali A, Upreti V et al (2009) Efficacy of autologous bone marrow-derived stem cell transplantation in patients with type 2 diabetes mellitus. *Stem Cells Dev* 18(10):1407–1416
- Bianco P, Riminucci M et al (2001) Bone marrow stromal stem cells: nature, biology, and potential applications. *Stem Cells* 19(3):180–192
- Cai X, Lin Y et al (2009) Bone marrow derived pluripotent cells are pericytes which contribute to vascularization. *Stem Cell Rev* 5(4):437–445
- Calvi LM, Adams GB et al (2003) Osteoblastic cells regulate the haematopoietic stem cell niche. *Nature* 425(6960):841–846
- Camargo FD, Chambers SM et al (2006) Hematopoietic stem cells do not engraft with absolute efficiencies. *Blood* 107(2):501–507
- Cao Y-A, Wagers AJ et al (2004) Shifting foci of hematopoiesis during reconstitution from single stem cells. *Proc Natl Acad Sci* 101(1):221–226
- Carlson AL, Fujisaki J et al (2013) Tracking single cells in live animals using a photoconvertible near-infrared cell membrane label. *PLoS One* 8(8):e69257
- Chen SL, Fang WW et al (2004) Effect on left ventricular function of intracoronary transplantation of autologous bone marrow mesenchymal stem cell in patients with acute myocardial infarction. *Am J Cardiol* 94(1):92–95
- Colmone A, Amorim M et al (2008) Leukemic cells create bone marrow niches that disrupt the behavior of normal hematopoietic progenitor cells. *Science* 322(5909):1861–1865
- Crisan M, Yap S et al (2008) A perivascular origin for mesenchymal stem cells in multiple human organs. *Cell Stem Cell* 3(3):301–313
- Daldrup-Link HE, Rudelius M et al (2005) Migration of iron oxide-labeled human hematopoietic progenitor cells in a mouse model: in vivo monitoring with 1.5-T MR imaging equipment. *Radiology* 234(1):197–205
- De Bari C, Dell'Accio F et al (2001) Multipotent mesenchymal stem cells from adult human synovial membrane. *Arthritis Rheum* 44(8):1928–1942
- Ding L, Morrison SJ (2013) Haematopoietic stem cells and early lymphoid progenitors occupy distinct bone marrow niches. *Nature* 495(7440):231–235

- Ding L, Saunders TL et al (2012) Endothelial and perivascular cells maintain haematopoietic stem cells. *Nature* 481(7382):457–462
- Dominici M, Le BK et al (2006) Minimal criteria for defining multipotent mesenchymal stromal cells. The International Society for Cellular Therapy position statement. *Cytherapy* 8(4):315–317
- Downes A, Mouras R et al (2011) Raman spectroscopy and CARS microscopy of stem cells and their derivatives. *J Raman Spectrosc* 42(10):1864–1870
- Duijvestein M, Vos AC et al (2010) Autologous bone marrow-derived mesenchymal stromal cell treatment for refractory luminal Crohn's disease: results of a phase I study. *Gut* 59(12):1662–1669
- Ema H, Morita Y et al (2006) Adult mouse hematopoietic stem cells: purification and single-cell assays. *Nat Protoc* 1(6):2979–2987
- Estrada EJ, Valacchi F et al (2008) Combined treatment of intrapancreatic autologous bone marrow stem cells and hyperbaric oxygen in type 2 diabetes mellitus. *Cell Transplant* 17(12):1295–1304
- Ferraro F, Lympieri S et al (2011) Diabetes impairs hematopoietic stem cell mobilization by altering niche function. *Sci Transl Med* 3(104):104ra101
- Friedenstein AJ, Chailakhyan RK et al (1987) Bone marrow osteogenic stem cells: in vitro cultivation and transplantation in diffusion chambers. *Cell Tissue Kinet* 20(3):263–272
- Fujisaki J, Wu J et al (2011) In vivo imaging of Treg cells providing immune privilege to the haematopoietic stem-cell niche. *Nature* 474(7350):216–219
- Furlani D, Ugurlucan M et al (2009) Is the intravascular administration of mesenchymal stem cells safe? Mesenchymal stem cells and intravital microscopy. *Microvasc Res* 77(3):370–376
- Gangji V, Hauzeur JP (2005) Treatment of osteonecrosis of the femoral head with implantation of autologous bone-marrow cells. Surgical technique. *J Bone Joint Surg Am* 87 Suppl 1(Pt 1):106–112
- Granero-Molto F, Weis JA et al (2009) Regenerative effects of transplanted mesenchymal stem cells in fracture healing. *Stem Cells* 27(8):1887–1898
- Greenbaum A, Hsu Y-MS et al (2013) CXCL12 in early mesenchymal progenitors is required for haematopoietic stem-cell maintenance. *Nature* 495(7440):227–230
- Hare JM, Traverse JH et al (2009) A randomized, double-blind, placebo-controlled, dose-escalation study of intravenous adult human mesenchymal stem cells (prochymal) after acute myocardial infarction. *J Am Coll Cardiol* 54(24):2277–2286
- Horton NG, Wang K et al (2013) In vivo three-photon microscopy of subcortical structures within an intact mouse brain. *Nat Photonics* 7(3):205–209
- Johnstone B, Hering TM et al (1998) In vitro chondrogenesis of bone marrow-derived mesenchymal progenitor cells 43. *Exp Cell Res* 238(1):265–272
- Kalajzic I, Staal A et al (2005) Expression profile of osteoblast lineage at defined stages of differentiation. *J Biol Chem* 280(26):24618–24626
- Kalajzic Z, Li H et al (2008) Use of an alpha-smooth muscle actin GFP reporter to identify an osteoprogenitor population. *Bone* 43(3):501–510
- Kassem M, Mosekilde L et al (1993) 1,25-dihydroxyvitamin D3 potentiates fluoride-stimulated collagen type I production in cultures of human bone marrow stromal osteoblast-like cells. *J Bone Miner Res* 8(12):1453–1458
- Keller G (2005) Embryonic stem cell differentiation: emergence of a new era in biology and medicine. *Genes Dev* 19(10):1129–1155
- Kermani AJ, Fathi F et al (2008) Characterization and genetic manipulation of human umbilical cord vein mesenchymal stem cells: potential application in cell-based gene therapy. *Rejuvenation Res* 11(2):379–386
- Kiel MJ, Yilmaz ÖH et al (2005) SLAM family receptors distinguish hematopoietic stem and progenitor cells and reveal endothelial niches for stem cells. *Cell* 121(7):1109–1121
- Kiel MJ, Radice GL et al (2007) Lack of evidence that hematopoietic stem cells depend on N-cadherin-mediated adhesion to osteoblasts for their maintenance. *Cell Stem Cell* 1(2):204–217



- Lane SW, Wang YJ et al (2011) Differential niche and Wnt requirements during acute myeloid leukemia progression. *Blood* 118(10):2849–2856
- Lapidot T, Kollet O (2002) The essential roles of the chemokine SDF-1 and its receptor CXCR4 in human stem cell homing and repopulation of transplanted immune-deficient NOD/SCID and NOD/SCID/B2m(null) mice. *Leukemia* 16(10):1992–2003
- Lapidot T, Dar A et al (2005) How do stem cells find their way home? *Blood* 106(6):1901–1910
- Lassailly F, Foster K et al (2013) Multimodal imaging reveals structural and functional heterogeneity in different bone marrow compartments: functional implications on hematopoietic stem cells. *Blood* 122(10):1730–1740
- Le Blanc K, Gotherstrom C et al (2005) Fetal mesenchymal stem-cell engraftment in bone after in utero transplantation in a patient with severe osteogenesis imperfecta. *Transplantation* 79(11):1607–1614
- Le BK, Tammik C et al (2003) HLA expression and immunologic properties of differentiated and undifferentiated mesenchymal stem cells. *Exp Hematol* 31(10):890–896
- Le BK, Frassoni F et al (2008) Mesenchymal stem cells for treatment of steroid-resistant, severe, acute graft-versus-host disease: a phase II study. *Lancet* 371(9624):1579–1586
- Levy O, Zhao W et al (2013) mRNA-engineered mesenchymal stem cells for targeted delivery of interleukin-10 to sites of inflammation. *Blood* 122:e23–e32
- Liang J, Zhang H et al (2012) Allogeneic mesenchymal stem cell transplantation in seven patients with refractory inflammatory bowel disease. *Gut* 61(3):468–469
- Lo Celso C, Fleming HE et al (2009a) Live-animal tracking of individual haematopoietic stem/progenitor cells in their niche. *Nature* 457(7225):92–96
- Lo Celso C, Wu JW et al (2009b) In vivo imaging of hematopoietic stem cells and their microenvironment. *J Biophotonics* 2(11):619–631
- Lo Celso C, Lin CP et al (2011) In vivo imaging of transplanted hematopoietic stem and progenitor cells in mouse calvarium bone marrow. *Nat Protoc* 6(1):1–14
- Luster AD, Alon R et al (2005) Immune cell migration in inflammation: present and future therapeutic targets. *Nat Immunol* 6(12):1182–1190
- Matsuzaki Y, Kinjo K et al (2004) Unexpectedly efficient homing capacity of purified murine hematopoietic stem cells. *Immunity* 20(1):87–93
- Mazo IB, Gutierrez-Ramos JC et al (1998) Hematopoietic progenitor cell rolling in bone marrow microvessels: parallel contributions by endothelial selectins and vascular cell adhesion molecule 1. *J Exp Med* 188(3):465–474
- Mazo IB, Honeczarenko M et al (2005) Bone marrow is a major reservoir and site of recruitment for central memory CD8+ T cells. *Immunity* 22(2):259–270
- Méndez-Ferrer S, Michurina TV et al (2010) Mesenchymal and haematopoietic stem cells form a unique bone marrow niche. *Nature* 466(7308):829–834
- Morikawa S, Mabuchi Y et al (2009) Prospective identification, isolation, and systemic transplantation of multipotent mesenchymal stem cells in murine bone marrow. *J Exp Med* 206(11):2483–2496
- Osawa M, Hanada K et al (1996) Long-term lymphohematopoietic reconstitution by a single CD34-low/negative hematopoietic stem cell. *Science* 273(5272):242–245
- Park D, Spencer JA et al (2012) Endogenous bone marrow MSCs are dynamic, fate-restricted participants in bone maintenance and regeneration. *Cell Stem Cell* 10(3):259–272
- Porada CD, Almeida-Porada G (2010) Mesenchymal stem cells as therapeutics and vehicles for gene and drug delivery. *Adv Drug Deliv Rev* 62(12):1156–1166
- Prohazky F, Dallman MJ et al (2013) From seeing to believing: labelling strategies for in vivo cell-tracking experiments. *Interface Focus* 3(3):20130001
- Quarto R, Mastrogiacomo M et al (2001) Repair of large bone defects with the use of autologous bone marrow stromal cells. *N Engl J Med* 344(5):385–386
- Runnels JM, Zamiri P et al (2006) Imaging molecular expression on vascular endothelial cells by in vivo immunofluorescence microscopy. *Mol Imaging* 5(1):31–40
- Sackstein R, Merzaban JS et al (2008) Ex vivo glycan engineering of CD44 programs human multipotent mesenchymal stromal cell trafficking to bone. *Nat Med* 14(2):181–187

- Sanchez-Aguilera A, Lee YJ et al (2011) Guanine nucleotide exchange factor Vav1 regulates perivascular homing and bone marrow retention of hematopoietic stem and progenitor cells. *Proc Natl Acad Sci U S A* 108(23):9607–9612
- Sarkar D, Vemula PK et al (2010) Engineered mesenchymal stem cells with self-assembled vesicles for systemic cell targeting. *Biomaterials* 31(19):5266–5274
- Sarkar D, Spencer JA et al (2011) Engineered cell homing. *Blood* 118(25):e184–e191
- Schroeder T (2008) Imaging stem-cell-driven regeneration in mammals. *Nature* 453(7193):345–351
- Seo BM, Miura M et al (2004) Investigation of multipotent postnatal stem cells from human periodontal ligament. *Lancet* 364(9429):149–155
- Shizuru JA, Negrin RS et al (2004) Hematopoietic stem and progenitor cells: clinical and preclinical regeneration of the hematolymphoid system. *Annu Rev Med* 56(1):509–538
- Sipkins DA, Wei X et al (2005) In vivo imaging of specialized bone marrow endothelial microdomains for tumour engraftment. *Nature* 435(7044):969–973
- Toma C, Wagner WR et al (2009) Fate of culture-expanded mesenchymal stem cells in the microvasculature: in vivo observations of cell kinetics. *Circ Res* 104(3):398–402
- Visnjic D, Kalajzic Z et al (2004) Hematopoiesis is severely altered in mice with an induced osteoblast deficiency. *Blood* 103(9):3258–3264
- von Andrian UH, Chambers JD et al (1991) Two-step model of leukocyte-endothelial cell interaction in inflammation: distinct roles for LECAM-1 and the leukocyte beta 2 integrins in vivo. *Proc Natl Acad Sci U S A* 88(17):7538–7542
- Wang L, Benedito R et al (2013) Identification of a clonally expanding haematopoietic compartment in bone marrow. *EMBO J* 32(2):219–230
- Winkler IG, Sims NA et al (2010) Bone marrow macrophages maintain hematopoietic stem cell (HSC) niches and their depletion mobilizes HSCs. *Blood* 116(23):4815–4828
- Wynn RF, Hart CA et al (2004) A small proportion of mesenchymal stem cells strongly expresses functionally active CXCR4 receptor capable of promoting migration to bone marrow. *Blood* 104(9):2643–2645
- Zhang J, Niu C et al (2003) Identification of the haematopoietic stem cell niche and control of the niche size. *Nature* 425(6960):836–841
- Zuk PA, Zhu M et al (2001) Multilineage cells from human adipose tissue: implications for cell-based therapies. *Tissue Eng* 7(2):211–228

## Chapter 8

# Live Imaging of Subcellular Structures and Cellular Processes in Mouse Intraperitoneal Organs

Liqin Cao and Kuniya Abe

**Abstract** Intravital microscopy is a powerful tool for discovery and analysis in cell biology, neurobiology, immunology and oncology and has increasingly become a method used in most biomedical research. Recently, advances in imaging system, fluorescence labeling and tissue immobilization techniques have made it possible to *in vivo* image subcellular structure dynamics and cellular processes in virtually all abdominal organs of live mice. In this chapter, we describe the considerations that comprise subcellular intravital imaging in mouse intraperitoneal organs. After discussing the topics such as choosing the suitable imaging modalities and optics, labeling strategies, tissue stabilization, anesthesia and animal handling, examples of imaging various organs with subcellular resolution using a tissue stabilization device made by the authors are presented. This chapter will be helpful to scientists who are interested in adding intravital microscopy to their technology toolbox. We have focused our discussions on *in vivo* imaging in abdominal organs, however, most of the points we make are relevant to imaging of any organs.

**Keywords** Intravital microscopy • Subcellular structures • Abdominal organs • Mouse

---

L. Cao (✉)

Mammalian Genome Dynamics, RIKEN BioResource Center,  
Tsukuba, Ibaraki 305-0074, Japan

5F Health and Medical Science Innovation Laboratory,  
WPI-International Institute for Integrative Sleep Medicine,  
University of Tsukuba, Tsukuba, Ibaraki 305-8575, Japan  
e-mail: [cao.liqin.ga@u.tsukuba.ac.jp](mailto:cao.liqin.ga@u.tsukuba.ac.jp)

K. Abe (✉)

Mammalian Genome Dynamics, RIKEN BioResource Center,  
Tsukuba, Ibaraki 305-0074, Japan  
e-mail: [abe@rtc.riken.jp](mailto:abe@rtc.riken.jp)

© Springer Science+Business Media Dordrecht 2014

R. Weigert (ed.), *Advances in Intravital Microscopy*:

*From Basic to Clinical Research*, DOI 10.1007/978-94-017-9361-2\_8

163

## 8.1 Introduction

Imaging of live animals at microscopic resolution (intravital microscopy, IVM) has provided enormous invaluable information on mammalian cell biology in the last two decades (Weigert et al. 2013; Grutzendler et al. 2002; Nimmerjahn et al. 2005; Li et al. 2012; Marchiando et al. 2010; Swirski et al. 2009; Masedunskas et al. 2011; Orth et al. 2011). For example, subcellular IVM of the mouse brain has revealed unexpected details of the dynamic nature of synaptic structures through development and reshaped the understanding of neurodegenerative diseases and of immune surveillance function of microglia (Grutzendler et al. 2002; Nimmerjahn et al. 2005). Imaging the salivary glands of live mice has shed novel insights into the mechanism of regulated exocytosis and disclosed discrepancies between *in vitro* and *in vivo* model systems (Masedunskas et al. 2011, 2012a; Masedunskas and Weigert 2008). However, performing subcellular intravital imaging in intraperitoneal organs of rodents has long been impeded due to organ motion caused by respiration and heart-beat. Research using IVM has suggested that mechanisms of inflammatory leukocyte recruitments in mouse kidney and liver differ markedly from those in other readily-visualized tissues such as the skin, muscle and mesentery (Hickey and Westhorpe 2013), underlining the importance of observing biological processes in their natural *in vivo* context. In the last few years, much effort has been made to develop technologies facilitating to access constantly abdominal organs of live rodents with minimal invasiveness and to minimize tissue motion artifacts with negligible impairments (Ritsma et al. 2013; Cao et al. 2012; Kim et al. 2012; Tanaka et al. 2012). The confluence of these developments has made it possible to longitudinally image murine internal organs with subcellular resolution under proper physiological conditions.

In this chapter, we provide an overview of the latest technical advances in subcellular IVM with a particular emphasis on practical considerations for imaging of abdominal organs in rodents. First, the most widely used imaging modalities and state-of-the-art optics such as miniaturized objectives and microlenses for IVM of rodent internal organs are described. Recommendations are made for choosing the appropriate microscope, objective and settings in order to perform IVM with high sensitivity and low phototoxicity for specific imaging studies. Next, general labeling strategies for IVM are outlined. The advantages and limitations of these strategies are discussed, and methods for avoiding fluorescence crosstalk (also termed bleed through or crossover) are addressed. Various approaches to accessing the target organs and minimizing tissue motion artifacts for long-term imaging without compromising tissue integrity are then introduced. Finally, considerations for animal preparation and handling, anesthesia, and physiologic monitoring of anesthetized animals are presented, and how animal preparation and anesthesia may confound the results of the imaging studies is discussed. We have also reviewed selected applications of IVM in murine abdominal organs, including examples from our own work. These studies are chosen because they illustrate how IVM can be used to image and investigate a wide range of physiological and subcellular processes in internal organs.

## 8.2 Choice of Imaging Modality and Optics

### 8.2.1 *Microscope*

A wide variety of light microscopy techniques are available for IVM (Li et al. 2012; Alencar et al. 2005; Mennone and Nathanson 2011; Yamauchi et al. 2006; Nishimura et al. 2008; Serrels et al. 2009; Pittet and Weissleder 2011). The type of system to be used depends largely on the kind of experiment to be performed. For imaging cellular processes and subcellular structures, laser scanning confocal, two-photon and spinning-disk microscopy are the most widely used. Detailed descriptions on these technologies are not presented here as many excellent discussions may be found elsewhere (Helmchen and Denk 2005; Zipfel et al. 2003; Wang et al. 2005), and only the main and distinctive features of these systems are briefly reviewed.

Laser scanning confocal microscope (LSCM) uses an emission pinhole to reject out-of-focus light, which greatly increases the contrast and the visibility of fine details in the specimen and allows performing optical sectioning. One of the advantages of LSCM is that the thickness of the optical section can be determined by tuning the size of pinhole to enable an optimal definition of subcellular structures (Masedunskas et al. 2011). The good lateral and axial resolution makes LSCM the type of microscopy that is best suited for imaging organelles and biological processes (Weigert et al. 2010). However, LSCM suffers from a limited depth penetration up to 50–100  $\mu\text{m}$  due to high absorption and scattering of UV or visible light in the tissue (Phan and Bullen 2010). Further, under LSCM microscope both in-focus and out-of-focus molecules can be excited, leading to photodamage and photobleaching, and is not suitable for long-term imaging.

Two-photon microscope (TPM) relies on the simultaneous absorption of two photons by a fluorophore. For a given fluorophore, two-photon excitation requires the use of excitation light at twice the one-photon wavelength, falling into the near infrared (NIR) or infrared (IR). TPM has a number of advantages. First, it can penetrate much deeper (up to 400  $\mu\text{m}$  in lymphoid tissue) into tissues than LSCM because the absorption and scattering of NIR or IR in biological specimens are minimal (Helmchen and Denk 2005; von Andrian and Mempel 2003). By adding extra options to the system such as optical parametric oscillators or regenerative amplifiers, the imaging depth can be further extended up to 700  $\mu\text{m}$  in the lymph node and 1,000  $\mu\text{m}$  in the brain (Andresen et al. 2009; Theer et al. 2003). Second, Two-photon excitation of fluorophores is limited to the focal plane and no pinhole is required to block off-focus emission in TPM. This significantly reduces the photodamage and photobleaching, and enables to successfully image embryogenesis in mice which has failed with LSCM due to the developmental arrest caused by phototoxicity (Squirrell et al. 1999). Third, TPM can excite various endogenous fluorophores that are simulated by UV in LSCM and visualize structures such as collagen fibers through second-harmonic generation, which allows intrinsic molecular imaging in living specimens without any exogenous labels (Wang et al. 2010; Pena et al. 2007). While TPM has unique advantages, it has poorer resolution when

compared with LSCM because the resolution of a microscopy system is directly proportional to the wavelength of excitation light (Piston 1998). Moreover, TPM is expensive and less affordable for most laboratories, and generally relies on a single excitation wavelength for all fluorophores.

Both conventional LSCM and TPM have an inherently slow acquisition speed that reaches at best a few frames per second, limiting the ability to observe events that occur on very fast timescales. To monitor the behavior of fast-moving fine structures inside the cells of live animals, spinning-disk confocal microscopy (SDCM) is a technique of choice. SDCM offers video rate imaging up to 1,000 frames per second. This rapid acquisition speed also helps to overcome the challenge of motion artifacts caused by heartbeat and respiration in intravital imaging, which is particularly pronounced for abdominal organs. SDCM gives a lower local dose of light relative to CLSM, which significantly reduces photobleaching/phototoxicity and allows long-term IVM (Graf et al. 2005). Applications of SDCM in neurobiology, immunology and cancer studies in live animals have been reported (Nishimura et al. 2008; Ewald et al. 2011a; Stirling et al. 2009; Jenne et al. 2011). While SDCM is a powerful tool for high-speed imaging, it has a more limited tissue penetration than TPM and theoretically more limited ability to remove out-of-focus light than CLSM due to crosstalk between the multiple pinholes (Shimozawa et al. 2013).

## 8.2.2 Objective Lenses

The choice of objectives is important especially for performing subcellular IVM. When deciding which lens is chosen for a particular application, balancing the desire of high-resolution image acquisition with the need of minimal exposure of the specimen to light to reduce phototoxicity and photobleaching should be taken into consideration. The resolution of an optical microscope can be defined by a simple equation  $R = \lambda / (2NA)$ , where  $R$  is resolution (the shortest resolvable distance between two objects),  $\lambda$  is the wavelength of the light,  $NA$  is the numerical aperture of the lens (Piston 1998). This relationship indicates that for a given imaging light, higher  $NA$  lens will produce higher resolution. The resolving power of a microscope is also dependent on contrast. In general, more light produces higher-contrast images (Webb and Brown 2013). The light throughput of an objective lens is proportional to its  $NA$  to the fourth power, and inversely proportional to the square of its magnification (Webb and Brown 2013; Abramowitz et al. 2002). Consequently, to obtain bright and high-resolution images, an objective lens with the highest  $NA$  and the lowest magnification capable of providing a pixel size that matches the Nyquist criterion should be used. The Nyquist criterion defines that the pixel size should be slightly less than one-half of the resolution, that is, approximately two points should be collected per resolution size for maximizing the structural information collection (Piston 1998; Brown 2007). Increasing the magnification to sample with smaller pixel size than that required by the Nyquist criterion leads to oversampling, subjecting the specimen to more light exposure and phototoxicity than is necessary and increasing the scanning time for a given image area which could raise the chances of introducing motion artifacts, without adding additional structural information.



Besides the resolving power, physical accessibility of the objective lens to the tissue of interest should also be taken into account in small animal IVM, particularly for longitudinal imaging at multiple time points in which minimal invasiveness is a matter of great concern. Stick-type objectives with a small footprint ranging from 1.3~3.5 mm in diameter have shown to allow access to virtually any abdominal organs of mice and provide optimal excitation for imaging the uneven and rounded surfaces of these organs (Fig. 8.1) (Cao et al. 2012; Alencar et al. 2005). These objective lenses have a relatively high NA and are optimized for use at red and NIR wavelengths, enabling subcellular IVM in various internal organs (Swirski et al. 2009; Cao et al. 2012). Recently, applications of using gradient refractive index (GRIN) microlenses for intravital imaging have been presented (Kim et al. 2012; Li and Yu 2008; Barretto et al. 2009, 2011). GRIN microlenses typically are cylindrical shape lenses that usually possess small diameters (350–1,000  $\mu\text{m}$ ), moderate lengths (20–100 mm) and relatively high NA (0.4–0.6), allowing minimally invasive cellular imaging of mouse internal organs (Fig. 8.1) (Kim et al. 2012; Li and Yu 2008). By combing GRIN lenses with high-NA plano-convex glass lenses cut from tiny, mass-produced ball lenses, imaging at subcellular resolution that is comparable to conventional microscopy has been achieved (Barretto et al. 2009).

## 8.3 Labeling Strategies for Intravital Microscopy

### 8.3.1 Fluorescent Proteins (FP)

Transgenic mice expressing selected FPs in specific cell lineages or whole animals have been extensively used for intravital imaging experiment. The versatile applications of FP mice include cell lineage identification, single-cell tracking, organelle dynamics observation and membrane trafficking analysis (Masedunskas et al. 2011; Cao et al. 2012; Kedrin et al. 2008). Fused multi-FP transgene strategies have led to

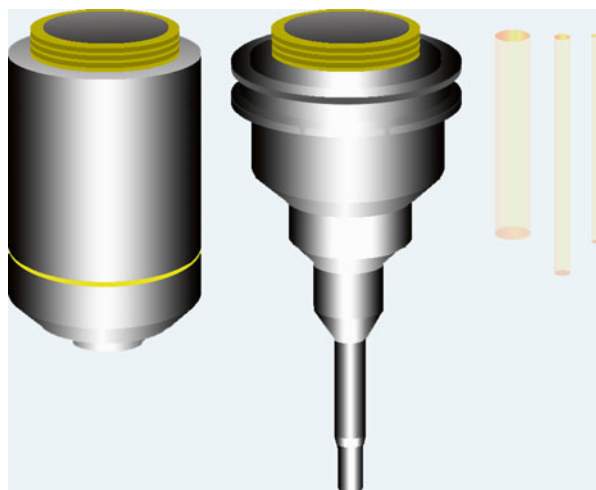


**Fig. 8.1** Schematic of optical lenses. Regular objective lens (*left*). Stick-type objective lens (*middle*). Gradient refractive index (GRIN) lenses with different diameters (*right*)

some elegant studies, such as the generation of the FUCCI reporter system that allows real-time monitoring of cell cycle progression and proliferative status of cancer cells implanted in mice and the brainbow mouse model that facilitates to analyze the neuronal circuitry (Dan et al. 2012; Livet et al. 2007). During the past few years, techniques of forster resonance energy transfer (FRET) and fluorescence recovery after photobleaching (FRAP) using FPs have gained increasing popularity. FRET has been used for co-localization, protein–protein interactions and cell signaling pathway studies, and FRAP presents itself as a useful tool to study the diffusion of various biomolecules in living cells (Balla 2009; Timpson et al. 2011; Berkovich et al. 2011). Further, photoconversion of FPs has provided the opportunity to label the subgroup of a specific cell population and track them in multiple image sessions (Kedrin et al. 2008).

While FP transgenic animal models offer the advantages of stably endogenous expression, high tissue specificity and precise temporal regulation, the generation of transgenic mice is costly and time-consuming. An alternative approach is to deliver the FP gene directly into the target organs of the adult animal via viral or plasmid DNA mediated gene transfer. Transduction of FP and other genes with the adenovirus vector has been accomplished in the murine kidney and liver, and therapeutic benefits have been demonstrated in liver disease models (Corridon et al. 2013; Daly 2004). Recently, transfection of naked plasmid DNA using a tissue suction device has proven to be an effective technique for *in vivo* site-specific gene transfer in mouse internal organs, and the expression of luciferase and green fluorescent protein in the liver, kidney and spleen were detected (Shimizu et al. 2012). The successful delivery and expression of plasmid DNA in other organs such as the heart and salivary gland have also been reported (Shimizu et al. 2012; Sramkova et al. 2009). These novel approaches offer the possibility to image various biological processes in live animals in a relatively short amount of times since the creation of genetically modified animals is not involved.

### 8.3.2 *Fluorescent Probes*

Numerous synthetic fluorescent probes that are suitable for IVM, including chemical compounds and nanocrystal quantum dots, have been developed in the last few decades. The main advantages of these probes are that they are easy to use, provide a wide array of image colors, enable studying various physiological and cellular functions and allow labeling of most cell compartments including cytoplasm, nucleus, subcellular structures and cell membrane (Parish 1999; Prohazka et al. 2013; Masedunskas et al. 2012b). The probe can be delivered to the target site via systematic injection of the molecules into the animal. For example, intravenous injection of angiosense or dextrans is a routine method to highlight the vasculature and enable studying blood flow patterns in the kidney, pancreas and other organs in rodents (Kang et al. 2006; Nyman et al. 2008). The nuclear dye Hoechst is also commonly administrated systematically. It can rapidly penetrate the cell and label

the nuclei *in vivo* (Parish 1999). Alternatively, some probes can be administrated to tissues locally. Mitochondria, lysosomes and nuclei have shown to be effectively labeled by mitotracker, lysotracker and DRAQ5, respectively, in the salivary glands, liver and pancreas by bathing these organs in the probe solution (Masedunskas et al. 2012b) (Cao, unpublished data). In comparison with endogenously expressed FPs, fluorescent dyes present challenges of toxicity and non-specific staining (Last'ovicka et al. 2009; Lee et al. 2005). Therefore, for each particular application pilot experiments should be performed to determine a suitable dose with which the staining is sufficiently strong, but toxicity and non-specific labeling are minimized. Local administration of the probe is more desirable whenever applicable because it is less noxious, less expensive due to reduced amount of probe required, and in general offers better control for non-specific staining in comparison to systematic injections.

### 8.3.3 Endogenous Fluorophores

Some molecules, including structure proteins collagen and elastin, enzymes/coenzymes NADH (nicotinamide adenine dinucleotide) and FAD (flavin adenine dinucleotide), vitamins, porphyrins and lipids lipofuscin, are endogenous fluorophores that can be visualized by either single photon microscopy via UV radiation or non-linear optical techniques such as TPM and second harmonic generation (SHG) (Huang et al. 2002; Perentes et al. 2009). In SHG case, incident photons interact with the non-centrosymmetric biological structures and produce new photons at twice the energy of their incident light (Weigert et al. 2013). The detection of endogenous emission through nonlinear excitation provides valuable information about cellular metabolic activity and tissue architecture (Huang et al. 2002; Perentes et al. 2009; Klinger et al. 2012). Since this approach requires no exogenous labelling which avoids the potential side effects of labelling and uses nonlinear excitation in the 700–900 nm range instead of the UV range which greatly minimizes photodamage risk and improves tissue penetration depth, it is becoming increasingly used in IVM both for basic research as well as medical diagnostics. For example, NADH is a sensitive indicator of both oxidative and glycolytic energy metabolism (Chance and Williams 1955; Williamson et al. 1967). Monitoring the change in NADH fluorescence facilitates to characterize the tissue redox status under pathological conditions in the liver and kidney (Paxian et al. 2004; Wu et al. 2007). Imaging and measuring the level of NADH from murine pancreatic islets provide information to understand the differential metabolic responses in the cytoplasm and mitochondria of pancreatic  $\beta$  cells under glucose stimulation and help to determine the causative gene essential for glucose-stimulated metabolic responses (Patterson et al. 2000; Piston et al. 1999). Analysis of NADH fluorescence has also been exploited to confirm the energy metabolism model in the brain (Kasischke et al. 2004), identify subtypes and grades of the cancer, and predict potential therapeutic efficacy in tumor studies (Ostrander et al. 2010). Collagen fibers, which serve to hold cells

together, generate a SHG signal under two-photon excitation and have been widely used for analyzing tissue structural organization. Imaging collagen fibers has enabled successful diagnosis of liver and lung fibrosis as well as distinguishing different steps of their pathological processes (Pena et al. 2007; Lee et al. 2004). Moreover, collagen fibers within the tissue can serve as valuable reference landmarks for tracking cell migration over long period of imaging times (Ritsma et al. 2013; Perentes et al. 2009). Combination of two-photon fluorescence and second-harmonic generated signal microscopy as two-modality microscopy allows for simultaneously detecting endogenous and exogenous fluorescent signals in conjunction with structural components in deep tissues, yielding multicolor images at high resolution. It is worth noting that for a given excitation power the absolute brightness of intrinsic emission signals are dramatically different among tissues, and significantly higher laser intensity is required to acquire reasonable signal-to-noise images for some tissues (Dela Cruz et al. 2010). The high laser power could lead to severe tissue damage, therefore the tissue type is important to consider when designing microscopic imaging experiments based on intrinsic emission.

### 8.3.4 *Fluorescence Crosstalk Minimization*

Fluorescence crosstalk is a common problem when imaging a sample that has been labelled by more than one fluorescent marker. Crosstalk can happen in both the excitation and emission. Since most fluorophores have the excitation curve and emission curve with a long tail towards the blue and red end of the spectrum, respectively (Fig. 8.2), excitation crosstalk between fluorophores usually occurs towards shorter wavelengths while emission crosstalk occurs towards longer wavelengths. For example, the 488 nm-laser used to excite EGFP can also simultaneously excite DsRed, whereas the DsRed emission filter can often detect the EGFP signal. Several strategies are commonly used to overcome the crosstalk problem. Firstly, gathering images sequentially rather than simultaneously by exciting each fluorophore at a time helps to minimize crosstalk between channels. However, when imaging the internal organs of live animals that experience tissue motion caused by heartbeat and respiration or the highly dynamic events in the cells, the sequential scan is often not an option. Secondly, carefully choosing fluorescent probes with widely separated excitation and emission profiles and associated filter sets can effectively avoid crosstalk. When designing multicolor-imaging experiments it is important to check the available equipment configurations including laser lines and detector filters before selecting fluorescent labels to ensure that the chosen probes offer the optimal combination of collecting specific fluorescent signals with minimal crosstalk with the use of available instrument. It is also critical to ensure that the fluorescence emission of all selected probes is at a similar level of brightness. Note that synthetic dyes or quantum dots usually have a much narrower emission spectrum (typically 30–60 nm) in comparison to FPs (~80–150 nm). In multicolor-imaging experiments using filter sets, control samples labeled for each fluorophore as well as unlabeled samples should be

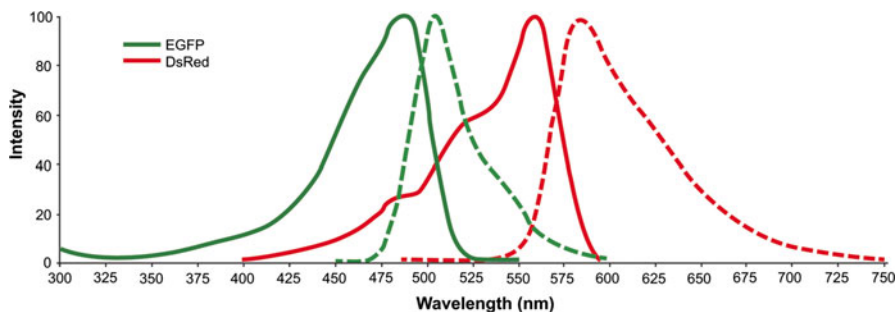


**Fig. 8.2** Normalized excitation (*solid lines*) and emission (*dashed lines*) spectra of EGFP and DsRed

prepared and imaged with the same imaging settings used for multiple labeled samples whenever possible. These images can serve as references to adjust laser intensity, gain and offset level of the detector to minimize emission bleed through and can also be used to correct images post acquisition. Thirdly, spectral imaging coupled with image analysis using linear unmixing algorithms can be employed to powerfully eliminate fluorescence spectral overlap artifacts in multifluorescence imaging. Spectral imaging and linear unmixing is an established method used in terrestrial remote sensing for decades (Hiraoka et al. 2002; Haraguchi et al. 2002; Radosevich et al. 2008). Recent advances in software and imaging hardware have extended the application of this technology to medical and bioscience field. This technique enables the identification of the emission fluorescence through the analysis of their unique spectral signatures, allowing the separation of the fluorescence emission of fluorophores that have closely overlapping emission spectra and the elimination of background and autofluorescence signals from images (Zhang et al. 2013). Therefore, spectral imaging opens the door to virtually unlimited use of fluorescent labels simultaneously in a specimen. Microscopes equipped for this technology are commercially available and becoming increasingly popular. While spectral imaging offers significant new advantages and possibilities, it also increases the complexity of the instrument and attentions must be paid to technical limitations and potential pitfalls.

## 8.4 Tissue Access and Motion Artifact Control

### 8.4.1 Tissue Access

To *in vivo* image mouse abdominal organs microscopically, different surgical tissue preparations are necessary to meet the experiment goal. For subcellular resolution imaging, exteriorization of the target organ in combination with careful tissue positioning and motion suppression is the most common method (Fig. 8.3a) (Cao et al. 2012; Dunn et al. 2002; Toiyama et al. 2010; Coppieters et al. 2010). This approach

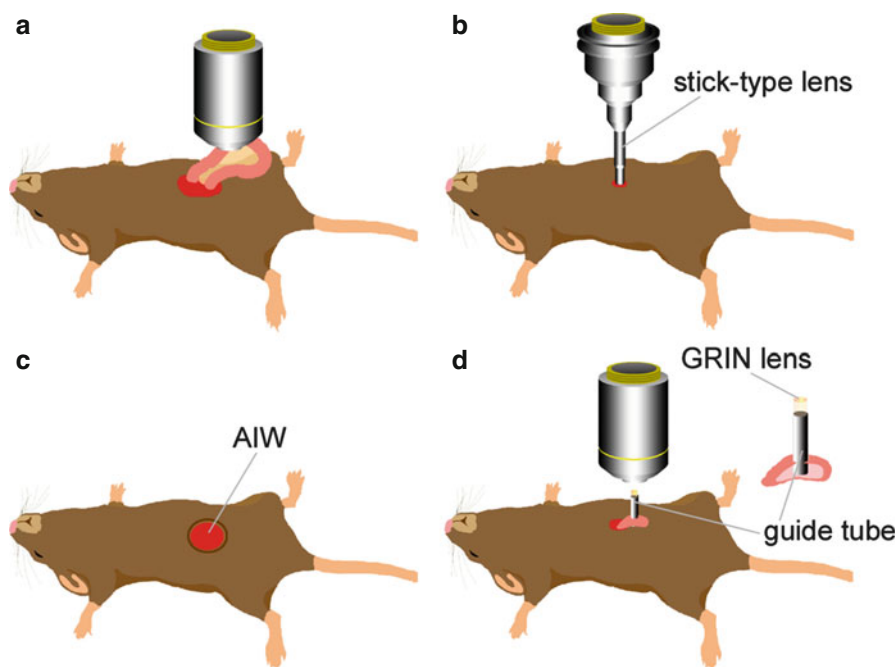


**Fig. 8.3** Abdominal tissue preparation strategy for intravital microscopy. (a) The tissue is exteriorized. (b) The miniaturized objective lens accesses the internal organ through a keyhole incision. (c) The abdominal imaging window (AIW) is implanted on top of the tissue which is glued firmly to the ring of the AIW. (d) The GRIN microlens is inserted into the tissue beneath the tissue surface and held in place by using a guide tube

requires in some cases considerably invasive surgical procedures when imaging using a regular microscope objective, precluding longitudinal image acquisition at subsequent time points (Coppieters et al. 2010; Zhong et al. 2008). Recent technique developments in miniaturized optical devices such as stick-type objectives, GRIN microlenses (both see Sect. 8.2.2) and fiber optic microprobes (Bao et al. 2008; Lin et al. 2008) facilitate to image exteriorized internal organs with less invasive surgical preparation, enabling repetitive imaging in the same animal within a prolonged period of time by replacing the organ in the peritoneal cavity, suturing the abdominal wall and skin separately over the incision and allowing the mouse to recover for a reasonable time before the next imaging session. The miniaturized lenses can also be applied to the surface of the internal organ through a small keyhole incision or natural orifices which further minimizes the invasiveness, and allow image acquisition with cellular resolution (Fig. 8.3b) (Kim et al. 2012; Alencar et al. 2005). For long-term repeatedly routine imaging, the chronic-transparent window is the technique of choice. The first optical window chamber was implanted in the rabbit ear in 1924 to allow imaging of angiogenesis *in vivo* (Sandison 1924). Subsequently, the conception and technique have been adopted to develop several kinds of windows for intravital imaging of mice: (i) the dorsal skin chambers to chronically visualize the subcutaneous tumor formation, metastatic process and



drug response (Alexander et al. 2008), (ii) the cranial window to image dendritic spine turnover, microglia and angioarchitecture as well as to measure cerebral blood flow (Drew et al. 2010; Xu et al. 2007), (iii) the mammary imaging window to orthotopically image breast tumor growth and microenvironments (Kedrin et al. 2008), (iv) the spinal chamber to monitor microglia and afferent axon dynamics in response to spinal cord injury (Farrar et al. 2012), and (v) the abdominal imaging window (AIW) to visualize biological processes in internal organs (Fig. 8.3c). The early AIWs composed of titanium rings and secured to the abdominal wall of a mouse were designed and manufactured to perform chronic observations of pancreas tumor growth and hepatic metabolism, respectively (Tsuzuki et al. 2001; Liu 2007). Recently, the AIW was further developed to enable imaging of many inner organs including the pancreas, liver, spleen, kidney, and small intestine at the cellular or subcellular scale (Ritsma et al. 2013, 2012). The new model of AIW consists of a titanium ring with a groove on the side and a coverslip on the top, which could be tightly secured to the skin and abdominal wall and held in place for an average of 5 weeks. The organ of interest is firmly secured to the window ring using glue to facilitate the acquisition of high-quality images. The AIW provides a powerful means to perform chronic study on many diseases that affect abdominal organs. It is important to note that assessments of possible complications that may relate to the surgical procedure should be undertaken at the end of the experiment.

Conventionally, *in vivo* imaging can access only the superficial 300–400  $\mu\text{m}$  of the internal organ due to the light absorption and scattering. This limitation has recently been surmounted by the use of particular tools such as GRIN lenses and glass microprisms (Chia and Levene 2009). Needle-like GRIN lenses fabricated in sub-millimeter in diameter can be inserted deep into the tissue and serve as a micro-endoscope with negligible damage to the surrounding tissue (Fig. 8.3d). They can be held in place by using a positioning control translator or a guide tube and have allowed intravital deep imaging in the rat kidney and mouse brain at the sites 3 and 1.5 mm below the cortex, respectively (Li and Yu 2008; Barretto et al. 2011). Microprisms with a high-reflective coating on the hypotenuse can also be inserted or chronically implanted into the tissue, turning the scanning pattern of the excitation laser from the horizontal plane to the vertical plane. This mini-periscope technique offers a penetration depth that extends up to the length of the prism ( $>1$  mm) and allows for wide field-of-view imaging ( $>900$   $\mu\text{m}$ ) with subcellular resolution (Chia and Levene 2009; Andermann et al. 2013). These innovations enable imaging within deep tissue areas that have been unreachable by the conventional optical systems, and open entirely new possibilities for studying cellular biology *in vivo*.

### 8.4.2 Motion Artifact Control

Motion artifacts caused by respiration and heartbeat is a crucial obstacle to subcellular intravital imaging of abdominal organs. Various strategies have been developed to address this issue, which include: (i) the employment of specific surgical protocols to expose and properly position the inner organ. For example, *in vivo*

imaging of subcellular structures in live rodent kidney has been firstly achieved by taking advantage of the longer left renal pedicle to facilitate kidney exteriorization and tissue immobilization (Dunn et al. 2002; Molitoris and Sandoval 2005). Subcellular imaging of the liver and pancreas were fulfilled by using more invasive surgical procedures such as tracheotomy and splenectomy (Coppieters et al. 2010; Zhong et al. 2008), (ii) the development of diverse tools to physically minimize tissue motion, such as the custom-made microstage device to provide immobilization platforms for virtually all internal organs (Cao et al. 2012), tissue stabilizers to apply pressure on the organ's surface to increase stabilization (Toiyama et al. 2010), and AIWs to restrain tissue movement by gluing the organ of interest to window ring (Ritsma et al. 2013), (iii) the innovation of techniques to provide adaptive movement compensation using visual feedback control of the objective lens to remove the relative motion between the tissue and the objective (Lee et al. 2008; Laffray et al. 2011), (iv) the utilization of fast-scanning imaging system such as spinning-disk microscopy or high-speed confocal and two-photon microscopes equipped with resonant scanning mirrors, and (v) the application of software to correct some motion artifacts by post-acquisition image processing (Cao et al. 2012). It is worth mentioning that care must be taken to ensure that the motion control approaches lead to no tissue damage and the physiological condition of the organ relevant to the specific study is properly maintained during the imaging session.

## 8.5 Animal Preparation and Anesthesia Considerations

### 8.5.1 Animal Preparation

Several parameters are necessary to be taken into consideration when preparing mice for intravital imaging because animal handling may greatly influence results, especially when comparing between experiments. For example, studies show that strain and gender difference has significant effects on metabolism, immunity, tumorigenesis and pharmacokinetics (Kolaczowska et al. 2001; Hildebrandt et al. 2008). Research has found that physiological and metabolic processes, including cardiovascular function, endocrinology, exocrinology, immune function and gastrointestinal function, are linked to the animal's circadian cycle (Schroder et al. 2013; Fonken et al. 2013; Summa et al. 2013). An organism's response to pharmacological treatments is also modulated by the circadian clock. Numerous observations have demonstrated that drug-induced response varies depending on the timing of the treatment in the day (Levi 2002; Antoch and Kondratov 2013). It is therefore critical to use the mice of same strain and gender, and control the treatment and imaging time to ensure reproducibility between imaging experiments in longitudinal studies. Furthermore, the behavior and food consumption of rodents are responsive to a daily cycle. The timing and length of food removal for fasting treatment should be controlled to warrant consistent caloric intake between groups of animals.

### 8.5.2 *Anesthesia Considerations*

General anesthesia is necessary for intravital imaging of mouse internal organs. According to the nature of the drugs, anesthesia can be administrated via intraperitoneal, intramuscular or intravenous injection or through inhalation. Commonly used injectable anesthetics for mice include ketamine, pentobarbital, thiopental, and tribromoethanol, and inhalation agents isoflurane, halothane and sevoflurane (Gargiulo et al. 2012a). Since strain, gender, age and body weight can have a marked impact on a mouse's response to anesthetic agents (Gargiulo et al. 2012a), all of these factors should be considered when choosing an anesthetic regimen. For example, female mice usually require a higher dose of ketamine than male mice (Gargiulo et al. 2012a). Transgenic and knockout mouse strains can exhibit altered sensitivity to anesthetics such as tribromoethanol and pentobarbital (Xie et al. 2000; Naveilhan et al. 2001). Another important factor to take into account is that anesthetic agents may influence physiological variables, further confounding imaging results (Dabbagh and Rajaei 2013; Abdel el Motal and Sharp 1985).

Here we briefly discuss the usage and physiological effects of ketamine and isoflurane, which are the most commonly used anesthetic drugs in mouse IVM, as examples. Detailed discussions on more anesthetics may be found in other comprehensive review articles (Gargiulo et al. 2012a, b). Ketamine is usually administrated to mice and rats via intraperitoneal injection at a dose ranging from 80 to 200 mg/kg depending on strain, gender and animal's health condition. To alleviate the muscle rigidity induced by ketamine, sedative xylazine is often co-injected at a 10:1 ratio of ketamine to xylazine, producing anesthesia up to 1 h. Re-administration of ketamine/xylazine combination can be performed to further extend the anesthesia. Ketamine may induce light respiratory depression, hypotension, bradycardia, as well as increase norepinephrine plasma levels (Anton et al. 2004; Erhardt et al. 1984). Furthermore, research has revealed that ketamine anesthesia suppresses inflammatory response but markedly increases apoptosis in splenic and hepatic tissues at 3 h after administration (Takahashi et al. 2010; Thompson et al. 2002). Inhalant isoflurane is often the anesthetic agent of choice for a long-term imaging session (>6 h) because it can be adjusted quickly as needed, allowing better control over the length and depth of anesthesia. Isoflurane is usually delivered at a relatively high dose (4 %) for inducing anesthesia, a moderate dose (2.5 %) for performing surgery and a lower dose (<2 %) for imaging. It is critical to use the lowest possible dose of isoflurane for the long survival times (Ewald et al. 2011a). Side effects of isoflurane include respiratory depression, hypotension, immune depression and acidosis (Gargiulo et al. 2012a; Kim et al. 2011; Sjoblom and Nylander 2007). Therefore, the effects of anesthetics on physiological parameters should be taken into considerations when choosing a suitable anesthetic agent for a specific imaging study.

General anesthesia induces hypothermia, which is potentially lethal and can affect the integrity of the imaging results as well because many physiological and cellular processes are very susceptible to changes in temperature. It is therefore

essential to keep mice warm by providing heat through warming pads, circulating water blankets or other means, and to monitor the core body temperature of an anesthetized animal using a rectal temperature probe (Gargiulo et al. 2012a). For a long-term imaging session under inhalation anesthesia, it is recommended to monitor physiologic variables such as breathe and heart rate, blood-oxygenation levels and vascular distension using an oximeter probe to ensure optimal conditions for the mouse during the entire imaging session. Alternatively, anesthesia can be monitored through constant visual inspection (Ewald et al. 2011a, b). In addition the anesthetic gas mixture should be humidified to avoid adverse effect on the lung with the long-term exposure to the dry air, and the animal should be supplemented with warm saline to compensate for the loss of fluid.

## 8.6 Applications of Subcellular IVM in Abdominal Organs

The first *in vivo* imaging of rodent abdominal organs at the subcellular level was achieved in the kidney of live rats using two-photon microscopy (Kang et al. 2006; Dunn et al. 2002; Sandoval et al. 2004). These pioneering studies demonstrated the internalization process of fluorescently labeled dextrans and folic acid in proximal tubular cells and reshaped the understanding of apical uptake of large molecules in the kidney. Subsequent technological developments in surgical procedures and devices minimizing organ motion have allowed subcellular intravital imaging of diverse visceral organs with invasiveness of various degrees (Cao et al. 2012; Coppieters et al. 2010; Zhong et al. 2008; Ritsma et al. 2012). Recently, Cao et al. (Cao et al. 2012) reported a simple custom-made microstage device that effectively reduces abdominal organ motions without affecting tissue integrity and physiology, facilitating to obtain imaging results that truly represent what occurs *in vivo* and opening the way for longitudinally imaging cell biology in the same animal (Fig. 8.4a, b). In this study, the use of the microstage device in combination with the intravital laser scanning imaging system (IV100, Olympus) equipped with novel stick-type objectives has enabled to visualize subcellular structures, determine reporter gene expression levels and image organelle dynamics in real-time in various internal organs (Fig. 8.4a–j). The study presents the first report for the quantitative longitudinal analysis of autophagy in response to nutrient starvation in abdominal organs of live mice. Furthermore, subcellular events such as exocytosis and mitochondrial fusion and fission can be followed (Fig. 8.4i, j).

Table 8.1 lists selected examples showing that IVM has been successfully used to study dynamic events within multiple internal organs with subcellular resolution, which leads to novel findings and enhanced understanding of cellular, physiologic and disease processes. For example, IVM of the spleen of *Cx3cr1<sup>gfp/+</sup>* mice revealed that the spleen is a site for storage and rapid deployment of undifferentiated monocytes which are an essential source for the body to regulate inflammation (Swirski et al. 2009). Imaging protein trafficking in the jejunal enterocytes of transgenic mice expressing fluorescent-tagged occludin and ZO-1 fusion proteins has linked occludin endocytosis to tumor necrosis factor ( $\alpha$ ) (TNF)-induced tight junction regulation (Marchiando et al. 2010). This study has demonstrated for the first time that the

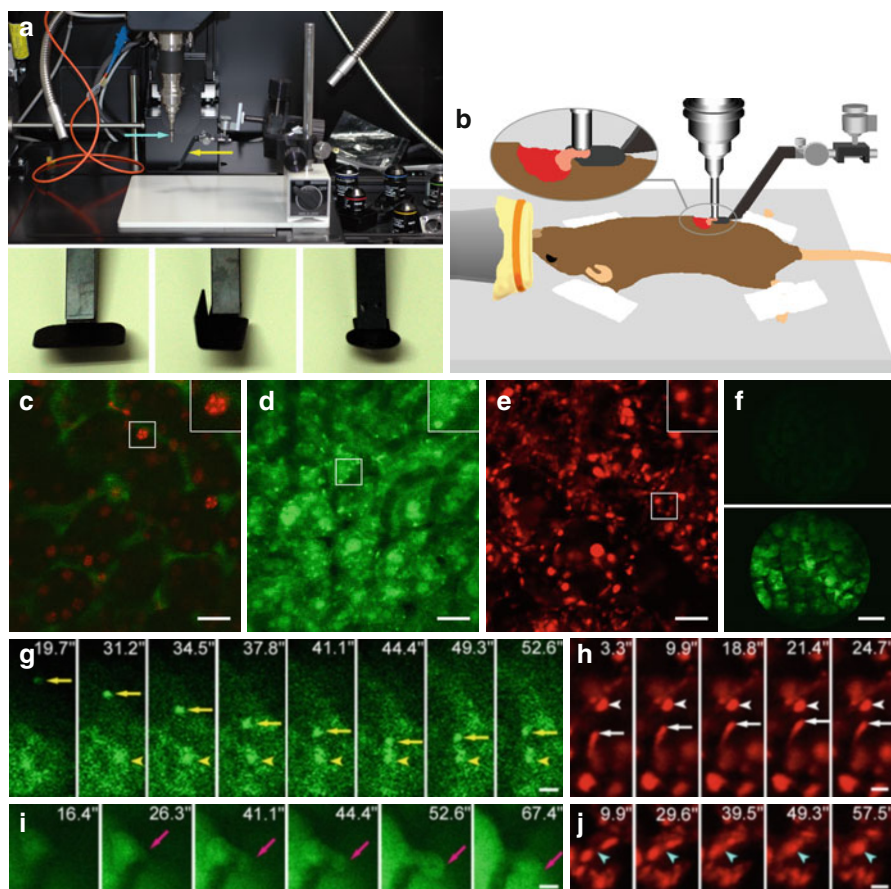


**Fig. 8.4** Intravital imaging of subcellular structures and gene expression in mouse abdominal organs. Images were collected from mRFP-MBD-nls, GFP-LC3, CAG/su9-DsRed2- Acr3-EGFP and F-XBP1ΔDBD-Venus transgenic mouse models in which methylated DNA, autophagic vesicles, mitochondria and endoplasmic reticulum (ER) stress are highlighted by mRFP, GFP, DsRed2 and Venus fluorescence, respectively. (a) Custom-made microstage device (yellow arrow), stick-type objective lens (blue arrow) and microstages of three types for organs of different morphology (lower panels). (b) Illustration showing the *in vivo* imaging of pancreas of an anesthetized mouse using the microstage device and stick-type water immersion lens. (c) Highly methylated chromocenters and vasculatures labeled by mRFP-MBD-nls and AngioSense 750 IVM (*pseudo green color*) in the kidney, respectively. (d) Autophagic vesicles labelled by GFP-LC3 in the liver cells. (e) Mitochondria labelled by DsRed2 in the pancreatic acinar cells. *Insets* in (c-e) are magnified pictures of the boxed area in corresponding images. (f) ER stress indicated by Venus fluorescence in the kidney 24 h later after the F-XBP1ΔDBD-Venus transgenic mice were injected with saline (upper panel) or tunicamycin (lower panel). (g) Time-lapse images of autophagosome movements in the pancreatic acinar cells of GFP-LC3 transgenic mice. One GFP-LC3 dot displaced rapidly (yellow arrow), while the other remained stationary (yellow arrowhead). (h) Time-lapse images of mitochondrial movements in the pancreatic acinar cells of CAG/su9-DsRed2-Acr3-EGFP transgenic mice, showing the change in distance between two mitochondria over time (white arrow and arrowhead). (i) Imaging an exocytosis event (Magenta arrow) in the pancreatic acinar cell of GFP-LC3 transgenic mice. (j) Imaging a mitochondrial fusion event (blue arrowhead) in the pancreatic acinar cell of CAG/su9-DsRed2-Acr3-EGFP transgenic mice. Scale bars, 20 μm (c-d), 10 μm (e), 50 μm (f), 2 μm (g) and 5 μm (h-j)

**Table 8.1** Examples of intravital imaging of various abdominal organs

Organ	Subject	Approach	Reference
Kidney	Endocytosis	Two-photon microscope	Dunn et al. (2002), Sandoval et al. (2004), Sandoval and Molitoris (2008)
	Apoptosis	Two-photon microscope	Kelly et al. (2003)
	Exocytosis	Multiphoton microscope	Toma et al. (2006)
	Functional studies in pathology	Multiphoton microscope	Kang et al. (2006)
	Changes in mitochondrial structure and function during kidney injury	Multiphoton microscope	Hall et al. (2012)
	DNA methylation	Laser scanning microscope	Cao et al. (2012)
Pancreas	DNA methylation, autophagy, exocytosis	Laser scanning microscope	Cao et al. (2012)
	Kinetic events in autoimmune diabetes development	Two-photon microscope	Coppieters et al. (2010, 2012)
Spleen	CD8+ T cells migrating along type I collagen fibers	Two-photon microscope	Ritsma et al. (2013)
	Splenic monocyte displacement	Laser scanning microscope	Swirski et al. (2009)
Liver	Mitochondrial polarization, liver injury	Spinning-disk confocal microscope	Zhong et al. (2008)
	DNA methylation, autophagy	Laser scanning microscope	Cao et al. (2012)
	Hepatic disposition of compound	Two-photon microscope	Liu et al. (2012)
	Oxygen distribution	Fluorescence microscope	Paxian et al. (2004)
	Hepatocyte apoptosis	Confocal microscope, confocal endomicroscope	Goetz et al. (2011)
	Metastasis	Two-photon microscope	Ritsma et al. (2012)
	Malaria parasite displacement	Spinning-disk confocal microscope	Thiberge et al. (2007)
Intestine	Functional dynamics of intestinal mucosa	Two-photon microscope	Klinger et al. (2012)
	Epithelial barrier function	Two-photon microscope	Watson et al. (2005)
	Occludin endocytosis	Multiphoton microscope	Marchiando et al. (2010)

internalization of occludin is caveolin-1–dependent and is critical for *in vivo* immune-mediated tight junction regulation, which has resolved a long-standing debate regarding the contribution of occludin to barrier function. These examples underscore IVM as an important and indispensable tool for the functional and pathological studies of intraperitoneal organs.



## 8.7 Conclusions and Perspectives

IVM has provided useful insights into cellular and tissue functions of abdominal organs. Recent advances in microscope optics, fluorescence probes, and tissue access and immobilization technologies allow researchers to repeatedly access a target internal organ and perform longitudinal imaging with subcellular resolution, which opens up a new avenue for studying cellular and physiological processes, organelle dynamics, disease progression, orthotopic tumor biology and therapeutic responses at the subcellular level in abdominal organs *in vivo*. Future improvements should focus on further developing miniaturized objective lenses and novel fluorophores for deep tissue imaging of organs and tumors with heterogeneous nature, refining surgical procedures and animal handling techniques for ensuring image recording at the animal's normal physiological state, and generating more animal models including knockout mice and transgenic mice expressing various fluorescent reporter molecules for visualization of diverse biological processes. With these improvements, IVM will continue to make unexpected discoveries and become an essential tool to understand biological processes and disease mechanisms in abdominal organs.

**Acknowledgments** This work was supported in part by the grant from the Ministry of Education, Culture, Sports, Science and Technology of Japan (No. 22570009 to Liqin Cao) and the RIKEN Foreign Researcher grant to Liqin Cao, and the grant from New Energy and Industrial Technology Development Organization (NEDO) project "Development of Basic Technology to Control Biological Systems using Chemical Compounds" to Kuniya Abe. We thank Olympus Corporation for microscopy technical support, and Drs. Atsushi Yoshiki and kazuyuki Mekada for maintaining the mouse strains.

## References

- Abdel el Motal SM, Sharp GW (1985) Inhibition of glucose-induced insulin release by xylazine. *Endocrinology* 116:2337–2340
- Abramowitz M, Spring KR, Keller HE, Davidson MW (2002) Basic principles of microscope objectives. *Biotechniques* 33:772–774, 776–778, 780–771
- Alencar H, Mahmood U, Kawano Y, Hirata T, Weissleder R (2005) Novel multiwavelength microscopic scanner for mouse imaging. *Neoplasia* 7:977–983
- Alexander S, Koehl GE, Hirschberg M, Geissler EK, Friedl P (2008) Dynamic imaging of cancer growth and invasion: a modified skin-fold chamber model. *Histochem Cell Biol* 130:1147–1154
- Andermann ML, Gilfoy NB, Goldey GJ, Sachdev RN, Wolfel M et al (2013) Chronic cellular imaging of entire cortical columns in awake mice using microprisms. *Neuron* 80:900–913
- Andresen V, Alexander S, Heupel WM, Hirschberg M, Hoffman RM et al (2009) Infrared multiphoton microscopy: subcellular-resolved deep tissue imaging. *Curr Opin Biotechnol* 20:54–62
- Antoch MP, Kondratov RV (2013) Pharmacological modulators of the circadian clock as potential therapeutic drugs: focus on genotoxic/anticancer therapy. *Handb Exp Pharmacol* 217:289–309

- Anton M, Wagner B, Haubner R, Bodenstein C, Essien BE et al (2004) Use of the norepinephrine transporter as a reporter gene for non-invasive imaging of genetically modified cells. *J Gene Med* 6:119–126
- Balla T (2009) Green light to illuminate signal transduction events. *Trends Cell Biol* 19:575–586
- Bao H, Allen J, Pattie R, Vance R, Gu M (2008) Fast handheld two-photon fluorescence microendoscope with a 475 microm×475 microm field of view for in vivo imaging. *Opt Lett* 33:1333–1335
- Barretto RP, Messerschmidt B, Schnitzer MJ (2009) In vivo fluorescence imaging with high-resolution microlenses. *Nat Methods* 6:511–512
- Barretto RP, Ko TH, Jung JC, Wang TJ, Capps G et al (2011) Time-lapse imaging of disease progression in deep brain areas using fluorescence microendoscopy. *Nat Med* 17:223–228
- Berkovich R, Wolfenson H, Eisenberg S, Ehrlich M, Weiss M et al (2011) Accurate quantification of diffusion and binding kinetics of non-integral membrane proteins by FRAP. *Traffic* 12:1648–1657
- Brown CM (2007) Fluorescence microscopy—avoiding the pitfalls. *J Cell Sci* 120:1703–1705
- Cao L, Kobayakawa S, Yoshiki A, Abe K (2012) High resolution intravital imaging of subcellular structures of mouse abdominal organs using a microstage device. *PLoS One* 7:e33876
- Chance B, Williams GR (1955) Respiratory enzymes in oxidative phosphorylation. III. The steady state. *J Biol Chem* 217:409–427
- Chia TH, Levene MJ (2009) Microprisms for in vivo multilayer cortical imaging. *J Neurophysiol* 102:1310–1314
- Coppieters K, Martinic MM, Kiosses WB, Amirian N, von Herrath M (2010) A novel technique for the in vivo imaging of autoimmune diabetes development in the pancreas by two-photon microscopy. *PLoS One* 5:e15732
- Coppieters K, Amirian N, von Herrath M (2012) Intravital imaging of CTLs killing islet cells in diabetic mice. *J Clin Invest* 122:119–131
- Corridon PR, Rhodes GJ, Leonard EC, Basile DP, Gattone VH 2nd et al (2013) A method to facilitate and monitor expression of exogenous genes in the rat kidney using plasmid and viral vectors. *Am J Physiol Renal Physiol* 304:F1217–F1229
- Dabbagh A, Rajaei S (2013) The role of anesthetic drugs in liver apoptosis. *Hepat Mon* 13:e13162
- Daly TM (2004) AAV-mediated gene transfer to the liver. *Methods Mol Biol* 246:195–199
- Dan S, Okamura M, Mukai Y, Yoshimi H, Inoue Y et al (2012) ZSTK474, a specific phosphatidylinositol 3-kinase inhibitor, induces G1 arrest of the cell cycle in vivo. *Eur J Cancer* 48:936–943
- Dela Cruz JM, McMullen JD, Williams RM, Zipfel WR (2010) Feasibility of using multiphoton excited tissue autofluorescence for in vivo human histopathology. *Biomed Opt Express* 1:1320–1330
- Drew PJ, Shih AY, Driscoll JD, Knutsen PM, Blinder P et al (2010) Chronic optical access through a polished and reinforced thinned skull. *Nat Methods* 7:981–984
- Dunn KW, Sandoval RM, Kelly KJ, Dagher PC, Tanner GA et al (2002) Functional studies of the kidney of living animals using multicolor two-photon microscopy. *Am J Physiol Cell Physiol* 283:C905–C916
- Erhardt W, Hebestedt A, Aschenbrenner G, Pichotka B, Blumel G (1984) A comparative study with various anesthetics in mice (pentobarbitone, ketamine-xylazine, carfentanyl-etomidate). *Res Exp Med (Berl)* 184:159–169
- Ewald AJ, Werb Z, Egeblad M (2011a) Dynamic, long-term in vivo imaging of tumor-stroma interactions in mouse models of breast cancer using spinning-disk confocal microscopy. *Cold Spring Harb Protoc* 2011:pdb.top97
- Ewald AJ, Werb Z, Egeblad M (2011b) Monitoring of vital signs for long-term survival of mice under anesthesia. *Cold Spring Harb Protoc* 2011:pdb.prot5563
- Farrar MJ, Bernstein IM, Schlafer DH, Cleland TA, Fetcho JR et al (2012) Chronic in vivo imaging in the mouse spinal cord using an implanted chamber. *Nat Methods* 9:297–302
- Fonken LK, Lieberman RA, Weil ZM, Nelson RJ (2013) Dim light at night exaggerates weight gain and inflammation associated with a high-fat diet in male mice. *Endocrinology* 154:3817–3825

- Gargiulo S, Greco A, Gramanzini M, Esposito S, Affuso A et al (2012a) Mice anesthesia, analgesia, and care, part I: anesthetic considerations in preclinical research. *ILAR J* 53:E55–E69
- Gargiulo S, Greco A, Gramanzini M, Esposito S, Affuso A et al (2012b) Mice anesthesia, analgesia, and care, part II: anesthetic considerations in preclinical imaging studies. *ILAR J* 53:E70–E81
- Goetz M, Ansems JV, Galle PR, Schuchmann M, Kiesslich R (2011) In vivo real-time imaging of the liver with confocal endomicroscopy permits visualization of the temporospatial patterns of hepatocyte apoptosis. *Am J Physiol Gastrointest Liver Physiol* 301:G764–G772
- Graf R, Rietdorf J, Zimmermann T (2005) Live cell spinning disk microscopy. *Adv Biochem Eng Biotechnol* 95:57–75
- Grutzendler J, Kasthuri N, Gan WB (2002) Long-term dendritic spine stability in the adult cortex. *Nature* 420:812–816
- Hall AM, Rhodes GJ, Sandoval RM, Corridon PR, Molitoris BA (2012) In vivo multiphoton imaging of mitochondrial structure and function during acute kidney injury. *Kidney Int* 83:72–83
- Haraguchi T, Shimi T, Koujin T, Hashiguchi N, Hiraoka Y (2002) Spectral imaging fluorescence microscopy. *Genes Cells* 7:881–887
- Helmchen F, Denk W (2005) Deep tissue two-photon microscopy. *Nat Methods* 2:932–940
- Hickey MJ, Westhorpe CL (2013) Imaging inflammatory leukocyte recruitment in kidney, lung and liver—challenges to the multi-step paradigm. *Immunol Cell Biol* 91:281–289
- Hildebrandt IJ, Su H, Weber WA (2008) Anesthesia and other considerations for in vivo imaging of small animals. *ILAR J* 49:17–26
- Hiraoka Y, Shimi T, Haraguchi T (2002) Multispectral imaging fluorescence microscopy for living cells. *Cell Struct Funct* 27:367–374
- Huang S, Heikal AA, Webb WW (2002) Two-photon fluorescence spectroscopy and microscopy of NAD(P)H and flavoprotein. *Biophys J* 82:2811–2825
- Jenne CN, Wong CH, Petri B, Kubes P (2011) The use of spinning-disk confocal microscopy for the intravital analysis of platelet dynamics in response to systemic and local inflammation. *PLoS One* 6:e25109
- Kang JJ, Toma I, Sipos A, McCulloch F, Peti-Peterdi J (2006) Quantitative imaging of basic functions in renal (patho)physiology. *Am J Physiol Renal Physiol* 291:F495–F502
- Kasischke KA, Vishwasrao HD, Fisher PJ, Zipfel WR, Webb WW (2004) Neural activity triggers neuronal oxidative metabolism followed by astrocytic glycolysis. *Science* 305:99–103
- Kedrin D, Gligorijevic B, Wyckoff J, Verkhusha VV, Condeelis J et al (2008) Intravital imaging of metastatic behavior through a mammary imaging window. *Nat Methods* 5:1019–1021
- Kelly KJ, Sandoval RM, Dunn KW, Molitoris BA, Dagher PC (2003) A novel method to determine specificity and sensitivity of the TUNEL reaction in the quantitation of apoptosis. *Am J Physiol Cell Physiol* 284:C1309–C1318
- Kim M, Park SW, Kim M, D’Agati VD, Lee HT (2011) Isoflurane activates intestinal sphingosine kinase to protect against renal ischemia-reperfusion-induced liver and intestine injury. *Anesthesiology* 114:363–373
- Kim JK, Lee WM, Kim P, Choi M, Jung K et al (2012) Fabrication and operation of GRIN probes for in vivo fluorescence cellular imaging of internal organs in small animals. *Nat Protoc* 7:1456–1469
- Klinger A, Orzekowsky-Schroeder R, von Smolinski D, Bleszenohl M, Schueth A et al (2012) Complex morphology and functional dynamics of vital murine intestinal mucosa revealed by autofluorescence 2-photon microscopy. *Histochem Cell Biol* 137:269–278
- Kolaczowska E, Chadzinska M, Seljelid R, Plytycz B (2001) Strain differences in some immune parameters can be obscured by circadian variations and laboratory routines: studies of male C57BL/6J, Balb/c and CB6 F1 mice. *Lab Anim* 35:91–100
- Laffray S, Pages S, Dufour H, De Koninck P, De Koninck Y et al (2011) Adaptive movement compensation for in vivo imaging of fast cellular dynamics within a moving tissue. *PLoS One* 6:e19928
- Last’ovicka J, Budinsky V, Spisek R, Bartunkova J (2009) Assessment of lymphocyte proliferation: CFSE kills dividing cells and modulates expression of activation markers. *Cell Immunol* 256:79–85

- Lee HS, Liu Y, Chen HC, Chiou LL, Huang GT et al (2004) Optical biopsy of liver fibrosis by use of multiphoton microscopy. *Opt Lett* 29:2614–2616
- Lee LM, Seftor EA, Bonde G, Cornell RA, Hendrix MJ (2005) The fate of human malignant melanoma cells transplanted into zebrafish embryos: assessment of migration and cell division in the absence of tumor formation. *Dev Dyn* 233:1560–1570
- Lee S, Nakamura Y, Yamane K, Toujo T, Takahashi S et al (2008) Image stabilization for in vivo microscopy by high-speed visual feedback control. *IEEE Trans Robot* 24:45–54
- Levi F (2002) From circadian rhythms to cancer chronotherapeutics. *Chronobiol Int* 19:1–19
- Li X, Yu W (2008) Deep tissue microscopic imaging of the kidney with a gradient-index lens system. *Opt Commun* 281:1833–1840
- Li W, Nava RG, Bribiesco AC, Zinselmeyer BH, Spahn JH et al (2012) Intravital 2-photon imaging of leukocyte trafficking in beating heart. *J Clin Invest* 122:2499–2508
- Lin KY, Maricevich M, Bardeesy N, Weissleder R, Mahmood U (2008) In vivo quantitative microvasculature phenotype imaging of healthy and malignant tissues using a fiber-optic confocal laser microprobe. *Transl Oncol* 1:84–94
- Liu Y (2007) Visualization of hepatobiliary excretory function by intravital multiphoton microscopy. *J Biomed Opt* 12:014014
- Liu X, Thorling CA, Jin L, Roberts MS (2012) Intravital multiphoton imaging of rhodamine 123 in the rat liver after intravenous dosing. *IntraVital* 1:54–59
- Livet J, Weissman TA, Kang H, Draft RW, Lu J et al (2007) Transgenic strategies for combinatorial expression of fluorescent proteins in the nervous system. *Nature* 450:56–62
- Marchiando AM, Shen L, Graham WV, Weber CR, Schwarz BT et al (2010) Caveolin-1-dependent occludin endocytosis is required for TNF-induced tight junction regulation in vivo. *J Cell Biol* 189:111–126
- Masedunskas A, Weigert R (2008) Intravital two-photon microscopy for studying the uptake and trafficking of fluorescently conjugated molecules in live rodents. *Traffic* 9:1801–1810
- Masedunskas A, Sramkova M, Parente L, Sales KU, Amornphimoltham P et al (2011) Role for the actomyosin complex in regulated exocytosis revealed by intravital microscopy. *Proc Natl Acad Sci U S A* 108:13552–13557
- Masedunskas A, Porat-Shliom N, Weigert R (2012a) Regulated exocytosis: novel insights from intravital microscopy. *Traffic* 13:627–634
- Masedunskas A, Milberg O, Porat-Shliom N, Sramkova M, Wigand T et al (2012b) Intravital microscopy: a practical guide on imaging intracellular structures in live animals. *Bioarchitecture* 5:143–157
- Mennone A, Nathanson MH (2011) Needle-based confocal laser endomicroscopy to assess liver histology in vivo. *Gastrointest Endosc* 73:338–344
- Molitoris BA, Sandoval RM (2005) Intravital multiphoton microscopy of dynamic renal processes. *Am J Physiol Renal Physiol* 288:F1084–F1089
- Naveilhan P, Canals JM, Valjakka A, Vartiainen J, Arenas E et al (2001) Neuropeptide Y alters sedation through a hypothalamic Y1-mediated mechanism. *Eur J Neurosci* 13:2241–2246
- Nimmerjahn A, Kirchhoff F, Helmchen F (2005) Resting microglial cells are highly dynamic surveillants of brain parenchyma in vivo. *Science* 308:1314–1318
- Nishimura S, Manabe I, Nagasaki M, Seo K, Yamashita H et al (2008) In vivo imaging in mice reveals local cell dynamics and inflammation in obese adipose tissue. *J Clin Invest* 118:710–721
- Nyman LR, Wells KS, Head WS, McCaughey M, Ford E et al (2008) Real-time, multidimensional in vivo imaging used to investigate blood flow in mouse pancreatic islets. *J Clin Invest* 118:3790–3797
- Orth JD, Kohler RH, Foijer F, Sorger PK, Weissleder R et al (2011) Analysis of mitosis and anti-mitotic drug responses in tumors by in vivo microscopy and single-cell pharmacodynamics. *Cancer Res* 71:4608–4616
- Ostrander JH, McMahon CM, Lem S, Millon SR, Brown JQ et al (2010) Optical redox ratio differentiates breast cancer cell lines based on estrogen receptor status. *Cancer Res* 70:4759–4766

- Parish CR (1999) Fluorescent dyes for lymphocyte migration and proliferation studies. *Immunol Cell Biol* 77:499–508
- Patterson GH, Knobel SM, Arkhammar P, Thastrup O, Piston DW (2000) Separation of the glucose-stimulated cytoplasmic and mitochondrial NAD(P)H responses in pancreatic islet beta cells. *Proc Natl Acad Sci U S A* 97:5203–5207
- Paxian M, Keller SA, Cross B, Huynh TT, Clemens MG (2004) High-resolution visualization of oxygen distribution in the liver in vivo. *Am J Physiol Gastrointest Liver Physiol* 286:G37–G44
- Pena AM, Fabre A, Debarre D, Marchal-Somme J, Crestani B et al (2007) Three-dimensional investigation and scoring of extracellular matrix remodeling during lung fibrosis using multiphoton microscopy. *Microsc Res Tech* 70:162–170
- Perentes JY, McKee TD, Ley CD, Mathiew H, Dawson M et al (2009) In vivo imaging of extracellular matrix remodeling by tumor-associated fibroblasts. *Nat Methods* 6:143–145
- Phan TG, Bullen A (2010) Practical intravital two-photon microscopy for immunological research: faster, brighter, deeper. *Immunol Cell Biol* 88:438–444
- Piston DW (1998) Choosing objective lenses: the importance of numerical aperture and magnification in digital optical microscopy. *Biol Bull* 195:1–4
- Piston DW, Knobel SM, Postic C, Shelton KD, Magnuson MA (1999) Adenovirus-mediated knockout of a conditional glucokinase gene in isolated pancreatic islets reveals an essential role for proximal metabolic coupling events in glucose-stimulated insulin secretion. *J Biol Chem* 274:1000–1004
- Pittet MJ, Weissleder R (2011) Intravital imaging. *Cell* 147:983–991
- Progatzy F, Dallman MJ, Lo Celso C (2013) From seeing to believing: labelling strategies for in vivo cell-tracking experiments. *Interface Focus* 3:20130001
- Radosevich AJ, Bouchard MB, Burgess SA, Chen BR, Hillman EM (2008) Hyperspectral in vivo two-photon microscopy of intrinsic contrast. *Opt Lett* 33:2164–2166
- Ritsma L, Steller EJ, Beerling E, Loomans CJ, Zomer A et al (2012) Intravital microscopy through an abdominal imaging window reveals a pre-micrometastasis stage during liver metastasis. *Sci Transl Med* 4:158ra145
- Ritsma L, Steller EJ, Ellenbroek SI, Kranenburg O, Borel Rinkes IH et al (2013) Surgical implantation of an abdominal imaging window for intravital microscopy. *Nat Protoc* 8:583–594
- Sandison JC (1924) A new method for the microscopic study of living growing tissues by the introduction of a transparent chamber in the rabbit's ear. *Anat Rec* 28:281–287
- Sandoval RM, Molitoris BA (2008) Quantifying endocytosis in vivo using intravital two-photon microscopy. *Methods Mol Biol* 440:389–402
- Sandoval RM, Kennedy MD, Low PS, Molitoris BA (2004) Uptake and trafficking of fluorescent conjugates of folic acid in intact kidney determined using intravital two-photon microscopy. *Am J Physiol Cell Physiol* 287:C517–C526
- Schroder EA, Lefta M, Zhang X, Bartos DC, Feng HZ et al (2013) The cardiomyocyte molecular clock, regulation of Scn5a, and arrhythmia susceptibility. *Am J Physiol Cell Physiol* 304:C954–C965
- Serrels A, Timpson P, Canel M, Schwarz JP, Carragher NO et al (2009) Real-time study of E-cadherin and membrane dynamics in living animals: implications for disease modeling and drug development. *Cancer Res* 69:2714–2719
- Shimizu K, Kawakami S, Hayashi K, Kinoshita H, Kuwahara K et al (2012) In vivo site-specific transfection of naked plasmid DNA and siRNAs in mice by using a tissue suction device. *PLoS One* 7:e41319
- Shimozawa T, Yamagata K, Kondo T, Hayashi S, Shitamukai A et al (2013) Improving spinning disk confocal microscopy by preventing pinhole cross-talk for intravital imaging. *Proc Natl Acad Sci U S A* 110:3399–3404
- Sjoblom M, Nylander O (2007) Isoflurane-induced acidosis depresses basal and PGE(2)-stimulated duodenal bicarbonate secretion in mice. *Am J Physiol Gastrointest Liver Physiol* 292:G899–G904
- Squirrell JM, Wokosin DL, White JG, Bavister BD (1999) Long-term two-photon fluorescence imaging of mammalian embryos without compromising viability. *Nat Biotechnol* 17:763–767

- Sramkova M, Masedunskas A, Parente L, Molinolo A, Weigert R (2009) Expression of plasmid DNA in the salivary gland epithelium: novel approaches to study dynamic cellular processes in live animals. *Am J Physiol Cell Physiol* 297:C1347–C1357
- Stirling DP, Liu S, Kubes P, Yong VW (2009) Depletion of Ly6G/Gr-1 leukocytes after spinal cord injury in mice alters wound healing and worsens neurological outcome. *J Neurosci* 29:753–764
- Summa KC, Voigt RM, Forsyth CB, Shaikh M, Cavanaugh K et al (2013) Disruption of the circadian clock in mice increases intestinal permeability and promotes alcohol-induced hepatic pathology and inflammation. *PLoS One* 8:e67102
- Swirski FK, Nahrendorf M, Etzrodt M, Wildgruber M, Cortez-Retamozo V et al (2009) Identification of splenic reservoir monocytes and their deployment to inflammatory sites. *Science* 325:612–616
- Takahashi T, Kinoshita M, Shono S, Habu Y, Ogura T et al (2010) The effect of ketamine anesthesia on the immune function of mice with postoperative septicemia. *Anesth Analg* 111:1051–1058
- Tanaka K, Morimoto Y, Toiyama Y, Matsushita K, Kawamura M et al (2012) In vivo time-course imaging of tumor angiogenesis in colorectal liver metastases in the same living mice using two-photon laser scanning microscopy. *J Oncol* 2012:265487
- Theer P, Hasan MT, Denk W (2003) Two-photon imaging to a depth of 1000 microm in living brains by use of a Ti:Al2O3 regenerative amplifier. *Opt Lett* 28:1022–1024
- Thiberge S, Blazquez S, Baldacci P, Renaud O, Shorte S et al (2007) In vivo imaging of malaria parasites in the murine liver. *Nat Protoc* 2:1811–1818
- Thompson JS, Brown SA, Khurdayan V, Zeinalzadedan A, Sullivan PG et al (2002) Early effects of tribromoethanol, ketamine/xylazine, pentobarbital, and isoflurane anesthesia on hepatic and lymphoid tissue in ICR mice. *Comp Med* 52:63–67
- Timpson P, McGhee EJ, Morton JP, von Kriegsheim A, Schwarz JP et al (2011) Spatial regulation of RhoA activity during pancreatic cancer cell invasion driven by mutant p53. *Cancer Res* 71:747–757
- Toiyama Y, Mizoguchi A, Okugawa Y, Koike Y, Morimoto Y et al (2010) Intravital imaging of DSS-induced cecal mucosal damage in GFP-transgenic mice using two-photon microscopy. *J Gastroenterol* 45:544–553
- Toma I, Kang JJ, Peti-Peterdi J (2006) Imaging renin content and release in the living kidney. *Nephron Physiol* 103:71–74
- Tsuzuki Y, Mouta Carreira C, Bockhorn M, Xu L, Jain RK et al (2001) Pancreas microenvironment promotes VEGF expression and tumor growth: novel window models for pancreatic tumor angiogenesis and microcirculation. *Lab Invest* 81:1439–1451
- von Andrian UH, Mempel TR (2003) Homing and cellular traffic in lymph nodes. *Nat Rev Immunol* 3:867–878
- Wang E, Babbey CM, Dunn KW (2005) Performance comparison between the high-speed Yokogawa spinning disc confocal system and single-point scanning confocal systems. *J Microsc* 218:148–159
- Wang BG, König K, Halbhüner KJ (2010) Two-photon microscopy of deep intravital tissues and its merits in clinical research. *J Microsc* 238:1–20
- Watson AJ, Chu S, Sieck L, Gerasimenko O, Bullen T et al (2005) Epithelial barrier function in vivo is sustained despite gaps in epithelial layers. *Gastroenterology* 129:902–912
- Webb DJ, Brown CM (2013) Epi-fluorescence microscopy. *Methods Mol Biol* 931:29–59
- Weigert R, Sramkova M, Parente L, Amornphimoltham P, Masedunskas A (2010) Intravital microscopy: a novel tool to study cell biology in living animals. *Histochem Cell Biol* 133:481–491
- Weigert R, Porat-Shliom N, Amornphimoltham P (2013) Imaging cell biology in live animals: ready for prime time. *J Cell Biol* 201:969–979
- Williamson JR, Herczeg BE, Coles HS, Cheung WY (1967) Glycolytic control mechanisms. V. Kinetics of high energy phosphate intermediate changes during electrical discharge and recovery in the main organ of *Electrophorus electricus*. *J Biol Chem* 242:5119–5124



- Wu L, Tiwari MM, Messer KJ, Holthoff JH, Gokden N et al (2007) Peritubular capillary dysfunction and renal tubular epithelial cell stress following lipopolysaccharide administration in mice. *Am J Physiol Renal Physiol* 292:F261–F268
- Xie W, Barwick JL, Downes M, Blumberg B, Simon CM et al (2000) Humanized xenobiotic response in mice expressing nuclear receptor SXR. *Nature* 406:435–439
- Xu HT, Pan F, Yang G, Gan WB (2007) Choice of cranial window type for in vivo imaging affects dendritic spine turnover in the cortex. *Nat Neurosci* 10:549–551
- Yamauchi K, Yang M, Jiang P, Xu M, Yamamoto N et al (2006) Development of real-time subcellular dynamic multicolor imaging of cancer-cell trafficking in live mice with a variable-magnification whole-mouse imaging system. *Cancer Res* 66:4208–4214
- Zhang Y, Hu B, Dai Y, Yang H, Huang W et al (2013) A new multichannel spectral imaging laser scanning confocal microscope. *Comput Math Methods Med* 2013:890203
- Zhong Z, Ramshesh VK, Rehman H, Currin RT, Sridharan V et al (2008) Activation of the oxygen-sensing signal cascade prevents mitochondrial injury after mouse liver ischemia-reperfusion. *Am J Physiol Gastrointest Liver Physiol* 295:G823–G832
- Zipfel WR, Williams RM, Webb WW (2003) Nonlinear magic: multiphoton microscopy in the biosciences. *Nat Biotechnol* 21:1369–1377

## Chapter 9

# Intravital Imaging of the Lactating Mammary Gland in Transgenic Mice Expressing Fluorescent Proteins

Andrius Masedunskas, Roberto Weigert, and Ian H. Mather

**Abstract** Mammals are critically dependent upon maternal milk in the first few weeks to months of life. All essential nutrients for neonatal survival are either synthesized within mammary secretory cells or transported across the epithelium from interstitial spaces and the systemic circulation (Larson and Smith 1974/1978). Major milk components include proteins, carbohydrates, ions and water (the “skim milk” phase) synthesized, processed, sorted and secreted by compartments in the classical secretory pathway (Burgoyne and Duncan 1998; Shennan and Peaker 2000; Truchet et al. 2014), and membrane-coated neutral lipid droplets (the “cream or milk fat” phase) secreted by a form of reverse pinocytosis at the apical surface (Mather and Keenan 1998; McManaman et al. 2007) (Fig. 9.1). In addition, prolactin, serum albumin, immunoglobulins and other proteins are transported by transcytosis into colostrum and milk through the endosomal system (Hunziker and Kraehenbuhl 1998; Ollivier-Bousquet 1998; Monks and Neville 2004; Wheeler et al. 2007). Thus, milk-secreting cells provide a unique model for investigating the synthesis, assembly and secretion of a diverse complement of constituents.

**Keywords** Milk secretion • Lactation • Mammary gland • Intravital imaging • Green fluorescent protein • Transgenic mouse strains • Milk lipids and proteins • Secretion kinetics

---

Roberto Weigert and Ian H. Mather are co-principal investigators.

A. Masedunskas • R. Weigert

Intracellular Membrane Trafficking Unit, National Institute of Dental and Craniofacial Research, National Institutes of Health, Bethesda, MD 20892, USA

e-mail: [weigert@mail.nih.gov](mailto:weigert@mail.nih.gov)

I.H. Mather (✉)

Intracellular Membrane Trafficking Unit, National Institute of Dental and Craniofacial Research, National Institutes of Health, Bethesda, MD 20892, USA

Department of Animal and Avian Sciences, University of Maryland, College Park, MD 20742, USA

e-mail: [imather@umd.edu](mailto:imather@umd.edu)

© Springer Science+Business Media Dordrecht 2014

187

R. Weigert (ed.), *Advances in Intravital Microscopy*:

*From Basic to Clinical Research*, DOI 10.1007/978-94-017-9361-2\_9

## 9.1 Introduction

### 9.1.1 Milk Secretion and the Mammary Gland

Mammals are critically dependent upon maternal milk in the first few weeks to months of life. All essential nutrients for neonatal survival are either synthesized within mammary secretory cells or transported across the epithelium from interstitial spaces and the systemic circulation (Larson and Smith 1974/1978). Major milk components include proteins, carbohydrates, ions and water (the “skim milk” phase) synthesized, processed, sorted and secreted by compartments in the classical secretory pathway (Burgoyne and Duncan 1998; Shennan and Peaker 2000; Truchet et al. 2014), and membrane-coated neutral lipid droplets (the “cream or milk fat” phase) secreted by a form of reverse pinocytosis at the apical surface (Mather and Keenan 1998; McManaman et al. 2007) (Fig. 9.1). In addition, prolactin, serum

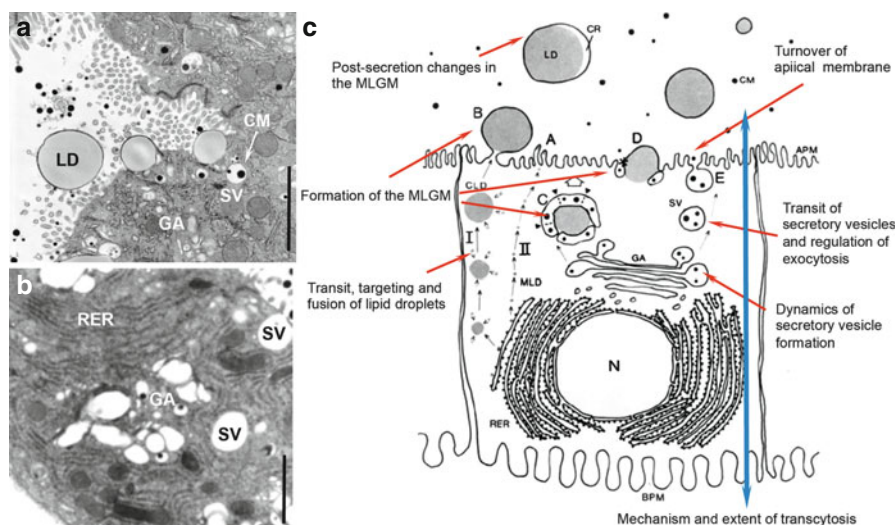


**Fig. 9.1** Secretion of milk from mammary epithelial cells (**a**, **b**) Electron micrographs of, (**a**) mouse, and (**b**) guinea pig secretory cells from lactating mammary gland. Note the lipid droplets budding from the apical plasma membrane and secretory vesicles containing mature casein micelles in (**a**), and the extensive rough endoplasmic reticulum and Golgi apparatus with swollen secretory vesicles containing lactose, water and other milk constituents in (**b**). Bars 2.5  $\mu$ m; (**c**) Pathways for the secretion of lipid droplets and skim milk components. Lipid droplets formed in the rough endoplasmic reticulum transit to the apical plasma membrane and either grow larger by fusing with other droplets to form cytoplasmic lipid droplets (Pathway I), or remain the same size as microvesicles (Pathway II). During secretion, droplets acquire an outer membrane layer either from the apical plasma membrane (mechanisms A, B), secretory vesicles (mechanism C), or endosomes (mechanism D). Skim milk components, including casein micelles are processed through the Golgi apparatus, packaged into secretory vesicles and secreted by exocytosis at the apical surface (mechanism E). Some major questions amenable to analysis by intravital imaging are highlighted. APM apical plasma membrane, BPM basal plasma membrane, CLD, cytoplasmic lipid droplet, CM casein micelle, CR cytoplasmic crescent of trapped cytoplasm, GA Golgi apparatus, LD milk lipid droplet, MLD microvesicle, N nucleus, RER rough endoplasmic reticulum, SV secretory vesicle. The micrograph in (**a**) is taken from Ogg et al. (2004), and the illustration in (**c**) from Mather and Keenan (1998), with permission

albumin, immunoglobulins and other proteins are transported by transcytosis into colostrum and milk through the endosomal system (Hunziker and Kraehenbuhl 1998; Ollivier-Bousquet 1998; Monks and Neville 2004; Wheeler et al. 2007). Thus, milk-secreting cells provide a unique model for investigating the synthesis, assembly and secretion of a diverse complement of constituents.

For experimental purposes, the mammary gland provides several advantages over other secretory systems. Because the gland is associated with the skin it is uniquely accessible to experimental manipulation. Unlike other epithelia, the secretion can be collected in lightly anesthetized or conscious animals by simple milking procedures and the streak canal of the nipple can be used as a conduit for the infusion of experimental agents. The entire gland is readily transduced by adenoviral vectors (Russell et al. 2003), such that recombinant tagged fusion proteins can be facily expressed in the secretory epithelium, and fluid-phase and membrane markers can be introduced into the luminal spaces to monitor the uptake and recycling of soluble and membrane-bound constituents. Uniquely among all epithelia, membranes are continuously consumed by the formation and budding of lipid droplets from the apical surface (Mather and Keenan 1998; McManaman et al. 2007), and membrane-bounded “exosomes”, nanoparticles and apical fragments are secreted in significant quantities (Wooding et al. 1977; Admyre et al. 2007; Argov-Argaman et al. 2010).

Paradoxically, despite these advantages and the importance of understanding how milk is made at the molecular and cellular levels, the field has been stuck in a time-war for well over 30 years. Our knowledge of how the major constituents of milk are synthesized and secreted is based on classical biochemical studies and microscopic examination of dead specimens. We have very little information for any species on the *dynamics and kinetics* of milk secretion, or the co-ordination of cellular activities within the secretory epithelium, or between neighboring alveoli. The generally accepted paradigm has survived largely because it has been untested by modern high-resolution light microscopy and intravital imaging techniques (Weigert et al. 2013).

In order to break this barrier, we have developed novel methods for imaging mammary epithelial cells in situ by confocal microscopy using lactating mice as the experimental model. High-resolution intravital images of untreated tissue can be acquired through the use of transgenic mice which express endogenous constituents labeled with green fluorescent protein (GFP) analogs.

### ***9.1.2 Previous Methods for Imaging the Mammary Gland***

Early attempts to image the mammary gland (Shan et al. 2003) relied on the use of clear acrylic windows implanted into the skin over the gland and were based upon technologies dating from the 1930s (Clark and Clark. 1932). Surgically prepared rodents (rats or mice) were implanted with mammary tumor fragments, or GFP-expressing cells and tumor development, angiogenesis and metastasis optically monitored through the window for several weeks. Tissue morphology was followed at low resolution and the vasculature highlighted by injection of rhodamine-dextran. In more recent applications, the use of glass windows enabled imaging with greater optical clarity, and the application of photoswitchable GFP analogs such as Dendra2 expressed in tumor cells allowed the identification of

subpopulations of marked cells following photoconversion of the marker (Kedrin et al. 2008).

In an alternative approach, mouse mammary glands were surgically prepared for single-session short-term imaging at higher resolution to monitor the trafficking patterns and kinetics of tumor cells, and to document tumor cell interactions with macrophages and underlying stromal components (Ahmed et al. 2002; Sidani et al. 2006; Wyckoff et al. 2007; Ewald et al. 2011a; Dovas et al. 2012). Mice have been successfully monitored for up to 40 h under isoflurane anesthesia with minimal inflammatory complications (Ewald et al. 2011b; Ewald et al. 2011c). However, none of these previous techniques were employed to analyze lactating glands at a sufficient resolution to enable the continuous tracking and analysis of intracellular organelles, transport vesicles and lipid droplets.

## 9.2 Procedures

### 9.2.1 Technical Considerations

One of the most important prerequisites for investigating the molecular dynamics of milk secretion *in vivo* is the ability to achieve sub-cellular resolution imaging. This can be realized by following several important principles: (1) employing the most sensitive confocal imaging systems available; (2) imaging at a shallow depth to avoid the light scattering effects of optically nonhomogeneous samples; (3) imaging with high numerical aperture (NA) objectives; and (4) developing a robust mammary gland immobilization technique. Although multiphoton microscopy is superior for deep tissue imaging, laser scanning confocal microscopes are preferred to achieve the highest spatial resolution when imaging at a shallow depth (0–20  $\mu\text{m}$ ). Such shallow depth is sufficient to reach the top cells, their apical surfaces and the lumina of the alveoli. Good signal to noise ratio at high resolution is critical, without which the sub-cellular events and the molecular machinery cannot be observed. Therefore it is very important to use the most sensitive microscopy systems available. New microscopes are designed with the most efficient optical paths and can be equipped with ultra-sensitive gallium arsenide phosphide (GaAsP), or hybrid detectors. The most important component of the optical path is the objective and great care should be taken in selecting the best one. In our hands, 60 $\times$  high NA oil immersion objectives outperform water immersion objectives at shallow depth. In a promising development, some manufacturers have introduced silicon immersion objectives that match the refractive index of tissues more closely. Researchers should examine and choose objectives carefully by collecting point spread function and brightness data from the tissues to be imaged. Finally, the main challenge to successfully perform intravital microscopy is to minimize the motion artifacts that are generated by heartbeat, respiration and peristaltic movements. This is especially true for applications that require imaging at high resolution, such as analyzing the dynamics of subcellular structures that are affected by small shifts of a few microns in any direction. We describe our approach in stabilizing the mammary gland below.

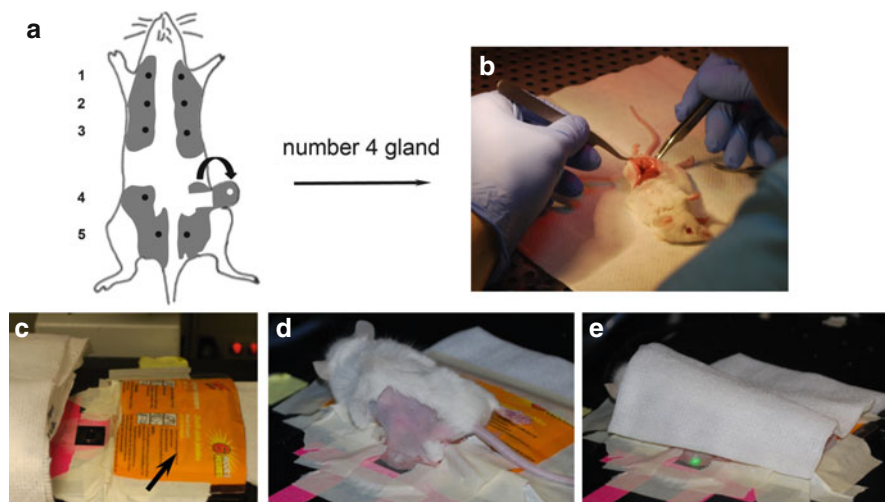


**Fig. 9.2** Preparation of mice for intravital imaging (a) Classification of mouse mammary glands (1, 2, 3, 4, 5) according to anatomical position. The number 4 gland used for intravital imaging is shown with a prepared skin flap (*curved arrow*); (b–e) Stages in preparation of the mammary skin flap and alignment of the mouse on the microscope stage; (b) Surgery; (c) Setting up of heating pad (*arrow*); (d) Positioning of mouse and skin flap; (e) Imaging

Additionally, we have discussed the practical details of establishing intravital systems and experimental models previously (Masedunskas et al. 2012b).

## 9.2.2 Animal Procedures

### 9.2.2.1 Surgery

Mice have five pairs of mammary glands, three thoracic and two inguinal, denoted by Arabic numerals, one through five, in the anterior to posterior direction (Fig. 9.2a). For practical purposes, the thoracic glands (numbers one through three) are inappropriate for high resolution imaging, because of proximity to the chest cavity and the difficulty of isolating the glands from respiratory motions and heartbeat. Of the two inguinal pairs, the number four glands are the most accessible, and we have routinely used the right-hand gland (defined in the supine position) as shown in Fig. 9.2a.

Mice are initially anesthetized by exposure to isoflurane (3.0–3.5 %) for 5 min, followed by an intraperitoneal injection of xylazine and ketamine (approx. 20 and 100 mg/kg body weight, respectively). Animals are then maintained under a deep plane of anesthesia throughout the surgical and imaging procedures using additional doses of xylazine and ketamine administered by either subcutaneous, or intraperitoneal injection, as appropriate. The adequacy of the anesthesia may be monitored throughout the procedure by watching for voluntary movements and every 10–20 min by checking for palpebral and toe pinch reflexes.



For surgery, the mice are kept warm with an overhead heating lamp and the skin surrounding the right-hand number four and five glands on the right side shaved using a hand-held electric razor. A mid-line incision is made starting close to the nipple of the number four gland and completed by proceeding dorsally in a perpendicular direction to a point about mid-way between the spinal and ventral midlines. This first incision is on the cranial side of the nipple (between the number three and four glands). A second incision is made from the point of the initial incision in a perpendicular direction between the number four and five glands to a point about mid-way between the spinal and ventral midlines and the skin with the attached gland carefully peeled away from the abdomen. This creates a skin flap, in which part of the number four mammary gland and associated vascular supply are separated from the abdominal wall (Fig. 9.2a, b). During this procedure, as much connective and adipose tissue as possible is removed with fine forceps to expose the underlying secretory parenchyma and the abdominal wall is protected with carbomer 940 gel and Parafilm. Any cut blood vessels are cauterized using a hand-held battery-powered cauterizer and blood is removed by washing with physiological saline. Throughout surgery, the exposed gland may be treated with specific pharmacological agents, or labeled with fluorescent dyes, depending upon experimental requirements. In the intravital images shown in this chapter, neutral lipid droplets were labeled by repeatedly washing the gland with 10  $\mu$ M BODIPY 665 in physiological saline (a total of 1 ml, applied over approx. 1 h).

After surgery, the mouse is placed face-down next to the microscope on a heating pad covered with a loose gauze cloth for warmth, and the mammary skin flap placed on the preheated and moistened microscope stage (Fig. 9.2c, d). A low-level barrier (e.g., a small wooden rod, or applicator) is then placed between the skin flap and the abdominal wall and the rear leg is taped down in order to isolate the gland from potential muscular contractions and body movements. The skin flap is further stabilized by overlaying it with a piece of Plexiglas, which is secured with appropriate spacers and tape. During this procedure, blood flow in the skin flap is intermittently monitored by standard fluorescence microscopy to ensure that no undue pressure is applied to the gland. This “setting-up” phase is the most technically demanding but also the most important for ensuring stable preparations for successful long-term time-lapse imaging. Typical imaging sessions lasted from 1 to 3 h (Fig. 9.2e) and the mice tolerated the xylazine/ketamine anesthesia with no obvious complications. In this short time frame inflammatory complications were minimal, as judged by the lack of infiltrating phagocytic cells in regions of interest. However, as expected, macrophages were frequently observed in interstitial spaces underlying the secretory epithelium. Macrophages are well-documented residents of the mammary gland and milk, they play important developmental roles and they are essential during lactation (Reed and Schwertfeger 2010).

#### 9.2.2.2 Collection of Mouse Milk

Mice are separated from their respective litters for approx. 4 h to allow time for milk to accumulate in luminal spaces and then anesthetized by exposure to isoflurane (3.0–3.5 %). A single intra-peritoneal dose of oxytocin (0.2 IU in 0.2 ml sterile saline) is injected to stimulate “milk let-down” and milk expressed with a hand-held milking device essentially as described (Teter et al. 1990). Milk is removed as soon

as it begins to accumulate in the milking apparatus and collected into capillary tubes, to reduce water losses due to evaporation in the vacuum line. All micrographs discussed in this review were acquired within 1–2 h after milking. [Animal procedures were approved by the NIH Institutional Animal Care and Use Committee].

### 9.2.3 Microscopy

Images were acquired using an Olympus Fluoview 1,000 confocal microscope (Olympus America) equipped with a 60× PLAPON oil immersion objective (NA 1.42). Acceptable confocal images were obtained to a depth of 15–20  $\mu\text{m}$ , which was sufficient to penetrate through one layer of myoepithelial and secretory epithelial cells and into the alveolar lumen. GFP and BODIPY 665 were detected using excitation wavelengths of 488 and 633 nm, and respective emission wavelengths of 520 nm (barrier filter BA 505–605) and either 633 or 688 nm (barrier filter BA 655–755 nm). Typically, the microscope was set to collect line-scan images (512×512 pixels; 12 bits/pixel) at a sampling speed of either 4.0 or 8.0  $\mu\text{s}/\text{pixel}$ . Time-lapse images were captured every 5 or 10 s for up to 2 h and stored as TIFF files. Movies were constructed from the stacked TIFF files using Image J (NIH) and MetaMorph (Molecular Devices) software.

## 9.3 Imaging Results

### 9.3.1 Use of Different GFP Mouse Strains

Transgenic mice expressing GFP, related fluorescent analogs, or other fluorophores were successfully used to image mammary secretory cells and follow the kinetics and dynamics of specific proteins and cellular structures. Fluorescent transgenic mice analyzed included animals expressing soluble GFP in the cytoplasm (Okabe et al. 1997), GFP-myosin IIA [a “knock-in” mouse strain, (Bao et al. 2007)], glycosyl phosphatidylinositol (GPI)-anchored GFP (Rhee et al. 2006), the Lifeact mouse, which expresses a 17-amino-acid peptide bound to GFP that associates with filamentous actin (F-actin) (Riedl et al. 2008), and either a Tomato-red-, or GFP-membrane mouse, in which the fluorophore is targeted to the plasma membranes of cells through the sorting motif MGCCFSKT from the MARCKS protein (Muzumdar, Tasic et al. Muzumdar et al. 2007).

### 9.3.2 General Structure and Physiology of the Gland

Mammary secretory cells are organized into alveolar structures in a simple epithelium (Fig. 9.3a), which is adjacent on the basal-lateral side with an encompassing layer of stellate-shaped myoepithelial cells forming an outer basket (Fig. 9.3a)

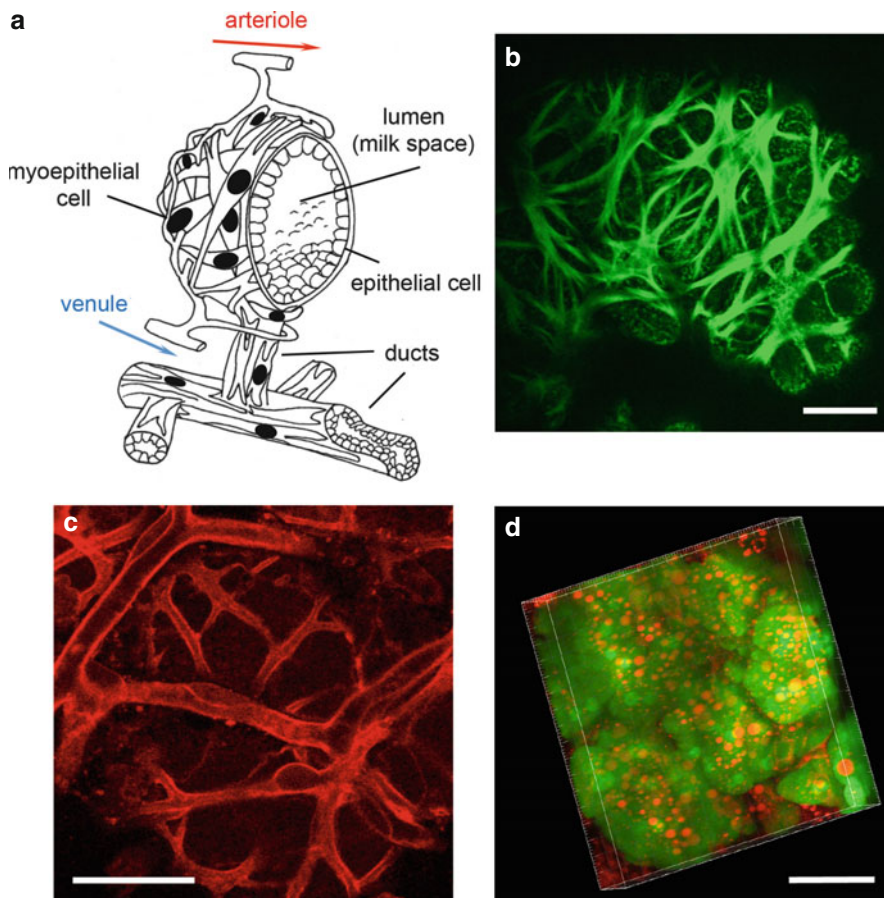


**Fig. 9.3** The mammary alveolus (a) Structure of the mammary alveolus showing the secretory epithelium surrounded by myoepithelial cells and blood capillaries. Milk collects in the central lumen of each alveolus and drains down through the ductal network [figure redrawn and revised from Reece (2004), with permission]; (b) Myoepithelial cells (green) highlighted by GFP-decorated F-actin in the GFP-Liveact mouse; (c) Capillary bed (red) in the Tomato red-membrane mouse; (d) Three-dimensional reconstruction showing alveolar structure in the GFP mouse stained with BODIPY 665 (red) to identify neutral lipid droplets. Bars, (b, c) 25  $\mu$ m, (d) 50  $\mu$ m

(Hollmann 1974). The entire structure is stabilized by a basal lamina and associated hemidesmosomes, focal contacts and extracellular matrix (Streuli 2003). Nutrients and precursors for milk synthesis are transported across the basal-lateral plasma membranes of the secretory cells from an extensive capillary bed underlying the myoepithelium, and completed milk constituents are secreted across the apical plasma membrane into luminal spaces. Tight junctions between lateral membranes effectively seal the epithelium and prevent the passage of materials around cells during lactation in most species (Pitelka 1978; Peaker 1983). During pregnancy these junctions are permeable and allow access of constituents, including ions and

macromolecules from interstitial spaces directly into the forming colostrum (Nguyen and Neville 1998). At peak lactation, the epithelial cells are estimated to secrete over three times their own volume in milk per day (Linzell 1972; Mather and Keenan 1983). Thus, there is a pronounced and continuous vectorial flow of precursors and secretory product across the epithelium during lactation.

Each alveolus is drained by a duct lined with epithelial cells and an associated myoepithelium, which anastomoses with adjacent ducts to form a branched network that terminates in a single duct draining one lobule of tissue. The most frequent structural analogy is to a bunch of grapes, with each grape representing a single alveolus and the stems, the ductular network. Multiple lobules are connected together to form single lobes, which drain through a lobar duct either into a gland cistern for storage, or into a sinus underlying the nipple. Thus, the milk collects in the lumina of each alveolus and is stored until the suckling stimulus triggers the release of oxytocin from the pituitary gland via a neuroendocrine reflex (the so-called “milk-ejection reflex”) (Cross 1977). Oxytocin, transported to the gland through the systemic circulation, binds to a G-protein coupled receptor on the myoepithelial cell surface (Gimpl and Fahrenholz 2001), and precipitates contraction of the myoepithelium, thus forcing the secreted milk from luminal spaces, through the ducts and into the outside world through single or multiple ducts (“streak canals”) in the nipple.

### ***9.3.3 Preliminary Intravital Survey of Transgenic Mouse Strains***

Initial inspection of intravital images of lactating mammary glands stained with BODIPY 665 revealed remarkable detail, at both the macroscopic and sub-cellular levels (Figs. 9.3b–d and 9.4). In all of the mouse strains, the overall structure of the alveolus and capillary bed were clearly delineated in both two-dimensional images (Figs. 9.3b, c and 9.4) and three-dimensional reconstructions (Fig. 9.3d). Myoepithelial cells were distinguished by GFP-Liveact-decorated actin cables in the Liveact mouse (Figs. 9.3b and 9.4a), and by plasma-membrane associated GPI in the GPI-GFP mouse (Fig. 9.4e). Paradoxically, because the myoepithelium and capillary endothelial cells did not express much GFP in the GFP mouse, they were highlighted by their relative lack of fluorescence, compared with the secretory epithelium (not shown). Capillary endothelial cells and circulating leukocytes were readily distinguished in the GFP-myosin IIA and either Tomato-red-, or GPI-membrane mouse by the presumed association of either marker with the plasma membrane (Figs. 9.3c and 9.4c, and data not shown). Erythrocytes were revealed in the blood plasma of both mouse strains by their lack of GFP, thus appearing as dark granules, which filled the available luminal spaces in time-lapse images.

Several structures and organelles could be resolved in the secretory epithelial cells, depending upon the mouse strain. All cell surfaces (apical, lateral, and basal) were distinguishable in GFP-membrane, Liveact, GFP-myosin IIA, and GPI-GFP

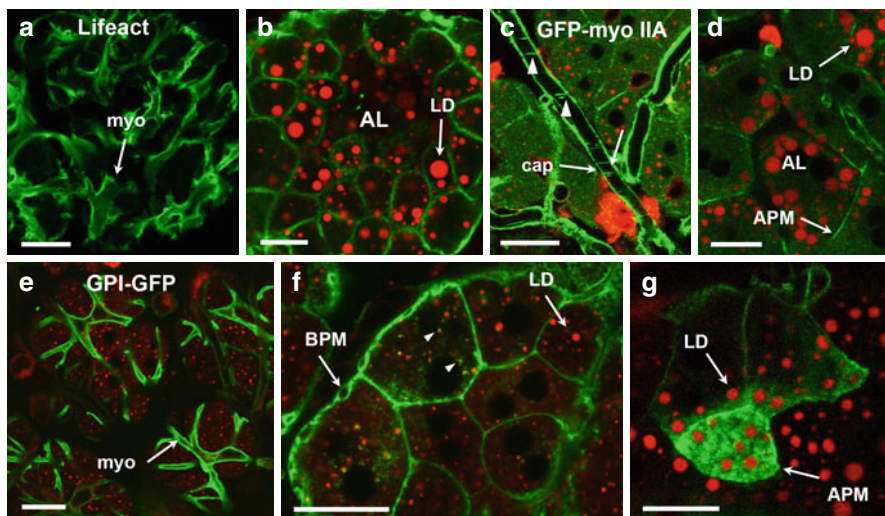


**Fig. 9.4** Intravital images of mammary epithelial cells of GFP transgenic mice (**a**, **b**) Lifeact mouse:- (**a**), myoepithelial cells highlighted by GFP-decorated actin cables, and (**b**), the secretory epithelium; (**c**, **d**) GFP-myosin IIA mouse:- (**c**), basal regions showing the capillary bed and circulating blood cells (*arrowheads*), and **d**, the secretory epithelium; (**e**, **g**) GPI-GFP mouse:- (**e**), basal regions showing myoepithelial cells highlighted by GPI-GFP on the plasma membrane, (**f**) secretory epithelial cells showing *GPI-GFP* on basal, lateral and apical surfaces and on intracellular membrane structures (*arrowheads*, vesicles?), and (**g**), grazing section of the apical surface with associated GPI-GFP and lipid droplets. *AL* alveolar lumen, *APM* apical plasma membrane, *BPM* basal plasma membrane, *cap* capillary, *LD* lipid droplet, *myo* myoepithelial cell, Neutral lipid was stained with BODIPY 665 (red), GFP is shown in green. Bars, (**a**–**g**) 20  $\mu$ m

mice (examples for latter three strains, Fig. 9.4b, d, f, g). BODIPY-stained lipid droplets could be resolved to 0.40  $\mu$ m. The largest droplets (>2.0  $\mu$ m) were in the apical cytoplasm and many were associated with the plasma membrane (Fig. 9.4g). GFP-GPI-labeled structures (vesicles?) were present throughout the cytoplasm (*arrowheads*, Fig. 9.4f). Cytoplasmic GFP revealed numerous dark granules, some of which moved in concerted fashion towards the cell apex and merged with the apical surface in time lapse images and are most probably secretory vesicles (not shown).

This initial screen of a few transgenic mouse lines provided important information on the distribution of myosin IIA, and F-actin on the basal, lateral and apical surfaces of secretory epithelial cells (Fig. 9.4b, d), and the targeting of the GPI-anchor to all surfaces of both myoepithelial and secretory epithelial cells and intracellular vesicles (Fig. 9.4e–g). Thus, intravital imaging of GFP transgenic mice allows the facile description of protein distributions in tissues at steady state without the use of immunohistochemistry and attendant complications of fixation artifacts, and problems with antibody specificity. These issues are especially relevant to lactating mammary tissue because of the difficulty of stabilizing the large quantities of neutral lipid in adipocytes, secretory-epithelial cells and milk with chemical



fixatives. However, expression of GFP, or GFP-fusion proteins is dependent upon the cell and tissue specificity of the promoter linked to the transgene. Therefore, *quantitative inter-cellular* comparisons of protein distributions in tissues are inevitably compromised. One possible way around this problem would be the use of “knock-in” mice, in which the encoded fluorescent fusion protein is expressed from a transgene that is controlled by an endogenous promoter.

### 9.3.4 Intravital Analysis of Lipid Droplets

The major lipids in milk are triacylglycerols synthesized in the rough endoplasmic reticulum (rER) and assembled into neutral lipid droplets (Bauman and Davis 1974). In the most widely accepted model, accretion of lipid occurs within the hydrophobic core of the rER membrane, and the nascent droplets are expelled into the cytoplasm coated with a monolayer of phospholipids derived from the cytoplasmic half of the rER bilayer (Martin and Parton 2006). A cohort of lipid-associated proteins, including proteins in the PAT family (McManaman et al. 2007; Russell et al. 2011), coat the outer surface and serve to stabilize the droplets in the cytoplasm. Droplets are then transported to the apical cytoplasm by unknown mechanisms and, based on analysis of light and electron micrographs, may either remain the same size (Pathway II, Fig. 9.1c), or expand by fusing with other droplets during transit (Pathway I, Fig. 9.1c) (Wooding 1977; Stemberger and Patton 1981; Mather and Keenan 1998).

In preliminary experiments, lipid droplet movement was followed from time lapse images captured over periods of from 1 to 2 h. BODIPY-stained lipid droplets were examined with respect to their position in the cell, their size, transport speed and fusion characteristics. Droplets increased in size by multiple fusion events, both during transport and after arrival in the cell apex. Fusion reactions were promiscuous, with no obvious size restrictions; small droplets fused with each other, or with larger droplets and many small droplets could be seen fusing with a single large droplet (examples, Fig. 9.5a, b).

Following arrival at the cell apex, the droplets acquire an outer envelope, comprising a phospholipid bilayer and associated integral and peripheral proteins (Fig. 9.1a, c). The origin of this outer bilayer has proved controversial, with possible contributions coming from the apical plasma membrane (Fig. 9.1c, mechanisms A, B), secretory vesicles (Fig. 9.1c, mechanism C), and endosomes (Fig. 9.1c, mechanism D) [discussed by Mather and Keenan (1998), and Heid and Keenan (2005)]. Lipid droplets emerge from the cell coated with this outer membrane layer, in an analogous fashion to the budding of enveloped viruses from the plasma membrane.

Thus, immediately after secretion milk-lipid droplets are coated with a monolayer of phospholipids and proteins acquired from the rER and cytoplasm, and a typical outer bilayer membrane [*in toto*, referred to as the milk-lipid globule membrane (MLGM)]. However, following secretion, ultrastructural studies indicate that



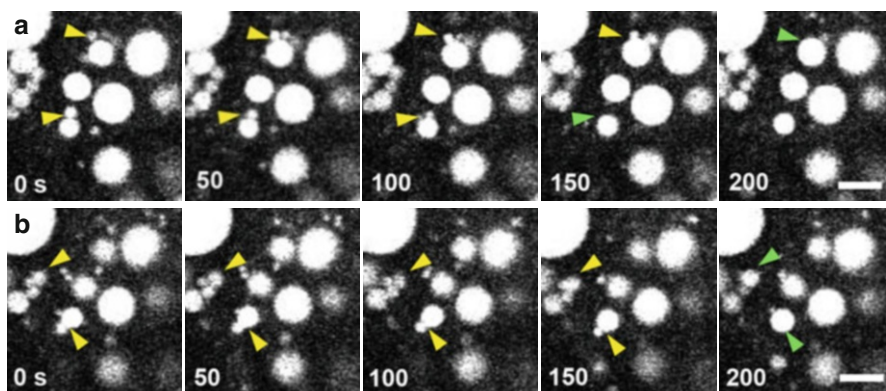


**Fig. 9.5** Time-lapse images of lipid droplets in the GFP-myosin IIA mouse (**a, b**) Two separate intervals from a one hour movie showing association (yellow arrowheads) and eventual fusion (green arrowheads) between lipid droplets in the apical cytoplasm. Time intervals are shown in seconds from an arbitrary starting point, in each case, of 0 s. Neutral lipid droplets were stained with BODIPY 665 (gray scale). Bars (**a**) 5  $\mu$ m

the MLGM may undergo extensive rearrangement during storage in the gland (Wooding 1971; Peixoto de Menezes and Pinto da Silva 1978). Material between the outer bilayer and the inner phospholipid monolayer (presumed cytoplasmic domains of integral proteins and peripheral constituents) appear to thicken, forming lens-like structures on the surface of the droplet. In some areas, the outer membrane and associated internal protein coat may be shed from the droplet in the form of vesicles (Wooding 1971) and contribute to membrane fragments in the skim milk (Wooding 1974; Patton and Jensen 1975). Additional membrane heterogeneity is implied from studies in which exogenous lipid reporters were shown to distribute in patches on the droplet surface when added to fresh milk samples (Lopez 2011). In all of these reports, the milk-lipid droplets were processed either by chemical fixation (Wooding 1971), or the addition of exogenous reagents (Lopez 2011) and therefore to some extent are compromised by the possible generation of experimental artifacts.

GFP transgenic mouse strains offer a simple solution to this problem. Milk can be readily collected from conscious or lightly anesthetized animals (Sect. 9.2.2.2) and the distribution of endogenous GFP constructs analyzed on the surface of unfixed lipid droplets by confocal microscopy immediately after milking. In preliminary experiments, we used the GFP-membrane mouse to examine the gross structure of the MLGM on secreted droplets. Most droplets were coated with the GFP-membrane marker, either around the entire surface, or in more localized regions (Fig. 9.6a–c). Three-dimensional reconstructions showed that the GFP marker was often condensed into areas, like continents and islands, although in most droplets lower quantities of GFP were detectable over most of the surface (Fig. 9.6d–i). These results imply that the outer bilayer remains on substantial regions of the droplet surface after secretion and that the membrane-associated GFP

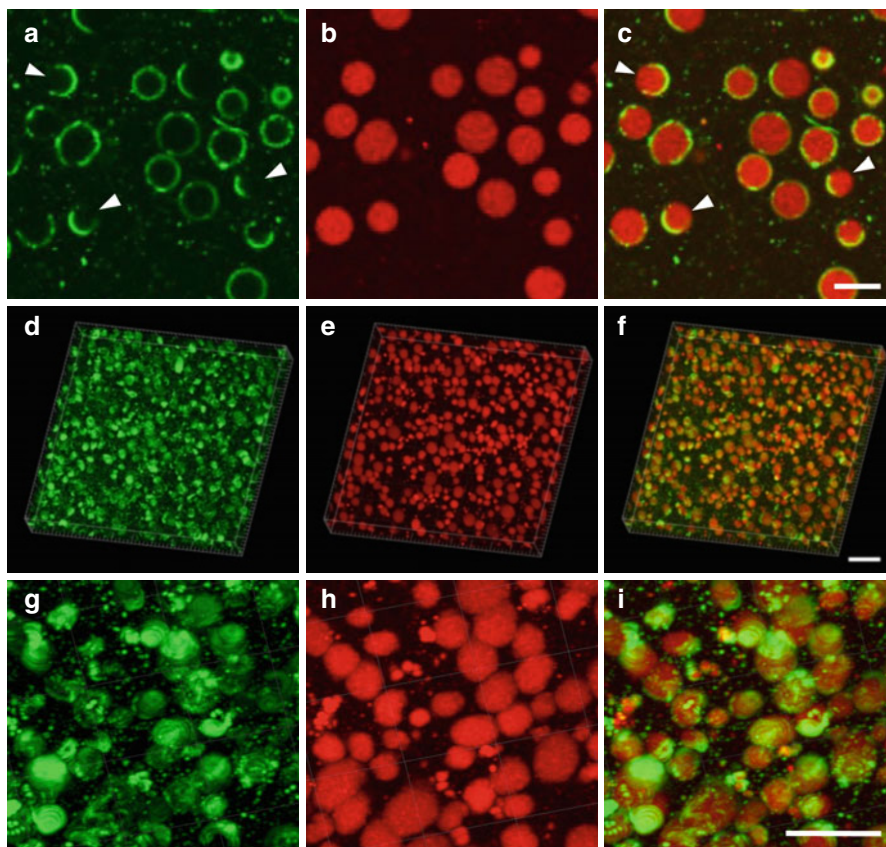


**Fig. 9.6** Milk-lipid droplets Milk samples from the GFP-membrane mouse; (a–c) Lipid droplets in a single optical section. Note that the GFP-membrane is associated with most of the lipid droplets but in many cases is unevenly distributed on the surface (*arrowheads*), (d–i) Lipid droplets in three-dimensional reconstructions showing uneven but global distribution of GFP-membrane on droplet surfaces. (a, d, g) GFP-membrane, (b, e, h) neutral lipid, (c, f, i) merged image. Bars, (a–c) 10  $\mu$ m, (d–f) 30  $\mu$ m, (g–i) 20  $\mu$ m

molecules laterally aggregate and condense in the plane of the bilayer. Similar conclusions were obtained from a FRAP analysis of the distribution of the integral protein, butyrophilin 1a1, fused to GFP and expressed in mouse mammary gland using an adenoviral vector (Jeong et al. 2013). The condensed areas are reminiscent of the lens-like structures seen in electron micrographs, suggesting that they are not fixation artifacts. However, we found little evidence that most of the outer membrane is shed in the form of vesicles into milk in disagreement with earlier ultrastructural studies [the “initial membrane” of (Wooding 1971)].

GFP transgenic mice that express integral marker proteins targeted to specific membrane compartments will be especially useful in determining the membrane origin of the outer MLGM bilayer. The substantial amount of GFP targeted to the

cell surface and secreted droplets in the GFP-membrane mouse, implies that the apical plasma membrane or endosomes are the most likely sources of membrane.

## 9.4 Major Unanswered Questions and the Way Forward

The introduction of intravital microscopy is revolutionizing the *in situ* analysis of cell function, membrane trafficking, and organelle dynamics in many systems (Masedunskas et al. 2012a; Weigert et al. 2013). Recent applications include kinetic analysis of fluid-phase endocytosis in the kidney (Sandoval et al. 2004), exocytosis of salivary proteins in the submandibular gland (Masedunskas et al. 2011), and trafficking of GLUT4 transporters to the plasma membrane in skeletal muscle (Lauritzen et al. 2010). Likewise the application of intravital imaging promises to provide significant and novel insights into the processing, trafficking and secretion of lipid and skim milk constituents in the mammary gland.

Many aspects of lipid droplet assembly, transport and secretion remain unclear. The rates of lipid droplet transport and secretion, and the molecular mechanisms underlying these processes are poorly characterized. The potential role of cytoskeletal motors in driving transport of lipid droplets to the cell apex is controversial [see Mather and Keenan (1998) for discussion], and the molecules required for the fusion of lipid droplets and how this process is regulated *in vivo* are unknown [see Valivullah et al. (1988) for *in vitro* data]. Formation of the MLGM and the budding of lipid droplets at the apical surface may require a cohort of three proteins – butyrophilin 1a1, xanthine oxidoreductase, and PLIN-2 (adipophilin) (Jeong et al. 2013), but their mode of action has not been resolved and the source of the outer membrane envelope is still unclear. Mechanisms underlying post-secretion changes to the MLGM, including the potential aggregation of membrane constituents are uncharacterized.

In the case of skim-milk proteins, early experiments established that proteins produced in the secretory epithelium, such as the caseins and  $\alpha$ -lactalbumin, were processed through the classical secretory pathway. Total transit times were within the range of 40–60 min for radiolabeled proteins in tissue explants and isolated perfused glands (Saacke and Heald 1974; Mather et al. 1984). However, within this time-frame, we have no estimates for the rate of secretory vesicle formation at the Golgi complex, the kinetics and potential role of cytoskeletal elements in transport to the apical surface, the molecular regulation of (presumed) SNARE-mediated fusion of the vesicles with the plasma membrane, or the fate of the vesicle membrane after exocytosis. Furthermore, it is unclear whether the secretion is constitutive, or regulated (Turner et al. 1992). Unlike tightly regulated exocrine systems, such as the pancreas, milk appears to collect continuously in luminal spaces between milkings. However, protein secretion from isolated mammary acini, is stimulated by exogenous calcium, suggesting some form of intermittent, or pulsatile regulation (Turner et al. 1992).

With respect to the fate of vesicle membrane inserted into the apical surface, it has been estimated that over 25–200 times as much membrane is added to the plasma membrane as can be potentially removed by formation of the MLGM (Mather and Keenan 1983). Thus, a substantial quantity of membrane has to be either recycled into the cell, or shed into milk. There is evidence for both endocytosis at the apical surface (Welsch et al. 1984), and membrane shedding (Wooding et al. 1977) but mechanisms for the regulation of such membrane turnover are unknown. Furthermore, it is unclear how the removal of membrane by endocytosis can be separated from the re-uptake of milk constituents, thus raising the possibility that soluble milk components may be recycled and further processed through endocytic pathways for re-export.

Immunoglobulins (IgG, sIgA, and sIgM) are transported across the epithelium into colostrum and milk by receptor-mediated transcytosis (Hunziker and Kraehenbuhl 1998; Wheeler et al. 2007). Transport through the cell is presumed to be mediated through the endosomal system. However, the exact pathways taken and whether, at some point they intersect with the Golgi apparatus and secretory pathway, is unclear. Other proteins from the serum and interstitial spaces, including serum albumin in the mouse (Monks and Neville 2004), prolactin and transferrin (Ollivier-Bousquet 1998) are also transported across the cell throughout lactation by poorly defined mechanisms.

Many of these uncertainties are amenable to analysis by intravital imaging using appropriate GFP transgenic mouse strains, and adenoviral or lentiviral vectors to transduce the mammary epithelium and express specific fluorescent reporter proteins. “Knock-in” mice with transgenes controlled by endogenous promoters will be especially useful for measuring the dynamics and kinetics of tagged proteins at physiological levels. Fluorescent fluid-phase markers may be used to kinetically dissect endocytosis at the apical and basal surfaces, or the transcytosis of materials from the capillary bed to the alveolar lumen, and in the reverse direction from milk to interstitial spaces. Selected mouse strains can be used to examine MLGM structure and the origin of intracellular lipid droplets by analyzing the dynamics and distribution of specific GFP reporters in cells and on the droplet surface.

Besides analysis of membrane and secretory dynamics in epithelial cells, these novel approaches will have wide application for the high resolution imaging of the myoepithelium, ductal epithelial cells, the capillary bed and stromal cells at all stages of mammary development, including pregnancy, lactation and involution. Furthermore, many mutant and transgenic mouse strains are available, which are defective in various aspects of mammary development and lactation that can be analyzed by similar methods.

**Acknowledgements** This work was funded by the intramural program of the NIH (National Institute of Craniofacial and Dental Research), Bethesda, MD, the Maryland Agricultural Experiment Station, University of Maryland, College Park, MD and grants from the USDA NRI Program (2005–04637), and NIH (1R01 HD048588-01A1) to I.H.M.

## References

- Admyre C, Johansson SM, Qazi KR, Filen JJ, Lahesmaa R, Norman M, Neve EP, Scheynius A, Gabrielsson S (2007) Exosomes with immune modulatory features are present in human breast milk. *J Immunol* 179:1969–1978
- Ahmed F, Wyckoff J, Lin EY, Wang W, Wang Y, Hennighausen L, Miyazaki J, Jones J, Pollard JW, Condeelis JS, Segall JE (2002) GFP expression in the mammary gland for imaging of mammary tumor cells in transgenic mice. *Cancer Res* 62:7166–7169
- Argov-Argaman N, Smilowitz JT, Bricarello DA, Barboza M, Lerno L, Froehlich JW, Lee H, Zivkovic AM, Lemay DG, Freeman S, Lebrilla CB, Parikh AN, German JB (2010) Lactosomes: Structural and compositional classification of unique nanometer-sized protein lipid particles of human milk. *J Agric Food Chem* 58:11234–11242
- Bao J, Ma X, Liu C, Adelstein RS (2007) Replacement of nonmuscle myosin II-B with II-A rescues brain but not cardiac defects in mice. *J Biol Chem* 282:22102–22111
- Bauman DE, Davis CL (1974) Biosynthesis of milk fat. In: Larson BL, Smith VR (eds) *Lactation, a comprehensive treatise*, 11th edn. Academic, New York and London, pp 31–75
- Burgoyne RD, Duncan JS (1998) Secretion of milk proteins. *J Mammary Gland Biol Neoplasia* 3: 275–286
- Clark ER, Clark EL (1932) Observations on living preformed vessels as seen in the transparent chamber inserted into a rabbit's ear. *Am J Anat* 49:441–477
- Cross BA (1977) Comparative physiology of milk removal. In: Peaker M (ed) *Comparative aspects of lactation*. Academic, London, pp 193–210
- Dovas A, Patsialou A, Harney AS, Condeelis J, Cox D (2012) Imaging interactions between macrophages and tumour cells that are involved in metastasis *in vivo* and *in vitro*. *J Microsc* 251:261–269
- Ewald AJ, Werb Z, Egeblad M (2011a) Dynamic, long-term *in vivo* imaging of tumor-stroma interactions in mouse models of breast cancer using spinning-disk confocal microscopy. *Cold Spring Harb Protoc*. doi:[10.1101/pdb.top97](https://doi.org/10.1101/pdb.top97)
- Ewald AJ, Werb Z, Egeblad M (2011b) Monitoring of vital signs for long-term survival of mice under anesthesia. *Cold Spring Harb Protoc*. doi:[10.1101/pdb.prot5563](https://doi.org/10.1101/pdb.prot5563)
- Ewald AJ, Werb Z, Egeblad M (2011c) Preparation of mice for long-term intravital imaging of the mammary gland. *Cold Spring Harb Protoc*. doi:[10.1101/pdb.prot5562](https://doi.org/10.1101/pdb.prot5562)
- Gimpl G, Fahrenholz F (2001) The oxytocin receptor system: structure, function and regulation. *Physiol Rev* 81:629–683
- Heid HW, Keenan TW (2005) Intracellular origin and secretion of milk fat globules. *Eur J Cell Biol* 84:245–258
- Hollmann KH (1974) Cytology and fine structure of the mammary gland. In: Larson BL, Smith VR (eds) *Lactation, a comprehensive treatise*, vol I. Academic, New York and London, pp 3–95
- Hunziker W, Kraehenbuhl JP (1998) Epithelial transcytosis of immunoglobulins. *J Mammary Gland Biol Neoplasia* 3:287–302
- Jeong J, Lisinski I, Kadegowda AKG, Shin H, Wooding FBP, Daniels BR, Schaack J, Mather IH (2013) A test of current models for the mechanism of milk-lipid droplet secretion. *Traffic* 14:974–986
- Kedrin D, Gligorijevic B, Wyckoff J, Verkhusha VV, Condeelis J, Segall JE, van Rhee J (2008) Intravital imaging of metastatic behavior through a mammary imaging window. *Nat Methods* 5:1019–1021
- Larson BL, Smith VR (1974/1978) *Lactation, a comprehensive treatise*. Academic Press, New York/London
- Lauritzen HP, Galbo H, Toyoda TT, Goodyear LJ (2010) Kinetics of contraction-induced GLUT4 translocation in skeletal muscle fibers from living mice. *Diabetes* 59:2134–2144
- Linzell JL (1972) Milk yield, energy loss in milk and mammary gland weight in different species. *Dairy Sci Abstr* 34:351–360
- Lopez C (2011) Milk fat globules enveloped by their biological membrane: unique colloidal assemblies with a specific composition and structure. *Curr Opin Colloid Interf Sci* 16:391–404



- Martin S, Parton RG (2006) Lipid droplets: a unified view of a dynamic organelle. *Nat Rev Mol Cell Biol* 7(5):373–378
- Masedunskas A, Sramkova AM, Parente L, Sales KU, Amornphimoltham P, Bugge TH, Weigert R (2011) Role for the actomyosin complex in regulated exocytosis revealed by intravital microscopy. *Proc Natl Acad Sci U S A* 108:13552–13557
- Masedunskas A, Porat-Shliom N, Weigert R (2012a) Regulated exocytosis: novel insights from intravital microscopy. *Traffic* 13:627–634
- Masedunskas M, Milberg O, Porat-Shliom N, Sramkova M, Wigand T, Amornphimoltham P, Weigert R (2012b) Intravital microscopy a practical guide on imaging intracellular structures in live animals. *Bioarchitecture* 2:143–157
- Mather IH, Keenan TW (1983) Function of endomembranes and the cell surface in the secretion of organic milk constituents. In: Mepham TB (ed) *Biochemistry of lactation*. Elsevier, Amsterdam, pp 231–283
- Mather IH, Keenan TW (1998) Origin and secretion of milk lipids. *J Mammary Gland Biol Neoplasia* 3:259–273
- Mather IH, Jarasch E-D, Bruder G, Heid HW, Mepham TB (1984) Protein synthesis in lactating guinea-pig mammary tissue perfused in vitro. I Radiolabelling of membrane and secretory proteins. *Exp Cell Res* 151:208–223
- McManaman JL, Russell TD, Schaack J, Orlicky DJ, Robenek H (2007) Molecular determinants of milk lipid secretion. *J Mammary Gland Biol Neoplasia* 12:259–268
- Monks J, Neville MC (2004) Albumin transcytosis across the epithelium of the lactating mouse mammary gland. *J Physiol* 560:267–280
- Muzumdar MD, Tasic B, Miyamichi K, Li L, Luo L (2007) A global double-fluorescent Cre reporter mouse. *Genesis* 45:593–605
- Nguyen D-AD, Neville MC (1998) Tight junction regulation in the mammary gland. *J Mammary Gland Biol Neoplasia* 3:233–246
- Ogg SL, Weldon AK, Dobbie L, Smith AJH, Mather IH (2004) Expression of butyrophilin (Btln1a1) in lactating mammary gland is essential for the regulated secretion of milk-lipid droplets. *Proc Natl Acad Sci U S A* 101:10084–10089
- Okabe M, Ikawa M, Kominami K, Nakanishi T, Nishimune Y (1997) ‘Green mice’ as a source of ubiquitous green cells. *FEBS Lett* 407:313–319
- Ollivier-Bousquet M (1998) Transferrin and prolactin transcytosis in the lactating mammary epithelial cell. *J Mammary Gland Biol Neoplasia* 3:303–313
- Patton S, RG Jensen (1975) Lipid metabolism and involvement in lipid droplet assembly during lactation. In: Holman RT (ed) *Progress in the chemistry of fats and other lipids*. Pergamon Press, Oxford, XIV, Part 4: pp 163–277
- Peaker M (1983) Secretion of water and ions. In: Mepham TB (ed) *Biochemistry of lactation*. Elsevier, Amsterdam, pp 285–305
- Peixoto de Menezes A, Pinto da Silva P (1978) Freeze-fracture observations of the lactating rat mammary gland. Membrane events during milk fat secretion. *J Cell Biol* 76: 767–778
- Pitelka DR (1978) Cell contacts in the mammary gland. In: Larson BL (ed) *Lactation, a comprehensive treatise*, vol IV. Academic, New York and London, pp 41–66
- Reece WO (2004) *Dukes’ physiology of domestic animals*. Comstock Publishing Associates, Cornell University Press, Ithaca-London
- Reed JR, Schwertfeger KL (2010) Immune cell location and function during post-natal mammary gland development. *J Mammary Gland Biol Neoplasia* 15:329–339
- Rhee JM, Purity MK, Lackan CS, Long JZ, Kondoh G, Takeda J, Hadjantonakis AK (2006) In vivo imaging and differential localization of lipid-modified GFP-variant fusions in embryonic stem cells and mice. *Genesis* 44:202–218
- Riedl J, Crevenna AH, Kessenbrock K, Yu JH, Neukirchen D, Bista M, Bradke F, Jenne J, Holak TA, Werb Z, Sixt M, Wedlich-Soldner R (2008) Lifeact: a versatile marker to visualize F-actin. *Nat Methods* 5:605–607
- Russell TD, Fischer A, Beeman NE, Freed EF, Neville MC, Schaack J (2003) Transduction of the mammary epithelium with adenovirus vectors in vivo. *J Virol* 77:5801–5809



- Russell TD, Schaack J, Orlicky DJ, Palmer C, Chang BHJ, Chan L, McManaman JL (2011) Adipophilin regulates maturation of cytoplasmic lipid droplets and alveolae in differentiating mammary glands. *J Cell Sci* 124:3247–3253
- Saacke RG, Heald CW (1974) Cytological aspects of milk formation and secretion. In: Larson BL, Smith VR (eds) *Lactation, a comprehensive treatise*, vol II. Academic, New York and London, pp 147–189
- Sandoval RM, Kennedy MD, Low PS, Molitoris BA (2004) Uptake and trafficking of fluorescent conjugates of folic acid in intact kidney determined using intravital two-photon microscopy. *Amer J Physiol cell physiol* 287:C517–C526
- Shan S, Sorg B, Dewhirst MW (2003) A novel rodent mammary window of orthotopic breast cancer for intravital microscopy. *Microvasc Res* 65:109–117
- Shennan DB, Peaker M (2000) Transport of milk constituents by the mammary gland. *Physiol Rev* 80:925–951
- Sidani M, Wyckoff J, Xue C, Segall JE, Condeelis JS (2006) Probing the microenvironment of mammary tumors using multiphoton microscopy. *J Mammary Gland Biol Neoplasia* 11:151–163
- Stemberger BH, Patton S (1981) Relationship of size, intracellular location, and time required for secretion of milk fat droplets. *J Dairy Sci* 64:422–426
- Streuli CH (2003) Cell adhesion in mammary gland biology and neoplasia [editorial and series of 8 reviews on cell adhesion in the mammary gland]. *J Mammary Gland Biol Neoplasia* 6:375–485
- Teter BB, Sampugna J, Keeney M (1990) Milk fat depression in C57Bl/6J mice consuming partially hydrogenated fat. *J Nutr* 120:818–824
- Truchet S, Chat S, Ollivier-Bousquet M (2014) Milk secretion: the role of SNARE proteins. *J Mammary Gland Biol Neoplasia* 19:119–130
- Turner MD, Rennison ME, Handel SE, Wilde CJ, Burgoyne RD (1992) Proteins are secreted by both constitutive and regulated secretory pathways in lactating mouse mammary epithelial cells. *J Cell Biol* 117:269–278
- Valivullah HM, Bevan DR, Peat A, Keenan TW (1988) Milk lipid globules: control of their size distribution. *Proc Natl Acad Sci U S A* 85:8775–8779
- Weigert R, Porat-Shliom N-P, Amornphimoltham P (2013) Imaging cell biology in live animals: ready for prime time. *J Cell Biol* 201:969–979
- Welsch U, Singh S, Buchheim W, Patton S (1984) Internalization of ferritin-Concanavalin A by the lactating mammary gland in vivo. *Cell Tissue Res* 235:433–438
- Wheeler TT, Hodgkinson AJ, Prosser CG, Davis SR (2007) Immune components of colostrum and milk – a historical perspective. *J Mammary Gland Biol Neoplasia* 12:237–247
- Wooding FBP (1971) The structure of the milk fat globule membrane. *J Ultrastruct Res* 37:388–400
- Wooding FBP (1974) Milk fat globule membrane material in skim-milk. *J Dairy Res* 41:331–337
- Wooding FBP (1977) Comparative mammary fine structure. *Symp Zool Soc London*. M. Peaker. Academic Press, London. 41:1–41
- Wooding FBP, Morgan G, Craig H (1977) Sunbursts and christiesomes – cellular fragments in normal cow and goat milk. *Cell Tissue Res* 185:535–545
- Wyckoff JB, Wang Y, Lin EY, Li JF, Goswami S, Stanley ER, Segall JE, Pollard JW, Condeelis J (2007) Direct visualization of macrophage-assisted tumor cell intravasation in mammary tumors. *Cancer Res* 67:2649–2656

## Chapter 10

# Fluorescent Dextrans in Intravital Multi-Photon Microscopy

Ruben M. Sandoval and Bruce A. Molitoris

**Abstract** Intravital Multi-photon microscopy stands unique among investigative tools because of the rich and dynamic information that can be rapidly collected and quickly analyzed. Additionally, data gathered from an intact *in vivo* subject in many cases is more meaningful than that derived from isolated *in vitro* methods that lack the complex interactions only found within intact organs. There are numerous fluorescent compounds that have been utilized in intravital microscopy studies to delineate compartments and label organelles. Dextrans are unique in that they are inert, are polymers and as such available in various sizes, and are easily modified to accept fluorophores. Here we describe how dextrans can be used to label different compartments within the kidney based solely on molecular weight. Parameters such as microvascular flow rates and vascular integrity, vesicular trafficking, and renal function can be studied using established techniques. Despite their broad versatility, precautions must be taken when using specified molecular weight sizes because preparations with a broad heterogeneity of their polymer sizes can lead to misinterpretation of data in parameters such as membrane integrity and renal function.

**Keywords** In vivo physiology • Kidney • Glomeruli filtration • Dextrans • GFR • RBC velocity • WBC dynamics • Endocytosis

### 10.1 Introduction

Decades before the advent of turn-key multi-photon systems with rapid-acquisition capabilities, and terabytes drives to store the large amounts of data generated, Arfors and Hint (Arfors and Hint 1971; Thorball 1981) used fluorescence microscopy and fluorescent dextrans to visualize the microcirculation. Today, intravital multi-photon microscopy has become more frequently used as it affords access to unprecedented amounts of dynamic information (Benninger et al. 2008;

---

R.M. Sandoval (✉) • B.A. Molitoris  
Indiana University School of Medicine,  
Indiana Center for Biological Microscopy,  
Indianapolis, Indiana  
e-mail: [rsandova@iupui.edu](mailto:rsandova@iupui.edu)

Dunn et al. 2002; Helmchen and Denk 2005; Masedunskas et al. 2012; Molitoris and Sandoval 2006; Niesner and Hauser 2011; Peti-Peterdi et al. 2012; Wyckoff et al. 2011; Zipfel et al. 2003). Observations ranging from simple morphology to concentration gradients and rates of flow across compartments can be collected using inherent autofluorescence normally found in tissues, and fluorescent molecules systemically delivered. Of the latter, no compound is arguably more versatile than fluorescently conjugated dextrans. Simple polymers of D-glucose occurring as a natural product of *L. mesenteroides*, they can be tailored in size from a few thousand Daltons to several million (Wang et al. 1989). It is this range in size that dictates which of the various physiologic processes can be studied. Today dextrans are widely used to study many aspects of vascular morphology and function, endocytosis and vesicular trafficking in tubular epithelial cells, and more recently renal function (Wang et al. 2010, 2012).

## 10.2 Dextran Characteristics and Use

Dextrans are inherently inert, highly water-soluble, relatively non-toxic and can be modified to accept several different chemical groups to facilitate labeling with fluorescent probes or to alter their inherent characteristics. These modifications include addition of side groups such as diethylaminoethyl (DEAE), which can be used to bind DNA and assist in transfecting cells (Pari and Xu 2004). Dextran sulfates can be used to improve *in situ* hybridization histochemistry (Hrabovsky and Petersen 2002) as well as preventing coagulation of blood in biological research (Hall and Ricketts 1952). For fluorescence microscopy, the most useful side groups to attach to dextrans are amino and carboxymethyl (CM) groups.

Amino groups located along the dextran scaffolding allow for the most simple and straightforward labeling procedure. Attachment of fluorophores containing reactive groups such as sulfonyl chlorides, isothiocyanates and various esters can be carried out in aqueous solutions at their respective optimal pHs followed by purification with dialysis membranes or gel columns (Probes 2003). Additionally, the chemistry to produce a consistent degree of labeling is well understood with little variation when reaction times are kept consistent.

Carboxymethyl (CM) dextrans are perhaps the most advantageous derivatives because the CM groups serve two purposes. Their presence has been implicated in the reduction of immune response after multiple exposures and rare anaphylactic events in humans (Richter 1975). These groups can also be used as attachment sites for fluorophores, although the labeling procedure is more protracted and complex. Katherine Luby-Phelps' chapter in *Methods in Cell Biology* (Vol. 29) outlines procedures in tables 1–3 for modifying and labeling dextrans by the methods of DeBelder and Granath, and Inman (Wang et al. 1989; de Belder and Granath 1973; Inman 1975).

In studying renal processes, the size of the dextran will determine the eventual location to which it will distribute and thus the type of information that can be determined. Because of the glomerular filtration barrier, larger molecular weight dextrans

are largely retained within the vasculature in the plasma but excluded from the Red Blood Cells (RBCs). Smaller molecular weight dextrans that can pass freely or with little hindrance across the filtration barrier are suited to study uptake and trafficking in proximal tubule cells, whose apical surface is augmented by microvilli, thus increasing surface area for internalization of filtered materials. Since the bulk of small fluorescent dextrans will pass freely down the nephron localization within the distal tubule lumen and collecting ducts allows for measurement of luminal diameters and concentrating events (Tanner et al. 2004).

### 10.3 Large Molecular Weight Dextrans That Are Not Cleared by the Kidney Can Be Used to Study Renal Hemodynamics

Because dextrans cannot penetrate the intact membranes of viable cells, those having large molecular weights circulating within the plasma can be used to determine the characteristics of flowing RBCs and White Blood Cells (WBCs) under normal and diseased states. Red blood cell flowing in large diameter renal vessels can easily exceed speeds of 1 mm/s making it unfeasible to calculate RBC speeds from traditionally acquired movies because acquisition rates on the microscope are far slower. However, the slow acquisition rate of the microscope does produce a motion artifact within the vessels which causes RBC's to appear deformed and "slanted" and this can be exploited to calculate speed. The majority of confocal microscopes in use today are laser-scanning systems that build composite images by compiling a series of raster scans of the specimen. The RBCs flowing across the blood vessel captured in this fashion having faster flow rates will produce images with a shallower angle to the RBCs in the blood vessel, while slower flow rates will produce steeper angles (Sipos et al. 2007). Intravital labeling of nuclei in white blood cells (WBCs) is accomplished using the nuclear dye Hoechst 33342 (Sharfuddin et al. 2008, 2009). This allows an additional parameter to distinguish WBCs from RBCs aside from their morphologic differences.

Figure 10.1 demonstrates how RBC flow is determined on a laser-scanning multi-photon system. By limiting the scan to a line drawn across a blood vessel a composite is generated that more readily shows the slope produced by the moving RBCs, which facilitates the determination of speed. The difference in slope generated by faster and slower moving RBCs is readily apparent in panels A and B. Converting the pixels in the horizontal axis (d) to distance and dividing the number of pixels in the vertical axis (t) converted to time, the speed can be generated.

Activation of WBCs causing reduced renal flow and function is a response common to many disease models. Panels C shows the rapid movement of WBCs across the peritubular capillaries in a normal rat, while in panel D activated WBCs 24 h after ischemic injury can be seen. Under normal physiologic conditions the WBCs remain round and quiescent (Panel C). Consequently, their velocity is similar to that of flowing RBCs and their labeled nuclei appear as streaks within the vasculature,

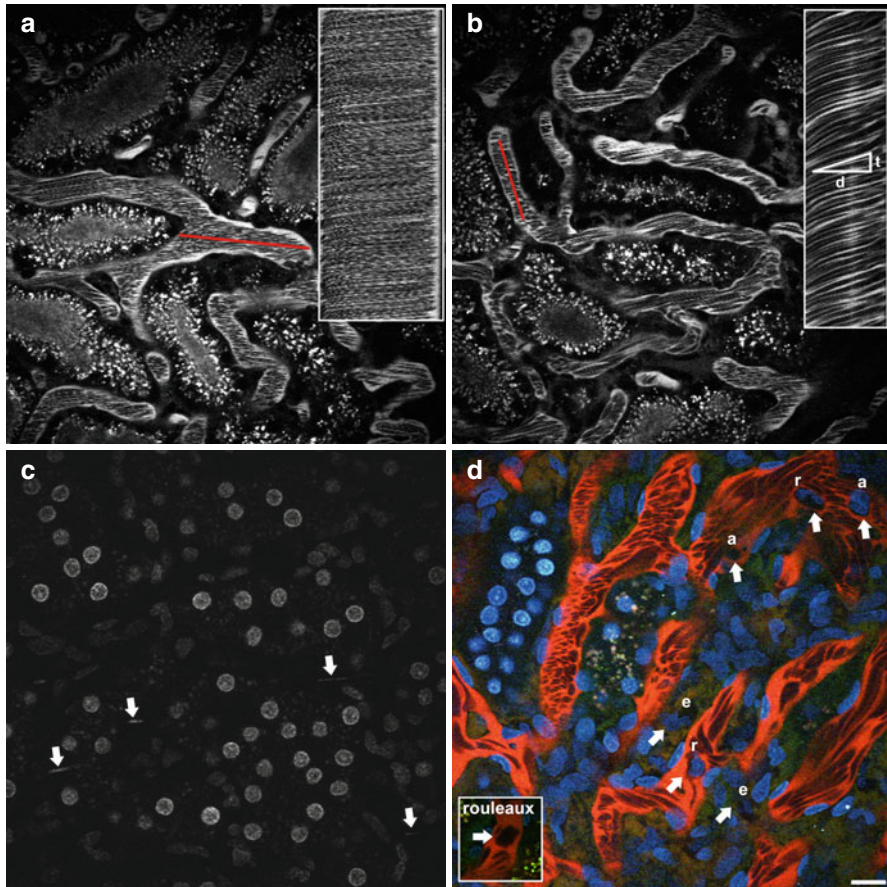


**Fig. 10.1** Large molecular weight (MW) dextrans are retained within the plasma and can be used to assess cellular flow rates. Panel (a) shows a peritubular blood vessel in a normal rat exhibiting fast flow of Red Blood Cells (RBC's). The large 150 kDa Rhodamine Dextran is excluded from the RBC's and thusly they appear as dark streaks within the vasculature. The slope of the streaks is a motion artifact from the acquisition; the faster the RBC's move when the image is collected the more shallow the slope. Hence, the slope of the RBC's can be used to determine speed. The inset in Panel (a) shows a linescan, generated by continuously imaging a single line and making a horizontal composite, which can be used to calculate RBC speed based on the acquisition speed of the microscope system and the magnification of the image. The speed for the RBCs in this vessel is 1,095  $\mu\text{m/s}$ . Panel (b) shows a smaller diameter peritubular blood vessel from the same rat showing RBCs moving at a 654  $\mu\text{m/s}$ . The accompanying linescan (*inset*) shows a steeper slope than that seen in Panel (a) with the demarcation of the parameters used to calculate speed; distance ( $d$ ) and time ( $t$ ) (Sipos et al. 2007). Aside from having the ability to determine RBC speed, dynamics of White Blood Cells (WBC's) can be directly measured. Panels (b, c) show WBC's within the peritubular capillaries labeled with the nuclear stain Hoeschst 33342 (cyan). In normal untreated rats WBC's typically circulate rapidly throughout the vasculature and their nuclei appear as streaks (Panel c, *streaks*, *arrows*). Panel (d) shows activated WBCs 24 h post ischemic injury, with WBCs adhere tightly to the vascular endothelia ( $a$ ) or rolling and crawling along the wall ( $r$ ) if the adherence is transient, and extravasated into the interstitial space ( $e$ ) (Sharfuddin et al. 2009; Sharfuddin et al. 2008). A picture inset outlines a rouleaux formation (*arrow*) common to many types of injuries and disease models. These structures are formed by tightly bound RBCs forming a "stacked coin" configuration resistant to dissociation in the flowing blood. (Bar = 15  $\mu\text{m}$ )



with their normal morphology being unapparent. Panel D shows activated WBCs causing obstruction of RBC flow leading to plasma streaming and regional hypoxia. The true morphology of WBCs becomes apparent upon activation with the nucleus clearly visible and typical amorphous shape of the cell clearly demarcated against the bright plasma.

#### **10.4 Smaller, Molecular Weight Dextrans That Are Cleared by the Kidney Can Be Used to Study the Dynamics of the Endosomal Compartment Within Tubular Epithelia**

Aside from the fact that small molecular weight dextrans are cleared from the vasculature via renal filtration, they share many of the same characteristics as their larger counterparts; mainly they are membrane impermeant. This characteristic that outlines RBCs and WBCs within the circulating blood now allows the detection of the endosomal pool within the highly active proximal tubules whose function is to reabsorb filtered molecules from being lost in the urine. The panels in Fig. 10.2 show the sequential trafficking of two, 3 kDa dextrans administered 22 min apart. Panel A shows a 3 kDa Texas Red dextran (red) given 22 min prior to imaging, accumulating towards the basal pole of proximal tubule cells within the late endosomes/lysosomes. Panels B and C show a 3 kDa Cascade Blue dextran (cyan) 5 and 30 min after a bolus infusion, with endocytic vesicles trafficking away from the sub-apical region towards the late endosomes/lysosomes. Quantitative analysis of the trafficking dynamics of the two dextrans is shown in Panel D. A progressive increase in the total area occupied, and total integrated fluorescence is delineated for the individual dextrans, as well as an increase in their colocalization (Dunn et al. 1989; Sandoval and Molitoris 2008). Thus utilization of differently charged fluorophores on the same sized dextran allows questions such as temporal handling based on charge differences to be probed and answered.

#### **10.5 Small Molecular Weight Dextrans Labeled with pH Sensitive Fluorophores Can Be Used to Study the pH of the Endosomal Pool**

Acidification within the endosomal pathway has been shown to be essential in the trafficking of materials to the lysosomes, but not the early and late endosomes as reported by Maxfield et al. where Bafilomycin A1 was used to inhibit the acidification of the vacuolar system (van Weert et al. 1995). This study used a 70 kDa dextran labeled with fluorescein (whose fluorescence decreases in progressively acidic environments) and rhodamine (whose fluorescence is pH independent). Determining the pH of the endosomal compartment can be accomplished in the same manner *in vivo* with the only caveat being it becomes necessary to use a smaller dextran that is readily filtered. Figure 10.3 shows the progressive acidification of vesicles in Panels



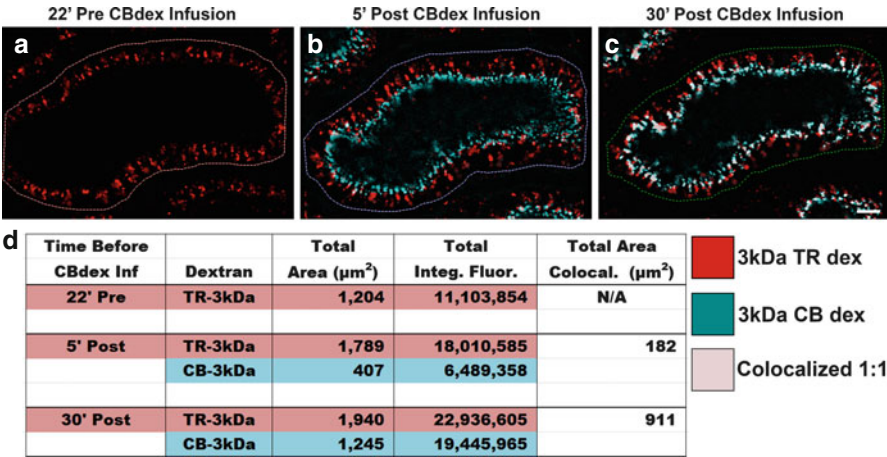


**Fig. 10.2** Small molecular weight (MW) dextrans can be used to measure vesicular trafficking *in vivo*. Twenty-two minutes prior to imaging, a rat was given an intra-venous (*i.v.*) injection of a 3 kDa Texas Red dextran (TR-dex, *red*), which accumulated within the early endosomes/lysosomes of proximal tubules (Panel **a**). A 3,000 MW Cascade Blue dextran (CB-dex, *blue*) was also introduced via an *i.v.* injection during imaging to show vesicular trafficking as it moves progressively from the early endosomes to the late endosomes/lysosomes. Panel (**b**) shows an image acquired 5 min post infusion with the CB-dex, showing CB-dex localized mainly to the microvilli and early endosomal compartment (*cyan*). An image taken 30 min post infusion shows the CB-dex colocalized with a portion of the lysosomes (now white because of the color merge, Panel **c**). Analysis of the individual channels within the images was performed on the highlighted proximal tubule shown in cross section (Panel **d**). A dramatic increase in the total integrated fluorescence (area in pixels  $\times$  fluorescence/ pixel; expressed in arbitrary units) is seen for the individual dextrans. An increase occurs in the area occupied by the individual dextrans; note the greater amount of colocalization that occurs as more of each dextran reaches the late endosomes/lysosomes. This was carried out as previous described (Dunn et al. 1989; Sandoval and Molitoris 2008) and generating binary masks of the images to calculate areas from individual channels and where colocalized. (Bar=8  $\mu\text{m}$ )

A and B, in which the yellow fluorescence within the endosomes changes to more orange and red with quenching of the green fluorescein emissions. Knowing the fluorescence emission curve of fluorescein (Panel D) at a known range of physiologic pHs allows for the determination vesicular pH based on the change in the ratio of Green/Red intensities that will decrease from the known initial value taken from the plasma having a pH of 7.2 (Panel C). Several regions were quantified and Table E shows the acidification that occurs.

### 10.6 The Clearance of Small Freely Filtered Dextrans Can Be Used to Determine Renal Function by Measuring Decay Rates from Any Systemic Blood Vessel

Rapid determination of renal function (glomerular filtration rate, GFR) has been a holy grail in medicine because of the ramifications of knowing this value has on a wide-range of medical procedures and treatments. Many current methods

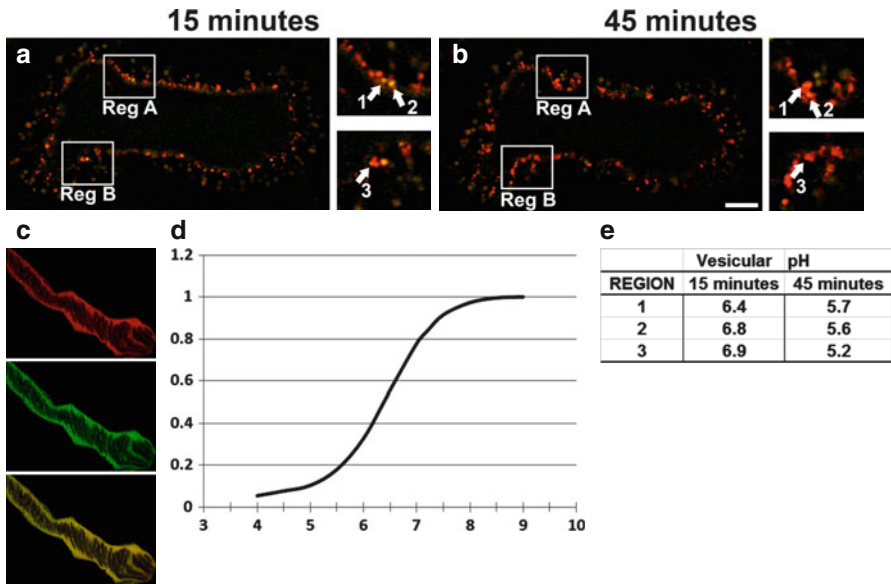


**Fig. 10.3** Exploiting the pH dependent fluorescence of Fluorescein, small molecular weight dual labeled fluorescein and Texas Red dextrans can be used to estimate the pH within the endosomal compartments. Panels (a, b) show accumulation at 15 and 45 min respectively, of a synthesized and purified 10 kDa amino-dextran conjugated to both Fluorescein and Texas Red. As the dual labeled dextran traffics to increasingly acidic compartments, the fluorescence of Fluorescein is quenched causing a shift in the ratio of red/green intensities since the emissions from Texas Red remains unaffected. Two distinct regions were analyzed (*Regions A and B*) with *arrows* pointing to the vesicles that were examined. Panels (c–e) show the analysis and extrapolation of the degree of fluorescence quenching for Fluorescein, which is ratioed against a constant Texas Red fluorescence. Using the ratio of green/red fluorescence in the plasma with a pH of ~7.2 (Panel c), subsequent ratios can be used to extrapolate the pH from the pH dependent fluorescence curve for Fluorescein (Panel d) (van Weert et al. 1995). The drop in measured pH for the individual vesicles examined in *Regions A and B* is presented in the *table* (Panel e); note the acidification that occurred in all the compartments and the accompanying color shift. (Bar=8  $\mu$ m)

involve the estimation of GFR by determining levels of endogenous markers that are normally cleared by the kidney. Creatinine is one such example (Molitoris et al. 2008). Here, a decrease in GFR is determined by the accumulation of this metabolic by-product in the blood. Unfortunately, accumulated levels that lead to a diagnosis of renal impairment occur long after the initial reduction in GFR and hence the window of treatment to restore function or further abate dysfunction has passed such as processes like acute kidney injury. There are currently other tests capable of measuring renal function; conducted using the clearance of small freely filtered molecules such as inulin or the radio contrast compound Iohexol (Schwartz et al. 2006). The only drawback to these tests is the time required to complete the analysis of their concentration in the plasma; at best these values are available approximately 24 h from the time the final blood sample was taken.

The use of a small, freely filtered, fluorescent dextran is a major technological advancement in the development of a rapid test for renal function (Wang et al. 2010; Wang et al. 2012). No longer needed are time and labor-intensive analytical methods

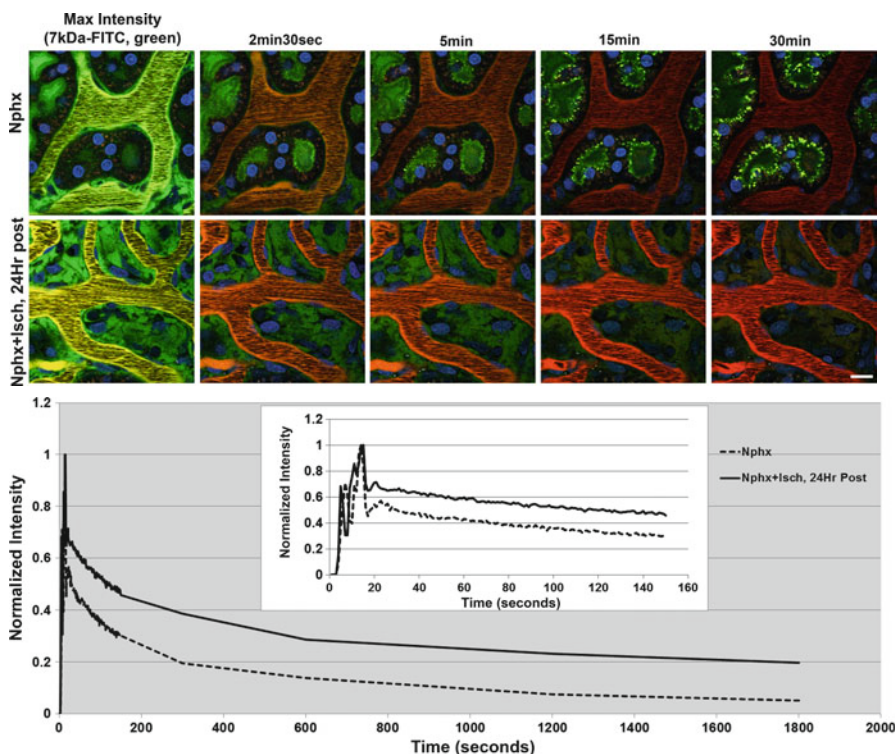


**Fig. 10.4** Measuring the rate of fluorescence decay for a freely filtered dextran from the plasma in any vessel can be used to determine the Glomerular Filtration Rate (GFR). The two distinct rows of images show identical time points after a single bolus infusion of a 7 kDa Fluorescein-dextran (green) for a model of unilateral nephrectomy alone (Nphx) or nephrectomy and 24 h post renal ischemia (Nphx+24 h Post Isch); respectively. Note the difference in plasma levels of the Fluorescein dextran (green) at the five identical time points between the two injury models. The maximum plasma intensity (MAX, which can vary slightly by a few seconds between individual rats and conditions) is used to normalize the quantitative data utilized to generate a decay curve (seen in the lower portion of the panel). A graph of the normalized intensity decay curves examined for 30 min is seen, with an inset showing the dynamic changes occurring within the first 150 s. This graphs is generated from a 150 frame movie originally collected, followed immediately by capturing an image every minute for ~30 min (~176 frames total). Using an estimated plasma volume, the GFR for the rat having only the nephrectomy was 0.41 mL/min/100 g body weight; the rat having the combined nephrectomy and ischemia was 0.16 mL/min/100 g body weight (Wang et al. 2010, 2012). (Bar = 15  $\mu$ m)

such as the use of an HPLC to determine the time-dependent decay in concentration of these other compounds. Figure 10.4 shows a series of sequential images taken of a peritubular blood vessel showing the time-dependent decay in fluorescence of a 7 kDa dextran following administration of a single bolus. The upper series is of a rat that underwent a unilateral nephrectomy 24 h prior to imaging (Nphx); the

lower series shows images from a rat that underwent the same procedure with the addition of renal ischemia on the remaining kidney (Nphx +isch, 24 h post). The curve generated shows the decay in vascular fluorescence from the image series, at time points taken every second for the first 100 s, then every minute for 30 min thereafter. A value for GFR is generated based a two-compartment model, and the use of an estimate for plasma volume based on weight.

## 10.7 Alteration in Vascular Integrity Can Be Determined Using Large Molecular Weight Dextrans

Permeability for any compound is defined as the concentration across two compartments separated by a barrier. The permeability factor (or coefficient) is the ratio of the concentration of the compound in the (downstream) compartment to which the compound migrates, divided by the concentration of the compartment holding the initial bolus of material (upstream). A compound that is freely filtered without hindrance has a permeability coefficient of 1.0 while a compound that is not filtered has a coefficient of 0.0. Thus, all compounds fall within this range of 0–1. The kidney is an ideal system in which to study this phenomenon. The glomerulus is composed of a series of interconnected, coiled and branching blood vessels called capillary loops. These vascular loops filter out small and moderately sized molecular weight compounds, both waste products and nutrients, into the nephron where nutrients are reclaimed and waste products pass into the urine. A cross section of the glomerulus allows the visualization of both compartments used to determine a compound's permeability coefficient called the glomerular sieving coefficient (GSC). Panels A and B in Fig. 10.5 show the GSC of two different dextrans of opposing molecular weights, a freely filtered 7 kDa dextran (Panel A) and a nearly impermeant 150 kDa dextran (Panel B). The image in panel A showing the freely filtered dextran in the urinary space (Bowman's space) silhouettes the podocytes encompassing the capillary loops. The GSC is calculated by dividing the fluorescence in the Bowman's space by the fluorescence in the plasma. It is crucial to take steps to subtract intensities from background images taken prior to infusion of the dextrans, select only the plasma in the capillary loops while avoiding the flowing RBCs, and correctly setting the detector offset (Sandoval et al. 2013).

The peritubular vasculature surrounding the tubular epithelia allows small and moderately sized molecular weight compounds to pass to and fro into the interstitial space to contact the basolateral membrane of tubular cells. The permeability of this barrier is increased after injury (Sutton et al. 2006). Panels C and D from Fig. 10.5 show the alteration in permeability before and after ischemic injury in studies that used a 150 kDa dextran which normally does not pass across the endothelial barrier into the interstitial space. Quantitation of the extent of leakage can be expressed as a percent area showing extravasated dextran of the total area from a single plane image.



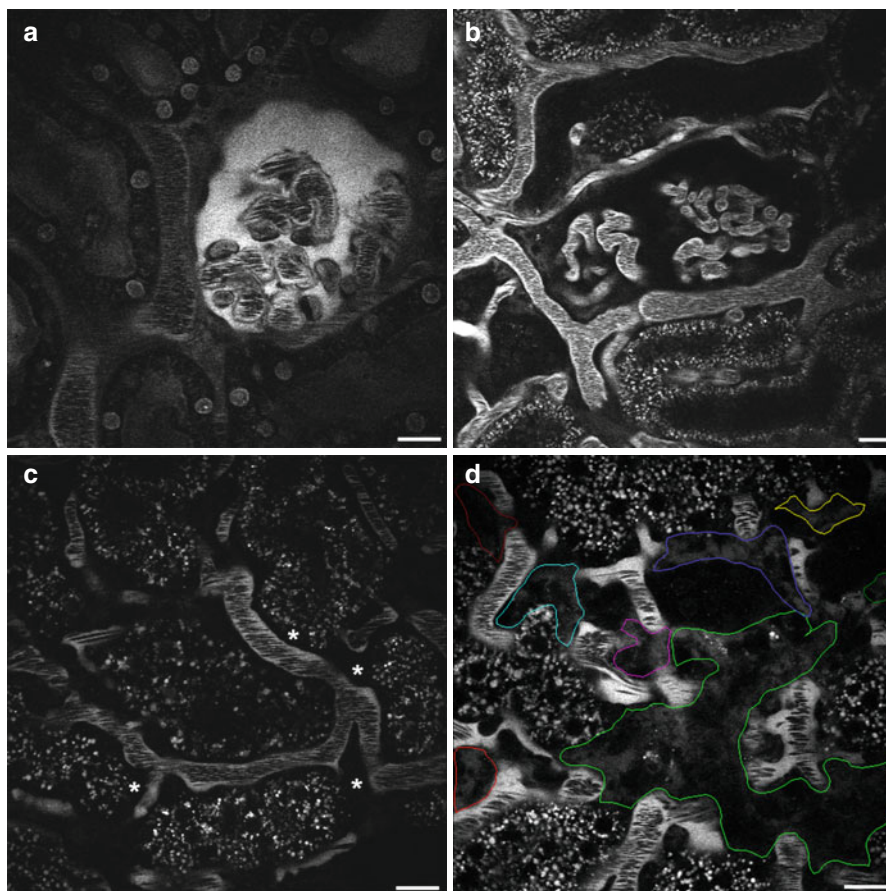


**Fig. 10.5** The integrity of the renal microvasculature can be assessed in normal and diseased states using larger molecular weight dextrans. Permeability factor, or sieving coefficient is most commonly used to analyze the fractional renal clearance of a compound from the blood into the urinary space within the glomerulus. Panels (a, b) show the glomerular sieving coefficient (GSC) across the glomerular capillary loops of a freely filtered 7 kDa dextran (a, 1.05), and a 150 kDa dextran with minimal renal clearance (b, 0.005); respectively. The GSC is calculated by ratioing the intensity of the filtered material in the Bowman's space by the intensity within the plasma. For compounds that are freely filtered analysis is best done using a continuous venous infusion due to rapidly fluxing intensities that can occur when using a single bolus. A detailed description of how to perform this calculation can be found in publications from our laboratory (Sandoval et al. 2012, 2013a, b). Deterioration of vascular integrity is a consequence of numerous disease processes and can be determined by noting the migration of a normally impermeant dextran into the interstitial space that is found between the tubular epithelia and the peritubular capillaries. Panels (c, d) show the peritubular vasculature in a normal and post ischemic rat; respectively, labeled with a 150 kDa dextran. In normal rats (Panel c) the dextran is retained within the vasculature and does not permeate out into the interstitial space (asterisk). In a model of post renal ischemia (Panel d), regions showing movement of the large 150 kDa dextran into the interstitial space are heterogeneous in distribution (Sutton et al. 2006). This phenomenon can be quantified by determining the area affected and reporting it as a percent of the total region analyzed. Here, the highlighted regions having the 150 kDa dextran within the interstitial space had a cumulative area of 12,138.4  $\mu\text{m}^2$ , out of the total area for the image of 44,826.6  $\mu\text{m}^2$ ; or approximately 27 %. It is important to standardize the time at which the images are acquired for analysis to avoid any bias that may be inadvertently introduced. (Bar=20  $\mu\text{m}$ )

## 10.8 Dextran Preparations Vary in Size Dispersion

The importance of size in the way dextrans are handled within a living subject during *in vivo* imaging has been described in detail within this chapter. The numerous parameters that can be studied are dependent on the dextran reaching the desired compartment or organelle; which often involves crossing barriers. Alternatively, determining the integrity of a compartment such as the vasculature before and after injury relies on a large dextran that is normally retained within the blood vessels. The presence of a broad distribution of sizes within a preparation can cause a dramatic difference in the way data are generated and interpreted.

An example of the importance of a narrowly dispersed dextran follows. When determining the GSC of a moderately sized molecular weight dextran, the presence of larger and smaller sized fractions, around the mean, will produce a range of GSC values that are time-dependent. A higher GSC will be initially reported as the kidney clears out the smaller more permeable molecular weight components shortly after infusion of the bolus (Sandoval et al. 2012). Analyzing images at more protracted time points will report a progressively lower GSC as renal clearance leaves behind increasingly larger size components. Panel A from Fig. 10.6 shows a graph with the representative size distribution of two preparations of a dextran with a molecular weight of 69.7, 70 and 150 kDa. The 70 kDa dextran has a very broad size distribution with components ranging in size from those that are freely filtered; to very large whose sizes exceed those of the 150 kDa dextran. In contrast, the 69 kDa dextran has a much narrower size distribution of the constituent components as is evident by the narrower bell shaped curve. When the GSC for the two dextrans are plotted over time, one can see the 70 kDa dextran had GSC values spanning an order of magnitude, however, the 69 kDa dextran had a far more consistent GSC. It should be noted that even a very narrowly dispersed preparation will display some minor change in GSC over time because the size is not perfectly uniform.

The term disparity (***D***) is the measure of the heterogeneity of sizes within a preparation of any polymer such as a dextran, and can refer to either molecular mass (***DM***) or degree of polymerization (***DX***). When referring to disparity in a dextran, the index typically reported is molecular mass (***DM***). When reporting this index for a polymerization reaction, this value can be as high as 10 or 20 depending on reaction factors; since dextrans are purified this value tends to be much lower (with a lower number having a narrower size distribution). Disparity is determined by dividing the molecular weight average by the number average molar mass; ***DM = Mw/Mn*** (Ioan et al. 2000). Molecular weight average (***Mw***) can be determined by using a static light scatter, small angle neutron scattering, X-ray scattering, and sedimentation velocity. Number average molar mass (***Mn***) is derived from methods such as gel permeation chromatography, viscometry, and colligative methods (relative lowering of vapor pressure, elevation of boiling point, depression of freezing point, osmotic pressure). Not every laboratory has the equipment or time to run these painstaking analytical procedures for every batch of fluorescent dextrans they receive prior to use. As intravital multi-photon microscopy becomes more widely



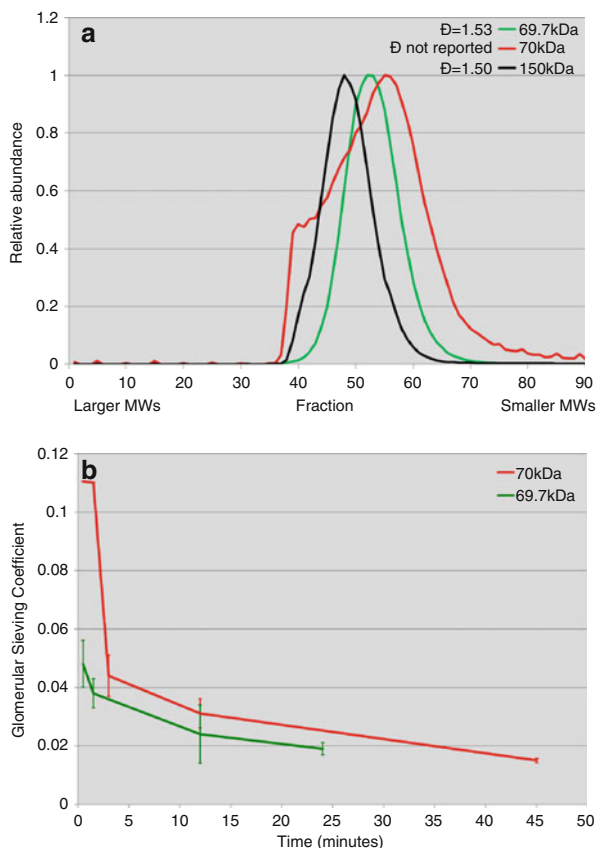


**Fig. 10.6** Dextrans, along with other polymeric compounds, can contain a range of molecular sizes that can affect permeability values. Panel (a) shows a graph of three dextrans analyzed through gel chromatography. The 150 kDa dextran and 69 kDa dextran both have a narrow size distribution and produce tight bell shaped curves when plotting relative abundance versus elution fractions. The 70 kDa dextran, from a different supplier, has a much broader size distribution indicating it contains a range of sizes spanning from smaller ones that are freely filtered across the glomerulus to some that are larger than the 150 kDa dextran. Panel (b) shows the glomerular sieving coefficient (GSC) for the 69 and 70 kDa dextran taken over time. One can see that the broadly dispersed 70 kDa dextran has a highly time-dependent GSC; elevated initially as the smaller fractions clear into the Bowman's space and are readily detected. Latter time points will report lower GSC values associated with the retention of larger molecular weight fractions (Sandoval et al. 2012). Disparity values ( $\bar{D}$ , formerly referred to as the polydispersity index (Gilbert et al. 2009)) for the 69 and 150 kDa dextran are 1.53 and 1.50; respectively. The 70 kDa dextran was not supplied with a disparity value, but it appears evident its value was much higher

used and accepted as a methodology, it will become important that manufacturers supply disparity values with their dextrans. Of the dextrans analyzed in Fig. 10.6, the 69 kDa dextran and the 150 kDa dextran have associated disparity values of 1.53 and 1.50 respectively; while the 70 kDa dextran was not supplied with this

value. This omission emphasizes the fact that when utilized for typical *in vitro* cell culture studies this characteristic is less crucial to arriving at correct values for the parameter studied.

## 10.9 Summary

Many of the applications for dextrans described here focus on their use in renal related studies. Parameters such as microvascular morphology and permeability however, can be used in the study of other organs amenable to intravital imaging on a multi-photon system. One factor that will greatly increase the versatility of dextrans is the continual expansion and enhancement of fluorophores. Advancements here to introduce new colors and increase quantum yield can only serve to enhance sensitivity and detection of dextrans within structure or compartments having very low accumulations. A prime example of this is the development of the pH sensitive pHrodo™ dyes by Life Technologies engineered to determine pH *in vitro* and *in vivo*. TdB Consultancy in Sweden is currently working to produce a line of dextrans with very narrow dispersion values tailor made for intravital fluorescence microscopy. As microscope systems have become increasingly sophisticated with the incorporation of more and better detectors it is possible to visualize and study up to four different processes each distinguished by its own color. The inert nature of dextrans makes them ideal for use in studies utilizing tissues expressing fluorescent proteins, fluorescent organelle markers, and natural tissue auto-fluorescence or second harmonics. It is also important to remember that some studies will call for more stringent preparations of dextrans whose narrower size distributions will help correctly describe the process under study.

**Acknowledgements** This work was supported by grants to BAM from the National Institute of Health (DK091623, 079312, 088934, 093274), and support from the Veterans Administration through a Merit Review Award.

## References

- Arfors KE, Hint H (1971) Studies of the microcirculation using fluorescent dextran. *Microvasc Res* 3:440–444
- Benninger RK, Hao M, Piston DW (2008) Multi-photon excitation imaging of dynamic processes in living cells and tissues. *Rev Physiol Biochem Pharmacol* 160:71–92
- de Belder A, Granath K (1973) Preparation and properties of fluorescein-labelled dextrans. *Carbohydr Res* 30:375–378
- Dunn KW, McGraw TE, Maxfield FR (1989) Iterative fractionation of recycling receptors from lysosomally destined ligands in an early sorting endosome. *J Cell Biol* 109:3303–3314
- Dunn KW et al (2002) Functional studies of the kidney of living animals using multicolor two-photon microscopy. *Am J Physiol Cell Physiol* 283(3):C905–C916
- Gilbert RG, Hess M, Jenkins AD, Jones RG, Kratochvil P, Stepto RFT (2009) Dispersity in polymer science. *Pure Appl Chem* 81(2):351–353

- Hall M, Ricketts CR (1952) The use of dextran sulphate as a blood anticoagulant in biological research. *J Clin Pathol* 5(4):366
- Helmchen F, Denk W (2005) Deep tissue two-photon microscopy. *Nat Methods* 2(12):932–940
- Hrabovsky E, Petersen SL (2002) Increased concentrations of radioisotopically-labeled complementary ribonucleic acid probe, dextran sulfate, and dithiothreitol in the hybridization buffer can improve results of in situ hybridization histochemistry. *J Histochem Cytochem* 50(10):1389–1400
- Inman JK (1975) Thymus-independent antigens: the preparation of covalent, hapten-ficoll conjugates. *J Immunol* 114(2 Pt 1):704–709
- Ioan CE, Aberle T, Burchard W (2000) Structure properties of Dextran. 2. Dilute solution. *Macromolecules* 33:5730–5739
- Masedunskas A et al (2012) Intravital microscopy: a practical guide on imaging intracellular structures in live animals. *Bioarchitecture* 2(5):143–157
- Molitoris BA, Sandoval RM (2006) Pharmacophotonics: utilizing multi-photon microscopy to quantify drug delivery and intracellular trafficking in the kidney. *Adv Drug Deliv Rev* 58(7):809–823
- Molitoris BA et al (2008) Technology insight: biomarker development in acute kidney injury – what can we anticipate? *Nat Clin Pract Nephrol* 4(3):154–165
- Niesner RA, Hauser AE (2011) Recent advances in dynamic intravital multi-photon microscopy. *Cytometry A* 79(10):789–798
- Pari GS, Xu Y (2004) Gene transfer into mammalian cells using calcium phosphate and DEAE-dextran. *Methods Mol Biol* 245:25–32
- Peti-Peterdi J, Burford JL, Hackl MJ (2012) The first decade of using multiphoton microscopy for high-power kidney imaging. *Am J Physiol Renal Physiol* 302(2):F227–F233
- Probes M (2003) Amine-reactive probes (technical protocol), Lifetechnologies
- Richter W (1975) Effect of substitution on reactivity of B 512 dextran fractions with anti-B 512 dextran in heterologous passive cutaneous anaphylaxis. *Int Arch Allergy Appl Immunol* 48(4):505–512
- Sandoval RM, Molitoris BA (2008) Quantifying endocytosis in vivo using intravital two-photon microscopy. *Methods Mol Biol* 440:389–402
- Sandoval RM, M BA (2013) Quantifying glomerular permeability of fluorescent macromolecules using 2-photon microscopy in Munich Wistar rats. *J Vis Exp* 74. doi:[10.3791/50052](https://doi.org/10.3791/50052).
- Sandoval RM et al (2012) Multiple factors influence glomerular albumin permeability in rats. *J Am Soc Nephrol* 23(3):447–457
- Sandoval RM, Wang E, Molitoris BA (2013) Finding the bottom and using it Offsets and sensitivity in the detection of low intensity values in vivo with 2-photon microscopy. *Intravital* 2(1):1–9
- Schwartz GJ et al (2006) Glomerular filtration rate via plasma iothexol disappearance: pilot study for chronic kidney disease in children. *Kidney Int* 69(11):2070–2077
- Sharfuddin AA, Sandoval RM, Molitoris BA (2008) Imaging techniques in acute kidney injury. *Nephron Clin Pract* 109(4):c198–c204
- Sharfuddin AA et al (2009) Soluble thrombomodulin protects ischemic kidneys. *J Am Soc Nephrol* 20(3):524–534
- Sipos A et al (2007) Advances in renal (patho)physiology using multiphoton microscopy. *Kidney Int* 72(10):1188–1191
- Sutton TA, Horbelt M, Sandoval RM (2006) Imaging vascular pathology. *Nephron Physiol* 103(2):p82–p85
- Tanner GA, Sandoval RM, Dunn KW (2004) Two-photon in vivo microscopy of sulfonefluorescein secretion in normal and cystic rat kidneys. *Am J Physiol Renal Physiol* 286(1):F152–F160
- Thorball N (1981) FITC-dextran tracers in microcirculatory and permeability studies using combined fluorescence stereo microscopy, fluorescence light microscopy and electron microscopy. *Histochemistry* 71(2):209–233
- van Weert AW et al (1995) Transport from late endosomes to lysosomes, but not sorting of integral membrane proteins in endosomes, depends on the vacuolar proton pump. *J Cell Biol* 130(4):821–834

- Wang Y-L, Taylor DL (1989) Fluorescence microscopy of living cells in culture, part A. Fluorescent analogs, labeling cells, and basic microscopy. *Methods Cell Biol* 29:iii–xiv, 1–333
- Wang E et al (2010) Rapid diagnosis and quantification of acute kidney injury using fluorescent ratio-metric determination of glomerular filtration rate in the rat. *Am J Physiol Renal Physiol* 299(5):F1048–F1055
- Wang E et al (2012) A portable fiberoptic ratiometric fluorescence analyzer provides rapid point-of-care determination of glomerular filtration rate in large animals. *Kidney Int* 81(1):112–117
- Wyckoff J et al (2011) High-resolution multiphoton imaging of tumors in vivo. *Cold Spring Harb Protoc* 2011(10):1167–1184
- Zipfel WR, Williams RM, Webb WW (2003) Nonlinear magic: multiphoton microscopy in the biosciences. *Nat Biotechnol* 21(11):1369–1377

## Chapter 11

# Intravital Microscopy of the Lung

Robert G. Presson, Irina Petrache, and Mary Beth Brown

**Abstract** Real time high quality imaging of intra-thoracic organs with sufficient resolution to study microcirculatory dynamics, inflammatory cell trafficking, and cellular and subcellular events during physiologic circulatory and breathing conditions remains a high priority in pulmonary and cardiovascular research. Recent technological developments especially in the area of two-photon microscopy (TPM) offer enhanced resolution and deeper penetration under the organ surface, thus allowing sampling of areas of interest to biologists and physiologists. Furthermore, with TPM one can image sub-cellular and molecular events in real time, such as protein trafficking, enzyme activation, and reactive oxygen species generation, which are pertinent to the pathogenesis of many diseases of interest to the research community. The application of TPM to organs in the thoracic cavity, and especially the lung has been hampered by cardiorespiratory motion and new techniques to mitigate these limitations have been developed. In this chapter, we will describe intravital imaging techniques applied to the lung through a historical perspective, and highlight several recent practical applications of these approaches.

**Keywords** Microscopy • Lung • Pulmonary • Real time • Microcirculation

### Abbreviations

TPM	Two Photon microscopy
FITC	Fluorescein Isothiocyanate
PMN	Polymorphonuclear cell

---

This work was supported by the NIH R01HL077328 (IP)

R.G. Presson, MD (✉)

Department of Anesthesia, Indiana University,  
1102 South Drive, Fessler Hall 204, Indianapolis, IN 46202, USA  
e-mail: [rpresson@iupui.edu](mailto:rpresson@iupui.edu)

I. Petrache

Department of Medicine, Indiana University, Indianapolis, IN, USA

Richard L. Roudebush Veteran Affairs Medical Center, Indianapolis, IN, USA

M.B. Brown

Department of Physical Therapy, Indiana University, Indianapolis, IN, USA

© Springer Science+Business Media Dordrecht 2014

221

R. Weigert (ed.), *Advances in Intravital Microscopy*:

*From Basic to Clinical Research*, DOI 10.1007/978-94-017-9361-2\_11

## 11.1 Techniques

The oldest technique for studying the pulmonary microcirculation and one of the most direct is intravital microscopy. This technique was first applied to the lung in 1661, when Marcello Malpighi transilluminated the frog lung with candlelight and used a microscope to observe erythrocytes moving through the pulmonary capillaries. This discovery completed the picture of the circulation developed by William Harvey through a series of experiments demonstrating that there had to be a direct connection between the venous and arterial systems throughout the body.

### 11.1.1 *Unrestrained Motion*

Since the seventeenth century, the essentials of intravital lung microscopy have remained the same as has the principal obstacle, respiratory motion. Early investigators either observed the lung without restraining respiratory motion, or suspended respiration and observed the lung in apnea. The tradeoffs of these techniques are illustrated by the classical study of (Wearn et al. 1934). These investigators dissected the chest wall of the cat down to the pleura, and transilluminated the lower edge of the lung with a quartz rod that was passed through an abdominal incision. Initial experiments were performed while the animals were breathing, and morphine was used to decrease the respiratory rate. Although these investigators reported that the difficulty of observing the moving lung grew less as their eyes became accustomed to the motion, they did not feel secure in detecting the finer capillary changes.

### 11.1.2 *Apnea*

Subsequent studies were performed animals were studied who were immobilized by the use of curare. Oxygen was insufflated into the trachea, which helped to prevent hypoxemia, but not hypercarbia and acidosis. Using this technique, Wearn made the important observation that pulmonary capillaries were intermittently perfused suggesting the possibility of a recruitable reserve. Although the experimental conditions in the first group were the most physiologic, respiratory motion interfered with the observations. In contrast, the ability to observe the microcirculation in the paralyzed animals was ideal but the observations were unavoidably affected by alterations in blood gases.

### 11.1.3 *Vacuum Manifold*

A significant advance in dealing with respiratory motion was made approximately 30 years later by Wagner who developed an implantable window that was encircled by a vacuum manifold (Wagner 1969). Gentle radial traction from the manifold



arrested cardiorespiratory motion in the observation field permitting serial measurements on the same microvascular networks without the need to alter ventilation. Using this device, Wagner et al. directly observed capillary recruitment in the dog lung when pulmonary artery pressure was raised by airway hypoxia, the first direct observation of capillary recruitment in an intact living animal.

Although the vacuum manifold effectively limited respiratory motion, it confined observations to a small area of the subpleural microcirculation. In addition, investigators had limited control of hemodynamics in the intact animal. The geometry of the implanted manifold also imposed limitations on the characteristics of the microscope objective. The diameter of the objective either had to be small enough to fit inside the walls of the frame or the working distance had to be long enough to focus on the lung without lowering the objective into the frame. This problem was most notable with large diameter, high NA objectives with short working distances and with windows developed for implantation in smaller species such as the rat that limited the dimensions of the frames (Fig. 11.1).

One solution to this problem is to couple the lung to a vacuum manifold that is not implanted in the closed chest wall. Because manifolds used for this preparation do not need to accommodate the thickness of the chest wall they are flat across the top and therefore can accommodate objectives of any diameter or working distance (Fig. 11.2). In this preparation a thoracotomy is performed and the ribs are retracted to expose the lung. The manifold is then lowered until it contacts the pleural surface (Fig. 11.3). Although respiratory motion is greatly reduced when the manifold is coupled to the lung by vacuum, there is typically more motion than that seen in the closed thorax preparation. Alternatively windows developed for use in smaller species may lack a means of arresting cardiorespiratory motion. In this case, observations must be made during respiration or apnea as discussed above.

#### ***11.1.4 Isolated Lung***

To address several of the above-mentioned problems, the isolated pump-perfused lung preparation was developed. In a typical preparation (Fig. 11.4), the main pulmonary artery is cannulated via the right ventricular outflow tract and the left atrium is cannulated via the left ventricle in small species or via the left atrial appendage in larger species. Perfusate (buffer, autologous blood, or a mixture) is pumped into the pulmonary artery with a peristaltic pump and drains passively from the left atrium into a temperature-controlled reservoir. Because the isolated lung has a relatively low metabolic rate and is not attached to a metabolically active animal,  $\text{CO}_2$  production is minimal and due to a lack of  $\text{O}_2$  consumption, there is essentially no alveolar-arterial  $\text{O}_2$  gradient. Thus ventilation with a 6 %  $\text{CO}_2$ -17 %  $\text{O}_2$ -77 %  $\text{N}_2$  gas mixture produces normal arterial blood gas tensions. The lack of metabolic activity also means that ventilation can be suspended for long periods without a significant change in blood gases. In this preparation fine control of arterial pressure, venous pressure and cardiac output can be achieved by changes in perfusion pump flow rate and venous reservoir height. The entire surface area of the lung is also available for observation.

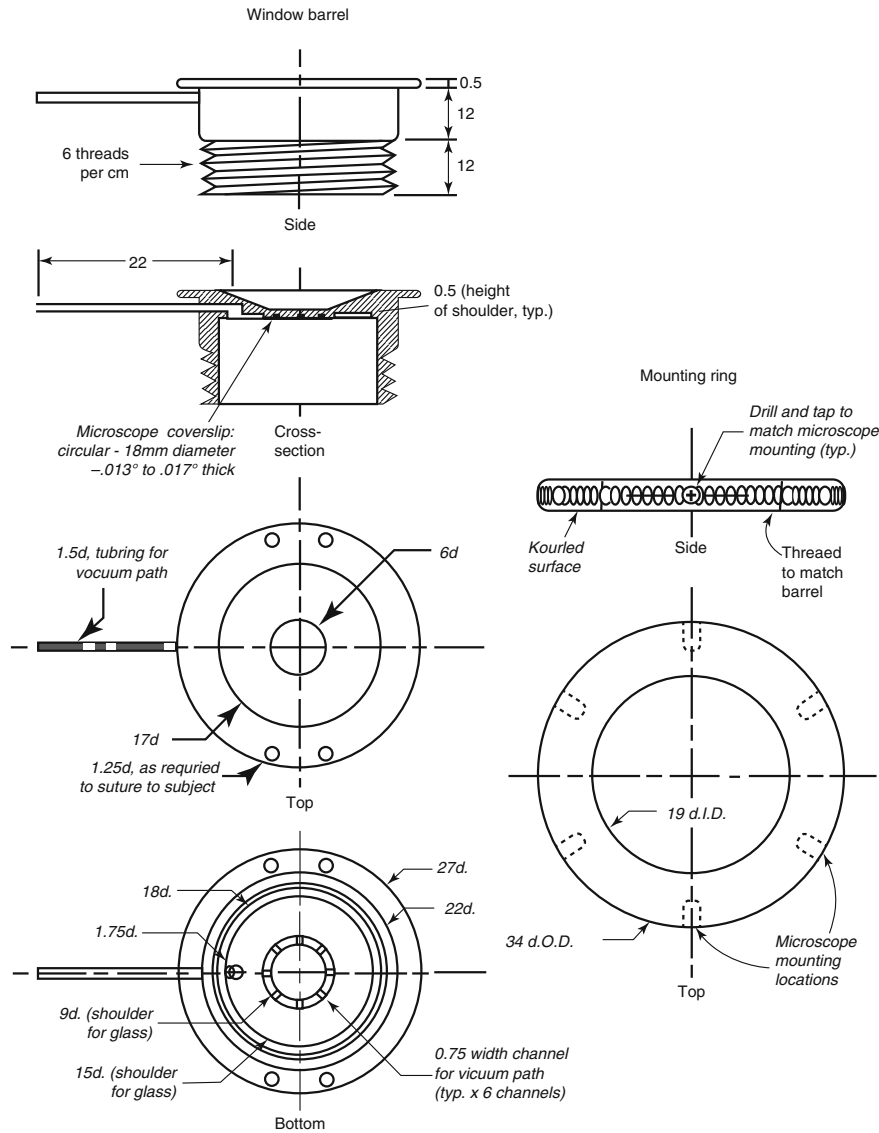
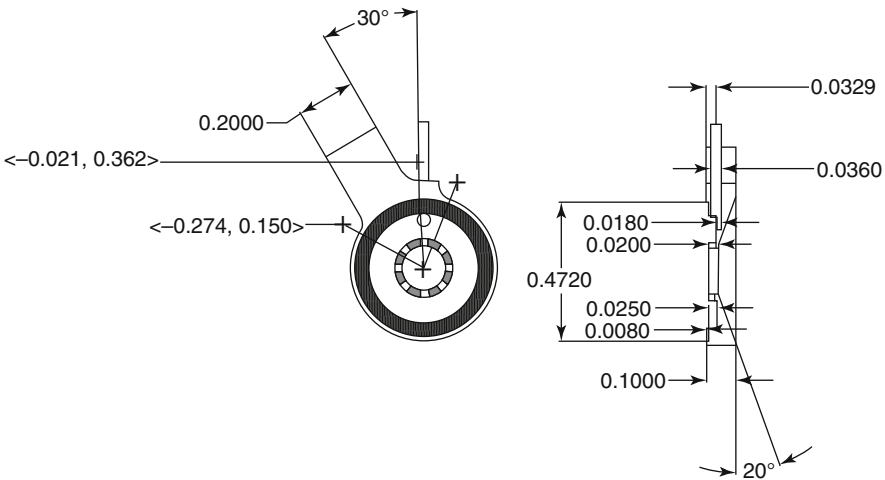


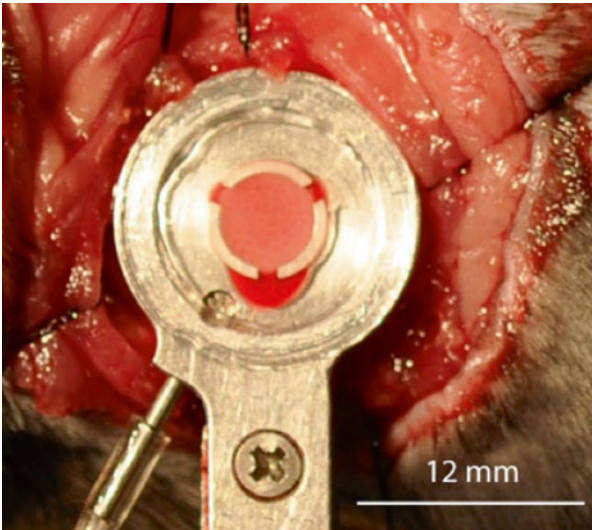
Fig. 11.1 Window for implantation in the rat

Unrestricted access to the great vessels allows for some unique techniques such as the one developed by Bhattacharya and colleagues. A microcatheter (e.g. PE-10) is passed retrograde through a pulmonary vein until it wedges in a small pulmonary vein blocking blood flow to this area. A fluorescent probe is then infused through the catheter to load the microcirculation drained by the vein. After several minutes the catheter is withdrawn and the area is reperfused removing intravascular indicator.



**Fig. 11.2** Manifold for mouse lung

**Fig. 11.3** Lung coupled to window in open mouse thorax



This technique allows loading of a small area of the microvascular endothelium with probe while avoiding significant background levels of circulating indicator.

In spite of its advantages, measurements obtained from the isolated lung vary from the intact animal (closed thorax, lungs perfused by the beating heart) for a number of reasons. First, it is commonly observed that vascular resistance is higher in the pump-perfused lung preparation. Because the distribution of resistance across the pulmonary circulation in the pump-perfused lung is similar to that in the intact animal, microvascular pressure will be higher in the pump-perfused lung resulting in a higher level of recruitment for a given flow rate.

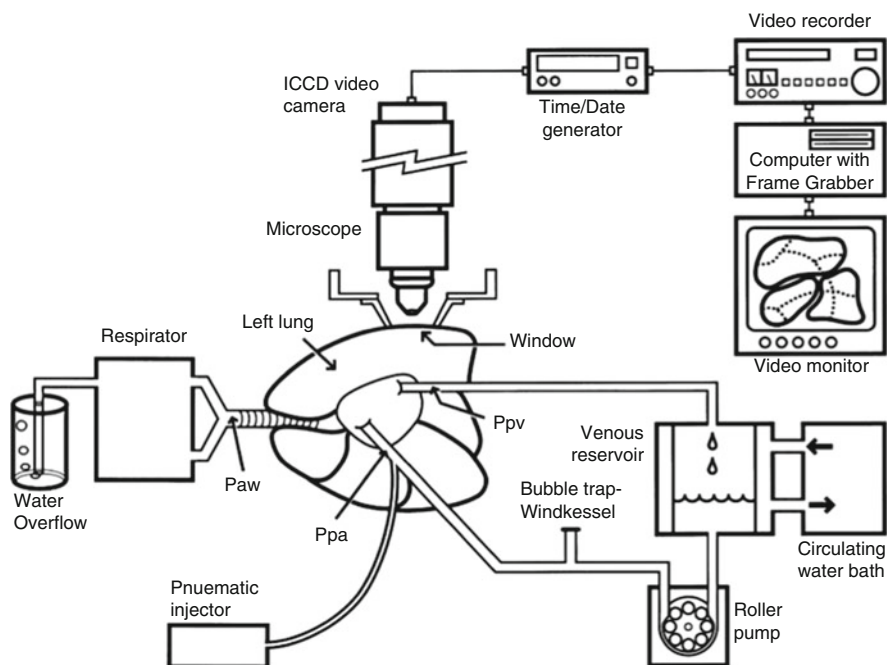


**Fig. 11.4** Pump perfused lung preparation for intravital microscopy

A second problem with the pump-perfused lung arises from exposure of the perfusate to the pump circuit. It is known that complement is activated by both the classical and alternate pathways when heparinized blood is recirculated through an extracorporeal perfusion circuit. Activated complement in turn causes neutrophil activation and sequestration in the pulmonary capillaries. This is a particular problem with studies of neutrophil trafficking in the pulmonary microcirculation. Inflammatory mediators may also alter vascular tone in the vessels supplying and draining the capillary bed.

Because the level of capillary recruitment is highly dependent on the degree of alveolar wall tension, studies of microvascular perfusion may differ between the isolated lung and the intact animal. When alveolar diameters are small and wall tension is low, capillaries begin to open at a low pressure. Recruitment then proceeds rapidly such that all capillaries open with only a small increase in pressure. Under these circumstances, recruitment has been described as sheet-like. A different pattern is observed when alveolar diameter is large and wall tension is high. In this case, recruitment occurs gradually, a segment at a time, over a broad range of pressure. Which of these patterns is observed in the excised lung is dependent on the degree of lung inflation. However, it can be difficult to know how much to adjust inflating pressure to achieve a lung volume equal to that in the closed thorax. Unlike the excised lung, there is a gradient of alveolar size in the lung suspended by negative pleural pressure in the closed chest with the alveoli at the top pulled open by the weight of the lung while those at the bottom are compressed.

The isolated lung is most commonly perfused with a peristaltic pump that produces steady flow. However the lung in the intact animal is perfused with pulsatile flow. In contrast to steady flow, it has been shown that capillary recruitment is nearly double during pulsatile flow. The accompanying increase in the cross sectional area of the capillary bed may explain in part why resistance is lower in the intact lung. Taken together, these observations provide an explanation why previously reported values of microvascular gas exchange reserve in the pump-perfused lung may differ from the intact animal.

### ***11.1.5 Gating and Frame Registration***

In cases where respiratory and cardiac-induced lung motion is not eliminated by a vacuum manifold, ventilation can be synchronized with image acquisition or gated. In this case ventilation is suspended briefly while an image is acquired (1–2 s). Imaging is then paused and ventilation is resumed for a set number of breaths. This cycle then repeats until imaging is complete. Due to a lower frequency of image acquisition, gating inherently decreases temporal resolution. Alternatively motion artifact can be removed in some cases by post acquisition-processing or frame registration. Briefly, pixels are shifted in sequential images to bring them into registration thus eliminating motion (Fig. 11.5).

## **11.2 Major Areas of Investigation**

### ***11.2.1 Gas Exchange Reserve***

The microcirculation of the normal lung has significant gas exchange reserve capacity in three forms: capillary recruitment, capillary distension, and transit time reserve. The first of these, recruitment, exists in the form of capillaries that are not perfused with red blood cells at rest, or even during moderate exercise. As oxygen demand increases, cardiac output and capillary transmural pressure rise causing recruitable capillaries to become perfused. These newly recruited capillaries directly increase gas exchange surface area. Increased capillary transmural pressure also causes distension of recruited capillaries, the second form of reserve, which increases the number of red blood cells in the gas exchange vessels. The third form of reserve, surplus capillary length, occurs because under basal conditions red blood cells become saturated with oxygen after crossing the first third of the capillary bed. The remaining two thirds of capillary length are utilized when red blood cell velocity increases, forcing the cells to move farther across the capillaries before they are completely saturated. This form of reserve is limited by the rate of diffusion of oxygen from alveolar gas to the hemoglobin in red blood cells. If transit times

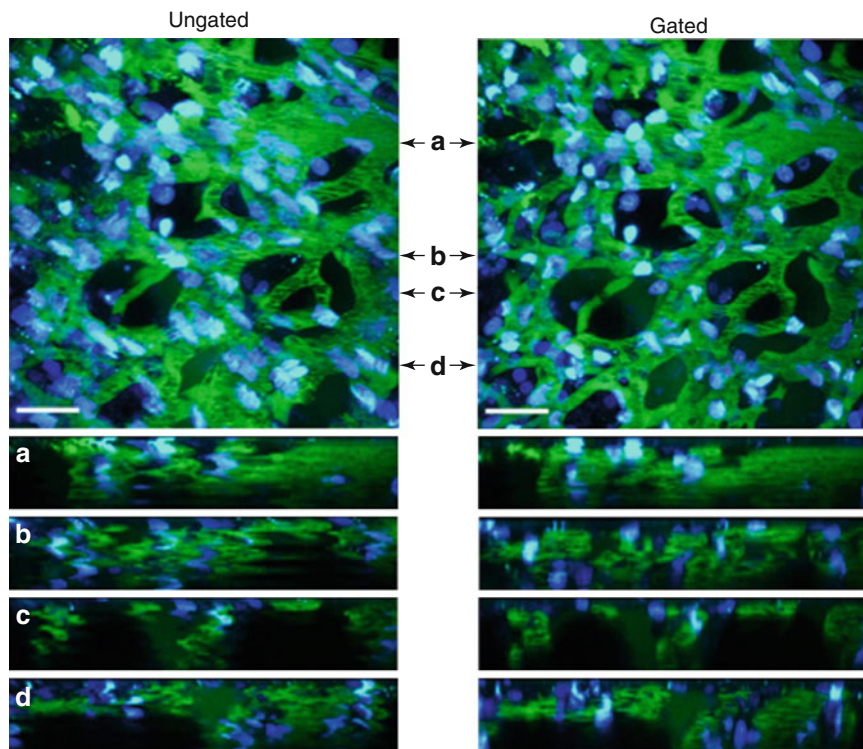


**Fig. 11.5** Gated imaging eliminates motion for maximum clarity in 3-dimensional TPM reconstructions. Comparison between non-gated (**a**) and gated (**b**) image acquisition of an identical field of view showing FITC-labeled (*green*) alveolar microvasculature in the intact rat. Reconstructions in the x-z orientation correspond to the indicated slice regions (**c**, **d**) from the 3-dimensional images. Nuclei are stained with intravenously-administered Hoechst 33258 dye (blue). Scale bars = 25  $\mu$ m (Reproduced from (Presson et al. 2011) with permission)

become too short ( $\sim < 0.25$  s under normal conditions), red blood cells may exit the capillary bed incompletely saturated. However, changes in capillary transit time are linked to the degree of recruitment and distension through their effect on capillary volume. For a given pulmonary blood flow, capillary transit time increases as capillary volume increases. In this way, recruitment and distension limit the fall in capillary transit times. Further, the transit time distribution becomes more homogeneous as pressure and flow increase with the longest transit times decreasing more than the shorter ones. This effect is presumably the result of more homogeneous recruitment and distension of pulmonary capillaries. Together these two effects help to prevent incompletely saturated red blood cells from exiting the pulmonary circulation.

The important relationships between these three forms of reserve capacity have been investigated in various species using a number of techniques. However because of technical limitations, measurement of microvascular reserve in the rat has generally



been limited to isolated pump perfused preparations or fixed tissue which may not accurately reflect reserve capacity in the intact animal (closed thorax, lungs perfused by the beating heart) for a number of reasons. For example, vascular resistance is typically increased in the isolated lung which may in turn effect capillary transmural pressure and thus the degree of recruitment and distension. Further, lung volume in the isolated lung, which has an important influence on microcirculatory perfusion through its effect on alveolar wall tension, may vary from the lung suspended in the closed thorax. Therefore actual values for pulmonary micro-vascular reserve in the intact rat remain uncertain. This is an important gap because a number of models of lung pathology (e.g. emphysema, pulmonary hypertension, and lung transplantation) are based on studies in this species. To fill this gap, we have developed an intravital microscopy model of the pulmonary microcirculation in the intact rat, and reported the first measurements of pulmonary microvascular reserve using this model (Presson et al. 2011).

### ***11.2.2 Leukocyte Trafficking***

One of the most exciting applications of intravital lung microscopy in the intact animal is the opportunity to study leukocyte trafficking. This achievement is due to elimination of leukocyte activation typically initiated by contact with foreign surfaces in the isolated pump perfused lung preparations. Therefore, leukocyte trafficking as a marker of both PMN and pulmonary endothelial cell activation during inflammation can be measured by quantifying leukocyte adhesion, rolling, and extravasation from the microcirculation into alveolar spaces. To determine leukocyte trafficking using TPM, leukocytes can be labeled either with intravenous rhodamine 6G for fluorescence imaging, or via transgenic expression of fluorescence proteins under cell-specific promoters (Fig. 11.6).

### ***11.2.3 Vascular Permeability***

Changes in vascular permeability are relevant to the development of pulmonary edema, lung inflammation, and infection. Typically, measurement of increased lung vascular permeability have relied on measuring wet and dry lung weight, or the degree of extravasation of injectable dye into airways. These measurement are tedious and imprecise. The intravital monitoring of intravascularly injected dye into the alveolar spaces offers the advantages of direct observation of increased permeability of the lung microcirculation upon application of an edemagenic agonist and that of quantification of kinetics and degrees of leaked plasma (Fig. 11.6). The limitations of this technique are the relatively short observation time, which is dependent on the duration of the preparation (hours) and the small area of observation of only dozens of alveoli, which may miss heterogeneous disease distributions.

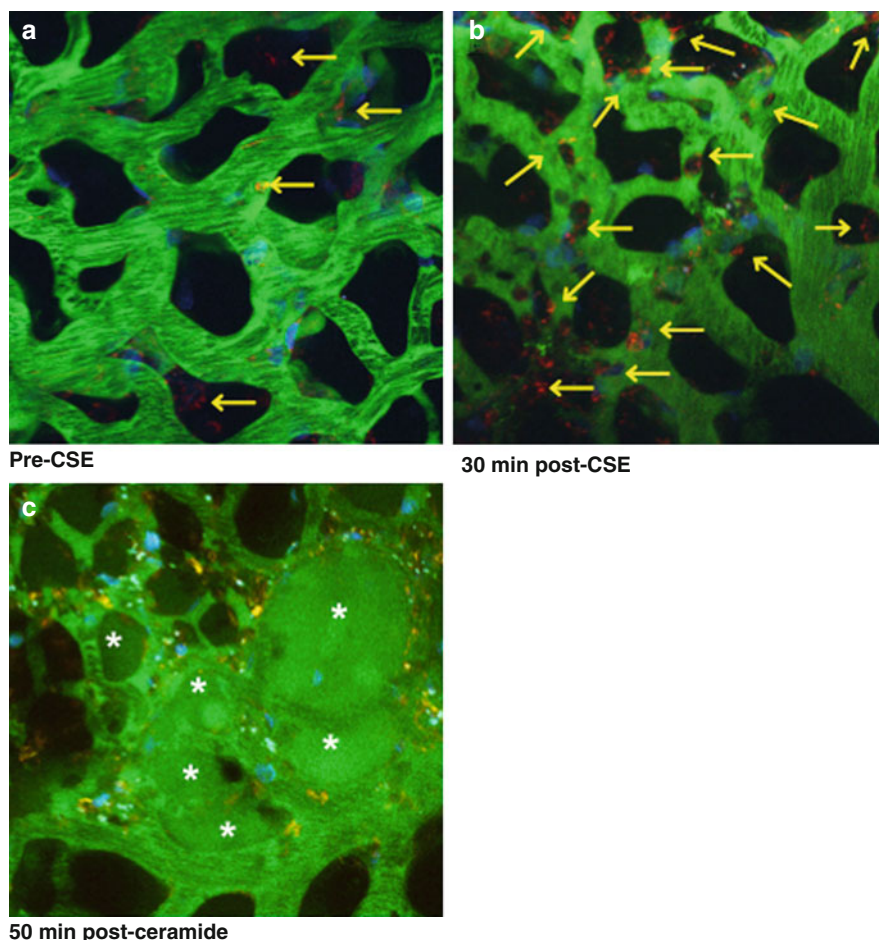


**Fig. 11.6** Capturing leukocyte trafficking and plasma extravasation in real-time in the pulmonary microvasculature of a living rat. Three-dimensional reconstruction of FITC-labeled vessels (*green*) surrounding alveoli (*dark regions*) and Rho-G6-labeled neutrophils (*orange*) imaged in intravital 2-photon microscopy before (a) and (b) 30 min after intratracheally-administered cigarette smoke extract (CSE), or 50 min after intravenous administration of ceramide 16:0 PEG (c). Nuclei are stained with intravenously administered Hoechst 33258 dye (blue). Note increasing neutrophil trafficking (*yellow arrows*) and plasma extravasation into airspaces (*asterisks*)

#### 11.2.4 Vasoreactivity

By injecting fluorescent plasma markers, such as labeled albumin, one can measure vascular diameters of specific vessels before and after interventions and directly gauge vascular constriction and dilation (Fig. 11.7). These measurements may be useful for screening of drug effects, as well as direct observation of ventilation perfusion relationship, for example hypoxic vasoconstriction.

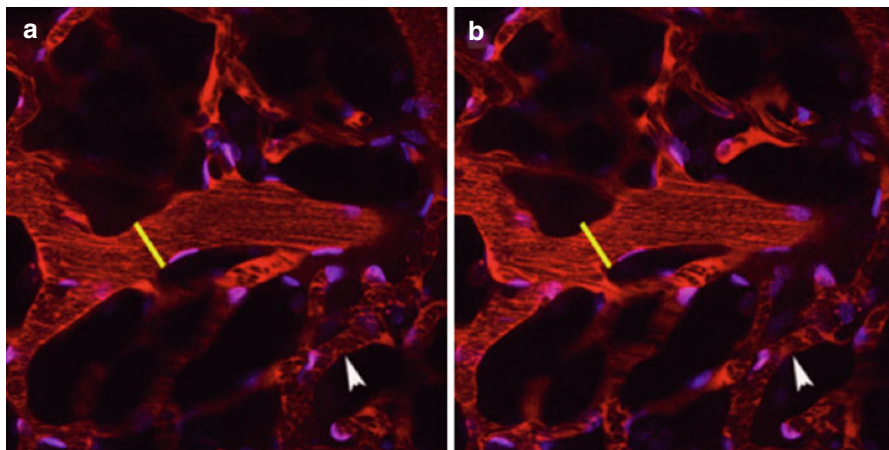


**Fig. 11.7** Vasoconstriction of a TR-labeled (red) pulmonary arteriole in response to hypoxia ( $\text{FiO}_2$  14 %) captured in an intact rat in real-time using 2-photon intravital microscopy during (a) Normoxia (b) Hypoxia (1 min). Note narrowing (constriction) of the pulmonary arteriole in hypoxia relative to the overlaid yellow line, which represents the diameter of the vessel during normoxia. Capillaries (white arrow head) surrounding normal alveolar airspaces (dark) remained unchanged in diameter during hypoxia. Nuclei are stained with intravenously administered Hoechst 33258 dye (blue) and circulating cells appear as black streaks within the vessels

### 11.2.5 Cellular Movement

Cellular movement such as migration/homing or engulfment (Megens et al. 2011), inter-cellular connections (Islam et al. 2012), as well as subcellular pathology and physiology such as structural details (e.g. endothelial glycocalyx (Yang et al. 2013)) molecular trafficking, and signal transduction are now made possible with improved resolution of microscopy and stability of lung preparations. Some of these advances have been recently reviewed (Kuebler 2011; Looney and Bhattacharya 2013). As an example, NO production and cellular localization can be distinctly visualized with TPEM, with minimal or no interference from lung autofluorescence (Fig. 11.8). Recently, inter-cellular waves of calcium signaling have been visualized using intravital lung microscopy (Westphalen et al. 2014).

In conclusion, there are exciting new developments in lung intravital microscopy which allow the visualization of previously unimagined details in the lung in real time. The cost and technical complexity of preps, the relative superficial sub pleural visualization, relatively short duration of real time monitoring, and the potential sampling error of non-homogeneous lung processes remain challenges to the widespread utilization of intravital imaging in lung research. As technology advances, it is likely these hurdles will be soon eliminated and intravital imaging in the intact animal and possibly in human lungs will become routine.

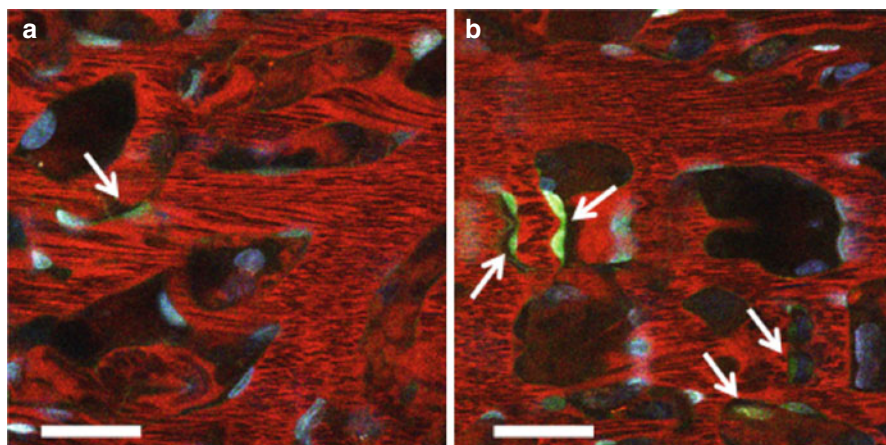


**Fig. 11.8** Increase in DAF-2DA-labeled nitric oxide fluorescence (NO indicator) (*green, arrows*) in TR-labeled (*red*) pulmonary microvasculature in response to i.v. sodium nitroprusside (SNP). Images were captured in an intact rat in real-time using 2-photon intravital microscopy: (a) pre-SNP (b) post-SNP. Nuclei are stained with intravenously administered Hoechst 33258 dye (blue) and circulating cells appear as *black streaks* within the vessels. Scale bar=25  $\mu$ m

**Acknowledgements** We would like to thank Wiltz Wagner Jr., PhD for his mentoring and key role in pioneering the lung intravital imaging technique.

## References

- Islam MN et al (2012) Mitochondrial transfer from bone-marrow-derived stromal cells to pulmonary alveoli protects against acute lung injury. *Nat Med* 18:759–765. doi:[10.1038/nm.2736](https://doi.org/10.1038/nm.2736)
- Kuebler WM (2011) Real-time imaging assessment of pulmonary vascular responses. *Proc Am Thorac Soc* 8:458–465. doi:[10.1513/pats.201101-005MW](https://doi.org/10.1513/pats.201101-005MW)
- Looney MR, Bhattacharya J (2013) Live imaging of the lung. *Annu Rev Physiol*. doi:[10.1146/annurev-physiol-021113-170331](https://doi.org/10.1146/annurev-physiol-021113-170331)
- Megens RT, Kemmerich K, Pyta J, Weber C, Soehnlein O (2011) Intravital imaging of phagocyte recruitment. *Thromb Haemost* 105:802–810. doi:[10.1160/TH10-11-0735](https://doi.org/10.1160/TH10-11-0735)
- Presson RG Jr et al (2011) Two-photon imaging within the murine thorax without respiratory and cardiac motion artifact. *Am J Pathol* 179:75–82
- Wagner WW Jr (1969) Pulmonary microcirculatory observations in vivo under physiological conditions. *J Appl Physiol* 26:375–377
- Wearn JT et al (1934) The normal behavior of the pulmonary blood vessels with observations on the intermittence of the flow of blood in the arterioles and capillaries. *Am J Physiol* 109:236–256
- Westphalen K et al (2014) Sessile alveolar macrophages communicate with alveolar epithelium to modulate immunity. *Nature*. doi:[10.1038/nature12902](https://doi.org/10.1038/nature12902)
- Yang Y, Yang G, Schmidt EP (2013) In vivo measurement of the mouse pulmonary endothelial surface layer. *J Vis Exp* 72:e50322. doi:[10.3791/50322](https://doi.org/10.3791/50322)

## Chapter 12

# Intravital Microscopy for Molecular Imaging in Cancer Research

Hongmei Yu and Sanjiv Sam Gambhir

**Abstract** Molecular imaging is an important tool in life sciences research and for clinical diagnosis and treatment. Among numerous imaging modalities, intravital microscopy (IVM) provides the best imaging spatial resolution *in vivo* and allows visualization of cellular and subcellular structures and functions. Because of its high resolution and the large number of available imaging agents, IVM has been used increasingly for the study of *in vivo* processes in many different fields. The application of IVM in cancer research and cancer treatment response assessment has been particularly fruitful. These IVM studies have disclosed that the cellular and subcellular dynamics during tumor progression and drug treatment *in vivo* are very different from those under *in vitro* conditions. Since the findings from IVM studies are obtained directly from intact living organisms, they may provide much more relevant information helpful to drug discovery and evaluation in clinics. In this chapter, we will briefly introduce the concepts of molecular imaging and the unique features of IVM. We will then highlight the most current IVM research in cancer biology and cancer drug response at the tissue, cellular and subcellular levels. We will end this chapter by outlining the future directions of IVM research.

**Keywords** Intravital imaging • Molecular imaging • Cancer • Drug delivery • Drug response • Imaging agents • Tumor microenvironment • Tumor stroma • Tumor circulation • Hypoxia • Tumor PO<sub>2</sub> • Tumor pH • Tumor extracellular matrix • Tumor cell heterogeneity • Cell tracking

## Abbreviations

<sup>18</sup> F-FDG	Fluorodeoxyglucose
CARS	Coherent anti-stokes raman scattering
CCL1	Chemokine (C-C motif) ligand 1

---

H. Yu • S.S. Gambhir (✉)

Molecular Imaging Program at Stanford, Stanford University, Stanford, CA, USA

Department of Radiology, Stanford University, Stanford, CA, USA

e-mail: [sgambhir@stanford.edu](mailto:sgambhir@stanford.edu)

© Springer Science+Business Media Dordrecht 2014

233

R. Weigert (ed.), *Advances in Intravital Microscopy*:

*From Basic to Clinical Research*, DOI 10.1007/978-94-017-9361-2\_12



CT	Computed tomography
DEVD	Aspartic acid-glutamic acid-valine-aspartic acid
ECM	Extracellular matrix
FAD	Flavin adenine dinucleotide
FCS	Fluorescence Correlation Spectroscopy
FLIM	Fluorescence-lifetime imaging microscopy
FRAP	Fluorescence recovery after photobleaching
FRET	Förster resonance energy transfer
GFP	Green fluorescent protein
IR/NIR	Infrared/ Near-infrared
IVM	Intravital microscopy
mKO2	Monomeric Kusabira-Orange 2
MMP	Metalloproteinase
MRI	Magnetic resonance imaging
NADH	Nicotinamide adenine dinucleotide
OFDI	Optical frequency domain imaging
PARP-1	Poly(ADP-ribose) polymerase-1
PARPi	Poly(ADP-ribose) polymerase-1 inhibitor
PET	Positron emission tomography
RFP	Red fluorescent protein
ROCK	Rho-associated protein kinase
scVEGF	Single-chain vascular endothelial growth factor
SERS	Surface enhanced Raman scattering
SHG	Second harmonic generation
SNR	Signal-to-noise ratio
SPECT	Single-photon emission computed tomography
TGF- $\beta$	Transforming growth factor beta
VEGF	Vascular endothelial growth factor
YFP	Yellow fluorescent protein

## 12.1 Introduction to Molecular Imaging

### 12.1.1 Definition

Modern molecular imaging is defined as the noninvasive, real-time visualization of biochemical events at the tissue, cellular and molecular level in living organisms (James and Gambhir 2012). This makes molecular imaging fundamentally different from traditional clinical imaging in which mostly anatomic information is obtained. The rich information from modern molecular imaging is greatly improving the early detection, treatment selection, treatment management, and prognostication of many diseases. These achievements are mainly attributed to the rapid advancement of the two essential components of modern molecular imaging - imaging modalities and imaging agents.



### ***12.1.2 Molecular Imaging Instrumentation***

There are many imaging modalities. The classical ones include PET, SPECT, MRI, CT, ultrasound and optical imaging modalities. Many are often used in both clinical and preclinical settings. Other novel imaging modalities include fluorescence optical microscopy, bioluminescence optical imaging, photoacoustic imaging, and Raman spectroscopy. This latter group is used primarily for preclinical studies at the current time. Each of the above imaging modalities has its own strengths and limitations in terms of imaging depth, sensitivity, costs, and spatial and temporal resolution (James and Gambhir 2012). These properties largely determine the specific applications of each modality. For instance, intravital microscopy (IVM) gives the highest spatial resolution (1–10  $\mu\text{m}$  or even sub-micrometer) and great flexibility for multiplexed imaging (monitoring multiple events simultaneously). The two properties are especially desired in studying cellular and subcellular events in living subjects. In the case of cancer, there exist large cellular and subcellular heterogeneities; each tumor and tumor cell can have very different pathological characteristics, activities and drug responses. Characterization of these heterogeneous elements and the underlying molecular mechanisms in vivo is the key to understanding the behavior of various cancers and designing effective treatments. These pressing needs demand high resolution imaging systems, such as IVM. In Part 2, we will discuss the current status of IVM in detail.

### ***12.1.3 Molecular Imaging Agents***

Molecular imaging agents (contrast agents or probes) are special classes of molecules and particles which bind or otherwise interact with their biological targets and enable non-invasive visualization of the targeted events. Every imaging agent needs to have sufficient specificity, sensitivity, and optimal pharmacokinetic properties for a specified in vivo imaging application. In order to comply with these requirements, these agents are designed to have at least two functional groups: one for the specific binding or reacting with the targets (e.g., small molecules, peptides, aptamers, antibodies or antibody fragments) and the other for providing signal(s) for its detection (e.g., radioisotopes, fluorophores, optical absorbers, inelastic light scattering materials). These imaging agents can be classified as non-targeted and targeted imaging agents (Fig. 12.1). Non-targeted imaging agents, such as fluorescent beads or particles, emit signal continuously independent of their binding states (Fig. 12.1a). The specificity of these agents is largely determined by their preferential accumulation into specific tissues. Targeted agents are designed to specifically bind to or interact with their targets. The targeting mechanism can involve specific antibodies for antigens, substrates for enzymes, ligands, agonists or antagonists for receptors, etc. (Fig. 12.1b) In particular, smart imaging agents can activate or switch

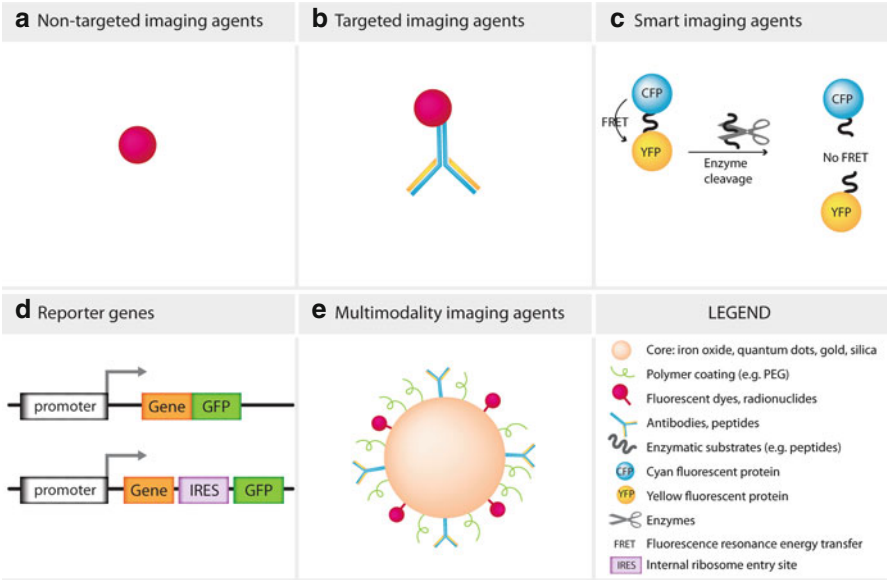


**Fig. 12.1** Major types of molecular imaging agents (a) Non-targeted imaging agents, such as fluorescent dyes, nanoparticles (b) Targeted imaging agents, such as fluorescent molecule conjugated antibodies; (c) smart imaging agents, such as fluorescence resonance energy transfer (FRET) caspase sensitive imaging agent. This caspase imaging agent is constructed by linking the cyan fluorescent protein (CFP) and yellow fluorescent protein (YFP) with a caspase-specific substrate (DEVD). Cleavage of DEVD by activated caspases results in the loss of fluorescence resonance energy transfer from CFP to YFP, thus reduced FRET signal. (d) Reporter genes, such as fusion reporter genes (*top*) and IRES-mediated bi-cistronic reporter genes (*bottom*). The fusion gene produces one single transcript and one polypeptide, whereas IRES-mediated bi-cistronic reporter gene produces one single transcript but two different polypeptides. (e) Multimodality imaging agents, such as a nanoparticle with an iron oxide core, a polymeric coating, and antibody and fluorescent dye conjugates for targeted MRI and optical imaging

signals exclusively in the presence of their intended *target*, which minimizes background signals and increases sensitivity (Fig. 12.1c). Reporter genes can be used to measure the location and levels of expression of specific genes of interest (Fig. 12.1d). Therefore, targeted imaging agents have increased specificity. Lastly, multimodality imaging agents are under rapid development (Fig. 12.1e). These agents contain in their backbone two or more of radioisotopes, fluorescent molecules, or nanoparticles that enable simultaneous PET, MRI, CT and/or optical imaging. Thus far, there are approximately 1,170 agents listed in the NCBI Molecular Imaging and Contrast Agents Database (MICAD). In this database, 41 % are PET imaging agents, 30 % are PET/CT imaging agents, 12 % are optical imaging agents, 9 % are MRI imaging agents, 3 % are multimodality imaging agents, 2 % are ultrasound imaging agents, and 1 % are x-ray/CT imaging agents. This variety of imaging agents makes it possible to visualize multiple biological targets and processes *in vivo*.

## 12.2 Basics of Intravital Microscopy (IVM)

Intravital Microscopy (IVM) is a unique molecular imaging modality that enables live animal imaging at microscopic spatial resolution. In this section, we discuss why IVM is such a unique modality in molecular imaging, and the requirements for conducting IVM work.

### 12.2.1 *Benefits of IVM in Molecular Imaging*

The key strength of IVM over other modalities is its high spatial resolution. Imaging resolution critically affects early detection, diagnosis, and therapy monitoring. However, most molecular imaging modalities, such as CT, MRI, PET, SPECT and ultrasound, provide images with limited resolution ( $>1.0$  mm). In contrast, IVM provides a spatial resolution of  $1\text{--}10\text{ }\mu\text{m}$  which is critically required to resolve cellular and subcellular structures. Another key feature of IVM is that IVM studies focus on *in vivo* processes, which can sometimes be readily translated into the clinic. The other major advantage of IVM is the diversity of available imaging agents, which are mainly fluorescence imaging agents. This means that many cellular and subcellular processes and their molecular mechanisms can be studied *in vivo* with IVM. These benefits allow us to study critical biological questions, in a way that was previously impossible, to understand the development of many diseases. For example, in oncology, we can study the spatial and temporal relation between different tumor cells and stromal cells, their dynamic interactions, and the response of tumor cells to certain treatments. As much current cancer research efforts focus on cellular and subcellular structures and functions, IVM work can serve as an important tool for studying these processes within the context of the entire intact microenvironment. Therefore, IVM is a unique and essential molecular imaging modality. In summary, the key strengths of IVM are:

1. Relatively high spatial resolution ( $1\text{--}10\text{ }\mu\text{m}$ )
2. A wide array of imaging agents
3. Multiplexed imaging capability

### 12.2.2 *IVM Instrumentation*

Using appropriate IVM instrumentation, imaging techniques, and agents are critical for successful IVM studies (Fig. 12.2). IVM instrumentation can include linear (e.g., single-photon confocal) and nonlinear microscopies (e.g., two-photon and other multiphoton systems), coherent anti-stokes raman scattering (CARS), fluorescence lifetime imaging microscopy (FLIM), optical frequency domain imaging

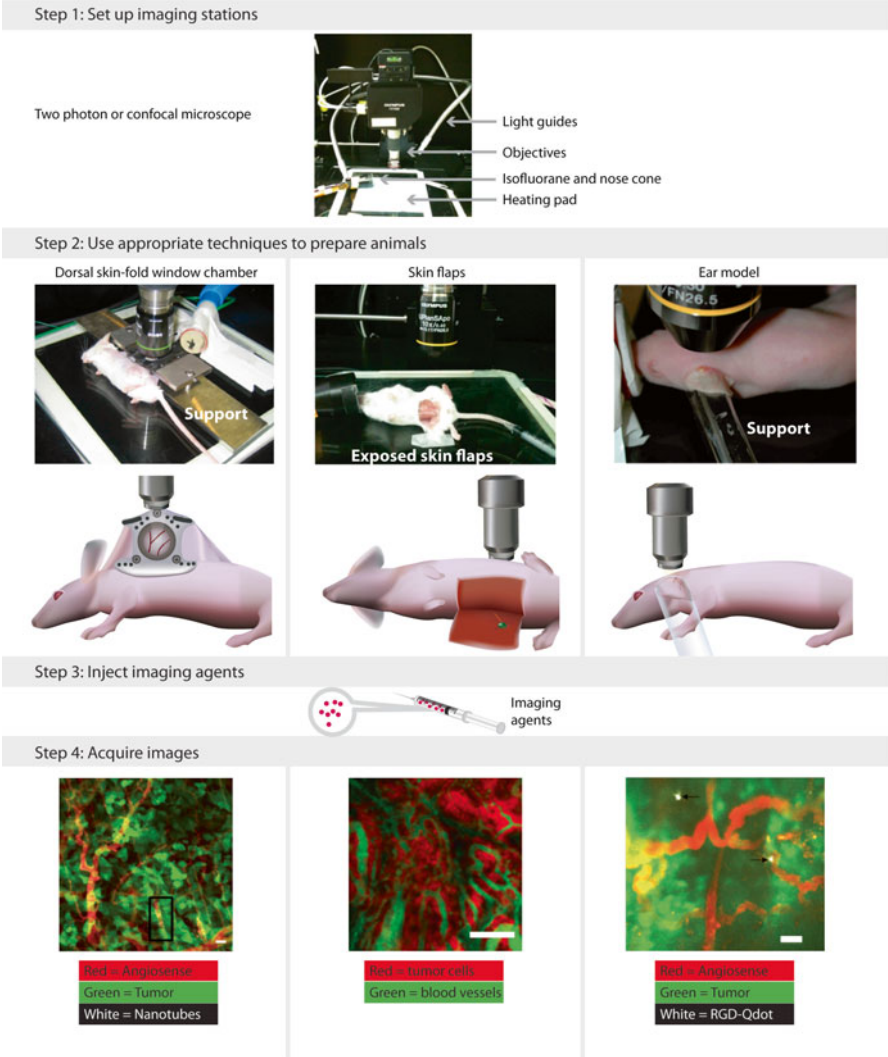


**Fig. 12.2** Typical workflow for IVM imaging: *Step 1*, set up imaging stations, such as two photon, and confocal microscopes with the appropriate objectives, light guides, heating pat and anesthesia system. *Step 2*, prepare animals for IVM imaging with the dorsal skin-fold window chamber model (*left*), skin flaps (*middle*), and ear model (*right*). In the dorsal skin-fold window chamber model and the ear model, special metal or glass supports are used to position the window chamber and the ear. *Step 3*, inject imaging agents into animals (e.g., intravenously, intradermally). *Step 4*, acquire images with the control software. An image acquired through a dorsal skin-fold window chamber with an IVM100 confocal system shows that RGD-Single walled nano-tubes bind to tumor blood vasculature (scale bar, 50  $\mu\text{m}$ ) (*bottom left*) (Smith et al. 2013) (Copyright 2013 Elsevier). The image acquired from an exposed mammary tumor with an IVM100 confocal system shows tumor angiogenesis (scale bar, 500  $\mu\text{m}$ ) (*bottom middle*). The image acquired through ears with an IVM100 confocal system shows RGD-Qdots bind to SKOV-3 tumor blood vessels (scale bar, 50  $\mu\text{m}$ ) (*bottom right*) (Smith et al. 2010) (Reprinted by permission from John Wiley & Sons)

**Table 12.1** Comparison of one-photon confocal and two-photon systems

	One-photon confocal	Two-photon
Removal of out-of-focus light	Pin-hole-based	Simultaneous absorption of two photons
Light source	Gas laser, UV and visible	Solid state laser
	Continuous laser	Pulsed laser (e.g., Ti:S resonator)
Excitation light and power	Fixed or tunable wavelength (405, 488, 648 nm, 0.01–0.1 W)	Tunable wavelength (690–1,200 nm, 0.4–2.5 W)
Detection mode	Photon multiplier tube (PMT) or CCD	PMT
Photo-toxicity, photo-bleaching	High	Low
Imaging depth	~100 µm	300–600 µm
Spatial resolution	Good	Good
Temporal resolution	Conventional: ~4 frames/s (fps)	Conventional: 4–30 fps
	Resonant Scan: 30 fps	Similar scanning techniques as in confocal are under development
	Swept filed: 100–1,000 fps	
	Spinning disk: 2,000 fps	
Cost	\$50,000–\$100,000	\$100,000–\$250,000

(OFDI), etc. Among these, confocal microscopy and two-photon microscopy are the most commonly used IVM instrumentation types. Both systems enable imaging of cellular and subcellular events in living systems, but imaging principles and system setups are different between the two.

Two-photon systems (2P) offer many benefits for *in vivo* imaging, including: (1) relatively deep tissue imaging due to decreased tissue absorption of longer wavelength light; and (2) less out-of-focus light due to the reduced two-photon excitation outside of the focal volume. 2P often requires objectives with high numerical aperture (NA) and high laser power to collect sufficient signal and obtain high Z-resolution. In practice, objectives with high NA have smaller working distances, which make imaging beyond 300 µm hard to achieve. Additionally, a high powered IR laser can overheat tissue and also saturate the detectors; consequently, infrared light blockers are often installed to protect systems from IR damage. This poses a significant problem considering the great interest and rapid progress in developing infrared and near infrared (IR/NIR) fluorophores for *in vivo* imaging. Compared with the 2P system, 1P systems offer comparable or better spatial resolutions but decreased imaging depth. Additional benefits with 1P are that there are many well-characterized imaging agents, options for lasers, objectives and built-in functionalities (Förster resonance energy transfer FRET, Fluorescence recovery after photobleaching FRAP). Therefore, the confocal microscope is a good choice for imaging thin tissues. The major differences between confocal and 2P systems are listed in Table 12.1.

### 12.2.3 IVM Imaging Techniques

Using the appropriate imaging technique is another key for successful IVM studies (Fig. 12.2). IVM requires the excitation and emission lights to be delivered and collected in a narrow optical path, which is very different from other whole body imaging modalities such as PET, CT and MRI. Furthermore, motions from heart-beat and respiration can have deleterious effects on high resolution IVM imaging. Therefore, tissues/organs to be imaged with IVM need to be effectively prepared to: (1) allow access of the optical components; (2) minimize motion artifacts; and (3) minimize perturbation of organ functions. To achieve these goals, three types of tissue preparations have been developed: window chambers, exposed tissue preparations, and *in situ* preparations (Fig. 12.2). In Table 12.2, we summarize these techniques and compare their strengths and limitations. For additional technique details, please refer to the review in (Jain et al. 2011) and other chapters (IVM: Principles and Technology).

### 12.2.4 IVM Imaging Agents

The third key requirement for IVM studies is the imaging agent (Figs. 12.1 and 12.2). In IVM studies, imaging agents critically help to increase the optical contrast or signal-to-noise ratio (SNR): the difference in intensity (or other measures) between the objects of interest and the adjacent background. Without sufficient optical contrast or SNR, it is difficult to obtain high resolution images, particularly under *in vivo* conditions where many endogenous molecules can give strong auto-fluorescence background (e.g., nicotinamide adenine dinucleotide NADH, flavin adenine dinucleotide FAD, collagen). Some endogenous contrast molecules can be used for IVM work. For examples, collagen produces a unique second harmonic generation (SHG) signal; lipids generate strong Raman signal, etc. But these applications are limited. For most applications, exogenous contrast agents are needed in order to image many different cell populations, cellular, and subcellular components. For IVM work, exogenous contrast agents can be either non-targeted or targeted optical imaging agents (Fig. 12.1). The targeted exogenous IVM imaging agents usually have one fluorescent functional component and another functional component for specific interaction with the target(s) of interest. Both functional components help to obtain high optical contrast. With higher molar extinction coefficients and quantum yields, the fluorescent components provide much higher fluorescence signal than the tissue autofluorescence background. (Molar extinction coefficient is a measurement of how strongly an imaging agent absorbs light at a given wavelength. Fluorescence quantum yield is the ratio of photons absorbed to photons emitted through fluorescence). Quantum dots, in particular, have extinction coefficients 10–50 times larger than fluorescent dyes and thus generate very high optical contrast for IVM work. IR/NIR fluorescent molecules (600–1,000 nm) are also very useful as the absorption



Table 12.2 IVM imaging techniques

Technique	Specific method	Examples (selected)	Strengths	Limitations
Window chambers	Dorsal skinfold	Lehr et al. (1993), Brown et al. (2010), Palmer et al. (2011), Li et al. (2009)	Long-term imaging	Some studies are not carried in orthotopic & natural environments
	Abdominal	Ritsma et al. (2013)	Stable and high resolution imaging	Spatial and mechanical constraints for tumor growth & other biological processes
	Mammary	Kedrin et al. (2008)	Easy registration	Inflammation after window implantation, the exudate can cover windows
	Cranial	Grinvald et al. (1991)		Limited field of view
	Lymph node	Ito et al. (2012)		Most windows are not commercially available
Exposed tissues	Mammary fat pad	Kotsuma et al. (2012)	Orthotopic sites	Technically challenging
	Liver	Tanaka et al. (2012)	Relatively easy and fast procedures	Frequent and long term imaging difficult (tissue damage and scar formation after repeated exposure)
	Pancreas	Coppieters et al. (2010)		Prone to motion artifacts
	Lung	Looney et al. (2011)		Hard for high resolution imaging & registration
	Heart	Lee et al. (2012)		Limited organs/tissues
In situ preparation	Cornea	Imanishi et al. (2004)		Invasive, sometimes lethal
	Eye model	Steven et al. (2011)	Little/no surgery involved	Limited to those superficial tissues
	Tail model	Leu et al. (2000)	Long-term & repetitive imaging	Sometimes non-orthotopic sites (e.g., tumors)
	Ear model	Hoshida et al. (2006), Smith et al. (2008)		

and autofluorescence of endogenous biomolecules in the UV/Vis region are high (Weissleder and Ntziachristos 2003). IR/NIR fluorescent molecules are less prone to interfering absorption and fluorescence from tissues, have reduced scattering, and enable enhanced tissue penetration. These properties can greatly help to overcome some limitations of IVM. However there are relatively few NIR fluorescent agents currently available. Besides phthalocyanines, cyanine and squaraine dyes (Escobedo et al. 2010), there are only a few NIR fluorescent proteins with bacterial phytochrome-based NIR fluorescent proteins being only recently reported (Filonov et al. 2011). Additional functional components for targeting can be antibodies or antibody fragments, peptides or molecular substrates. These groups enable the imaging agents to preferentially localize to their targets rather than the background and therefore enhance the contrast. Other functional units (e.g., polyethylene glycol) that increase the circulation half-life and uptake of the agents can further improve the imaging contrast.

Many exogenous IVM imaging agents are available for high contrast IVM imaging of specific tissues, cellular, and subcellular events. New probes are continuously being developed. It is expected that IVM studies will be greatly empowered by future probes with: (1) IR and NIR spectrum; (2) photo-conversion capability; (3) smart detection; (4) self-amplification; (5) multimodality imaging and clinical translation potential. In the next sections, we will discuss specific applications of these IVM tools in cancer research.

## 12.3 IVM Applications

IVM has been applied in many research areas, including immunology, developmental biology, neuroscience, and cancer biology. These IVM studies have greatly improved our understanding of various human diseases and have helped build the IVM toolbox. In subsequent discussions, we will focus on IVM studies in the cancer field. We will highlight some novel imaging agents and techniques being developed, and elaborate on how they are applied in studying cancer biology and cancer drug response at the tissue level and at the cellular and subcellular levels.

### 12.3.1 *Imaging Tumors at the Tissue Level*

Tumors are abnormal organs with multiple cell populations co-evolving with their microenvironment (Hanahan and Weinberg 2011; Egeblad et al. 2010). This notion highlights the complicated composition, organization and development of many solid tumors. Indeed, tumors often have multiple tumor cell subpopulations and non-tumor stromal cell types, non-cellular components (e.g., soluble growth factors, cytokines; extracellular matrix ECM), and functional units (blood vessels and lymphatics). These components interact with each other, and together they create a

tumor microenvironment of complicated circulatory systems, pH and oxygen profiles, ECM structure and other chemo-mechanical factors. Mapping and characterizing these factors is the first step in understanding the roles of the tumor microenvironment in tumor development and treatment response.

### 12.3.1.1 Circulatory System

Solid tumors often have abnormal circulation and this abnormal circulation is critical to tumor hypoxia, acidosis, high interstitial pressure, lymphangiogenesis, tumor progression and metastasis. IVM has become a major tool for high resolution analysis of the distribution, structure and functions of tumor circulation. Common imaging agents used for these assays are fluorescently labeled macromolecules (e.g., IgG, albumin, dextran, and fluorescent beads and polymers). These imaging agents are either intravenously injected to analyze the blood vessel functions or subcutaneously (or intradermally) injected to image the lymphatic functions (Padera et al. 2002; Hoshida et al. 2006; Isaka et al. 2004). For example, in IVM tail models (Padera et al. 2002), ear models (Hoshida et al. 2006), skinfold window chamber models (Isaka et al. 2004), it has been clearly shown that tumor vasculatures are tortuous and rich in fenestrations, vesicles and vesico-vacuolar channels. These tumor vessels lack the normal basement membrane and perivascular coverage. The inter-endothelial junctions are loose (100 nm–2  $\mu$ m) whereas the leukocyte-endothelial interactions are strong. Therefore most tumor vessels are highly permeable (Fukumura et al. 2010). Similarly, tumor lymphatic vessels are often collapsed in the center of tumors but enlarged at the tumor periphery. This leads to reduced clearance of excess interstitial fluid from tumors (Padera et al. 2002; Leu et al. 2000). The defects in blood vessels and lymph systems together contribute to the high interstitial pressure, diffusion-dominant transport, and increased tumor lymphatic metastasis (Hoshida et al. 2006; Al-Rawi and Jiang 2011).

In the above work, fluorescently labeled macromolecules and particles with different sizes are particularly useful. In particular, dextran with size ranging from 2.36 to 27 nm, and fluorescent microspheres with sizes ranging from 20 nm to 5  $\mu$ m, have been quite convenient to pinpoint the pore cut-off size in tumor vessels. Additionally, these imaging agents allow for the simulation of macromolecule transport in the tumor interstitial space. Combining IVM with FRAP and Fluorescence Correlation Spectroscopy (FCS) techniques allows for the quantification of the intratumoral diffusion, convection, and binding (Jain et al. 2011). These studies have assisted the rational design and selection of effective anti-tumor drugs based on their size, shape, charge and the diffusion distance in tumors. Besides these “inert” imaging agents, novel targeted imaging agents have been developed, such as  $\alpha$ v $\beta$ 3 integrin targeted imaging agents (Snoeks et al. 2010), VivoTag-680 conjugated  $\alpha$ v $\beta$ 3 integrin antagonist imaging agent (Kossodo et al. 2010), and Cy5.5 conjugated scVEGF (single-chain vascular endothelial growth factor) imaging agent (Backer et al. 2007). These novel imaging agents can provide further opportunities to image and study specific molecular events in tumor angiogenesis.

### 12.3.1.2 Hypoxia and pH

Many solid tumors have a hypoxic and acidic tumor microenvironment. Tumor hypoxia and acidosis can cause a landscape change in tumor genomics, proteomics, metabolic and signaling networks, and can also promote tumor invasion, metastasis and drug resistance (Parks et al. 2013; Harris 2002; Wilson and Hay 2011). It has been postulated that the loss of balance between tumor growth and poor oxygen delivery is the cause of tumor hypoxia and acidosis. This idea is supported by the facts that about 70 % of human cancers have a high uptake of  $^{18}\text{F}$ -FDG in clinical PET imaging (Parks et al. 2013) and that tumors have decreased blood and oxygen supply (Vaupel et al. 1989). However PET imaging and electrode based measurements do not have sufficient resolution for spatial correlation between the two. In order to fully understand the relation between tumor blood and oxygen delivery, and tumor hypoxia and acidosis, high resolution mapping of the spatial and temporal relationship of tumor pH, partial pressure of oxygen ( $\text{PO}_2$ ) and blood vessels is needed. IVM, together with other molecular imaging modalities, such as NMR, provides a fresh view of the causes of and relation between the changes in tumor  $\text{PO}_2$ , pH, blood supply and metabolism. In such IVM studies, the  $\text{PO}_2$  profiles in tumors are derived from phosphorescence quenching imaging of oxygen sensitive porphyrine and the pH profiles are generated from fluorescence ratiometric imaging of pH sensitive seminaaphthorhodafluors (SNARFs) (Martin and Jain 1994; Helmlinger et al. 1997; Dellian et al. 1996). It has been found that the pH and  $\text{PO}_2$  profiles in tumors are highly heterogeneous: hypoxic areas co-exist with oxygenated areas; acidic regions co-exist with relatively basic regions; highly glycolytic cancer cells (lower pH) can locate in oxygen-rich environments. Importantly, the pH and  $\text{PO}_2$  profiles in a tumor do not necessarily correlate with each other or blood supply; both pH and  $\text{PO}_2$  can independently control VEGF expression in tumors (Fukumura et al. 2001). These early imaging-based results have been confirmed and explained by recent biochemical analysis of tumor tissue: indeed, oncogene activation alone can cause tumor glycolysis and acidosis (Elstrom et al. 2004); and hypoxia can increase acidosis through hypoxia-inducible factor (HIF)-dependent pH-regulating systems (Wilson and Hay 2011). Furthermore, imaging mixed tumor populations expressing wild type HIF1 $\alpha$  and HIF1 $\alpha$ -/- mutant through a skinfold window chamber has shown that HIF1 $\alpha$ -/- cells remain alive at regions distal to blood vessels (Brown et al. 2001). This stimulating result suggests HIF1 $\alpha$  is necessary for some tumor cells to migrate but not to survive, which echoes recent research on the multiple functions of HIF1 $\alpha$  in tumor pathology. Interestingly, recent IVM studies have also shown that the acidic peritumoral region is associated with the up-regulation of glucose transporter-1 (GLU-1) and this acidic extracellular pH is necessary for tumor cell migration and invasion (Estrella et al. 2013). It is not clear if HIF1 $\alpha$  is involved in GLU-1 over-expression in this case. It will be very interesting to conduct imaging correlation work and mechanistic studies to see if these observations are related. These examples highlight the contributions of IVM to the research of tumor hypoxia and acidosis.

Specialized imaging agents are critical to the above IVM work. Accurate quantification of  $\text{PO}_2$  and pH *in vivo* is often difficult due to variability within tissues,

cells, and the distribution and photo-bleaching effects of imaging agents. Because of these issues, great effort has been put into developing better imaging agents in recent years. Among those, ratiometric imaging agents, which include a reference dye or use emission wavelength shifts, allow better estimation of  $\text{PO}_2$  and pH in living subjects. For ratiometric imaging of oxygen, oxygen-sensitive fluorescent agents (e.g., Phosphor oxyphor G2, iridium complex BTP), or bioreductive fluorescent agents using  $\text{O}_2$  as a substrate (e.g., nitroimidazole and indolequinone based imaging agents), are linked with oxygen-insensitive reference fluorophores (e.g., NIR dyes Cy) (Apte et al. 2011). For ratiometric imaging of pH, small molecule-based imaging agents which can shift their emission spectrum under specific pH are commonly used. These imaging agents include fluorescein based imaging agents (e.g., BCECF), benzoxanthene dyes (e.g., SNARFs), BODIPY and cyanine-based pH indicators (Han and Burgess 2010). Conjugation of these pH sensitive molecules with nanoparticles, peptides and proteins, has shown improved signal, sensitivity, pharmacokinetics and tissue specificity. Furthermore, targeted molecular imaging agents have also been developed as the molecular mediators in hypoxia and acidosis are identified. Examples include HypoxiSense 680 [PerkinElmer] and fluorescence antibody targeting carbonic anhydrase IX (Bao et al. 2012), peptides with the oxygen-dependent degradation domain of HIF-1  $\alpha$  (Kuchimaru et al. 2010). These targeted imaging agents can help to dissect the molecular networks involved in tumor hypoxia and will likely eventually impact strategies for cancer diagnosis and therapy.

In summary, IVM studies have been able to provide high resolution mapping of tumor  $\text{PO}_2$  and pH *in vivo*. This imaging based research has demonstrated that tumor hypoxia and acidosis are spatially and temporally heterogeneous and are controlled by interrelated regulation networks.

### 12.3.1.3 Extracellular Matrix Composition and Remodeling

The extracellular matrix (ECM) is an important component of the tumor microenvironment. Tumor cells and stromal cells can deposit, degrade and dynamically remodel ECM at different tumor development stages. The tumor ECM, in turn, regulates a broad range of tumor cell activities from promoting tumor cell growth to building up metastatic foci. These roles of tumor ECM are closely related to their biochemical properties, and biophysical properties (Yu et al. 2011). IVM studies have greatly helped the characterization of ECM composition, structure and dynamic process and the understanding of ECM functions in tumor development.

IVM has been widely used to characterize type I collagen (Col I) in many tumor models due to the unique and robust SHG signals associated with Col I (Williams et al. 2005). These SHG signals arise from the highly noncentrosymmetric triple-helix structure of Col I. By combining Col I SHG and cell labeling techniques, it has been found that tumors have increased collagen density; the changes of stiffness, distribution and orientation of Col I are often associated with tumor progression (Yu et al. 2011; Provenzano et al. 2008; Provenzano et al. 2006; Levental et al. 2009). In

particular, increased Col I density promotes mammary tumor initiation and progression. The reorganized Col I at the tumor-stromal interface facilitates local invasion. Most interestingly, increased collagen crosslinking and stiffening can force tumor malignant transformation (Provenzano et al. 2008; Provenzano et al. 2006; Levental et al. 2009). On the other hand, IVM at the single cell level has shown that both fibroblasts and macrophages can interact with and remodel collagen. Activated fibroblast can deposit Col I. Migrating fibroblasts can drag, push, and degrade collagen fibers in a  $\beta 1$  integrin and matrix metalloproteinase (MMPs) dependent manner (Perentes et al. 2009). Macrophages can also degrade collagen intra-cellularly or extra-cellularly (via MMPs). Thus, remodeled Col I, tumor cells and tumor stromal cells form an interactive network promoting tumor progression. Besides collagen, there are many other important ECM components, such as fibronectin, tenascin, decorin, fibromodulin, hyaluronic acid, SPARC, lumican, and osteopontin. The precise roles of these proteins in tumor progression are not yet clear (Frantz et al. 2010). Imaging these ECM components *in vivo* requires novel imaging agents for specific ECM proteins and specific function of interest. These imaging agents are still very limited and require further development and validation. For example, fibronectin FRET imaging agents have been used in cell culture work but not yet *in vivo* (Smith et al. 2007). Quantum dots-conjugated hyaluronic acid has been tried for *in vivo* real-time imaging but the imaging properties are to be improved (Bhang et al. 2009). It is expected that many new imaging agents for these ECM components will be developed in the future and imaging these ECM proteins *in vivo* will likely be possible.

Secreted proteases and enzymes play key roles in ECM remodeling and tumor progression. MMPs, cathepsins, urokinase-type plasminogen activator (uPA) are some of the well known proteases involved in tumor development. Because of their important roles, there has been great interest in developing optical imaging agents to visualize the distribution and activity of these proteases in tumors. Activity-based imaging agents are the most often used to detect these proteases as they give high signal-to-background ratio *in vivo* and enable differentiation of active and inactive proteases (Blum et al. 2005). For example, a fusion reporter of a collagen binding peptide and Renilla luciferase has been conjugated with a quencher dabcyI and MMP-2/9 substrate peptide to map MMP2/9 activity in tumors *in vivo* (Xia et al. 2011). The absorption spectrum of dabcyI overlaps with the emission spectrum of Renilla luciferase such that removing the quenchers by MMP-2 restores the bioluminescent emission. A similar imaging agent composed of Cy5.5, MMP substrate, a BHQ-3 fluorescence quencher and an RGD targeting sequence has been shown to have great tumor specificity and stability *in vivo* (Zhu et al. 2011). Additionally, nanoparticles are also used as quenchers to generate activatable fluorescent imaging agents for MMPs (Lee et al. 2009). Activity-based imaging agents are also available for the cathepsin families (Mahmood and Weissleder 2003), thrombin (Pinto and Schanze 2004), etc. Although these imaging agents can give high tumor-specific fluorescence signals *in vivo*, they still suffer from the non-specific cleavage by other enzymes and the low stability in serum. Currently, most of these imaging agents are used in whole body imaging, histology, or cell culture studies. It is expected that their applications in IVM will increase in the future.

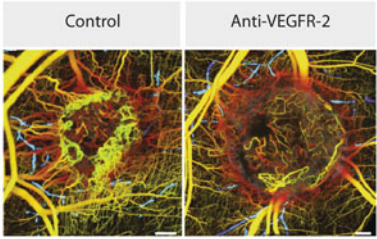


#### 12.3.1.4 Implications in Imaging Drug Distribution

Any drug has to reach its target tissues and cells before being effective. To reach its targets, a drug needs to leave the bloodstream, diffuse into the interstitial space and enter the target organs and tissues. It is known that the distribution of many anti-cancer drugs is insufficient and heterogeneous, but it is often unclear what causes this poor drug distribution and how to address it. IVM has been a powerful tool in providing insights into these questions. Careful studies with IVM have revealed that besides the size, charge, and hydrophobicity of the drugs, the tumor vasculature, interstitial pressure, pH, oxygenation and ECM all critically affect drug distribution (Goel et al. 2012; Amornphimoltham et al. 2010). The leaky and chaotic tumor circulation results in poor perfusion and reduced drug distribution in tumors. The high interstitial pressure and poor drainage, due to high solid stress and abnormal lymphatic function, further increase blood flow resistance and reduce the convective transport of drugs. Additionally, the dense ECM network with reduced pore size forms a barrier that limits drug diffusion in the interstitial space (Tufto et al. 2007; Erikson et al. 2008). Acidic and hypoxic conditions in tumors affect the physico-chemical properties of drugs (e.g., charge), the expression of drug transporters on cells, and drug activity (e.g., doxorubicin uses oxygen to generate free radicals and damage DNA) (Trédan et al. 2007). These findings suggest that drug distribution in tumors can be improved by increasing tumor blood flow, increasing vessel permeability, reducing interstitial fluid pressure (IFP), modifying tumor ECM and targeting tumor hypoxia and acidity. Indeed, therapeutic effects have been improved using these strategies (Fig. 12.3a) (Goel et al. 2012).

The value of IVM for cancer treatment studies can be exemplified from research on anti-angiogenic therapy. Anti-angiogenic therapy in clinical cancer therapy remains a puzzle. It has been shown in the pre-clinical setting that anti-angiogenic drugs could cut off tumor blood supply and thus starve and shrink tumors. However, many anti-angiogenic agents showed modest effects in clinical trials and sometimes resulted in more aggressive tumors (Bergers and Hanahan 2008). Multiple mechanisms could contribute to this drug resistance but remain to be tested (Bergers and Hanahan 2008). Thus far, some IVM studies showed that the up-regulation of alternative pro-angiogenic signaling pathways (e.g., FGF) and reduction in VEGF signals are the major reasons for anti-VEGF drug resistance (Fukumura et al. 2010). On the other hand, other studies revealed that alternative factors can influence drug delivery (Tada et al. 2007; Smith et al. 2008). Reduced vascular permeability by anti-angiogenesis therapy can also hinder the extravasation of many drugs (Bhirde et al. 2009; Mikhail and Allen 2010; Pink et al. 2012) and lead to hypoxia and increase cancer stem cells and tumor metastasis (Gaustad et al. 2012; Rapisarda and Melillo 2012; Conley et al. 2012). Additionally, tumor vasculature is very heterogeneous; VEGF-dependent and -independent vascular zones coexist and interconvert dynamically (Manning et al. 2013). Tumor cells can also enter the blood stream when they are close to a structured tumor-associated vessel (Beerling et al. 2011). These diverse findings from IVM studies demonstrate that many factors can contribute to the lack of efficacy of anti-angiogenic therapy, and suggest that anti-angiogenic

**a** Effects of anti-angiogenic VEGFR-2 treatment



**b** Effects of hyaluronidase treatment

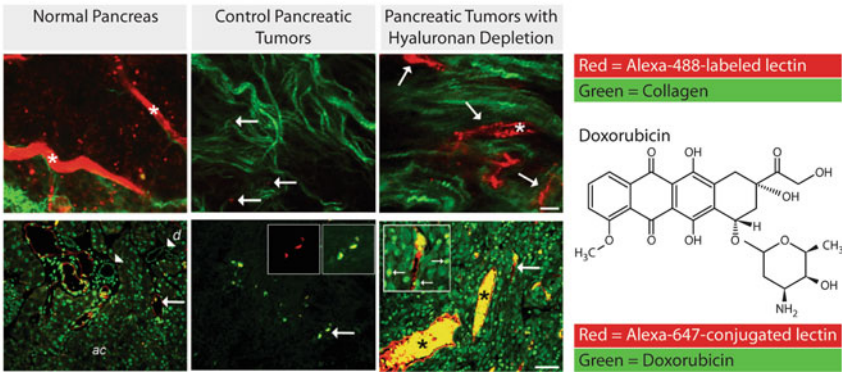


**Fig. 12.3** Examples of IVM imaging at the tissue level **(a)** Optical frequency domain images show the response to anti-angiogenic VEGFR-2 by mouse mammary tumor cells (MCAIV) grown in a dorsal skin-fold window chamber. Antiangiogenic VEGFR-2 treatment leads to reduced density, length and diameters of intratumor vessels compared to those in the control tumors. The lymphatic vascular network is in blue (scale bar, 500  $\mu\text{m}$ ) (Vakoc et al. 2009) (Reprinted by permission from Macmillan Publishers Ltd: *Nature Medicine*, copyright 2009). **(b)** Two-photon images show that hyaluronidase treatment increased the perfusion of tumor blood vessels (*top*) and the delivery of doxorubicin (*bottom*) in a pancreatic ductal adenocarcinoma of transgenic mice (scale bar, 50  $\mu\text{m}$ ). The autofluorescence of doxorubicin allows for the imaging of its distribution (*left*). *ac* acini, *d* duct. Asterisks highlight the large, functional lectin-positive vessels loaded with doxorubicin. Arrows in the top panels indicate well-perfused functional vessels. In the bottom panel, arrows in left image show thin-walled vessel and arrowheads point out the ductal epithelium; arrows in the middle and right images show the regions magnified in respective insert boxes; small arrows in the inserts show the distribution of doxorubicin in the nuclear (green) and extracellular space (Provenzano et al. 2012) (Reprinted by permission from Elsevier, copyright 2012)

reagents should be applied to specific cancer types in a controlled manner (e.g., timing, location, and combination therapy). These results and potential therapeutic strategies need to be further tested for extrapolation to the clinical setting.

Tumor ECM can impact drug effects by direct influence on the diffusion and distribution of drugs in the tumor interstitium and by indirectly affecting the response of tumor cells to drugs. Two-photon FRAP work has shown that increased collagen content in tumors is associated with slow diffusion of molecules, and treating tumors with collagenase can improve the diffusion of drugs (Alexandrakis et al. 2004; Magzoub et al. 2008). Interestingly, hyaluronidase (HA) treatment does not

improve molecular diffusion in tumors. But treating pancreatic ductal adenocarcinomas with HA reduced the interstitial fluid pressure, opened the microvasculature, and improved efficacy of chemotherapeutic drugs (Fig. 12.3b) (Eikenes et al. 2005; Provenzano et al. 2012). Indirectly targeting fibroblast-mediated ECM remodeling with TGF- $\beta$  inhibitors also improved the distribution and efficacy of therapeutics in breast carcinoma (Liu et al. 2012; Salnikov et al. 2005).

These studies suggest that targeting ECM processing and remodeling might be a useful strategy to improve cancer therapy. However, improving drug distribution by targeting ECM is often not straightforward. Just like anti-angiogenesis therapy, inhibitors for MMP showed promising results in preclinical studies but failed in clinical trials. ECM proteins and their related proteases and factors have more complicated functions than expected (Yu et al. 2011; Mueller and Fusenig 2004). Some MMPs have ECM-independent functions and can have protective roles (Folgueras et al. 2004). Tumor cells can switch from mesenchymal, amoeboidal and collective modes of migration and invasion depending on tumor ECM, proteases and signaling. Thus, inhibitions of MMPs, TGF- $\beta$  and other factors can often lead to adverse effects (Matise et al. 2012; Meulmeester and Ten Dijke 2011). Considering that some of these studies are based on a snap-shot of tumor progression and that ECM remodeling is a highly dynamic process, further real-time IVM imaging is necessary to better understand how to target ECM in cancer therapy.

In summary, IVM has been a useful tool in understanding drug delivery and distribution in tumors. The results from this research have helped in designing new drugs, developing novel therapeutic strategies and elucidating mechanisms of drug effects. However, drug efficacy does not only depend on drug distribution at the tissue level. Recent IVM imaging of single cell and subcellular pharmacokinetics showed that the proteomic heterogeneity in individual cells can be a major reason for limited drug action when tumor cells are exposed to sufficient drugs *in vivo* (Thurber et al. 2013). Therefore, imaging the structure and composition of tumors at the cellular and subcellular levels is another important direction leading to the understanding of drug resistance and response. In the next section, we will discuss IVM work at the cellular and subcellular levels and related work on drug response.

### 12.3.2 *Imaging Tumors at the Cellular and Subcellular Levels*

#### 12.3.2.1 **Cell Tracking**

Tumors are heterogeneous and can have multiple tumor cell subpopulations and stromal cell populations within a single tumor (Marusyk et al. 2012; Pietras and Ostman 2010). These various populations can have different cellular states, spatial-temporal distributions, cell-cell interactions, as well as different functions during tumor development. Identifying the roles of each cell population in tumor development is always a critical task in cancer research and clinics. IVM, with its high

resolution at the cellular level and diverse imaging agents, is an ideal tool for tracking cells and cell activities in their native *in vivo* environment.

Tracking cells requires specific labeling of cells of interest. There are three basic cell labeling methods: *ex vivo* labeling, direct *in vivo* labeling, and transgenic methods. For *ex vivo* labeling, specific cell populations are isolated and labeled with imaging agents *in vitro* and injected back into the hosts. Since cell specificity is achieved in the cell isolation and purification steps, a wide range of imaging agents can be used, such as fluorescent reporter genes, fluorescent molecules and particles. For short-term cell labeling and imaging experiments, CFSE (Carboxyfluorescein succinimidyl ester), Dil (1,1'-Diocadecyl-3,3',3'-tetramethylindocarbocyanine perchlorate), quantum dots, etc. are often used. This transient cell labeling technique allows, for example, the visualization of T cell dynamics in lymph nodes, and tumor cell extravasation during metastasis (Stoll et al. 2002; Bajénoff et al. 2006; Voura et al. 2004). Because of the problems of dye retention, transfer, dilution and toxicity, reporter genes are preferred for long-term cell labeling (Hulit et al. 2012). By tracking cancer cells stably expressing GFP, CFP, RFP (green, cyan, red fluorescent proteins), etc., it has been found that tumor cells move much faster *in vivo* than *in vitro* (Condeelis and Segall 2003). Tumor cells are able to utilize collective, amoeboidal or mesenchymal migration strategies (Friedl and Alexander 2011), and take active or passive approaches for intravasation and extravasation (Kedrin et al. 2008). IVM in combination with whole body bioluminescence imaging has demonstrated that intravenously injected lymphoma cells home to spleen and bone marrow first and then disseminate to lymph nodes only a few days after (Ito et al. 2012). Furthermore, the reporter gene approach allows studying the molecular mechanisms involved in these processes. For example, by expressing mutant proteins or using inhibitors, it has been found that the migration speed and modes of tumor cells *in vivo* are regulated by signaling networks involved in actin polymerization, actomyosin contraction and cell adhesion, such as Arp2/3-cofilin-mena pathways, Rho family small GTPase, Integrin and focal adhesion kinase pathways (Philippart et al. 2008; Olson and Sahai 2009; McGhee et al. 2011; Timpson et al. 2011). Although simple and fast, the *ex vivo* labeling method has major drawbacks: the isolation and *in vitro* labeling can alter cell properties, and the implantation sites are often not the native environments.

In the direct *in vivo* labeling, imaging agents are systemically administered and taken up by a specific cell population. Systemic delivery of imaging agents is fast. Many imaging agents ranging from small molecules to antibody conjugated particles can be administrated *in vivo* to label cells for short-term imaging. But some major problems of these imaging agents include: high background signal, low specificity and stability *in vivo*. For example, dextran, DiR, etc. can be injected *in vivo* to label macrophages, but many other cells such as dendritic cells and cancer cells can also take up these dyes. Cell type-specific imaging agents, such as those based on unique surface ligands, receptors, antigens, or subcellular molecules, can have better specificity (Fig. 12.1b) (Kobayashi and Choyke 2011). However, creating such highly specific markers is not easy and remains an important research area in molecular imaging.

Transgenic reporter animal approaches allow for tracking of cells in their native environment for prolonged periods. This approach is extremely valuable when studying the tumor associated stromal cells, including immune cells, fibroblasts, mesenchymal cells, endothelial cells, and recruited bone marrow cells (Fig. 12.1d). Experiments with direct *in vivo* cell labeling and transgenic mice expressing GFP, YFP and RFP have shown that dendritic like cells, myeloid cells and carcinoma-associated fibroblasts migrate faster at the tumor periphery than within the tumor, whereas the regulatory T-cells (Tregs) mainly migrate near blood vessels (Egeblad et al. 2008). As these tumor stromal cells are involved in tumor lymphangiogenesis, immune surveillance, hypoxia response, ECM remodeling, tumor progression and metastasis (Mueller and Fusenig 2004; Tlsty and Coussens 2006; McMillin et al. 2013), these IVM studies can really help in understanding the dynamic interactions between stromal and tumor cells. The transgenic animal approach is also extremely useful in lineage tracing of heterogeneous tumor cells. As tumor cell heterogeneity can arise from genetic, epigenetic clonal evolution, environmental effects, or cancer stem cell differentiation (Magee et al. 2012), it is necessary to label a few tumor cells in their native environment and follow their fate for prolonged periods *in vivo*. It has not been until recently, that the technology breakthroughs in lineage tracing, transgenic mouse models and imaging techniques have made it possible to perform such long-term cell fate tracking experiments *in vivo* (Livet et al. 2007). With “Brainbow” mosaic expressing multicolor fluorescent proteins in individual cells and tracing their fates in the native environment (Fig. 12.4a), it has become evident

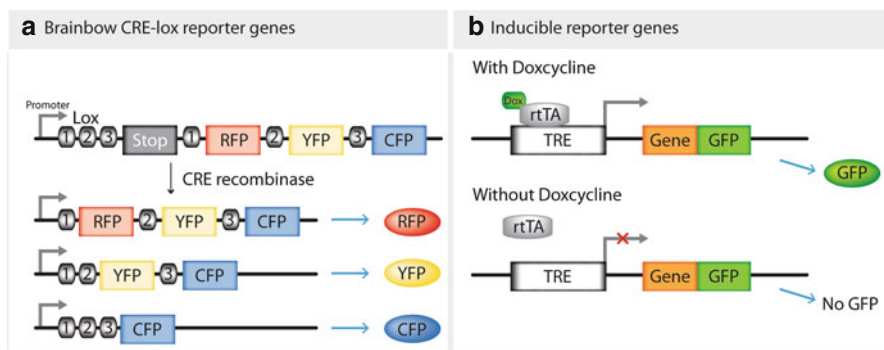


**Fig. 12.4** Reporter genes (a) an example of the brainbow CRE/loxP site-specific recombination systems. In this brainbow system, DNA transcriptional STOP cassette and fluorescent reporter genes (e.g., RFP, YFP, CFP) are flanked by pairs of mutually incompatible lox variants (three lox pairs here). The introduction of CRE results in random recombination between these loxP pairs. Each of these recombinations leads to the expression of a distinct XFP, such as RFP, YFP or CFP. This strategy is extremely useful in long-term cell-lineage tracing experiments (b) an example of the inducible reporter gene systems. In this tetracycline (Tet)-or doxycycline (Dox)-inducible system, the transcription of the gene of interest and the fluorescent protein genes is under the control of Tet response element (TRE). In the presence of doxycycline, the reversed tetracycline transactivator (rtTA) binds to TRE and turns on the transcription of TRE-controlled genes. In the absence of doxycycline, rtTA can not bind to TRE and thereby prevents the transcription of TRE-controlled genes

that stem-cell-like cells that are long-lived and able to self-renew or divide to produce new progenitors do exist in papillomas, intestinal cancer, and glioblastoma models (Driessens et al. 2012; Schepers et al. 2012; Chen et al. 2012). These multipotent stem cells maintain human adenomas and the pattern of clonal expansion in tumor evolution (Humphries et al. 2013) and can also propagate glioblastoma growth after chemotherapy (Chen et al. 2012). These studies, for the first time, provide solid data supporting the idea that a small subset of cells drives tumor growth, and that it is necessary to target these cells in cancer therapy.

### 12.3.2.2 Subcellular Components and Processes

Microscopy has been an essential tool to study the dynamics of molecular localization, interaction and function of subcellular components during cell division, apoptosis, migration, metabolism, transcription and translation *in vitro*. Imaging subcellular processes *in vivo* is still very challenging due to the motion artifacts from live animals and the low signal to noise ratio *in vivo*. However with recent technical advancement in minimizing motion effects and the availability of better imaging agents, subcellular IVM imaging has become possible.

IVM has been used to image cell division *in vivo*. One of the classic methods for imaging cell division is to use GFP-tagged human histone H2B (H2B-GFP) to visualize chromatin structure and nuclear dynamics (Fig. 12.1d) (Hadjantonakis and Papaioannou 2004; Yamamoto et al. 2004; Orth et al. 2011; Janssen et al. 2013). This reporter gene can be further modified to include a tetracycline regulatory element such that H2B-GFP is only expressed when doxycycline is added (Fig. 12.4b). With this inducible H2B-GFP reporter, the cell cycling time of stem cells and their progenitors, the repopulation potential of stem cells, and the interactions between stem cells within their niches have been studied *in vivo* (Foudi et al. 2009; Wilson et al. 2008). One of the drawbacks of these H2B-GFP reporter systems is the requirement for high resolution images to analyze the morphology of H2B-GFP tagged chromatin for accurate cell cycle staging. This is a great challenge for *in vitro* and *in vivo* work. Therefore, a more elegant cell cycle reporter system is to directly color code each G1, S, or G2/M phase. For example, the Fucci reporter uses the cell-cycle-dependent proteolysis of Cdt1 and Geminin to control the expression of mKO2 and Azami green, such that the nuclei of cells appear in different color when cells cycle through G1/S/G2/M phase (Sakaue-Sawano et al. 2008). This reporter gene makes it very convenient to track the cell-cycle stages in real-time *in vivo*.

IVM and reporter genes have also been used to visualize the intracellular signaling pathways involved in cancer cell migration, invasion, and metastasis. In these studies, tumor cells are engineered to express fusion proteins composed of proteins of interest with fluorescent proteins, and injected into animals and tracked with IVM. Using these approaches, it has been found that ROCK regulates the phosphorylation and organization of myosin light chain and thus cancer cell motility *in vivo* (Wyckoff et al. 2006). Rac and Rho-kinase signaling control the switch between



the mesenchymal and amoeboid movement of cancer cells *in vivo* (Sanz-Moreno et al. 2008) whereas TGF $\beta$  signaling is associated with single cell movement (Giampieri et al. 2009; Kardash et al. 2010). Similar work has revealed a series of important proteins regulating tumor invasion and migration *in vivo*, which is impossible to be studied in isolated cells.

Imaging caspase activity and apoptosis is another important area of IVM research. Some of this research takes advantage of genetically-encoded FRET imaging agents to report caspase activity under *in vivo* conditions. In these cases, the caspase sensor is constructed to have CFP and GFP linked by a caspase-3 cleavage sequence DEVD (Fig. 12.1c). Tumor cells are engineered to express this reporter gene construct and then injected into animals. The non-apoptotic cells give FRET signals, but the apoptotic cells lose FRET signals as activated caspase-3 cleaves DEVD (Keese et al. 2010; Breart et al. 2008). Other studies use systemically administered imaging agents, such as near-infrared FLIVO<sup>TM</sup> and caspase-triggered nanoaggregation imaging agent, to study apoptosis. The FLIVO<sup>TM</sup> imaging agent is a small molecule fluorescent inhibitor for active caspases and can give red fluorescence in apoptotic cells with little background (Tsai et al. 2007). Caspase-triggered nanoaggregation imaging agent has a DEVD caspase cleavage peptide linked with a polymeric fluorescence backbone which can aggregate and self-amplify signal upon caspase cleavage (Shen et al. 2013). These imaging agents can be a good alternative when the introduction of reporter genes into cells is not feasible, and when FRET signals are difficult to quantify *in vivo*.

FRAP, FLIM, photoswitching, etc. techniques have also been incorporated for IVM imaging of subcellular processes. For example, FRAP IVM imaging has shown that the immobile fraction of E-cadherin in cell-cell junctions is five times more *in vivo* than *in vitro* and E-cadherin mobility correlates with cell migration (Serrels et al. 2009). FLIM has also been combined with IVM to study the metabolic products in tumor cells *in vivo*. For examples, NADH and FAD have very different two-photon fluorescence life times depending on their bound states and can serve as reporters for mitochondrial activity. Mapping these endogenous NADH and FAD with FLIM-IVM within live cells has shown a stepwise change of intracellular metabolic states during cancer development (Skala et al. 2007; Provenzano et al. 2009).

### 12.3.2.3 Implications in Monitoring Drug Response

Currently, 70 % of oncology drugs that enter Phase 2 clinical trials fail to enter Phase 3. Among those drugs that do enter Phase 3 trials, 59 % fail (Kola and Landis 2004). This high failure rate is mainly due to the lack of drug efficacy in the clinic, the lack of predictive animal models and the lack of understanding of drug mechanisms *in vivo*. IVM might be a valuable tool to address these issues.

One area of IVM research is in cancer immunotherapy. These IVM studies have disclosed that the infiltration of cytotoxic T cells (CTL) in tumors is very heterogeneous and their tumor-elimination activities are limited by access to tumor cells

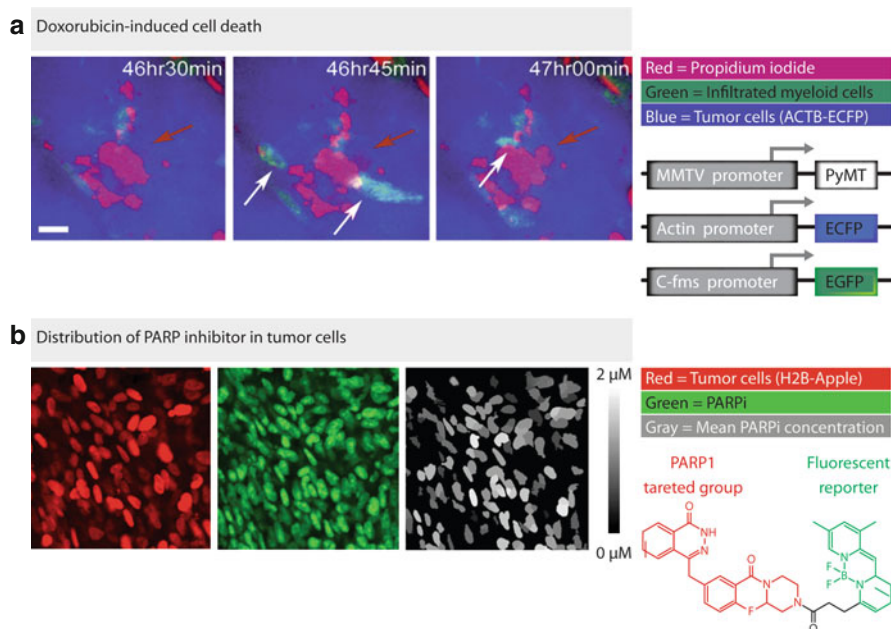


**Fig. 12.5** Examples of IVM imaging at the cellular and subcellular levels (a) Spinning disk confocal images show doxorubicin-induced cell death in exposed mammary tumors in real-time. Reporter mice are generated by crossing MMTV-PyMT and ACTB-ECFP and c-fms-EGFP mouse strains such that tumor cells express ECFP and stromal macrophage express EGFP (left). The death of tumor cells (red arrow) and stromal cells induced by doxorubicin is visualized by propidium iodide (PI) administered intraperitoneally. Doxorubicin also induces the infiltration of stromal cells (white arrow) (scale bar, 10  $\mu$ m) (Nakasone et al. 2012) (Reprinted by permission from Elsevier, copyright 2012). (b) IVM images show PARP inhibitors (PARPi) distribution in a HT-1080 tumor implanted in a dorsal skin-fold window chamber. Proliferating tumor cells are labeled with H2B-Apple, tumor associated macrophages (TAM) are labeled with Clio-680 nanoparticles, PARPi is synthesized with a fluorescent group attached to the PARP1 targeted group (left). The PARPi is accumulated in most tumor cells and some TAMs (Thurber et al. 2013) (Reprinted by permission from Macmillan Publishers Ltd, copyright 2013)

(Boissonnas et al. 2007). Additionally, CD44 has been found to mediate cell migration and stable interactions between killer cells and tumor cells (Mrass et al. 2008). Such IVM based work greatly contributed to the discovery of novel anti-tumor immune therapies. Another important area of study is the stroma mediated drug sensitivity and resistance in chemotherapies (McMillin et al. 2013). Many drugs, such as dexamethasone, doxorubicin, vemurafenib, ruxolitinib, can be affected by the tumor stroma. But the mechanisms are not clear. Recently, Nakasone et al. addressed the question with IVM and transgenic mouse models for breast cancer (Nakasone et al. 2012). Their imaging results have shown that the sensitivity to doxorubicin changes with tumor stage. This stage dependent drug sensitivity was found to be related to the leakiness of blood vessels and the recruitment of CCR2+ myeloid cells but not the intrinsic properties of tumor cells (Fig. 12.5a). Further

studies have shown that infiltrated CD11b+GR1+ myeloid precursors can also mediate the anti-VEGF resistance in colorectal cancer (Shojaei et al. 2007). However, the roles of myeloid cells in tumor drug response can be drug and tumor type specific (Germano et al. 2013). Therefore, more IVM studies are still needed in this area.

Subcellular mechanisms are also important in drug sensitivity and resistance of tumor. Janssen et al. set out to understand the mechanisms of docetaxel-induced tumor cell death *in vivo* (Janssen et al. 2013). They expressed H2B tagged photo-switchable Dendra2 and FRET caspase-3 biosensor simultaneously in tumor cells to track the mitotic progression and the onset of apoptosis within tumors. They showed, in contrast to the *in vitro* conditions, that docetaxel-induced apoptosis was independent of mitosis *in vivo* but rather dependent on the heterogeneous microenvironment. This hypothesis was tested in a related IVM study with Src-inhibitor applied to a subcutaneously grafted p53-mutant pancreatic tumor (Nobis et al. 2013). With a FLIM-FRET Src sensor, dasatinib-inhibition of Src activity was found to be limited within 50–100  $\mu\text{m}$  from the vasculature. Cyclopamine was then administered to modify ECM structure for enhancing dasatinib effects. Although dasatinib efficacy was improved, it was mainly localized to the peri-vascular region (25–50  $\mu\text{m}$  away from vessels) and the spatial limit remained similar as in the controls. This result suggests that tumor ECM may not be a limiting factor for dasatinib, which is in agreement with the recent finding from another group (Thurber et al. 2013). Imaging the intracellular kinetics of the PARP-1 inhibitor (PARPi) distribution in real time in live animals showed that the responses of tumor cells to PARPi are heterogeneous regardless of efficient drug delivery and sufficient nuclei accumulation of PARPi (Fig. 12.5b) (Thurber et al. 2013). This result suggests PARPi efficacy may be linked to both the intrinsic heterogeneity of individual cells and the stromal cells. These few cases together demonstrate that drug response *in vivo* is complicated and no single mechanism can explain all observations. In order to identify the exact mechanisms of drug response *in vivo*, more thorough IVM work will be required.

In summary, using different models, drugs, and methods, these IVM studies all demonstrate that drug sensitivity and responses are strongly affected by the *in vivo* environment and the cellular and subcellular heterogeneity. These initial studies have shown the great potential of IVM in these areas of investigation. With the advancement of imaging instrumentation, improved imaging techniques and imaging agents, IVM will undoubtedly impact the development of anti-cancer therapy and ultimately assist in clinical cancer management.

## 12.4 Future Directions

Although IVM has provided significant gains in our understanding of basic *in vivo* biology, there are still many potential advances in instrumentation and imaging probes that may allow further insight and the full realization of IVM strategies. Improving imaging depth and increasing multiplexing capability is a major goal in

IVM work. Improvements in instrumentation are covered elsewhere in this book (See Chapter IVM: Principles and Technology). It will be important to expand our current library of IVM imaging agents, particularly IR and NIR fluorescent imaging agents, because of their apparent benefits in deep tissue imaging. The ability to use multiple imaging agents, each one specific for a given process of interest, will be highly important. This will require a team science approach in which biologists, chemists, molecular pharmacologists, and IVM specialists work hand-in-hand to develop a larger library of well validated agents. It will be important to show that such developed agents actually measure specific processes of interest through careful validation studies. In addition, it will be important to continue to make IVM more quantitative so that images obtained using specific imaging probes can be quantified to show the levels of underlying molecular targets or processes of interest.

Another important future direction is multimodality imaging. In multimodality imaging, a single imaging agent is often used for imaging with different imaging modalities to maximize the information from complementary methods (James and Gambhir 2012; Gambhir 2013). The limited field of view and imaging depth in IVM restrict its abilities to study the traffic of tumor cells and tumor metastasis. Combining IVM and other whole-body imaging modalities can often overcome such limitations. For these purposes, fusion reporter genes and reporter mice for luciferase-GFP and for PET-luciferase-RFP are available (Cao et al. 2004; Ray et al. 2004; Yan et al. 2013) and some multimodality imaging agents have also been developed (Tsourkas et al. 2005). It is expected that there will be many more important applications of multimodality imaging in the future (Cherry 2006; Culver et al. 2008).

The development of novel endomicroscopy (e.g., Raman, confocal), microcatheters, etc. instrumentation is another exciting direction. These types of instruments will likely allow new ways of imaging mouse models in which different tissue compartments (e.g., gastrointestinal tract) can be accessed. By allowing microscopes that go into the body one may be able to open up entirely new ways to study molecular and cellular events that are currently quite difficult to perform.

In summary, many important questions in cancer pathology and drug response remain to be answered. IVM based imaging research has already shown its power in addressing some of these questions. We can foresee that IVM will continue to make even more significant contributions in these research areas which hopefully will lead to a greater understanding of fundamental biology and for potential translational benefit.

## References

- Alexandrakis G, Brown EB, Tong RT et al (2004) Two-photon fluorescence correlation microscopy reveals the two-phase nature of transport in tumors. *Nat Med* 10:203–207
- Al-Rawi AAM, Jiang WG (2011) Lymphangiogenesis and cancer metastasis. *J Cell Mol Med* 16:1405–1416
- Amornphimoltham P, Masedunskas A, Weigert R (2010) Intravital microscopy as a tool to study drug delivery in preclinical studies. *Adv Drug Deliv Rev* 63:119–128

- Apte S, Chin FT, Graves EE et al (2011) Molecular imaging of hypoxia: strategies for probe design and application. *Curr Org Synth* 8:593–603
- Backer MV, Levashova Z, Patel V et al (2007) Molecular imaging of VEGF receptors in angiogenic vasculature with single-chain VEGF-based probes. *Nat Med* 13:504–509
- Bajénoff M, Breart B, Huang AYC et al (2006) Natural killer cell behavior in lymph nodes revealed by static and real-time imaging. *J Exp Med* 203:619–631
- Bao B, Groves K, Zhang J et al (2012) In vivo imaging and quantification of carbonic anhydrase IX expression as an endogenous biomarker of tumor hypoxia. *PLoS One* 7:e50860
- Beerling E, Ritsma L, Vriskoop N et al (2011) Intravital microscopy: new insights into metastasis of tumors. *J Cell Sci* 124:299–310
- Bergers G, Hanahan D (2008) Modes of resistance to anti-angiogenic therapy. *Nat Rev Cancer* 8:592–603
- Bhang SH, Won N, Lee T-J et al (2009) Hyaluronic acid-quantum dot conjugates for in vivo lymphatic vessel imaging. *ACS Nano* 3:1389–1398
- Bhirde AA, Patel V, Gavard J et al (2009) Targeted killing of cancer cells in vivo and in vitro with EGF-directed carbon nanotube-based drug delivery. *ACS Nano* 3:307–316
- Blum G, Mullins SR, Keren K et al (2005) Dynamic imaging of protease activity with fluorescently quenched activity-based probes. *Nat Chem Biol* 1:203–209
- Boissonnas A, Fetler L, Zeelenberg IS et al (2007) In vivo imaging of cytotoxic T cell infiltration and elimination of a solid tumor. *J Exp Med* 204:345–356
- Breart B, Lemaître F, Celli S, Bouso P (2008) Two-photon imaging of intratumoral CD8+ T cell cytotoxic activity during adoptive T cell therapy in mice. *J Clin Invest* 118:1390–1397
- Brown EB, Campbell RB, Tsuzuki Y et al (2001) In vivo measurement of gene expression, angiogenesis and physiological function in tumors using multiphoton laser scanning microscopy. *Nat Med* 7:864–868
- Brown E, Munn LL, Fukumura D, Jain RK (2010) In vivo imaging of tumors. *Cold Spring Harbor Protoc.* 2010:pdb.prot5452, Vol 7
- Cao Y-A, Wagers AJ, Beilhack A et al (2004) Shifting foci of hematopoiesis during reconstitution from single stem cells. *Proc Natl Acad Sci U S A* 101:221–226
- Chen J, Li Y, Yu T-S et al (2012) A restricted cell population propagates glioblastoma growth after chemotherapy. *Nature* 488:1–6
- Cherry SR (2006) Multimodality in vivo imaging systems: twice the power or double the trouble? *Annu Rev Biomed Eng* 8:35–62
- Condeelis J, Segall J (2003) Intravital imaging of cell movement in tumours. *Nat Rev Cancer* 3:921–930
- Conley SJ, Gheordunescu E, Kakarala P et al (2012) Antiangiogenic agents increase breast cancer stem cells via the generation of tumor hypoxia. *Proc Natl Acad Sci U S A* 109:2784–2789
- Coppieters K, Martinic MM, Kiosses WB et al (2010) A novel technique for the in vivo imaging of autoimmune diabetes development in the pancreas by two-photon microscopy. *PLoS One* 5:e15732
- Culver J, Akers W, Achilefu S (2008) Multimodality molecular imaging with combined optical and SPECT/PET modalities. *J Nucl Med* 49:169–172
- Dellian M, Helminger G, Yuan F, Jain RK (1996) Fluorescence ratio imaging of interstitial pH in solid tumours: effect of glucose on spatial and temporal gradients. *Br J Cancer* 74:1206–1215
- Driessens G, Beck B, Caauwe A et al (2012) Defining the mode of tumour growth by clonal analysis. *Nature* 488:1–5
- Egeblad M, Ewald AJ, Askautrud HA et al (2008) Visualizing stromal cell dynamics in different tumor microenvironments by spinning disk confocal microscopy. *Dis Model Mech* 1:155–167
- Egeblad M, Nakasone ES, Werb Z (2010) Tumors as organs: complex tissues that interface with the entire organism. *Dev Cell* 18:884–901
- Eikenes L, Tari M, Tufto I et al (2005) Hyaluronidase induces a transcapillary pressure gradient and improves the distribution and uptake of liposomal doxorubicin (Caelyx) in human osteosarcoma xenografts. *Br J Cancer* 93:81–88

- Elstrom RL, Bauer DE, Buzzai M et al (2004) Akt stimulates aerobic glycolysis in cancer cells. *Cancer Res* 64:3892–3899
- Erikson A, Tufto I, Bjønnum AB et al (2008) The impact of enzymatic degradation on the uptake of differently sized therapeutic molecules. *Anticancer Res* 28:3557–3566
- Escobedo JO, Rusin O, Lim S, Strongin RM (2010) NIR dyes for bio imaging applications. *Curr Opin Chem Biol* 14:64–70
- Estrella V, Chen T, Lloyd M et al (2013) Acidity generated by the tumor microenvironment drives local invasion. *Cancer Res* 73:1524–1535
- Filonov GS, Piatkevich KD, Ting L-M et al (2011) Bright and stable near-infrared fluorescent protein for in vivo imaging. *Nat Biotechnol* 29:757–761
- Folgueras AR, Pendás AM, Sánchez LM, López-Otín C (2004) Matrix metalloproteinases in cancer: from new functions to improved inhibition strategies. *Int J Dev Biol* 48:411–424
- Foudi A, Hochedlinger K, Van Buren D et al (2009) Analysis of histone 2B-GFP retention reveals slowly cycling hematopoietic stem cells. *Nat Biotechnol* 27:84–90
- Frantz C, Stewart KM, Weaver VM (2010) The extracellular matrix at a glance. *J Cell Sci* 123:4195–4200
- Friedl P, Alexander S (2011) Cancer invasion and the microenvironment: plasticity and reciprocity. *Cell* 147:992–1009
- Fukumura D, Xu L, Chen Y et al (2001) Hypoxia and acidosis independently up-regulate vascular endothelial growth factor transcription in brain tumors in vivo. *Cancer Res* 61:6020–6024
- Fukumura D, Duda DG, Munn LL, Jain RK (2010) Tumor microvasculature and microenvironment: novel insights through intravital imaging in pre-clinical models. *Microcirculation* 17:206–225
- Gambhir SS (2013) Molecular imaging primer, 1st edn. Available at the Apple bookstore for iPad or Mac)
- Gaustad J-V, Simonsen TG, Leinaas MN, Rofstad EK (2012) Sunitinib treatment does not improve blood supply but induces hypoxia in human melanoma xenografts. *BMC Cancer* 12:388
- Germano G, Frapolli R, Belgiovine C et al (2013) Role of macrophage targeting in the antitumor activity of trabectedin. *Cancer Cell* 23:249–262
- Giampieri S, Manning C, Hooper S et al (2009) Localized and reversible TGFbeta signalling switches breast cancer cells from cohesive to single cell motility. *Nat Cell Biol* 11:1287–1296
- Goel S, Wong AH-K, Jain RK (2012) Vascular normalization as a therapeutic strategy for malignant and nonmalignant disease. *Cold Spring Harb Perspect Med* 2:a006486
- Grinvald A, Shoham D, Shmuel A et al (1991) In-vivo optical imaging of cortical architecture and dynamics. *Brain* 34:1–91
- Hadjantonakis A-K, Papaioannou VE (2004) Dynamic in vivo imaging and cell tracking using a histone fluorescent protein fusion in mice. *BMC Biotechnol* 4:33
- Han J, Burgess K (2010) Fluorescent indicators for intracellular pH. *Chem Rev* 110:2709–2728
- Hanahan D, Weinberg RA (2011) Hallmarks of cancer: the next generation. *Cell* 144:646–674
- Harris AL (2002) Hypoxia – a key regulatory factor in tumour growth. *Nat Rev Cancer* 2:38–47
- Helmlinger G, Yuan F, Dellian M, Jain RK (1997) Interstitial pH and pO<sub>2</sub> gradients in solid tumors in vivo: high-resolution measurements reveal a lack of correlation. *Nat Med* 3:177–182
- Hoshida T, Isaka N, Hagendoorn J et al (2006) Imaging steps of lymphatic metastasis reveals that vascular endothelial growth factor-C increases metastasis by increasing delivery of cancer cells to lymph nodes: therapeutic implications. *Cancer Res* 66:8065–8075
- Hulit J, Kedrin D, Gligorijevic B et al (2012) The use of fluorescent proteins for intravital imaging of cancer cell invasion. *Methods Mol Biol* 872:15–30
- Humphries A, Cereser B, Gay LJ et al (2013) Lineage tracing reveals multipotent stem cells maintain human adenomas and the pattern of clonal expansion in tumor evolution. *Proc Natl Acad Sci U S A* 110:E2490–E2499
- Imanishi Y, Batten ML, Piston DW et al (2004) Noninvasive two-photon imaging reveals retinyl ester storage structures in the eye. *J Cell Biol* 164:373–383
- Isaka N, Padera TP, Hagendoorn J et al (2004) Peritumor lymphatics induced by vascular endothelial growth factor-C exhibit abnormal function. *Cancer Res* 64:4400–4404



- Ito K, Smith BR, Parashurama N et al (2012) Unexpected dissemination patterns in lymphoma progression revealed by serial imaging within a murine lymph node. *Cancer Res* 72: 6111–6118
- Jain RK, Munn LL, Fukumura D (2011) Tumor models in cancer research. In: Teicher BA (ed) *Cancer drug discovery and development*. Springer, New York; pp 641–679
- James ML, Gambhir SS (2012) A molecular imaging primer: modalities, imaging agents, and applications. *Physiol Rev* 92:897–965
- Janssen A, Beerling E, Medema R, van Rheenen J (2013) Intravital FRET imaging of tumor cell viability and mitosis during chemotherapy. *PLoS One* 8:e64029
- Kardash E, Reichman-Fried M, Maître J-L et al (2010) A role for Rho GTPases and cell-cell adhesion in single-cell motility in vivo. *Nat Cell Biol* 12:47–53
- Kedrin D, Gligorijevic B, Wyckoff J et al (2008) Intravital imaging of metastatic behavior through a mammary imaging window. *Nat Methods* 5:1019–1021
- Keese M, Yagublu V, Schwenke K et al (2010) Fluorescence lifetime imaging microscopy of chemotherapy-induced apoptosis resistance in a syngenic mouse tumor model. *Int J Cancer* 126:104–113
- Kobayashi H, Choyke PL (2011) Target-cancer-cell-specific activatable fluorescence imaging probes: rational design and in vivo applications. *Acc Chem Res* 44:83–90
- Kola I, Landis J (2004) Can the pharmaceutical industry reduce attrition rates? *Nat Rev Drug Discov* 3:711–715
- Kossodo S, Pickarski M, Lin S-A et al (2010) Dual in vivo quantification of integrin-targeted and protease-activated agents in cancer using fluorescence molecular tomography (FMT). *Mol Imaging Biol* 12:488–499
- Kotsuma M, Parashurama N, Smith BR et al (2012) Nondestructive, serial in vivo imaging of a tissue-flap using a tissue adhesion barrier Applications for IVM imaging in the mammary fat pad and lymph node. *Intr Vital* 1:69–76
- Kuchimaru T, Kadosono T, Tanaka S et al (2010) In vivo imaging of HIF-active tumors by an oxygen-dependent degradation protein probe with an interchangeable labeling system. *PLoS One* 5:e15736
- Lee S, Ryu JH, Park K et al (2009) Polymeric nanoparticle-based activatable near-infrared nano-sensor for protease determination in vivo. *Nano Lett* 9:4412–4416
- Lee S, Vinegoni C, Feruglio PF et al (2012) Real-time in vivo imaging of the beating mouse heart at microscopic resolution. *Nat Commun* 3:1054
- Lehr HA, Leunig M, Menger MD et al (1993) Dorsal skinfold chamber technique for intravital microscopy in nude mice. *Am J Pathol* 143:1055–1062
- Leu AJ, Berk DA, Lymboussaki A et al (2000) Absence of functional lymphatics within a murine sarcoma: a molecular and functional evaluation. *Cancer Res* 60:4324–4327
- Levental KR, Yu H, Kass L et al (2009) Matrix crosslinking forces tumor progression by enhancing integrin signaling. *Cell* 139:891–906
- Li Z, Wilson KD, Smith B et al (2009) Functional and transcriptional characterization of human embryonic stem cell-derived endothelial cells for treatment of myocardial infarction. *PLoS One* 4:13
- Liu J, Liao S, Diop-Frimpong B et al (2012) TGF- $\beta$  blockade improves the distribution and efficacy of therapeutics in breast carcinoma by normalizing the tumor stroma. *Proc Natl Acad Sci* 109:16618–16623
- Livet J, Weissman TA, Kang H et al (2007) Transgenic strategies for combinatorial expression of fluorescent proteins in the nervous system. *Nature* 450:56–62
- Looney MR, Thornton EE, Sen D et al (2011) Stabilized imaging of immune surveillance in the mouse lung. *Nat Methods* 8:91–96
- Magee JA, Piskounova E, Morrison SJ (2012) Cancer stem cells: impact, heterogeneity, and uncertainty. *Cancer Cell* 21:283–296
- Magzoub M, Jin S, Verkman AS (2008) Enhanced macromolecule diffusion deep in tumors after enzymatic digestion of extracellular matrix collagen and its associated proteoglycan decorin. *FASEB J* 22:276–284

- Mahmood U, Weissleder R (2003) Near-infrared optical imaging of proteases in cancer. *Mol Cancer Ther* 2:489–496
- Manning CS, Jenkins R, Hooper S et al (2013) Intravital imaging reveals conversion between distinct tumor vascular morphologies and localized vascular response to Sunitinib. *Intra Vital* 2:1–12
- Martin GR, Jain RK (1994) Noninvasive measurement of interstitial pH profiles in normal and neoplastic tissue using fluorescence ratio imaging microscopy. *Cancer Res* 54:5670–5674
- Marusyk A, Almendro V, Polyak K (2012) Intra-tumour heterogeneity: a looking glass for cancer? *Nat Rev Cancer* 12:323–334
- Matise LA, Palmer TD, Ashby WJ et al (2012) Lack of transforming growth factor-beta signaling promotes collective cancer cell invasion through tumor-stromal crosstalk. *Breast Cancer Res* 14:R98
- McGhee EJ, Morton JP, Von Kriegsheim A et al (2011) FLIM-FRET imaging in vivo reveals 3D-environment spatially regulates RhoGTPase activity during cancer cell invasion. *Small GTPases* 2:239–244
- McMillin DW, Negri JM, Mitsiades CS (2013) The role of tumour-stromal interactions in modifying drug response: challenges and opportunities. *Nat Rev Drug Discov* 12:217–228
- Meulmeester E, Ten Dijke P (2011) The dynamic roles of TGF- $\beta$  in cancer. *J Pathol* 223:205–218
- Mikhail AS, Allen C (2010) Block copolymer micelles for delivery of cancer therapy: transport at the whole body, tissue and cellular levels. *J Control Release* 138:214–223
- Mrass P, Kinjyo I, Ng LG et al (2008) CD44 mediates successful interstitial navigation by killer T cells and enables efficient antitumor immunity. *Immunity* 29:971–985
- Mueller MM, Fusenig NE (2004) Friends or foes – bipolar effects of the tumour stroma in cancer. *Nat Rev Cancer* 4:839–849
- Nakasone ES, Askautrud HA, Kees T et al (2012) Imaging tumor-stroma interactions during chemotherapy reveals contributions of the microenvironment to resistance. *Cancer Cell* 21:488–503
- Nobis M, McGhee EJ, Morton JP et al (2013) Intravital FLIM-FRET imaging reveals dasatinib-induced spatial control of Src in pancreatic cancer. *Cancer Res* 73:4674–4686
- Olson MF, Sahai E (2009) The actin cytoskeleton in cancer cell motility. *Clin Exp Metastasis* 26:273–287
- Orth JD, Kohler RH, Foijer F et al (2011) Analysis of mitosis and antimetabolic drug responses in tumors by in vivo microscopy and single-cell pharmacodynamics. *Cancer Res* 71:4608–4616
- Padera TP, Kadambi A, Di Tomaso E et al (2002) Lymphatic metastasis in the absence of functional intra tumor lymphatics. *Science* 296:1883–1886
- Palmer GM, Fontanella AN, Shan S et al (2011) In vivo optical molecular imaging and analysis in mice using dorsal window chamber models applied to hypoxia, vasculature and fluorescent reporters. *Nat Protoc* 6:1355–1366
- Parks SK, Mazure NM, Counillon L, Pouyssegur J (2013) Hypoxia promotes tumor cell survival in acidic conditions by preserving ATP levels. *J Cell Physiol* 228:1854–1862
- Perentes JY, McKee TD, Ley CD et al (2009) In vivo imaging of extracellular matrix remodeling by tumor-associated fibroblasts. *Nat Methods* 6:2008–2010
- Philipp U, Roussos ET, Oser M et al (2008) A Mena invasion isoform potentiates EGF-induced carcinoma cell invasion and metastasis. *Dev Cell* 15:813–828
- Pietras K, Ostman A (2010) Hallmarks of cancer: interactions with the tumor stroma. *Exp Cell Res* 316:1324–1331
- Pink DBS, Schulte W, Parseghian MH et al (2012) Real-time visualization and quantitation of vascular permeability in vivo: implications for drug delivery. *PLoS One* 7:e33760
- Pinto MR, Schanze KS (2004) Amplified fluorescence sensing of protease activity with conjugated polyelectrolytes. *Proc Natl Acad Sci U S A* 101:7505–7510
- Provenzano PP, Eliceiri KW, Campbell JM et al (2006) Collagen reorganization at the tumor-stromal interface facilitates local invasion. *BMC Med* 4:38
- Provenzano PP, Inman DR, Eliceiri KW et al (2008) Collagen density promotes mammary tumor initiation and progression. *BMC Med* 6:11

- Provenzano PP, Eliceiri KW, Keely PJ (2009) Multiphoton microscopy and fluorescence lifetime imaging microscopy (FLIM) to monitor metastasis and the tumor microenvironment. *Clin Exp Metastasis* 26:357–370
- Provenzano P, Cuevas C, Chang A et al (2012) Enzymatic targeting of the stroma ablates physical barriers to treatment of pancreatic ductal adenocarcinoma. *Cancer Cell* 21:418–429
- Rapisarda A, Melillo G (2012) Overcoming disappointing results with antiangiogenic therapy by targeting hypoxia. *Nat Rev Clin Oncol* 9:378–390
- Ray P, De A, Min J-J et al (2004) Imaging tri-fusion multimodality reporter gene expression in living subjects. *Cancer Res* 64:1323–1330
- Ritsma L, Steller EJA, Ellenbroek SIJ et al (2013) Surgical implantation of an abdominal imaging window for intravital microscopy. *Nat Protoc* 8:583–594
- Sakaue-Sawano A, Ohtawa K, Hama H et al (2008) Tracing the silhouette of individual cells in S/G2/M phases with fluorescence. *Chem Biol* 15:1243–1248
- Salnikov AV, Roswall P, Sundberg C et al (2005) Inhibition of TGF-beta modulates macrophages and vessel maturation in parallel to a lowering of interstitial fluid pressure in experimental carcinoma. *Lab Invest* 85:512–521
- Sanz-Moreno V, Gadea G, Ahn J et al (2008) Rac activation and inactivation control plasticity of tumor cell movement. *Cell* 135:510–523
- Schepers AG, Snippert HJ, Stange DE et al (2012) Lineage tracing reveals Lgr5+ stem cell activity in mouse intestinal adenomas. *Science* 730:730–735
- Serrels A, Timpson P, Canel M et al (2009) Real-time study of E-Cadherin and membrane dynamics in living animals: implications for disease modeling and drug development. *Cancer Res* 69:2714–2719
- Shen B, Jeon J, Palmer M et al (2013) Positron emission tomography imaging of drug-induced tumor apoptosis with a caspase-triggered nanoaggregation probe. *Angewandte Chemie* 52:10511–10514
- Shojaei F, Wu X, Malik AK et al (2007) Tumor refractoriness to anti-VEGF treatment is mediated by CD11b+Gr1+ myeloid cells. *Nat Biotechnol* 25:911–920
- Skala MC, Riching KM, Gendron-Fitzpatrick A et al (2007) In vivo multiphoton microscopy of NADH and FAD redox states, fluorescence lifetimes, and cellular morphology in precancerous epithelia. *Proc Natl Acad Sci U S A* 104:19494–19499
- Smith ML, Gourdon D, Little WC et al (2007) Force-induced unfolding of fibronectin in the extracellular matrix of living cells. *PLoS Biol* 5:12
- Smith BR, Cheng Z, De A et al (2008) Real-time intravital imaging of RGD-quantum dot binding to luminal endothelium in mouse tumor neovasculature. *Nano Lett* 8:2599–2606
- Smith BR, Cheng Z, De A et al (2010) Dynamic visualization of RGD-quantum dot binding to tumor neovasculature and extravasation in multiple living mouse models using intravital microscopy. *Small* 6:2222–2229
- Smith BR, Zavaleta C, Rosenberg J et al (2013) High-resolution, serial intravital microscopic imaging of nanoparticle delivery and targeting in a small animal tumor model. *Nano Today* 8:126–137
- Snoeks TJA, Löwik CWGM, Kaijzel EL (2010) ‘In vivo’ optical approaches to angiogenesis imaging. *Angiogenesis* 13:135–147
- Steven P, Bock F, Hüttmann G, Cursiefen C (2011) Intravital two-photon microscopy of immune cell dynamics in corneal lymphatic vessels. *PLoS One* 6:e26253
- Stoll S, Delon J, Brotz TM, Germain RN (2002) Dynamic imaging of T cell-dendritic cell interactions in lymph nodes. *Science* 296:1873–1876
- Tada H, Higuchi H, Wanatabe TM, Ohuchi N (2007) In vivo real-time tracking of single quantum dots conjugated with monoclonal anti-HER2 antibody in tumors of mice. *Cancer Res* 67:1138–1144
- Tanaka K, Morimoto Y, Toiyama Y et al (2012) In vivo time-course imaging of tumor angiogenesis in colorectal liver metastases in the same living mice using two-photon laser scanning microscopy. *J Oncol* 2012:265487

- Thurber G, Yang K, Reiner T et al (2013) Single-cell and subcellular pharmacokinetic imaging allows insight into drug action in vivo. *Nat Commun* 4:1505
- Timpson P, McGhee EJ, Morton JP et al (2011) Spatial regulation of RhoA activity during pancreatic cancer cell invasion driven by mutant p53. *Cancer Res* 71:747–757
- Tlsty TD, Coussens LM (2006) Tumor stroma and regulation of cancer development. *Annu Rev Pathol* 1:119–150
- Trédan O, Galmarini CM, Patel K, Tannock IF (2007) Drug resistance and the solid tumor micro-environment. *J Natl Cancer Inst* 99:1441–1454
- Tsai YC, Mendoza A, Mariano JM et al (2007) The ubiquitin ligase gp78 promotes sarcoma metastasis by targeting KAI1 for degradation. *Nat Med* 13:1504–1509
- Tsourkas A, Shinde-Patil VR, Kelly KA et al (2005) In vivo imaging of activated endothelium using an anti-VCAM-1 magnetooptical probe. *Bioconjug Chem* 16:576–581
- Tufto I, Hansen R, Byberg D et al (2007) The effect of collagenase and hyaluronidase on transient perfusion in human osteosarcoma xenografts grown orthotopically and in dorsal skinfold chambers. *Anticancer Res* 27:1475–1481
- Vakoc BJ, Lanning RM, Tyrrell JA et al (2009) Three-dimensional microscopy of the tumor micro-environment in vivo using optical frequency domain imaging. *Nat Med* 15:1219–1223
- Vaupel P, Kallinowski F, Okunieff P (1989) Blood flow, oxygen and nutrient supply, and metabolic microenvironment of human tumors: a review. *Cancer Res* 49:6449–6465
- Voura EB, Jaiswal JK, Mattoussi H, Simon SM (2004) Tracking metastatic tumor cell extravasation with quantum dot nanocrystals and fluorescence emission-scanning microscopy. *Nat Med* 10:993–998
- Weissleder R, Ntziachristos V (2003) Shedding light onto live molecular targets. *Nat Med* 9:123–128
- Williams RM, Zipfel WR, Webb WW (2005) Interpreting second-harmonic generation images of collagen I fibrils. *Biophys J* 88:1377–1386
- Wilson WR, Hay MP (2011) Targeting hypoxia in cancer therapy. *Nat Rev Cancer* 11:393–410
- Wilson A, Laurenti E, Oser G et al (2008) Hematopoietic stem cells reversibly switch from dormancy to self-renewal during homeostasis and repair. *Cell* 135:1118–1129
- Wyckoff JB, Pinner SE, Gschmeissner S et al (2006) ROCK- and myosin-dependent matrix deformation enables protease-independent tumor-cell invasion in vivo. *Curr Biol* 16:1515–1523
- Xia Z, Xing Y, Jeon J et al (2011) Immobilizing reporters for molecular imaging of the extracellular microenvironment in living animals. *ACS Chem Biol* 6:1117–1126
- Yamamoto N, Jiang P, Yang M et al (2004) Cellular dynamics visualized in live cells in vitro and in vivo by differential dual-color nuclear-cytoplasmic fluorescent-protein expression. *Cancer Res* 64:4251–4256
- Yan X, Ray P, Paulmurugan R et al (2013) A transgenic tri-modality reporter mouse. *PLoS One* 8:e73580
- Yu H, Mouw JK, Weaver VM (2011) Forcing form and function: biomechanical regulation of tumor evolution. *Trends Cell Biol* 21:47–56
- Zhu L, Xie J, Swierczewska M et al (2011) Dual-functional, receptor-targeted fluorogenic probe for in vivo imaging of extracellular protease expressions. *Bioconjug Chem* 22:1001–1005

## Chapter 13

# Imaging Drug Distribution and Effects at the Single Cell Level In Vivo

Randy Giedt, Katy Yang, and Ralph Weissleder

**Abstract** Current pharmacokinetic and pharmacodynamic studies mostly focus on large scale organ-level measurements of drug distribution and performance. These approaches neglect the more refined single-cell and subcellular analyses that provide insight into how drugs truly function at the cellular level in an *in vivo* environment. Recently, improved methods in intravital imaging have introduced the possibility of *in vivo* single-cell pharmacokinetic and pharmacodynamic studies. Combined with improved modeling, these studies can reveal how drugs work or fail at single-cell resolution *in vivo*.

**Keywords** Drug delivery • Single cell imaging • Pharmacokinetics • Pharmacodynamics • Fluochromes • Fluorescent reporters • FLAP • FRET

### 13.1 Introduction

Therapeutic drugs are often developed in stages. First, candidate biological functions and chemical formulations are identified and validated *in vitro*. Promising compounds are then screened for distribution characteristics (pharmacokinetics, or PK); desired and undesired bioactivity effects as a function of dose (pharmacodynamics, or PD); overall metabolism; and toxicity limits. The results of these studies are then utilized to predict human dosage. Finally, the compound moves into clinical trials that assess its effects in humans. The process is expensive, its success rate is low, and system-level read-outs are often not obtained *in vivo*. Furthermore, when

---

R. Giedt • K. Yang

Center for Systems Biology, Massachusetts General Hospital,  
185 Cambridge St, CPZN 5206, Boston, MA 02114, USA

R. Weissleder, MD, PhD (✉)

Center for Systems Biology, Massachusetts General Hospital,  
185 Cambridge St, CPZN 5206, Boston, MA 02114, USA

Department of Systems Biology, Harvard Medical School,  
200 Longwood Ave, Boston, MA 02115, USA

e-mail: [rweissleder@mgd.harvard.edu](mailto:rweissleder@mgd.harvard.edu)

drugs fail in later clinical testing, extensive analyses of the underlying reasons – commonplace in other industries – are often not pursued.

Current PK models are typically coarse-grain, multi-compartmental models (Sun et al. 1999). While coarse-grain models typically incorporate patient-to-patient differences in drug absorption and distribution, metabolics, physiological states, etc., they neglect more refined variability measurements at the single-cell level. Recent evidence of, for example, tumor heterogeneity, indicates that including single-cell PK may create more instructive models of tumor response for designing chemotherapeutic agents (Spencer et al. 2009; Campos et al. 2013; Heppner 1984). Similarly, current PD studies in both animal models and humans are often based on *in vitro* cell response data combined with *in vivo* large-scale physiological measurements of therapeutic activity and drug toxicity. These large-scale calculations/appraisals/evaluations often miss/exclude the factors and their dynamics that ultimately govern efficacy: specific signaling pathway analysis over time, emergence of resistance, unexpected bystander effects, immune response effects, and response heterogeneity among cell populations, among others. Improved knowledge of *in vivo* PD may not only expand our understanding and use of successful candidate drugs but also create an avenue for understanding the reasons behind unexpected drug failures.

Recent advances in intravital imaging techniques combined with novel chemistries have shown tremendous promise in advancing drug development methods. Specifically, novel observable small-molecule fluorescent drugs with similar affinity and PK to their therapeutic counterparts (Budin et al. 2011; Yang et al. 2012; Prescher and Bertozzi 2005; Reiner et al. 2012; Devaraj and Weissleder 2011) are being developed and utilized with fluorescent pathway read-outs for more detailed, single-cell, *in vivo* PK/PD analyses (Fig. 13.1). We can now study drug PK at single-cell resolution in order to address questions such as, “What is the single-cell heterogeneity of drug distribution?”, “How does a drug distribute throughout a tumor?”, and “How do factors such as the state of the vasculature affect the efficacy of therapeutic agents?”, among others. In addition, time-lapse information about drug distribution at the single-cell level opens the possibility for improved mathematical models of PK. These labeled drugs, advances in mouse models, and improved computational approaches have opened new opportunities. In the future, we believe that intravital imaging will be used in *in vivo* environments to elucidate previously inaccessible PK/PD properties: measuring single-cell heterogeneity, improving drug dosing and toxicity analyses, studying closely related chemical structures *in vivo*, and uncovering bystander effects will result in improved modeling of drug effects. The goal of this review is to summarize some of the foundational work in this emerging field, thereby supplementing other recent reviews (Pittet and Weissleder 2011; Condeelis and Weissleder 2010).



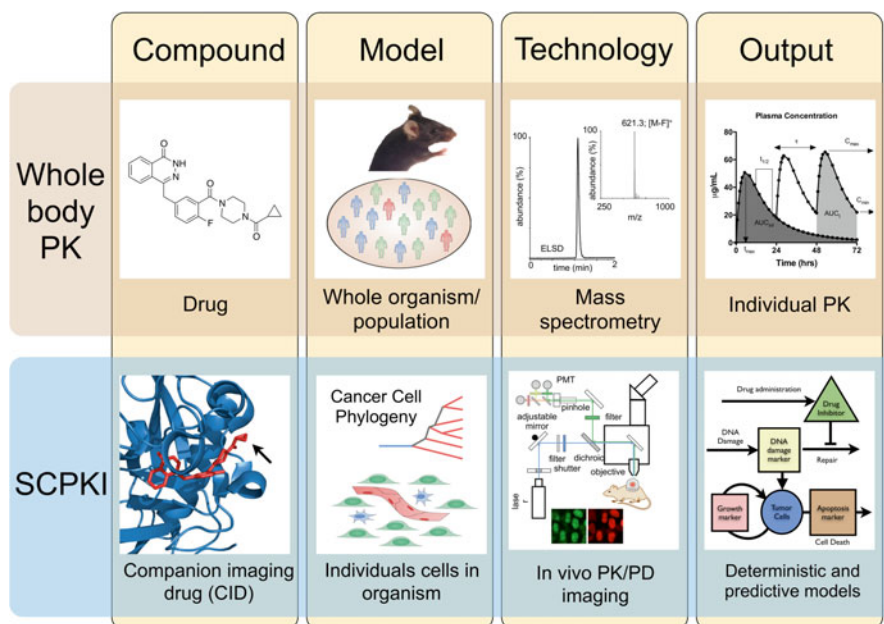


**Fig. 13.1** SCPki adds to conventional PK/PD analysis by providing single-cell resolution data. Whole-body pharmacokinetics (*top row*) are relatively standardized measurements taken in drug development. The drug is typically studied by mass spectrometry for drug detection in both animal models and the clinic. Data is analyzed using compartmental or non-compartmental plasma concentration analyses. Single cell pharmacokinetic imaging (SCPki, *bottom row*) integrates cell signaling pathway analysis and drug perturbation with therapeutic efficacy (*bottom right*). Intravital microscopy techniques can use companion imaging agents to track drugs *in vivo* in individual cells with variable genetic and epigenetic backgrounds. Various cell signaling reporters can then be integrated into the framework to provide real-time feedback on signaling and drug effects

## 13.2 Technology Development

### 13.2.1 Fluorescent Imaging Drugs

Table 13.1 summarizes common approaches to rendering therapeutic drugs fluorescent (so-called “companion imaging drugs”, or CID). Large-molecular-weight drugs (e.g. therapeutic antibodies, nanoparticles) are often easily labeled with reactive fluorochromes (e.g. Cyanine type dyes, Alexa Fluor, and VivoTag dyes). Given the large size of these therapeutic compounds, single-fluorochrome labeling generally does not significantly affect biodistribution and/or function. Small-molecule

**Table 13.1** Fluorescent companion imaging drugs

Type	Common tags	Examples
Small molecule	Direct labeling	BODIPY derivatives preferred (newer derivatives being developed); CFDA (carboxy-fluorescein diacetate)
	Two step bioorthogonal labeling	Activatable BODIPY; cell membrane permeable dyes (such as CFDA)
Antibody	Direct labeling	Many fluorochromes; specific choice less critical
Nanoparticle drugs	Direct labeling	Many fluorochromes and fluorescent nanoparticles; specific choice less critical

drug labeling, on the other hand, can be more challenging, and the choice of fluorochrome and attachment strategies become more critical. Overall, two different approaches have been pursued: (i) directly attaching a fluorophore to a drug (Reiner et al. 2012; Zhang et al. 2012) and (ii) bioorthogonal two-step systems with *in vivo* recombination (Devaraj et al. 2009).

### 13.2.1.1 Direct Labeling

Direct labeling is a viable (and often preferable) option for many small molecules, particularly if non-critical anchor points can be identified so that fluorochrome labeling does not interfere with target binding (Fig. 13.2). A crystal structure within the drug bound to the intended protein target is particularly useful in designing attachment points. Occasionally it may be necessary to utilize short linkers to attach fluorochromes, depending on the target. Ideal fluorochromes are highly water soluble, low molecular weight, cell-membrane permeable, bright, and stable. Several fluorochromes fulfill these prerequisites: BODIPY-FL (including some more water-soluble derivatives), Fluorescein diacetate, and perhaps Oregon Green 488, among others (Lavis and Raines 2008). Undoubtedly, newer fluorochromes will be developed to extend current capabilities and designs.

### 13.2.1.2 Bioorthogonal Labeling

A second method of producing CID utilizes the inverse Diels-Alder cycloaddition reaction between trans-cyclooctene (TCO) and tetrazine (Tz) (Devaraj et al. 2008, 2009, 2010; Blackman et al. 2008). In this scheme, a drug of interest is labeled with TCO in a manner that minimizes alterations. A Tz-labeled fluorophore is then used either to reveal the TCO-labeled drug *in vivo* or to label the drug *in vitro*. Both the TCO and Tz are relatively small and non-perturbing moieties, which often simplifies cellular delivery. The bioorthogonal reaction has extremely fast kinetics and highly selective conversion into a fluorescent drug conjugate (Devaraj et al. 2009). Recent developments of activatable Tz-BODIPY dyes have further advanced this labeling scheme, as the Tz-BODIPYs are essentially non-fluorogenic whereas the clicked product becomes brightly fluorescent, vastly improving SNR (Carlson et al. 2013).

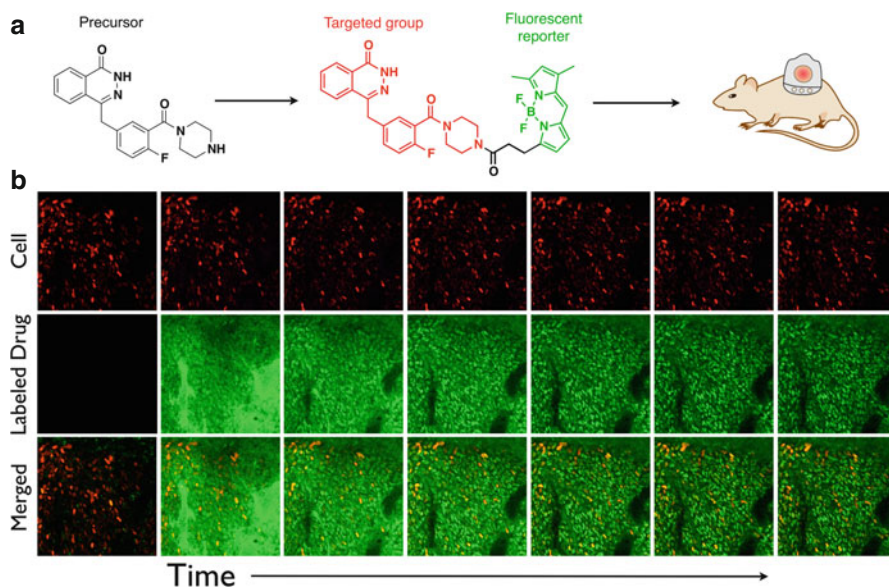


**Fig. 13.2** Fluorescently labeled drugs allow *in vivo* PK analysis. (a) Fluorescently labeled drugs are typically created by conjugating a fluorescent tag with a precursor drug target for use in *in vivo* imaging applications. (b) As an example of fluorescently labeled drug PK analysis, a PARP inhibitor was tagged with Bodipy-FL and observed over 3 h as it distributed from the vasculature into a tumor in an *in vivo* system (Image taken in part from Thurber et al. (2013))

### 13.2.2 Fluorescent Protein Reporters for PK/PD Imaging

Fluorescent reporters are essential to drug imaging. Fluorescent proteins (FP) are used for four different applications (Fig. 13.3): (i) to mark cells of interest (e.g. cancer cells and/or immune cells); (ii) to delineate cell boundaries in order to simplify analyses (e.g. cell membrane FP and/or nuclear proteins); (iii) as pathway reporters (e.g. DNA damage or pERK); and (iv) as cell fate reporters (e.g. cell cycle, apoptosis, proliferation).

#### 13.2.2.1 Generic Reporters

Generic reporters are used in the blue (e.g. Cerulean), yellow/green (e.g. EGFP), red (e.g. mCherry, mApple), and far red (e.g. iRFP) channels to label cells. One major consideration is how the reporters combine with fluorescent drugs (often BODIPY labeled) and additional pathway read-outs. Supplemental systems to study cell-cell variation include Brainbow (Livet et al. 2007) and the Lentiviral Gene Ontology (LeGO) system. Using the LeGO method, cells are transduced with red (mCherry), green (Venus), or blue (Cerulean) fluorescent proteins, either alone or in combination, to produce a palette of potential colors via an RGB color system (Weber et al. 2011, 2012). Applications of this system include probing questions related to how

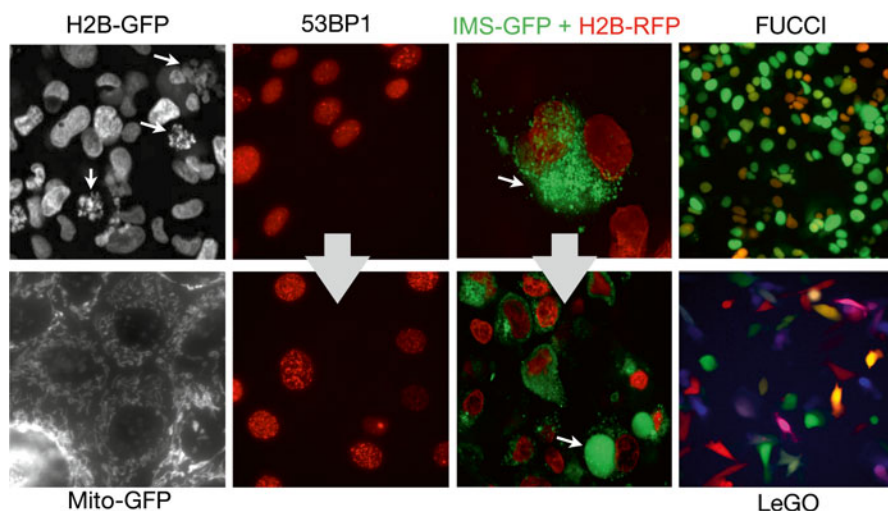


**Fig. 13.3** Genetic reporters allow PD analysis. H2B-GFP allows detailed analysis of nuclear morphology, including arrests and apoptosis (*white arrows*). Mito-GFP is often used to delineate mitochondrial morphology. A particularly useful DNA damage marker is 53BP1-FP, which changes its phenotype from diffuse nuclear distribution (*top*) to punctuate nuclear staining (*bottom*) during DNA damage. Column three illustrates the use of MOMP markers, i.e. the use of IMS-GFP combined with H2B-RFP to measure apoptosis. Fucci is an example of a robust cell cycle indicator, and the LeGO system functions very well as a marker of clonal proliferation (Figure taken in part from Earley et al. (2012) and Orth et al. (2011))

drug dosing affects the long-term proliferation rates of individual clonal populations (Weber et al. 2011; Malide et al. 2012); how cellular diversity changes under pharmaceutical treatment (Kreso et al. 2013); and the likelihood of specific cells metastasizing.

### 13.2.2.2 Boundary Markers

Boundary markers include spatially localized FP expression to delineate cell membranes and/or cellular structures of interest (e.g. nucleus, mitochondria). One example of a nuclear marker, a probe based on fusing a fluorescent protein (EGFP) with a core histone protein (H2B), has been used to monitor nuclear localization in single cells as well as mitosis *in vivo* (Orth et al. 2011). H2B is a histone protein involved in chromatin structure that, when fused to a fluorescent protein, facilitates visual observation of chromosomal status (condensation, segregation, etc.), thereby/consequently enabling interpretation of the relative cell cycle state as well as the general nuclear localization in individual cells. Other useful boundary markers delineate the cell plasma membrane using either a FP to mark the entire cell (described above) or a membrane targeting sequence fused to an FP (such as the N-terminal 20 amino acids of neuromodulin (Skene and Virag 1989)). On a smaller scale, mitochondria

have been imaged *in vivo* via genetically constructed mouse models with a Dendra2 based (Gligorijevic et al. 2009) photoactivable construct that ubiquitously targets across cell types in the widely expressed Rosa26 locus (Pham et al. 2012). Using a photoactivatable probe in this *in vivo* setting allows the observer to monitor both the static condition of mitochondria as well as the movement, fusion, and fission rates of these organelles at a single-cell level.

### 13.2.2.3 Pathway Reporters

Pathway reporters potentially allow imaging of specific cellular pathways and their behavior in the presence of therapeutic interventions, which is critically important to understanding single cell *in vivo* PD. In recent years, advanced fluorescent techniques based on photobleaching and recovery methods, such as Fluorescence Recovery After Photobleaching (FRAP), Fluorescence Loss in Photobleaching (FLIP), Fluorescence Localization After Photobleaching (FLAP), and a molecular interaction tool, Fluorescence Resonance Energy Transfer (FRET), have come online *in vitro* and show promise for *in vivo* applications (Ishikawa-Ankerhold et al. 2012). These biosensors have numerous beneficial characteristics, including rapid measurement acquisition and the ability to measure molecular interaction distances (Aoki et al. 2013). Komatsu and colleagues have recently developed a FRET backbone system, Eevee, that rapidly develops a variety of signaling molecule indicators in intracellular applications. Specifically, the lab used this system to create an array of biosensors to study cancer biology. One of these probes, a phospho-ERK indicator, significantly has *in vivo* applications (Komatsu et al. 2011). More traditional pathway reporters tag relevant proteins or sensors that indicate interaction with important molecules or ions. While many of these technologies have yet to be translated into a *whole mouse environment*, indicators of relevant biological functions/PD being used *in vivo* are emerging. One such probe is the genetically encoded calcium indicator (GECI), which has been utilized as an *in vivo* neuronal calcium signaling indicator (Watanabe 1997). With advances in underlying technologies (Zhao et al. 2011) and increased focus on neuronal research, these indicators will likely play an important role in general intravital imaging as well as PD analysis of calcium flux.

### 13.2.2.4 Cell Fate Reporters Are Particularly Important

Cell fate reporters are particularly important for PD analyses, especially in studies dealing with chemotherapeutic agent development. Types of cell fate reporters include cell cycle indicators that visually map cell arrest or apoptosis. A probe in which  $\beta$ 1-tubulin was fused to TagRFP, for example, was utilized *in vivo* to follow microtubule changes during mitosis (Orth et al. 2011). In another applicable example, mitochondrial outer-membrane potential (MOMP), which is an early step in apoptosis, was measured by fluorescently tagging a mitochondrial inner-membrane

protein (Smac mitochondrial import sequence residues 1–59) (Earley et al. 2012; Albeck et al. 2008; Du et al. 2000). This system quantified apoptosis by observing the fluorescent leakage from the mitochondria to the cytoplasm during mitochondrial depolarization. Furthermore, some of the reporters described as boundary markers may also serve as cell fate reporters. For example, while H2B-EGFP can delineate the cell nucleus, it can also function as a mitotic reporter, as described above. Additionally, because H2B localizes with chromatin, the fragmentation that occurs during apoptosis can be visualized using H2B-EGFP.

### 13.2.3 Image and Data Processing

Analyzing intravital images is a particularly challenging image processing application that blocks the acquisition and use of large amounts of data within a reasonable time frame. Automating image analysis to create and subsequently use large, robust data sets could dramatically improve applications that include modeling as well as SCPKI. Though the last decade has seen considerable progress in *in vitro* image analysis, intravital imaging involves unique challenges. Generally, image sets display highly complex and dense environments, constant cell movement and rearrangement in both the X-Y and Z planes, lower fluorescent signal-to-noise ratios than are normally present in cell culture, and heterogeneous feature appearance (Carpenter 2009). To date, relatively little work has been done in this field due to its inherent complexities.

Recognizing predefined image properties is typically referred to as “segmentation”, which in this context refers to applying an algorithm to an image to create a binary image in which the background is separated from the foreground (Gonzalez et al. 2009). Different image segmentation methods (for example, thresholding methods (Sezgin and Sankur 2004)) have been developed over the past 40 years to meet diverse modern image processing needs, with a wide range of implementation complexities depending on the specific image and application qualities. Simple image segmentation methods involve thresholding algorithms that separate pixels based on different techniques for global image property analysis. More complex and/or varied methods include local-area image segmentation (Long et al. 2009; Jaqaman et al. 2010), edge detection to elucidate desired image properties (Bergmeir et al. 2012), watershed and/or energy-function based methods (Lin et al. 2007), and model-based feature determination (Jaqaman et al. 2010), among many other strategies.

An image-processing pipeline for single-cell pharmacology (SCP) analysis involves several steps. First, single cells must be separated from one another, typically via a fluorescent cellular or subcellular marker combined with a segmentation algorithm. Second, PK and/or PD recognition must be implemented. PK identification could utilize fluorescently-labeled drug imaging, as described above, and PD determination could employ a cell fate/outcome reporter. Third, PK and/or PD must be linked to the previously defined individual cells. This is done using some algo-



rithm that consistently links moving cells from frame to frame, even with changes in cell appearance and/or 3-D movement (Jaqaman et al. 2008; Racine et al. 2007; Ponti et al. 2005). Combining these steps in a typically noisy environment presents a significant challenge to creating robust and repeatable analysis methods that can answer specific biological or PK/PD questions *in vivo*.

Analytic approaches to such data sets depend on the experimental designs and hardware used to acquire images. Obviously, generating these data sets requires coordinating genetic reporters to maximize the number of individual color channels. Further, cell tracking requires images to be acquired frequently enough to minimize the distance that cells move between images. Going forward, both software design and improved acquisition equipment will likely play a major role in advancing automatic data analysis, since higher-quality data strengthens analysis.

One analysis strategy recently implemented for SCPKI used an adaptive thresholding algorithm for cell segmentation in conjunction with a Bodipy-FL-labeled PARP inhibitor and the previously-described H2B nuclear marker to determine drug distribution *in vivo* (Giedt et al. 2013). Using this protocol, H2B-labeled cancer cells were first segmented based on their nuclei via Ray's thresholding method, which is an adaptive, iterative segmentation method that has several advantages for intravital microscopy image analysis (Ray and Saha 2009). First, using an adaptive thresholding method that segments images based on local characteristics rather than global image properties facilitates reliable and repeatable segmentation despite the presence of heterogeneous nuclear marker expression (due to both biological stochasticity and variability in the Z-height when segmenting single slice images). Second, the algorithmic iteration reduces the amount of user input required and consequently permits a more robust and easily repeatable segmentation procedure. This algorithm also allows intravital image segmentation and analysis using simple 2-D images, as overlapping cells are separated by eliminating the dimmer of the two cells in a local thresholding framework. Following cancer cell nuclei segmentation, cells were linked frame-to-frame using a tracking algorithm (Jaqaman et al. 2008). After cell linking, the relative concentration of BODIPY-FL-labeled drug was measured by quantifying the fluorescence intensity of the labeled drug in a defined area within specific cell nuclei. In this manner, drug concentration, distribution, and heterogeneity were monitored over time in an *in vivo* environment via/using an automated format (Fig. 13.4).

#### 13.2.4 Orthotopic Organ Imaging

Imaging tissues at (sub)cellular resolutions in the native organ environment is a desirable goal for SCPKI. New water immersion “stick” and long working distance objectives (Lee et al. 2012a), as well as microendoscopes, can access difficult-to-image tissues. In addition to improved objectives and faster imaging approaches, motion restriction methods are essential to (sub)cellular *in vivo* organ imaging.

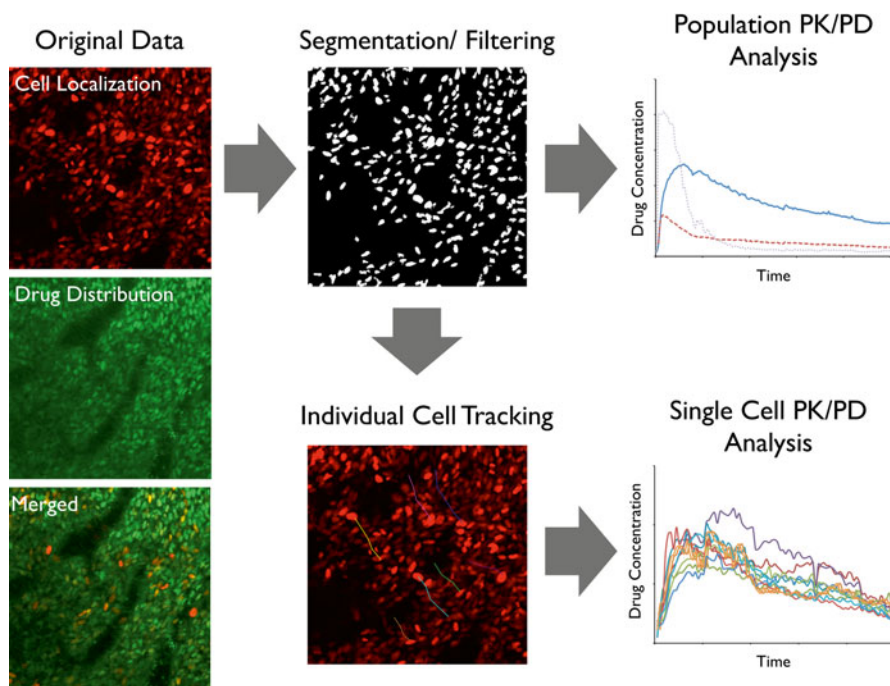


**Fig. 13.4** Combining labeled drugs with genetic reporters allows for automated analysis. To automatically analyze PK/PD conditions, a cell indicator must first be segmented, and after segmentation, population statistics can be analyzed. By tracking individual cells over time, it is also possible to delineate single-cell PK/PD analyses (Figure taken in part from Giedt et al. (2013))

#### 13.2.4.1 Motion Suppression

A well established and popular method of minimizing animal movement during imaging is the dorsal skinfold window chamber which can be immobilized on the microscope stage (Brown et al. 2001). Titanium or stainless steel window chambers are surgically implanted in mice to enable the injection and observation of human xenografts through a coverslip viewing area. This mechanical restraint normally creates sufficient stability for detailed imaging and is thus well suited to pharmacological tumor biology applications, such as PK/PD analysis of chemotherapeutic treatments.

In addition to window chambers, simple external mechanical interventions can also be used to restrict movement in orthotopic settings. One such method utilizes an adjustable rigid metal stand with an attached circular or U-shaped metal ring containing a secured coverslip, all anchored on a base plate. By physically placing the end of this apparatus against the tissue area of interest (a surgically exposed organ, for example), motion in the X-Y plane can be restricted by the soft compression of the stabilizer's outer ring against the tissue. Motion in the Z-plane can be similarly restricted by compression from the coverslip. As an additional benefit,

incorporating a coverslip into the system simplifies and improves image acquisition by increasing the sample's in-focus range (Lee et al. 2012b).

Mitigating or even eliminating motion artifacts can also be accomplished by using the improved, ultrafast confocal and 2-photon scanning microscopes (see (Tanaami et al. 2002)) that have become commercially available. Adapted/Augmented mechanical and acquisition methods, including new resonant scanners/fast axis mirrors, in conjunction with new sample scanning methods, such as line or spinning disk excitation, now allow for image acquisition of *in vivo* samples at rates of ~400 frames per second or greater. By utilizing these technologies, motion artifacts caused by traditionally longer image acquisition times of ~500 ms to 2 s can be eliminated. In addition, these technologies permit *in vivo* acquisition of detailed, fast-action events at the single-cell level.

While mechanical stabilization methods are helpful, they often cannot completely eliminate motion defects, especially in high-movement areas such as the heart or lungs. A supplementary / ancillary strategy for image stabilization involves retrospectively gating temporally serial images in relation to some physiologic cycle (for example, the respiratory or cardiac cycle). Briefly, retrospective gating schemes typically acquire a large number of images for post-processing/selection. These images are then sorted using an algorithm that determines movement and/or focus, and individual images are either selected or eliminated in order to create a coherent time-lapse sequence for an in-focus region. These retrospective methodologies can be combined with physical restraint to reliably image characteristics such as cell movement, cellular or intracellular behavior, and drug distribution, to name a few, over long time periods in high-motion environments. Some examples that combine retrospective gating with mechanical restriction of movement include the intravital imaging of kidney movement despite the animal breathing cycle (Lee et al. 2012b) and viewing cardiomyocytes in a live, beating heart (Lee et al. 2012a).

### 13.3 Some Examples of PK/PD Imaging

Most recent examples of intravital PK/PD imaging have focused on cancer therapeutics. Emerging imaging techniques and model systems, however, also have the potential to evaluate drugs targeting cardiovascular (Lee et al. 2012b) and neurological diseases.

#### 13.3.1 *Taxol*

One relevant study focused on the SCPDI of a classic chemotherapeutic agent. In this work, cells transfected with H2B-EGFP were observed *in vivo* following treatment with taxol, an anti-mitotic microtubule stabilizing agent. Time-lapse, high-resolution imaging at the single-cell level tracked cell division behavior in

the absence and presence of taxol treatment. A key finding of this study was that cells responded to treatment differently in *in vitro* versus *in vivo* environments. Specifically, while cells in culture underwent apoptosis following Paclitaxel treatment, cells *in vivo* survived longer and in many cases became multinucleate. More broadly, this study demonstrated that multiple cellular PD phenotypes, including mitotic arrest, multinucleation, and apoptosis, could be observed *in vivo* (Orth et al. 2011). Taken as a whole, this research illustrates intravital microscopy's ability to elucidate drug-mediated events at the cellular and subcellular level in single cells.

### 13.3.2 Poly ADP Ribose Polymerase (PARP): Inhibitors

This class of candidate drugs inhibit DNA repair. These agents perform extremely well *in vitro*, but recent clinical trials have not conclusively proven the efficacy of the PARP inhibitor class. To study PK's possible role in this failure, a fluorescent (BODIPY-FL) version of AZD2281 was synthesized and validated. Breast and ovarian cancer cell lines were transduced with H2B, described above, fused to Apple fluorescent protein (Reiner et al. 2012), which was used to identify cancer cell nuclei (the predominant localization of PARP1) *in vivo*. Using both window chamber and orthotopic cancer models, SCPKI was observed and modeled, thereby illustrating the potential benefits of an intravital approach (Reiner et al. 2012; Thurber et al. 2013). Collectively, these studies show that the olaparib reached its cellular target in virtually all tumor cells and that drug distribution was an unlikely reason for observed clinical failures.

### 13.3.3 Other Examples

Either labeled drugs or intravital imaging can be utilized to answer specific questions about drug development. For example, BI-2536, an inhibitor of Polo-like kinase 1 (PLK1) (Budin et al. 2011), and MLN8054, an inhibitor of Aurora Kinase A (Yang et al. 2012), have both been fluorescently labeled using TCO-Tz bioorthogonal chemistry and have been shown to be effective agents *in vitro* for potential *in vivo* study. In another example, hepatic drug clearance has been monitored and modeled using intravital microscopy by observing the clearance of sodium fluorescein or rhodamine 123, providing an *in vivo* framework for improving coarse-grain PK analyses (Weiss et al. 2013). A study focusing on pharmacokinetic factors explored nanoparticle delivery targeted to  $\alpha(v) \beta(3)$  integrin (receptor for vitronectin), which is overexpressed in tumor cells and tumor vasculature, *in vivo* (Shuhendler et al. 2012). These studies, among others, and reviews of nanoparticle imaging (Chen et al. 2013; Yu et al. 2013; Han et al. 2013) illustrate the wide variety of applications for intravital microscopy in the realm of drug development.

## 13.4 Future Needs

Advances in intravital imaging technologies and analyses have initiated PK/PD studies at the single-cell level. This newly emerging field is expected to be a critical adjunct to conventional macroscopic PK/PD analysis and add to the understanding of drug action *in vivo*. However, there are a number of challenges that the field still faces.

### 13.4.1 Improved Fluorochromes

An area of interest for both intravital microscopy and the wider biological community is improving fluorochromes. Of particular concern for intravital imaging are a probe's overall brightness, signal to noise ratio, quantum efficiency, and photostability. Indeed, one of the most common difficulties associated with developing genetic or chemical probes for intravital imaging is insufficient brightness and/or signal to noise ratio in *in vivo* applications. Intravital environments are noisy and motile, making typically benign image capture parameters critically important for successful imaging. Improved fluorochromes would enable shorter image acquisition times and consequently allow for longer observation periods, thereby increasing the spatial resolution of both drug distribution and localized PD reporters and decreasing any potential system perturbation that fluorophores may introduce.

### 13.4.2 An Expanded Set of Robust Pathway Markers

Development of novel drugs necessitates corresponding pathway markers to monitor drug action specificity and potency. Indeed, the lack of fluorophore-labeled drugs and the need for corresponding genetic pathway markers that function well *in vivo* are the major impediments to the more widespread use of intravital microscopy in drug development and analyses. Additionally, creating stable markers for general cancer pathways (i.e. not designed to correspond to the action of a specific drug) to be used in evaluating and/or screening candidate molecules for possible unexpected actions and/or general efficacy would also be valuable for drug development. Well functioning apoptosis indicators for various stages of the apoptotic cycle would be particularly advantageous. Such indicators could serve as endpoints in drug efficacy measurements and help decode how cancer cells survive chemotherapeutic treatments. The combination of effective, easily identifiable markers of general cancer cell status and the PK single cell analyses described above would enormously benefit SCPKI and cancer drug development by aiding both drug creation/innovation and failure analyses.

### 13.4.3 *Improved Open-Source Analysis Tools*

Intravital imaging data sets are often visually complicated, with a diverse set of confounding factors. While it's unlikely that there will ever be a "one size fits all" approach to dealing with cell segmentation and data acquisition, even for more specialized applications like *in vivo* imaging, there is a need for easily accessible and widely applicable open-source methods for handling intravital images and data. An open source platform with PK/PD analysis and other pertinent processing tools, such as cell segmentation, tracking etc., would be invaluable for advancing drug development. Additionally, the broader biological research community needs further development of novel algorithms for the unique image processing issues involved with intravital imaging, including segmenting whole cells in contact with each other, tracking cells with high movement rates over long time periods in 3-D, and segmentation of 3-D data sets. In terms of intravital drug development, an ideal solution would be to create a system that combines real-time segmentation and cell tracking with relevant readouts (for example, fluorescence intensity of cells in multiple channels) for use during imaging sessions. Such a system would increase the efficiency and data yield of intravital imaging experiments. Finally, improved data sharing methods for intravital imaging experiments and biological knowledge would dramatically hasten research and drug development while conserving resources for the community at large. Approaches such as "GoogleCell" (Callaway 2012) would pool both data and resources to engender/precipitate more robust *in vivo* studies using a variety of equipment and data that would not otherwise be available to any single investigator.

### 13.4.4 *Organ Function Evaluation Methodology*

While much work to date has relied on window chambers, other improved orthotopic imaging approaches would allow us to study native environments and entire organs that are not easily accessible via window chamber. Indeed, studies focusing on organs such as the brain, heart, pancreas, and kidneys, among others, would benefit from improved orthotopic methods. For these organs, one of the largest problems is motion and related artifacts from both macroscale whole animal movement and microscopic cell movement. Finding additional methods to deal effectively with cell movement is a critical challenge. One potentially helpful area of study is the development of prospective gating strategies for use with intravital microscopy in real time. Such methods would greatly aid the study of high-movement areas such as the heart.



### 13.4.5 Modeling and Systems Biology Approaches

Continued advancement in intravital imaging methods and techniques that lead to improved single-cell quantitative data present us with the opportunity to create new, robust PK/PD models. In particular, incorporating single-cell measures of heterogeneity into the current coarse-grained, systemic PK/PD models could improve drug design by increasing knowledge of how drugs distribute in solid tumors and how diversely tumor cells respond to specific biological targets in an *in vivo* environment (Fig. 13.5). Improvements in these models will address tumor vasculature differences, individual cell location, cell heterogeneity in terms of both PK and PD, and, eventually, intracellular distribution and its respective heterogeneity *in vivo* (Thurber and Weissleder 2011). Practically, these improved models may help us determine

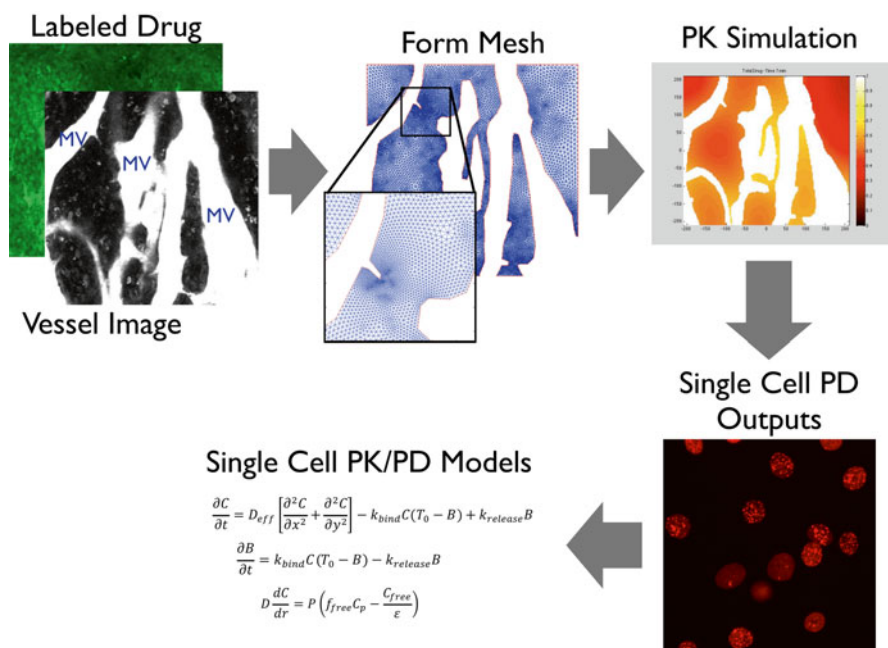


**Fig. 13.5** Intravital microscopy improves single-cell PK/PD models. The first step in creating models is to determine the relevant anatomy in the imaging area, typically by separating the vasculature from tumor/tissue areas. The tissue distribution area can then be simulated by a framework for computer analysis (mesh). From this data, relevant PK analyses and simulations can be constructed and combined with single-cell PD outputs. This data facilitates the creation of improved single-cell PK/PD models that can/may/will improve drug development and analysis (Figure taken in part from Thurber et al. (2013))

optimal drug concentrations based on biological efficacy rather than systemic toxicity and conduct failure analyses of unsuccessful drug candidates. Additionally, data from these models may generate opportunities for utilizing systems biology approaches to identifying new drug targets (Sorger and Schoeberl 2012).

## References

- Albeck JG et al (2008) Quantitative analysis of pathways controlling extrinsic apoptosis in single cells. *Mol Cell* 30:11–25
- Aoki K, Kamioka Y, Matsuda M (2013) Fluorescence resonance energy transfer imaging of cell signaling from in vitro to in vivo: basis of biosensor construction, live imaging, and image processing. *Dev Growth Differ* 55:515–522
- Bergmeir C, Garcia Silvente M, Benitez JM (2012) Segmentation of cervical cell nuclei in high-resolution microscopic images: a new algorithm and a web-based software framework. *Comput Methods Programs Biomed* 107:497–512
- Blackman ML, Royzen M, Fox JM (2008) Tetrazine ligation: fast bioconjugation based on inverse-electron-demand Diels-Alder reactivity. *J Am Chem Soc* 130:13518–13519
- Brown EB et al (2001) In vivo measurement of gene expression, angiogenesis and physiological function in tumors using multiphoton laser scanning microscopy. *Nat Med* 7:864–868
- Budin G, Yang KS, Reiner T, Weissleder R (2011) Bioorthogonal probes for polo-like kinase 1 imaging and quantification. *Angew Chem Int Ed Engl* 50:9378–9381
- Callaway E (2012) Structural biologists share their toys. *Nature* 483:15–16
- Campos M et al (2013) Simultaneous phenotypic and genetic characterization of single circulating tumor cells from colon cancer patients. *Histol Histopathol* 28(11):1439–50
- Carlson JC, Meimetus LG, Hilderbrand SA, Weissleder R (2013) BODIPY-tetrazine derivatives as superbright bioorthogonal turn-on probes. *Angew Chem Int Ed Engl* 52:6917–6920
- Carpenter AE (2009) Extracting rich information from images. *Methods Mol Biol* 486:193–211
- Chen O et al (2013) Compact high-quality CdSe-CdS core-shell nanocrystals with narrow emission linewidths and suppressed blinking. *Nat Mater* 12:445–451
- Condeelis J, Weissleder R (2010) In vivo imaging in cancer. *Cold Spring Harb Perspect Biol* 2:a003848
- Devaraj NK, Weissleder R (2011) Biomedical applications of tetrazine cycloadditions. *Acc Chem Res* 44:816–827
- Devaraj NK, Weissleder R, Hilderbrand SA (2008) Tetrazine-based cycloadditions: application to pretargeted live cell imaging. *Bioconjug Chem* 19:2297–2299
- Devaraj NK, Upadhyay R, Haun JB, Hilderbrand SA, Weissleder R (2009) Fast and sensitive pretargeted labeling of cancer cells through a tetrazine/trans-cyclooctene cycloaddition. *Angew Chem Int Ed Engl* 48:7013–7016
- Devaraj NK, Hilderbrand S, Upadhyay R, Mazitschek R, Weissleder R (2010) Bioorthogonal turn-on probes for imaging small molecules inside living cells. *Angew Chem Int Ed Engl* 49:2869–2872
- Du C, Fang M, Li Y, Li L, Wang X (2000) Smac, a mitochondrial protein that promotes cytochrome c-dependent caspase activation by eliminating IAP inhibition. *Cell* 102:33–42
- Earley S et al (2012) In vivo imaging of drug-induced mitochondrial outer membrane permeabilization at single-cell resolution. *Cancer Res* 72:2949–2956
- Giedt RJ, Koch PD, Weissleder R (2013) Single cell analysis of drug distribution by intravital imaging. *PLoS One* 8:e60988
- Gligorijevic B, Kedrin D, Segall JE, Condeelis J, van Rhee J (2009) Dendra2 photoswitching through the Mammary Imaging Window. *J Vis Exp* 28:1278

- Gonzalez RC, Woods RE, Eddins SL (2009) Digital image processing with Matlab. Gatesmark Publishing, Knoxville
- Han HS et al (2013) Spatial charge configuration regulates nanoparticle transport and binding behavior in vivo. *Angew Chem Int Ed Engl* 52:1414–1419
- Heppner GH (1984) Tumor heterogeneity. *Cancer Res* 44:2259–2265
- Ishikawa-Ankerhold HC, Ankerhold R, Drummen GP (2012) Advanced fluorescence microscopy techniques – FRAP, FLIP, FLAP, FRET and FLIM. *Molecules* 17:4047–4132
- Jaqaman K et al (2008) Robust single-particle tracking in live-cell time-lapse sequences. *Nat Methods* 5:695–702
- Jaqaman K et al (2010) Kinetochore alignment within the metaphase plate is regulated by centromere stiffness and microtubule depolymerases. *J Cell Biol* 188:665–679
- Komatsu N et al (2011) Development of an optimized backbone of FRET biosensors for kinases and GTPases. *Mol Biol Cell* 22:4647–4656
- Kreso A et al (2013) Variable clonal repopulation dynamics influence chemotherapy response in colorectal cancer. *Science* 339:543–548
- Lavis LD, Raines RT (2008) Bright ideas for chemical biology. *ACS Chem Biol* 3:142–155
- Lee S et al (2012a) Real-time in vivo imaging of the beating mouse heart at microscopic resolution. *Nat Commun* 3:1054
- Lee S, Vinegoni C, Feruglio PF, Weissleder R (2012b) Improved intravital microscopy via synchronization of respiration and holder stabilization. *J Biomed Opt* 17:96018–96011
- Lin G et al (2007) A multi-model approach to simultaneous segmentation and classification of heterogeneous populations of cell nuclei in 3D confocal microscope images. *Cytometry A* 71:724–736
- Livet J et al (2007) Transgenic strategies for combinatorial expression of fluorescent proteins in the nervous system. *Nature* 450:56–62
- Long F, Peng H, Liu X, Kim SK, Myers E (2009) A 3D digital atlas of *C. elegans* and its application to single-cell analyses. *Nat Methods* 6:667–672
- Malide D, Metais JY, Dunbar CE (2012) Dynamic clonal analysis of murine hematopoietic stem and progenitor cells marked by 5 fluorescent proteins using confocal and multiphoton microscopy. *Blood* 120:e105–e116
- Orth JD et al (2011) Analysis of mitosis and antimitotic drug responses in tumors by in vivo microscopy and single-cell pharmacodynamics. *Cancer Res* 71:4608–4616
- Pham AH, McCaffery JM, Chan DC (2012) Mouse lines with photo-activatable mitochondria to study mitochondrial dynamics. *Genesis* 50:833–843
- Pittet MJ, Weissleder R (2011) Intravital imaging. *Cell* 147:983–991
- Ponti A et al (2005) Periodic patterns of actin turnover in lamellipodia and lamellae of migrating epithelial cells analyzed by quantitative Fluorescent Speckle Microscopy. *Biophys J* 89:3456–3469
- Prescher JA, Bertozzi CR (2005) Chemistry in living systems. *Nat Chem Biol* 1:13–21
- Racine V et al (2007) Visualization and quantification of vesicle trafficking on a three-dimensional cytoskeleton network in living cells. *J Microsc* 225:214–228
- Ray N, Saha BN (2009) Edge sensitive variational image thresholding. *ICIP* 6:37–40
- Reiner T et al (2012) Imaging therapeutic PARP inhibition in vivo through bioorthogonally developed companion imaging agents. *Neoplasia* 14:169–177
- Sezgin M, Sankur B (2004) Survey over image thresholding techniques and quantitative performance evaluation. *J Electron Imaging* 13:146–165
- Shuhendler AJ et al (2012) A novel solid lipid nanoparticle formulation for active targeting to tumor  $\alpha(v)\beta(3)$  integrin receptors reveals cyclic RGD as a double-edged sword. *Adv Healthc Mater* 1:600–608
- Skene JH, Virag I (1989) Posttranslational membrane attachment and dynamic fatty acylation of a neuronal growth cone protein, GAP-43. *J Cell Biol* 108:613–624
- Sorger PK, Schoeberl B (2012) An expanding role for cell biologists in drug discovery and pharmacology. *Mol Biol Cell* 23:4162–4164

- Spencer SL, Gaudet S, Albeck JG, Burke JM, Sorger PK (2009) Non-genetic origins of cell-to-cell variability in TRAIL-induced apoptosis. *Nature* 459:428–432
- Sun H et al (1999) Population pharmacokinetics. A regulatory perspective. *Clin Pharmacokinet* 37:41–58
- Tanaami T et al (2002) High-speed 1-frame/ms scanning confocal microscope with a microlens and Nipkow disks. *Appl Opt* 41:4704–4708
- Thurber GM, Weissleder R (2011) A systems approach for tumor pharmacokinetics. *PLoS One* 6:e24696
- Thurber GM et al (2013) Single-cell and subcellular pharmacokinetic imaging allows insight into drug action in vivo. *Nat Commun* 4:1504
- Watanabe S (1997) Fluorescent indicators for Ca<sup>2+</sup> based on green fluorescent proteins and calmodulin. *Tanpakushitsu Kakusan Koso* 52:1770–1771
- Weber K et al (2011) RGB marking facilitates multicolor clonal cell tracking. *Nat Med* 17:504–509
- Weber K, Thomaschewski M, Benten D, Fehse B (2012) RGB marking with lentiviral vectors for multicolor clonal cell tracking. *Nat Protoc* 7:839–849
- Weiss M, Liu X, Thorling CA, Roberts MS (2013) Functional characterization of hepatic transporters using intravital microscopy. *Eur J Pharm Sci* 49(5):845–849
- Yang KS, Budin G, Reiner T, Vinegoni C, Weissleder R (2012) Bioorthogonal imaging of aurora kinase A in live cells. *Angew Chem Int Ed Engl* 51:6598–6603
- Yu JH et al (2013) High-resolution three-photon biomedical imaging using doped ZnS nanocrystals. *Nat Mater* 12:359–366
- Zhang Z et al (2012) Leveraging kinase inhibitors to develop small molecule tools for imaging kinases by fluorescence microscopy. *Mol Biosyst* 8:2523–2526
- Zhao Y et al (2011) An expanded palette of genetically encoded Ca(2)(+) indicators. *Science* 333:1888–1891

## Chapter 14

# Nonlinear Endomicroscopy Imaging Technology for Translational Applications

Gunnsteinn Hall, Wenxuan Liang, and Xingde Li

**Abstract** Nonlinear endomicroscopic imaging technology has emerged as a strong candidate for potentially enabling clinical translation of the powerful multiphoton imaging microscopy technology. With the development of ultrafast light sources followed by the initial demonstration of multiphoton microscopy in 1990, the field of nonlinear optical imaging has been expanded rapidly towards assessing biological tissue microstructures and functions. In this book chapter we present an overview of the underlying theory of nonlinear signal generation, tight focusing and resolution, and explore the multiple challenges associated with designing nonlinear ultracompact endoscopic probes that are needed for *in vivo* imaging of internal organs and the various solutions available. Specifically, we cover light delivery, beam scanning and signal collection. Finally, we review a few emerging applications, including preterm birth diagnosis, lung and breast cancer imaging.

**Keywords** Non-linear microscopy • Microendoscopy • Endogenous fluorescence • Clinical imaging • Pre-clinical research • MEMS scanners • Breast cancer • Lung cancer • Cervical imaging

### 14.1 Introduction

Nonlinear imaging covers a broad range of imaging modalities which involve nonlinear optical processes. The term nonlinear optical process (or nonlinear optics) refers to cases where the dielectric material polarization depends nonlinearly on the electric field. This is typically only observed under high light intensities. At high intensities, photons can interact with each other and the surrounding material with an elevated probability, leading to a diverse range of nonlinear phenomena, including multiphoton absorption, harmonic generation, coherent anti-Stokes Raman scattering and stimulated Raman scattering (Shen 1984; Boyd 2003).

---

G. Hall • W. Liang • X. Li (✉)

Department of Biomedical Engineering, Johns Hopkins University,  
720 Rutland Avenue, Baltimore, MD 21205, USA

e-mail: [xingde@jhu.edu](mailto:xingde@jhu.edu)

© Springer Science+Business Media Dordrecht 2014

281

R. Weigert (ed.), *Advances in Intravital Microscopy*:

*From Basic to Clinical Research*, DOI 10.1007/978-94-017-9361-2\_14

Multiphoton (MP) and second-harmonic generation (SHG) imaging microscopy have shown promise for clinical applications. Skala et al. (2007) showed that MP intensity and lifetime measurements can be used to differentiate between cancerous tissue from normal tissue. Nadiarnykh et al. (2010) demonstrated that SHG microscopy can be sensitive to changes in the extracellular matrix during the development of ovarian cancer and Provenzano observed a change in the ECM during development of breast cancer towards the onset of metastasis (Provenzano et al. 2008).

Coherent Anti-Stokes Raman Spectroscopy (CARS) and Stimulated Raman Scattering (SRS), involving three photons, can sensitively probe the vibrational signatures of molecules, which can be very useful for visualizing lipids in tissues (Evans and Xie 2008; Saar et al. 2010). These techniques have shown some promise for tumor diagnosis (Saar et al. 2011), and CARS microscopy has been used to monitor drug delivery to tissues *in vivo* (Saar et al. 2011).

All of these previously mentioned studies were performed on excised tissues with large benchtop microscopes. In order to utilize these promising techniques for translational applications *in vivo*, miniaturization of the microscope is required. On the way to miniaturization, several engineering problems need to be resolved, particularly regarding light delivery and collection, as well as beam scanning for image formation. This chapter will review some key challenges and solutions.

The first small microscope was demonstrated by Helmchen et al. (2001) for the brain imaging of freely moving rats. The prototype was however quite bulky. Myiang et al. (2006) demonstrated the first, fully integrated fiber-optic scanning endomicroscope, which had a ultra-compact scanning head of an outer diameter of 2.4 mm and a rigid length of ~3.5 cm with the rest fully flexible. Following this demonstration the major emphasis has been mostly on improving the quality of the endomicroscope with a similar level of miniaturization.

More recently, Zhang et al. (2012) demonstrated the feasibility of SHG imaging endomicroscopy for monitoring changes in the mouse cervix during pregnancy and its potential for preterm birth diagnosis. The potential of endomicroscopy to access tissues with its unique contrast and 3D capability at high resolution is likely to lead to further translational applications in the near future considering many of the engineering challenges have been resolved and thus the performance of the endomicroscope has been continuously improved.

The requirement for translational applications on the endomicroscope probe can vary greatly depending on the application. For preclinical small animal studies the size often needs to be smaller, for example, in mouse imaging. However, the major challenges remain the same in all cases. In this book chapter we will review the essential components of nonlinear endomicroscopy design and in the end some potential applications will be visited.

## 14.2 Fundamentals of Nonlinear Microscopy

The beginning of the nonlinear optics field can be traced back to theoretical work on two photon absorption by Maria Goeppert-Mayer (1931) in the 1930s in her doctoral thesis. Although the principles behind the various nonlinear imaging



modalities were known for a long time, the technology has only become available since around 1990. This chapter will be focused on multiphoton and SHG microscopy as these modalities have shown the most potential for endoscopic applications.

The main advantage of multiphoton imaging over a comparable linear modality such as confocal microscopy lies in the use of near-infrared light (NIR) for excitation which scatters less in the tissue and thus allows deeper imaging. Studies comparing multiphoton and confocal imaging microscopy (Centonze and White 1998) have shown significant improvement in the depth penetration of multiphoton over confocal and improved viability due to the “confinement” of the excitation to the focal volume and NIR excitation avoiding the use of UV excitation (Squirrell et al. 1999). The resolution of the two are comparable, as in spite of multiphoton using a longer wavelength, it has a square dependence on the excitation power while confocal imaging generally uses a larger than diffraction limited pinhole which trades off resolution for improved signal strength. In addition, multiphoton imaging can use full-field geometry for collecting the emission signal where a confocal pinhole is not needed.

SHG microscopy was demonstrated a few years following the establishment of multiphoton microscopy (Campagnola et al. 1999). In terms of the optical setup, SHG and multiphoton microscopy are almost identical. The only difference is that the emission of SHG occurs at exactly half the excitation wavelength. Therefore, with the appropriate choice of emission filters, the SHG signal can be isolated.

Other types of nonlinear contrast mechanisms have also been explored for endomicroscopic applications, including CARS and SRS (Legare et al. 2006; Balu et al. 2010). The setups for these are quite different from that of MP and SHG and they have not been explored widely, so the following discussion will only be focused on MP and SHG, although all of the design criteria apply to all nonlinear imaging modalities.

The instantaneous two-photon fluorescence from a point-object excited with focused light can be written (Denk et al. 1990; Xu and Webb 1996; Diaspro et al. 2006) with units of photons  $s^{-1}$  (count rate)

$$F(t) = \delta_2 \eta I(t)^2 = \delta_2 \eta P(t)^2 \left( \frac{\pi (NA)^2}{\lambda hc} \right)^2, \quad (14.1)$$

where  $\delta_2$  is the two-photon absorption cross-section specified in units of Goppert-Mayer (GM) which is equivalent to  $10^{-50} \text{ cm}^4 \text{ s photon}^{-1}$ , NA is the numerical aperture of the objective lens,  $\lambda$  is the center wavelength of the excitation laser, and  $\eta$  is the fluorescence quantum efficiency/yield representing the fraction of excited electrons that return to the ground state by emitting a fluorescent photon;  $I(t)$  is the irradiance distribution at the geometric focal point (with units of photons  $\text{cm}^{-2} \text{ s}^{-1}$ ) which is related to the instantaneous power  $P(t)$  (units of W). The relation can be obtained by writing the spatially varying irradiance in the transverse focal plane as  $I(\mathbf{r}, t) = I(t) \text{IPSF}(\mathbf{r})$ , where IPSF represents the intensity point-spread-function and  $I(t)$  is the irradiance at the geometric focus. The total power can be found by

integration, e.g.  $P(t) = \iint I(\mathbf{r}, t) E_{\text{photon}} dA = I(t) E_{\text{photon}} \iint \text{IPSF}(\mathbf{r}) dA$ , where  $E_{\text{photon}} = hc/\lambda$ . For focused beams, it can be shown (Born and Wolf 1999) that

$$\text{IPSF}(r) = \left( \frac{\lambda J_1(2\pi \text{NA } r / \lambda)}{\pi \text{NA } r} \right)^2$$

in the focal plane. By analytical integration, we finally obtain the irradiance at the focus as  $I(t) = \pi P(t) (\text{NA}/\lambda)^2 / E_{\text{photon}}$ , which has been applied in the equation above.

The detected time-averaged fluorescence intensity with a collection efficiency  $\phi$  can be written as

$$\langle F \rangle_{\text{det}} = \phi \delta_2 \eta g P_{\text{avg}}^2 \left( \frac{\pi (\text{NA})^2}{\lambda hc} \right)^2, \quad (14.2)$$

where  $P_{\text{avg}} = \langle P(t) \rangle$  and  $g = \langle P^2(t) \rangle / \langle P(t) \rangle^2$  represents an efficiency factor that is pulse-shape dependent and is generally higher for shorter and more highly peaked pulses. For a constant source (CW beam)  $g = 1$ , whereas for square pulses of with width  $\tau$  and repetition rate  $R$ ,  $g = 1/(\tau R)$ ; for other pulse shapes this factor is multiplied by a shape-specific factor, which we will denote by  $g_s$  (0.588 for  $\text{sech}^2$  pulses for instance). Therefore, we can write  $g = g_s / \tau R$  for arbitrary pulsed shapes. For femtosecond pulses the detected fluorescence from a point-object can be written

$$\langle F \rangle_{\text{det, pulsed}} = \phi \delta_2 \eta \frac{g_s}{\tau R} P_{\text{avg}}^2 \left( \frac{\pi (\text{NA})^2}{\lambda hc} \right)^2, \quad (14.3)$$

For a pulsed laser, the relationship between average power and peak power can be estimated as follows. Let us assume that the laser outputs pulses with a repetition rate of  $R$ , and each pulse has a pulse width  $\tau$ . The average power measured can be written  $P_{\text{avg}} = P_{\text{peak}} \tau R$  (assuming square pulses). For typical cases of  $R = 80$  MHz and  $\tau = 100$  fs, the ratio of the peak and average intensity is  $P_{\text{peak}}/P_{\text{avg}} = 125000$ . Therefore, the peak power is significantly larger than the average power and is typically on the order of several kW assuming the average power on tissue is about few tens of mW.

For convenience and ease of measurement the two-photon absorption cross-section  $\delta_2$  and the fluorescence quantum yield  $\eta$  are combined into  $\sigma_2 = \delta_2 \eta$ , which is defined as the action cross section (in units of GM). Strong fluorophores have a large  $\sigma_2$ , for example GFP which is an important marker for gene expression has a cross section ranging from  $\sim 10$  to  $\sim 40$  GM at 800 nm to its peak at  $\sim 920$  nm (Blab et al. 2001). On the other hand intrinsic fluorophores have a relatively much lower cross section, for example nicotinamide adenine dinucleotide (NADH) has a cross section ranging from 0.02 to 0.09 GM from 690 to 730 nm and flavins such as FAD (flavin adenine dinucleotide) about  $\sim 0.1$ – $0.8$  GM for 700–730 nm. Therefore, imaging of intrinsic signals with similar excitation typically produce  $\sim 100$ – $1,000$  times lower signals than GFP and require increasing the average power by 10–30 times for comparable signal levels.

The overall fluorescence signal also depends upon the extent of the underlying sample. In reality the detected signal is integrated over the full volume. For a homogeneous sample that is uniform throughout the focal volume, it has been shown that the dependence of the excitation on the NA is much less than for a point object, as for a homogeneous object, for a lower NA the focal volume would be larger and contribution would be obtained from more spatial regions than for a point object (Xu and Webb 1996; Dunn et al. 2000). So, in cases of small samples there is a strong dependence on the NA of the objective lens, whereas in homogeneous samples throughout the focal volume, the NA dependence is mostly through the collection efficiency. In practical cases, it is reasonable to assume that the situation is intermediate, and therefore it can be expected that there is a mild dependence of the collected fluorescence signal on the NA.

SHG imaging signal generation effectively follows the comparable equations as presented for two photon fluorescence, although as a coherent modality, the cross section depends on electric dipole organization due to the strong dependence on phase-matching between the excitation and emission light, in addition to the dipole concentration (Moreaux et al. 2000). Furthermore, due to phase-matching conditions SHG generation is mostly generated along the forward direction, although a backward-generated component also exists (Mertz and Moreaux 2001; Legare et al. 2007; Lacomb et al. 2008). Through tissue scattering, some of the forward generated SHG can be efficiently collected for image formation. SHG imaging can be performed with the same instrument as two-photon fluorescence imaging, whether a benchtop microscope or an endomicroscope, with the proper emission filters.

Other nonlinear modalities, such as CARS and SRS, also have a nonlinear dependence on the incident light for absorption of the pump and probe beams, and effectively depend on many of the same factors as the formalism above for two-photon absorption. For a more detailed discussion, see (Evans and Xie 2008) for instance.

## 14.3 Endomicroscope System Design

### 14.3.1 *Ultrafast Pulse Generation and Properties of Short Pulses*

#### 14.3.1.1 Ultrafast Light Source

As can be inferred from Eq. 14.3, a very high electric field is needed for nonlinear signal generation, and by using short pulses, the electric field inside the pulses can be made very high, while maintaining a much lower average power (due to the relatively long time between pulses) to avoid burning or damaging the sample. A critical component for multiphoton microscopy is an ultrafast laser which can output pulses of  $\sim 100$  fs with a repetition rate of typically  $\sim 80$  MHz. The source for the initial demonstration of multiphoton microscopy in 1990 utilized a mode-locked dye laser with pulsewidth of  $\sim 100$  fs at 80 MHz (Denk et al. 1990).

At present, the most commonly-used source is based on a solid state mode-locked Ti:Sapphire laser. Initially these sources required significant maintenance, but recently they have been much improved such that they are sealed and completely based on computer control. These lasers typically have an output power above 1 W at 800 nm and modern versions are tunable approximately from 680 to 1,080 nm with a high output power. Solid state lasers are characterized by a metal-doped crystalline gain medium. They offer a high output power, and depending on the gain medium, are widely tunable in the near infrared range. Another example of a solid state laser is the chromium-doped forsterite laser with a 1,230–1,270 nm tuning range.

Fiber lasers, equipped with a doped fiber as the nonlinear gain medium, are another option (Murari et al. 2011). They are typically very compact and robust, but are less flexible in terms of wavelength selection and generally not tunable. In terms of power they are typically limited to a few hundred milliwatts, which is satisfactory for many imaging applications.

#### 14.3.1.2 Spectral and Temporal Pulse Relationship

The relationship between the temporal pulses and spectral properties is now examined. The electric field amplitude of a pulse  $e(t)$  in time-domain is conveniently expressed in terms of a slowly varying amplitude  $a(t)$  and an optical carrier function (Weiner 2009), i.e.

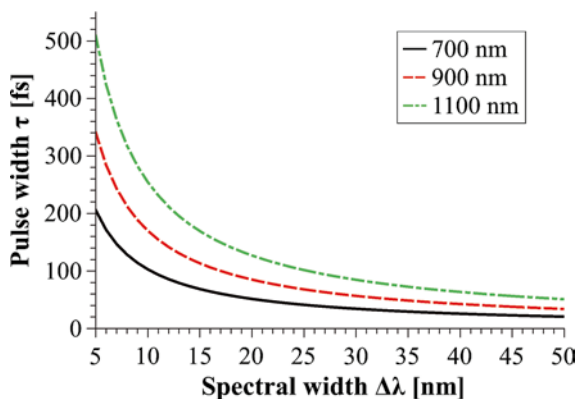
$$e(t) = \text{Re}\{a(t)e^{j\omega_0 t}\} = \frac{1}{2}\left[a(t)e^{j\omega_0 t} + a^*(t)e^{-j\omega_0 t}\right], \quad (14.4)$$

The spectrum can be written as  $E(\omega) = 0.5[A(\omega - \omega_0) + A^*(-\omega - \omega_0)]$ , where  $A(\omega)$  is the Fourier transform of the envelope function  $a(t)$ . This relationship forms the basis of the relationship between the spectral and temporal properties of pulses.

The most widely used measure of pulse duration is the intensity full width at half maximum (FWHM), and can be denoted  $\tau$ . The bandwidth is measured as the FWHM of the power spectrum and is denoted by  $\Delta\nu$  (in Hz), which is related to wavelength through  $c = \nu\lambda$ , and  $d\nu/d\lambda = -c\lambda^{-2}$ , so that  $\Delta\lambda \approx \frac{\lambda^2}{c}\Delta\nu$ . A commonly employed pulse shape is given in the time-domain as  $a(t) = \text{sech}(t/t_p)$ , where  $\tau = 1.763t_p$ . By Fourier transforming the pulse and examining its spectral form, the time-bandwidth product (TBP) is determined to be  $\tau\Delta\nu = 0.315$  (Weiner 2009). A pulse is considered transform limited when the phase is flat in the spectral domain. When this is fulfilled, the pulse width is optimal in the time domain. Under influences of spectral phase, the pulses can broaden temporally, reducing the nonlinear signal generation, as will be discussed for fibers in the next section. Figure 14.1 shows transform limited relationships between  $\Delta\lambda$  and  $\tau$  for sech pulses at three different central wavelengths ranging from 700 to 1,000 nm.

In practice, an optical autocorrelator is typically used to measure pulse widths, and the autocorrelator is either based on an interferometric autocorrelation or

**Fig. 14.1** Relation between spectral bandwidth and pulse widths in case of transform limited sech pulses at three different central wavelengths of 700, 900 and 1,100 nm



intensity autocorrelation (Weiner 2009), which are both based on splitting up the pulses and interfering in a nonlinear crystal in slightly different configurations. In order to obtain further information about the pulse shape, the autocorrelation technologies have been further expanded to methods such as frequency-resolved optical gating (FROG) (Trebin and Kane 1993) and spectral phase interferometry (SPIDER) (Iaconis and Walmsley 1998) which can fully determine the pulse shape (Weiner 2009).

### 14.3.2 Light Delivery and Excitation: Dispersion Compensation

One of the major challenges of in a miniaturized portable nonlinear endomicroscopy system in comparison to a benchtop nonlinear microscope lies in the delivery of the excitation light to the sample. Endomicroscopes use a single-mode optical fiber for excitation light delivery, where the single-mode beam emanating from the small core size is imaged onto the sample for diffraction-limited resolution. The fiber, like any glass material, has dispersive characteristics where light of shorter wavelengths (towards blue) travels slower than light of longer wavelengths (towards red), which temporally spreads out the ultrafast pulse. As the nonlinear signal production efficiency scales inversely with the temporal pulse width, it is critical to compensate for this effect. This is accomplished by precompensating for the dispersion before the pulse enters the fiber by selectively speeding up the shorter wavelengths (blue) with respect to the longer wavelengths (red). A number of devices that exhibit anomalous dispersion such as prisms, diffraction gratings, chirped mirrors, photonic crystal fiber (PCF) and photonic bandgap fiber (PBF) can be used for precompensation. PBF and PCF guide light based on photonic bandgap or closely spaced air holes which is different from conventional optical fibers that are based on total internal reflection. The majority of the light is carried in lower refractive index regions which can have a large area and minimal nonlinear effects, making these

types of special fibers suitable for delivering distortion-free pulses. However, they operate within a limited range of wavelengths and the amount of compensation depends on their physical length which is not tunable once fixed. Grating and prism pairs on the other hand are easy to tune and can operate over a broad wavelength range.

In addition to the linear dispersion of the pulses (and higher order dispersion), nonlinear effects also affect the pulses. At typical excitation wavelengths around  $\sim 800$  nm the fiber core is  $3\text{--}5$   $\mu\text{m}$  in diameter. Due to the small area of the core and short pulse width, the excitation light fluence is very high, leading to nonlinear effects such as self-phase modulation (SPM) which can further broaden the pulse width (Agrawal 2001). This eventually limits the amount of power that can be used for delivery, as the broadening due to this effect depends nonlinearly on the photon density in the fiber core.

### ***14.3.3 Light Focusing Through a Miniature Objective Lens for High Resolution***

In order to focus the light to a small spot for high resolution, a miniature high numerical aperture (NA) objective lens is required. In addition, tight focusing helps create a high electric field in the focal volume as required for efficient nonlinear signal generation and 3D optical sectioning. The first demonstrations of miniature MP endomicroscopy utilized gradient-index lenses (GRIN) with an NA of 0.46 resulting in a lateral and axial resolution of  $\sim 2$  and  $\sim 20$   $\mu\text{m}$ , respectively (Myaing et al. 2006). Typical nonlinear imaging microscopy applications use NAs of  $\sim 0.8\text{--}1.0$ , and thus to a rough approximation have lateral/axial resolutions of  $\sim 0.4/2$   $\mu\text{m}$  or up to  $\sim 0.3/0.75$   $\mu\text{m}$  for a high 1.2-NA lens (Zipfel et al. 2003). Furthermore, for coherent modalities such as SHG imaging it has been proposed that an NA of higher than  $\sim 0.80$  can be severely affected by the Gouy phase shift (Moreaux et al. 2000). More recently, more advanced miniature objectives have been designed (Zhang et al. 2012) that can have a design NA of  $\sim 0.8$  (and practically an effective NA of  $\sim 0.5$  due to underfilling the lens while scanning the beam) for producing a comparable resolution as a benchtop microscope. However, due to the trade-off between focal length and aperture size, these typically have a relatively short working distance (WD) of a few hundred microns. That is satisfactory for a large number of cases, as the depth in MP and SHG microscopy is limited to  $200\text{--}300$   $\mu\text{m}$ , depending on the tissue scattering properties (Helmchen and Denk 2005).

The theoretical diffraction-limited optical resolution for a generalized  $N$  photon absorption process can be approximated from the full-width at half maximum (FWHM) of the intensity point-spread function to the  $N$ -th power. Under the paraxial approximation (valid for  $\text{NA} \leq 0.7$ ) we obtain (Born and Wolf 1999):



$$\text{Lateral resolution (FWHM)}: D_{xy}^N \approx \frac{0.51}{\sqrt{N}} \cdot \frac{\lambda}{\text{NA}}, \quad (14.5)$$

$$\text{Axial resolution (FWHM)}: D_z^N \approx \frac{1.77}{\sqrt{N}} \cdot \frac{n\lambda}{(\text{NA})^2}, \quad (14.6)$$

where  $n$  is the refractive index in the image space. The approximation sign stems from the estimation of the  $N$ -photon process width dependence as  $1/\sqrt{N}$ , which in general does not have an analytic expression. We have verified numerically that the approximation is accurate to within 3.5 %. As an example for two-photon endomicroscopic imaging using a water-immersion based micro-objective with an NA of 0.80, the theoretical transverse and axial resolutions at 890 nm are  $\sim 0.4$  and  $\sim 2.3$   $\mu\text{m}$ , respectively. In practice the resolution is usually worse due to optical aberrations and by not filling the lens back aperture.

### 14.3.4 Collection and Detection of Emission Photons

The fluorescent emission is typically collected with a fiber and weakly focused on a highly sensitive detector such as a photomultiplier tube (PMT) to match the active area. This allows for the detector to be at the proximal end, which is critical for probe miniaturization as detectors are generally spacious and require cables and electronics. Two configurations exist for the fiber optic collection of light as illustrated in Fig. 14.2. In the first configuration (a) a single fiber is used for both excitation light delivery and emission collection, and in the second configuration (b) two separate fibers are used in the second configuration (b), where a single mode fiber for excitation light delivery and a multimode fiber for emission collection. The single fiber approach is easier to implement and help achieve a small size and flexibility, as the separate-fiber approach requires a miniature dichroic within the probe for the separation of emission and excitation which needs to be mounted and aligned properly. However, when aligned properly, the use of a large area multimode fiber potentially allows a larger collection efficiency. This approach was used by Helmchen et al. (2001) in an early application. The single fiber method places higher constraints on the micro-objective, as it is critical to focus the emission back onto the fiber for collection. Since the emission is typically much lower wavelength than the excitation (for example 890 nm excitation and 445 nm emission for typical SHG microscopy), this requires a highly achromatic design. To reduce these requirements, a double clad fiber (DCF) is used which uses an extra cladding layer to guide the emission photons as first demonstrated by Myaing et al. (2006). The use of DCFs allows efficient excitation and emission collection. More recently, larger DCFs have been used to increase the collection efficiency (Zhang et al. 2012). GRIN lenses have high chromatic aberrations and

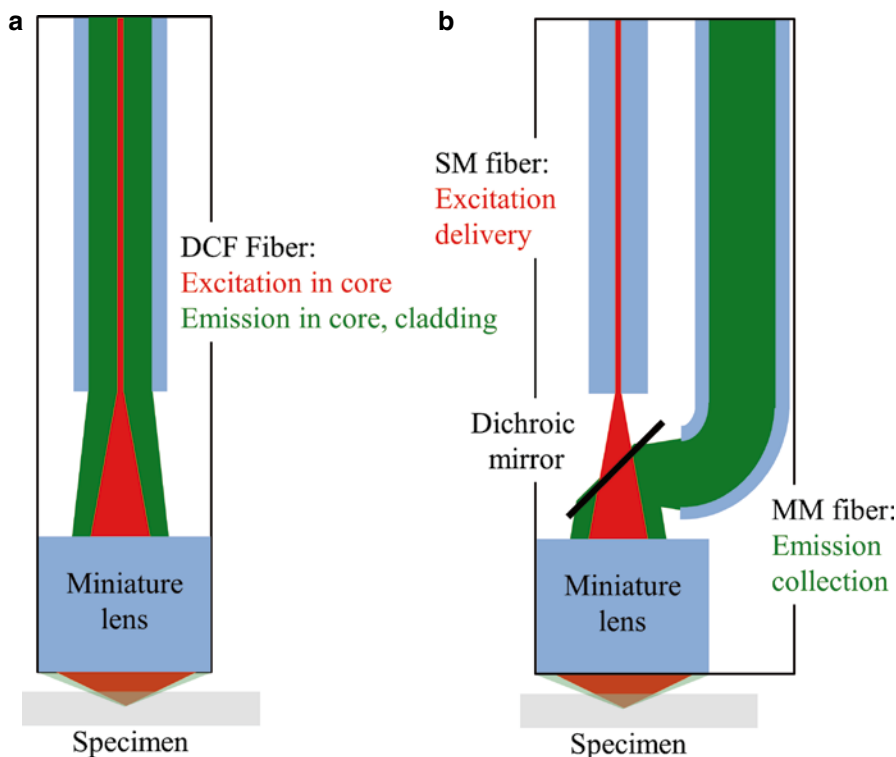


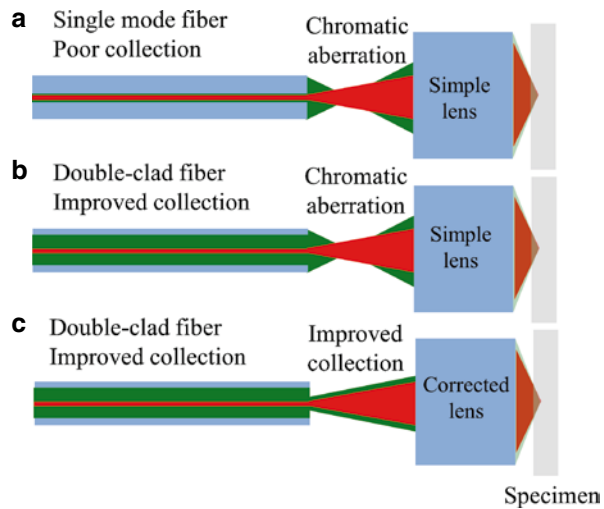
**Fig. 14.2** Schematics of the two configurations for fiber-optic excitation light delivery and emission collection, utilizing (a) a single fiber for both, and (b) two fibers, one for excitation and a second one for collection

therefore require a large collection area. Compound lenses have been demonstrated to have lower chromatic aberration and improve collection efficiency (Wu et al. 2009; Zhao et al. 2010) and recently a superachromatic micro-objective has been demonstrated for high resolution and very minimal chromatic aberration and high collection efficiency (Zhang et al. 2012). Figure 14.3 illustrates the benefits of utilizing a combination of chromatic correction and a large cladding DCF in configuration (c) over that of a standard single-mode fiber and simple lenses with chromatic errors in (a).

### 14.3.5 Point Scanning for Image Formation

As a point-detection based modality, scanning of the focal point is needed for image formation along with synchronization between the scanning and detection. The scanner needs to be situated within the probe and therefore needs to be miniaturized as well. Two main types of miniaturizable scanners exist as described below.

**Fig. 14.3** Illustration of collection efficiency for different combinations of the single-fiber and lens design. (a) Poor collection with combined chromatic aberration and small diameter collection of a single-mode fiber. (b) Improved collection through the use of a double clad fiber (DCF) with a large cladding area for collection. (c) Further improvement is achieved by combining an improved lens design with a DCF



#### 14.3.5.1 Piezoelectric (PZT) Scanners

This scanning mechanism uses a piezoelectric actuator to generate the mechanical deflection. The fiber is attached to the PZT actuator leaving a free-standing cantilever, which amplifies the motion when driven at its mechanical resonance and displaces the fiber tip, causing a movement of the excitation spot.

The mechanical resonance frequency of a fiber cantilever is given by

$$f = \frac{\beta}{4\pi} \sqrt{\frac{E}{\rho}} \left( \frac{R}{L^2} \right), \quad (14.7)$$

where  $\beta$  is the constant of the zeroth-order vibration mode of the cantilever and is given by 3.52,  $E$  and  $\rho$  are the Young's modulus and mass density of the cantilever, respectively. For a typical application with a free standing length of 1 cm, the resonance frequency is about 1 kHz. The mechanical resonance can be chosen to some degree by varying the length of the free fiber end, and by adding weight or changing the Young's modulus to it as described by Huo et al. (2010).

There are at least two approaches, one based on a monolithic cylindrical four-quadrant actuator (Smithwick et al. 2001; Liu et al. 2004; Myaing et al. 2006) and another one based on actuators that are often bimorph or trimorph. The cylindrical actuator can be used to generate spiral, or Lissajous scan patterns by driving the orthogonal electrode pairs with appropriately modulated or frequency- and phase-shifted sinusoidal waveforms. A piezoelectric bimorph is a cantilever consisting of two stacked piezoelectric layers, which can produce a one-dimensional displacement through electrical activation where one layer extends while the other contracts. For larger deflections, the number of layers can be increased, as is done for example in the trimorph. More layers are also possible (Ballas 2007). A single bending actuator with some structural modifications may also be used to generate a Lissajous

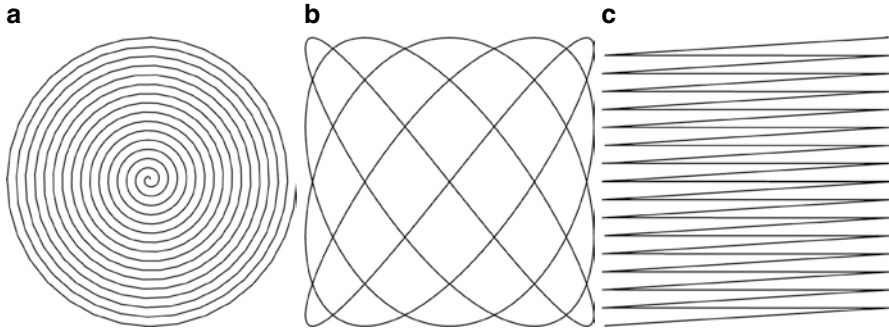


**Fig. 14.4** Examples of three commonly used scan patterns for endomicroscopy: (a) Spiral scan, (b) Lissajous scan pattern (here with drive frequency ratio of 4:5 for illustration), and (c) Raster scan

scan (Helmchen et al. 2001; Flusberg et al. 2005). Another design using two bending actuators arranges them orthogonally and has a fast and slow axis based on the construction (Le Harzic et al. 2008; Rivera et al. 2011). It can be used to generate a raster scan pattern by driving the fast and slow actuators with sinusoidal and ramp waveforms, respectively. Scanners using bending actuators offer more flexibility in the scan patterns but often require a much higher drive voltage. The cylindrical scanner on the other hand is easier to fabricate and due to its symmetric nature and it is also easier to integrate with the overall probe.

#### 14.3.5.2 MEMS Scanners

MEMS-based scanners (Piyawattanametha et al. 2006; Tang et al. 2009) are built around reflective coatings deposited on micromachined silicon plates with gimbal mounts. These plates act as mirrors which can then be rotated around the mounts using electrostatic forces generated by a comb drive or by electrothermal forces. Additionally circuits for driving the mirrors can be fabricated on the same silicon die, leading to monolithic scanners. MEMS scanners can implement raster scans very easily and have the potential for region-of-interest windowing but are significantly more complicated to fabricate. Also, MEMS scanners tend to be larger than piezoelectric scanners due to the decoupling between light delivery and scanning. Thus the light beam often needs to be folded, which requires some free space for operation. This also makes the design asymmetric and more complicated to integrate into the distal end of an endomicroscope.

#### 14.3.5.3 Scan Patterns

Based on the kind of scanner used, several two-dimensional scan patterns can be achieved for moving the focused excitation spot on the sample. Three common examples are spiral, Lissajous and raster scans. The spiral scan, shown in Fig. 14.4a,

consists of opening and closing spiral trajectories requiring amplitude modulation of the PZT drive waveforms leading to a circular field-of-view. Such scanning is easy to implement on tubular PZT actuators which are compact and easy to integrate with the probe. Image reconstruction is also relatively straightforward. However, it suffers from highly non-uniform spatiotemporal characteristics due to the fact that the tangential velocity of the excitation spot increases as it gets further away from the center of rotation although the angular velocity is maintained. In practice this leads to higher incident flux and oversampling in the center and lower incident flux and less sampling at the periphery.

The drive signals for one “circle” of spiral scanning can be given by

$$\begin{aligned} x_{\text{spiral}}(t) &= m(t) \sin(2\pi f_0 t), \\ y_{\text{spiral}}(t) &= m(t) \sin(2\pi f_0 t + \pi/2), \end{aligned} \quad (14.8)$$

where  $m(t) = \text{tri}(t/T_{\text{frame}})$  (triangular modulation with width  $2T_{\text{frame}}$ ) and  $f_0$  is the resonance frequency. Each circle has a period defined by  $f_0$ , and the number of points per circle depends on the sampling density which should be comparable to the optical resolution. For proper sampling the sampling should oversample the optical resolution by at least a factor of  $\sim 2$  (the Nyquist theorem). The number of circles per frame should be chosen based on similar considerations. The overall time per frame is determined from  $T_{\text{frame}} = N_{\text{circles/frame}}/f_0$ . The open-loop phase refers to each frame where the spiral is scanned outward from the origin, whereas the closed-loop phase refers to the scanning towards the origin. These are repeated periodically for continuous operation.

The Lissajous scan pattern is based on driving the two axes with sinusoidal waveforms at slightly different frequencies at constant amplitude. In order to obtain a closed curve, the frequency ratio must be rational. Figure 14.4b shows an example of a Lissajous pattern for a drive frequency ratio of 4:5. The advantage of Lissajous scanning over spiral scanning includes improved sampling uniformity, more uniform fluence distribution and a near rectangular field-of-view (Liang et al. 2012). However, the disadvantage is that reconstruction is computationally intensive due to the complex trajectory, and it is more sensitive to drive perturbations. It has been noted that employing frequencies relatively far from resonance (semi-resonant), improved stability can be achieved (Moon et al. 2010) yet limiting the scanning amplitude to only 25 % of the maximal displacement and thus requiring 4 times higher driving voltages. The Lissajous drive signals can be written as

$$\begin{aligned} x_{\text{Lissajous}}(t) &= a \sin(2\pi f_x t), \\ y_{\text{Lissajous}}(t) &= a \sin(2\pi f_y t), \end{aligned} \quad (14.9)$$

where  $t$  is from 0 to the end of one period  $T_{\text{frame}}$ , and the periods of the two axes are given by  $T_x = 2\pi/f_x$  and  $T_y = 2\pi/f_y$ . When the drive frequency ratio  $f_x/f_y$  can be written as a fully reduced fraction  $f_x/f_y = T_y/T_x = m/n$  (where  $m$  and  $n$  are natural numbers), the scan pattern forms a closed loop and repeats itself retracing another frame with a

frame period given by  $T_{\text{Frame}} = mT_x = nT_y$ . Additionally, in order to obtain a dense enough scan trace, and for both axes to stay close to the resonance frequency of the fiber cantilever, usually both  $m$  and  $n$  should be at least several hundred, which means the typical frame rate will be several Hz if the drive signal frequency is on the order of kHz. As a specific example, selecting  $T_x = 734 \mu\text{s}$  ( $f_x \sim 1.362 \text{ kHz}$ ) and  $T_y = 736 \mu\text{s}$  ( $f_y \sim 1.359 \text{ kHz}$ ) corresponds to a fully reduced drive frequency ratio of  $m/n = 368/367$ , which yields a frame period of  $368 \times 734 \mu\text{s} = 367 \times 736 \mu\text{s} = 270.1 \text{ ms}$ , corresponding to a frame rate of  $\sim 3.7 \text{ Hz}$ .

Scanners to implement raster scanning are relatively harder to fabricate – requiring asymmetric piezoelectric structures or MEMS mirrors, which are also typically larger than tubular piezoelectric actuators and more complicated to integrate with the overall probe design. The required drive voltage is often very high (e.g. more than 200 V peak-to-peak). However, the scan pattern, shown in Fig. 14.4(c), can be easily described in Cartesian space making image reconstruction very simple. In addition, raster scans have excellent spatiotemporal characteristics with uniform incident flux and sampling density within the field-of-view.

For raster scanners, the two axes are ramped with different frequencies, one with a slow scan (frame scanning) whereas the other axis obtains a line scan. The drive signals can be represented in terms of sawtooth waveforms as follows

$$\begin{aligned} x_{\text{raster}}(t) &= \text{sawtooth}\left(\frac{t}{T_{\text{line}}}\right), \\ y_{\text{raster}}(t) &= \text{sawtooth}\left(\frac{t}{T_{\text{frame}}}\right), \end{aligned} \quad (14.10)$$

where  $\text{sawtooth}(t) = t - \text{floor}(t/T)$  represents a sawtooth waveform with period  $T$ .  $T_{\text{line}}$  and  $T_{\text{frame}}$  are the periods for the fast line scan ( $x$ ) and slower frame scanning axis ( $y$ ), respectively. In this representation the signal can repeat itself, as it retraces itself back and forth. For nonresonant operation the waveform can be jerked back to the initial point at the end of a scan and repeated. Figure 14.4c shows example waveforms. In practice the sawtooth waveform is often low-pass filtered to match the bandwidth of the galvanometer which cannot make instantaneous stops and turns. Raster scanning can also be achieved with triangular and sinusoidal drive signals as discussed by Duma et al. (2011). Another desirable feature of nonresonant raster scanners is the ability for random access scanning, where the probe can be quickly pointed or scanned over a given area (Sawinski and Denk 2007). This is also generally limited to the more involved asymmetric scanners.

Figure 14.5 shows a photograph of a tubular, four-quadrant monolithic piezoelectric beam scanner with a  $250 \mu\text{m}$  diameter DCF fiber threaded through the central hole. The overall diameter of the scanner including a housing unit is 2.1 mm and the cantilever has a mechanical resonance frequency of 1.1 kHz. With a peak-to-peak drive voltage of about 80 V, the fiber scan range is about  $500 \mu\text{m}$ . The overall field of view (FOV), representing the extent of the endomicroscopy images, is



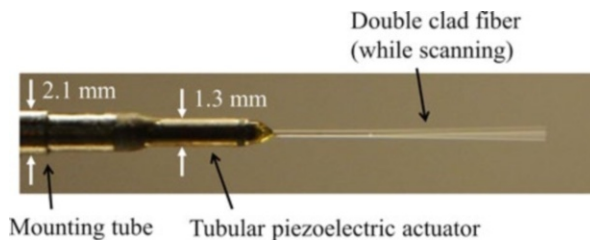


**Fig. 14.5** Photograph of a 1.3-mm-diameter monolithic, four-quadrant, tubular piezoelectric actuator mounted on a 2.1 mm-diameter housing tube. The double clad fiber (with a diameter of 250  $\mu\text{m}$ ) is threaded through the actuator and is being scanned at its mechanical resonance frequency

determined by the maximal displacement of the scanned fiber  $d_{\text{fib}}$  and the magnification of the micro-objective lens, i.e.  $\text{FOV} = d_{\text{fib}}/M$ . For high resolution imaging  $M$  is about  $\sim 4\text{--}5$  and therefore the overall imaging FOV is typically around 100  $\mu\text{m}$ .

#### 14.3.5.4 Axial Scanning and 3D Image Formation

As nonlinear imaging methods have an inherent optical sectioning capability, where the signal generation is localized at the focus, the incorporation of a mechanism for scanning the focal point along the optical axis (Z-scanning) enables the construction of a three-dimensional image of the sample. Z-scanning can also be useful for locating a feature or region of interest.

Multiple approaches can be taken for accomplishing this. One approach is to use a piston-cylinder based design with either pneumatic or mechanical actuation (Rouse et al. 2004). This requires very high precision manufacturing. A more straightforward way is to use a micromotor (Helmchen et al. 2001; Flusberg et al. 2005; Le Harzic et al. 2008) which offers low-voltage operation. However, these can be difficult to miniaturize. An alternative is to use a MEMS-based linear actuator for moving the objective lens such as demonstrated by Liu et al. for 3D confocal endomicroscopy (Liu et al. 2013). Another technique that is easier to implement is using a shape memory alloy (SMA) wire in conjunction with a helical spring (Wu et al. 2010). The SMA wire can be contracted by low-voltage, low-power ( $\sim 5$  mW at 100 mV) electrical heating, compressing the spring. Interrupting the current relaxes the wire and allows the spring to recover, providing bidirectional motion for moving the lens. In addition, methods based on tuning the lens focal length (such as with a deformable lens) can be used for performing Z-scanning (Grewe et al. 2011). Additionally, thermomechanical scanners have been demonstrated previously (Choi et al. 2006). Recently, miniature MEMS based designs with a scanning and deformable mirror surface have been made for full 3D imaging (Strathman et al. 2013).

## 14.4 Translational Applications

### 14.4.1 Cervical Imaging for Preterm Birth Diagnosis

Preterm birth (PTB) accounts over 12.7 % of all births in the United States. PTB is one of the leading causes of infant mortality and frequently leads to severe problems for surviving infants (Behrman et al. 2007). The causes of PTB are not well understood. However, studies indicate that changes occur in the cervix prior to the onset of uterine contractility in both term and PTB (Behrman et al. 2007). Premature changes in the cervix could be indicative of impending PTB. The cervix is rich in connective tissue largely composed of collagen fibers that have an intrinsic SHG contrast and thus can be visualized with SHG microscopy (Williams et al. 2005; Akins et al. 2010; Campagnola 2011). The progressive structural changes in fibrillar collagens are directly related to cervical mechanical strength and thus potentially can serve as a diagnostic indicator for women at risk for PTB. Zhang et al. developed a portable fiber-optic SHG endomicroscope system for studying changes in the cervix during pregnancy with mouse models (Zhang et al. 2012). A schematic of the setup is illustrated in Fig. 14.6. A custom microobjective with an NA of 0.80

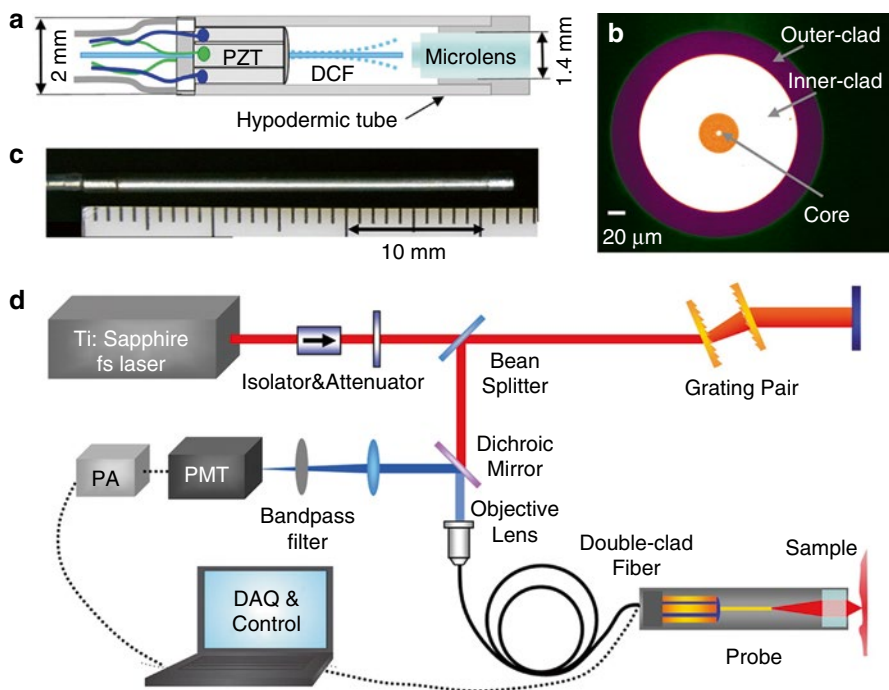


**Fig. 14.6** Schematic of an SHG endomicroscope system utilized in cervical tissue imaging (Reproduced from Zhang et al. (2012) with permission)

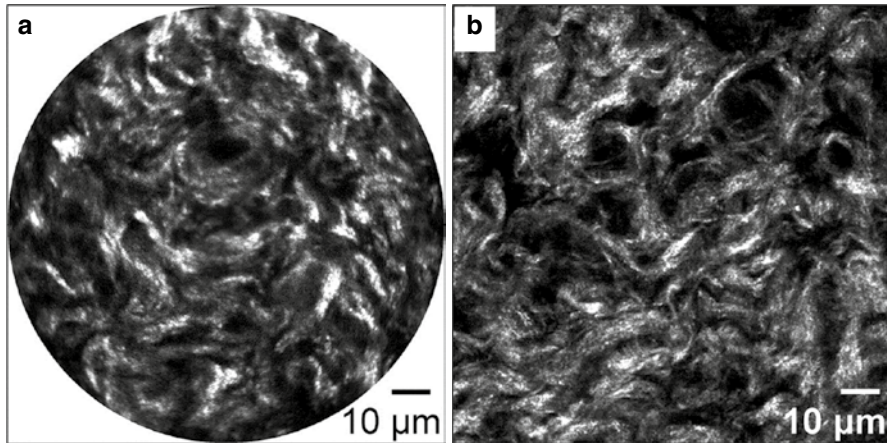


**Fig. 14.7** Comparison of cervical images obtained with an endomicroscope (a) and a bench-top microscope (b) (Image reproduced from Zhang et al. (2012) with permission)

was used, achieving a lateral and axial resolution of 0.76 and 4.36  $\mu\text{m}$  respectively (FWHM). The field of view on the sample was 110  $\mu\text{m}$ . As shown in Fig. 14.7, the image quality of cervical SHG images obtained with the endomicroscope is comparable with ones obtained on a benchtop microscope. The changes in the cervical collagen fiber architecture throughout pregnancy can be visualized using SHG endomicroscopy as shown in Fig. 14.8. This study was performed on excised mouse cervixes and indicates that significant remodeling occurs in the cervix from start of pregnancy towards birth. The collagen fiber sizes change from small to large and the overall collagen content is higher as represented by the fractional area coverage and these changes were shown to be statistically significant and verified by histology (Zhang et al. 2012). Figure 14.9 shows the increase in collagen fiber diameter and overall fiber coverage (A) and (B), as well as overall increase in intensity (C). This shows clearly that the fiber architecture is modified throughout pregnancy which is in agreement with the known cervical ripening prior to birth (Timmons et al. 2010). To become clinically useful it needs to be shown that in cases of preterm birth the progression in the fiber architecture is abnormal or resembles that of late stages at an early time point. The SHG endomicroscopy technology could also potentially serve as an enabling tool for assessing PTB treatment outcomes, thus ultimately promoting the development of PTB therapeutics.

#### 14.4.2 Lung Cancer Imaging

It has been demonstrated that multiphoton microscopy can be used for label-free diagnosis of lung cancer. Wang et al. through the combined use of SHG and multiphoton were able to differentiate lung adenocarcinoma (LAC) and squamous cell

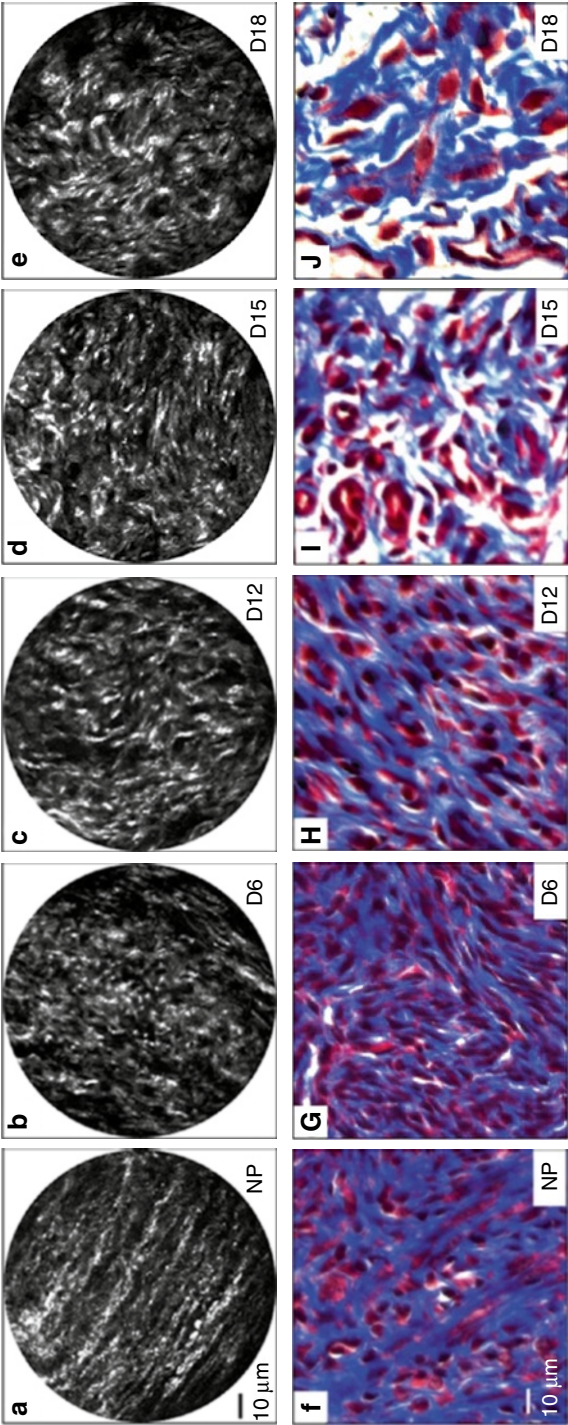


**Fig. 14.8** Endomicroscopy images of cervical tissue sections from nonpregnant (NP) (a) and pregnant mice at gestation days 6 (b), 12 (c), 15 (d), and 18 (e). Significant morphological changes in cervical collagen are evident over the course of pregnancy. Microscopic images of trichrome stained samples (f–j) at the same gestational time points show gross changes in collagen morphology, confirming the SHG endomicroscopy findings (Figure reproduced from Zhang et al. (2012) with permission)

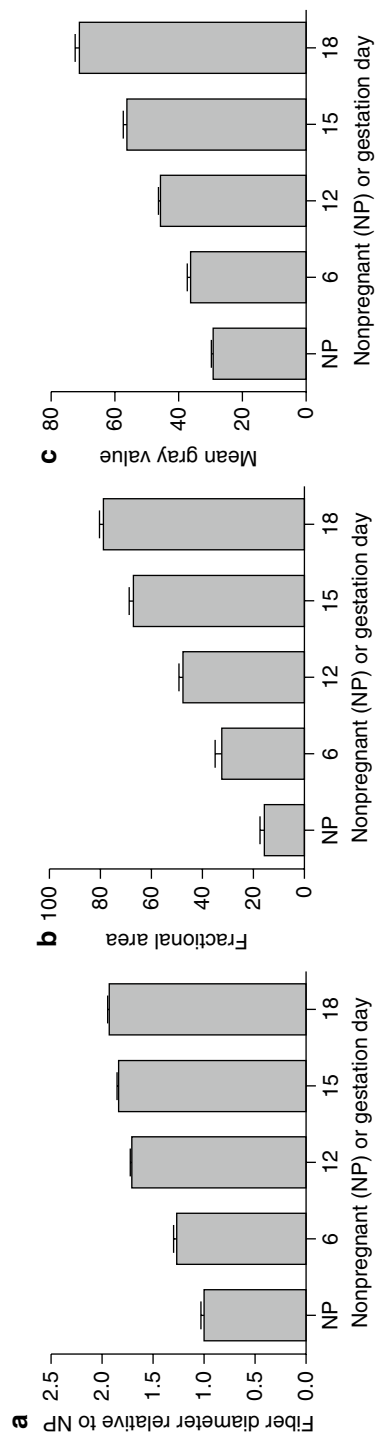


**Fig. 14.9** Quantitative analysis of the fiber diameter (a), fibrillar fractional area coverage (b), and intensity-based mean gray value (c). Features were measured in non-pregnant (NP), gestation days 6, 12, 15, 18 mouse cervical sections. Error bars represent standard error of the mean (Figure reproduced from Zhang et al. (2012) with permission)



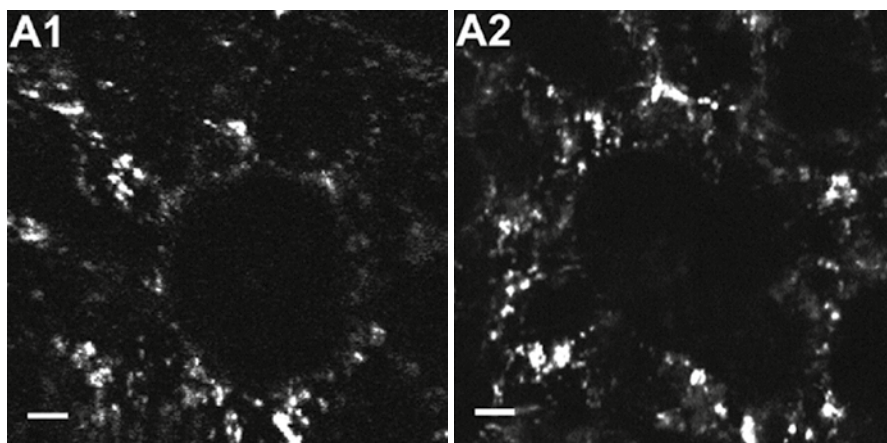


**Fig. 14.10** Imaging comparison of *ex vivo* mouse lung tissue as captured with a multiphoton endomicroscope (a) and benchtop microscope (b) (Reproduced from Rivera et al. (2011) with permission)

(SCC) carcinoma from normal lung tissue (Wang et al. 2009). Recently, Rivera et al. have demonstrated endomicroscopic imaging of *ex vivo* lung tissue with comparable image quality between the endomicroscope and benchtop microscope as compared in Fig. 14.10 (Rivera et al. 2011) using a power of 75 mW at the sample. With further work, it should be possible to utilize the endomicroscope to differentiate between normal and diseased lung tissue.

### 14.4.3 Breast Tissue Imaging

As mentioned above, SHG imaging microscopy has been shown to have the potential for early detection of breast cancer and evaluating metastatic potential based on changes in the collagen fiber architecture (Provenzano et al. 2008; Conklin et al. 2011; Kakkad 2012). The feasibility of using an SHG endoscope to diagnose these changes lies in its potential use in the clinic, both during biopsy retrieval and potentially for guiding surgery and delineating cancer margins. Figure 14.11 demonstrates representative examples of SHG endoscopic images from human breast cancer tissue and underlines the potential of using this technology for clinical applications. The collagen fiber architecture can be visualized clearly using about ~40 mW excitation.

### 14.4.4 Other Potential Applications

In addition to these highlighted endomicroscopic studies, many other potential applications have been demonstrated on benchtop microscope platforms that could be extended to endoscopy as well. For an overview of other applications targeted



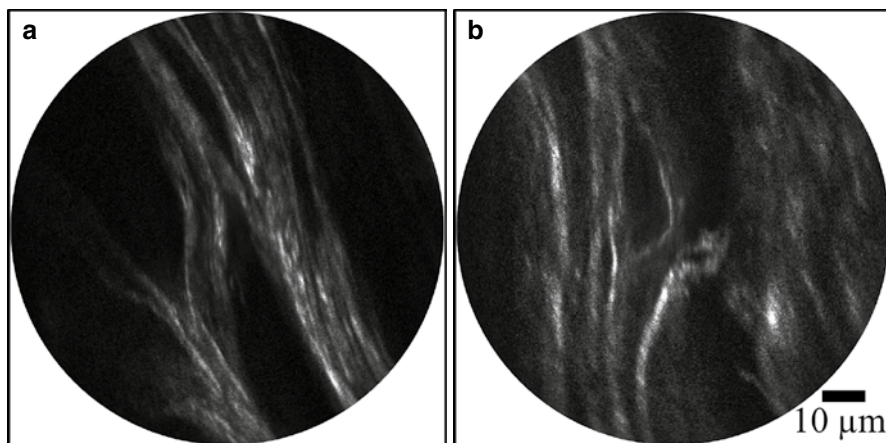


**Fig. 14.11** Representative images of SHG images from human breast biopsies obtained with our SHG endomicroscope

towards cancer, see for example the review by Perry et al. (2012). Another review more focused on clinical applications of SHG imaging was written by Campagnola (2011).

**Acknowledgements** We would like to thank previous members of our laboratory and our collaborators for their contributions to developing the multiphoton endomicroscope technology, including Dr. Mon T. Myaing, Dr. Yicong Wu, Dr. Yuying Zhang, Dr. Kartikeya Murari, Jiefeng Xi, Carmen Kut and Dr. Ming-Jun Li. We are also grateful to Dr. Kristine Glunde and Dr. Zaver Bhujwalla for providing the breast cancer tissues for imaging and to Dr. Mala Mahendroo and Dr. Kate Luby-Phelps for collaborating with us on the cervical imaging project. We acknowledge the financial support from the National Institutes of Health (including R01CA153023 and P50CA103175) and the Hartwell Foundation.

## References

- Agrawal GP (2001) Nonlinear fiber optics. Academic Press, San Diego
- Akins ML, Luby-Phelps K et al (2010) Second harmonic generation imaging as a potential tool for staging pregnancy and predicting preterm birth. *J Biomed Opt* 15(2):026020
- Ballas RG (2007) Piezoelectric multilayer beam bending actuators: static and dynamic behavior and aspects of sensor integration. Springer, Berlin/New York
- Balu M, Liu G et al (2010) Fiber delivered probe for efficient CARS imaging of tissues. *Opt Express* 18(3):2380–2388
- Behrman RE, Butler AS et al (2007) Preterm birth: causes, consequences, and prevention. National Academies Press, Washington, DC
- Blab GA, Lommerse PHM et al (2001) Two-photon excitation action cross-sections of the auto-fluorescent proteins. *Chem Phys Lett* 350(1–2):71–77
- Born M, Wolf E (1999) Principles of optics: electromagnetic theory of propagation, interference and diffraction of light. Cambridge University Press, Cambridge/New York
- Boyd RW (2003) Nonlinear optics. Academic Press, San Diego
- Campagnola P (2011) Second harmonic generation imaging microscopy: applications to diseases diagnostics. *Anal Chem* 83(9):3224–3231

- Campagnola PJ, Wei MD et al (1999) High-resolution nonlinear optical imaging of live cells by second harmonic generation. *Biophys J* 77(6):3341–3349
- Centonze VE, White JG (1998) Multiphoton excitation provides optical sections from deeper within scattering specimens than confocal imaging. *Biophys J* 75(4):2015–2024
- Choi H, Chen SC et al (2006) Design of a nonlinear endomicroscope biopsy probe. <http://dx.doi.org/10.1364/BIO.2006.TuI69>
- Conklin MW, Eickhoff JC et al (2011) Aligned collagen is a prognostic signature for survival in human breast carcinoma. *Am J Pathol* 178(3):1221–1232
- Denk W, Strickler J et al (1990) Two-photon laser scanning fluorescence microscopy. *Science* 248(4951):73–76
- Diaspro A, Chirico G et al (2006) Two-photon fluorescence excitation and related techniques in biological microscopy. *Q Rev Biophys* 38(02):97
- Duma V-F, Lee K-S et al (2011) Experimental investigations of the scanning functions of galvanometer-based scanners with applications in OCT. *Appl Optics* 50(29):5735
- Dunn AK, Wallace VP et al (2000) Influence of optical properties on two-photon fluorescence imaging in turbid samples. *Appl Optics* 39(7):1194
- Evans CL, Xie XS (2008) Coherent anti-stokes Raman scattering microscopy: chemical imaging for biology and medicine. *Annu Rev Anal Chem (Palo Alto Calif)* 1:883–909
- Flusberg BA, Cocker ED et al (2005) Fiber-optic fluorescence imaging. *Nat Methods* 2(12):941–950
- Göppert-Mayer M (1931) Über Elementarakte mit zwei Quantensprüngen. *Ann Phys* 401(3):273–294
- Grewe BF, Voigt FF et al (2011) Fast two-layer two-photon imaging of neuronal cell populations using an electrically tunable lens. *Biomed Opt Express* 2(7):2035
- Helmchen F, Denk W (2005) Deep tissue two-photon microscopy. *Nat Methods* 2(12):932–940
- Helmchen F, Fee MS et al (2001) A miniature head-mounted two-photon microscope. High-resolution brain imaging in freely moving animals. *Neuron* 31(6):903–912
- Huo L, Xi J et al (2010) Forward-viewing resonant fiber-optic scanning endoscope of appropriate scanning speed for 3D OCT imaging. *Opt Express* 18(14):14375–14384
- Iaconis C, Walmsley IA (1998) Spectral phase interferometry for direct electric-field reconstruction of ultrashort optical pulses. *Opt Lett* 23(10):792–794
- Kakkad SM (2012) Collagen I fiber density increases in lymph node positive breast cancers: pilot study. *J Biomed Opt* 17(11):116017
- Lacomb R, Nadiarnykh O et al (2008) Quantitative second harmonic generation imaging of the diseased state osteogenesis imperfecta: experiment and simulation. *Biophys J* 94(11):4504–4514
- Le Harzic R, Weinigel M et al (2008) Nonlinear optical endoscope based on a compact two axes piezo scanner and a miniature objective lens. *Opt Express* 16(25):20588–20596
- Legare F, Evans CL et al (2006) Towards CARS endoscopy. *Opt Express* 14(10):4427–4432
- Legare F, Pfeffer C et al (2007) The role of backscattering in SHG tissue imaging. *Biophys J* 93(4):1312–1320
- Liang W, Murari K et al (2012) Increased illumination uniformity and reduced photodamage offered by the Lissajous scanning in fiber-optic two-photon endomicroscopy. *J Biomed Opt* 17(2):021108
- Liu XM, Cobb MJ et al (2004) Rapid-scanning forward-imaging miniature endoscope for real-time optical coherence tomography. *Opt Lett* 29(15):1763–1765
- Liu L, Wang EK et al (2013) Confocal microendoscopic 3D imaging using MEMS scanners for both lateral and axial scans. 26th IEEE international conference on micro electro mechanical systems (Mems 2013). Taipei, Taiwan; pp. 1085–1088.
- Mertz J, Moreaux L (2001) Second-harmonic generation by focused excitation of inhomogeneously distributed scatterers. *Opt Commun* 196(1–6):325–330
- Moon S, Lee SW et al (2010) Semi-resonant operation of a fiber-cantilever piezotube scanner for stable optical coherence tomography endoscope imaging. *Opt Express* 18(20):21183–21197
- Moreaux L, Sandre O et al (2000) Membrane imaging by second-harmonic generation microscopy. *J Opt Soc Am B* 17(10):1685
- Murari K, Zhang Y et al (2011) Compensation-free, all-fiber-optic, two-photon endomicroscopy at 155  $\mu\text{m}$ . *Opt Lett* 36(7):1299

- Myaing MT, MacDonald DJ et al (2006) Fiber-optic scanning two-photon fluorescence endoscope. *Opt Lett* 31(8):1076–1078
- Nadiarnykh O, LaComb RB et al (2010) Alterations of the extracellular matrix in ovarian cancer studied by Second Harmonic Generation imaging microscopy. *BMC Cancer* 10:94
- Perry SW, Burke RM et al (2012) Two-photon and second harmonic microscopy in clinical and translational cancer research. *Ann Biomed Eng* 40(2):277–291
- Piyawattanametha W, Barretto RPJ et al (2006) Fast-scanning two-photon fluorescence imaging based on a microelectromechanical systems two-dimensional scanning mirror. *Opt Lett* 31(13):2018
- Provenzano PP, Inman DR et al (2008) Collagen density promotes mammary tumor initiation and progression. *BMC Med* 6:11
- Rivera DR, Brown CM et al (2011) Compact and flexible raster scanning multiphoton endoscope capable of imaging unstained tissue. *Proc Natl Acad Sci U S A* 108(43):17598–17603
- Rouse AR, Kano A et al (2004) Design and demonstration of a miniature catheter for a confocal microendoscope. *Appl Opt* 43(31):5763–5771
- Saar BG, Freudiger CW et al (2010) Video-rate molecular imaging in vivo with stimulated Raman scattering. *Science* 330(6009):1368–1370
- Saar BG, Contreras-Rojas LR et al (2011) Imaging drug delivery to skin with stimulated Raman scattering microscopy. *Mol Pharm* 8(3):969–975
- Sawinski JR, Denk W (2007) Miniature random-access fiber scanner for in vivo multiphoton imaging. *J Appl Phys* 102(3):034701
- Shen YR (1984) *The principles of nonlinear optics*. Wiley, New York
- Skala MC, Riching KM et al (2007) In vivo multiphoton microscopy of NADH and FAD redox states, fluorescence lifetimes, and cellular morphology in precancerous epithelia. *Proc Natl Acad Sci U S A* 104(49):19494–19499
- Smithwick QYJ, Seibel EJ et al (2001) Control aspects of the single-fiber scanning endoscope. *Proc SPIE* 4253(4253):176–188
- Squirrell JM, Wokosin DL et al (1999) Long-term two-photon fluorescence imaging of mammalian embryos without compromising viability. *Nat Biotechnol* 17(8):763–767
- Strathman M, Liu Y et al (2013) Dynamic focus-tracking MEMS scanning micromirror with low actuation voltages for endoscopic imaging. *Opt Express* 21(20):23934
- Tang S, Jung W et al (2009) Design and implementation of fiber-based multiphoton endoscopy with microelectromechanical systems scanning. *J Biomed Opt* 14(3):034005
- Timmons B, Akins M et al (2010) Cervical remodeling during pregnancy and parturition. *Trends Endocrinol Metab* 21(6):353–361
- Trebino R, Kane DJ (1993) Using phase retrieval to measure the intensity and phase of ultrashort pulses: frequency-resolved optical gating. *J Opt Soc Am A* 10(5):1101
- Wang CC, Li FC et al (2009) Differentiation of normal and cancerous lung tissues by multiphoton imaging. *J Biomed Opt* 14(4):044034
- Weiner AM (2009) *Ultrafast optics*. Wiley, Hoboken
- Williams RM, Zipfel WR et al (2005) Interpreting second-harmonic generation images of collagen I fibrils. *Biophys J* 88(2):1377–1386
- Wu Y, Xi J et al (2009) Scanning fiber-optic nonlinear endomicroscopy with miniature aspherical compound lens and multimode fiber collector. *Opt Lett* 34(7):953–955
- Wu Y, Zhang Y et al (2010) Fiber-optic nonlinear endomicroscopy with focus scanning by using shape memory alloy actuation. *J Biomed Opt* 15(6):060506
- Xu C, Webb WW (1996) Measurement of two-photon excitation cross sections of molecular fluorophores with data from 690 to 1050 nm. *J Opt Soc Am B* 13(3):481
- Zhang Y, Akins ML et al (2012) A compact fiber-optic SHG scanning endomicroscope and its application to visualize cervical remodeling during pregnancy. *Proc Natl Acad Sci U S A* 109(32):12878–12883
- Zhao Y, Nakamura H et al (2010) Development of a versatile two-photon endoscope for biological imaging. *Biomed Opt Express* 1(4):1159–1172
- Zipfel WR, Williams RM et al (2003) Nonlinear magic: multiphoton microscopy in the biosciences. *Nat Biotechnol* 21(11):1369–1377

## Chapter 15

# Intravital Multiphoton Endoscopy

David M. Huland, Dimitre G. Ouzounov, David R. Rivera, Chris M. Brown,  
and Chris Xu

**Abstract** When a patient has symptoms that could be indicative of cancer a clinical oncologist will perform a series of tests to reach an accurate diagnosis. The gold standard method for reaching a final diagnosis frequently involves locating and extracting tissue biopsies, which are then processed and studied at the cellular level by a pathologist. From this procedure a pathology report will be compiled that contains the diagnosis of the cancer type and grade. Deep penetration, low-resolution, imaging tests (e.g., magnetic resonance imaging MRI) scans, computed tomography (CT) scans, Ultrasound, etc.) can track the extent and spread of disease and serve as an initial screen for disease in tissues that are not easily accessed using conventional biopsy or optical imaging techniques (e.g. periphery lung, pancreas, small intestine). However, to date, these low resolution imaging tests have not been able to be used as stand alone diagnostic tests because they lack the ability to visualize disease at the cellular level and thus have been unable to match the sensitivity and specificity of diagnosis based upon biopsied tissue processed into histopathology slides. Finally, by compiling the data obtained from all these tests, the oncologist can determine the stage of the cancer (i.e., the severity or extent of the cancer) and use this information to provide the patient with a prognosis and course of treatment.

**Keywords** Microendoscopy • Cancer imaging • Multiphoton microscopy • Non-linear microscopy • GRIN lenses • Miniaturized optics • Intravital • Clinical imaging

---

D.M. Huland (✉) • D.G. Ouzounov • D.R. Rivera • C.M. Brown • C. Xu  
School of Applied and Engineering Physics, Cornell University,  
146 Clark Hall, Ithaca, NY 14853, USA  
e-mail: [dmh56@cornell.edu](mailto:dmh56@cornell.edu)

© Springer Science+Business Media Dordrecht 2014  
R. Weigert (ed.), *Advances in Intravital Microscopy*:  
*From Basic to Clinical Research*, DOI 10.1007/978-94-017-9361-2\_15

305

## 15.1 Introduction

### 15.1.1 *Current Clinical Practices for Cancer Diagnosis and Treatment*

When a patient has symptoms that could be indicative of cancer a clinical oncologist will perform a series of tests to reach an accurate diagnosis. The gold standard method for reaching a final diagnosis frequently involves locating and extracting tissue biopsies, which are then processed and studied at the cellular level by a pathologist. From this procedure a pathology report will be compiled that contains the diagnosis of the cancer type and grade. Deep penetration, low-resolution, imaging tests (e.g., magnetic resonance imaging MRI) scans, computed tomography (CT) scans, Ultrasound, etc.) can track the extent and spread of disease and serve as an initial screen for disease in tissues that are not easily accessed using conventional biopsy or optical imaging techniques (e.g. periphery lung, pancreas, small intestine). However, to date, these low-resolution imaging tests have not been able to be used as stand alone diagnostic tests because they lack the ability to visualize disease at the cellular level and thus have been unable to match the sensitivity and specificity of diagnosis based upon biopsied tissue processed into histopathology slides. Finally, by compiling the data obtained from all these tests, the oncologist can determine the stage of the cancer (i.e., the severity or extent of the cancer) and use this information to provide the patient with a prognosis and course of treatment.

Currently, the pathological analysis of tissue biopsies is one of the most effective methods for cancer diagnosis. In the clinic several types of biopsies are often performed, including:

1. Needle biopsies, in which a few cells (i.e., fine needle aspiration biopsy) or a small piece of tissue (i.e., core biopsy) is removed from the lesion,
2. Endoscopic or laparoscopic biopsies, in which a part of the lesion or the entire lesion is removed by a miniature surgical tool that is passed through the working channel of the endoscope/laparoscope or through a secondary incision, and
3. Surgical biopsies, in which a part of the lesion (i.e., incisional biopsy) or the entire lesion (i.e., excisional biopsy) is surgically removed (Young et al. 2011).

During diagnostic and surgical clinical procedures biopsy samples are typically located using some type of low magnification imaging modality. For example, needle biopsies are often guided using ultrasound, x-rays, CT or MRI scans, while endoscopic and surgical biopsies use white light imaging as guidance. After extraction, the biopsy samples are prepared for pathological analysis in a series of steps. For postoperative pathological analysis the biopsy samples are: (1) fixed, (2) dehydrated and cleared, (3) embedded with paraffin, (4) sectioned by a microtome, (5) mounted onto a microscope slide and (6) stained (Gartner and Hiatt 2007; Young et al. 2006). For intraoperative pathological analysis the biopsies are processed into frozen sections, whereby they are: (1) frozen, using compressed carbon dioxide or by immersion in a cold fluid, (2) sectioned by a microtome inside of a cryostat and (3) stained (Ross and Pawlina 2011). For intraoperative diagnosis, frozen sections are used in place of traditional sections since they allow for faster pathological analysis (e.g., ~10–30 min

vs. several days), but they often are of poorer quality than the traditional sections (Young et al. 2006; Ross and Pawlina 2011). Furthermore, frozen sections are often used intraoperatively for margin assessment during tumor resection.

Staining is a vital step in the tissue preparation process because it allows the pathologist to visualize and distinguish between the many cellular and tissue components, as well as accurately grade the cancer. Although a variety of stains have been developed Hematoxylin and Eosin are the most commonly used stains for routine pathology (Young et al. 2011). After processing is complete, a pathologist examines the tissue sections at the cellular level using a white light microscope and compiles the pathology report, which contains the final diagnosis. Note that if this routine histopathological analysis is unable to specifically identify the disease, then the pathologist can use supplementary techniques such as immunohistochemistry and electron microscopy (Young et al. 2011).

Although there are a number of cancer treatment options (e.g., chemotherapy, radiation therapy, photodynamic therapy, etc.), a particularly effective treatment is surgical resection of the tumor from the body. Depending on the cancer type this therapeutic procedure can be performed through traditional open surgery or a minimally invasive laparoscopic/endoscopic approach. In the open surgery approach the tumor is accessed and resected via a long exterior surgical incision. Using a minimally invasive laparoscopic/endoscopic approach, the tumor is resected by surgical tools controlled directly by the surgeon or with robotic assistance (e.g. da Vinci system) through several smaller exterior incisions. In both procedures the resection is guided using low-magnification white light imaging. Since this low-magnification imaging is unable to resolve cellular details, the resected tissue mass is prepared into frozen sections and analyzed intraoperatively by a pathologist to determine whether more tissue will need to be resected (i.e., tumor margin assessment) (Ross and Pawlina 2011). Although these practices are effective and widely adopted in the clinic, there are several limitations concerning the pathological analysis of endoscopic biopsies.

### ***15.1.2 Limitations of Endoscopic Cancer Diagnosis and Tumor Resection***

Frequently the clinical assessment of tissue health requires a physician to use a low-magnification, white-light (LMWL) endoscope that penetrates into the body to directly image the tissues *in situ*. Using this LMWL imaging as guidance, biopsy samples are extracted, processed into histopathology sections, and analyzed. Although LMWL endoscopy is widely used and effective for cancer diagnosis and tumor resection, these procedures have several limitations (Makino et al. 2012; Jain et al. 2012), including:

1. delayed diagnosis, due to the time required for biopsy processing and pathological analysis,
2. high procedural costs, due to the time delays imposed by intraoperative pathological analysis, which is necessary to determine how the biopsy/resection procedures will proceed in the operating room,



**Table 15.1** Tissue components visualized via multiphoton excitation of intrinsic emitters (Rivera 2013)

Process	Source	Tissue components visualized	Ref.
2PE	NADH, flavins, retinol, folic Acid	Cell cytoplasm, striated muscle fibers (i.e., skeletal & cardiac muscles)	Zipfel et al. (2003b), Huang et al. (2002)
2PE	Elastin	Elastic fibers (e.g., connective tissue, blood vessel walls)	Zipfel et al. (2003b)
3PE	Serotonin, melatonin, tyrosine, tryptophan, 5-HIAA, 5-HTOL	Cell cytoplasm, cell nuclei	Zipfel et al. (2003b)
SHG	Collagen	Collagen fibers (e.g., connective tissue, blood vessel walls, components of neuronal tissue & muscle tissue)	Zipfel et al. (2003b), Friedl et al. (2007), Campagnola et al. (2002), Rehberg et al. (2011)
SHG	Tubulin	Microtubules (e.g., cilia, mitotic spindles), cell cytoskeleton	Friedl et al. (2007), Campagnola et al. (2002), Dombeck et al. (2003)
SHG	Myosin	Striated muscle fibers (i.e., skeletal & cardiac muscles)	Zipfel et al. (2003b), Friedl et al. (2007), Campagnola et al. (2002), Rehberg et al. (2011), Both et al. (2004)
THG	Myosin	Striated muscle fibers (i.e., skeletal & cardiac muscles)	Friedl et al. (2007), Rehberg et al. (2011)
THG	Lipids & Lipid Bodies	Neuronal tissue (e.g., axons, dendrites, myelin sheaths), cell cytoplasm	Friedl et al. (2007), Witte et al. (2011), Débarre et al. (2006), Farrar et al. (2011)
THG	Hemoglobin	RBCs, blood vessels	Friedl et al. (2007), Rehberg et al. (2011), Witte et al. (2011)
THG	Collagen	Collagen fibers (e.g., connective tissue, blood vessel walls, components of neuronal tissue & muscle tissue)	Friedl et al. (2007), Rehberg et al. (2011)
THG	Elastin	Elastic fibers (e.g., connective tissue, blood vessel walls)	Sun et al. (2007)

3. patient discomfort and health risks, due to the numerous (including many benign) biopsies that are necessary to rule out carcinoma,
4. inaccurate cancer diagnosis due to incorrect biopsy sampling, because the biopsies are located using low-magnification, white-light (LMWL) imaging, which is often unable to locate early lesions as well as distinguish between benign and malignant lesions, and

**Table 15.2** Tissue components visualized by histopathology and multiphoton excitation of intrinsic emitters (Rivera 2013)

	Histopathological stain	Multiphoton imaging of unstained tissue
Cell nuclei	Hematoxylin, Masson’s Trichome, Van Gieson, Iron Hematoxylin	Dark-appearing, no fluorescence
Cell cytoplasm	Eosin, Masson’s Trichome, Van Gieson,	2PE, 3PE
Collagen fibers	Eosin, Masson’s Trichome, Van Gieson, Periodic Acid-Schiff	SHG, THG
Elastic fibers	Weigert’s, Orcein’s, Verhoeff’s	2PE, THG
Striated muscle	Hematoxylin & Eosin, Masson’s Trichome, Iron Hematoxylin	2PE, SHG, THG
Blood cells	RBC’s: Giesma, Eosin, Masson’s Trichome, Iron Hematoxylin	THG (RBC’s & WBC’s)
	WBC’s: Giesma, Hematoxylin & Eosin	
Myelin	Hematoxylin & Eosin, Iron Hematoxylin	THG

5. Inaccurate tumor resection, because LMWL imaging is unable to precisely define the boundaries of the tumor. Therefore, it is highly beneficial to develop new microscopic imaging tools that can provide minimally invasive, real-time, accurate disease diagnosis.

15.1.3 Multiphoton Microscopy

Multiphoton microscopy has the potential to be a versatile tool for clinical cancer diagnosis and treatment. Specifically, multiphoton microscopy provides several advantages over standard one-photon microscopy, including: (1) inherent optical sectioning, (2) ability to image deeper into tissues due to longer wavelength excitation and (3) reduced photodamage (Denk et al. 1990; Zipfel et al. 2003a; Helmchen and Denk 2005). Additionally, multiphoton excitation has the unique ability to generate fluorescence from intrinsic molecules (e.g., NADH, flavins) as well as produce harmonic generations (e.g., second harmonic generation (SHG) & third harmonic generation (THG)) within tissues, thereby producing real-time images of unprocessed, unstained tissues with resolution and detail comparable to gold standard histology (Makino et al. 2012; Jain et al. 2012; Pavlova et al. 2012; Zipfel et al. 2003b). Table 15.1, details the types of tissue components that can be visualized using multiphoton excitation of intrinsic emitters, while Table 15.2 and Fig. 15.1 provide a comparison between multiphoton imaging and histology. Furthermore, multiphoton microscopy has demonstrated the ability to accurately identify a variety of lesions within tumor-laden tissues in a manner comparable to conventional histopathological analysis (Makino et al. 2012; Jain et al. 2012; Pavlova et al. 2012).

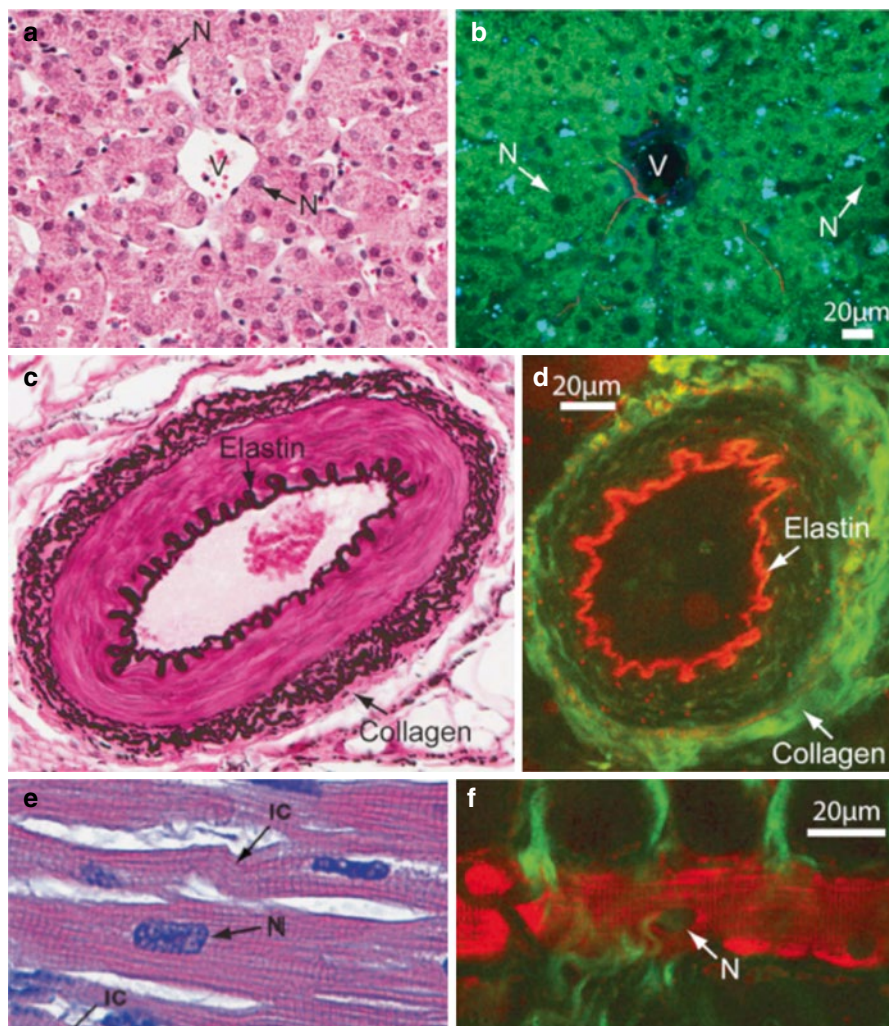


**Fig. 15.1** Common tissue components visualized via histology and multiphoton excitation of intrinsic emitters. (a, b) Comparison of cell nuclei & cytoplasm: liver hepatocytes radiating outward from a central vein (V). (a) H&E, the nuclei (N, blue) and cytoplasm (pink) of the hepatocytes are visible. (b) MPM, the nuclei (N) of the hepatocytes appear black (non-fluorescent), while the cytoplasm is brightly fluorescent via 2PE (green pseudocolor) (Makino et al. 2012). (c, d) Elastin & collagen comparison: artery in cross-section, displaying characteristic layers of the artery wall. (c) Trichome w/Verhoeff's elastic stain, elastic fibers (black) and collagen fibers (pink) are visible. (d) MPM, 2PE of elastin (red pseudocolor) and SHG of collagen (green pseudocolor) are visible (Zipfel et al. 2003a). (e, f) Striated muscle comparison: longitudinal images of cardiac muscle cells, where the characteristic striations (i.e., vertical banding pattern) are visible. (e) H&E, the nuclei (N, blue) and extensive cytoplasm (pink) of the myocytes are visible (Young et al. 2006). (f) MPM, the nuclei (N, black) and extensive cytoplasm (2PE of NADH, red pseudocolor) of the myocytes are visible along with collagen connective tissue components (SHG, green pseudocolor) (Zipfel et al. 2003a)

The ability to acquire diagnostic quality images solely from intrinsic tissue fluorophores and harmonic generations is a significant advantage for multiphoton imaging because to date, few contrast agents have been approved for use in live patients due to dye toxicity concerns. Additionally, multiphoton imaging of intrinsic fluorophores can provide valuable spectroscopic information in terms of changes in the intensity and emission wavelength as tissues develop abnormalities (Pavlova et al. 2012; Zipfel et al. 2003b). Therefore, multiphoton endoscopes (MPEs) that enter the body via a natural orifice or a small surgical incision and are capable of providing real-time, cellular level images from unstained tissues would be valuable clinical tools. These endoscopes could be used clinically to provide real-time surgical margin assessment during tumor resection, and serve as either guides or replacements (i.e., optical biopsy) for conventional biopsies.

### 15.1.4 Multiphoton Endoscopy

A challenge faced in the realization of a clinically useful multiphoton endoscope is achieving multiple imaging parameters (e.g., high resolution, fast frame rates, large field of view (FOV), axial sectioning, etc.) within a compact device size that is suitable for minimally invasive procedures. High spatial resolution is necessary to resolve cellular details within tissues that can be used to assess the tissue health state. A large image FOV is useful so that a clinician can survey a large region of tissue and identify sites of interest. Fast frame rates are necessary to mitigate *in vivo* motion artifacts that are caused by natural bodily functions (e.g., respiration, heart beats, and smooth muscle contractions) and can be generated using distal resonant optomechanical structures. Finally, axial sectioning is valuable for clinical diagnostics since it enables the visualization of informative three-dimensional structural tissue details.

To date, several research groups have developed multiphoton endoscopes (Engelbrecht et al. 2008; Myaing et al. 2006; Wu et al. 2009a, 2010; Le Harzic et al. 2008; Sawinski and Denk 2007; Helmchen et al. 2001; Bao et al. 2008; Piyawattanametha et al. 2006; Piyawattanametha et al. 2009; Tang et al. 2009; Hoy et al. 2011). These devices consist of a distal miniaturized scanning mechanism and lens assembly that are encapsulated in a protective outer housing. The current generation of distally scanned endoscopic instruments is progressing towards reducing instrument size while improving instrument performance, however, limitations of the current generation of endoscopes do exist including: non-uniform laser scanning (Engelbrecht et al. 2008; Myaing et al. 2006; Wu et al. 2009a, 2010), slow frame rates (Le Harzic et al. 2008; Sawinski and Denk 2007; Helmchen et al. 2001; Bao et al. 2008), large device sizes (Bao et al. 2008; Piyawattanametha et al. 2006; Piyawattanametha et al. 2009; Tang et al. 2009; Hoy et al. 2011), and slow axial sectioning (Wu et al. 2010; Le Harzic et al. 2008; Helmchen et al. 2001; Bao et al. 2008; Piyawattanametha et al. 2009). To date, these devices have been unable to demonstrate the ability to acquire *in vivo* images of tissues solely from intrinsic fluorescence and harmonic generation. Table 15.3 displays a comparison between

**Table 15.3** Performance matrix of current multiphoton endoscopes

MPE type	Scanner description	Scanner size (mm×mm)	MPE size (mm×mm)	FOV (μm×μm)	Resolution (FWHM) X-Y, Z (μm)	Frame rate (frames/s)	Built-In axial sectioning	Intrinsic fluorescence images
[Ref.]								
Cornell MPE	Res./non-res. fiber, raster	1×26	Ø3×40	110×110	0.8, 10	4 fps; (512×512 pixels)	No	Yes
Cornell MME	Res./non-res. multifiber, raster	1×26	Ø3×40	110×110	0.8, 10	4 fps; (512×512 pixels)	Yes	Yes
Engelbrecht et al. (2008), Myaing et al. (2006), Wu et al. (2009a, 2010)	Res. fiber, spiral	Ø0.4×8	Ø2.4×~45 Wu et al. (2009a, 2010)	Ø160 Wu et al. (2009a, 2010) or Ø200 (Engelbrecht et al. 2008)	0.98, 7.7 Engelbrecht et al. (2008) or 1.6, 11.4 Wu et al. (2009a, 2010)	3 fps Myaing et al. (2006), Wu et al. (2009a, 2010) or 8 fps Engelbrecht et al. (2008); 512×512 pixels	Yes (Wu et al. 2010)	No
Le Harzic et al. (2008)	Non-res. fiber, raster	1.9×34	Ø7×100	420×420	0.6, 5.8	0.1 fps; (512×512 pixels)	Yes	No
Sawinski and Denk (2007)	Non-res. piezolever fiber, raster	6.4×12.7	~15×25×NR	250×250	0.75, NR	0.2–0.5 fps; (512×512 pixels)	No	No
Helmchen et al. (2001)	Res. fiber, Lissajous	2×28	13×75×NR	135×135	NR	0.5 fps; (128×128 pixels)	Yes	No
Bao et al. (2008), Bewersdorf et al. (2006)	Non-res. E.M. tuning fork fiber, raster	Ø5×NR	Ø7×43 Bewersdorf et al. (2006)	475×475	1, 14.5	0.8 fps; (1,024×1,024 pixels)	Yes	No
Piyawattanametha et al. (2006), Piyawattanametha et al. (2009), Hoy et al. (2011)	MEMS; raster Piyawattanametha et al. (2006), Piyawattanametha et al. (2009) & Lissajous Hoy et al. (2011)	0.6×3.2×3	10×19×20 Piyawattanametha et al. (2009) or Ø9.6×23 Hoy et al. (2011)	295×100 Piyawattanametha et al. (2009) or 150×150 Hoy et al. (2011)	1.29, 10.3 Piyawattanametha et al. (2009) or 1.27, 13.5 Hoy et al. (2011)	1–15 fps (400×135 pixels) Piyawattanametha et al. (2009) or 7 fps (512×512 pixels) Hoy et al. (2011)	Yes Piyawattanametha et al. (2009)	No

Notes: the FOV reported for the Cornell endoscopes (described in this work) is the uniform FOV; in reality these devices have a FOV up to 208×110 μm. Furthermore note that the Cornell Multifocal Multiphoton Endoscope (MME) acquires three images simultaneously at the reported performance parameters. NR not reported, Ø diameter



current MPEs and the instruments described in this chapter. The majority of the limitations of current MPEs are in part due to the design of the distal scan mechanisms. Within these endoscopes, various distal miniaturized scanners have been demonstrated, including resonant-based (e.g., spiral (Engelbrecht et al. 2008; Myaing et al. 2006; Wu et al. 2009a, 2010) or Lissajous (Helmchen et al. 2001) scan pattern) and non-resonant-based cantilever fiber scanners (Le Harzic et al. 2008; Sawinski and Denk 2007; Bao et al. 2008) as well as microelectromechanical systems (MEMS) scanning mirrors (Piyawattanametha et al. 2006; Piyawattanametha et al. 2009; Tang et al. 2009; Hoy et al. 2011).

Of these scanners, the resonant-based spiral scanners are most successful in terms of high performance optomechanical design (Brown et al. 2006) resulting small dimensions (e.g., scanner outer diameter (o.d.)  $\approx 1$ , rigid distal tip  $\approx 12$  mm) and fast image acquisition speeds [e.g., 8 frames/s with  $512 \times 512$  pixels per frame, approximately  $200\text{-}\mu\text{m}$  diameter field-of-view (FOV<sub>xy</sub>)] (Engelbrecht et al. 2008; Lee et al. 2010). However, spiral scanners are limited and in multiphoton imaging applications by non-uniform spatial coverage and sampling time, in comparison to a raster scanner, resulting in the acquisition of images that are highly uneven in terms of the two-photon excitation generated throughout the frame. For example, the pixel dwell time of a typical spiral scanner is non-uniform with differences as high as 800 times between the center and periphery of the scan (Engelbrecht et al. 2008), meaning that the power at the periphery must be much higher ( $>10\times$ ) than that at the center to achieve equivalent two-photon excitation throughout the image frame.

Although a raster scan pattern provides a more uniform spatial coverage, current miniaturized fiber raster scanners are limited in terms of their physical dimensions and/or scan speeds. Le Harzic et al. previously demonstrated a piezodriven X-Y scanner (length = 34 mm, width = 1.9 mm) capable of a uniformly sampled FOV<sub>xy</sub> up to  $420\text{ }\mu\text{m}$  by  $420\text{ }\mu\text{m}$ , but this device is limited by its frame rate (i.e., 0.1 frames/s with  $512 \times 512$  pixels per frame) and size (i.e., 1 cm outer diameter) (Le Harzic et al. 2008). Sawinski and Denk demonstrated a piezo lever fiber raster scanner, however this device is also limited by its frame rate (i.e., up to 0.5 frames/s with  $512 \times 512$  pixels) and size (i.e., all dimensions  $>1$  cm) (Sawinski and Denk 2007). Additionally, Bao et al. demonstrated a fiber raster scanner that is driven by an electromagnetic tuning fork (length = 43 mm, width = 5 mm), resulting in a uniformly sampled FOV<sub>xy</sub> up to  $475\text{ }\mu\text{m}$  by  $475\text{ }\mu\text{m}$ , but this device is also limited by its frame rate (i.e., 0.8 frames/s with  $1,024 \times 1,024$  pixels per frame) (Bao et al. 2008). Slow image acquisition speeds and large device sizes are not ideal for minimally invasive, *in vivo* imaging procedures. Recently, MEMS scanning mirrors have been developed as an alternative to optical fiber scanning, capable of fast raster (Piyawattanametha et al. 2006, 2009; Tang et al. 2009) and Lissajous scanning (Hoy et al. 2011). Although 2D MEMS scanning mirrors with miniature dimensions (e.g.,  $750 \times 750\text{ }\mu\text{m}$  mirror size) have demonstrated fast line acquisition rates on the order of 1–3 kHz, the overall miniaturization of these MEMS scanners (i.e., their probe O.D.s) is limited by the die size of the actuator, which is typically  $3 \times 3$  mm (Piyawattanametha et al. 2006, 2009; Hoy et al. 2011). To that end, MPEs that use MEMS scanners have device dimensions  $\sim 1$  cm or greater, which is not ideal for minimally invasive procedures within a live patient (Piyawattanametha et al. 2006, 2009; Tang et al. 2009; Hoy et al. 2011). As stated previously, axial sectioning is



a useful ability for a MPE. To date, axial sectioning in flexible MPEs has been achieved through the use of built-in one-dimensional actuators (e.g., shape memory alloys, DC motors) that mechanically move the two-dimensional scanner and optics within the distal housing (Wu et al. 2010; Le Harzic et al. 2008; Helmchen et al. 2001; Bao et al. 2008; Piyawattanametha et al. 2009). However, these one-dimensional actuators are slow and add additional size to the endoscopes. During *in vivo* imaging, tissues move rapidly in three dimensions relative to the imaging device due to natural bodily movements. Therefore, ideally an MPE should acquire multiple axial sections simultaneously to acquire meaningful 3D images from live tissues.

In this work, we detail our efforts to improve upon the shortcomings of current MPEs, and develop endoscopes that are capable of translating the benefits of multiphoton microscopy into the clinic. We will focus predominately on three different approaches:

1. A compact and flexible raster scanning MPE (Rivera et al. 2011, 2012a, b; Brown et al. 2012),
2. A rigid GRIN needle based MPE (Huland et al. 2012, 2013),
3. A dual modality MPE with variable magnification and field of view (Ouzounov et al. 2013a, b).

In summary, this work describes our efforts to develop clinically useful, compact multiphoton endoscopes capable of providing a minimally invasive, real-time diagnosis of a patient's tissue health state.

## 15.2 Compact and Flexible Raster Scanning MPE

### 15.2.1 Introduction

A number of groups have demonstrated miniaturized instruments capable of confocal, optical coherence tomography (OCT), TPF, and SHG imaging (Engelbrecht et al. 2008; Myaing et al. 2006; Wu et al. 2009a, b, 2010; Le Harzic et al. 2008; Sawinski and Denk 2007; Helmchen et al. 2001; Bao et al. 2008; Piyawattanametha et al. 2006, 2009; Tang et al. 2009; Hoy et al. 2011; Seibel and Smithwick 2002; Hendriks et al. 2011; Goetz et al. 2007; Dickensheets and Kino 1996; Hofmann et al. 1999; Fu et al. 2007). The primary constituents of these devices are typically a miniaturized scanning mechanism and lens assembly that is encapsulated in a protective housing with dimensions suitable for minimally invasive procedures (i.e. a probe outer diameter on the order of a few millimeters with a rigid length of several centimeters). Within these micro-endoscopes, various distal miniaturized scanners have been demonstrated, including resonant-based [e.g., Lissajous (Helmchen et al. 2001; Wu et al. 2009b) or spiral (Engelbrecht et al. 2008; Myaing et al. 2006; Wu et al. 2009a; Seibel and Smithwick 2002; Hendriks et al. 2011) scan pattern] and non-resonant-based cantilever fiber scanners (Le Harzic et al. 2008; Sawinski and Denk

2007; Hendriks et al. 2011; Goetz et al. 2007) as well as microelectromechanical systems (MEMS) scanning mirrors (Piyawattanametha et al. 2006, 2009; Tang et al. 2009; Dickensheets and Kino 1996; Hofmann et al. 1999; Fu et al. 2007). Of these scanners, the resonant-based spiral scanners are the most successful in terms of their miniaturized dimensions (e.g., o.d.  $\approx 1$  mm) and fast image acquisition speeds [e.g., 8 frames/s with  $512 \times 512$  pixels per frame, approximately 200- $\mu\text{m}$  diameter field-of view (FOV<sub>xy</sub>)] (Engelbrecht et al. 2008); however, these resonant devices are fundamentally limited by non-uniform spatial coverage and sampling time in comparison to current miniaturized raster scanners. Current miniaturized raster scanners are, however, limited in terms of their physical dimensions and/or scan speeds. Slow image acquisition speeds are not ideal because of the motion artifacts typically faced in real-time *in vivo* clinical imaging environments. Additionally, although 2D MEMS scanning mirrors with miniature dimensions (e.g.,  $750 \times 750$   $\mu\text{m}$  mirror size) have recently demonstrated fast line acquisition rates on the order of 1–3 kHz, the overall miniaturization of these MEMS scanners (i.e. probe o.d.) is limited by the die size of the actuator, which is typically  $3 \times 3$  mm (Piyawattanametha et al. 2006; Tang et al. 2009).

Here, we present an endoscope that utilizes a miniaturized resonant/nonresonant cantilever fiber raster scanner design that is compact (width/thickness  $\leq 1$  mm, total length  $\approx 2.6$  cm), achieves  $\geq 650$   $\mu\text{m}$  fiber-tip deflection for both the resonant and non-resonant axes, and allows for imaging at approximately 4.1 frames/s ( $512 \times 512$  pixels). The fiber scanner's small dimensions enable it to be packaged along with a miniaturized high N.A. gradient-index (GRIN) assembly to form a compact and flexible TPF/SHG endoscope, with an outside diameter of 3 mm and a rigid length of 4 cm. The temporal pulse widths at different endoscope output powers were characterized as well as the imaging resolution of the device. Finally, we demonstrate that our multiphoton endoscope prototype is able to obtain *ex vivo* and *in vivo* tissue images solely based on intrinsic fluorescence and SHG signal. These results show the potential for our endoscope prototype to be used as a real-time *in vivo* diagnostic tool for medical diagnostics.

## 15.2.2 Design and Characterization

### 15.2.2.1 Miniaturized Raster Scanner

The miniaturized fiber raster scanner is driven by high-performance two-layer piezoelectric actuators or bimorphs (T215-A4CL, Piezo Systems, Inc.). These bimorphs are suitable for the fabrication of a miniaturized scanning mechanism because of their small dimensions (e.g., width = 0.5–1 mm, thickness = 380  $\mu\text{m}$ ) and ability to achieve deflection on the order of hundreds to thousands of microns. In our device, two bimorphs are aligned such that their bending axes are

perpendicular to each other and serve as the resonant and non-resonant drivers for the lateral X-Y scanning. A commercial double clad optical fiber (DCF SM-9/105/125-20A, NuFern) is mounted as a cantilever onto these axes and is driven resonantly in one dimension and non-resonantly in the other. The DCF has a core, inner cladding, and an outer cladding with diameters of 9, 105, and 125  $\mu\text{m}$ , respectively. The length of the cantilevered DCF that would enable high speed resonant scanning on the order of 1 kHz was determined from (Kinsler et al. 1982):

$$\nu = \frac{\beta R}{4\pi L^2} \sqrt{\frac{E}{\rho}} \quad (15.1)$$

where E is the Young's modulus (silica),  $\rho$  is the density (silica), R is fiber radius, L is the cantilever fiber overhang length, and  $\beta$  is a constant that is dependent upon the boundary conditions of the cantilever and the vibration mode number. In our calculation, we use the boundary condition of a fixed-free cantilever beam and the zeroth-order vibration mode ( $\beta \approx 3.52$ ). From this calculation, we chose a fiber overhang length of approximately 9 mm for our scanner resulting in a measured resonant frequency of 1.05 kHz. A 3-mm length piezo bimorph was sufficient to provide a fiber-tip deflection range of over 1 mm at a peak-to-peak drive voltage (Vpp) of 50 V. In order to achieve large non-resonant fiber-tip deflection, while minimizing the overall rigid length of the cantilever, we optimized the active length of the nonresonant piezo bimorph using the following equation:

$$D = 2c \left( L_1^2 + 2L_1 L^2 \right) \left( \frac{V_{\text{applied}}}{V_{\text{spec}}} \right) \quad (15.2)$$

where D is the non-resonant fiber-tip deflection ( $\mu\text{m}$ ), c is a proportionality constant, L1 is the free length of the non-resonant piezo bimorph, and L2 is the total length of the resonant piezo bimorph and the overhang length of the optical fiber (i.e., 12 mm). Using this calculation as a guide, we chose a non-resonant piezo length of 14 mm, which theoretically predicted deflection up to 763  $\mu\text{m}$  at 200 Vpp. Although the application of relatively high voltage to the piezo bimorphs is necessary for high fiber-tip deflection (i.e., 200 Vpp to achieve non-resonant fiber-tip deflection up to 650  $\mu\text{m}$ ), we note that the electrical current within these bimorphs is small, with estimated currents of 30 and 1  $\mu\text{A}$  for the resonant and non-resonant bimorphs, respectively.

It should be noted that in order to generate a purely linear fiber-tip motion in our resonant axis with minimal displacement out of the plane of actuation, we incorporated a small stiffening rod into the scanner to break the cylindrical symmetry of the optical fiber. Additionally, we note that our scanner has the ability to arbitrarily position the resonant axis line-scans in a direction orthogonal to the non-resonant axis by applying a dc offset voltage to the non-resonant bimorph. This may be of clinical use for measuring fast, dynamic physiological phenomena.

### 15.2.2.2 Three-Millimeter Outer Diameter Multiphoton Endoscope

The prototype miniaturized raster scanner has a width/thickness  $\leq 1$  mm, a total length of approximately 2.6 cm, and is capable of fiber-tip deflection of  $1.0\text{ mm} \times 0.65\text{ mm}$ . The small width and thickness of the scanner allow it to be packaged, along with a commercial multi-element GRIN lens assembly (GT-MO-080-018-810, GRIN-TECH), into a waterproof stainless steel housing with an outer diameter of 3 mm and a rigid length of 4 cm. The 0.8-N.A. GRIN assembly has a total length of 7.62 mm and is protected by a 1.4-mm o.d. stainless steel housing. The miniature size of the scanner and lens assembly enable the distal end of the endoscope to have dimensions that are well suited for a minimally invasive probe. Figure 15.2a shows a mechanical assembly diagram of the distal end, and Fig. 15.2b shows a photograph of the external protective housing that encapsulates the miniaturized scanner and lens assembly. Within the protective housing, the double-clad fiber tip is centered laterally and separated approximately 200  $\mu\text{m}$  axially from the 1-mm diameter back aperture of the GRIN assembly (Fig. 15.2c). For endoscopic imaging, a tabletop setup is used (Fig. 15.2d).

### 15.2.2.3 Pulse Characterization

We pre-compensate the fiber dispersion by imposing an appropriate quadratic chirp on the input pulses with a rotating cylindrical lens and grating (Le Harzic et al. 2008), which has the advantage of allowing continuous tuning of the second-order dispersion over a large range without perturbing the spatial alignment. Figure 15.3a shows the second order autocorrelation traces of the initial laser output as well as at 50-mW output from our endoscope. We are able to achieve a 290-fs pulse width at 50-mW output from the core of the DCF. The measured optical spectra are shown in Fig. 15.3b. The characteristic spectrum narrowing due to the optical nonlinearity and the normal dispersion of the fiber is clearly visible. Figure 15.3c shows the measured pulse widths over a range of endoscope power outputs. These results are in close agreement with numerical simulations based on the nonlinear Schrodinger's equation (Sawinski and Denk 2007).

### 15.2.2.4 Optical Resolution

The lateral and axial resolutions of our device are characterized by the transmission image of a high-resolution United States Air Force (USAF) test target and the axial response of the two-photon excited fluorescence signal from a 500-nm thin film of Rhodamine B (RhB) dye, respectively. Figure 15.4a shows a transmission image of a high-resolution USAF test target, where the smallest line-width group (group 9) is displayed. The group 9 elements have line widths ranging from 977 nm (group 9, element 1) down to 775 nm (group 9, element 3) and are all discernible in this image. Figure 15.4b shows an inverted

**Fig. 15.2** Three-millimeter o.d. raster scanning endoscope components and setup. **(a)** Mechanical assembly of the endoscope components. **(b)** Photograph of the prototype. **(c)** Optical path of the internal components of the distal end. **(d)** Tabletop endoscope imaging setup. (Rivera et al. 2011)

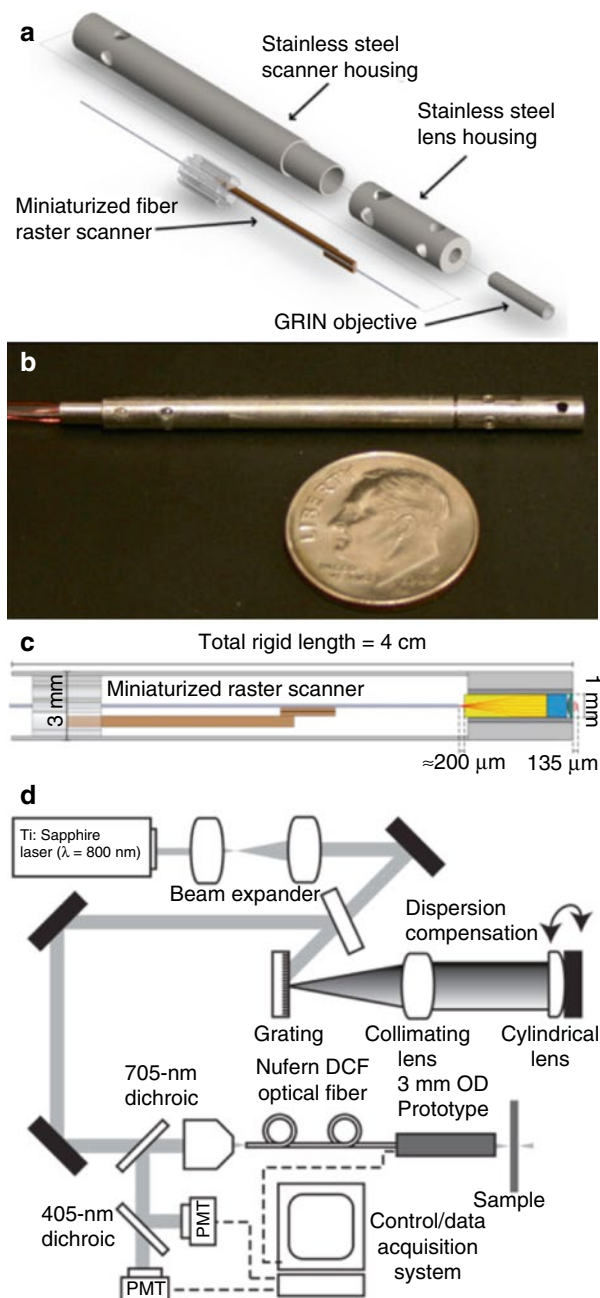
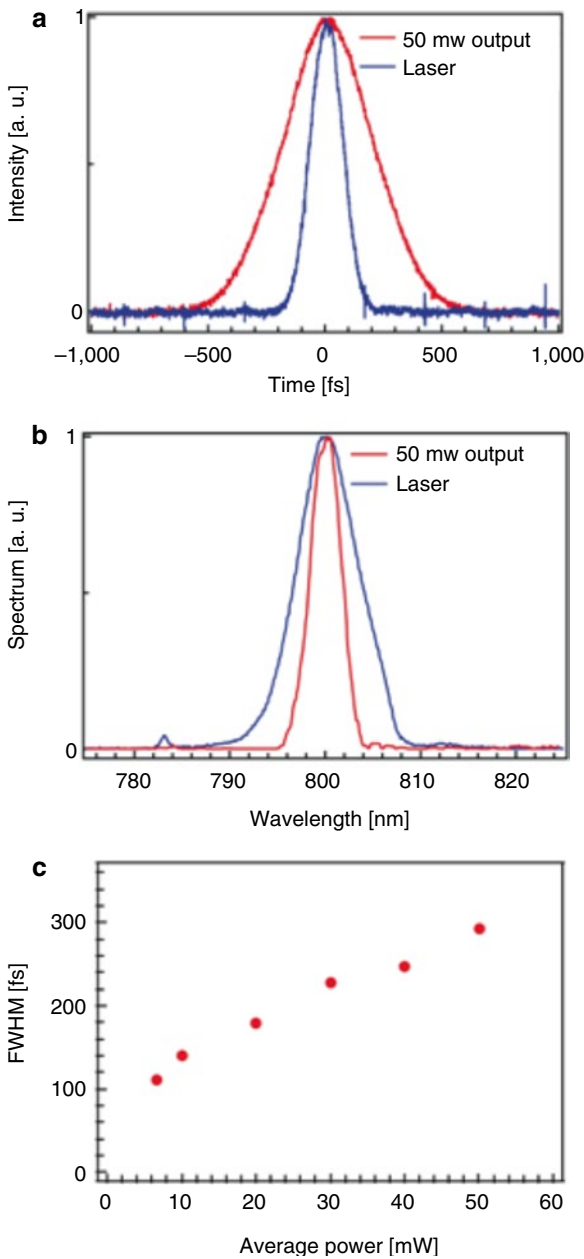


**Fig. 15.3** Pulse characterization. **(a)** Autocorrelation pulse-width measurements for the Ti:Sapphire output and for 50-mW endoscope output. The measured pulse widths are approximately 100 and 290 fs, respectively. **(b)** Spectra for the Ti:Sapphire output and for endoscope output at 50 mW. **(c)** Measured pulse widths of the endoscope output as a function of output power, assuming a deconvolution factor of 1.54 for a Sech2 pulse (Rivera et al. 2011)

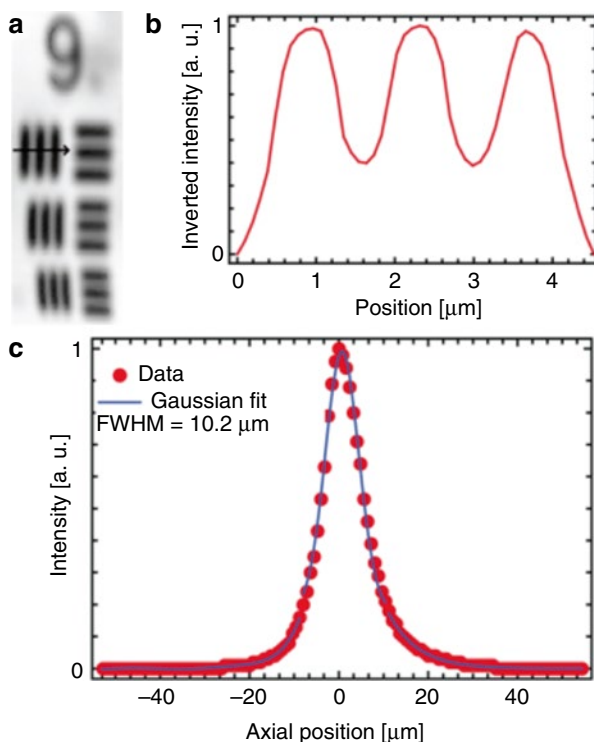


line-intensity profile across the vertical lines in group 9, element 1. Given the line widths of 977 nm and the measured peak-to-trough ratio of 0.46, we determine a one-photon lateral resolution of approximately 1.1  $\mu\text{m}$  full width at half maximum (FWHM), which corresponds to a two-photon lateral resolution of



**Fig. 15.4** Lateral and axial resolution. (a) Transmission image of high-resolution USAF test target. Group 9, elements 1–3 are displayed with line widths ranging from 977 to 775 nm.

FOV<sub>xy</sub> = 10 × 30 μm. (b) Intensity line profile across the vertical bars of group 9, element 1. Using the intensity ratios between the peak and trough values, we determine a one-photon lateral resolution of approximately 1.1 μm (FWHM), which corresponds to a two-photon lateral resolution of approximately 0.8 μm (FWHM). (c) A two-photon axial resolution of approximately 10 μm (FWHM of the thin film response) is determined using a RhB thin film scan (Rivera et al. 2011)



approximately 0.8 μm (FWHM). Figure 15.4c shows the intensity profile produced as a result of stepping a 500-nm RhB thin film axially through the focal plane of the endoscope prototype. The FWHM of the intensity profile is approximately 10 μm. Using the magnification of the endoscopic lenses ( $M = 1/4.8$ ) and the measured mode field diameter (MFD) of the DCF (MFD  $\approx 9.1$  μm at 800 nm), the theoretical two-photon lateral and axial resolutions are approximately 0.8 μm (FWHM) and 9.4 μm (FWHM of the thin film response), respectively. The demonstrated lateral and axial resolutions should be sufficient for resolving subcellular details in biological tissues.

### 15.2.2.5 Scan Uniformity Characterization

A raster scan pattern is superior to a spiral or Lissajous scan pattern because of the uniformity in its spatial scan pattern and pixel dwell time throughout the sample. In order to demonstrate the high uniformity in our raster scanner, Fig. 15.5a shows a transmission image of a 400 line-pair per mm (LP/mm) Ronchi ruling, without any image processing. The large deflection range in the resonant scan is evident by the

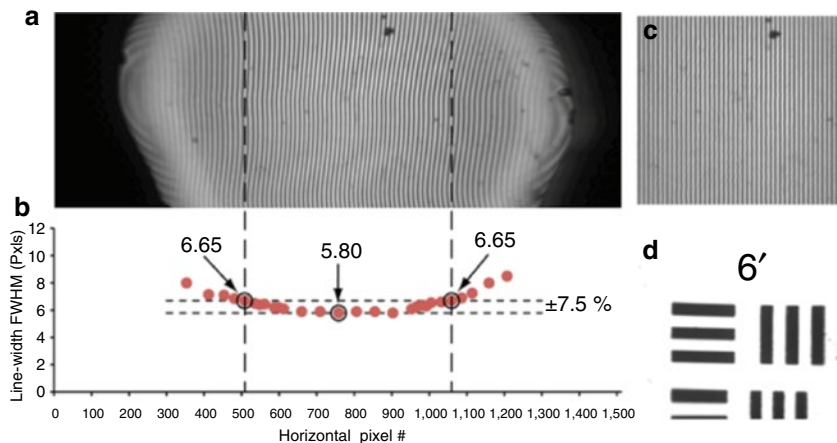


**Fig. 15.5** Raster scan uniformity characterization. **(a)** Transmission image of a 400 LP/mm Ronchi ruling (line width = 1.25 μm). **(b)** Plot of the measured line widths of the Ronchi ruling as a function of the horizontal pixel number across the image. A horizontal range of approximately 110 μm corresponds to a line-width deviation of ±7.5 %. **(c)** Cropped and postprocessed Ronchi ruling image from **a** (FOV<sub>xy</sub> ≈ 110 μm × 110 μm). The Ronchi ruling lines in **c** are corrected to be of uniform width across the image FOV<sub>xy</sub>. **(d)** Cropped and postprocessed transmission image of USAF test target group 6, elements 2–3 (line widths: 7.0 to 6.2 μm, FOV<sub>xy</sub> ≈ 110 μm × 110 μm) (Rivera et al. 2011)

appearance of the black regions on the horizontal edges of Fig. 15.5a, which indicate that the fiber tip is scanning well past the 1-mm back aperture of the GRIN lens. The visible FOV<sub>xy</sub> that is contained within the GRIN lens is approximately 208 × 110 μm. We measured the line widths horizontally across the Ronchi ruling as shown in Fig. 15.5b. Over a horizontal range of approximately 110 μm, there is a line-width deviation of approximately ±7.5 %. Thus, a uniform pixel dwell time over a reasonably large FOV<sub>xy</sub> (110 × 110 μm) can be achieved (dashed region within Fig. 15.5a).

In the Ronchi ruling image (Fig. 15.5a), it is apparent that the 1.25 μm width vertical lines do not appear to be perfectly straight throughout the entire image. This imperfection is attributed to a slight variation in our scanner's resonant deflection, which is dependent upon the non-resonant scan position. Although it leads to image distortions if uncorrected, such an imperfection has negligible impact on the sampling uniformity of the scanner. We observe that the variation in the resonant axis deflection is consistent, stable and repeatable between frames for given drive parameters (i.e., drive frequency and applied voltage to the piezos). The repeatability of the scan pattern enables us to develop an image remapping algorithm to correct the original unprocessed Ronchi ruling image (see Fig. 15.5c for the corrected Ronchi ruling image), which can then be applied to correct subsequently acquired images (e.g., Fig. 15.5d).

For comparison, the pixel dwell time of a typical spiral scanner is nonuniform with differences as high as 800 times between the center and periphery of the scan (Friedl et al. 2007). It is impractical to compensate for such large scan nonuniformities with power modulation because of the following factors: (i) To achieve equivalent two-photon excitation between the center and periphery of the spiral scan, the power at the periphery must be much higher ( $>10\times$ ) than that at the center; a single dispersion compensation setup cannot provide optimal compensation over such a large power variation because of the nonlinear pulse broadening effects within the optical fiber (see Fig. 15.3c). (ii) The high power levels required at the periphery of the spiral scan will add significant cost and complexity to the laser source, and may preclude the use of fiber-based laser sources, which are widely considered to be an ideal source for use in the clinical setting because of their robustness, small footprint, and low cost.

#### 15.2.2.6 *Ex Vivo* Intrinsic Fluorescence Imaging

An ideal optical diagnostic tool will acquire high-quality images with minimal frame averaging and without tissue staining or processing. The use of tissue staining, although common for ex vivo imaging (e.g., in the laboratory setting), is not ideal for many in vivo clinical imaging applications; therefore, we demonstrate the potential of our device to be used as an in vivo imaging instrument by acquiring intrinsic TPF/SHG signal from label-free ex vivo mouse tissue. Because of the raster scanner's highly uniform pixel dwell time, minimal frame averaging was necessary in order to obtain high quality images. Figure 15.6a shows unaveraged ex vivo images of SHG from collagen fibers taken from a mouse tail at three representative depths within the tissue. In these images, individual strands are discernible. Figure 15.6b shows unaveraged intrinsic fluorescence images of ex vivo mouse lung at different depths where anatomical details such as the alveolar walls and lumens are visible. Figure 15.6c shows five frame-averaged images at three different axial depths of the two-photon excited intrinsic fluorescence from ex vivo mouse colon tissue. Mouse colon tissue consists of closely packed tubular glands (crypts) covered by a layer of columnar absorptive cells and mucus secreting goblet cells. The cellular structures in Fig. 15.6c represent the intrinsic fluorescence emitted from these epithelial cells. The morphological details present in the unstained images displayed in Fig. 15.6 indicate that our prototype shows potential for future clinical use. No tissue damage was observed during the course of the ex vivo imaging session, and the imaging conditions were comparable to those shown by other investigators to have negligible tissue mutagenicity (Helmchen et al. 2001). For comparison, we imaged two-photon excited intrinsic fluorescence from ex vivo mouse tissue using a commercial multiphoton microscope (Fluoview FV1000D, Olympus). Figure 15.7 shows unstained images acquired from both systems at comparable depths within the tissue. This figure was obtained with comparable amounts of two-photon excited fluorescence at the sample per frame in each system. These images demonstrate that the multiphoton endoscope is capable of acquiring images of anatomical features that are similar in appearance to those obtained from a conventional multiphoton microscope.

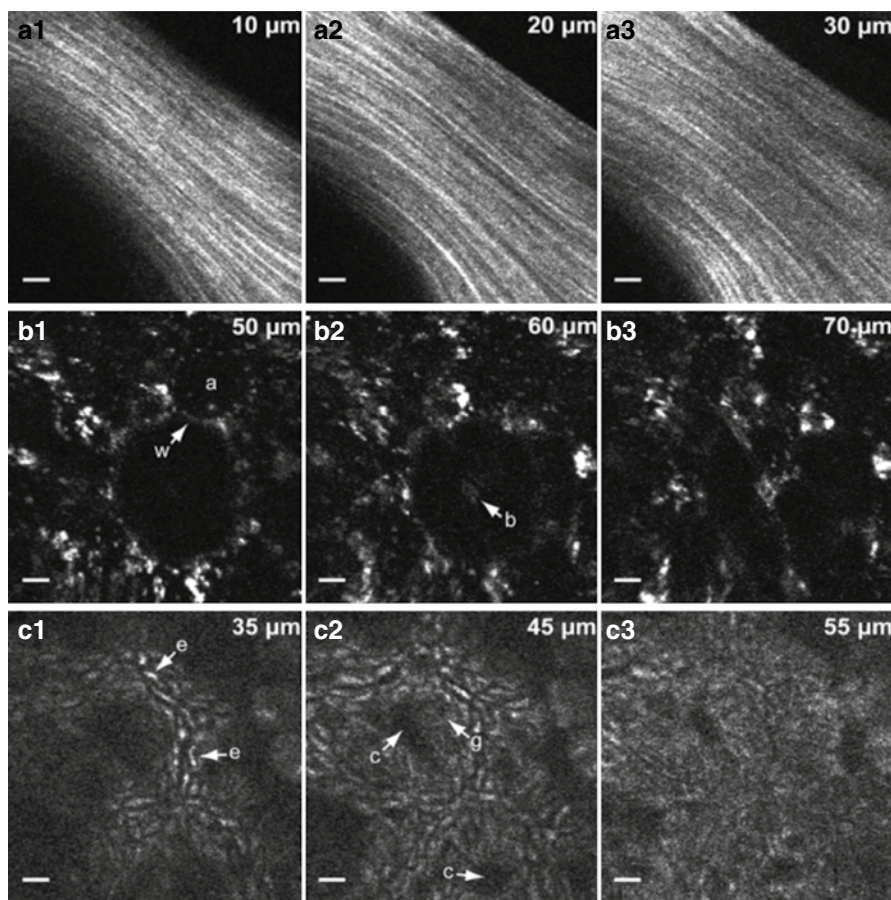


**Fig. 15.6** TPF/SHG images of ex vivo mouse tissue. (a) Unaveraged SHG images of mouse tail tendon at 10, 20, and 30  $\mu\text{m}$  from the surface. (b) Unaveraged intrinsic fluorescence images of mouse lung at 50, 60, and 70  $\mu\text{m}$  from the tissue surface. In b1, alveolar walls (w) and lumens (a) are clearly visible; in b2, a bronchiole (b) is distinguishable. (c) Five frames averaged intrinsic fluorescence images of mouse colon at 35, 45, and 55  $\mu\text{m}$  from the surface. In c1, enterocytes (e) are visible; in c2, crypts (c) and goblet cells (g) are present. Scale bars, 10  $\mu\text{m}$ . All images were acquired at 4.1 frames/s, 800-nm excitation, and the uniformly sampled FOVxy of approximately  $110 \times 110 \mu\text{m}$  is displayed. For the images in a, the power at the sample is approximately 30 mW; for the images in b and c, the power at the sample is 75 mW (Rivera et al. 2011)

## 15.2.3 In Vivo Imaging of Unstained Tissues

### 15.2.3.1 In Vivo Imaging Setup

In this experiment, the imaging apparatus was housed inside a light-tight enclosure to reduce background signal detected by the device (Fig. 15.8). Inside the enclosure, MPME position was controlled remotely by mounting the device on a flexible arm (FLEX- BAR Positioning Arm, Flexbar Machine Corp.) allowing for six degrees of

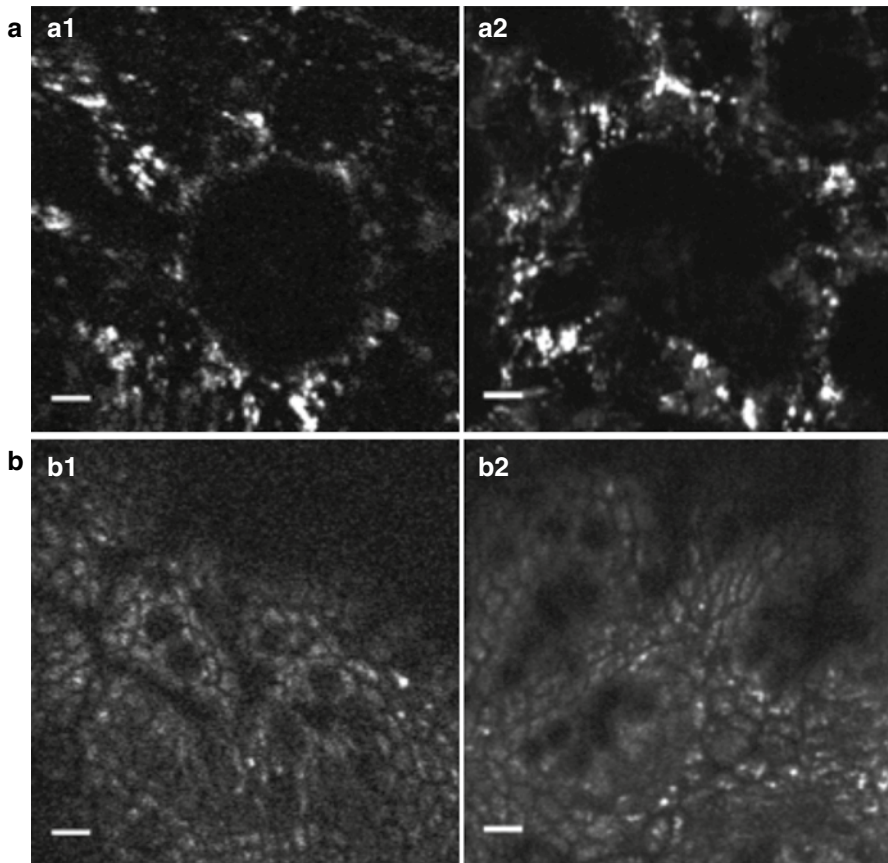


**Fig. 15.7** Imaging comparison between the multiphoton endoscope and a commercial multiphoton microscope. **(a)** Unaveraged intrinsic fluorescence images of ex vivo mouse lung. *a1* shows the image acquired from the multiphoton endoscope, and *a2* shows the image acquired from the Olympus multiphoton microscope. **(b)** Five frames averaged intrinsic fluorescence images of ex vivo mouse colon. *b1* shows the image acquired from the multiphoton endoscope, and *b2* shows the image acquired from the Olympus multiphoton microscope. Scale bars, 10  $\mu\text{m}$ . Comparable amounts of two-photon excited fluorescence at the sample per frame were maintained in each system. The displayed images were acquired with 800-nm excitation and a FOVxy of approximately  $110\ \mu\text{m} \times 110\ \mu\text{m}$  (Rivera et al. 2011)

freedom of gross movement. The flexible arm was mounted on a precision motorized micromanipulator (MP-285, Sutter Instrument Co.) allowing for submicron XYZ axis motion control of the endoscope. An infrared (IR) imaging system was used to assist with navigation of the endoscope and monitor the respiration rate of the anesthetized rat to ensure normal breathing during the imaging procedure. The imaging system used two IR (illumination wavelength 940 nm) LEDs (M940L2, Thorlabs) to illuminate the animal while acquiring images from two CCD camera systems. Illumination light from the IR LEDs was blocked from the MPME PMTs using a short-pass filter (FF01-720/SP-25, Semrock). The IR filter, combined with the poor quantum efficiency of the PMTs at the



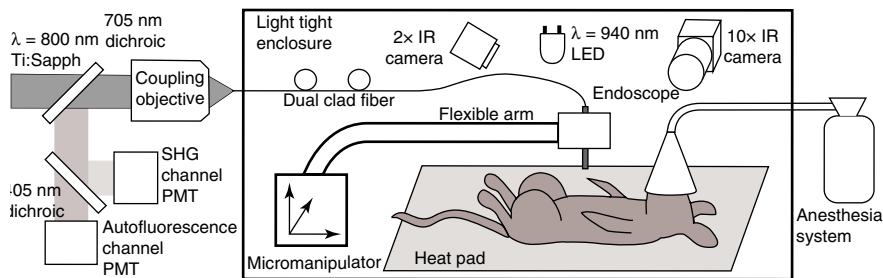


**Fig. 15.8** In vivo imaging experimental layout. Note that the 800-nm excitation light is precompensated for the DCF dispersion prior to fiber coupling (Brown et al. 2012)

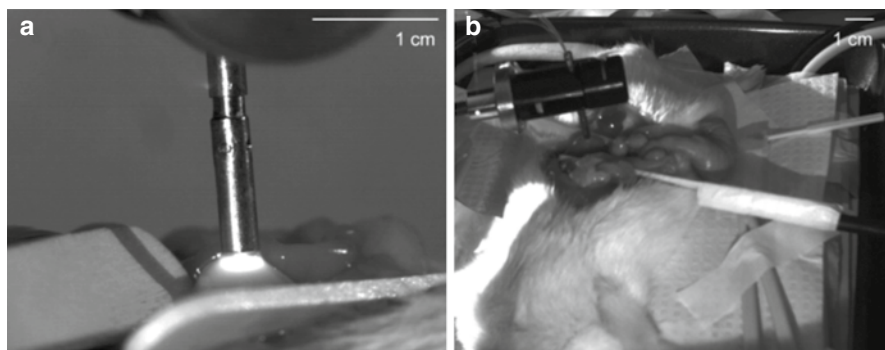


**Fig. 15.9** Infrared camera images: (a) 10× view of 3 mm OD endoscope acquiring in vivo kidney image; (b) 2× view of rat and mounted endoscope (Brown et al. 2012)

IR illumination wavelength, allowed for simultaneous MPME and IR widefield imaging during the experimental procedure. Together, the two IR imaging systems allowed for 10× and 2× magnification IR imaging of the device and anesthetized rat (Fig. 15.9).

### 15.2.3.2 Animal Preparation for *In Vivo* Imaging

A male rat (250–350 g, Sprague–Dawley, Charles River Laboratories International, Inc.) model was used in this experiment. Prior to surgery, the rat was sedated in an induction chamber with a gas anesthetic (~5 % isoflurane-oxygen mixture). After reaching the appropriate level of sedation for surgery, the animal was fitted with a nose cone to maintain the sedation (~2–3 % isoflurane-oxygen mixture), placed on a temperature-controlled heat pad (set to 36 °C) to maintain body temperature and mechanically restrained in a dorsal recumbent position. A small ventral-midline abdominal incision was made to expose the internal organs to the MPME. After imaging the kidney and the liver, a second incision was made in the colon to expose its inner surface to the device. Prior to imaging each organ, the organ was isolated then elevated with tongue depressors to reduce motion artifact (Fig. 15.9). The



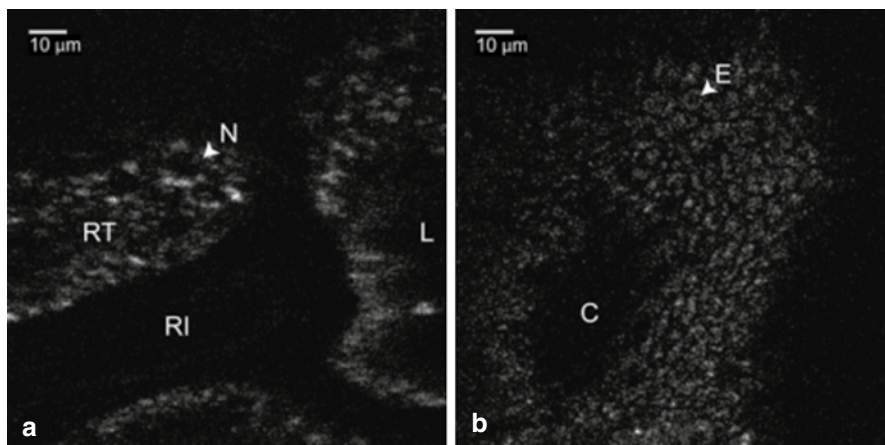


**Fig. 15.10** Unaveraged, unstained multiphoton endoscope images of rat kidney and colon. Images show intrinsic fluorescence emission (420–690 nm): (a) Image of superficial kidney renal cortex, approximately 20  $\mu\text{m}$  below the surface of the organ showing epithelial cellular nuclei (N) 5 to 10  $\mu\text{m}$  in diameter, renal tubules (RT) composed of epithelial cells, renal interstitium (RI)—the loose connective tissue and vascular supply in the kidney, and renal lumen (L) inside the renal tubules; (b) image 20–30  $\mu\text{m}$  below the surface of the interior colon showing a cross-sectional view of a crypt (C) and a variety of enterocyte cells lining the intestine (E). Note that dark cellular nuclei are viewable in many of these cells (Brown et al. 2012)

endoscope was then maneuvered into position for image acquisition using the flexible arm and micromanipulator. A total of 10 rats were imaged using these procedures. After the initial iterations, we achieved a consistent procedural throughput for the last several runs where the entire imaging session (e.g., imaging kidney, liver, and colon) required approximately 40 min. All animal procedures were conducted in accordance with a Cornell University Institutional Animal Care and Use Committee approved protocol and relevant standard operating procedures.

### 15.2.3.3 *In Vivo* Results, Discussion and Conclusion

During the *in vivo* imaging sessions, the image plane of the MPME was positioned ~20 to 30  $\mu\text{m}$  below the tissue surface to obtain the *en face* unstained, unaveraged *in vivo* MPME images shown in Figs. 15.10 and 15.11. Due to axial motion of the live tissue relative to the MPME image plane, images acquired may be above or below this depth. The recognizable tissue features were highly consistent in all imaged rats. These images show many features that are recognizable in histological tissue samples (Gartner and Hiatt 2007). Figure 15.10a shows an image of intrinsic fluorescent signal in the rat kidney. In this image, optical cross-sections of tubular nephrons are visible in the periphery of the organ along with features such as cells, renal tubules, renal interstitium, and renal lumen. Figure 15.10b shows an image of

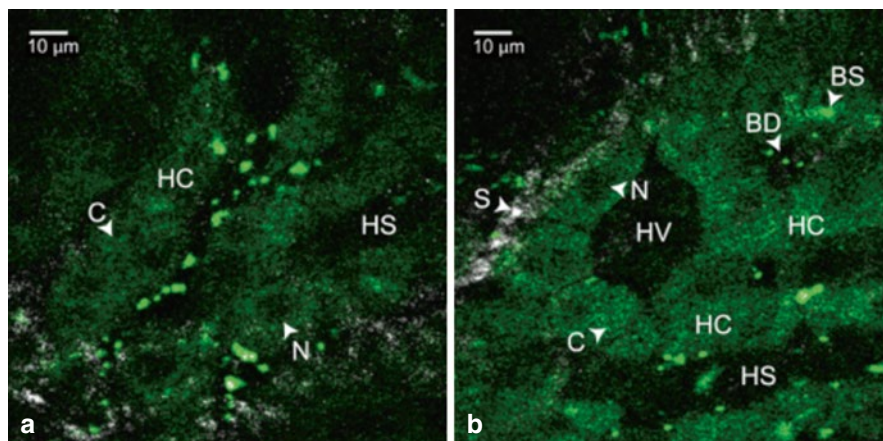


**Fig. 15.11** Unaveraged, unstained multiphoton endoscope images of rat liver located approximately 20  $\mu\text{m}$  below organ surface. The pseudo-color images show *grey* SHG signal ( $<405\text{ nm}$ ) and *green* intrinsic fluorescent emission (420 to 690 nm). (a) Liver image shows 20–30  $\mu\text{m}$  diameter hepatocytes with a dark 5–10  $\mu\text{m}$  diameter nucleus (N) and bright surrounding cytoplasm (C), hepatic chords (HC) composed of chains of hepatocytes, and a hepatic sinusoid (HS)—the blood filled space between hepatic chords. (b) Liver image shows features including: bile ductile (BD), bile salts (BS), septa (S)—a fine fibrillar connective tissue that covers the surface of the hepatocytes, and a hepatic venule (HV) (Brown et al. 2012)

intrinsic fluorescent signal from the interior wall of the rat colon. This image shows an optical cross-section of a colon crypt. Figure 15.11a and 15.22b show intrinsic fluorescence (pseudocolored green) and SHG (gray) images  $\sim 20\text{--}30\text{ }\mu\text{m}$  below the surface of the rat liver. These images show hepatocytes (i.e., functional liver cells) surrounded by a collagenous tissue capsule. The hepatocytes are arranged in cords, forming structural units. The blood-filled spaces between the cords are sinusoids. Since blood is a strong light absorber, we see an absence of intrinsic signal in the sinusoid. Strong SHG signal can be seen in the septa of the liver. Images in Figs. 15.10 and 15.11 were interpreted with the assistance of a certified pathologist. When imaging kidney, liver, and colon tissue with this device, over  $\sim 75\%$  of recorded images were free of streaking or warping of features within the image frame even though the organ moves relative to the MPME due to respiration and cardiac motion. This can be credited to rigid mounting of the endoscope during image acquisition, isolating tissue while imaging, the 4.1 frame/s image acquisition speed, and the high uniformity of the resonant-nonresonant fiber scanner. The demonstrated device can be further improved by achieving faster frame rates with high signal-to-noise ratio, distal axial sectioning, larger image FOVs while maintaining high-image resolution, and decreasing the device size. Several developments can be used to address these issues and are discussed below. For example, by incorporating lensed fibers a larger FOV can be achieved in a miniature endoscope (Rivera et al. 2012a). Furthermore, a higher frame rate and axial sectioning can be achieved by incorporating a multifocal approach in the MPME (Rivera et al. 2012b). To the best

of our knowledge, this research demonstrates the first multiphoton images from unstained tissue in a live animal using a compact and flexible MPME device. These images show many of the features that are commonly seen in biopsied histopathology slides from these tissues, indicating the potential of the MPME device for in vivo diagnostics of tissue health.

## ***15.2.4 Multifocal Multiphoton Endoscope***

### **15.2.4.1 Introduction**

To achieve fast frame rates necessary to mitigate in vivo motion artifacts and to provide high procedural throughputs, these endoscopes use miniaturized two dimensional scanners capable of fast scan speeds. Although a variety of miniaturized scanners have been demonstrated, the resonantly actuated, single optical fiber, spiral scanners have been the most successful due to their small size and ability to achieve fast scan speeds (e.g., 8 Hz with a 200  $\mu\text{m}$  diameter field of view (FOV),  $512 \times 512$  pixels) (Engelbrecht et al. 2008). However, while increasing the resonant frequency of a single optical fiber enables fast frame rates, this also decreases the amount of two-photon excited fluorescence per image frame, which results in a low signal-to-noise ratio (SNR) per frame. Although SNR is improved by frame averaging, this reduces the effective frame rate for image acquisition. To achieve axial sectioning within tissue, endoscopes require distal mechanical motion. Axial sectioning is valuable for clinical diagnostics since it enables the visualization of informative three-dimensional structural tissue details. To date, axial sectioning in flexible multiphoton endoscopes has been achieved through the use of built-in one-dimensional actuators (e.g., shape memory alloys, DC motors) that mechanically move the two-dimensional scanner and optics within the distal housing (Wu et al. 2010; Helmchen et al. 2001; Bao et al. 2008). However, these one-dimensional actuators are slow and pose limitations to overall device miniaturization.

To obtain a multiphoton endoscope capable of a fast frame rate without reducing the SNR per frame and axial sectioning, we translate a well-established technique of microscopy, multifocal multiphoton microscopy (MMM) (Bewersdorf et al. 2006; Kim et al. 2007; Carriles et al. 2008), into a multifocal multiphoton endoscope (MME). The demonstrated MME is capable of longitudinal parallel image acquisition, while maintaining good SNR per frame. Multiple focal points are achieved by incorporating three parallel but axially offset double clad fibers (DCF) into a previously demonstrated miniaturized raster scanner (Rivera et al. 2011). This fiber array scanner is paired with a high NA gradient index (GRIN) lens assembly. The fabricated MME prototype has an outer diameter (o.d.) of 3 mm with a rigid distal length of 4 cm. It achieves lateral and axial resolutions, for two-photon imaging, of 0.8 and 10  $\mu\text{m}$ , respectively, matching our previous results (Rivera et al. 2011). For a proof of principle, we demonstrate simultaneous axial image acquisition (4 frames/s per focal plane) at three depths by obtaining images of ex vivo mouse lung solely from

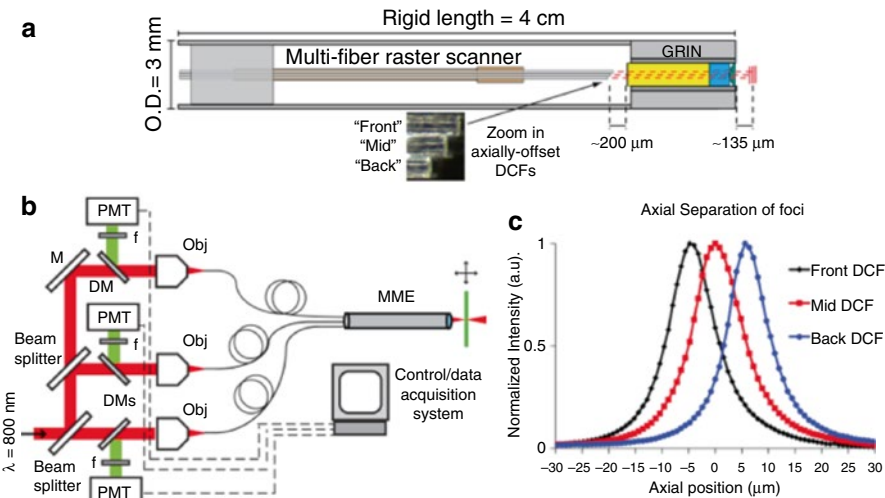


**Fig. 15.12** (a) MME components. *Inset*: Close-up of the axially offset DCFs. (b) MME imaging setup. (c) Axial intensity profile of the thin film response from each DCF. The “Front” DCF is focused the furthest distance in front of the lens, followed by the “Mid” and “Back” DCF, which is focused the shortest distance (Rivera et al. 2012b)

the intrinsic signal of endogenous tissue fluorophores. To the best of our knowledge, this is the first endoscope to demonstrate spatial multiplexing.

**15.2.4.2 MME Fabrication and Specifications**

The primary constituents of the MME are a miniaturized multi-fiber raster scanner and a commercial 1.4 mm o.d. GRIN lens assembly (GT-MO-080-018-810, GRINTECH). The miniature raster scanner is fabricated by mounting three DCFs (SM-9/105/125-20A, NuFern) onto two piezo bimorphs, with perpendicular bending axes. The DCFs are bonded alongside each other to form a rectangular fiber array that is simultaneously driven resonantly along the thin dimension at 1 kHz and nonresonantly along the thick dimension at 4 Hz (i.e., 4 frames/s). The DCF array has a core-to-core separation distance of 125  $\mu\text{m}$ . The end faces of the DCFs are offset axially by  $\geq 75 \mu\text{m}$  and are focused by the GRIN lens assembly to achieve three focal points with  $\geq 4.8 \mu\text{m}$  axial separation (Fig. 15.12a, c). A schematic of the internal components of the fabricated MME is displayed in Fig. 15.12a.

**15.2.4.3 MME Imaging Setup**

The experimental setup for the multifocal multiphoton imaging is shown in Fig. 15.12b. The entire setup (including the laser) is housed on a mobile optical table. Femtosecond excitation pulses at 800 nm from a Ti:Sapphire laser (MaiTai,

Newport) are pre-compensated for fiber dispersion and divided into three beam paths that independently couple the excitation light into the cores of the 1 m long DCFs. The three fibers are actuated by the miniaturized resonant/non-resonant scanner and imaged by the GRIN lens assembly to produce three raster-scanned image planes separated by  $\geq 4.8 \mu\text{m}$  axially and  $\sim 25 \mu\text{m}$  laterally. The multiphoton excited signal generated by a particular illumination fiber is epicollected through the GRIN lens to the core and inner clad of that particular DCF (i.e., the fiber array also serves as a descanned array detector). Signals transmitted through the DCFs are reflected by dichroic beam splitters (DM, FF705-Di01- $25 \times 36$ , Semrock), transmitted through a pair of 720-SP filters (FF01-720/SP-25, Semrock) to an Ultra Bi-Alkali photomultiplier tube (PMT) (R7600U-200, Hamamatsu). Image acquisition is done with a modified version of ScanImage (Pologruto et al. 2003). Note that the DCFs used here are not strictly single moded at 800 nm, but by optimizing the launch conditions and using two-photon excitation we have not observed degradation of image quality under typical experimental perturbations.

#### 15.2.4.4 Axial Separation of Foci

To measure the axial separation distance of the three illumination fibers, a 500 nm Rhodamine B (RhB) thin film was stepped axially through the focal planes of the three fibers, and the epi-fluorescence signal was recorded. The results of the measurement are displayed in Fig. 15.12c, and show that at the sample the “Front” DCF’s focal point is separated by  $\sim 4.8 \mu\text{m}$  from that of the “Mid” DCF, which is separated by  $\sim 5.6 \mu\text{m}$  from the focal point of the “Back” DCF. The three fibers’ focused illumination maintains  $\sim 10 \mu\text{m}$  two-photon axial resolution (FWHM of the thin film response). In fact, we observed that the fibers could be placed up to  $\sim 2 \text{ mm}$  away from the front surface of the GRIN lens without degrading the axial resolution. This indicates that future MMEs could incorporate a larger number of axially offset illumination fibers than the three fibers demonstrated herein.

#### 15.2.4.5 Lateral Separation of Foci

Since the transverse magnification of the GRIN lens is  $\sim 0.2$  and the core-to-core separation of the DCFs is  $125 \mu\text{m}$ , there is a lateral separation of  $\sim 25 \mu\text{m}$  between each foci at the sample. To show the lateral shift in the FOV between the three fibers we acquired transmission images of a U.S. Air Force test target whereby for each fiber the distance to the target was optimized to focus the displayed feature (Fig. 15.13a). In Fig. 15.13a the number 6, from group 6 of the target, is positioned so that it is at the top of the image acquired using the “Front” DCF. By keeping the target in this position and then alternating the other two fibers as the illumination source, the lateral shift between the fibers becomes apparent.



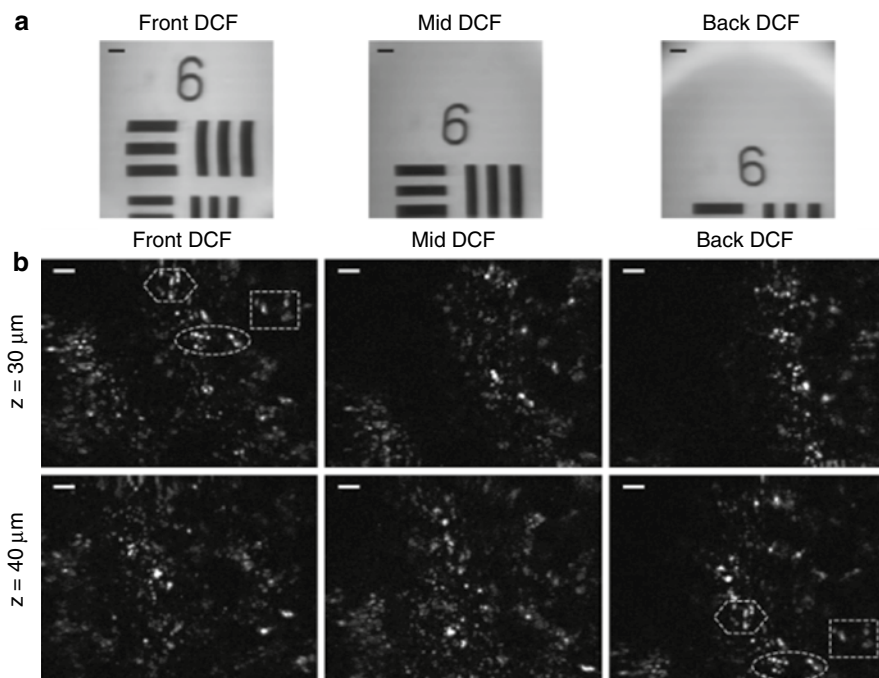


**Fig. 15.13** (a) Approximately 25  $\mu\text{m}$  lateral shift in FOV: Transmission images of a U.S. Air Force test target acquired from the illumination of each of the three DCFs. The  $\text{FOV} \approx 100 \times 100 \mu\text{m}$  (b) Simultaneous axial sectioning: Intrinsic fluorescence images of ex vivo mouse lung (2 frames averaged) obtained from each fiber at different stage depths into the tissue. The indicated features come into focus initially in the image obtained from the “Front” DCF ( $z=30 \mu\text{m}$ ) and then come into focus 10  $\mu\text{m}$  deeper ( $z=40 \mu\text{m}$ ) for the image obtained from the “Back” DCF, but are shifted  $\sim 50 \mu\text{m}$  laterally. Images are acquired at 4 frames/s with an  $\text{FOV} \approx 130 \mu\text{m} \times 100 \mu\text{m}$ . The power from each fiber focused at the sample is  $\sim 50 \text{ mW}$ . Scale bars are 10  $\mu\text{m}$  for all images in (a) and (b) (Rivera et al. 2012b)

#### 15.2.4.6 Simultaneous Axial Sectioning of *Ex Vivo* Mouse Lung

For a proof of principle, we demonstrate the ability of our MME to acquire multiphoton images simultaneously at three axial depths by imaging unstained ex vivo mouse lung (Fig. 15.13b). In order to illustrate the differences in the images obtained from the three fibers, we performed an axial scan of the mouse lung sample through the focal planes of the illumination fibers. Figure 15.13b shows multiphoton images at two representative stage depths into the tissue. Note that  $z=0 \mu\text{m}$  (not shown) is the stage position where the surface of the lung comes into focus in the image obtained by the “Front” DCF. The indicated features come into focus initially in the image obtained from the “Front” DCF ( $z=30 \mu\text{m}$ ) and then come into focus 10  $\mu\text{m}$  deeper ( $z=40 \mu\text{m}$ ) for the image obtained from the “Back” DCF, but are shifted laterally by  $\sim 50 \mu\text{m}$ .



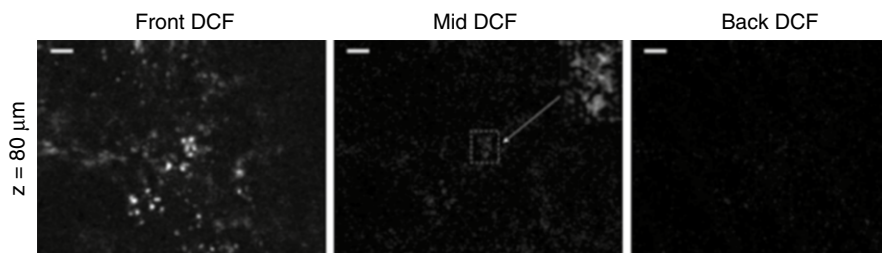


**Fig. 15.14** Channel crosstalk imaging comparison. MPM images of mouse lung ( $\sim 80 \mu\text{m}$  below surface) obtained via illumination solely from the “Front” DCF and collection from all fibers. The inset image obtained from the “Mid” DCF is a magnified image of the indicated central feature. The inset image’s intensity values are multiplied by an additional factor of 5 from the original image to better display the “ghost” feature. The power from each fiber focused at the sample is  $\sim 50 \text{ mW}$ . Scale bars are  $10 \mu\text{m}$  (Rivera et al. 2012b)

#### 15.2.4.7 MME Crosstalk Assessment

Much like MMM, crosstalk between neighboring foci is a concern for our MME, particularly for imaging deep into scattering tissues. We measured the crosstalk in our MME by illuminating one fiber at a time and measuring the fluorescence collected from all fibers. For a non-scattering medium (RhB thin film) we found that the fiber crosstalk is less than 1 %. For highly scattering lung tissue where previous investigators report scattering lengths averaging  $\sim 42 \mu\text{m}$  for illumination wavelengths averaging  $\sim 590 \text{ nm}$  (Cheong et al. 1990), we found that crosstalk was minimal ( $\leq 10 \%$  up to  $\sim 80 \mu\text{m}$  imaging depth) when imaging mouse lung ex vivo as shown in Fig. 15.14. Figure 15.14 displays images of ex vivo mouse lung obtained by illuminating the “Front” fiber only, and collecting the fluorescence through all three fibers simultaneously. The displayed image is  $\sim 80 \mu\text{m}$  beneath the tissue surface, and shows that crosstalk is tolerable in the adjacent fiber (“Mid” DCF) as indicated by the appearance of a weak “ghost” image, and crosstalk between non-adjacent fibers (i.e., the ghost image collected by the back fiber) is below the noise level of the system. The observed negligible crosstalk between nonadjacent fibers provides support for the use of a larger number of illumination fibers in future MMEs. We also note that there are several solutions to further mitigate channel crosstalk. It was previously demonstrated that crosstalk in MMM can be reduced by using de-scanned detection with a matched array of detectors, whereby each focus is imaged onto a separate detector with an optimized detection area (Kim et al. 2007). This detection technique has demonstrated significant imaging depth in ex vivo mouse brain tissue (Kim et al. 2007). Since our fiber array scanner also acts as a matched, descanned array detector, the crosstalk in our MME could be further mitigated by optimizing the size and separation of the fiber detector area (i.e., optimizing the size of the inner cladding layer as well as the separation between the fibers). Furthermore, fiber crosstalk could also be suppressed by utilizing nanosecondtime decorrelated excitation and detection. Time multiplexing has been previously implemented in MMM to improve imaging depth and acquire images simultaneously from multiple axial planes (Carriles et al. 2008).

#### 15.2.4.8 MME Tissue Damage Discussion

A clinically applicable multiphoton endoscope should acquire diagnostic quality multiphoton images without tissue staining. However, obtaining multiphoton images solely from the fluorescence of weakly emitting, endogenous tissue fluorophores (e.g., NADH), requires the use of highly energetic femtosecond pulses at the sample (Xu et al. 1996). A major concern of using high excitation intensities is tissue photodamage. Multifocal multiphoton microscopy has proven to be particularly valuable if photodamage is dominated by higher order ( $n > 2$ ) nonlinear processes at the excitation wavelength (Bewersdorf et al. 2006). At multiphoton excitation wavelengths (e.g., 750–800 nm) used to excite endogenous fluorophores, one-photon heating is negligible (Schönle and Hell 1998), and photodamage is likely a higher order ( $n > 2$ ) non-linear process (Hopt and Neher 2001). The effects of additional foci on sample heating is expected to be small due to the large foci separation distance and the shallow imaging depths (limited by crosstalk) that is best suited for MME. Furthermore, the lateral separation distance of the foci could be increased significantly to reduce the heating contributions from the neighboring foci. Experimentally, no tissue damage was observed in our ex vivo imaging sessions, and previous groups have imaged deep within mouse brain in vivo at excitation powers up to 300 mW ( $\lambda_{exc} = 830$  nm) without damaging the tissue (Kleinfeld et al. 1998).

#### 15.2.4.9 Parallel Transverse Image Acquisition

The rigid length of our prototype is 4 cm. However, MME provides a possible solution to significantly reduce the rigid length. For example, the multifoci can be positioned to illuminate the same focal plane (i.e., parallel transverse image acquisition). The non-resonant scan range can then be reduced to the inter-fiber distance. By stitching together the sub-fields of the fibers, the total FOV is maintained. The smaller scan range can be achieved by a shorter piezo scanner, providing a pathway for reducing the rigid length of the endoscope. Therefore, MMEs not only improve the image acquisition rate without sacrificing SNR but also reduce the rigid length of the device without reducing the FOV.

#### 15.2.4.10 Conclusions and Outlook

In conclusion, we have demonstrated an MME that uses a fiber-array scanner to achieve parallel longitudinal image acquisition. The demonstrated parallelism is essential for multiphoton endoscopes to acquire high SNR images at a high frame rate without excessive tissue photodamage. Although only three fibers are demonstrated in our fiber scanner, it is straightforward to increase the number of fibers so that further improvement in frame rate can be achieved. Such a multifocal approach is valuable for multiphoton endoscopes to become practical tools in the clinic.

### 15.2.5 *Use of a Lensed Fiber*

#### 15.2.5.1 Introduction

In fiber-scanning microendoscopes, light is delivered through an optical fiber that is mounted to a miniaturized actuator (e.g., piezoactuator (Wu et al. 2009a, b; Rivera et al. 2011; Seibel and Smithwick 2002), or electromagnetic tuning fork (Goetz et al. 2007)), which deflects the fiber tip in a two-dimensional scan pattern (e.g., Lissajous (Wu et al. 2009b), spiral (Wu et al. 2009a; Seibel and Smithwick 2002), or raster (Rivera et al. 2011; Goetz et al. 2007)). In order to acquire high resolution images, the scanned light is then focused onto the sample by endoscopic lenses, which also limits the FOV of the device. Therefore, the lateral resolution of the device is determined by the output spot size of the scanning fiber ( $D_{spot}$ ) and by the transverse magnification ( $M$ ) of the endoscopic lenses:  $resolution = M \times D_{spot}$ . Meanwhile, the FOV of the probe is defined by the distance swept by the scanning fiber tip ( $d_{tip}$ ) and by the transverse magnification ( $M$ ) of the miniature lens used:  $FOV = M \times d_{tip}$ . Because both the lateral resolution and the FOV have the same dependence on the lens magnification, it is not possible to optimize the fiber-scanning endoscope to obtain a large FOV and high spatial resolution simultaneously. To quantify the performance of a fiber-scanning endoscope, we define the following figure of merit (FOM):  $FOM = FOV/resolution$ . This FOM essentially corresponds to the number of independently resolvable points in the transverse direction of the FOV.

Here, we propose to reduce the size of the fiber output beam ( $D_{spot}$ ) through the use of a lensed fiber, thereby requiring less lens demagnification to achieve high lateral resolution. The reduced requirement for high lens demagnification has the added benefit of allowing for a larger image FOV. The output beam size and divergence of the lensed fiber are characterized and compared to that of its normal single-mode fiber counterpart. Additionally, for a proof of principle, we use a previously demonstrated miniaturized raster scanner to scan a normal single-mode fiber, along with its lensed counterpart, to show that although both fibers have the same image FOV, the lensed fiber's lateral resolution is higher by more than a factor of 2 (Rivera et al. 2011). Finally, in order to prove that the lensed fiber can be used simultaneously as an excitation delivery and epifluorescence collection fiber, in a similar fashion to the double-clad fibers (DCFs) used in fiber-scanning fluorescence endoscopes, we measured comparable fluorescence collection to that of a normal DCF with the lensed DCF.

#### 15.2.5.2 Output Beam Reduction

The lensed fibers used here were manufactured by fabricating a high performance miniature conical lens directly at the tip of the optical fiber via a precise laser lensing process; see Fig. 15.15a (OpTek Systems, Oxford, UK). This type of lensed fiber and its manufacturing process is well-known in the fiber-optic

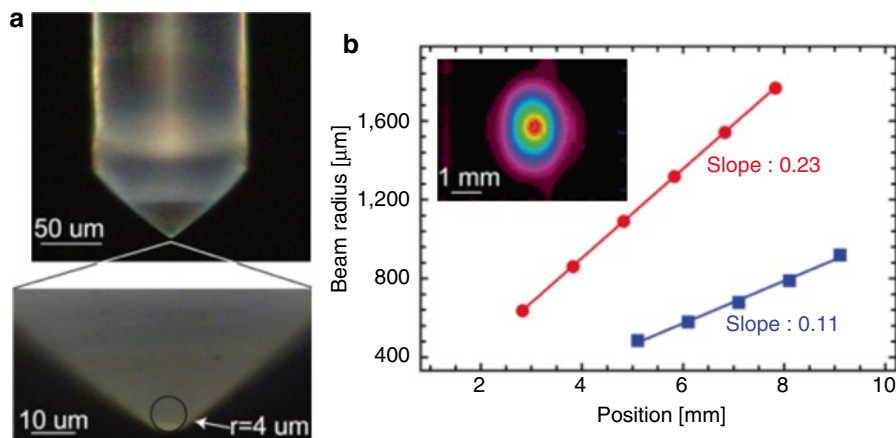


**Fig. 15.15** (a) Microphotographs of the lensed SM980 fiber. The ROC of the lens is 4  $\mu\text{m}$ . (b) Plots of the beam radius measured in the far field (from the fiber tip) for the normal (blue) and lensed (red) SM980. Inset, image of the beam spatial intensity distribution of the lensed SM980 (4  $\mu\text{m}$  ROC) obtained with a beam profiler (LBP-HR, Newport) (Rivera et al. 2012a)

communication industry (Presby et al. 1990). The formed miniature lens occurs over the final  $\sim 100\ \mu\text{m}$  of the distal tip of the optical fiber and focuses the excitation light at a distance in front of the lens apex that is  $\sim$ twice the lens radius of curvature (ROC), thereby reducing the output beam. To quantify the beam reduction between normal and lensed fibers, we measured the beam radius for each fiber type at several positions in the far field and determined the beam divergence and waist diameter, assuming that the output beams are well approximated as a Gaussian beam [Fig. 15.15b]. In this measurement, lensed and non-lensed versions of two types of fibers were investigated with 980 nm CW illumination: single-mode fibers at 980 nm (SM980-5.8–125, Thorlabs) and DCFs (DCF SM-9/105/125-20A, Nufern). The lensed fibers reported herein contained lenses with 4  $\mu\text{m}$  ROC, as measured by an optical microscope [see Fig. 15.15a]. We measured a beam waist diameter of 5.6  $\mu\text{m}$  with a divergence angle of  $\sim 0.11$  rad for the normal SM980. For the lensed SM980 fibers, we determined that the lens reduced the normal SM980 beam diameter by a factor of  $\sim 2$  times (beam waist diameter  $\sim 2.6\ \mu\text{m}$ , located  $\sim 8\ \mu\text{m}$  in front of the fiber tip, divergence angle  $\sim 0.23$  rad). Therefore, we conclude that these lensed fibers achieve the appropriate reduction in the output beam for our application. Although lensed fibers have been utilized previously in nonlinear imaging probes (Bao and Gu 2009), they were not fabricated to achieve a high-resolution, large FOV device.

Although there are other solutions for reducing the output beam of the optical fiber, lensed fibers are currently the best solution for endoscopy applications. For example, tapering the distal end of the optical fiber could also reduce the output beam. However, fiber tapers typically occur over distances much longer than the 100  $\mu\text{m}$  length occupied by the miniature lens. These long tapers cause tapered

fibers to be fragile, which makes them not ideal for the fabrication of a robust clinical device. Alternatively, an optical fiber with a tiny core could also achieve a small output beam. However, for clinical use, optical delivery fibers must be several meters in length and be able to effectively deliver the energetic femtosecond pulsed excitation that is necessary for fluorescence imaging (i.e., multiphoton imaging). These conditions are particularly problematic for small core optical fibers. In particular, multiphoton excited fluorescence signal is inversely proportional to the pulse width of the excitation source. Additionally, it is well established that fiber nonlinearity and dispersion broaden the excitation pulses delivered over meters of optical fiber (Agrawal 2007).

Although effects of dispersion can be negated by compensation techniques, fiber nonlinearity is not easily compensated. Because fiber nonlinearity increases dramatically with the reduction of the core size, a small core fiber that is several meters in length suffers from large pulse broadening as the excitation power is increased (Ouzounov et al. 2002). Therefore, the incorporation of a several meters long, small core optical fiber into a fluorescence endoscope is not practical. This is a particularly serious issue in the case of acquiring multiphoton images from the fluorescence of weakly emitting, endogenous tissue fluorophores (e.g., NADH), which require the use of high illumination powers at the sample (Xu et al. 1996). Because the miniature lens fabricated at the tip of a lensed fiber occurs over a length of 100  $\mu\text{m}$ , the effects of nonlinearity are minimal, thereby making lensed fibers ideal for nonlinear fluorescence imaging applications.

### 15.2.5.3 High Resolution and Large Field of View Lensed Fiber Scanner

We have previously demonstrated a miniaturized resonant/non-resonant fiber raster scanner that was incorporated into a compact and flexible multiphoton endoscope (3 mm OD, 4 cm rigid distal tip), capable of acquiring images of unstained ex vivo mouse tissue (Rivera et al. 2011). To show the high-resolution and large FOV that lensed fiber scanners are capable of, we incorporated lensed (4  $\mu\text{m}$  ROC) and non-lensed SM980 fibers into the raster scanner and paired it with a miniature gradient-index (GRIN) assembly (GT-MO-080-0415-810, GRINTECH). The multielement GRIN assembly is well suited for use with the lensed fiber due to its large input N.A. of 0.4. For this measurement, a 980 nm CW source was coupled to each optical fiber and a transmission imaging setup was used to image a high-resolution U.S. Air Force test target (Fig. 15.16). Transmission images of the target with the same 440  $\mu\text{m}$  diameter FOV were obtained using each fiber type, whereby for each fiber the distance to the target was optimized to properly focus the displayed features. The displayed images contain the smallest group that each fiber type could resolve, groups 8 and 9 [Fig. 15.17a, c]. To quantify the lateral resolution for each fiber at the target, we analyzed the intensity line profiles across the indicated image feature [Figs. 15.17a, c]. The intensity profile at the edge of the feature is the step-response function, and its derivative is the cross section of the point spread

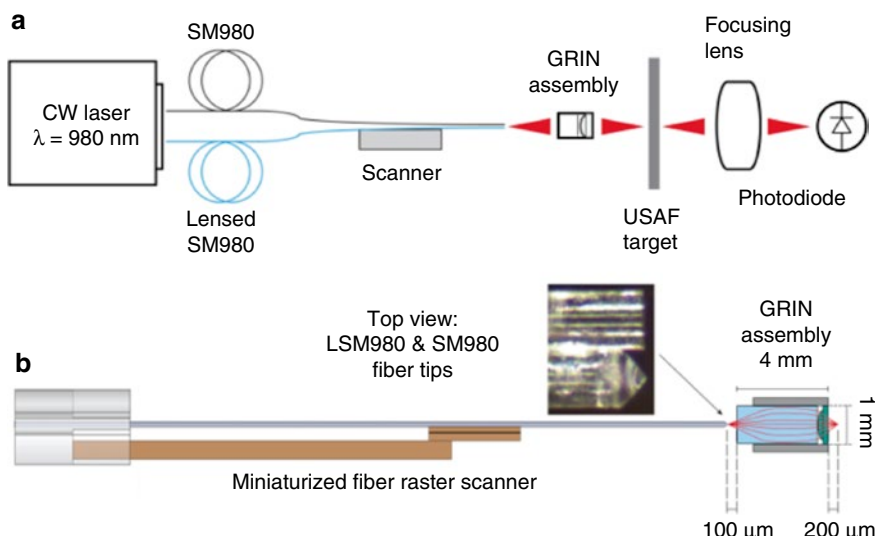


**Fig. 15.16** (a) Transmission imaging setup. (b) Alignment diagram of the scanner and GRIN assembly. *Inset*, top view showing the lensed SM980 (LSM980) and normal SM980 fiber tips (Rivera et al. 2012a)

function (PSF). In Fig. 15.17b, d, we show the intensity profile across the feature and its derivative. We determined that the one-photon lateral resolution (FWHM of the PSF) is approximately 1.1  $\mu$ m for the lensed SM980 and 2.4  $\mu$ m for the normal SM980. The FOM for the lensed fiber scanner ( $\text{FOM} = 440 / 1.1 = 400$ ) is more than twice that of lensed fibers.

#### 15.2.5.4 Fluorescence Collection Using Double Clad Lensed Fibers

A number of groups have utilized DCFs into fluorescence microscopy/endoscopy because they enable simultaneous delivery of excitation illumination and collection of emitted epifluorescence (Wu et al. 2009a; Rivera et al. 2011; Fu et al. 2005). To show that these lensed fibers are suitable for fluorescence endoscopy, we compared the collection ability of a Nufern double-clad lensed fiber (4  $\mu$ m ROC) to that of a normal Nufern DCF. For this measurement, 800 nm Ti:sapphire illumination was initially precompensated for fiber dispersion and then independently coupled into the core of a normal Nufern DCF and a lensed Nufern DCF, each 1 m in length. Each fiber was then independently aligned to a pair of 0.4 N.A. microscope objectives (RMS10X, Olympus), which focused the illumination into a cuvette containing 6.5  $\mu$ M Fluorescein dye. The epifluorescence emitted from the sample was then refocused back to the fibers, reflected off of a 705 nm dichroic mirror (DM) and delivered to an Ultra bialkali PMT for the photon counting measurements. We observed that the fluorescence signal collected by each fiber, as a function of the power delivered to the sample, was comparable. This measurement



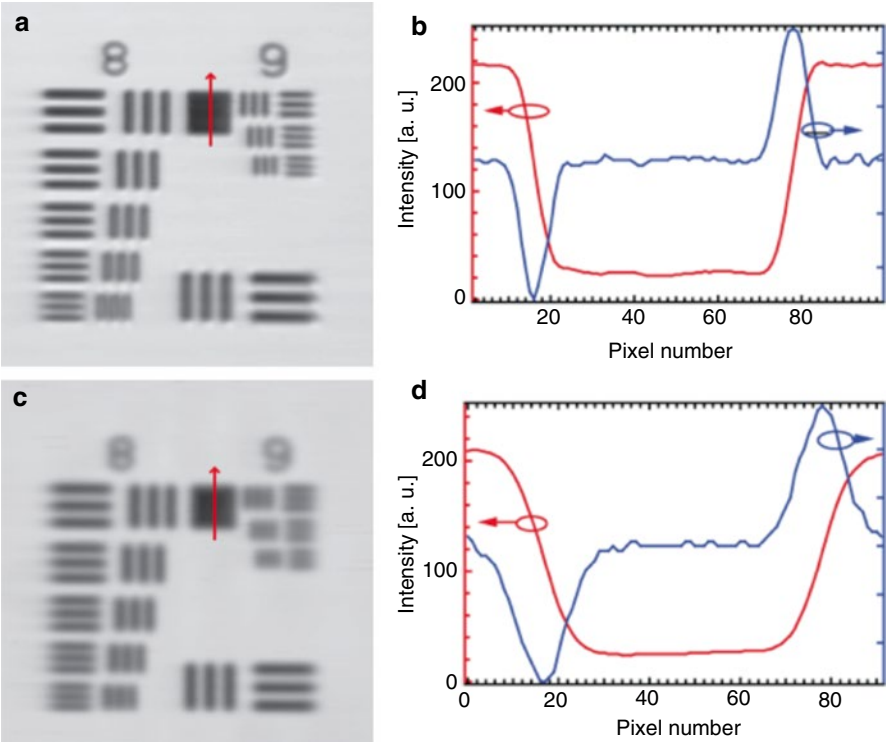


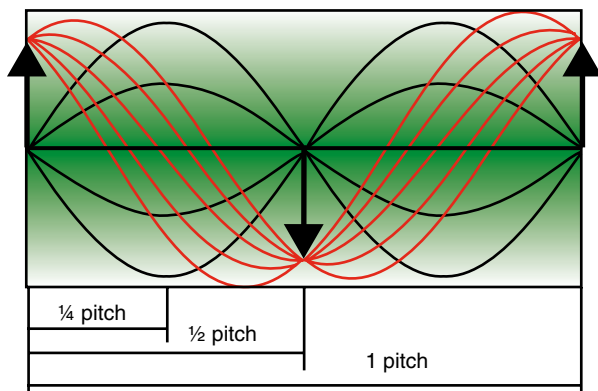
**Fig. 15.17** Transmission images of groups 8 and 9 from a high-resolution U.S. Air Force test target acquired using the lensed SM980 (a) and the normal SM980 (c). (b, d) Plots of the intensity line profile (red) across the feature indicated in (a) and (c), respectively, and its derivative (blue). The one-photon lateral resolution (FWHM) is 1.1 and 2.4  $\mu\text{m}$  for the lensed and the normal SM980, respectively (Rivera et al. 2012a)

indicates that lensed double-clad optical fibers are well suited for use in fluorescence endoscopy. We note that for this measurement, the same pulse widths were maintained for each fiber. Furthermore, we note that the miniature GRIN lens used in the resolution and FOV measurements has significant chromatic aberrations. For this reason we used well-corrected Olympus objectives for the collection measurements.

**15.2.5.5 Conclusion**

In conclusion, we have demonstrated the application of lensed fibers to reduce the output beam of an optical fiber, thereby enabling the construction of a compact fiber-scanning fluorescence endoscope that is capable of a large FOV and high spatial resolution.

**Fig. 15.18** Pitch length of a GRIN lens



## 15.3 Multiphoton Endoscopy Using Gradient Index Lens Systems

### 15.3.1 Introduction

While MPE using compact and flexible endoscope systems, such as the one described in part 2, have made great progress in the past years, their design becomes very challenging when attempting to push the outer diameter of the device below 2 mm. This is due to the need to encapsulate a miniaturized scanning mechanism inside the distal protective housing. This design requirement further poses several challenges including uniformity of the scan and sensitivity, durability and reliability of the scanner. Gradient index (GRIN) lenses, while rigid, can be manufactured in diameters as small as 350  $\mu\text{m}$  and thus offer a potential for use inside a biopsy needle to either guide and/or replace the biopsy entirely. They can be used to relay the excitation light and the MP signals to and from an external microscope deep into soft tissue. As only the GRIN lens penetrates the tissue, the remaining scanning and collection optics do not need to be miniaturized to the same extent as in the flexible devices and larger, higher quality and more reliable optics can be used.

GRIN lenses use a radially decreasing refractive index from the center of the lens to the outside edge to bend and focus light. This is achieved by nonuniformly doping the lens with a cation species with a decreasing concentration towards the outer side of the lens. The resulting refractive index profile declines approximately quadratically with radial distance from the central axis of the lens. As a result light rays travel in an approximately sinusoidal path down the axis of the lens. A lens that allows for exactly one full sine wave would be characterized as having a pitch of 1 (Fig. 15.18). Whereas a lens with a pitch of 0.25 would take a collimated beam and focus it to a point on the other surface. The gradient index profile of the lens can be manipulated allowing for lenses of different numerical aperture (NA).

Various previous systems have been used together with multiphoton microscopy to image rodent brains (Flusberg et al. 2005a; Levene et al. 2004; Jung et al. 2004; Jung and Schnitzer 2003) and in a clinical study for non-penetrative imaging of chronic leg ulcers with delayed wound healing (König et al. 2007). Further, GRIN systems have been used to image deep inside soft tissue via hypodermic needles (Pillai et al. 2011). However, these studies generally involved the use of short GRIN systems (<4 cm) intended for small animals and external clinical use. For a human clinical application significantly longer systems would be required. Biopsy needles can be as long as 25 cm in the case of a prostate biopsy, for example. We therefore investigated the effect of GRIN system length on the multiphoton imaging performance and integrated these systems into a compact and portable device that has the potential to be used in a clinical setting.

### 15.3.2 GRIN Endoscope Design and Long GRIN Systems

Previously reported GRIN multiphoton endoscopes use a combination of a relay and objective GRIN lenses in either a doublet (relay/objective) or triplet (objective/relay/objective) configuration. The lower NA relay lens serves to avoid a tight focus of the high energy excitation pulses within the glass while adding length to the endoscope system. The relay lens is designed to deliver collimated light to the back of the objective lens. The higher NA of the final objective lens allows for high resolution multiphoton imaging. In our studies we decided on the use of doublet systems over triplet as they have been shown to provide similar fields of views at reduced lens cost, greater image magnification, lower NA for coupling the laser beam and lower autofluorescence at the endoscope surface (Jung et al. 2004). With the help of GRINTECH GmbH, we designed several different doublet systems of 1 and 2 mm diameter for 800 nm excitation light. The different systems are summarized in Table 15.4. Each system is composed of a 0.1 NA relay lens of varying length and pitch and a 0.5 NA objective lens of pitch <0.25. Working distances were 100–140  $\mu\text{m}$  in air on either side and the lenses are protected by a stainless steel tube of 0.1 mm thickness yielding a total system outer diameter of 1.2 and 2.2 mm.

Our initial goal was to characterize the multiphoton imaging performance of the longer GRIN lenses. To achieve this we used a custom built horizontal multiphoton microscope together with a Ti:Sapphire laser (Tsunami, Spectra Physics, Inc.) at 800 nm. The lateral and axial resolution of the GRIN lens systems was measured in air using the full width at half maximum (FWHM) two-photon excited fluorescence from subresolution (0.2  $\mu\text{m}$ ) fluorescent beads and a 500 nm thin film of Rhodamine B (RhB) dye, respectively. The results are summarized in Table 15.4. An example of the obtained beam profiles is shown in Fig. 15.19 using the longest GRIN system (2C). As is evident from this data, the lateral resolution deteriorates only minimally with increasing relay length and relay pitch. The axial resolution, however, is affected significantly more with the longest GRIN system (2C) having an axial FWHM of 25  $\mu\text{m}$ . The majority of this deterioration is probably due to accumulation of spherical aberrations with increasing relay length, as suggested by the asymmetric

Table 15.4 Summary of optical characterization results

GRIN system	Part number	Diameter (mm)	Length (mm)	Relay lens pitch	FWHM (μm)		Diameter of FOV (μm)
					Lateral	Axial	
1A	GT-ERLS-100-075-11-50-NC	1.00	35.9	0.75	0.94	10.8	199
1B	GT-ERLS-100-175-11-50-NC	1.00	79.9	1.75	0.97	12.0	195
2A	GT-ERLS-200-075-11-50-NC	2.00	81.4	0.75	0.99	12.6	370
2B	GT-ERLS-200-125-11-50-NC	2.00	132.6	1.25	1.05	15.6	365
2C	GT-ERLS-200-275-11-50-NC	2.00	285.0	2.75	1.17	25.0	359

Five different doublet grin systems were designed by and purchased from Grintech GmbH. The lateral and axial two-photon resolution were determined in air using subresolution fluorescent beads and a thin rhodamine film respectively (Huland et al. 2012)

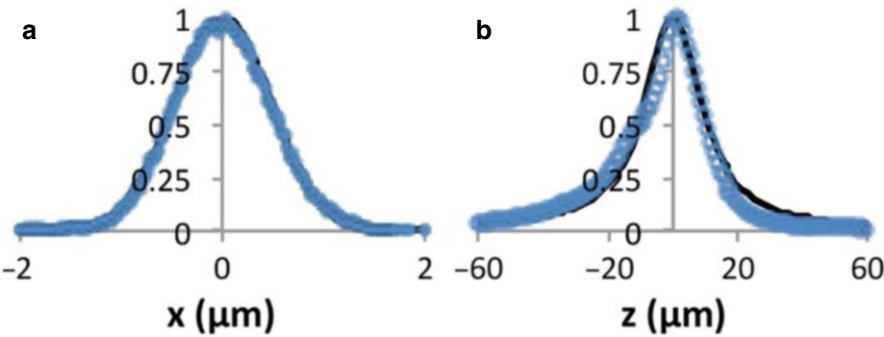
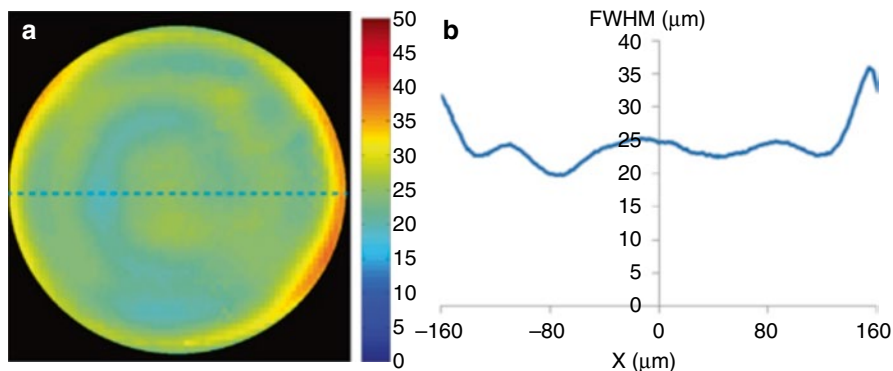


Fig. 15.19 Two-photon lateral and axial resolution of GRIN system 2C (285 mm length). (a) Lateral intensity line profile across a subresolution fluorescent bead with a Gaussian fit in black. (b) Axial intensity profile across a thin film rhodamine slide with a Lorentzian fit in black (Huland et al. 2012)

thin film response in Fig. 15.19 (b). The field of view for all systems is, as expected from the chosen relay/objective combination, close to a five times magnification of the diameter of the lens.

The results in Table 15.4 and Fig. 15.19 summarize the on axis performance of the systems. A significant concern with the use of these lenses for medical applications, however, is their off-axis performance as well. Imaging a z-stack of our thin film RhB slide through the entire FOV of the GRIN systems allows us to obtain this data efficiently for the axial resolution. We can identify and fit individual off-axis



**Fig. 15.20** Off-axis performance. Axial FWHM of GRIN system 2C in  $\mu\text{m}$  plotted (a) Across the FOV and (b) Across a line (dashed blue in (a)) through the center of the FOV (Huland et al. 2012)

areas of  $\sim 6$  by  $6 \mu\text{m}$  size and fit a Lorentzian function to each individual area to produce a plot that characterizes the axial resolution across the entire FOV. An example using GRIN system 2C is shown in Fig. 15.20. Off-axis lateral resolution was also measured for system 1B using sub-resolution fluorescent beads and the FWHM remained below  $1.2 \mu\text{m}$  up to the edge of the FOV. These results indicate that off-axis performance of the GRIN systems remains within  $\sim 20\%$  of the on-axis performance for most of the FOV ( $\sim 80\%$  of the area).

For multiphoton imaging through long GRIN systems, another concern is whether we can maintain ultrashort pulses at the sample after passing through long lengths of glass. To ensure this, we tested the effect on the excitation pulses of the longest GRIN system (2C). An initial  $80 \text{ fs}$  pulse width was broadened to  $740 \text{ fs}$  after passing through the system without dispersion compensation. We were able to recover an  $85 \text{ fs}$  pulse width at the sample though using a precompensation setup with a rotating cylindrical lens and grating (Durst et al. 2009), suggesting that a setup that accounts for the second order dispersion is sufficient for sub  $100 \text{ fs}$  pulses.

### 15.3.3 Compact and Portable GRIN Endoscope Design

The initial characterizations above were conducted using a custom built benchtop multiphoton microscope. The use of this in a clinical setting would not be practical so we designed a compact, portable fiber-coupled multiphoton system that can be used together with our GRIN endoscope systems to form a potentially clinical multiphoton GRIN endoscope. The design for this device is shown in Fig. 15.21 and fully described in (Huland et al. 2012). In summary, a Ti:Sapphire is used to deliver a  $800 \text{ nm}$  femto-second source via a hollow core PCF fiber of  $2 \text{ m}$  length (HC-800B, Thorlabs, Inc) to the device. Anomalous dispersion in the fiber is precompensated for by a  $10 \text{ cm}$  rod of dispersive glass (SF10). An aspheric lens on the endoscope collimates the

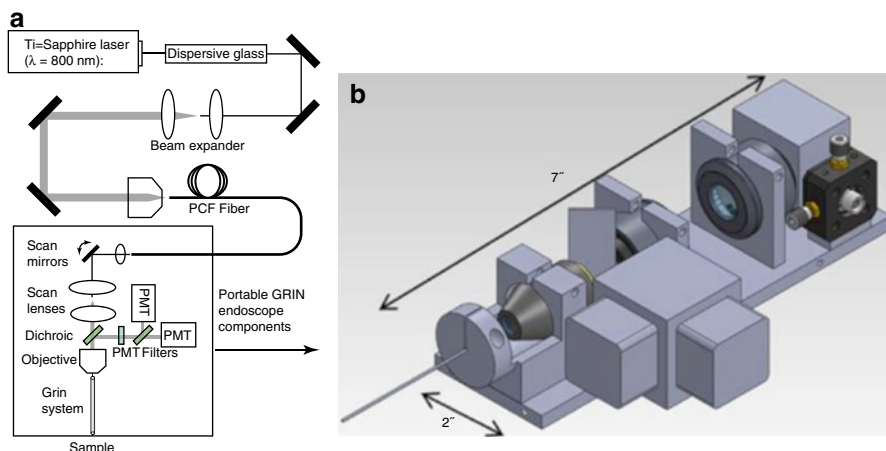


**Fig. 15.21** Portable GRIN endoscope. Optical drawing (a) and solidworks drawing (b) of the GRIN based endoscope system. Total system length of the portable device is 10.6" (including GRIN system) (Huland et al. 2012)

excitation pulses to a  $\sim 2$  mm diameter beam, before it is delivered to small aperture (3 mm) galvo scanning mirror system (6210H, Cambridge technology. These scanners provide a reliable, uniform, and fast imaging rate (up to 4 frames/s at 512 by 512 pixels). Two scan lenses (LSM02-BB and LSM03-BB, Thorlabs, Inc.) and an objective lens (0.3NA RMS10X-PF, Thorlabs, Inc.) couple the excitation beam into the proximal side of the GRIN lens system. The design is compatible with any of the characterized GRIN systems with 0.1 NA relay lens. Unless otherwise noted, we used our longest 1 mm diameter GRIN system (1B) for all characterizations and demonstrations. Fluorescence signal from the sample is epi-collected through the GRIN lens system and the microscope objective and separated into two channels for detection of autofluorescence ( $\sim 410$ – $680$  nm) and second harmonic generation (SHG) ( $\sim 400$  nm) by ultrabialkali photomultiplier tubes (Hamamatsu, Inc.).

The resulting system weighs less than 2lbs and is able to image a  $\sim 200$   $\mu\text{m}$  FOV at 4 frame/s (512 by 512 pixels). The device was measured, as described above, to have an axial resolution of 6.5  $\mu\text{m}$  FWHM in air and 7.4  $\mu\text{m}$  FWHM in water and a lateral resolution of 0.85  $\mu\text{m}$  FWHM in both air and water. The resulting pulse width at the sample is  $\sim 120$  fs.

### 15.3.4 In Vivo GRIN MPE Imaging

To demonstrate the capabilities of the portable and compact GRIN MPE we tested it on several organs in unstained tissues of live rats using a similar method as described in part 2. All animal procedures were reviewed and approved by the Cornell



Institutional Animal Care and Use Committee. To rapidly move the endoscope between organs, it was mounted on a flexible mechanical arm (18041-XL-Special, Flexbar Machine Corporation), which in turn, was mounted on a 3D stage (MP-285, Sutter Instruments) for fine movement control during imaging of the selected organ. Images were obtained with approximately 75 mW excitation power at the sample and at a rate of 4 frames/s. Signal was collected into two channels and pseudo-colored with autofluorescence in green and SHG in red. The same IR imaging system described in part 2.3.1 was used to guide the endoscope during imaging and monitor animal anesthesia.

A male rat (250–350 g, Sprague–Dawley, Charles River Laboratories International, Inc.) was anesthetized using a ~2–5 % isoflurane-oxygen mixture. A feedback controlled heat blanket set to 36 °C was used to help maintain rat body temperature. As described before, the abdominal organs were exposed using a ventral-midline incision and the kidney and liver were isolated and elevated using tongue depressors. The GRIN MPE obtained images of the surface of these organs. The inner lining of the colon was exposed with another incision and imaged in a similar fashion. Example images are shown in Fig. 15.22.

A significant challenge in these *in vivo* experiments is to overcome the motion artifacts evident when imaging at high resolution. The strongest source for these was motion due animal respiration originating predominately from the movement of the diaphragm. As a result, images obtained from the colon (furthest away from the diaphragm) suffered significantly less with >90 % of the images obtained showing little to no motion artifacts, while for the kidney this decreased to ~70 % and for the liver ~65 % at normal anesthesia respirations of around 45 breaths per minute. Increasing the isoflurane percentage in the anesthesia gas mixture allowed us to temporarily reduce the animals respirations to ~25 breaths/min. This improved the amount of high-quality liver images to ~80 %. While human respiratory rate is significantly lower than that of rodents at around 12–20 breaths/min and can be more easily controlled in a clinical setting, we note that motion artifacts due to cardiac and circulatory motion could be significantly more challenging to overcome in a human patient.

Overall, these images show great promise for clinical GRIN endoscopy. Throughout our imaging experiments we did not observe any laser induced tissue damage and our imaging conditions were comparable to those previously shown to have negligible tissue mutagenicity (Dela Cruz et al. 2010; Ramasamy et al. 2011). We can identify many of the important tissue features and our obtained images reveal similar anatomical features as seen in histology slides making them potentially useful for *in vivo* diagnosis of tissue health (Gartner and Hiatt 2007).

### 15.3.5 Three-Photon GRIN Endoscopy

A significant advantage of the GRIN lens approach to MPE is that it is not limited to a single imaging modality. As we can utilize larger external optics, we can utilize different imaging techniques to scan the back of the GRIN lens system. Therefore,

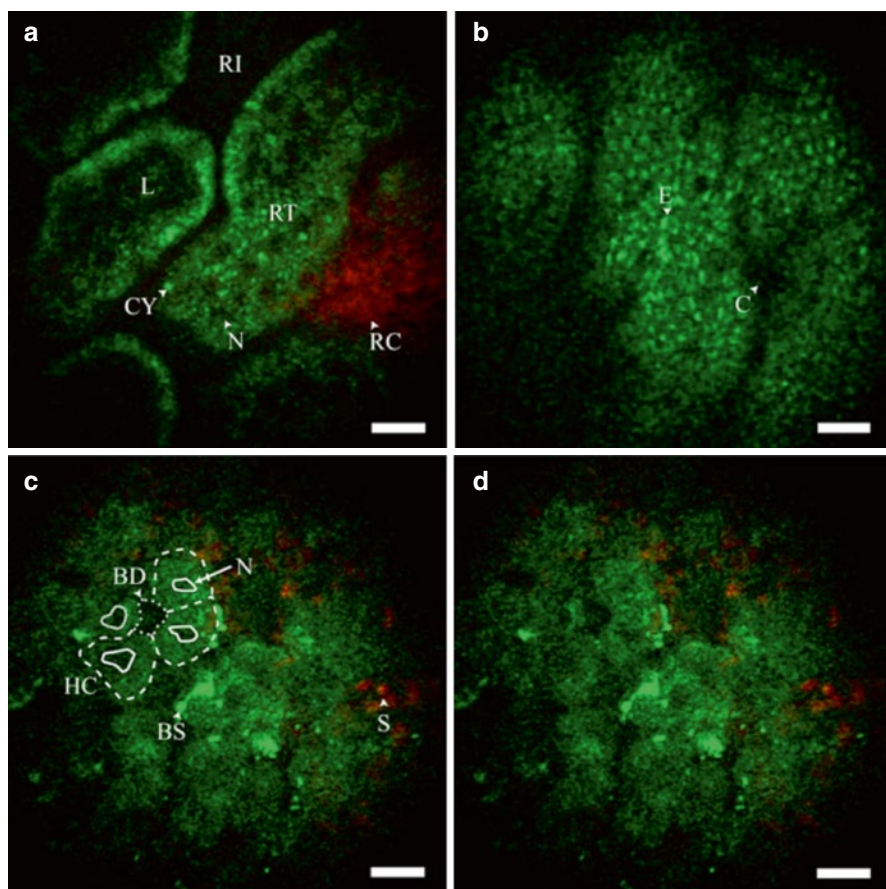


**Fig. 15.22** Unaveraged in vivo images of unstained rat tissue. The pseudo-color images show red SHG signal ( $<405$  nm) and green intrinsic fluorescent emission (405–700 nm). (a). Image of the superficial kidney renal cortex shows dark renal interstitium (RI), dark cellular nuclei (N) and bright intrinsic fluorescent cytoplasm (CY) that form the epithelial cells in the renal tubules (RT), SHG signal from the tough fibrous layer that forms the renal capsule (RC), and the dark blood filled lumen (L) inside the renal tubules. (b). Image of the inner colon wall shows bright intrinsic fluorescent signal from enterocytes (E) surrounding dark circular crypts (C). (c) Image of the rat liver showing  $\sim 20$   $\mu\text{m}$  diameter hepatocytes (coarse dashed line) with dark nuclei (N, solid line) chained together to form hepatic chords (HC), a dark bile duct (BD, fine dashed line) and bright intrinsically fluorescent bile salts (BS), as well as SHG emission from the septa (S) a fibrous tissue bands that separates hepatocyte nodules. (d). Image of the rat liver without figure labels shown for clarity. In these images, scale bars are 20  $\mu\text{m}$  (Huland et al. 2012)

we decided to explore the use of our compact and portable GRIN endoscope as a 3 photon (3P) endoscope (Huland et al. 2013). This allows the use of longer excitation wavelengths which have been shown to have several advantages. For a clinical setting the previously described use of a Ti:Sapp laser may be impractical as an excitation source. At longer wavelengths, however, we can use more compact and more reliable, and less expensive fiber based laser systems. Additionally, studies have

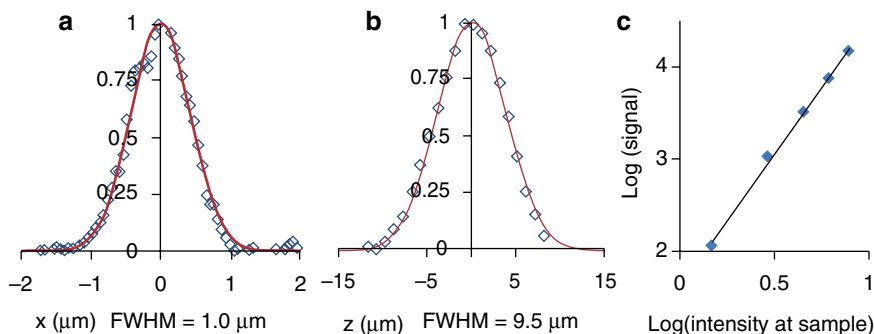


**Fig. 15.23** Three-photon lateral and axial resolution of the GRIN lens endoscope system. (a) Lateral and (b) axial intensity line profile across a subresolution fluorescent bead (blue diamonds). The Gaussian fits are indicated by the red lines. (c) Log-log plot of fluorescence signal as a function of excitation power at the sample. The slope is 2.9, indicating that the signal is generated by 3P excitation. Data in (c) used a Satsuma (Amplitude Systems, 1,035 nm, 5.7 MHz repetition rate) (Huland et al. 2013)

indicated that use of longer wavelengths could lead to reduced phototoxicity (Chen et al. 2002; Fu et al. 2006).

For 3P endoscopic imaging we used a fiber based laser at 1,040 nm (IMRA  $\mu$ Jewel, 1 MHz repetition rate). The compact and portable GRIN endoscope as described above is mostly compatible with this new wavelength. Changes only had to be made to the pulse delivery. For this demonstration we used a 1.6 m long hollow core photonic band-gap fiber (HC-1060-2, NKT Photonics). Dispersion compensation is achieved using a 65 cm of dispersive SF11 glass resulting in a pulse width of  $\sim 510$  fs. The use of the longer wavelength decreased the imaging performance of the device only slightly as we could take advantage of the improved point spread function of the three photon process (Fig. 15.23), yielding a lateral FWHM of 1.0  $\mu$ m and axial FWHM of 9.5  $\mu$ m. To test the capability of this setup for imaging of unstained tissue, we imaged *ex vivo* mouse lung. A 3 month old female, wild type mouse (Jackson Labs) was euthanized and a lung lobe removed. The sample was not stained and imaged within 1 h of euthanasia, by mounting it on a microscope slide using agarose gel. Due to the decreased repetition rate, we were able to obtain images at 5.9 mW average excitation power at a frame rate of 2 frames/s (512 by 512 pixels). Signal was separated into two channels using a 532 nm notch dichroic (NFD01-532, Semrock Inc.) into autofluorescence and SHG. It is noteworthy, that third harmonic generation could potentially be added as another imaging contrast, but was not possible in our experiments due to the GRIN lens transmission dropping significantly below  $\sim 370$  nm. Resulting images and a confirmation of 3P autofluorescence generation are shown in Fig. 15.24. On these images we can identify strong SHG originating presumably from the pleura on the surface of the lung as well as individual circular alveoli, demonstrating that these images could potentially provide diagnostic information on the tissue health.

To the best of our knowledge, this is the first demonstration of 3P imaging of unstained tissues through a compact and portable system with the potential for

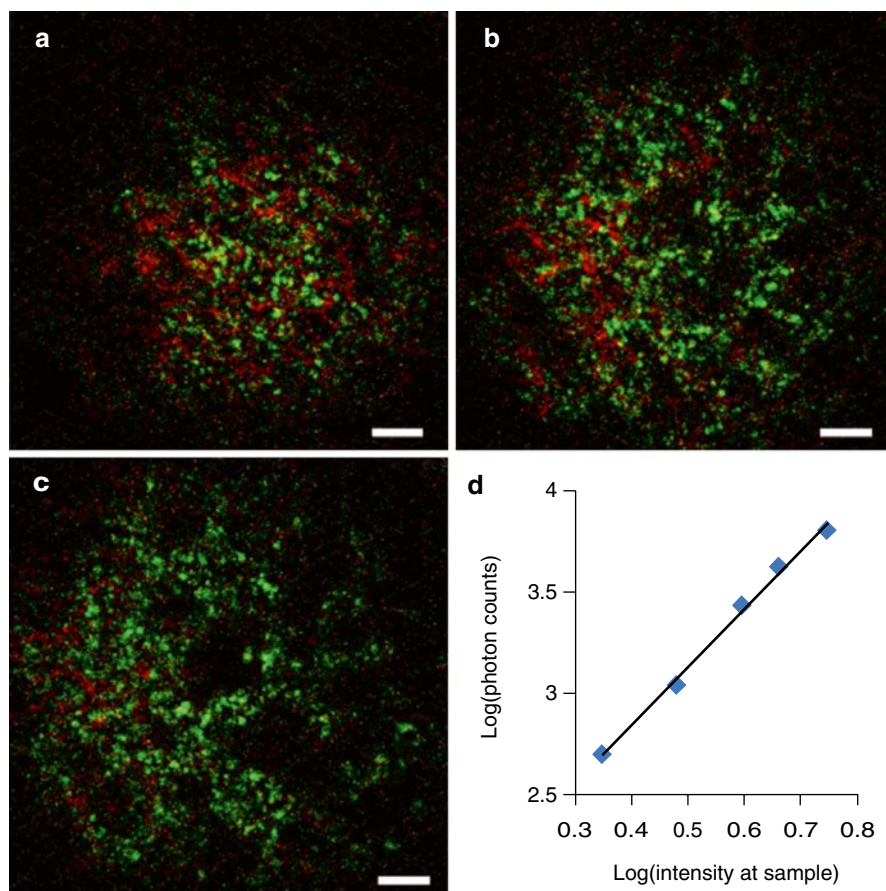


**Fig. 15.24** Unaveraged image of ex vivo unstained mouse lung acquired at 2 frames/s. *Green*: 3P autofluorescence. *Red*: SHG. Scale bar is 20  $\mu\text{m}$ . Images taken at (a) 20  $\mu\text{m}$ , (b) 30  $\mu\text{m}$ , and (c) 40  $\mu\text{m}$  below the tissue surface. (d) Log-log plot of autofluorescence signal as a function of excitation power at the sample. The slope is 2.9, indicating that the signal is generated by 3P excitation (Huland et al. 2013)

endoscopic tissue diagnosis. The combination of longer wavelength and 3P excitation, together with the convenient fiber-based excitation source, may make 3P endoscopy a valuable alternative to the conventional 2P approach.

### 15.3.6 Conclusions

While GRIN lens based endoscopic approaches are limited to rigid applications, they offer several advantages over the flexible multiphoton endoscopes. The diameter of GRIN endoscope probes can be as small as 350  $\mu\text{m}$ , which would allow them to be inserted into needles as small as 22 gauge (inner diameter of 413  $\mu\text{m}$ ). This

would decrease the FOV (to  $\sim 70\ \mu\text{m}$  when using the doublet design described here), but otherwise we would expect similar imaging performance. The GRIN lens systems described here are also inexpensive enough, that one could imagine them becoming a disposable probe tip, eliminating the need to sterilize the endoscope between procedures. Further, the ability to use larger optics allows for the use of durable galvo based scanning mirrors, more efficient collection optics, and the potential to use other imaging modalities in combination with multiphoton imaging. As such, this approach shows great promise to guide and/or replace current biopsy procedures to diagnose tissue health.

## 15.4 Dual Modality Endomicroscope with Variable Magnification and Field-of-View

### 15.4.1 Introduction

Imaging with our successful flexible and rigid prototypes, we realized that the practicality of the devices is severely constrained by the lack of zoom capability. The FOV of high-spatial resolution probes is relatively small and as result it is difficult and time consuming to investigate large area of interest. More importantly, the restricted FOV does not allow examining the tissue architecture which contains essential diagnostic information. For example, well established clinical practice is to extract tissue sample (Fig. 15.25a), processed it into histology sections and study them ex vivo under conventional light microscope using at least two magnifications: low magnification (Fig. 15.25c) for architecture viewing and high magnification (Fig. 15.25d) for cellular details. Variable magnification and FOV are essential for the proper diagnostic.

All high-spatial resolution imaging modalities such as optical coherence tomography (Huang et al. 1991), multiphoton microscopy (Denk et al. 1990; Zipfel et al. 2003b), and confocal microscopy (Minsky 1988), when incorporated into compact endoscope (Bao et al. 2008; Rivera et al. 2011; Brown et al. 2012; Seibel and Smithwick 2002; Flusberg et al. 2005a; Kiesslich et al. 2005; Xi et al. 2012; Wu et al. 2009c; Kim et al. 2010) they provide a relative small FOV (hundreds of microns, typically), which significantly reduces their utility in clinical applications. Miniature objective lens cannot simultaneously provide high-spatial resolution and large FOV, therefore optical zoom capability is essential functionality for a practical endoscope. Whereas, optical zoom is easily implemented in a conventional, tabletop light microscope by switching among multiple objective lenses (Fig. 15.25b), this approach is difficult, if not impossible, to implement in a miniature endoscopic probe due to steric size limitations.



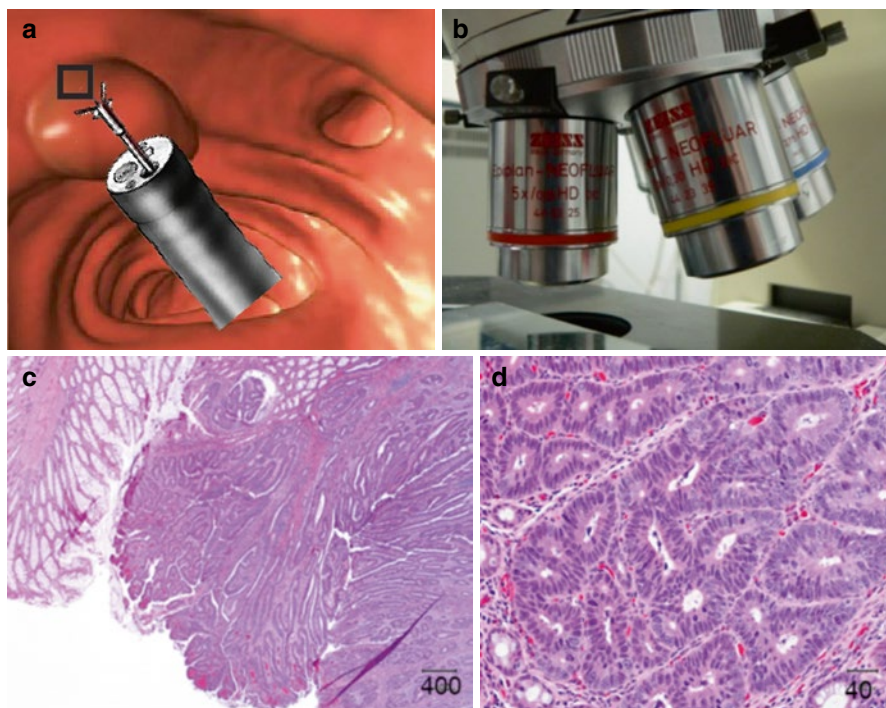


**Fig. 15.25** Tissue biopsy. (a) The tissue is examined with a colonoscope and a sample is excised from the area of interest. (b) The sample tissue is prepared into histology slides and then studied under an optical microscope at different magnifications to assess the tissue health. Optical zoom is trivial with conventional microscopes; physically switching multiple objective lenses with different magnifications. (c) Low magnification (20 $\times$ ) H&E image. (d) High magnification (200 $\times$ ) H&E image (Colon H&E imaged courtesy of Dr. Mukherjee, Weil Cornell Medical College)

#### 15.4.2 Miniature Varifocal Lens Design, Fabrication, Characterization and Testing

Various high-spatial resolution optical imaging modalities as MPM (Denk et al. 1990), OCT (Huang et al. 1991) and confocal (Minsky 1988) have been implemented in small endoscopic probes. Nevertheless that all these techniques derive their signal from different physical processes, the endoscopic devices have similar architecture (Flusberg et al. 2005b) that includes fiber delivery of the excitation light and collection of relevant signal, a scanning mechanism, a miniature objective lens. A large number of different types of objective lenses have been reported and demonstrated: simple monolithic gradient-index lens (GRIN) (Myaing et al. 2006;



Wu et al. 2009a; Fu et al. 2007; Bird and Gu 2003; Liu et al. 2009), compound GRIN lenses (Engelbrecht et al. 2008; Rivera et al. 2011; Barretto et al. 2009), compound spherical (Bao et al. 2008; Liang et al. 2002), or aspherical (Bao et al. 2008; Liang et al. 2002), micromachined lenses (Dickensheets and Kino 1996) and glass or plastic lenses (Carlson et al. 2005; Kester et al. 2007). These objective lenses satisfy the functional requirements in terms of resolution, size and cost, but achieving optical zoom capability in endoscopes has been elusive. A zoom endoscopic lens based on a dual zone lens was reported (Chen et al. 2010), but nearly half of the excitation power incident on the sample does not produce useful information. An endoscope probe that provides high-spatial resolution imaging with optical zoom capability has never before been demonstrated.

Traditional varifocal/zoom lenses, including catadioptric lenses (Ermolaeva et al. 2012; Shafer 1995; Shen et al. 2012; Betensky 1997), achieve their functionality by moving one or more of its components. This approach is not practical for endoscopic devices which distal end has very small size and is not easily accessible during normal operation. We developed a miniature catadioptric varifocal lens based on the principle of wavelength division multiplexing, i.e. separating the optical paths of excitation light with different wavelengths. The lens provides two magnifications and FOVs and the zoom operation is achieved by switching the wavelength of the excitation light without any mechanical adjustments of the lens components.

The objective lens, 3 mm outside diameter (OD) and ~8 mm in length, includes 3 optical elements (Fig. 15.26a). The FOV and magnification variation is enabled by two dichroic coatings deposited at the central part of the front surface of element #3 and at the peripheral region of the front surface of element #2. Note, that the central part of the front surface of element #2 is uncoated. The excitation light emerges from the tip of the fiber to the left in Fig. 15.26a, then it is directed by element #1 to the dichroic coating at the central part of the front surface of element #3. What happens next depends on the excitation/incident light wavelength. The light is either reflected (if the wavelength is within the reflection region of the coating, e.g.,  $\lambda_i=800$  nm) toward the patterned dichroic coating on the outer region of the front surface of element #2 and then focused to the sample with high numerical aperture (NA), or transmitted (if the wavelength is within the transmission region of the coating, e.g.,  $\lambda_i=406$  nm) and focused to the sample with low NA. Therefore, the change of magnification/FOV is achieved by switching only the wavelength of the excitation light, no mechanical adjustments of lens elements are required.

The design parameters are listed in Table 15.5. High-resolution multiphoton imaging mode is designed to operate between 800 and 900 nm. At  $\lambda_i=800$  nm, the calculated full width at half maximum (FWHM) of the lateral point spread function (PSF) is ~0.7  $\mu\text{m}$  (Fig. 15.28a), and the Strehl ratio is approximately 1 over the central 160- $\mu\text{m}$  FOV, indicating diffraction limited optical performance. The low-magnification imaging mode operates between 350 and 730 nm. At  $\lambda_i=406$  nm, the lateral resolution (FWHM) is ~4.5  $\mu\text{m}$ , and the FOV is 1.3 mm. The imaging planes of the miniature varifocal lens have small curvature in both imaging modalities. Such a curved image plane allows significantly better aberration correction than a planar image plane, and is inconsequential for *in vivo* tissue imaging. The radius of

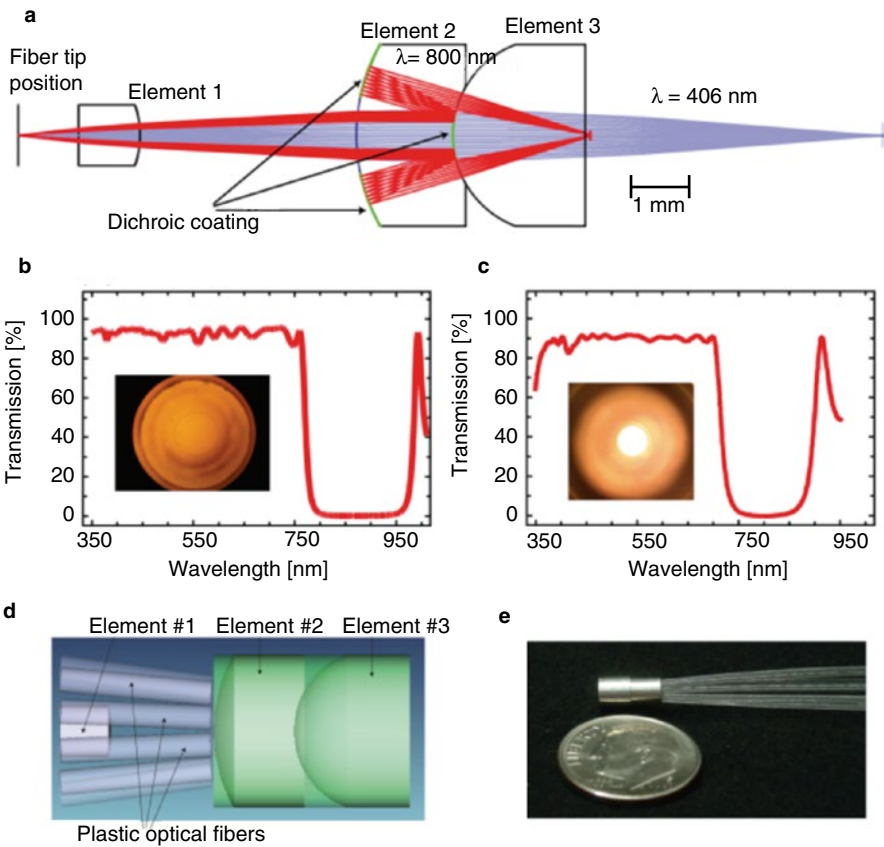


**Fig. 15.26** (a) Lens design layout, drawn to scale. (b) Transmission spectrum of the patterned dichroic coating deposited on the proximal surface of element #2 (shown in the *inset*). The patterned structure of the coating is clearly seen. (c) Transmission spectrum of the dichroic coating deposited on the proximal surface of element #3 (shown in the *inset*). (d) 3D lens layout, indicating the positions of the plastic fibers for signal collection. (e) Photograph of the objective lens assembly (Ouzounov et al. 2013b)

**Table 15.5** Design specifications for miniature zoom objective (Ouzounov et al. 2013b)

Parameters	High-mag mode	Low-mag mode
Sample space	Water	Air
Magnification	−0.2×	−1.47×
NA	0.55 (at 800 nm)	0.075 (at 405 nm)
FOV	160 μm	1.3 mm
One-photon resolution	0.7 μm	4.5 μm
Wavelength	800–900 nm	350–730 nm

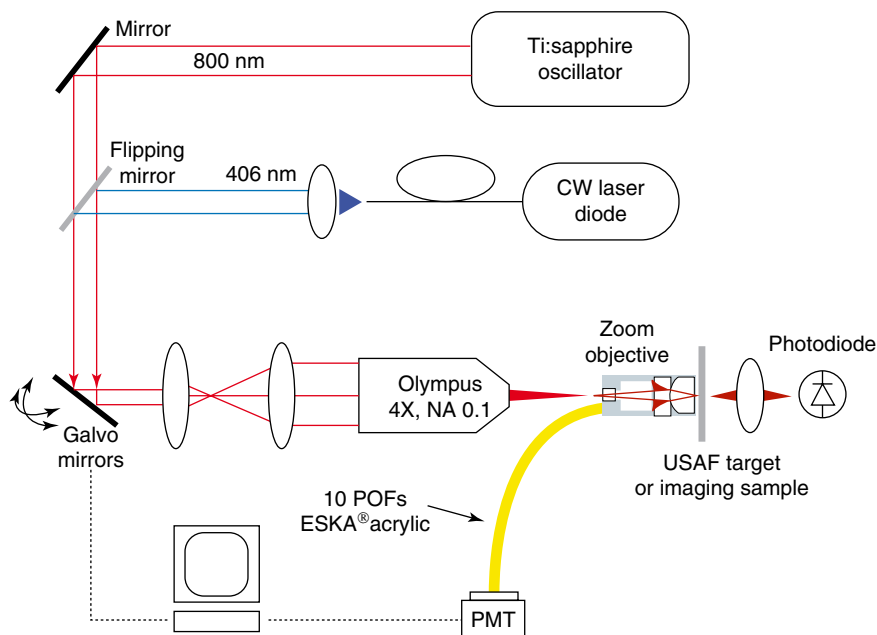


Fig. 15.27 Lens characterization and imaging setup (Ouzounov et al. 2013b)

curvature of the image surface is  $-1.09$  mm and  $-2.01$  mm for high magnification and low magnification mode, respectively. For *in vivo* imaging, this is not an issue because tissue features are not flat anyway. The curvature of the imaging plane surface will have little effect on signal collection, because the POFs collect through non-imaging pathways. The tolerance analysis we performed is based on calculating the root-mean-squared (rms) wavefront error, i.e., deviations from an ideal spherical wavefront. The nominal error of the lens design is 0.007.

The dichroic coatings on elements 2 and 3 (Fig. 15.26a–c) that enable the varifocal operation lead to non-reciprocal propagation of the excitation and the fluorescence light. Therefore, epi-collection of the two-photon excited fluorescence signal through the excitation pathway is inefficient. As a result, we use 10 large-core (500  $\mu\text{m}$  OD) plastic optical fibers (POFs) (ESKA® acrylic, Mitsubishi) located next to the proximal surface of element 2 (Fig. 15.26d) to collect the fluorescence signal and the scattered light at low magnification mode. Different locations of the imaging planes results in different collection efficiency, which is smaller for the low magnification mode due to the longer working distance. However, the much higher signal level at low magnification mode, due to the linear contrast mechanism, overcomes the collection efficiency reduction.

The optical elements were manufactured (Fig. 15.26e) and assembled by Optics Technology Inc, Pittsford, NY.

The performance of this miniature objective was characterized by transmission imaging a US Air Force (USAF) test target. Figure 15.27 shows the experimental setup. A mode-locked Ti:Sapphire laser (Tsunami, Spectra Physics) operating at

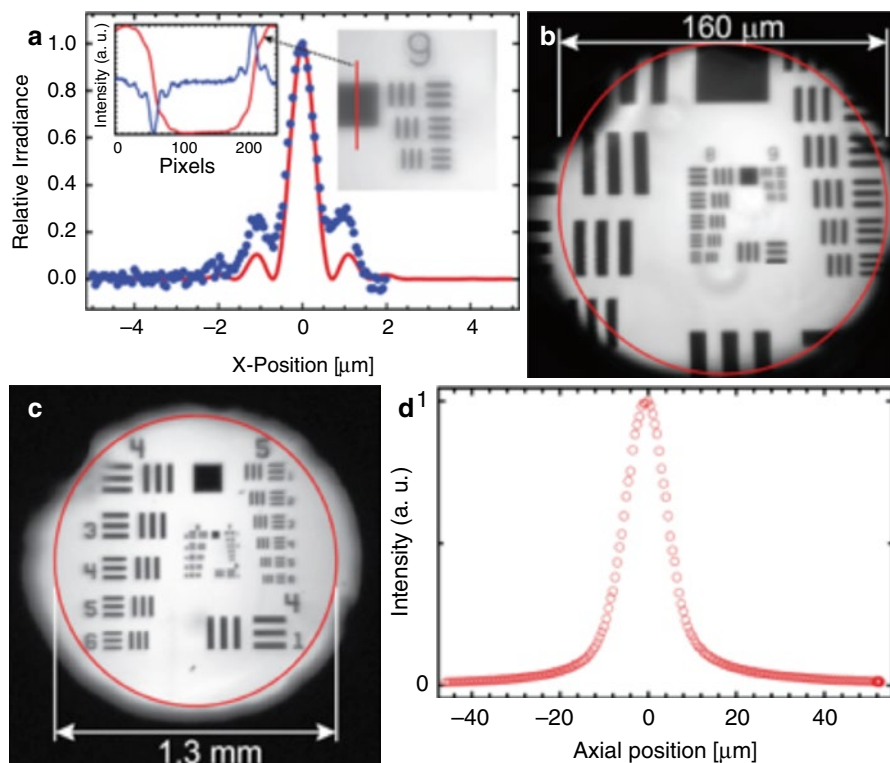


**Fig. 15.28** (a) Calculated (red solid line) and measured (blue dashed line) lateral point spread function for the high-resolution imaging mode. Inset: Group 9 of USAF resolution target imaged using the high-resolution imaging mode at 800 nm. Inset: Intensity line profile across the indicated feature and its derivative. (b) USAF resolution target imaged using the high magnification mode ( $\lambda_i=800$  nm). (c) USAF resolution target imaged in transmission using the low magnification mode ( $\lambda_i=406$  nm). (d) Axial scan of a thin Rhodamine B film showing the two-photon axial resolution (FWHM) of 10.5  $\mu\text{m}$  (Ouzounov et al. 2013b)

800 nm was used for characterization and imaging in high-resolution mode. For low-magnification, large FOV imaging, we use a fiber-coupled continuous wave (CW) semiconductor laser operating at 406 nm (LP406-SF20, Thorlabs). The laser beam is raster-scanned by a pair of galvo mirrors and is focused to the object plane of the zoom endoscope lens by a low NA objective (Olympus, 0.1 NA, 4 $\times$ ). To quantify the lateral resolution, for both modes, we analyzed the intensity line profile across the edge of a target feature (Fig. 15.28a, the feature used for high-magnification mode). The intensity profile at the edge of the feature is the edge-response function and its derivative is the line-spread function, which corresponds to the cross section of the point spread function (PSF). The lateral resolution of the high-magnification mode (FWHM) is  $\sim 0.75$   $\mu\text{m}$  (Fig. 15.28a), which corresponds to a two-photon resolution (FWHM) of  $\sim 0.5$   $\mu\text{m}$ . The obstruction at the center of the back aperture causes the side lobes of the PSF, a well-known feature for a reflective objective lens. However, the quadratic dependence on the excitation intensity in

two-photon excitation process will suppress significantly these side lobes. The FOV of the high-magnification mode is  $\sim 160\text{ }\mu\text{m}$  (Fig. 15.28b). The output beam of the miniature zoom lens operating in high-magnification mode has an annular profile, which reduces the axial resolution (Gu et al. 1993; Sheppard 1977). We characterized the two-photon axial resolution of the high-magnification mode by stepping a 500-nm Rhodamine B thin film through its focus. The measured FWHM of the thin film response is  $\sim 10.5\text{ }\mu\text{m}$  (Fig. 15.28d), which is sufficient for resolving cellular layers in biological tissues. Using the USAF test target, the one-photon lateral resolution of the low-magnification mode was measured to be  $\sim 4.5\text{ }\mu\text{m}$ . The low-magnification imaging mode achieved a large FOV of 1.3 mm (Fig. 15.28c).

The transmission of the varifocal lens is  $\sim 40$  and  $\sim 70\%$ , respectively, for the high and low magnification modes. In this prototype, the only coatings deposited were the patterned dichroic coatings on the proximal surfaces of elements #2 and #3 (Fig. 4.4) needed for varifocal operation. Anti-reflection coatings on the other optical surfaces will result in significantly higher power transmission.

To test the imaging capabilities of the dual magnification objective, we acquired *ex vivo* images from various unstained mouse tissues. The two-photon fluorescence and one-photon reflected/scattered light emitted from these tissues was epi-collected using the ten large core plastic optical fibers, and detected by an ultra bi-alkali (R7600U-200, Hamamatsu) PMT, which has an active area of  $\sim 400\text{ mm}^2$ . Short pass filters (FF720-SDi01-25 $\times$ 36, Semrock) were used in front of the PMT. The PMT output current was amplified and converted to voltage (C7319, Hamamatsu), and then digitalized at 16 bits at 10 MHz by a data acquisition card (NI PCI-6115, National Instruments). Prior to imaging, the excised tissue samples (i.e., a segment of colon, a single lung lobe and a whole kidney obtained from an adult CD-1 mouse) were embedded in agarose gel and mounted on microscope slides. The slide was mounted on a 3D translation stage (MP-285, Sutter). Low magnification images were acquired first. To acquire high magnification images, the site of interest was placed at the center of the FOV, and then the sample was moved axially to the image plane of the high magnification mode. Image acquisition is performed with the software ScanImage.

We show a high-resolution two-photon image of unstained mouse colon tissue (inner epithelial lining of the colon) in Fig. 15.29a. Typical features (e.g., enterocytes, goblet cells and crypts) are visible. A corresponding low magnification, reflection/scattering image of mouse colon is shown in Fig. 15.29b. Figure 15.29c shows a high-magnification multiphoton image of unstained mouse lung, where characteristic features including alveolar walls and lumens are clearly distinguishable. The corresponding low magnification image is shown in Fig. 15.29d. All images were acquired at a rate of 2 frames/s. The average power at the sample during multiphoton imaging was  $\sim 25\text{ mW}$ .

We show a low magnification image of unstained mouse kidney in Fig. 15.30a. High magnification two-photon fluorescence and second harmonic generation (SHG) images of unstained mouse kidney at the surface and  $\sim 80\text{ }\mu\text{m}$  below the surface are shown in Fig. 15.30b, c, respectively. In Fig. 15.30b, the fibrous components of the kidney capsule are visible. Figure 15.30c displays optical cross section of the proximal convoluted tubules, which are separated by renal interstitium (i.e. dark, non-fluorescent spaces containing sparse amount of connective tissue).

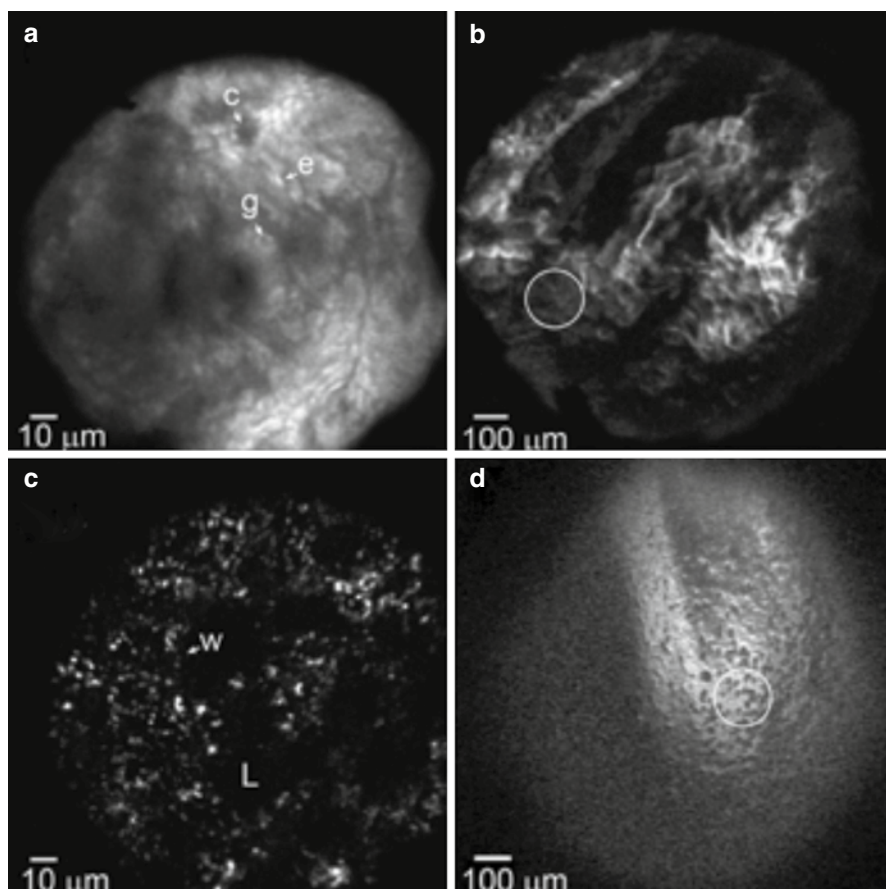


**Fig. 15.29** High-magnification two-photon intrinsic fluorescence images of unstained ex vivo mouse colon (a) and lung (c). Lung image is un-averaged; colon image is averaged over 3 frames. In (a), enterocytes (e), goblet cells (g) and crypts (c) are visible. In (c), alveolar walls (w) and lumens (L) are distinguishable. (b) Low magnification reflection/scattering image of unstained mouse colon (b) and lung (d). All images are acquired at 2 frames per second. Average power at the sample during multiphoton imaging was ~25 mW. The white circle in (b) and (d) indicates the approximate location of the site from which the multiphoton image shown in (a) and (c) is obtained (Ouzounov et al. 2013b)

### 15.4.3 Endomicroscope Probe Design, Fabrication, Characterization and Testing

#### 15.4.3.1 Endomicroscope Design

We integrated the varifocal miniature lens described above with a previously demonstrated (Rivera et al. 2011) miniaturized resonant/non-resonant fiber raster scanner into a fully functional endomicroscope probe with 5 mm OD and 5 cm rigid length (Fig. 15.31 (a)). The scanner consists of two scanning optical fibers that are bonded alongside each other: a hollow-core photonic band-gap fiber



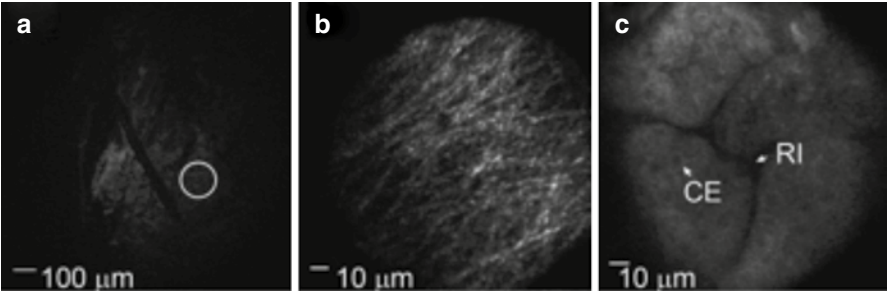


**Fig. 15.30** (a) Low magnification reflection/scattering image of unstained mouse kidney. High-magnification two-photon intrinsic fluorescence and SHG image of unstained ex vivo mouse kidney at the surface (b) and approximately 80  $\mu\text{m}$  below the surface (c). In (b), the collagen fibers of the kidney capsule are well distinguishable. In (c), cuboidal epithelium (CE) and the renal interstitium (RI) are visible. The white circle in (a) indicates the approximate location of the site from which the multiphoton images shown in (b) and (c) is obtained (Ouzounov et al. 2013b)

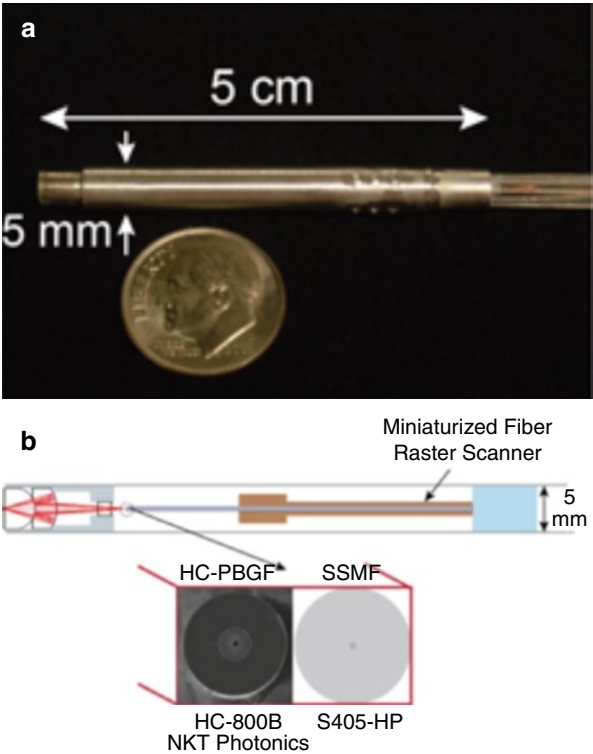
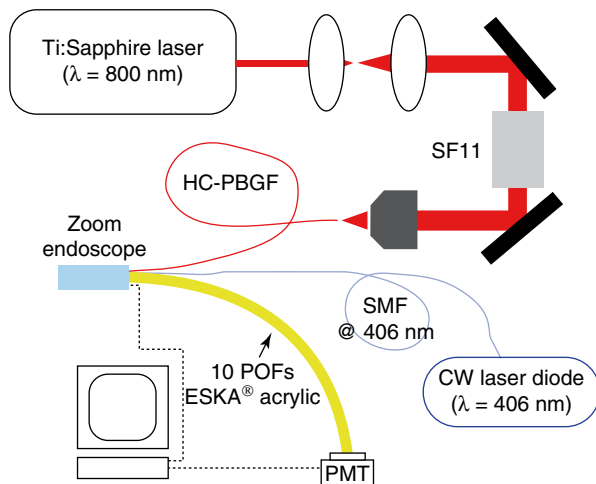


**Fig. 15.31** Dual modality endomicroscope. (a) Photograph of the endomicroscope with optical zoom. (b) Schematic illustration of the optical and mechanical configurations of the endomicroscope (Ouzounov et al. 2013a)

**Fig. 15.32** Endoscope characterization and imaging setup (Ouzounov et al. 2013a)



(HC-PBGF) with a transmission window at 800 nm (HC-800-2, NKT Photonics) for high-resolution multiphoton imaging, and a standard single mode fiber (SSMF) at 400 nm for large FOV, one-photon reflectance imaging. The fibers are bonded with instant adhesive (Loctite 495) and the distal end faces of the two fibers lie in the same plane. The schematic of the endomicroscope is shown in Fig. 15.31b.

#### 15.4.3.2 Endomicroscope Characterization

The experimental setup used for instrument characterization and for tissue imaging shown in Fig. 15.32 is similar to the one used for stand-alone lens. To compensate for the anomalous dispersion of HC-PBGF, the femtosecond pulses are positively pre-chirped by passing through a piece of SF11 glass and then coupled into the HC-PBG fiber (~1 m long, Fig. 15.25b) of the endomicroscope. The CW laser output fiber is spliced to the SSMF of the endomicroscope (Fig. 15.25b).

The device performance was characterized by imaging a US Air Force (USAF) test target in transmission. The lateral resolution (FWHM of PSF) of the high-magnification mode is ~0.75  $\mu\text{m}$  (Fig. 15.33a), which corresponds to a two-photon resolution (FWHM) of ~0.5  $\mu\text{m}$ . The side lobes of the PSF are caused by the obstruction at the center of the back aperture, which is a well-known feature of reflective objective lenses. These side lobes are significantly suppressed during two-photon imaging due to nonlinear nature of the signal. The FOV of the high-magnification mode is ~160  $\mu\text{m}$  (Fig. 15.33b). The low-magnification mode one-photon lateral resolution was determined to be ~4.5  $\mu\text{m}$ . The FOV of the low-magnification imaging mode is 1.15 mm (Fig. 15.33c). The output beam of the miniature zoom lens operating in high-magnification mode has an annular profile, which reduces the axial resolution (Gu et al. 1993; Sheppard 1977). We characterized the two-photon axial resolution of the high-magnification mode by stepping a 500-nm Rhodamine B thin film through its focus. The measured FWHM of the thin film response is

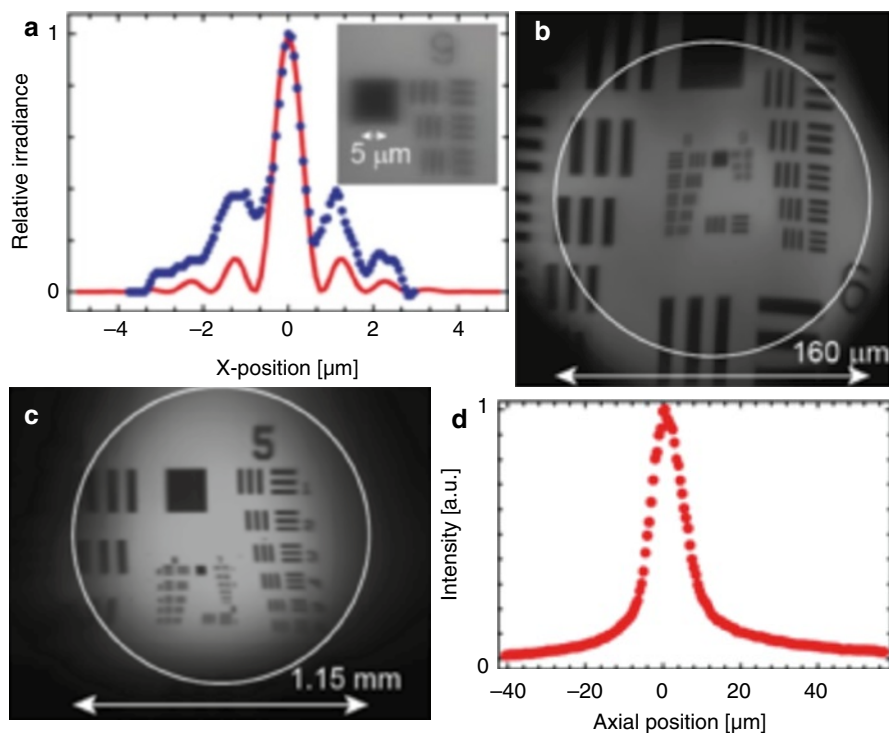


**Fig. 15.33** Dual modality endomicroscope characterization. (a) Calculated (red solid line) and measured (blue dashed line) lateral point spread function for the high-resolution imaging mode. *Inset:* Group 9 of USAF high-resolution target imaged in transmission using the high-resolution imaging mode at 800 nm. (b) USAF resolution target imaged in transmission using the high-magnification mode ( $\lambda_i = 800$  nm). (c) USAF resolution target imaged in transmission using the low-magnification mode ( $\lambda_i = 406$  nm). (d) Axial scan of a thin Rhodamine B film showing the two-photon axial resolution (FWHM) of 10.5  $\mu\text{m}$  (Ouzounov et al. 2013a)

$\sim 10.5$   $\mu\text{m}$  (Fig. 15.33d), which is sufficient for resolving cellular layers in biological tissues. The lateral and axial resolution for both operational modes of the completed endomicroscope prototype is similar to that of the stand-alone catadioptric varifocal lens, indicating that packaging of the miniature lens into a fully functional dual modality endomicroscope did not deteriorate its optical performance.

## 15.4.4 Ex Vivo and In Vivo Imaging of Unstained Rodent Tissues

### 15.4.4.1 Ex Vivo Imaging

To demonstrate the capability of the dual modality, dual magnification operation, we obtained *ex vivo* images from an unstained tumor-laden mouse lung lobe ( $\sim 3$  mm by  $\sim 5$  mm), and identified normal and abnormal tissue regions within the lobe using

both imaging modalities of the endomicroscope. Images were obtained from three different areas, indicated in Fig. 15.34a, within the tumor-laden lobe. Figure 15.34b–e show images from mildly affected site, Fig. 15.34f–h and i show images from site with inflammation and Fig. 15.28j–m show images from site with neoplasia. We identify the sites of interest by using the low-magnification reflectance modality to navigate the surface of the excised lung sample. These images, shown in Fig. 15.34d, h and l, exhibit very different surface morphology, which indicates different states of tissue health. In Fig. 15.34d, we observe normal lung parenchyma containing typical alveolar tissue, which is harder to discern in Fig. 15.34h and almost impossible to differentiate in Fig. 15.34l. Corresponding low magnification H&E images from the same sites are shown in Fig. 15.34c, g and k, respectively. It is not possible to perfectly match the locations of these two types of images due to typical artifacts associated with histological tissue processing. However, we placed small burn marks using a small blood vessel cauterize as fiducial markers and we were able to achieve a good correlation between the indicated areas in the low resolution H&E images (Fig. 15.34c, g and k) and the corresponding reflectance images (Fig. 15.34d, h and l). After completing each of the low-magnification images, we switched to the multiphoton modality and acquired high-resolution multiphoton images within those regions (Fig. 15.34e, i and m). Multiphoton microscopy of unstained tissues has been demonstrated to provide tissue diagnostics that are comparable to gold standard histology (Pavlova et al. 2012; Zipfel et al. 2003a; Mukherjee et al. 2009). Furthermore, it has been shown (Pavlova et al. 2012) that MPM is capable of differentiating between normal, inflammatory and neoplastic regions within mouse lung tissue. Therefore, to correctly diagnose the health state of the different regions within the excised tumor-laden mouse lung lobe, we compared the acquired multiphoton endomicroscopy images (Fig. 15.34e, i and m) to their corresponding H&E images (Fig. 15.34b, f and j, respectively) and to the multiphoton microscopy images reported in (Pavlova et al. 2012). Figure 15.34e shows a representative high-resolution multiphoton endomicroscopy image from the area indicated (red circle) in Fig. 15.34d. In Fig. 15.34e, mildly affected lung parenchyma is visible, where characteristic features such as alveolar walls and lumens are distinguishable. Moreover, in this image a few alveolar macrophages may be seen within the dark-appearing alveolar lumens. Figure 15.34b shows the corresponding H&E image to Figure 15.34e (i.e., both images are from the same tissue region) and contains similar morphological features, including intra-alveolar macrophages containing numerous eosinophilic crystals. A high-resolution multiphoton endomicroscopy image obtained within the region shown (red circle) in Fig. 15.10h is shown in Fig. 15.34i. Figure 15.10i and its corresponding H&E image (Fig. 15.34f) displays a relatively large number of macrophages that have migrated and infiltrated into the alveolar lumens, thereby indicating that this region is a site of inflammation (Pavlova et al. 2012). In the H&E image, the eosinophilic crystals within the macrophage cytoplasm are evident. Figure 15.34m displays a multiphoton image obtained within the area indicated (red circle) in Fig. 15.34i. In Fig. 15.34m and its corresponding H&E image (Fig. 15.34j) the normal alveolar architecture is effaced by neoplastic epithelial cells forming glandular and papillary structures. These results demonstrate that

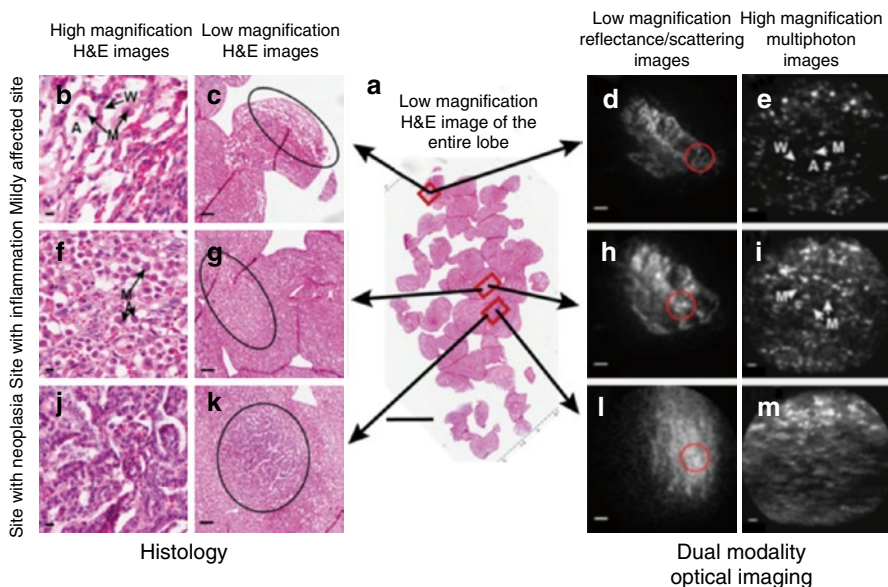


**Fig. 15.34** Ex vivo images of unstained tumor-laden mouse lung tissue. (a) Low magnification image of an H&E-stained section from the periphery of the entire lung lobe. The locations of the sites imaged are indicated. (b–e) A site that contains mildly affected lung tissue. (b) High Magnification H&E image shows mildly expanded alveolar septa surrounding lumens containing increased numbers of alveolar macrophages containing brightly eosinophilic crystals (M). (c) Low magnification H&E of the same site. (d) Low-magnification reflection/scattering image of this region within the mouse lung, in which the alveolar tissue is distinguishable. (e) High-magnification two-photon intrinsic fluorescence image of unstained ex vivo mouse lung tissue from the area displayed in (b). Alveolar lumens (A) and walls (W) are distinguishable as well as most likely a few macrophages within the lumens. (f–i) A site with moderate infiltrates of macrophages. (f) High magnification H&E image confirms that alveolar lumens are filled with large numbers of macrophages containing abundant intracytoplasmic eosinophilic crystals. (g) Low magnification H&E image of this site. (h) Low-magnification reflection/scattering image of this inflammatory site, in which the alveolar structure is not well distinguishable. (i) High-magnification two-photon intrinsic fluorescence image of unstained ex vivo mouse lung tissue from the area displayed in (h). A large number of cells, most likely macrophages, have migrated into the alveolar lumens, which is characteristic of inflammation. (j–m) A site with neoplasia proliferation of alveolar epithelial cells. (j) High magnification H&E image confirms that alveolar architecture is effaced by atypical epithelial cells forming glandular and papillary structures. (k) Low magnification H&E image of this site. (l) Low-magnification reflection/scattering image of this abnormal site, the alveolar structure is not well distinguishable. (m) High-magnification two-photon intrinsic fluorescence image of unstained ex vivo mouse lung tissue from the area displayed in (l). Compact mass of cells covers the whole area and the alveolar structure is not seen. The indicated area in (c), (g) and (k) correlates to the corresponding reflectance image in (d), (h) and (l). The red circle in (d), (h) and (l) indicates the approximate location of the site from which the multiphoton image shown in (e), (i) and (m) is obtained. Scale bars in (a), 1 mm. Scale bars in (c), (g), (k), (d), (h) and (l) are 100  $\mu$ m. Scale bars in (b), (f), (j), (e), (i) and (m) are 10  $\mu$ m (Ouzounov et al. 2013a)

our probe can use the low-magnification, large FOV modality to identify tissue sites that may have different health states and then use the high-magnification multiphoton modality to closely examine these sites and obtain diagnostic quality images. Therefore, our dual modality endomicroscope is able to provide an assessment of tissue health that is comparable to standard histopathological examinations that use an optical microscope with variable magnification.

**Mouse model.** LSL-K-ras G12D mice (Jackson et al. 2001) obtained from the Mouse Models of Human Cancer Consortium were backcrossed onto a pure 129SvEv genetic background. K-ras G12D activation and Cre-mediated recombination were induced through administration of  $3.16 \times 10^9$  viral particles of Ad-Cre virus combined with 0.144  $\mu\text{L}$  2 M  $\text{CaCl}_2$  and MEM 1 $\times$  (with Earle's salts, without L-glutamine and phenol red; Cellgro/Mediatech) to 40  $\mu\text{L}$  per mouse. Adult mice were anesthetized with 2.5 % Avertin intraperitoneally to effect (1 g tribromoethanol and 1 mL tert-amyl alcohol stock solution diluted in sterile saline and filtered before use). Virus was administered intratracheally following endotracheal intubation with a 24 gauge Monoject Veterinary I.V. catheter. The mouse was euthanized and the lungs were harvested 31 weeks post viral infection. All animal housing and experimentation was performed in accordance with institutional animal care and use guidelines.

### Tissue Processing

Mice were euthanized by carbon dioxide asphyxiation. The lung lobes were removed and kept in chilled PBS until imaging. The tissue was embedded in agarose gel, plated on a standard glass microscope slide, kept immersed in PBS, and imaged within 1 h of euthanasia. After imaging, lobes were fixed overnight in formalin and transferred to 70 % ethanol before being embedded in paraffin for serial sectioning and standard hematoxylin and eosin staining for subsequent histological analyses.

#### 15.4.4.2 In Vivo imaging

To demonstrate further the capability of our endomicroscope, we acquired *in vivo* images of kidney (Fig. 15.35) from anesthetized rats without any exogenous contrast. In Fig. 15.35, we show low-magnification reflectance and high magnification intrinsic multiphoton fluorescence images of the rat kidney. The kidney surface morphology and the fibrous components of the kidney capsule can be seen in the low magnification images show. High magnification multiphoton images were taken at various depths within the outermost regions of the kidney cortex. These images exhibit optical cross sections of the proximal convoluted tubules, which are lined by cuboidal epithelium and separated by renal interstitium (i.e., dark, non-fluorescent spaces containing sparse amounts of connective tissue). Note that these



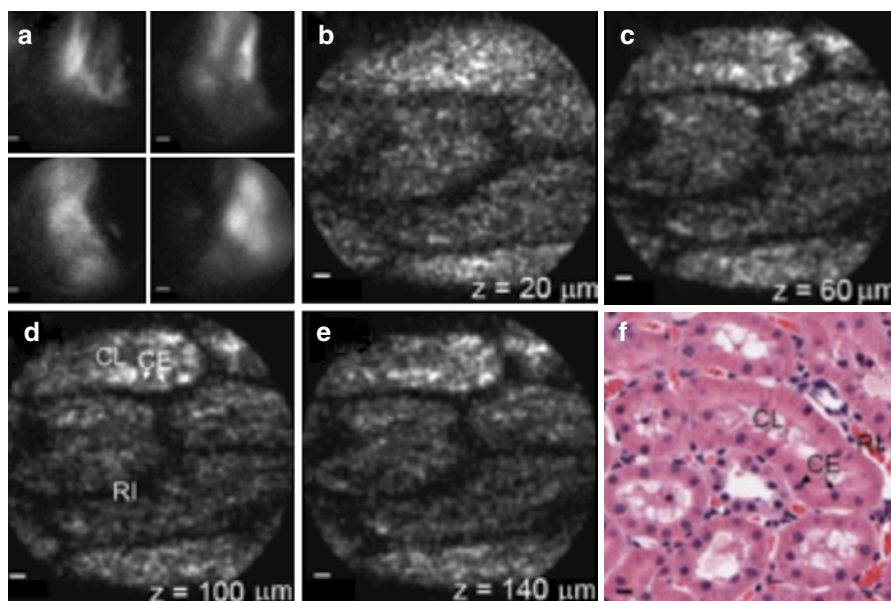


**Fig. 15.35** In vivo Images of unstained rat kidney tissues. (a), Low magnification reflection/scattering images of unstained in vivo rat kidney. The fibrous structure of the kidney capsule and outermost features of the kidney cortex are visible. (b–e), High-magnification two-photon intrinsic fluorescence image of unstained in vivo rat kidney 20  $\mu\text{m}$  below the surface (b), at  $\sim 60 \mu\text{m}$  below the surface (c), at  $\sim 100 \mu\text{m}$  below the surface (d) and at  $\sim 140 \mu\text{m}$  below the surface (e). (f) High magnification H&E image shows similar features and information as two-photon intrinsic fluorescence images. (b–f) show cross sections of proximal convoluted tubules, each tubule contains a central lumen (CL) lined with cuboidal epithelium (CE) and separated by the poorly fluorescent renal interstitium (RI) containing sparse connective tissue components. Scale bars in (a), 100  $\mu\text{m}$ . Scale bars in (b–f), 10  $\mu\text{m}$  (Ouzounov et al. 2013a)

features are clearly visible in images taken deep into the tissue (down to  $\sim 140 \mu\text{m}$  beneath the kidney surface), which demonstrates that our fluorescence collection scheme consisting of large POFs is capable of endoscopic imaging deep into scattering tissues. All images were taken using  $\sim 60 \text{ mW}$  average power at 4.1 frames/s (3 frames averaged). When the endomicroscope is pressed gently against the tissue, the motion artifacts (animal respiration, heart-beat, etc.) within the obtained images are mainly suppressed which makes a larger number of averages possible. Although we also intubated the animal imaged, pressing the probe against the tissue has significantly larger effect on motion artifacts reduction.

For the *in vivo* imaging experiments we used a normal male rat model (250–350 g, Sprague-Dawley, Charles River Laboratories International, Inc). The rat to be imaged was placed into an induction chamber with gas anesthetic ( $\sim 5 \%$  isoflurane-oxygen mixture) until reaching the sufficient level of sedation for intubation. The rat was intubated by inserting a small angiocatheter (Hallowell EMC, Rat Intubation Pack) into its trachea and extending the tube slightly past the

vocal folds. A commercial otoscope (Welch Allyn Model 21700) was used to guide the angiocatheter into its proper position during this procedure. The rat was then connected to a veterinary ventilator (Hallowell EMC MicroVent 1) in order to reduce imaging artifacts due to respiration. After intubation the animal was restrained on a temperature-controlled heat pad (36 °C) to maintain body temperature. The sedation (~2–3 % isoflurane-oxygen mixture) was maintained through the ventilator system during the imaging session. To expose the internal organs, a small ventral-midline abdominal incision was made and each organ was isolated and elevated with tongue depressors to further reduce the motion artifacts before imaging. The endomicroscope, attached to a mechanical arm connected to a precision motorized 3D stage (MP-285, Sutter Instrument Co.), is placed on top of the organ for image acquisition. All animal treatment was in compliance with Cornell University Institutional Animal Care and Use Committee approved protocol and procedures. The average power on the sample was approximately 60 mW, frame rate of 4.1 frame/s. The pulse duration was 110 fs and the wavelength was 800 nm.

We set up an infrared imaging system to help with endomicroscope positioning and monitoring of the animal during the imaging. The system includes an IR LED (M940L2, Thorlabs) operating at 940 nm and a CCD camera (DCU223M, Thorlabs) with a zoom lens (MVL7000, Thorlabs). The IR illumination wavelength of 940 nm does not interfere with the low magnification and high magnification imaging because of the short pass filters used (FF01-720/SP-25, Semrock) in the signal path and low PMT sensitivity at this wavelength.

### 15.4.5 Conclusions

Tissue biopsy procedures are the current practice for clinical assessment of tissue health. Tissue biopsy is guided by conventional wide field, white light endoscopes that offer a large FOV, but do not provide quality diagnostic information. Our dual modality endoscope with variable optical magnification provides, as demonstrated in the results presented above, high-spatial resolution diagnostic quality imaging. White light, wide field imaging naturally complements our dual modality endomicroscope. A video endoscope integrated with our device would provide imaging at three resolutions/FOVs: ~ 2 cm FOV with ~ 100  $\mu\text{m}$  resolution through white light imaging, ~ 1 mm FOV, 4.5  $\mu\text{m}$  resolution through the low magnification mode, and ~ 200  $\mu\text{m}$  FOV, <1  $\mu\text{m}$  resolution through the high magnification multiphoton imaging mode. Such multi-magnification/FOV imaging approach completely parallels the tissue biopsy procedure (i.e., white light imaging in vivo, and then dual magnification imaging of the stained biopsy specimen using a bench-top microscope ex vivo), and will allow for real time diagnostics in the clinic without tissue removal.

Maximizing the signal collection efficiency is essential for a practical multiphoton endomicroscope to achieve diagnostic quality image without inflicting damage to the tissue. Presently, most endoscopic objectives and probes are designed for

optimal excitation, and then using the same imaging optics to epi-collect the fluorescence back into the delivery fiber or to a single large core fiber (Engelbrecht et al. 2008; Le Harzic et al. 2008; Flusberg et al. 2005a). Most biological tissues are extremely heterogeneous and strongly scatter light at the short fluorescence and second harmonic generation wavelengths, therefore the contribution of ballistic fluorescence photons in epi-collection diminishes quickly with increasing imaging depth (Helmchen and Denk 2005). When imaging deep into scattering tissue, efficient collection of the scattered fluorescence photons that emerge from the tissue surface from a diffusely radiating region (Beaurepaire and Mertz 2002) is essential. By collecting the scattered fluorescence photons through 10 large core POFs, our endomicroscope improves the collection efficiency by increasing the effective collection FOV and NA; therefore, it is inherently well suited for imaging deep into highly scattering tissues. With our current device we can achieve 140  $\mu\text{m}$  imaging depth without noticeable degradation of image quality and this depth limit is due to the working distance of the device. A larger working distance (e.g.,  $\sim 500 \mu\text{m}$ ) varifocal objective lens can be achieved based on the same catadioptric concept, which will help properly evaluate the extent of tumor invasion during cancer staging (Kiesslich and Neurath 2007). Multiphoton imaging is inherently suited for deep tissue imaging, and our novel collection scheme based on harvesting non-ballistic fluorescence photons can further enhance this capability.

A future improvement for the varifocal lens is to achieve par-focal operation, i.e., the imaging planes of the two optical magnification modes overlap. The endoscope repositioning when switching between the two modalities would be eliminated. In addition, the catadioptric lens enables the combination of high-resolution multiphoton imaging with a number other of imaging modalities and thus may provide additional clinical value by combining the complementary diagnostic capabilities of several modalities in a single device. The low-magnification mode could be implemented as one-photon imaging, including any of reflectance (demonstrated in this paper), narrow-band, or laser-induced fluorescence imaging modality. The dichroic coatings spectral properties and the excitation light delivery fibers can be selected in such ways that a single device can implement all these modalities by choosing the appropriate laser sources. The low-magnification mode can also be implemented through multiphoton imaging modalities because the novel, non-reciprocal fluorescence collection approach (i.e., the separation between the excitation and collection optical path) enables high collection efficiency in a low NA, large FOV excitation system.

In summary, we have designed, built, and tested, an endomicroscope that, for the first time, achieves variations of optical magnification and FOV in a miniature device. By combining, in the same device, a high-resolution modality with a large FOV modality, our device extends significantly the clinical utility of high resolution endomicroscopy. Our endomicroscope enables surveying large tissue areas with a coarse spatial resolution and identifying the sites of interest to be imaged with high-spatial resolution. The optical zoom operation achieved without any mechanical adjustments is enabled by a novel miniature objective lens design utilizing the principle of wavelength division multiplexing. The demonstrated

endomicroscope overcomes a major limitation (i.e., small FOV) in existing high resolution endoscopic imaging, particularly in its clinical translation for real-time tissue diagnostics.

## 15.5 Summary and Conclusions

The strength of nonlinear microscopy lies in its ability to produce high resolution, real time images of unstained tissue. As a result, it has great potential to be useful in the clinical identification of abnormal tissue, as a tool for diagnostic imaging and surgical margin assessment. The work presented here describes endoscopic instrumentation development efforts and experimental validation of endoscopic imaging devices and techniques.

As the optical performance of these devices approaches clinical usefulness, a key step in the translation of this technology is to verify that the excitation light used does not damage the tissue. While some studies have suggested that the excitation powers used for our studies are below the damage threshold (Dela Cruz et al. 2010; Ramasamy et al. 2011), further studies of tissue damage under femtosecond pulse illumination are necessary to provide clear guidelines for the safety of MPE. These studies will undoubtedly play a major role in the design and fabrication of the next generation of multiphoton endoscopes.

**Acknowledgements** We thank members of the Xu, Webb, and Weiss research groups, as well as Douglas Scherr, Sushmita Mukherjee, Ashutosh Tewari, and Manu Jain of Weill Cornell Medical College and Julie Bentley of the University of Rochester for discussions and technical suggestions. We also thank Wendy Williams of the Cornell Center for Animal Resources and Education for her assistance with the *in vivo* imaging experiments. Our project was supported by the National Institutes of Health (NIH)/National Cancer Institute grant R01-CA133148 and the NIH/National Institute of Biomedical Imaging and Bioengineering grant R01-EB006736.

## References

- Agrawal GP (2007) Nonlinear fiber optics. Academic, Boston
- Bao H, Gu M (2009) A 04-mm-diameter probe for nonlinear optical imaging. *Opt Express* 17(12):10098
- Bao H, Allen J, Pattie R, Vance R, Gu M (2008) Fast handheld two-photon fluorescence endoscope with a 475  $\mu\text{m} \times 475 \mu\text{m}$  field of view for *in vivo* imaging. *Opt Lett* 33(12):1333
- Barretto RPJ, Messerschmidt B, Schnitzer MJ (2009) *In vivo* fluorescence imaging with high-resolution microlenses. *Nat Methods* 6(7):511–512
- Beaurepaire E, Mertz J (2002) Epifluorescence collection in two-photon microscopy. *Appl Opt* 41(25):5376
- Betensky EI (1997) Zoom relay lens for a family of catadioptric objective lenses. In: *Optical science, engineering and instrumentation'97*, pp. 90–96
- Bewersdorf J, Egner A, Hell SW (2006) *Handbook of biological confocal microscopy*. Springer Science+Business Media, New York

- Bird D, Gu M (2003) Two-photon fluorescence endoscopy with a micro-optic scanning head. *Opt Lett* 28(17):1552
- Both M, Vogel M, Friedrich O, von Wegner F, Künsting T, Fink RHA, Uttenweiler D (2004) Second harmonic imaging of intrinsic signals in muscle fibers *in situ*. *J Biomed Opt* 9(5): 882–892
- Brown CM, Reinhall P, Karasawa S, Seibel E (2006) Optomechanical design and fabrication of resonant microscanners for a scanning fiber endoscope. *Opt Eng* 45(4):043001
- Brown CM, Rivera DR, Pavlova I, Ouzounov DG, Williams WO, Mohanan S, Webb WW, Xu C (2012) *In vivo* imaging of unstained tissues using a compact and flexible multiphoton microendoscope. *J Biomed Opt* 17(4):0405052012
- Campagnola PJ, Millard AC, Terasaki M, Hoppe PE, Malone CJ, Mohler WA (2002) Three-dimensional high-resolution second-harmonic generation imaging of endogenous structural proteins in biological tissues. *Biophys J* 82(1 Pt 1):493–508
- Carlson K, Chidley M, Sung K-B, Descour M, Gillenwater A, Follen M, Richards-Kortum R (2005) *In vivo* fiber-optic confocal reflectance microscope with an injection-molded plastic miniature objective lens. *Appl Opt* 44(10):1792–1797
- Carriles R, Sheetz KE, Hoover EE, Squier JA, Barzda V (2008) Simultaneous multifocal, multiphoton, photon counting microscopy. *Opt Express* 16(14):10364
- Chen IH, Chu SW, Sun CK, Cheng PC, Lin B-L (2002) Wavelength dependent damage in biological multi-photon confocal microscopy: a micro-spectroscopic comparison between femtosecond Ti:sapphire and Cr:forsterite laser sources. *Opt Quantum Electron* 34(12): 1251–1266
- Chen M, Xu C, Webb WW (2010) Endoscope lens with dual fields of view and resolutions for multiphoton imaging. *Opt Lett* 35(16):2735–2737
- Cheong WF, Prael SA, Welch AJ (1990) A review of the optical properties of biological tissues. *IEEE J Quantum Electron* 26(12):2166–2185
- Débarre D, Supatto W, Pena A-M, Fabre A, Tordjmann T, Combettes L, Schanne-Klein M-C, Beatarepaire E (2006) Imaging lipid bodies in cells and tissues using third-harmonic generation microscopy. *Nat Methods* 3(1):47–53
- Dela Cruz JM, McMullen JD, Williams RM, Zipfel WR (2010) Feasibility of using multiphoton excited tissue autofluorescence for *in vivo* human histopathology. *Biomed Opt Express* 1(5):1320–1330
- Denk W, Strickler J, Webb W (1990) Two-photon laser scanning fluorescence microscopy. *Science* 248(4951):73–76
- Dickensheets DL, Kino GS (1996) Micromachined scanning confocal optical microscope. *Opt Lett* 21(10):764
- Dombeck DA, Kasischke KA, Vishwasrao HD, Ingelsson M, Hyman BT, Webb WW (2003) Uniform polarity microtubule assemblies imaged in native brain tissue by second-harmonic generation microscopy. *Proc Natl Acad Sci U S A* 100(12):7081–7086
- Durst ME, Kobat D, Xu C (2009) Tunable dispersion compensation by a rotating cylindrical lens. *Opt Lett* 34(8):1195
- Engelbrecht CJ, Johnston RS, Seibel EJ, Helmchen F (2008) Ultra-compact fiber-optic two-photon microscope for functional fluorescence imaging *in vivo*. *Opt Express* 16(8):5556
- Ermolaeva E, Livshits I, Vasiliev V Catadioptric varifocal objective (2012). In: SPIE optical engineering + applications, p 848804.
- Farrar MJ, Wise FW, Fetcho JR, Schaffer CB (2011) *In vivo* imaging of myelin in the vertebrate central nervous system using third harmonic generation microscopy. *Biophys J* 100(5): 1362–1371
- Flusberg BA, Jung JC, Cocker ED, Anderson EP, Schnitzer MJ (2005a) *In vivo* brain imaging using a portable 3.9 gram two-photon fluorescence microendoscope. *Opt Lett* 30(17):2272
- Flusberg BA, Cocker ED, Piyawattanametha W, Jung JC, Cheung ELM, Schnitzer MJ (2005b) Fiber-optic fluorescence imaging. *Nat Methods* 2(12):941–950
- Friedl P, Wolf K, von Andrian UH, Harms G (2007) Biological second and third harmonic generation microscopy. *Curr Protoc Cell Biol* Chapter 4, p. Unit 4.15

- Fu L, Gan X, Gu M (2005) Nonlinear optical microscopy based on double-clad photonic crystal fibers. *Opt Express* 13(14):5528
- Fu Y, Wang H, Shi R, Cheng J-X (2006) Characterization of photodamage in coherent anti-Stokes Raman scattering microscopy. *Opt Express* 14(9):3942
- Fu L, Jain A, Cranfield C, Xie H, Gu M (2007) Three-dimensional nonlinear optical endoscopy. *J Biomed Opt* 12(4):040501
- Gartner LP, Hiatt JL (2007) Color textbook of histology, 3rd edn. Saunders Elsevier, Philadelphia
- Goetz M, Fottnar C, Schirmacher E, Delaney P, Gregor S, Schneider C, Strand D, Kanzler S, Memadathil B, Weyand E, Holtmann M, Schirmacher R, Weber MM, Anlauf M, Klöppel G, Vieth M, Galle PR, Bartenstein P, Neurath MF, Kiesslich R (2007) In-vivo confocal real-time mini-microscopy in animal models of human inflammatory and neoplastic diseases. *Endoscopy* 39(4):350–356
- Gu M, Sheppard CJR, Zhou H (1993) Optimization of axial resolution in confocal imaging using annular pupils. *Opt Int J Light Electron Opt* 93(2):87–90
- Helmchen F, Denk W (2005) Deep tissue two-photon microscopy. *Nat Methods* 2(12):932–940
- Helmchen F, Fee MS, Tank DW, Denk W (2001) A Miniature Head-Mounted Two-Photon Microscope. *Neuron* 31(6):903–912
- Hendriks BHW, Bierhoff WCJ, Horikx JJJ, Desjardins AE, Hezemans CA, Hooft GW't, Lucassen GW, Mihajlovic N (2011) High-resolution resonant and nonresonant fiber-scanning confocal microscope. *J Biomed Opt* 16(2):026007
- Hofmann U, Muehlmann S, Witt M, Doerschel K, Schuetz R, Wagner B (1999) Electrostatically driven micromirrors for a miniaturized confocal laser scanning microscope. In: Symposium on micromachining and microfabrication. Santa Clara, CA; pp. 29–38
- Hopt A, Neher E (2001) Highly nonlinear photodamage in two-photon fluorescence microscopy. *Biophys J* 80(4):2029–2036
- Hoy CL, Ferhanoğlu O, Yildirim M, Piyawattanametha W, Ra H, Solgaard O, Ben-Yakar A (2011) Optical design and imaging performance testing of a 9.6-mm diameter femtosecond laser microsurgery probe. *Opt Express* 19(11):10536–10552
- Huang D, Swanson EA, Lin CP, Schuman JS, Stinson WG, Chang W, Hee MR, Flotte T, Gregory K, Puliafito CA (1991) Optical coherence tomography. *Science* 254(5035):1178–1181
- Huang S, Heikal AA, Webb WW (2002) Two-photon fluorescence spectroscopy and microscopy of NAD(P)H and flavoprotein. *Biophys J* 82(5):2811–2825
- Huland DM, Brown KM, Howard SS, Ouzounov DG, Pavlova I, Wang K, Rivera DR, Webb WW, Xu C (2012) *In vivo* imaging of unstained tissues using long gradient index lens multiphoton endoscopic systems. *Biomed Opt Express* 3(5):1077–1085
- Huland DM, Charan K, Ouzounov DG, Jones JS, Nishimura N, Xu C (2013) Three-photon excited fluorescence imaging of unstained tissue using a GRIN lens endoscope. *Biomed Opt Express* 4(5):652–658
- Jackson EL, Willis N, Mercer K, Bronson RT, Crowley D, Montoya R, Jacks T, Tuveson DA (2001) Analysis of lung tumor initiation and progression using conditional expression of oncogenic K-ras. *Genes Dev* 15(24):3243–3248
- Jain M, Robinson BD, Scherr DS, Sterling J, Lee M-M, Wysock J, Rubin MA, Maxfield FR, Zipfel WR, Webb WW, Mukherjee S (2012) Multiphoton microscopy in the evaluation of human bladder biopsies. *Arch Pathol Lab Med* 136(5):517–526
- Jung JC, Schnitzer MJ (2003) Multiphoton endoscopy. *Opt Lett* 28(11):902
- Jung JC, Mehta AD, Aksay E, Stepnoski R, Schnitzer MJ (2004) *In vivo* mammalian brain imaging using one- and two-photon fluorescence microendoscopy. *J Neurophysiol* 92(5):3121–3133
- Kester RT, Tkaczyk TS, Descour MR, Christenson T, Richards-Kortum R (2007) High numerical aperture microendoscope objective for a fiber confocal reflectance microscope. *Opt Express* 15(5):2409
- Kiesslich R, Neurath MF (2007) Endomicroscopy is born – do we still need the pathologist? *Gastrointest Endosc* 66(1):150–153
- Kiesslich R, Goetz M, Vieth M, Galle PR, Neurath MF (2005) Confocal laser endomicroscopy. *Gastrointest Endosc Clin N Am* 15(4):715–731



- Kim KH, Buehler C, Bahlmann K, Ragan T, Lee W-CA, Nedivi E, Heffer EL, Fantini S, So PTC (2007) Multifocal multiphoton microscopy based on multianode photomultiplier tubes. *Opt Express* 15(18):11658
- Kim P, Chung E, Yamashita H, Hung KE, Mizoguchi A, Kucherlapati R, Fukumura D, Jain RK, Yun SH (2010) In vivo wide-area cellular imaging by side-view endomicroscopy. *Nat Methods* 7(4):303–305
- Kinsler LE, Frey AR, Coppens AB, Sanders JV (1982) *Foundamentals of acoustics*, 3rd edn. Wiley, New York
- Kleinfeld D, Mitra PP, Helmchen F, Denk W (1998) Fluctuations and stimulus-induced changes in blood flow observed in individual capillaries in layers 2 through 4 of rat neocortex. *Proc Natl Acad Sci* 95(26):15741–15746
- König K, Ehlers A, Riemann I, Schenkl S, Bückle R, Kaatz M (2007) Clinical two-photon microendoscopy. *Microsc Res Tech* 70(5):398–402
- Le Harzic R, Weinigel M, Riemann I, König K, Messerschmidt B (2008) Nonlinear optical endoscopy based on a compact two axes piezo scanner and a miniature objective lens. *Opt Express* 16(25):20588
- Lee CM, Engelbrecht CJ, Soper TD, Helmchen F, Seibel EJ (2010) Scanning fiber endoscopy with highly flexible, 1 mm catheterscopes for wide-field, full-color imaging. *J Biophotonics* 3(5–6):385–407
- Levene MJ, Dombeck DA, Kasischke KA, Molloy RP, Webb WW (2004) *In vivo* multiphoton microscopy of deep brain tissue. *J Neurophysiol* 91(4):1908–1912
- Liang C, Sung K-B, Richards-Kortum RR, Descour MR (2002) Design of a high-numerical-aperture miniature microscope objective for an endoscopic fiber confocal reflectance microscope. *Appl Opt* 41(22):4603–4610
- Liu G, Xie T, Tomov IV, Su J, Yu L, Zhang J, Tromberg BJ, Chen Z (2009) Rotational multiphoton endoscopy with a 1  $\mu\text{m}$  fiber laser system. *Opt Lett* 34(15):2249
- Makino T, Jain M, Montrose DC, Aggarwal A, Sterling J, Bosworth BP, Milsom JW, Robinson BD, Shevchuk MM, Kawaguchi K, Zhang N, Brown CM, Rivera DR, Williams WO, Xu C, Dannenberg AJ, Mukherjee S (2012) Multiphoton tomographic imaging: a potential optical biopsy tool for detecting gastrointestinal inflammation and neoplasia. *Cancer Prev Res (Phila)* 5(11):1280–1290
- Minsky M (1988) Memoir on inventing the confocal scanning microscope. *Scanning* 10(4):128–138
- Mukherjee S, Wysock JS, Ng CK, Akhtar M, Perner S, Lee MM, Rubin MA, Maxfield FR, Webb WW, Scherr DS (2009) Human bladder cancer diagnosis using Multiphoton microscopy. *Proc Soc Photo Opt Instrum Eng*, p 7161.
- Myaing MT, MacDonald DJ, Li X (2006) Fiber-optic scanning two-photon fluorescence endoscope. *Opt Lett* 31(8):1076
- Ouzounov DG, Moll KD, Foster MA, Zipfel WR, Webb WW, Gaeta AL (2002) Delivery of nanjoule femtosecond pulses through large-core microstructured fibers. *Opt Lett* 27(17):1513
- Ouzounov DG, Rivera DR, Webb WW, Bentley J, Xu C (2013a) Miniature varifocal objective lens for endomicroscopy. *Opt Lett* 38(16):3103–3106
- Ouzounov DG, Rivera DR, Williams WO, Stupinski JA, Southard TL, Hume KH, Bentley J, Weiss RS, Webb WW, Xu C (2013b) Dual modality endomicroscope with optical zoom capability. *Biomed Opt Express* 4(9):1494–1503
- Pavlova I, Hume KR, Yazinski SA, Flanders J, Southard TL, Weiss RS, Webb WW (2012) “Multiphoton microscopy and microspectroscopy for diagnostics of inflammatory and neoplastic lung. *J Biomed Opt* 17(3):036014
- Pillai RS, Lorensen D, Sampson DD (2011) Deep-tissue access with confocal fluorescence microendoscopy through hypodermic needles. *Opt Express* 19(8):7213–7221
- Piyawattanametha W, Barretto RPJ, Ko TH, Flusberg BA, Cocker ED, Ra H, Lee D, Solgaard O, Schnitzer MJ (2006) Fast-scanning two-photon fluorescence imaging based on a microelectromechanical systems two-dimensional scanning mirror. *Opt Lett* 31(13):2018

- Piyawattanametha W, Cocker ED, Burns LD, Barretto RP, Jung JC, Ra H, Solgaard O, Schnitzer MJ (2009) *In vivo* brain imaging using a portable 2.9 g two-photon microscope based on a microelectromechanical systems scanning mirror. *Opt Lett* 34(15):2309–2311
- Pologruto TA, Sabatini BL, Svoboda K (2003) ScanImage: flexible software for operating laser scanning microscopes. *Biomed Eng Online* 2(1):13
- Presby HM, Benner AF, Edwards CA (1990) Laser micromachining of efficient fiber microlenses. *Appl Opt* 29(18):2692–2695
- Ramasamy R, Sterling J, Fisher ES, Li PS, Jain M, Robinson BD, Shevchuck M, Huland D, Xu C, Mukherjee S, Schlegel PN (2011) Identification of spermatogenesis with multiphoton microscopy: an evaluation in a rodent model. *J Urol* 186(6):2487–2492
- Rehberg M, Krombach F, Pohl U, Dietzel S (2011) Label-free 3D visualization of cellular and tissue structures in intact muscle with second and third harmonic generation microscopy. *PLoS One* 6(11):e28237
- Rivera DR, Brown CM, Ouzounov DG, Pavlova I, Kobat D, Webb WW, Xu C (2011) Compact and flexible raster scanning multiphoton endoscope capable of imaging unstained tissue. *Proc Natl Acad Sci U S A* 108(43):17598–17603
- Rivera DR, Brown CM, Ouzounov DG, Webb WW, Xu C (2012a) Multifocal multiphoton endoscope. *Opt Lett* 37(8):1349–1351
- Rivera DR, Brown CM, Ouzounov DG, Webb WW, Xu C (2012b) Use of a lensed fiber for a large-field-of-view, high-resolution, fiber-scanning microendoscope. *Opt Lett* 37(5):881–883
- Ross MH, Pawlina W (2011) *Histology: a text and atlas*, 6th edn. Lippincott Williams & Wilkins, Baltimore
- Sawinski J, Denk W (2007) Miniature random-access fiber scanner for *in vivo* multiphoton imaging. *J Appl Phys* 102(3):034701
- Schönle A, Hell SW (1998) Heating by absorption in the focus of an objective lens. *Opt Lett* 23(5):325
- Seibel EJ, Smithwick QYJ (2002) Unique features of optical scanning, single fiber endoscopy. *Lasers Surg Med* 30(3):177–183
- Shafer DR (1995) Catadioptric optically compensated zooming with one moving element. In: SPIE's 1995 international symposium on optical science, engineering, and instrumentation. San Diego, CA; pp. 235–240
- Shen B, Chang J, Ouyang J, Zhang L, Wei A (2012) Design of reflective active zoom systems with four mirrors. In: *Photonics Asia*, p. 85571C
- Sheppard CJR (1977) The uses of lenses with annular aperture in scanning optical microscopy. *Optik* 48:329–334
- Sun CK, Yu CH, Tai SP, Kung CT, Wang IJ, Yu HC, Huang HJ, Lee WJ, Chan YF (2007) *In vivo* and *ex vivo* imaging of intra-tissue elastic fibers using third-harmonic-generation microscopy. *Opt Express* 15(18):11167
- Tang S, Jung W, McCormick D, Xie T, Su J, Ahn YC, Tromberg BJ, Chen Z (2009) Design and implementation of fiber-based multiphoton endoscopy with microelectromechanical systems scanning. *J Biomed Opt* 14(3):034005
- Witte S, Negrean A, Lodder JC, de Kock CPJ, Testa Silva G, Mansvelder HD, Louise Groot M (2011) Label-free live brain imaging and targeted patching with third-harmonic generation microscopy. *Proc Natl Acad Sci U S A* 108(15):5970–5975
- Wu Y, Leng Y, Xi J, Li X (2009a) Scanning all-fiber-optic endomicroscopy system for 3D nonlinear optical imaging of biological tissues. *Opt Express* 17(10):7907
- Wu T, Ding Z, Wang K, Chen M, Wang C (2009b) Two-dimensional scanning realized by an asymmetry fiber cantilever driven by single piezo bender actuator for optical coherence tomography. *Opt Express* 17(16):13819
- Wu Y, Xi J, Cobb MJ, Li X (2009c) Scanning fiber-optic nonlinear endomicroscopy with miniature aspherical compound lens and multimode fiber collector. *Opt Lett* 34(7):953

- Wu Y, Zhang Y, Xi J, Li MJ, Li X (2010) Fiber-optic nonlinear endomicroscopy with focus scanning by using shape memory alloy actuation. *J Biomed Opt* 15(6):060506
- Xi J, Chen Y, Zhang Y, Murari K, Li M-J, Li X (2012) Integrated multimodal endomicroscopy platform for simultaneous en face optical coherence and two-photon fluorescence imaging. *Opt Lett* 37(3):362–364
- Xu C, Zipfel W, Shear JB, Williams RM, Webb WW (1996) Multiphoton fluorescence excitation: new spectral windows for biological nonlinear microscopy. *Proc Natl Acad Sci U S A* 93(20):10763–10768
- Young B, Lowe JS, Stevens A, Heath JW (2006) Wheater’s functional histology: a text and colour atlas. Churchill Livingstone Elsevier, Philadelphia, p 448
- Young B, Stewart W, O’Dowd G (2011) Wheater’s basic pathology: a text, atlas and review of histopathology, 5th edn. Churchill Livingstone/Elsevier, Philadelphia
- Zipfel WR, Williams RM, Christie R, Nikitin AY, Hyman BT, Webb WW (2003a) Live tissue intrinsic emission microscopy using multiphoton-excited native fluorescence and second harmonic generation. *Proc Natl Acad Sci U S A* 100(12):7075–7080
- Zipfel WR, Williams RM, Webb WW (2003b) Nonlinear magic: multiphoton microscopy in the biosciences. *Nat Biotechnol* 21(11):1369–1377

## Chapter 16

# Fluorescence Lifetime Imaging for Diagnostic and Therapeutic Intravital Microscopy

Washington Y. Sanchez, Zhen Song, Wolfgang Becker, Karsten Koenig,  
and Michael S. Roberts

**Abstract** Intravital imaging is now widely performed using wide-field microscopy, endoscopy, and state-of-the-art multiphoton microscopy for research and clinical assessment applications. Fluorescence lifetime imaging is increasingly being used as a complementary technology to greatly enhance the specificity and sensitivity in the analysis of the various fluorophores present within an intravital image. The fluorescence lifetime of a fluorophore. The fluorescence lifetime distribution for a fluorophore is an intrinsic property, arising from the emission of photons of light in the decaying to its original energy state after its molecules are excited by a specific wavelength of light and remain in an excited state for a range of times. This behavior for individual autofluorescent fluorophores, dyes, drugs, fluorescent proteins and antibodies is most frequently summarized in terms of their average fluorescence lifetime. Fluorescence lifetime differences are then used to identify and discriminate between molecules in various applications, including the assessment of drug distribution and metabolism, and in quantifying cell responses for toxicology. Fluorescence lifetime imaging microscopy (FLIM) and tomography involves the spatial representation of

---

W.Y. Sanchez (✉)

Faculty of Health Sciences, Therapeutics Research Centre, School of Medicine,  
University of Queensland, Brisbane, QLD, Australia  
e-mail: [w.sanchez1@uq.edu.au](mailto:w.sanchez1@uq.edu.au)

Z. Song

School of Pharmacy & Medical Science, University of South Australia,  
Adelaide, SA, Australia

W. Becker

Becker and Hickl GmbH, Nahmitzer Damm 30, 12277 Berlin, Germany

K. Koenig

Department of Biophotonics and Lasertechnology, Saarland University,  
Saarbruecken, Germany

JenLab GmbH, Jena, Germany

M.S. Roberts

Faculty of Health Sciences, Therapeutics Research Centre, School of Medicine,  
University of Queensland, Brisbane, QLD, Australia

School of Pharmacy & Medical Science, University of South Australia,  
Adelaide, SA, Australia

the fluorescent lifetimes of all molecules within image collected over a specified time period and resolution. Autofluorescence lifetime differences between normal and cancerous tissues have been used to define surgical margins during intraoperative surgery. Recent advances have enabled the rapid and robust collection of fluorescence lifetime information from tissues with high-resolution at video-rate speeds using endoscopic probes. Fluorescence lifetime imaging, combined with multi-spectral and anisotropic analysis, yields detailed redox state data from within a cell, arising from its metabolic state and enables intravital analysis of the transport and metabolism of fluorescent probes in cells. Intravital fluorescence lifetime imaging is becoming an indispensable diagnostic approach with broad therapeutic and clinical applications.

## 16.1 Introduction

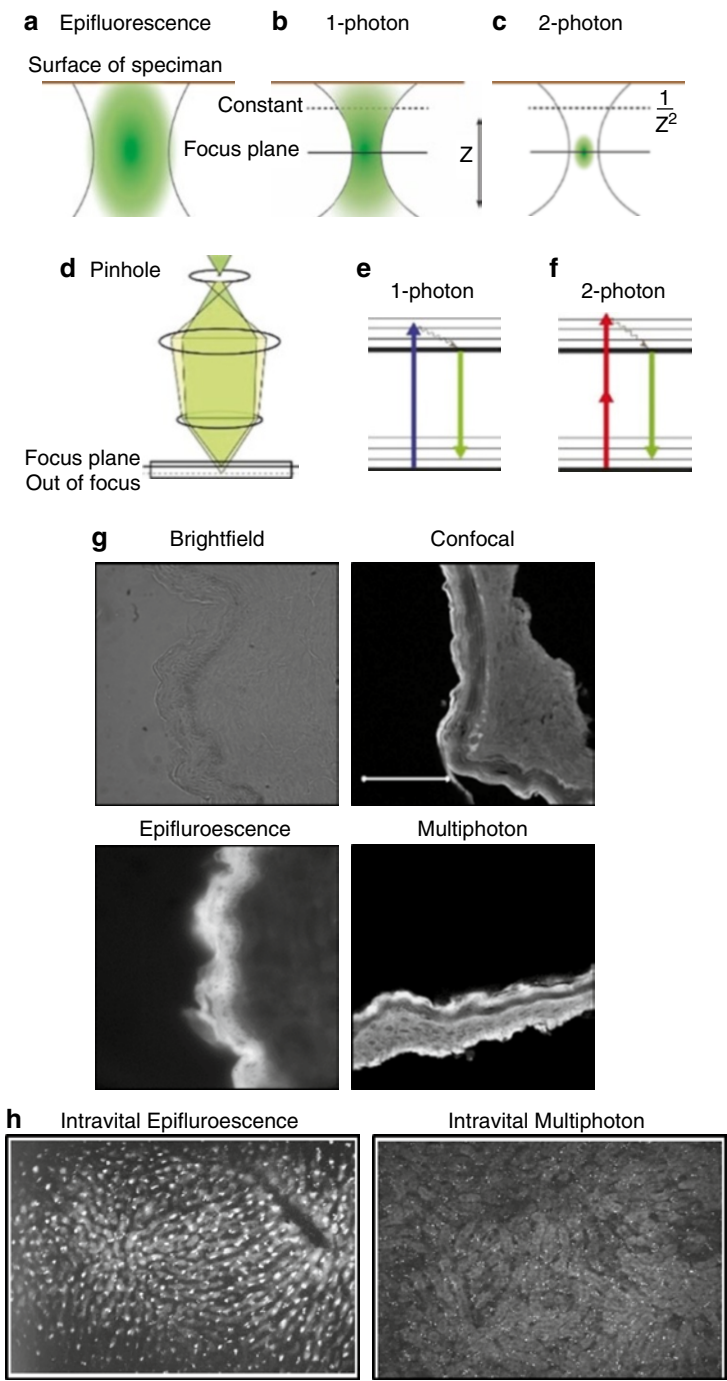
Fluorescence lifetime imaging (FLIM) is an essential complementary tool for intravital microscopy. FLIM adds an additional layer of information of the physico-chemical states of autofluorescent fluorophores and stained tissues. Combined with spectral and anisotropic imaging, a complex sample with a heterogeneous mix of fluorophores can be more precisely resolved with an enhanced sensitivity for each component. FLIM is now increasingly being used to rapidly assess disease states, progression and therapeutic delivery and efficacy with intravital microscopy. In this chapter, the theory and use of FLIM for intravital microscopy will be overviewed.

## 16.2 Intravital Multiphoton Tomography and Fluorescence Lifetime Imaging

Intravital fluorescence microscopy has now been used to image below the surface of tissue and organs for more than 60 years. One early application of this technique was the demonstration of the uptake of fluorescein from the sinusoids to hepatocytes and thence to the biliary canaliculae in rat livers *in vivo* (Hanzon 1952). Major developments of the technique include an improvement in focusing by confocal and multiphoton microscopy. In confocal microscopy, a pinhole is used to restrict the focus to a small focal volume, whereas in multiphoton tomography, the focus is limited to a plane (Fig. 16.1a–f). Figure 16.1g shows fluorescence, confocal fluorescence and multiphoton imaging of skin, and intravital epifluorescence microscopy and

---

**Fig. 16.1** Comparison of the optical diagram of (a) epifluorescence (b) confocal (c) two-photon. Epifluorescence is acquired when an area of specimen is uniformly illuminated. Both confocal and multi-photon images require point to point scanning thus the focus area is much smaller. Confocal microscopy obtains 3D resolution by limiting the observation volume by place a pinhole in front of the detect to avoid any out of focus light (d), whereas two-photon microscopy limits the excitation volume, since two/multi-photon will only occur when photon flux is extremely high. (e) and (f) are Jablonski energy diagrams of 1-photon excitation and 2-photon excitation. Intravital epifluorescence image (e) (Adapted from Hanzon (1952)). (g) Brightfield, confocal, epifluorescence, and multiphoton imaging of the skin. (h) Intravital epifluorescence (left panel) and two-photon microscopy (right panel) of the liver





intravital multiphoton tomography for liver (Fig. 16.1h). While intravital epifluorescence microscopy captures a greater proportion of off-focal plane layers of tissue, as shown by elevated intensity of vitamin A within the Kupffer cells (Fig. 16.1h), multiphoton microscopy captures fluorescence within the narrow focal volume ( $\sim 2 \mu\text{m}$  using a 10 $\times$  objective) to achieve higher sub-cellular resolution.

Key advantages of the multiphoton technique over the traditional fluorescence approach are: (1) a much deeper tissue depth of penetration, (2) narrow focal volume ( $\sim 1 \mu\text{m}^3$ ), and (3) less tissue photo-toxicity as a consequence of using laser light having a wavelength twice as long (half the energy) necessary to excite the sample (König 2008). A major advance in imaging has been the development of multiphoton microscopy for *in vivo* human studies to diagnose human skin conditions and to examine solute and nanoparticle distribution into skin. Figure 16.2 shows the first

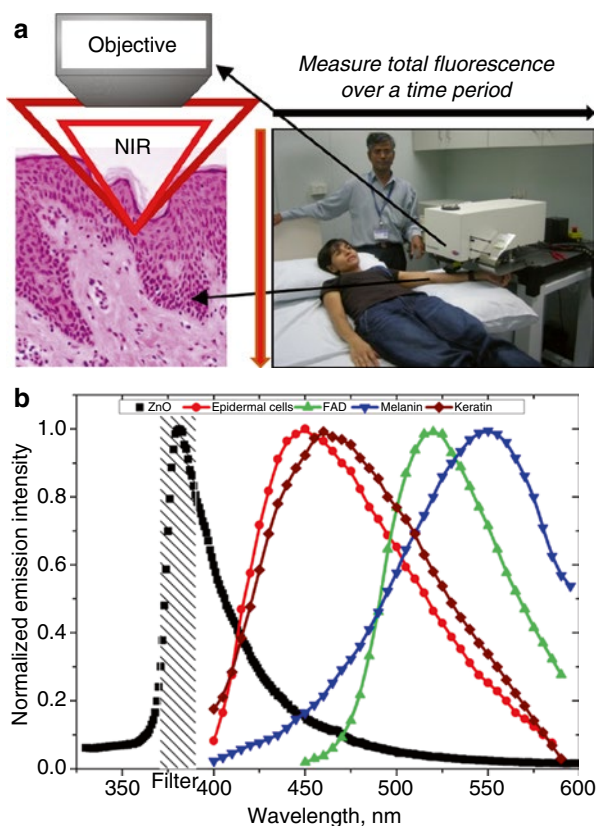
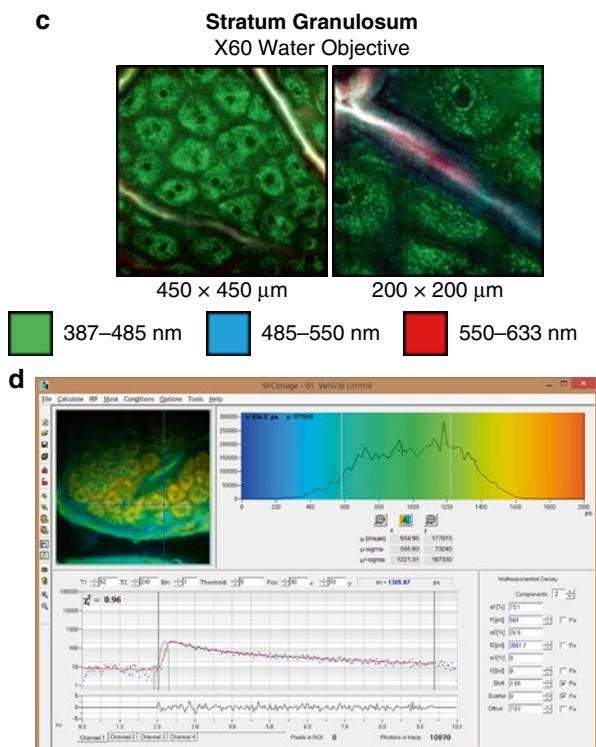


**Fig. 16.2** The processes of fluorescence imaging, spectral imaging, fluorescence lifetime and fluorescence lifetime imaging (FLIM). (a) Schematic of non-invasive multiphoton imaging and photograph of a volunteer being imaged with the DermaInspect® multiphoton microscope, equipped with fluorescence lifetime imaging; (b) Fluorescence emission spectra of various autofluorescence components and zinc oxide nanoparticles (Adapted from Zvyagin et al. (2008)); (c) Representative pseudo-colored images of human skin imaged with a multiphoton microscope at three spectral channels: 387–485 nm (green), 485–550 nm (blue), and 550–633 nm (red); (d) Representative pseudo-colored fluorescence lifetime image of human skin processed with SPCImage (Becker and Hickl)

**Fig. 16.2** (continued)



commercial CE approved instrument, the DermaInspect® whereby laser light may be focused in a plane below the surface of the skin of a volunteer and the reflected fluorescence intensity arising from fluorophores in the skin is measured in appropriate photomultiplier or other detection device (Fig. 16.2a, b). While reactive oxygen species (ROS)-associated photodamage can be induced using near-infrared light (NIR) for multiphoton microscopy, this is dependent on a number of factors including the length of exposure, laser intensity, wavelength, and pulse-length. Key factors such as laser and power and beam dwell time must be optimized to be below the published threshold for phototoxicity and minimal erythema dose for multiphoton imaging (Fischer et al. 2008). Clinical multiphoton microscopes such as the DermaInspect® fail to induce DNA damage or erythema in skin, relative to ultraviolet exposed skin, using the appropriate laser power settings for typical measurements (i.e. ~2 mW for the stratum corneum, ~30 mW for depths up to 100 μm) (König 2008).

There are a number of intrinsic molecules in the human skin that can be excited by light at various wavelengths. These molecules, in turn, emit fluorescence light at a range of different emission wavelengths and with a lifetime (Table 16.1). The Zeiss and other confocal/multiphoton devices typically deploy filter wheels/cubes or monochromator to provide spectral separation.

We have modified such a device to add a filter wheel to differentiate fluorophores with different spectral emission characteristics, a process often referred to as spectral imaging. We have described, as an application of that technique, the separation of the endogenous fluorophores in the skin from an externally applied physical

**Table 16.1** Excitation, emission, and fluorescence lifetime properties of autofluorescent compounds and proteins

Autofluorescent fluorophore	Excitation (nm)	Emission (nm)	State	Lifetime (ns)	Reference
NAD(P)H	720–780 (2P)	400–550	<i>Free</i>	0.39, 1.14	Gafni and Brand (1976), Lakowicz et al. (1992), Wakita et al. (1995), Niesner et al. (2004), Bird et al. (2005), Yu et al. (2012), Vergen et al. (2012)
			<i>Bound</i>	2.2–2.5	
FAD	720–900 (2P)	480–650	<i>Free</i>	40 <sup>a</sup> , 130 <sup>b</sup> , 2.0–2.8, 5.2	Nakashima et al. (1980), König and Riemann (2003), Skala et al. (2007b), Yu et al. (2012), Islam et al. (2013), Damayanti et al. (2013)
			<i>Bound</i>	0.08, 0.7, 1.7	
Melanin	720–880 (2P)	510–600		0.2, 0.5–1.9, 7.9	König and Riemann (2003), Yu et al. (2012), Dancik et al. (2013)
Retinol	700–830 (2P)	500 (max)	<i>Free</i>	1.75, 5.0	Collini et al. (2002), Zipfel et al. (2003)
			<i>Bound</i>	0.7, 3.6, 12	
Protoporphyrin IX (PPIX)	800 (2P)	590 (max)		5.2, 19	Schneckenburger et al. (1993), Wang et al. (2010)
Lipofuscin	366 (1P, max)	500–605 nm		0.3, 1.2, 4.8	Gaillard et al. (1995), Jung et al. (2010)
Keratin	750–900	400–600		1.4	Pena et al. (2005), Ehlers et al. (2007), Yu et al. (2012)
Elastin	700–740	570–590		0.2–0.4, 2.3–2.5	König and Riemann (2003), Zipfel et al. (2003), Yu et al. (2012)
Collagen	800 (SHG; 2P)	400 (SHG)		0	Yu et al. (2012)

<sup>a</sup>FAD monomer<sup>b</sup>FAD dimer

sunscreen, nano zinc oxide (Zvyagin et al. 2008; Roberts et al. 2008). As shown in Fig. 16.2c, the luminescent zinc oxide has a much lower emission peak wavelength than the various endogenous autofluorescent compounds in the skin. The use of a bandpass filter BP380 (which selectively allows the transmission of 372–388 nm fluorescence) enables the quantitation of the zinc oxide in the presence of other autofluorescent solutes and has been used to show that there is negligible penetration of topically applied zinc oxide in the viable epidermis. The epidermal fluorescence mainly arises from nicotinamide adenine dinucleotide (NADH), a coenzyme involved in redox reactions. It is often written as NAD(P)H, as its

fluorescence characteristics cannot be distinguished from another naturally occurring fluorophore, NADPH. It is also apparent that the various endogenous fluorophores in the skin also show different emission peak wavelengths. Figure 16.2c shows different images of the skin observed with a multiphoton microscope at three spectral channels for emission: 387–485 nm (green), 485–550 nm (blue), and 550–633 nm (red). As discussed later, the excitation wavelength in two-photon imaging is usually twice that associated with the single photon (confocal) excitation of a solute. The intensity of fluorescence emitted will depend on the concentration and environment of the NAD(P)H, the presence of other compounds also emitting in the same detection band, the intensity of excitation and the duration of emission collection. This variation in intensity can be used to provide a deep image of cells below the surface.

An alternative but complementary approach to spectral imaging is to recognize that a pure compound excited by light will emit photons that decay over time to define a lifetime distribution for that solute (Fig. 16.3). The presence of more than one solute or microenvironments in a small area will create a range of times the molecules of the fluorophores present remain within the excited state prior to decaying to its original energy state via the emission of photons of light. This range defines the lifetime distribution for solutes in that small area (Fig. 16.3) and enables a temporal resolution of solutes. The behavior of individual autofluorescence lifetime distribution for a given area and all of these lifetimes can also be mapped over a  $x$ ,  $y$  or  $x$ ,  $z$  space to give a spatial distribution. The collection of this spatial distribution in lifetimes is achieved using FLIM. The map of the spatial distribution of fluorescence lifetimes for each pixel captured within the field of view using fluorescence lifetime imaging (FLIM) is a valuable way to study such phenomena by confocal, multiphoton, wide-field microscopy or endoscopy (So et al. 1998; Becker et al. 2004). In the process of acquiring the spatial distribution map of lifetimes from a sample by FLIM microscopy, each pixel may contain the fluorescence from several components. These components may represent a single fluorophore in multiple physio-chemical states or multiple fluorophores in their physio-chemical states (Lakowicz et al. 1992; Vishwasrao et al. 2005; Islam et al. 2013). Examples of intravital intensity and FLIM maps are shown in Fig. 16.4.

The mean lifetime is the average time a molecule exists within an excited state following the absorption of energy from an exogenous source (e.g. photon of light) (Fig. 16.3a). The decay process of an excited molecule to its ground state can occur via several means including fluorescence (including fluorescence quenching and Förster (also called fluorescence) resonance energy transfer [FRET] (Förster 2012), phosphorescence, intersystem crossing and internal conversion (Fig. 16.3a). A key determinant of these processes is the environment in which the fluorophore is placed. Small solutes, such as L-tryptophan, phenol, hydroquinone, N-methylpicolinium perchlorate, and iodide, have, for instance, all be shown to quench the emitted fluorescence of fluorescein in solution (Watt and Voss 1979) in a manner similar to illustrated in Fig. 16.3c. Whilst most studies on fluorescence are concerned with the directed changes in fluorescence intensity or lifetime caused by a quencher (Fig. 16.3c, d), the change in fluorescence lifetime for a fluorophore in

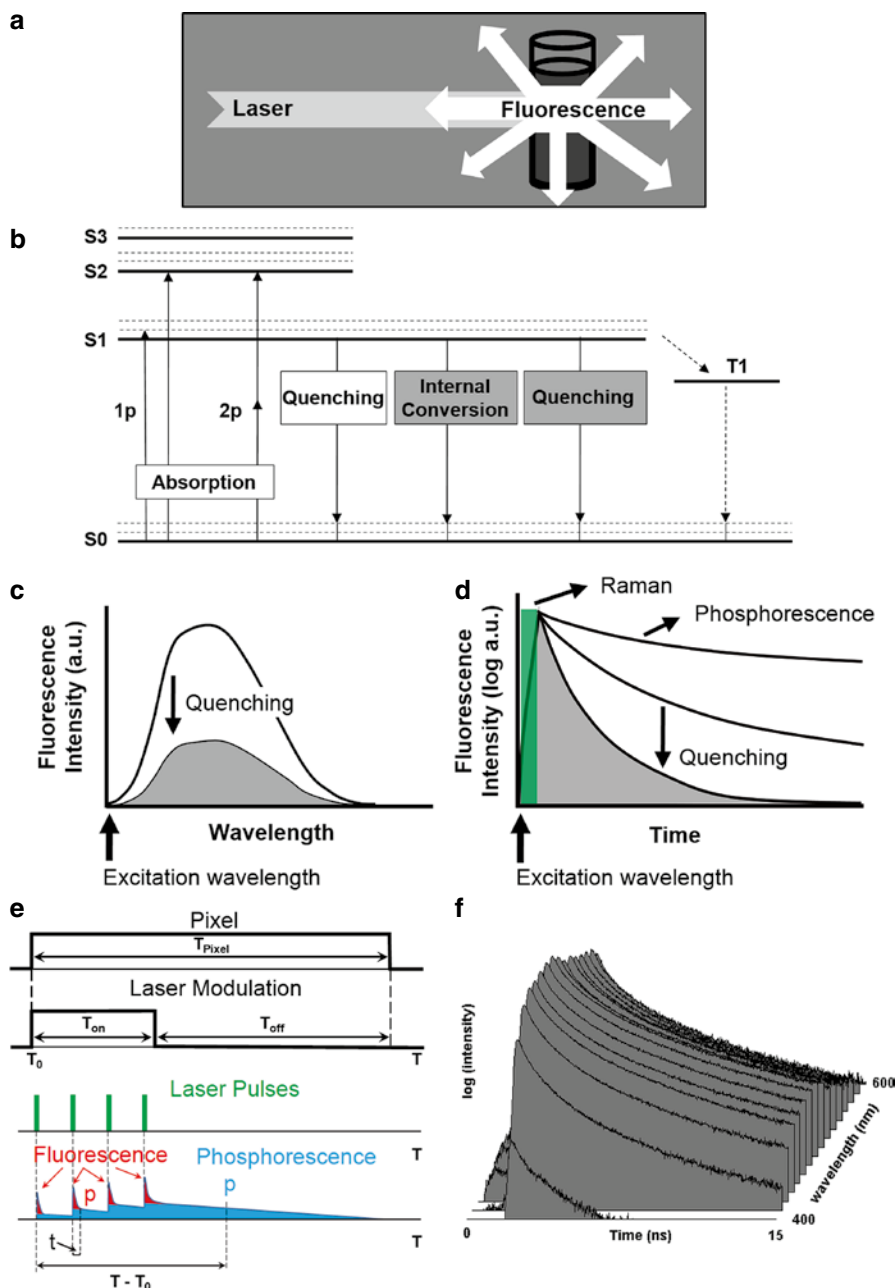


**Fig. 16.3** Processes of emission after exciting a fluorescent molecule (**a**, **b**), including quenching (**c**), fluorescence and phosphorescence lifetime decay curves (**d**) and acquisition modes (**e**) across multiple emission spectra (**f**) (Adapted from Becker (2005))

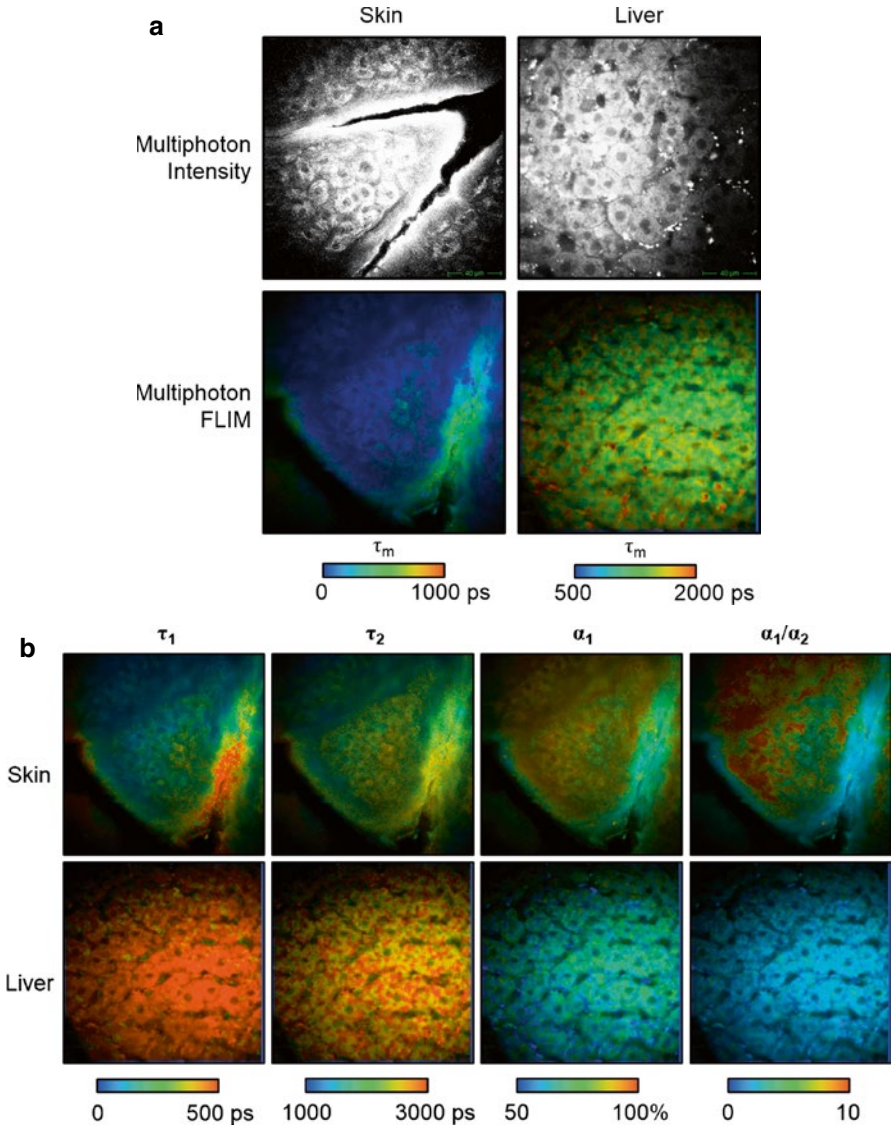


**Fig. 16.4** Examples of human skin and rat liver intravital intensity and FLIM maps. **(a)** Intravital multiphoton intensity images (*top*) and fluorescence lifetime pseudocolored images (*bottom*) of human skin (*left*) and rat liver (*right*). **(b)** Differences in fluorescence lifetime parameters ( $\tau_1$ ,  $\tau_2$ ,  $\alpha_1$ ,  $\alpha_1/\alpha_2$ ) between human skin (*top*) and rat liver (*bottom*)

the presence of an quencher will only equal that corresponding change in fluorescence intensity for a fluorophore by the quencher when the interaction can be described as strict collisional or dynamic quenching (Perrin 1929). In this situation, the quencher must interact with fluorophore by diffusing to it during the fluorophore's



excited lifetime state. The effect of the interaction is that the fluorophore does not emit a photon in returning to the ground state (Fig. 16.3d). This interaction is often expressed by the Stern-Volmer equation:

$$F_0 / F = 1 + K_{SV}Q \quad (16.1)$$

in which the fluorophore fluorescence divided by that in the presence of quencher concentration is related to 1 plus the product of a Stern-Volmer constant-  $K_{SV}$  (or measure of quencher affinity for fluorophore) and quencher concentration- $Q$ .  $K_{SV}$  equals  $k_q\tau_0$  where  $k_q$  is the bimolecular quenching rate constant (proportional to the sum of the diffusion coefficients for fluorophore and quencher) and  $\tau_0$  is the excited state lifetime in the absence of quencher. On the other hand, if the quencher binds with the fluorophore before excitation of the fluorophore, the resulting complex has non-fluorescent ground state and this is referred to as static quenching. In the case of static quenching, the lifetime of the sample will not be reduced since those fluorophores that are not complexed will have normal excited state properties (Weber 1948). Obviously, if a known quencher for a fluorophore does not interact with it when it is bound to a protein or in a membrane, we can deduce that the fluorophore is inaccessible to the quencher. By using quenchers that distribute into a given region of the protein or membrane, one can use the lack of or presence of a quenching interaction to define if the fluorophore is or not co-located. Oxygen is the best known quencher of almost all fluorophores. The iodide quenching referred to earlier possibly relates to an intersystem crossing to a triplet state and a slow emission, quenched by other processes. The decay time for each path varies taking femtoseconds for internal conversion, pico- and nanoseconds for fluorescence, and microseconds-seconds for phosphorescence (Ishikawa-Ankerhold et al. 2012). The fluorescence lifetime specifically refers to the time of a fluorophore remains excited prior to returning the ground state via fluorescence radiative and non-radiative decay (Chen and Periasamy 2003; van Munster and Gadella 2005).

The fluorescence lifetime of a fluorophore is a function of its physio-chemical properties. As a result, the lifetime is largely consistent regardless of the type of microscopy used to image a fluorophore or the excitation intensity, mode (i.e. single versus multiphoton), wavelength, or exposure time (Chen and Periasamy 2003). In addition the fluorescence lifetime is consistent irrespective of fluorophore concentration or intensity, given an adequate signal-to-noise ratio (Lakowicz et al. 1992). However, the fluorescence lifetime is subject to change as a result of physio-chemical alterations in the state of the fluorophore. Specifically, direct interactions with the fluorophore by other molecules and/or changes to the local environment (i.e. pH, ion concentration, temperature, refractive index of the medium, polarity) can alter the fluorescence lifetime (Becker et al. 2004; van Munster and Gadella 2005; Berezin and Achilefu 2010). As one example of these changes, we have measured the fluorescence lifetime of fluorescein under varying intravital conditions (Roberts et al. 2008). We showed differences in the fluorescence lifetime of fluorescein due to pH-dependent ionization of the dye in the bile versus other areas of the liver (Roberts et al. 2008). As a second example, the lifetimes of a fluorophore

probe (2,7-bis-(2-carboxyethyl)-5-(and-6)-carboxyfluorescein (BCECF) varies with pH (range: pH 4.5, 2.75 ns; pH 8.5, 3.90 ns) has been used to map the pH of uppermost layer of the epidermis (stratum corneum) over its pH range of 4.5–7.2 (Hanson et al. 2002). The pH maps suggest that the intra-corneocyte regions are close to neutral pH (average pH 6.7), whereas the intercellular region are more acidic (average pH 6.0) and the pH increases at greater distances from the stratum corneum surface. An important observation is that whereas the fluorescence intensity will decrease with increasing depth due to a reduced penetration, fluorescence lifetimes and FLIM yield concentration independent measurements of pH changes. More recently, fluorescence probes for both proton activity and hydration of stratum corneum were used to show that a mild synthetic cleanser mixture promotes stratum corneum hydration (Bloksgaard et al. 2013).

As shown in Fig. 16.3f, the fluorescence lifetime of a sample can vary with the emission wavelength, due to the selective excitation of the physio-chemical states of a single fluorophore and/or multiple fluorophores at various wavelengths. Specific emission wavelength bands alone or in combination with spectral imaging can be used to distinguish between a heterogeneous mix of fluorophores, their physio-chemical states and potential interactions with other molecules. The tissue autofluorescence, studied using intravital microscopy emission spectra (Fig. 16.4a) and FLIM mapping (Figs. 16.4b and 16.5a–b) has been used to discriminate normal and diseased tissue (König 2012) along with the localization of fluorescent diagnostic or therapeutic agents and their metabolites. The individual parameters that can be measured of a bi-exponential decay curve (individual lifetimes:  $\tau_{1/2}$ , lifetime amplitude coefficient:  $\alpha$ , ratio of amplitude coefficient  $\alpha_1/\alpha_2$ ) are demonstrated from intravital skin and liver FLIM imaging in Fig. 16.4. Individual lifetime parameters can be aggregated, which is described Sect. 16.4.1.

A relatively technique, phosphorescence lifetime imaging, can be used to take advantage of the longer lifetime properties of certain dyes, drugs and nanoparticles to isolate their signal from background fluorescence. For example, topically applied zinc oxide nanoparticles display a distinctive phosphorescence lifetime signal that can be isolated due to the absence of a significant background endogenous phosphorescence signal (Fig. 16.5b). Moreover, both the fluorescence and phosphorescence signal can be measured simultaneously on excised tissue and for intravital imaging.

## 16.3 FLIM Techniques

A fluorescence lifetime imaging (FLIM) technique for biological imaging has to combine high photon efficiency, high lifetime accuracy, resolution of multi-exponential decay profiles, simultaneous recording in several wavelength intervals and optical sectioning capability.

There is a number of different techniques to detect the fluorescence lifetime, and to combine fluorescence lifetime detection with imaging. The techniques can be

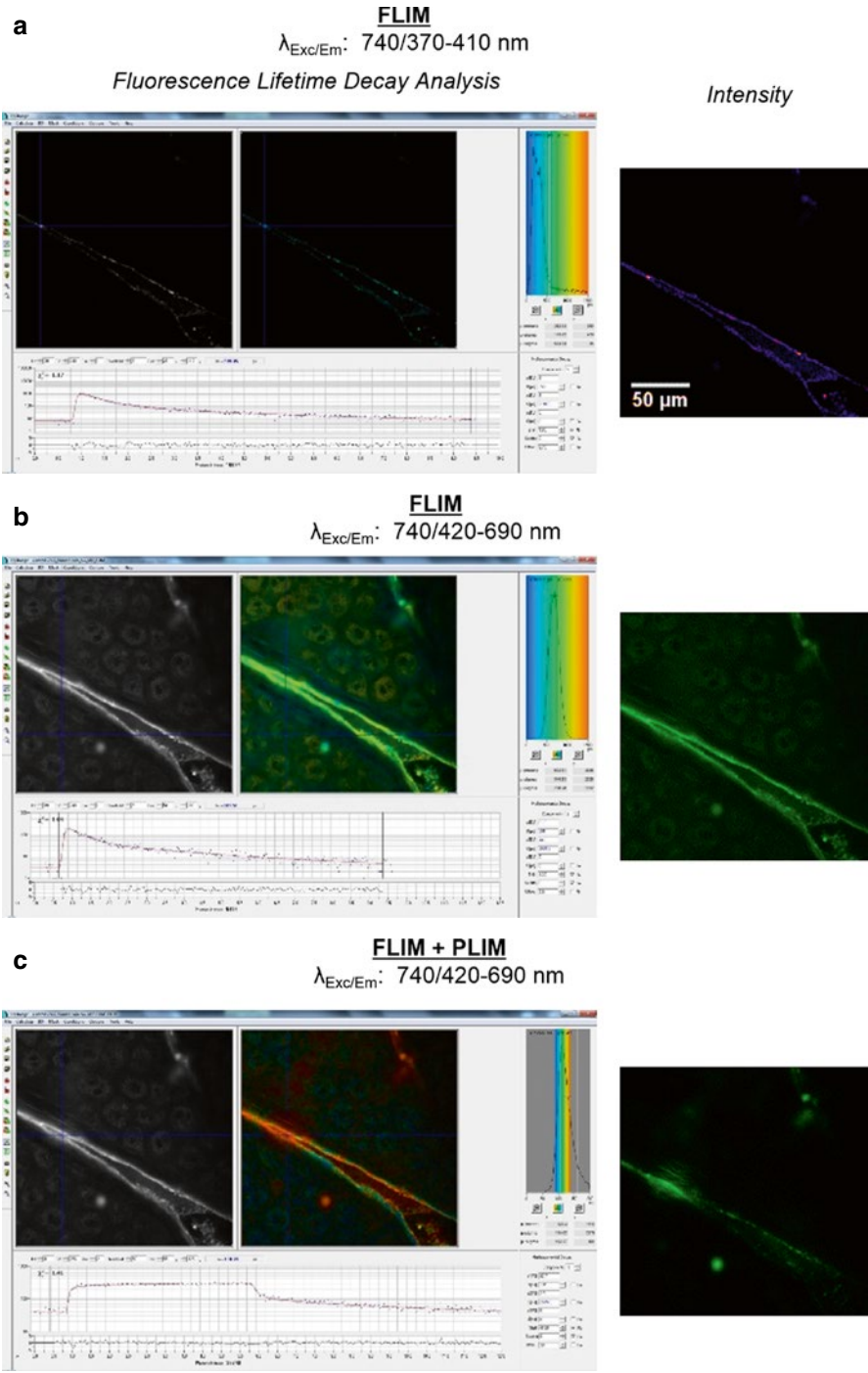


**Fig. 16.5** Multispectral fluorescence (a, b) and phosphorescence (c) lifetime imaging of the viable epidermis of human skin

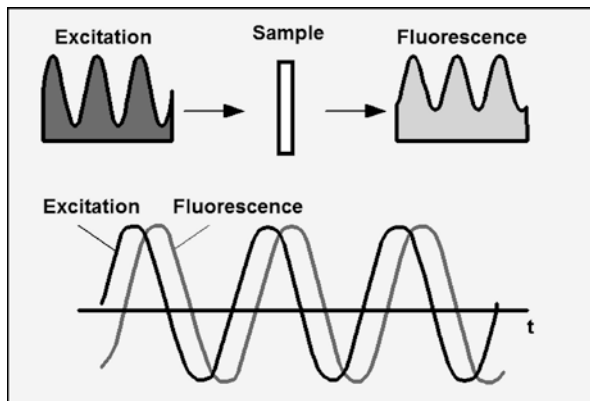
classified into time-domain and frequency-domain techniques, photon counting and analog techniques, and point-scanning and wide-field imaging techniques. It also matters whether a technique acquires the signal waveform in a few time gates (Buurman et al. 1992) or in a large number of time channels (Becker et al. 2004), and whether this happens simultaneously (Buurman et al. 1992; Becker 2005), or sequentially (Dowling et al. 1997; Straub and Hell 1998). Virtually all combinations are in use. This leads to a wide variety of instrumental principles. Different principles differ in their photon efficiency, i.e. in the number of photons required for a given lifetime accuracy (Ballew and Demas 1989; Köllner and Wolfrum 1992; Gerritsen et al. 2002; Philip and Carlsson 2003), the acquisition time required to record these photons, the photon flux they can be used at, their time resolution, their ability to resolve the parameters of multi-exponential decay functions, multi-wavelength capability, optical sectioning capability, and compatibility with different imaging and microscopy techniques. Please see (Becker and Bergmann 2008) or (Becker 2012a) for an overview.

### 16.3.1 Time Domain FLIM

Techniques commonly used in time-domain FLIM are gated image intensifiers (Dowling et al. 1997; Straub and Hell 1998) and multi-dimensional TCSPC (Becker 2005). Gated image intensifiers have the advantage that they acquire data in all pixels of the image simultaneously. However, they have to acquire the temporal profiles sequentially, i.e. by scanning a gate over the decay functions. Because there are usually more pixels in the image than time channels in one pixel image intensifiers are able to achieve short acquisition times. The disadvantage is that the gating results in low photon efficiency. The total exposure of the sample is therefore large. Moreover, there is no inherent depth resolution. The lifetime data are therefore contaminated by out-of focus signals. Gated image intensifiers have therefore been combined with structured illumination techniques (Cole et al. 2001). However, this further decreases the photon efficiency.

Multi-dimensional TCSPC is based on scanning the sample by a high-repetition rate laser and the detection of single photons of the fluorescence signal. Each photon is characterized by its time in the laser period, its wavelength, and the coordinates in the scanning area. The recording process builds up a photon distribution over these parameters. The result can be interpreted as an array of pixels, each containing a full fluorescence decay curve or several fluorescence decay curves for different wavelength. The technique can be modified to record fast dynamic changes in the fluorescence lifetime along a one-dimensional scan, or to simultaneously record phosphorescence and fluorescence lifetime images. The advantage of TCSPC is that it works at near-ideal photon efficiency and delivers an extremely high time resolution. Moreover, the scanning technique allows the photons to be detected from an accurately defined focal plane in the sample only. TCSPC FLIM data are therefore not contaminated by out-of-focus blur. It can be almost ideally combined with multiphoton microscopes, and is thus able to obtain clear lifetime images of deep tissue layers.

**Fig. 16.6** Frequency-domain FLIM. The fluorescence lifetime is derived from the decrease in the modulation degree and from the phase shift between the fluorescence and the excitation



Time-domain FLIM permits the direct measurement of the decay curves in the individual pixels based on the detected arrival time of a single emission photon following a pulse of excitation light (femtosecond pulse-width) (Becker and Bergmann 2008). This data is captured at high resolution, involves repeated measurements to capture a sufficient quantity of photons to generate an accurate portrait of the decay curve across the time domain. The key advantage of the time domain method is that it permits the direct measurement of the decay curve, which is fit into an exponential function according to the number of components, assessed by determining the goodness of fit by Poisson statistics. In practice, only a maximum of two to three components can be resolved. The fluorescence lifetime from a pixel, and subsequently its amplitude coefficient, is calculated from the slope of the fitted exponential decay curve, described by Eq. 16.2:

$$F(t) = \sum_{i=1}^n a_i e^{-t/\tau_i}, n \geq 1 \quad (16.2)$$

where  $\tau_i$  is the fluorescence lifetime of the  $i_{th}$  component or specie and  $a_i$  represents the amplitudes of the exponential components. In practical, multi-exponential decay profiles are common in fluorescence lifetime spectroscopy of biological samples. The instrument response function represents the photons from the excitation pulse scattered from a non-fluorescent sample that yields second harmonic generation (e.g. sugar, collagen) with a zero-value lifetime.

### 16.3.2 Frequency Domain FLIM

Frequency-domain FLIM records differences in the phase and the modulation degree between a modulated or pulsed excitation and the fluorescence signal (Fig. 16.6). These values are either translate into the fluorescence lifetime, or used directly by phasor plot analysis, see ‘Data Analysis’.

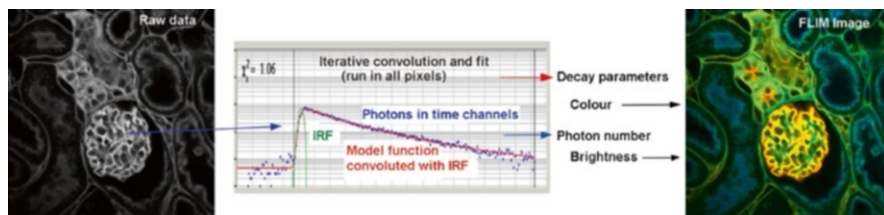


**Fig. 16.7** Time-Domain FLIM data analysis. The raw data (*left panel*) are images containing lifetime decay information in each pixel. The parameters of fluorescence lifetime decay are determined first de-convolution to exclude IRF, then fitted to multiple exponential curves. The *color coded image* representing one of the decay parameter (Adapted from Becker (2012a))

Detection of frequency-domain FLIM data is possible by wide-field-excitation and a gain-modulated camera (Lakowicz and Berndt 1991), or by confocal or multiphoton scanning techniques and detecting the fluorescence by gain-modulated point-detectors (Gratton and Barbieri 1986). In both cases the gain in the detection signal path is modulated by an oscillator frequency,  $f_{osc}$ , slightly different from the laser pulse or modulation frequency,  $f_{laser}$ . The phase shift and the amplitude of the fluorescence signal then transfer into a signal at the difference frequency,  $f_{laser} - f_{osc}$ . This is the same ‘heterodyne’ principle as it is used in a radio. The advantage is that the different frequency can be made independent of and much lower than the modulation frequency. The phase and the amplitude are determined at the difference frequency where filtering and signal processing can be performed by digital techniques.

Frequency-domain FLIM treats the fluorescence signal as an analog waveform, not as individual photon detection events. It is therefore able to work at extremely high intensities, where single photon detection becomes impossible. Problems may occur at extremely low intensities, when the detector on average delivers less than one photon within the time interval of the phase calculation. What then happens depends on the details of the electronics used. Both the modulation of the excitation light and the modulation of the detectors need not be sinusoidal. The best efficiency is obtained by using short laser pulses, and by modulating the detectors by square-wave signals (Philip and Carlsson 2003).

## 16.4 FLIM Data Analysis

### 16.4.1 Time Domain Data

Time-domain FLIM data are arrays of pixels each of which contains a (usually large) number of intensity values (or photon numbers) for consecutive times after the excitation pulse, see Fig. 16.7, left and middle. The photon numbers in the consecutive channels represent the shape of the measured fluorescence decay function.



This shape is the convolution of the true fluorescence decay function with the instrument response function, IRF.

$$f_m(t) = \int_{\tau=0}^t f(\tau) IRF(t-\tau) d\tau \quad (16.3)$$

where  $f_m(t)$  is the measured fluorescence function, while  $f(t)$  is the true fluorescence decay function. The IRF is the signal shape the system would record for an infinitely short fluorescence lifetime, mathematically, it is the convolution of the laser pulse shape with the detector response. It contains the temporal response function of the detector, the temporal response function of the recording electronics, and the shape of the excitation pulse. The IRF can either be measured or calculated from the fluorescence decay data themselves (Becker 2012b).

The common way to analyse such data is an iterative de-convolution process. The function of a suitable decay model is convoluted with the IRF. The fit procedure then optimises the model parameters until the best fit to the photon numbers in the time channels is achieved. The principle is in use for analysis of single fluorescence decay curves for many years (O'Connor 1984). For FLIM, the fit procedure has to be repeated for all pixels of the image.

The simplest decay model is a single exponential function. It is described by a single decay time. In most cases, however, fluorescence in biological systems contains several decay components of different lifetime. To extract the full information from such decay profiles models containing two or three exponential functions must be used. The fit procedure then delivers several decay times and amplitude coefficients as shown in Eq. 16.2. Amplitude-weighted or mean lifetime  $\tau_m$  is determined by:

$$F(t) = \sum_{i=1}^n a_i e^{-t/\tau_i}, n \geq 1 \quad (16.2)$$

where

$$\sum_{n=1}^i a_i = 1 \quad (16.4)$$

The final FLIM image is obtained by assigning the brightness to the total photon number in the pixel, and the colour to a selected decay parameter (Fig. 16.7, right). This can be the lifetime of a single-exponential decay, an amplitude- or intensity-weighted average of the lifetimes in a multi-exponential decay, a ratio of lifetimes or amplitudes, or a FRET efficiency.

Fluorescence lifetimes can also be obtained by calculating the first moment of the fluorescence waveform. The first moment of the waveform represents the average arrival time of the photons (Liebert et al. 2003) after the excitation pulses (Eq. 16.5).

$$\tau_m = M_1 = \int t N(t) dt / N \quad (16.5)$$

where  $N = \int N(t)dt$  represents total photon number in trace or total fluorescence (Becker and Bergmann 2006; Roberts et al. 2011). It is linearly related to the fluorescence lifetime of a single-exponential decay: The lifetime is the difference of the first moments of the decay curve and the IRF. The advantage of moment analysis is that it avoids any numerical instability and automatically delivers the lifetime at an ideal signal-to-noise ratio. The disadvantage is that it delivers systematic errors if the data contain background light or if the decay function does not drop all the way to zero in the time interval recorded. Procedures calculating lifetimes from only two, three, or four time intervals can be considered a variation of the moment technique (Gerritsen et al. 2002). Using the aggregate lifetime parameter  $\tau_m$  (Eq. 16.5), a general overview of the change in lifetime and relative contribution of each parameter can be measured. However, variants of this approach have been described such as the ‘mean NADH lifetime’ (Eq. 16.6), which has been used to compare the redox state of normal versus pre-cancerous tissue (Skala et al. 2007b):

$$\text{mean NADH lifetime} = (\alpha_1 \times \tau_1) + (\alpha_2 \times \tau_2) \quad (16.6)$$

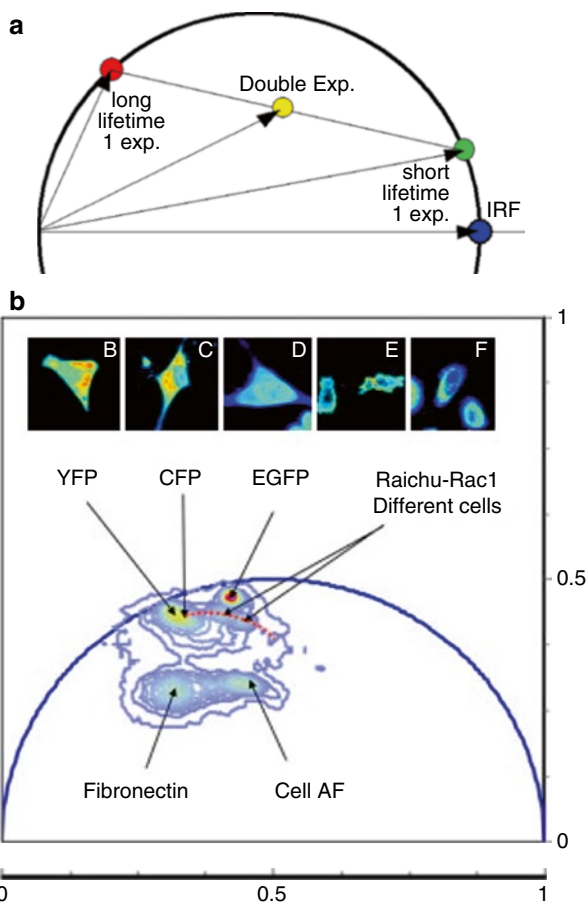
Time-domain analysis has been extended by ‘multi-parameter’ analysis (Weidtkamp-Peters et al. 2009). This technique builds up two-dimensional histograms of pixel frequencies over several decay parameters obtained in one detection channel, or decay parameters and intensity ratios obtained in different detection channels. In these histograms, signatures of fluorophores or fluorophore fractions can be found, marked, and the corresponding pixel be back-annotated in the images.

### 16.4.2 Frequency Domain Data

Frequency-Domain data contain two numbers in each pixel: A phase and a modulation degree. Such data can be analysed elegantly by the ‘Phasor’ approach (Digman et al. 2008). Phasor analysis does not explicitly aim on determining fluorescence lifetimes or decay components for the pixels. Instead, it uses the phase and the modulation degree directly. For each pixel, a pointer (the phasor) is defined and displayed in a polar plot. The phase is used as the angle of the pointer, the modulation degree as the amplitude. The end points of the phasors of all pixels are combined in a single ‘phasor plot’. The phasor plot has several remarkable features:

- The phasors of pixels with single-exponential decay profiles end on a semicircle. The location on the semicircle depends on the fluorescence lifetime (Fig. 16.8a).
- Phasors of pixels with multi-exponential decay profiles, i.e. sums of several decay components, end inside the semicircle. Combinations of different lifetimes are on a straight line between the phasors of the components (Fig. 16.8b).

**Fig. 16.8** Phasor analysis. (a): Principle. (b): Five different cells, transfected with (B) YFP, (C) paxillin-CFP, (D) EGFP, and (E) RAICHU-Rac1. (F) is an untransfected cell emitting only autofluorescence (From Digman et al. (2008)). [Copyright permission being sought]



- Phasors of decay profiles which result from the convolution of several processes end outside the semicircle. An example is the emission of a FRET-excited acceptor, which is the convolution of the decay function of the interacting donor with the fluorescence decay of the acceptor.

Pixels with different signature in the phasor plot are then back-annotated in the image by giving them different colours. A practical example is shown in Fig. 16.8b. It shows a phasor plot for several cells, B to F, shown at the top of the figure. The cells were transfected with (B) YFP, (C) paxillin-CFP, (D) EGFP, and (E) RAICHU-Rac1. (F) is an untransfected cell. As can be seen in the lower part of the figure, the fluorophores form different spots in the phasor plot, as does the autofluorescence of the untransfected cells. Note that all spots are inside the semicircle, i.e. none of the fluorophores delivers a perfectly single-exponential decay in the cell environment.

Phasor analysis is not restricted to data obtained in frequency-domain systems. It can be applied to Fourier-transformed time-domain data as well (Digman et al. 2008).



**Fig. 16.9** Clinical multiphoton microscope that can be equipped with TCSCP FLIM (From König (2012)). [Copyright permission being sought]

## 16.5 Intravital FLIM Instrumentation

For the most part, intravital fluorescence lifetime imaging has been restricted to the benchtop microscopes, using custom and/or specialized equipment to obtain an optimal image from the target tissues of mice and rats. For human intravital imaging, one of the most notable systems is the DermaInspect® (Fig. 16.2a) multiphoton microscopy equipped with TCSPC FLIM. The DermaInspect® has been used to perform numerous intravital FLIM studies of human tissue (König et al. 1999; König and Riemann 2003; Leite-Silva et al. 2013), typically for examining transdermal penetration of nanoparticles and skin metabolism (Roberts et al. 2008, 2011; Prow et al. 2012; Leite-Silva et al. 2013; Sanchez 2013). Initially the DermaInspect®, like most microscopy systems, was a fixed imaging station where volunteers and patients are imaged at various locations on the body. This system was also compatible for traditional intravital animal imaging using dedicated objective interfaces for humans and animals. One drawback of this system is that certain locations are extremely difficult to image due to accessibility and space constraints. With the advent of the MPTFlex DermaInspect® (Fig. 16.9), the objective head is attached to a flexible arm that can be easily manipulated to image any site on body with minimal disruption to the volunteer/patient (Speicher et al. 2010; Koehler et al. 2011; König 2012). This system can also accommodate a GRIN (gradient index) lens specifically for intravital imaging of both animals and humans (König 2008; Wang et al. 2010). The GRIN microendoscope has a high numerical aperture and long working distance as well as reduced aberration that is ideal for intravital imaging of organs and tissues in small animals.

Endoscopic probes have been adapted for intravital FLIM imaging. Both frequency- and time-domain techniques are used for endoscopic FLIM. One of the earliest reported usage of FLIM endoscopy used the frequency-domain technique

for intravital human imaging (Mizeret et al. 1997). While this system measured at a video rate, there were a number of limitations including a very low pixel resolution (i.e.  $32 \times 32$  pixels) and the analytical assumption of a single-exponential decay curve (i.e. the presence of only one lifetime component).

The next developmental step saw the creation of a time-domain FLIM endoscope, which was a flexible fiber-bundled endoscope (Siegel et al. 2003). For time-domain FLIM analysis, a stretched exponential (Kohlraush-Williams-Watts) function was used, under the assumption that there is a continuous set of lifetime components in a biological sample rather than a discrete number expressed as single- or a fixed number of multi-exponential components, to model lifetime data from human tissue. One advantage of this system was the use of a low cost pulsed diode laser for sample excitation to keep the overall cost of the instrument down. However, the long imaging acquisition time proved to be a practical limitation (Siegel et al. 2003). A similar system was also used to develop a rigid arthroscope for FLIM imaging (Requejo-Isidro et al. 2004). Montro et al. published the use of a flexible and high-speed (i.e. video) frequency-domain FLIM endoscope, using gated-optical image intensifiers (Munro et al. 2005), which was a substantial improvement over the first-generation frequency-domain FLIM endoscopes (Mizeret et al. 1997).

A side-viewing FLIM endoscope, fiber bundled, was reported with compatibility with flexible endoscopic probes as well as intravascular catheters (Elson et al. 2007). This system used a gated microchannel plate image intensifier, coupled to a flexible fiber bundle, with a GRIN lens objective on the endoscope head. Interestingly, to fit the measured FLIM data, a Laguerre polynomial analysis was chosen due to computational advantages over traditional multi-exponential fitting. More on this technique can be read (Jo et al. 2005). A major advantage of this system was the ability to resolve lifetimes across multiple spectral channels. However, as with other endoscopic FLIM systems, lengthy acquisition time along with artefacts from sample-movement were some of the limitations encountered (Elson et al. 2007). This system was also used for intravital FLIM endoscopy of human patients to discriminate normal tissue from glioblastoma multiforme (Sun et al. 2010) and oral carcinoma (Sun et al. 2013) tissues. Interestingly, while both cancerous tissues displayed a weaker tissue autofluorescence, the former displayed a longer NAD(P)H lifetime compared to normal tissue while the latter displayed a shorter lifetime. Despite these differences, intravital FLIM endoscopy proved to be an effective tool to distinguish normal and cancerous tissues.

Wide-field FLIM is perhaps the most attractive application of intravital FLIM imaging in terms of cost and simplicity for instrumentation and data analysis. Wide-field FLIM can be effectively deployed for intravital imaging for cutaneous diagnostics and intraoperative purposes. Unlike benchtop microscope systems and endoscopic FLIM, which operates within a sub-mm field-of-view, wide-field FLIM assembles a spatial map of fluorescence lifetimes on a macroscopic scale. Wide-field FLIM microscopes use a multi-channel plate or CCD/CMOS detector for measuring the fluorescence emission of biological samples, excited by a solid-state laser- or light emitting diode (Esposito et al. 2005; Galletly et al. 2008; Colyer et al. 2009).

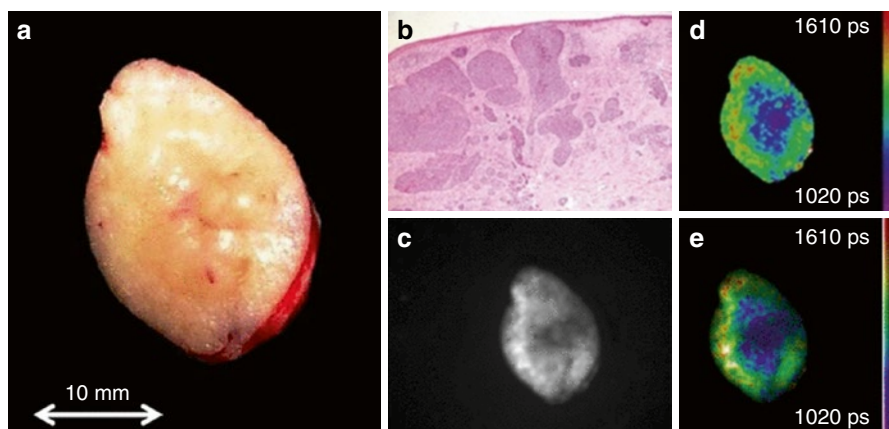


**Fig. 16.10** Wide-field FLIM of a human excised skin biopsy of suspected BCC lesion. (a) Color photograph of the excised skin biopsy. (b) Histopathology of the excised skin biopsy stained with haematoxylin and eosin (H&E). (c) Autofluorescence image of the biopsy, excited at 355 nm, filtered through a 375 nm long pass filter. Pseudocolored lifetime image of excised skin biopsy (d), and with intensity weighting (e) (From Galletly et al. (2008)). [Copyright permission being sought]

The utility of intravital wide-field FLIM was demonstrated in principle by examining the autofluorescence lifetime differences between normal and basal cell carcinoma (BCC) lesion within a human excised skin biopsy (Galletly et al. 2008). A 355 nm pulsed ultraviolet laser (80 MHz) was used to excite the skin biopsy sample via a holographic diffuser connected by a fiber optic cable. The resulting autofluorescence emission was filtered through either a 375 nm or 455 nm long pass filter prior to entering a gated optical image intensifier (GOI), coupled to a CCD camera for recording. The GOI permits snapshots of the fluorescence emission to be taken over time (i.e. 1,000 ps snapshots every 250 ps for 25 time points, acquisition time: ~20 s per sample) to generate the fluorescence decay curve. The fluorescence lifetime data was fit either to a single-exponential or stretched exponential model, as described earlier, to construct a pseudocolored image according to the average fluorescence lifetime of each pixel. The data showed remarkable discrimination between normal, non-cancerous tissue and the BCC lesion (Fig. 16.10), which was validated by traditional H&E histopathology.

A novel scanning-less implementation of wide-field FLIM was reported whereby single-photon counting of the fluorescence emission was recorded by a photon-multiplier (Spitz et al. 2008). Sample excitation was achieved using a pulsed (4 MHz) single-photon Ti:sapphire laser, which was tunable between 430 and 500 nm. The resulting emission was spectrally filtered before being further divided according to both horizontal and vertical polarization components, which were recorded simultaneously on the TCSPC photo-multiplier. The resulting average fluorescence lifetime for each pixel was calculated based on the delay between the laser pulse and arrival of the photons to the detector. Although this study did not examine any biological samples *in vivo*, the unique implementation of wide-field



FLIM to simultaneously record the fluorescence lifetime and time-resolved anisotropic lifetimes is a proof-of-principle for its potential application in intravital imaging.

For an intraoperative setting, wide-field FLIM microscopy should be capable of robustly measuring lifetime parameters at video frame rates. Substantial progress has been made on this goal using the existing a solid-state laser diode laser source, for UV excitation at 355 nm at high repetition rates (80 MHz), with emission fluorescence spectrally filtered and collected via a GOI coupled to a CCD camera (McGinty et al. 2010). The fluorescence emission can be recorded in the standard approach, whereby FLIM acquisition takes  $\sim 20$  s, or at a ‘rapid’ rate to achieve acceptable video frame rates while maintaining sufficient lifetime resolution of the sample (Fig. 16.11). However, one limitation of the latter approach is the level noise measured. Despite this, rapid lifetime measurements successfully contrasted normal and cancerous human pancreatic tissue obtained from surgical resection (McGinty et al. 2010). As with many of the systems presented here, the acquisition of lifetime data to detect disease states from excised tissue samples is a proof-of-principle for this technique to be used for intravital applications.

Promising developments have been made using the phasor technique to analyse FLIM data acquired from time-domain wide-field FLIM. The advantages of this approach include a rapid data processing time, which is compatible with video frame rates, and the ability to easily resolve multiple lifetime components. Typically, phasor-based wide-field systems employ high spatial, high temporal resolution, and high throughput 3D detectors (H33D) for single-photon counting (Colyer et al. 2009, 2012). The excitation sources generated pulsed laser light to illuminate the sample, with fluorescence emission relayed by a series of mirrors and filters (according to the desired spectral range) to the H33D detector. Emission photons from the sample are firstly converted to photoelectrons, via a photocathode, prior to penetration through a series of three microchannel plates (MCP). Following passage through the MCPs, the amplified photoelectron signal fire to a position-sensing anode to generate  $x, y$  coordinates of the initial photon of light. Time-to-digital converters (TDC) are used to measure: (1) the coarse timing information (macrotime  $T$ ) to determine spatial position of electrons contacting the position-sensing anode, and (2) the time between the MCP output pulse and the subsequent laser pulse (nanotime  $\tau$ ). The nanotime  $\tau$  parameter for each pixel is used to generate the phasor plot ( $g, s$  coordinates) of the sample, whereby multiple lifetime components can be visualized. Phasor analysis of sample fluorescence can be calculate rapidly permit wide-field FLIM video for intravital imaging.

## 16.6 FLIM of Tissue Autofluorescence

The long-standing approach for assessing the toxicity and disease progression of tissue is histopathology. A sample is obtained via biopsy prior to fixation and staining to visualize the morphology of the cells and tissue structures. Furthermore, a

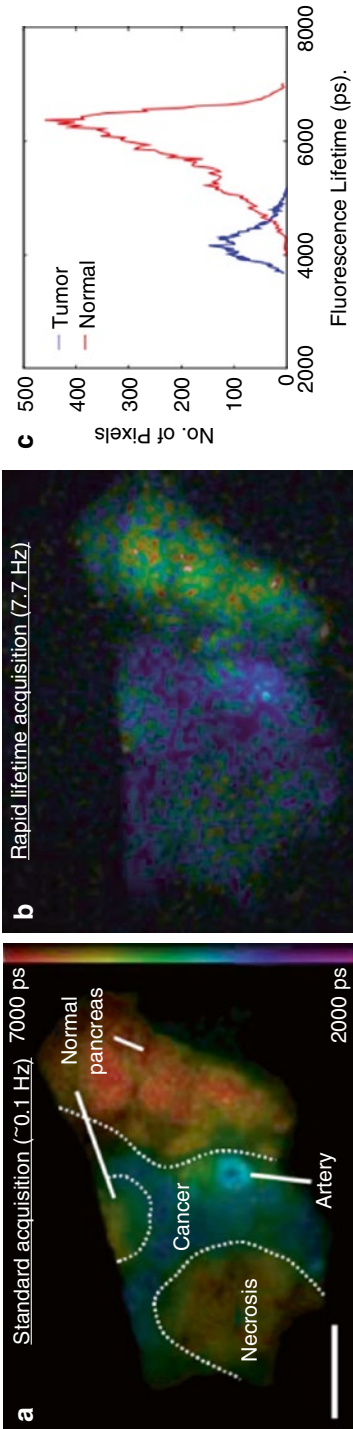


**Fig. 16.11** Wide-field FLIM: standard (a) versus rapid (b) lifetime acquisition. Representative pseudocolored FLIM images (a, b) with corresponding lifetime histograms (c) are displayed (From McGinty et al. (2010)). [Copyright permission being sought]

variety of stains and antibodies can be used to contrast specific cell types, proteins, lipids and messenger RNA, to name a few. While this approach can be very informative, it has several disadvantages including physical discomfort experienced by the patient during the biopsy procedure, tissue destruction, time and cost for sample processing and analysis.

Many of these use-cases can be achieved through intravital microscopy with FLIM for label-free analysis of tissue autofluorescence. Tissue autofluorescence is best resolved using two-photon microscopy, whereby simultaneous absorption of two near-infrared photons of light are used to excite a fluorophore at the energy level equivalent to half the wavelength of an incident photon. Excitation sources such as the tunable Titanium:Sapphire multiphoton laser have an excitation range between 720 and 920 nm (two-photon) with a pulse frequency of 80 Mhz. The excitation range can be widened through the use of an optical parametric oscillator, extending the maximum two-photon excitation wavelengths up to 1,300 nm (König 2012).

Various autofluorescent fluorophores in cells and tissues can be excited using multiphoton microscopy including nicotinamide adenine dinucleotide (NADH and its reduced phosphorylated form NADPH), flavin adenine dinucleotide (FAD), elastin, melanin, collagen (via SHG), porphyrins, lipofuscin, and keratin. The addition of FLIM permits the analysis of these fluorophores in their various physio-chemical states as a result from microenvironment changes or direct interactions with other molecules or proteins.

### ***16.6.1 Autofluorescent Fluorophores Involved in Cell Metabolism***

Two of the most key autofluorescent molecules for metabolic FLIM analysis are the cofactors NAD(P)H and FAD. Both molecules are central components of the intracellular metabolic and redox regulatory pathways. Figure 16.12 shows the involvement of both NAD(P)H and FAD in the energy production by glycolysis (cytosolic) and aerobic respiration (mitochondria) within the cell.

NAD(P)H is also involved in the regulation of apoptosis, reductive biosynthesis, cell signaling, antioxidation and biosynthesis. The most studied physio-chemical states of NAD(P)H using FLIM are in its free and protein bound forms (bi-exponential decay curve), which corresponds to lifetimes of ~0.39 and 2.2–2.5 ns respectively (Table 16.1). Both free and protein bound NAD(P)H can be easily resolved at a two-photon excitation wavelength of 740 nm and emission peak at 460 nm (Yu et al. 2012). FLIM analysis of the free and protein bound lifetimes, and relative contributions, are typically achieved with a biexponential decay model. The oxidized forms of NAD(P)H, NAD<sup>+</sup> and NADP<sup>+</sup>, do not exhibit fluorescence (Heikal 2010).

FAD is a redox cofactor and like NADH, an intracellular electron transporter and critical component of several metabolic pathways (Heikal 2010). In contrast to NAD(P)H, only the oxidised form of FAD is fluorescent and displays multiple lifetime components based on protein binding. The lifetime is reported to be

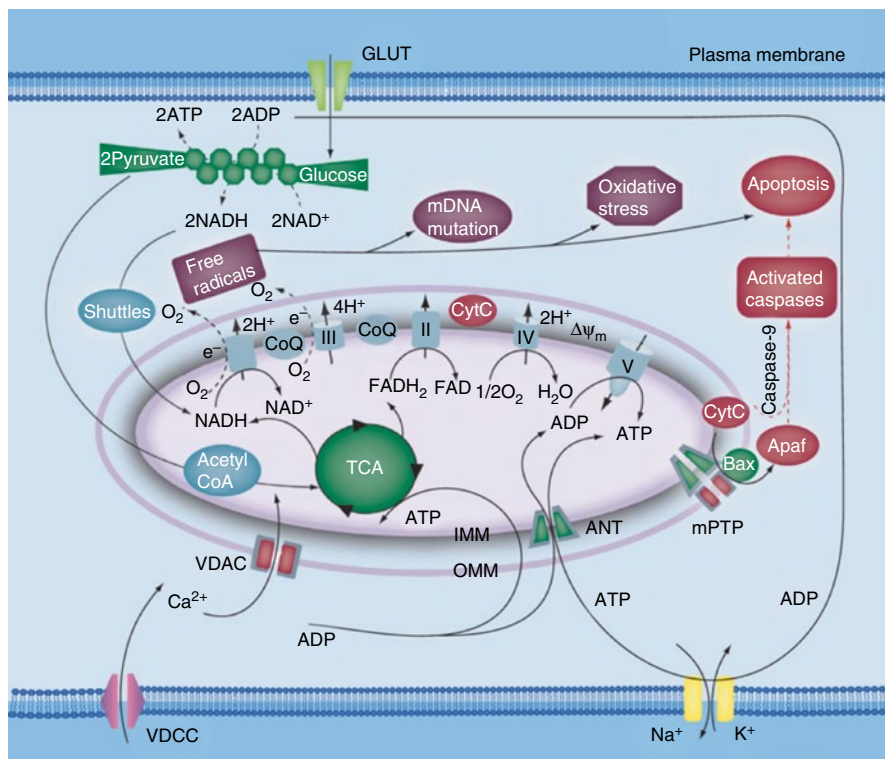


**Fig. 16.12** NAD(P)H and FAD involvement in glucose-related bioenergetics pathways (From Heikal (2010)). [Copyright permission being sought]

approximately ~2.0–2.8 ns for free FAD, and shorter lifetime component of ~0.7 ns for protein-bound FAD. FAD is excited at 730–740 nm and emits at a peak wavelength of ~520–550 nm (Kao et al. 2008; Yu et al. 2012).

### 16.6.2 Autofluorescent Fluorophores

Melanin refers to an aggregate of molecules within the melanin family of compounds (e.g. pheomelanin, eumelanin, neuromelanin) responsible for tissue pigmentation, UV filtering and reactive oxygen species scavenging. Melanin has an ultrafast energy conversion of absorbed UV light into heat and other chemical reactions due to low scattering and a highly efficient capacity to dissipate UV radiation via nonradiative means (99.9 %) (Meredith and Riesz 2007). A two-photon excitation wavelength between 720 and 880 nm can excite melanin, which has a broad emission range (peak at ~580 nm) (Yu et al. 2012) and multiple lifetimes of approximately 0.2, 0.5–1.9 and 7.9 ns (Table 16.1).

Porphyrins are organic aromatic molecules predominantly responsible for red autofluorescence in mammalian cells and tissues. The most well-known porphyrin is the haemoglobin cofactor, heme. Another key porphyrin is protoporphyrin IX (PPIX), which is used for photodynamic therapy and tissue staining after intracellular synthesis from the precursor 5-aminolevulinic acid (5-ALA). The optimal excitation wavelength for porphyrins ranges from 800 nm towards the upper wavelength limit for multiphoton lasers. The emission wavelength displays a peak at 590 nm, with several fluorescence lifetimes are reported: 5.2 and 19 ns (Table 16.1).

### 16.6.3 Autofluorescent Proteins

Elastin is an important structural protein found in connective tissue, responsible for adding elasticity to various tissues. Elastin is visible at a two-photon excitation peak wavelength of 750 nm, yielding fluorescence between 450 and 510 nm (Yu et al. 2012) and lifetimes of ~0.2 and 2.5 ns (Table 16.1). However, tissue such as the skin is often imaged at 760–780 nm in order to simultaneously capture NAD(P)H, FAD, keratin and elastin simultaneously with second harmonic generation (SHG) from collagen.

Collagen is the major component of connective tissue and heavily abundant within the tissues and organs of the body. Collagen has both weak autofluorescence and strong SHG optical properties. As SHG is not fluorescence, but rather the scattered photons at  $\frac{1}{2}$  the incident photon wavelength, collagen has no lifetime (Roberts et al. 2011).

Lipofuscin is a heterogeneous mix of oxidized proteins (30–70 %), lipids, metals (~2 %) and sugars that accumulate as yellow-brown pigment granules within the skin, liver, brain and other vital organs (Höhn and Grune 2013). Lipofuscin intralysosomal formation is associated with age and is believed to be a result of reduced degradation of oxidized protein and elevated reactive oxygen species levels within the cell. Intracellularly, lipofuscin may act to inhibit lysosomal and proteasomal degradation of proteins, leading to cellular toxicity and contributing to aging (Brunk and Terman 2002; Höhn and Grune 2013). Lipofuscin autofluorescence can be visualized with an excitation wavelength of 800 nm (two-photon) and emission between 500 and 550 nm. Several fluorescence lifetimes have been reported for lipofuscin including 0.32, 1.2 and 4.8 ns (Table 16.1). As a result, a multiexponential decay model should be adopted to resolve lipofuscin lifetime by intravital FLIM microscopy (Berezin and Achilefu 2010).

Keratin is a family of proteins that arrange to form epithelial-specific intermediary filaments. Keratins play a role in the regulation of intracellular strength, motility, division and apoptosis (Pan et al. 2013). Keratin autofluorescence can be detected using a broad two-photon excitation range of 760–860 nm, with fluorescence emission visible between 485 and 525 nm (Yu et al. 2012). The fluorescence lifetime of keratin follows a monoexponential decay curve and is approximately

1.4 ns (Ehlers et al. 2007). However, due to spectral overlay with several other autofluorescent molecules described above, multiexponential decay curves are required to resolve these individual lifetimes with time domain FLIM analysis.

## 16.7 Intravital Applications of FLIM

### 16.7.1 Cell Metabolism

Metabolic analysis by FLIM is largely centered around changes in the lifetime and proportion of NAD(P)H and FAD in their free and protein-bound states. Initially, the cellular redox state was assessed redox fluorometry by measuring changes in the steady-state fluorescence emission of NAD(P)H using single or multiphoton microscopy. This technique was improved by attempting to spectrally resolve the free and protein-bound species of NAD(P)H, an approach known as redox ratio fluorometry (Huang et al. 2002). Both forms of analysis had several drawbacks including the presence of contaminating non-specific background, light scattering, and poorly separated spectra for free and bound NAD(P)H. Related to this is examining the ratio of FAD to NAD(P)H intensity, also known as the redox ratio (Chance et al. 1979). This is considered a favorable approach as the oxidized form of FAD is fluorescent whereas the opposite is true for NAD(P)H. Thus the intensity ratio between both molecules is considered to directly related to the redox state of the cells. The advent of FLIM solved many of the challenges faced by redox ratio imaging due to excellent resolution of NAD(P)H and FAD speciation-associated lifetimes (Lakowicz et al. 1992; Kao et al. 2008; Islam et al. 2013).

Many of the foundational metabolic FLIM studies were performed *in vitro*, where a number of variables can be precisely controlled. The fluorescence lifetime changes associated with controlled metabolic events are generally considered to be consistent for intravital imaging. In a landmark metabolic FLIM study, the fluorescence lifetime of normal breast epithelial cells were examined during changes in cell confluency, nutrient deprivation and other metabolic challenges. The increase in cell confluency over time was found to be associated with a decrease in the average lifetime of NAD(P)H. This tendency corresponds with an increase in the ratio of free:bound NAD(P)H in cells (Bird et al. 2005). The increase in cell population over time, in culture, reduces oxygen and nutrient availability that is believed to increase the NADH/NAD<sup>+</sup> ratio and therefore the relative abundance of free NADH and the corresponding fast NAD(P)H lifetime. However, other factors such as cell morphology and the state of the cytoskeleton are also hypothesized to contribute to confluency-associated lifetime changes of NAD(P)H (Ghukasyan and Kao 2009). A reduction in the lifetime of NAD(P)H was also observed from serum starvation (nutrient deprivation) and inhibition of the electron transport chain by potassium cyanide, an inhibitor of complex IV of the electron transport chain (ETC) responsible channeling electrons to O<sub>2</sub> and pumping protons to the inter-membrane space of the mitochondria. As a result of KCN inhibition, intracellular NADH oxidation



is inhibited and therefore elevated NADH abundance as indicated by an increase in both fluorescence and free lifetime component (Huang et al. 2002; Bird et al. 2005).

Similarly, the inhibition of ETC complex I by rotenone (an inhibitor that prevents oxidation of NADH to NAD<sup>+</sup>) caused both a decrease in the average fluorescence lifetime of NAD(P)H and increase in the free:bound NAD(P)H ratio in human corneal epithelial cells and HeLa cells *in vitro* (Ghukasyan and Kao 2009; Gehlsen et al. 2012). A resulting increase in glycolysis after ETC inhibition by rotenone is also considered to increase the flux of free NADH in the cytoplasm over protein-bound NADH within the mitochondria (Erecińska et al. 1996). While both rotenone and KCN ostensibly inhibit the ETC, their divergent mechanisms of action are reflected in the dynamic changes of NAD(P)H lifetimes and free:bound ratios. KCN treatment over time leads to a recovery of free:bound ratio to its initial state, whereas rotenone treatment leads to a persistently elevated free:bound ratio (Ghukasyan and Kao 2009).

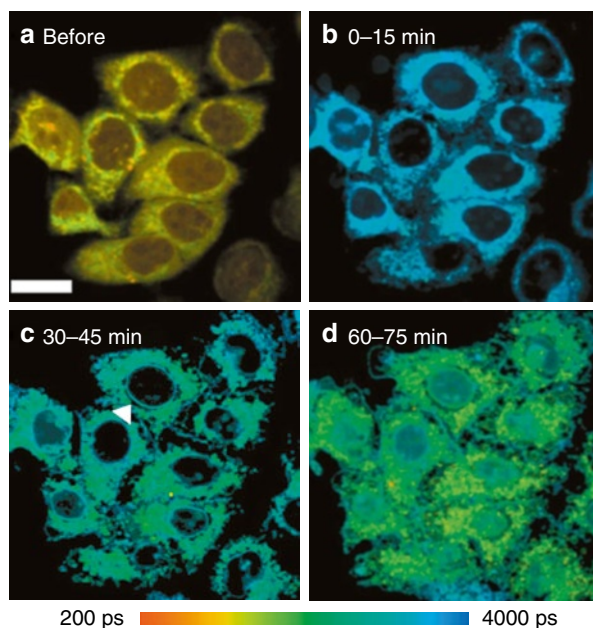
As a result of these *in vitro* studies it can be considered that the level oxidative phosphorylation for energy production within the cell is inversely proportional to the free:bound NAD(P)H ratio measured by FLIM. A reduction in this oxidative metabolic rate can coincide with decrease in the average weighted lifetime due to the predominance of the free NAD(P)H species. Overall, these observation have largely formed the basis of assessing the metabolic state of tissue with FLIM via intravital microscopy (Skala et al. 2007b; Sanchez et al. 2010; Thorling et al. 2011b, 2013; Deka et al. 2013). Promising work continues to be made in using the lifetime properties of autofluorescent compounds, such as NAD(P)H and FAD, to observe and characterize the differentiation of stem cells (König et al. 2011).

### 16.7.2 Metabolic Viability, Apoptosis and Necrosis

FLIM analysis of tissue autofluorescence is an effective imaging approach to assess cell toxicity and death. One of the first studies to explore this examined autofluorescence lifetime changes as a result of phototoxicity from near-infrared laser excitation (König et al. 1996). Phototoxicity was associated with a decrease in the average fluorescence lifetime of cellular autofluorescence.

The induction of apoptosis by staurosporine, an inhibitor of ATP-kinase binding, is associated with an increase in the fluorescence lifetime of NAD(P)H (Fig. 16.13) and decrease in the free to protein-bound ratio (Wang et al. 2008; Yu et al. 2011). These lifetime changes coincided morphological alterations characteristic of apoptosis and also preceded elevated caspase 3 activity (Wang et al. 2008). Furthermore, the increase in NAD(P)H lifetime preceded a reduction in the mitochondrial membrane potential and changes in intracellular ATP levels (Yu et al. 2011). Unlike apoptosis, the induction of necrosis by H<sub>2</sub>O<sub>2</sub> failed to elicit significant lifetime or ratio changes in NAD(P)H and were resolved by morphological examination alone (Wang et al. 2008; Ghukasyan and Kao 2009). This suggests that the NAD(P)H fluorescence lifetime is a robust early indicator of apoptotic cell death, with distinct

**Fig. 16.13** Fluorescence lifetime changes ( $\tau_m$ ) in NAD(P)H associated with the induction of apoptosis in HeLa after treatment with staurosporine (1  $\mu$ M) (From Wang et al. (2008)). [Copyright permission being sought]

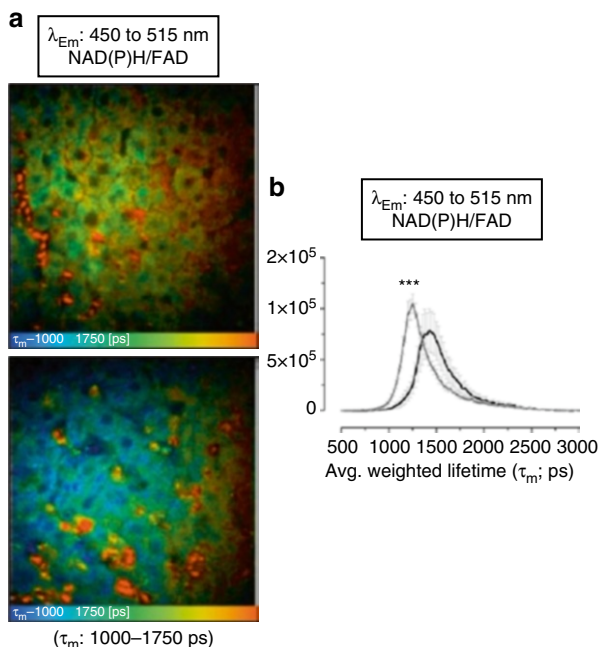


lifetime changes from cell proliferation, oxygen and nutrient deprivation, and the inhibition of oxidative phosphorylation.

FLIM of NAD(P)H lifetime within excised human skin can also be used to measure the metabolic viability of tissue (Sanchez et al. 2010). Excised skin kept at non-optimal temperatures for medium-term storage (i.e. room temperature and 37 °C over 5–7 days) demonstrates a progressive increase in both the fast and slow lifetimes of NAD(P)H relative to *in vivo* and freshly excised skin. In wound healing models for corneal epithelium, the presence of an initial challenge (scratch or erosion by NaOH) immediately cause a decrease in the average lifetime and increase in free:bound protein NAD(P)H relative to the control, which persisted during the recovery phase. As the measured NAD(P)H lifetime changes follow closely that of rotenone treatment, the authors hypothesize that glycolysis is elevated during wound healing within this model (Gehlsen et al. 2012).

The metabolic activity associated with wound healing appears to be tissue dependent. In a skin wound healing model, a punch biopsy was taken on the back of Sprague Dawley rats, removing the entire epidermis and dermis of the skin. Wound healing was measured at the site of the punch biopsy, specifically the center and edge of the wound, by multiphoton FLIM over 20 days. The free:bound NAD(P)H ratio at the center and edge of the wound was significantly lower than the normal healthy skin within the first 4–6 days of wound healing. The closure of the wound and formation of normal-appearing skin at the edges corresponded with a tendency for the free:bound ratio to increase above the normal skin controls. From this study, it appears that oxidative phosphorylation was the major source of energy production during wound healing (Deka et al. 2013).

**Fig. 16.14** Fluorescence lifetime changes in NAD(P)H/FAD in hepatocytes associated with ischemic reperfusion injury (*bottom*). (a) Representative  $\lambda_m$  intravital images of sham and I/R injury in the liver. (b)  $\lambda_m$  lifetime histograms of sham and I/R injury liver NAD(P)H/FAD (From Thorling et al. (2013))



FLIM analysis of cellular autofluorescence can be used to assess the tissue damage resulting from ischemia-reperfusion (I/R) injury. I/R injury in the rat liver is associated with an overall decrease in the average lifetime of NAD(P)H (Fig. 16.14) and increase in free:bound ratio (Thorling et al. 2011a, 2013). These lifetime changes follow the model of impaired oxidative phosphorylation for cellular energy production and apoptosis-associated lifetime changes (Wang et al. 2008; Yu et al. 2011), which correspond to histological detection of apoptosis after I/R injury within the liver (Thorling et al. 2011b).

### 16.7.3 pH Sensing

Intracellular pH can be measured by examining the change in both NADH and FAD fluorescence lifetimes without the addition of exogenous dyes. The fluorescence lifetimes of NADH and FAD were found to decrease with increasing pH both in aqueous solutions and intracellularly *in vitro* (Ogikubo et al. 2011; Islam et al. 2013). Lifetime changes of exogenous fluorescent dyes can also be used to measure the pH of tissues as demonstrated by the use of 2',7'-bis-(2-carboxyethyl)-5-(and-6)-carboxyfluorescein in the stratum corneum to resolve the acidic surface and lipid-rich intercellular spaces versus the more neutral corneocytes (Hanson et al. 2002).

#### **16.7.4 FLIM Anisotropy**

FLIM can be combined with anisotropy to improve the resolution of the physio-chemical states of a fluorophore within a complex intracellular environment. FLIM-anisotropy has been used to resolve the free and multiple protein-bound forms of NADH, as well as measure the intracellular viscosity, before and after hypoxia. This is achieved by correlating the fluorescence lifetime, rotational diffusion time and two-photon initial anisotropy of NADH in solution (free and titrated with a NADH-binding protein involved in OXPHOS) with cellular NADH fluorescence (Vishwasrao et al. 2005). The effectiveness of FLIM-anisotropy is limited by the degree of spectral and lifetime overlap from contaminating fluorophores. Therefore, the characterization of the physio-chemical states of a fluorophore, under isolated and controlled conditions, by FLIM-anisotropy is an essential foundational step prior to applying these techniques in intravital imaging.

#### **16.7.5 Oxygen Sensing**

Oxygen is known to quench fluorescence and reduce the fluorescence or phosphorescence lifetime of a fluorophore in a diffusion-limited manner. Thus, FLIM microscopy is an ideal non-invasive approach to measure oxygen distribution in tissue. Dyes such ruthenium (Zhong et al. 2003; Bowman et al. 2003), porphyrins (Amao 2003) and pyrene butyric acid (Ribou et al. 2007) can be used as oxygen sensors by measuring the decrease in fluorescence lifetime with increasing oxygen levels as indicated by the Stern-Volmer relationship (Amao 2003).

#### **16.7.6 Cancer Diagnostics**

Substantial progress has been made in discriminating between normal and cancerous tissue by non- or minimally invasive intravital FLIM. Given the metabolic differences between normal and tumor tissue, namely the predominance of glycolysis over oxidative phosphorylation in pyruvate oxidation, NAD(P)H and FAD are ideal autofluorescent metabolic indicators due to their involvement in both pathways. One of the first studies comparing the autofluorescence lifetime of normal and cancerous tissue found that malignancy-associated stroma in the breast showed a shorter lifetime than benign tissue (Tadrous et al. 2003). The sample was unfixed and excited with pulsed laser light at a wavelength of 415 nm. The time-domain lifetime data was fitted to a single component. This study was a landmark investigation that demonstrated FLIM analysis of cellular autofluorescence can be used to discriminate normal and cancerous tissues.

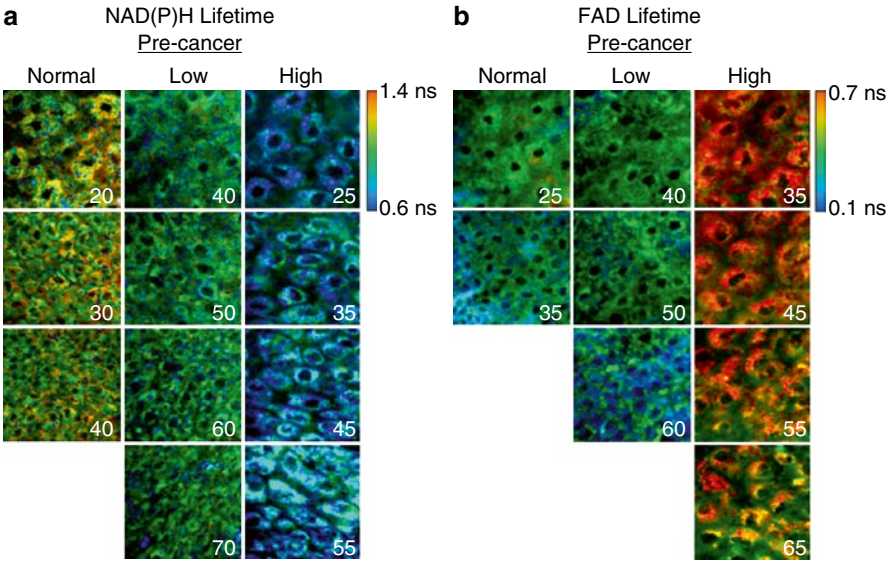


**Fig. 16.15** NAD(P)H (a) and FAD (b) fluorescence lifetime differences between normal (left panels), low-grade (center) and high-grade (right panels) pre-cancer oral cancer (From Skala et al. (2007b)). [Copyright permission being sought]

In 2007 a pair of studies were published performing intravital FLIM microscopy on a hamster cheek pouch model of oral cancer (Skala et al. 2007a, b). Normal and oral cancer tissue were examined for lifetime differences in the NAD(P)H and FAD fluorescence lifetimes and relative contributions (i.e. proportion of a lifetime component within a pixel) using multiphoton FLIM TCSPC. Both studies demonstrate a significant decrease in the long ( $\tau_2$ ) protein-bound NAD(P)H lifetime and contribution ( $\alpha_2$ ) in low- and high-grade precancer epithelium compared to normal tissue (Fig. 16.15). Moreover, high-grade precancer tissue showed a significant increase in the short ( $\tau_1$ ) protein-bound lifetime of FAD, relative to normal tissue. These changes were hypothesized to be related to a well-known metabolic phenotype observed in cancer cells known as the ‘Warburg effect’. The Warburg effect describes a bioenergetics phenotype in neoplastic cells whereby glycolysis is used to generate adenosine triphosphate (ATP) from pyruvate over oxidative phosphorylation under aerobic conditions (Nakajima and Van Houten 2013). As a result, oxidative phosphorylation is inhibited leading to a dominant glycolytic metabolic phenotype. Skala et al. demonstrate that when normal breast cells were exposed to an oxidative phosphorylation inhibitor,  $\text{CoCl}_2$ , a decrease in the protein-bound NAD(P)H lifetime is observed (Skala et al. 2007a), similar to lifetime differences observed in cancer tissue described earlier.

Similar to the work of Skala et al., the autofluorescence lifetime properties normal and cancer tissue was examined in a mouse model of breast cancer (Fig. 16.16), which displays phenotypic similarity to ductal carcinoma *in situ* (Conklin et al.



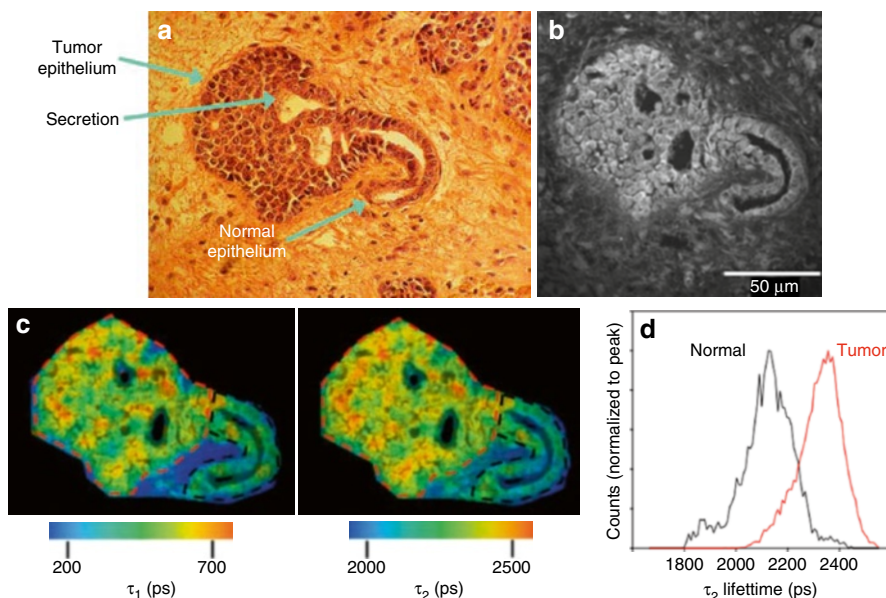


**Fig. 16.16** Fluorescence lifetime properties of FAD ( $\lambda_{\text{Exc}}$ : 890 nm) for normal versus cancerous breast epithelia (From Conklin et al. (2009)). (a) H&E stained mouse breast tumor. (b) Fluorescence intensity image of the sequential unstained slide at 890 nm excitation. (c) Color maps of the s1 (left) and s2 (right) components of the fluorescence lifetime, which illustrate the relatively longer lifetime values in tumor cells when compared to normal epithelium. (d) Range of lifetime values of the two ROIs drawn in (c)

2009). Multiphoton TCSPC FLIM was performed on biopsy sections after excitation at 780 and 890 nm to capture NAD(P)H and FAD fluorescence respectively. Tumor epithelia displayed high fluorescence intensity compared to normal tissue along with significantly longer NAD(P)H and FAD lifetimes compared to normal epithelia. While this study did not perform intravital imaging, the data generated further supports the role of FLIM for diagnostic purposes to discriminate normal and cancerous tissues, particularly using wide-field and/or endoscopic FLIM. Indeed this has been demonstrated with endoscopic FLIM of human patients with glioblastoma multiforme, where longer NAD(P)H lifetimes in cancerous tissue were used to contrast against normal brain tissue (Sun et al. 2010). Similarly, endoscopic FLIM was also used to contrast normal and cancerous tissue in human patients with HNC (Sun et al. 2013). Interestingly, there appears to be tissue-specific lifetime changes associated with cancer, as some neoplastic tissue display an increase in NAD(P)H lifetime for breast or brain cancer (Conklin et al. 2009; Sun et al. 2010) while others show a decrease for oral/HNC cancer (Skala et al. 2007a, b; Sun et al. 2013).

The spectral and lifetime properties of a human melanoma and basal cell carcinoma lesions were performed by intravital multiphoton FLIM using the DermaInspect<sup>®</sup> microscope (Dimitrow et al. 2009; Seidenari et al. 2013). This study showed that melanocytes and melanoma cells could be selectively excited by target-



ing melanin at 800 nm, which minimized NAD(P)H and FAD autofluorescence from neighboring keratinocytes. While there were no lifetime differences between normal and lesional tissue, for keratinocyte or melanocyte/melanoma autofluorescence, the lifetime properties between keratinocytes and melanocytes/melanoma were pronounced. Combined with spectral imaging, resolution of normal melanocytes and melanoma infiltration, within the depth range of multiphoton microscopy, is significantly improved with fluorescence lifetime imaging (Dimitrow et al. 2009). However, FLIM could not be used to distinguish between benign and melanocytic lesions. Despite this, the lifetime properties of melanin were used to observe the distribution of melanin/melanocytes (normal and melanoma) in normal and melanocytic lesions (Fig. 16.17a–e). Similarly, the lifetime properties of basal cells can be used to image their infiltration through the epidermis (Fig. 16.17f).

Aside from autofluorescence, the fluorescence lifetime parameters of probes designed to label cancer cells can be measured using intravital FLIM for diagnostic and therapeutic purposes. For example, one study reports the use of a near infrared probe conjugated to an anti-HER2/neu antibody to detect breast cancer cells engrafted into the forelimb of a mouse (Ardeshirpour et al. 2012). After sufficient tumor development on the forelimb, the probe-conjugated antibodies were injected via the tail-vein. The tumor region was imaged every 30 min for 5 h at an excitation wavelength of 717 nm (one-photon), with fluorescence emission collected through a longpass 780 nm filter to isolate the NIR probe's signal. The FLIM data was fit to a single exponential decay model. Interestingly, the lifetime of the NIR probe changed with binding of antibody to the HER2 expressing tumor cells *in vivo*. Using this approach, patient specific cancer biomarkers can be targeted to improve therapeutic targeting and surgery.

Finally, phasor analysis of time-domain FLIM can also be used to rapidly resolve the various sub-cellular autofluorescence lifetime components in cancer cells *in vitro* (Stringari et al. 2012). Both exponential decay fitting and phasor analysis of time-domain FLIM data is expected to evolve as a complementary analytical approaches for intravital FLIM microscopy of cancer and other disease states.

### 16.7.7 Nanoparticle, Drug Delivery and Metabolism

Intravital microscopy with fluorescence lifetime imaging has been used to study the uptake, distribution and metabolism of nanoparticles and drugs in animals and humans (Roberts et al. 2011). The fluorescence lifetime properties of a nanoparticle or drug can be used in combination with multi-spectral imaging to enhance its contrast from background fluorescence, measuring binding interactions and identify metabolic products.

For example, intravital FLIM imaging has been a critical technique in assessing both the penetration and toxicity of topically applied zinc oxide nanoparticles into the viable epidermis of *in vivo* human skin (Roberts et al. 2008). Zinc oxide nanoparticles are routinely used as a physical sunblock to prevent UV-induced photodamage. However, given their nano-size and formulation with chemical components, which may act as penetration enhancers, concerns have been raised about

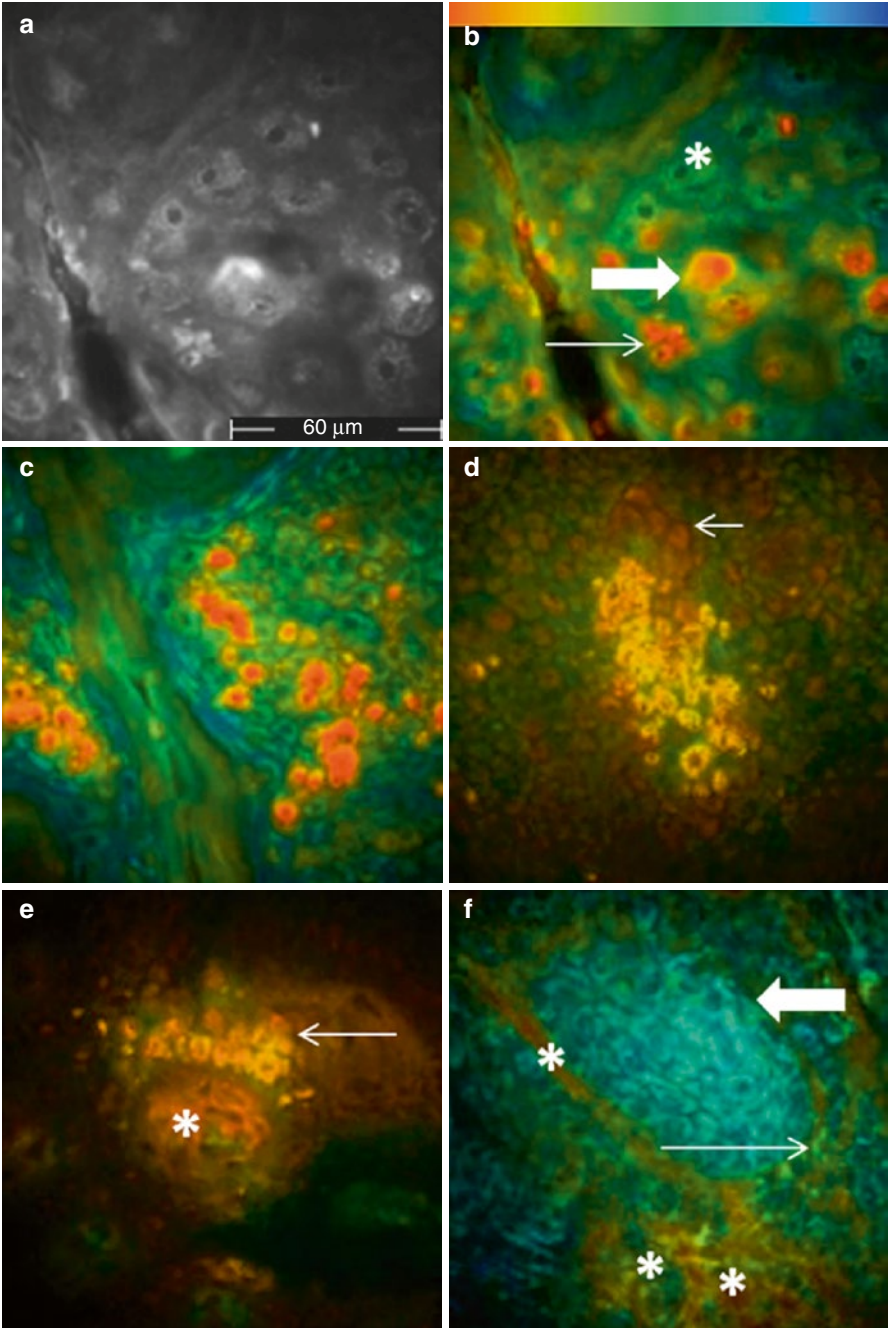


**Fig. 16.17** Multiphoton laser tomography and fluorescence lifetime imaging of healthy skin (**a**: intensity, **b**: lifetime), melanocytic lesions (**c–e**) and basal cell carcinoma (**f**), with colour coded *green* large keratinocytes (keratinocytes without pigment, *asterisk*), large *orange* melanin-containing keratinocytes (*thick arrow*), small red melanocytes (*thin arrow*), *red-range* cells: melanocytes, and a nest of *blue* basaloid cells (*thick arrow*), infiltrating *green* normal keratinocytes (*thin arrow*) and *asterisks* indicate blood vessels (Adapted from Seidenari et al. (2013)). [Copyright permission being sought]

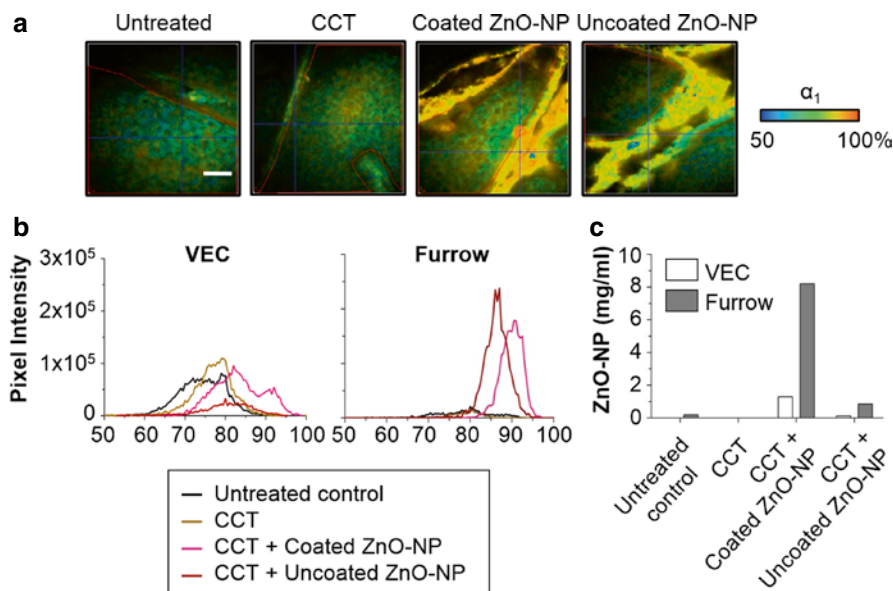


**Fig. 16.18** Penetration of topically applied coated/uncoated zinc oxide nanoparticles to *in vivo* human skin ( $\lambda_{\text{Exc}}$ : 740 nm). **(a)** Pseudocolored images from intravital FLIM microscopy of human skin after the topical application of zinc oxide nanoparticles. **(b)** Short lifetime amplitude coefficient ( $\alpha_1$ ) histogram from two gated regions within the skin: viable epidermal cells and skin furrows. **(c)** Concentration of zinc oxide nanoparticles within these regions after interpolating from a standard curve (Adapted from Leite-Silva et al. (2013))

their potential to penetrate past the stratum corneum into the viable epidermis (Robertson et al. 2010). Moreover, several *in vitro* studies demonstrate that micromolar doses of zinc oxide induced cellular toxicity of keratinocytes and other cell types. The fluorescence lifetime properties of zinc oxide are distinguishable from cellular autofluorescence by examining either the lower short/long lifetimes (multi-exponential decay) (Roberts et al. 2008) and >90 % short lifetime amplitude coefficient ( $\alpha_1$ ) (Lin et al. 2011). The DermaInspect® multiphoton microscope coupled with multi-spectral FLIM have largely demonstrated that zinc oxide nanoparticles accumulate at the skin surface with minimal penetration into the viable layers (Fig. 16.18) (Roberts et al. 2008; Lin et al. 2011; Leite-Silva et al. 2013). Moreover, topical application of zinc oxide nanoparticles fails to alter the redox state of the viable epidermis (Lin et al. 2011; Leite-Silva et al. 2013), due to the absence of lifetime changes associated with apoptosis (Ghukasyan and Kao 2009).

Similar to zinc oxide nanoparticles, gold nanoparticles have a fluorescence lifetime properties that can be contrasted against cellular autofluorescence (Qu et al. 2008; Labouta et al. 2011). Multiphoton-FLIM microscopy of excised human skin demonstrate penetration of topically applied gold nanoparticles into the viable epidermis in the presence of toluene, an organic solvent penetration enhancer, but not an aqueous solution (Labouta et al. 2011). Moreover, the redox ratio of the viable epidermis,

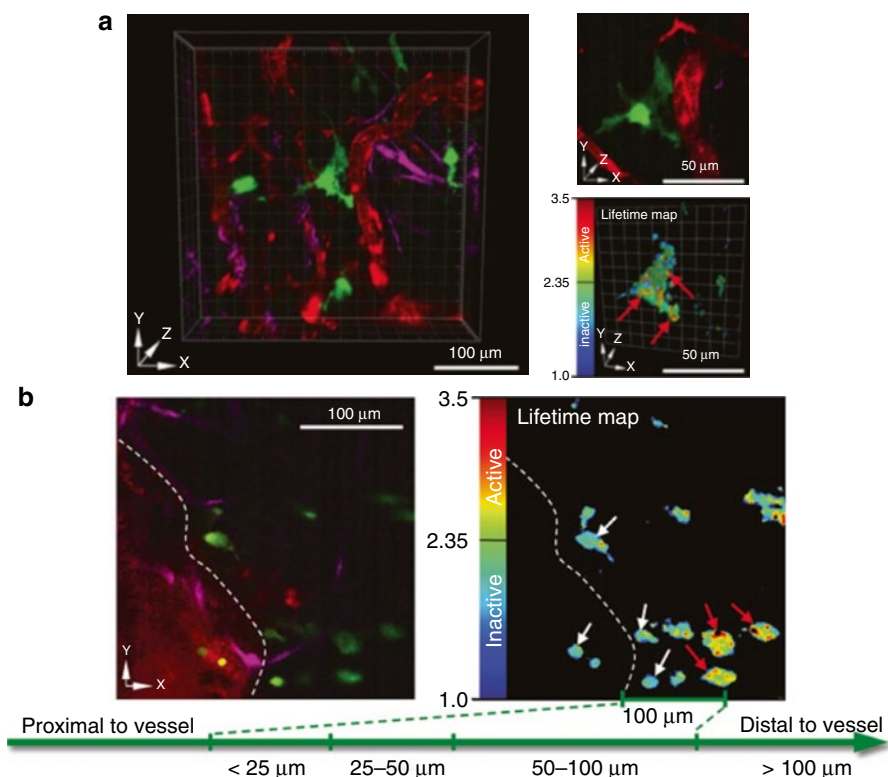


**Fig. 16.19** Intravital FLIM of PDAC tumor cells, expressing an Src-FRET biosensor, before (a) and after (b) administration of dasatinib (Src kinase inhibitor). Multiphoton images of PDAC cells (green), collagen SHG (purple) and microvasculature (red; Qtracker 655 quantum dots) are displayed in the left panel (a) and (b) (From Nobis et al. (2013)). [Copyright permission being sought]

measured as the NAD(P)H  $\alpha_1/\alpha_2$  ratio, displayed a tendency to be elevated after treatment with toluene compared to aqueous solutions suggesting an inhibition in cellular metabolic activity (Labouta et al. 2011). FLIM can also be used to assess the cutaneous delivery of fluorescently labelled siRNA by flexible liposomes (Geusens et al. 2010). While performed on excised human skin, these examples demonstrate the value of FLIM to simultaneously assess the penetration of topically applied actives into the skin and the metabolic state of the target tissues in response to treatment.

Intravital FLIM to assess the distribution of drug delivery and activity using *in vivo* animal models is a powerful tool for therapeutic drug development. For example, stably transfected primary mouse pancreatic ductal adenocarcinoma (PDAC) with an Src-FRET biosensor were engrafted into a mouse and monitored using intravital FLIM microscopy (Nobis et al. 2013). The Src biosensor displays a FRET effect when Src is in 'inactivated', corresponding to a decreased fluorescence lifetime compared to 'active' Src where no FRET effect occurs (Fig. 16.19). Treatment with dasatinib, a small molecule Src kinase inhibitor, results in the induction of a

FRET effect as seen by a reduction in the lifetime of the biosensor, indicating the deactivation of Src. Intravital FLIM microscopy of the Src-FRET biosensor allowed for: (1) the assessment of dasatinib efficacy after administration over time and spatially within the tumor, (2) observation of differences in drug responsiveness within the tumor subpopulation, and (3) monitor dasatinib activity in PDAC cells distally from the microvasculature (Nobis et al. 2013).

Intravital FLIM can be used to monitor drug uptake and metabolism within the liver, as demonstrated by the model fluorescent dye fluorescein where the unmetabolized and glucuronidated-fluorescein can be resolved according to their specific lifetimes (Roberts et al. 2008; Thorling et al. 2011a). In theory, quantitation of fluorescein metabolism by intravital FLIM in the liver can be used to model hepatic damage due to ischemia-reperfusion injury, which already displays compromised fluorescein uptake and clearance (Thorling et al. 2013).

Several *in vitro* studies also display the utility of FLIM to assess drug delivery, release and uptake in target cells. In particular, fluorescent drugs like doxorubicin (dox) have proven particularly useful as the lifetime of dox permits the specific measurement of cellular uptake of free (Bakker et al. 2012) or nanoparticle-conjugated dox (Romero et al. 2013; Basuki et al. 2013), and lifetime changes mark intercalation with DNA within cell nuclei (Chen et al. 2012; Weber et al. 2013).

## 16.8 FRET-FLIM

### 16.8.1 *Conventional Methods Studying Protein-Protein Interactions*

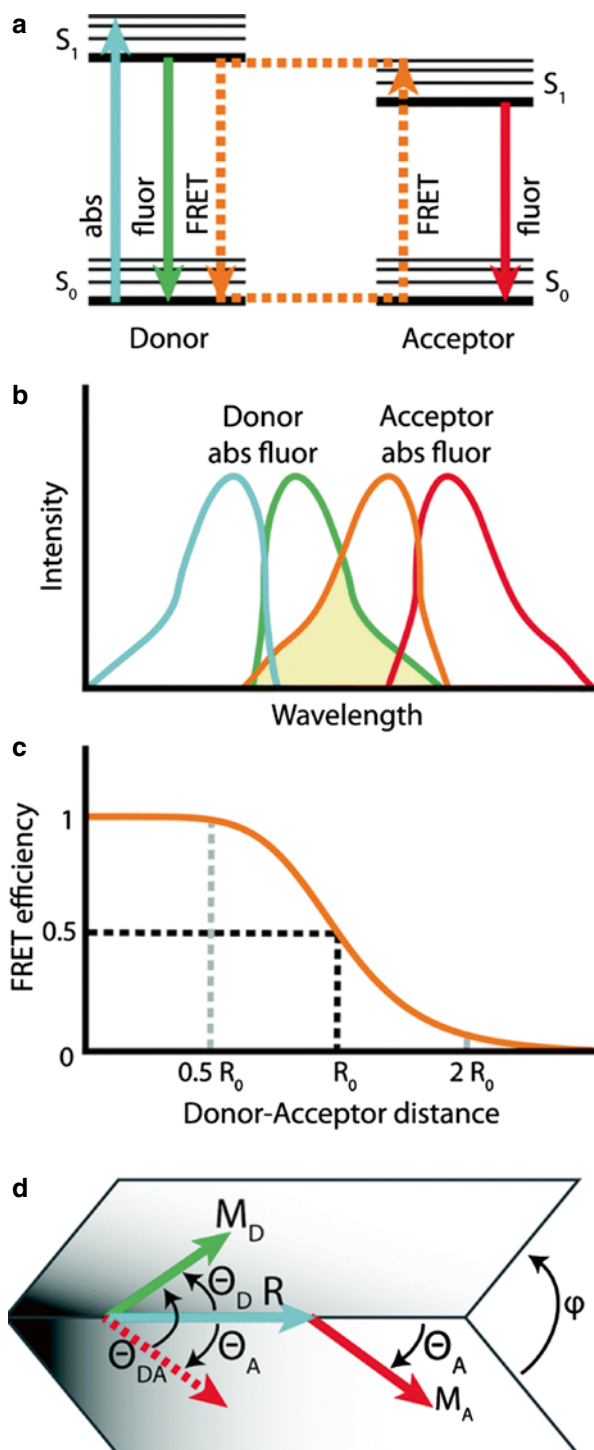
*In vitro* analysis such as using recombinant, bacterially expressed proteins, or Yeast 2-hybrid studies, pose limitations when protein interactions are studied in isolation. Therefore, the result only reveals whether proteins are able to interact without considering *in vivo* physiological conditions.

### 16.8.2 *FRET: Introduction*

Combining fluorescence microscopy and Förster (also called “fluorescence”) resonance energy transfer (FRET) is a feasible approach to study protein-protein interactions. FRET describes the photo-physical phenomenon of energy transfer from a donor to an acceptor molecule, provided they are in close proximity (Fig. 16.20). FRET can be used as a spectroscopic ruler to quantify the fluorescence signals, which are sensitive to molecular conformation, association, and separation. For protein-protein interaction to happen, the distance is in the range of 1–10 nm, which is not possible by co-localization using conventional fluorescence microscopy, even with confocal microscopy, which has a diffraction limit of Lateral 250 nm, axially



**Fig. 16.20** Förster resonance energy transfer. (a) Following the absorption of photons by the donor molecule, the excited state of the fluorophore can decay radiatively by fluorescence or non-radiatively transfer to another fluorophore within a threshold distance (acceptor). The acceptor fluorophore can then return to the ground state by fluorescence emission. (b) Donor absorption (blue), donor fluorescence (green), acceptor absorbance (orange) and acceptor fluorescence (red). The spectral overlap (yellow) between the donor fluorescence (green) and acceptor absorbance (orange) is necessary for FRET to be possible. (c) FRET efficiency decreases with the distance between the donor and acceptor. The 'Förster distance',  $R_0$ , represents the distance between donor and acceptor when the energy transfer efficiency reaches 50 % (Adapted from Prevo and Peterman (2014)). [Copyright permission being sought]





500 nm. Proteins can be co-localized due to their location – within the same focus volume, without interacting with each other, while not interaction with each other.

### 16.8.3 FRET Efficiency Definition

FRET efficiency is defined as:

$$E_{FRET} = \frac{R_0^6}{R_0^6 + R^6} \quad (16.7)$$

Where  $E_{FRET}$  – efficiency of energy transfer is proportional to the reciprocal of the sixth order of the inter-molecular distance.  $R_0$  – Critical radius, characteristic parameter of any specific FRET pair, is the distance between donor and acceptor molecule, when the energy transfer efficiency is 50 % (Borst et al. 2006).

$$R_0 = 0.211 (\kappa^2 \cdot n^{-4} \cdot Q_D \cdot J)^{1/6} (\text{in } ^\circ) \quad (16.8)$$

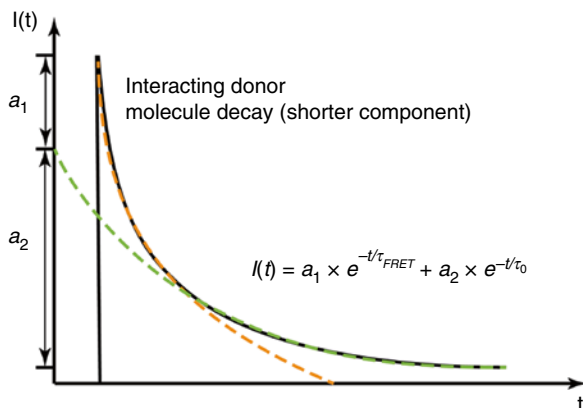
where  $\kappa^2$  is the dipole orientation factor ( $0 < \kappa^2 < 4$ ),  $n$  is the refractive index of the sample,  $Q_D$  – quantum yield of the donor and  $J$  is the spectral overlap between donor emission and acceptor absorption spectra.

In evaluating FRET efficiency, there are a number of approaches to take including ratio imaging, acceptor photo-bleaching, and FLIM-FRET. For FRET measurement using the ratio imaging approach, sufficient separation in excitation spectra is typically required for selective stimulation of the donor molecule, where a larger overlap (>30 %) between the donor emission and the acceptor excitation spectrum is required in order to obtain efficient energy transfer. It is also essential to have a reasonable separation in emission spectra between donor and acceptor molecules to avoid emission spectra cross-talking (Pollok and Heim 1999).

The second approach, acceptor photo-bleaching, capitalizes on the decrease of donor fluorescence under FRET conditions corresponding increase of the donor fluorescence when FRET is disrupted by photo-bleaching of the acceptor fluorophore. However, there are some key drawbacks with the ratio imaging and acceptor bleaching FRET approaches. For both approaches, the main drawback is emission spectra cross-talking whereby the donor emission is detectable in the acceptor channel. Thus, direct excitation of acceptor is required and the efficacy of this approach is dependent upon a high donor/acceptor concentration ratio.

The third approach is to spatially resolve FRET by fluorescence lifetime imaging (FRET- FLIM). FLIM overcomes the drawbacks of intensity based FRET analysis by monitoring the localized changes in donor fluorescence lifetime, thus providing an enormous advantage for imaging dynamic events within the living cells and organelles (Bastiaens and Squire 1999; Elangovan et al. 2002).

**Fig. 16.21** Measuring FRET from a time-domain (double-exponential) FLIM decay curve



### 16.8.4 Determination of FRET Efficiency Using FLIM

The donor decay comprises the interacting and non-interacting molecules can be fitted to double exponential curve (Fig. 16.21):

$$I(t) = a_1 \times e^{-t/\tau_{FRET}} + a_2 \times e^{-t/\tau_0} \quad (16.9)$$

With and representing the lifetime of interacting donor molecules and non-interacting donor molecules, and are the intensity factors of the two decay components. The FRET efficiency can be determined by

$$E_{FRET} = 1 - (\tau_{FRET} / \tau_0) \quad (16.10)$$

and the ratio of interacting and non-interacting donor molecule corresponds to  $\alpha_1/\alpha_2$ .

## 16.9 Summary

Intravital fluorescence lifetime imaging is an increasingly being used technique for both research and clinical diagnostic imaging. The unique lifetime properties of fluorophores, which remain generally unchanged with concentration or excitation light, enable FLIM to spectroscopically distinguish between fluorescent compounds and their various conformations. Moreover, as the fluorescence lifetime changes due to either microenvironment differences (e.g. temperatures, pH) or direct binding interactions, conformational and component changes within a fluorophore can be simultaneously measured spatially and temporally.

The two major means of acquiring fluorescence lifetime data are time- and frequency-domain FLIM. The latter is typically associated with phasor lifetime analysis, although this technique can be used for time-correlated single photon counting (TCSPC; time-domain FLIM). Time-domain FLIM yields a decay curve from which the lifetimes of multi-exponential components can be quantified. Frequency-domain FLIM plots the modulation and phase lifetimes within a phasor plot to distinguish between multiple components according to their lifetime properties.

Using either time- or frequency-domain FLIM, instrumentation for intravital FLIM has advanced considerably over the past 15 years. Intravital FLIM can be performed using wide-field microscopy, constructing a decay curve using either TCSPC or time-gated channels with a camera. This can further be adapted for intra-operative imaging through the use of an endoscope for diagnostic imaging. Multiphoton microscopy, using a static or flexible imaging head, has also emerged as a strong intravital FLIM instrument for both research and clinical purposes.

Intravital FLIM of tissue autofluorescence is a particularly useful diagnostic technique to assess the redox and thus metabolic state of cells and tissues in response to drug treatment. Moreover, the autofluorescence lifetime can be an early indicator of programmed cell death and metabolic decay. The use of novel dyes, probes, fluorescently labelled peptides, proteins or antibodies can add significant depth in assessing the tissue state as well as identifying cell and tissue types.

FRET effects, either as natural occurrence between autofluorescent molecules or two fluorescently labelled components, can be resolved efficiently using FLIM – within an intravital setting – overcoming existing difficulties in spectral overlap between donor and acceptor fluorescent molecules.

In summary, FLIM is an indispensable technique essential to any intravital imaging platform.

**Acknowledgements** This work was supported by the Australian National Health & Medical Research Council and the Australian Research Council.

## References

- Amao Y (2003) Probes and polymers for optical sensing of oxygen. *Microchim Acta* 143:1–12. doi:[10.1007/s00604-003-0037-x](https://doi.org/10.1007/s00604-003-0037-x)
- Ardehshirpour Y, Chernomordik V, Zielinski R et al (2012) In vivo fluorescence lifetime imaging monitors binding of specific probes to cancer biomarkers. *PLoS One* 7:e31881. doi:[10.1371/journal.pone.0031881](https://doi.org/10.1371/journal.pone.0031881)
- Bakker G-J, Andresen V, Hoffman RM, Friedl P (2012) Fluorescence lifetime microscopy of tumor cell invasion, drug delivery, and cytotoxicity. *Methods Enzymol* 504:109–125
- Ballew RM, Demas JN (1989) An error analysis of the rapid lifetime determination method for the evaluation of single exponential decays. *Anal Chem* 61:30–33. doi:[10.1021/ac00176a007](https://doi.org/10.1021/ac00176a007)
- Bastiaens PIH, Squire A (1999) Fluorescence lifetime imaging microscopy: spatial resolution of biochemical processes in the cell. *Trends Cell Biol* 9:48–52

- Basuki JS, Duong HTT, Macmillan A et al (2013) Using fluorescence lifetime imaging microscopy to monitor theranostic nanoparticle uptake and intracellular doxorubicin release. *ACS Nano* 7:10175–10189. doi:[10.1021/nn404407g](https://doi.org/10.1021/nn404407g)
- Becker W (2005) Advanced time-correlated single photon counting techniques. Springer, Berlin/ New York. doi:[10.1007/3-540-28882-1](https://doi.org/10.1007/3-540-28882-1)
- Becker W (2012a) Fluorescence lifetime imaging—techniques and applications. *J Microsc* 247:119–136. doi:[10.1111/j.1365-2818.2012.03618.x](https://doi.org/10.1111/j.1365-2818.2012.03618.x)
- Becker W (2012b) The bh TCSPC handbook, 5th edn. Becker & Hickl GmbH, Berlin
- Becker W, Bergmann A (2006) Timing stability of TCSPC experiments. In: Becker W (ed) *Opt. East 2006*. International Society for Optics and Photonics, Proc SPIE 6372, p 637209
- Becker W, Bergmann A (2008) Lifetime-resolved imaging in nonlinear microscopy. In: Masters BR, So PTC (eds) *Handbook of biomedical nonlinear optical microscopy*. Oxford University Press, Oxford
- Becker W, Bergmann A, Hink MA et al (2004) Fluorescence lifetime imaging by time-correlated single-photon counting. *Microsc Res Tech* 63:58–66. doi:[10.1002/jemt.10421](https://doi.org/10.1002/jemt.10421)
- Berezin MY, Achilefu S (2010) Fluorescence lifetime measurements and biological imaging. *Chem Rev* 110:2641–2684. doi:[10.1021/cr900343z](https://doi.org/10.1021/cr900343z)
- Bird DK, Yan L, Vrotsos KM et al (2005) Metabolic mapping of MCF10A human breast cells via multiphoton fluorescence lifetime imaging of the coenzyme NADH. *Cancer Res* 65:8766–8773. doi:[10.1158/0008-5472.CAN-04-3922](https://doi.org/10.1158/0008-5472.CAN-04-3922)
- Bloksgaard M, Brewer JR, Pashkovski E et al (2013) Effect of detergents on the physicochemical properties of skin stratum corneum: a two-photon excitation fluorescence microscopy study. *Int J Cosmet Sci*. doi:[10.1111/ics.12089](https://doi.org/10.1111/ics.12089)
- Borst JW, Nougalli-Tonaco I, Hink MA et al (2006) Protein-protein interactions in vivo: use of biosensors based on FRET. In: Geddes CD, Lakowicz J (eds) *Reviews in fluorescence*. Springer, New York, pp 341–357
- Bowman RD, Kneas KA, Demas JN, Periasamy A (2003) Conventional, confocal and two-photon fluorescence microscopy investigations of polymer-supported oxygen sensors. *J Microsc* 211:112–120. doi:[10.1046/j.1365-2818.2003.01192.x](https://doi.org/10.1046/j.1365-2818.2003.01192.x)
- Brunk UT, Terman A (2002) The mitochondrial-lysosomal axis theory of aging. *Eur J Biochem* 269:1996–2002. doi:[10.1046/j.1432-1033.2002.02869.x](https://doi.org/10.1046/j.1432-1033.2002.02869.x)
- Buurman EP, Sanders R, Draaijer A et al (1992) Fluorescence lifetime imaging using a confocal laser scanning microscope. *Scanning* 14:155–159. doi:[10.1002/sca.4950140305](https://doi.org/10.1002/sca.4950140305)
- Chance B, Schoener B, Oshino R et al (1979) Oxidation-reduction ratio studies of mitochondria in freeze-trapped samples. NADH and flavoprotein fluorescence signals. *J Biol Chem* 254: 4764–4771
- Chen N-T, Wu C-Y, Chung C-Y et al (2012) Probing the dynamics of doxorubicin-DNA intercalation during the initial activation of apoptosis by fluorescence lifetime imaging microscopy (FLIM). *PLoS One* 7:e44947. doi:[10.1371/journal.pone.0044947](https://doi.org/10.1371/journal.pone.0044947)
- Chen Y, Mills JD, Periasamy A. Protein localization in living cells and tissues using FRET and FLIM. *Differentiation*. 2003;71(9–10):528–541.
- Cole MJ, Siegel J, Webb SED et al (2001) Time-domain whole-field fluorescence lifetime imaging with optical sectioning. *J Microsc* 203:246–257. doi:[10.1046/j.1365-2818.2001.00894.x](https://doi.org/10.1046/j.1365-2818.2001.00894.x)
- Collini M, Leo B, Baldini G et al (2002) Probing protein aggregation by time-resolved fluorescence during beta-lactoglobulin crystal growth. *Eur Biophys J* 31:111–117. doi:[10.1007/s00249-002-0208-4](https://doi.org/10.1007/s00249-002-0208-4)
- Colyer R, Siegmund O, Tremsin A et al (2009) Phasor-based single-molecule fluorescence lifetime imaging using a wide-field photon-counting detector. *Proc Soc Photo Opt Instrum Eng*. doi:[10.1117/12.809496](https://doi.org/10.1117/12.809496)
- Colyer RA, Siegmund OHW, Tremsin AS et al (2012) Phasor imaging with a widefield photon-counting detector. *J Biomed Opt* 17:016008. doi:[10.1117/1.JBO.17.1.016008](https://doi.org/10.1117/1.JBO.17.1.016008)
- Conklin MW, Provenzano PP, Eliceiri KW et al (2009) Fluorescence lifetime imaging of endogenous fluorophores in histopathology sections reveals differences between normal and tumor

- epithelium in carcinoma in situ of the breast. *Cell Biochem Biophys* 53:145–157. doi:[10.1007/s12013-009-9046-7](https://doi.org/10.1007/s12013-009-9046-7)
- Damayanti NP, Craig AP, Irudayaraj J (2013) A hybrid FLIM-elastic net platform for label free profiling of breast cancer. *Analyst* 138:7127–7134. doi:[10.1039/c3an01097j](https://doi.org/10.1039/c3an01097j)
- Dancik Y, Favre A, Loy CJ et al (2013) Use of multiphoton tomography and fluorescence lifetime imaging to investigate skin pigmentation in vivo. *J Biomed Opt* 18:26022. doi:[10.1117/1.JBO.18.2.026022](https://doi.org/10.1117/1.JBO.18.2.026022)
- Deka G, Wu W, Kao F (2013) In vivo wound healing diagnosis with second harmonic and fluorescence lifetime imaging. *J Biomed Opt* 18:061222. doi:[10.1117/1.JBO.18.6.061222](https://doi.org/10.1117/1.JBO.18.6.061222)
- Digman MA, Caiolfa VR, Zamai M, Gratton E (2008) The phasor approach to fluorescence lifetime imaging analysis. *Biophys J* 94:L14–L16. doi:[10.1529/biophysj.107.120154](https://doi.org/10.1529/biophysj.107.120154)
- Dimitrow E, Riemann I, Ehlers A et al (2009) Spectral fluorescence lifetime detection and selective melanin imaging by multiphoton laser tomography for melanoma diagnosis. *Exp Dermatol* 18:509–515. doi:[10.1111/j.1600-0625.2008.00815.x](https://doi.org/10.1111/j.1600-0625.2008.00815.x)
- Dowling K, Hyde SCW, Dainty JC et al (1997) 2-D fluorescence lifetime imaging using a time-gated image intensifier. *Opt Comm* 135:27–31
- Ehlers A, Riemann I, Stark M, König K (2007) Multiphoton fluorescence lifetime imaging of human hair. *Microsc Res Tech* 70:154–161. doi:[10.1002/jemt.20395](https://doi.org/10.1002/jemt.20395)
- Elangovan M, Day RN, Periasamy A (2002) Nanosecond fluorescence resonance energy transfer-fluorescence lifetime imaging microscopy to localize the protein interactions in a single living cell. *J Microsc* 205:3–14
- Elson DS, Jo JA, Marcu L (2007) Miniaturized side-viewing imaging probe for fluorescence lifetime imaging (FLIM): validation with fluorescence dyes, tissue structural proteins and tissue specimens. *New J Phys* 9:127. doi:[10.1088/1367-2630/9/5/127](https://doi.org/10.1088/1367-2630/9/5/127)
- Erecińska M, Nelson D, Silver IA (1996) Metabolic and energetic properties of isolated nerve ending particles (synaptosomes). *Biochim Biophys Acta* 1277:13–34
- Espósito A, Oggier T, Gerritsen H et al (2005) All-solid-state lock-in imaging for wide-field fluorescence lifetime sensing. *Opt Express* 13:9812–9821
- Fischer F, Volkmer B, Puschmann S et al (2008) Assessing the risk of skin damage due to femtosecond laser irradiation. *J Biophotonics* 1:470–477. doi:[10.1002/jbio.200810050](https://doi.org/10.1002/jbio.200810050)
- Förster T (1912) Energy migration and fluorescence. 1946. *J Biomed Opt* 17:011002
- Gafni A, Brand L (1976) Fluorescence decay studies of reduced nicotinamide adenine dinucleotide in solution and bound to liver alcohol dehydrogenase. *Biochemistry* 15:3165–3171. doi:[10.1021/bi00660a001](https://doi.org/10.1021/bi00660a001)
- Gaillard ER, Atherton SJ, Eldred G, Dillon J (1995) Photophysical studies on human retinal lipofuscin. *Photochem Photobiol* 61:448–453
- Galletly NP, McGinty J, Dunsby C et al (2008) Fluorescence lifetime imaging distinguishes basal cell carcinoma from surrounding uninvolved skin. *Br J Dermatol* 159:152–161. doi:[10.1111/j.1365-2133.2008.08577.x](https://doi.org/10.1111/j.1365-2133.2008.08577.x)
- Gehlsen U, Oetke A, Szaszák M et al (2012) Two-photon fluorescence lifetime imaging monitors metabolic changes during wound healing of corneal epithelial cells in vitro. *Graefes Arch Clin Exp Ophthalmol* 250:1293–1302. doi:[10.1007/s00417-012-2051-3](https://doi.org/10.1007/s00417-012-2051-3)
- Gerritsen HC, Asselbergs MAH, Agronskaia AV, Van Sark WJHM (2002) Fluorescence lifetime imaging in scanning microscopes: acquisition speed, photon economy and lifetime resolution. *J Microsc* 206:218–224. doi:[10.1046/j.1365-2818.2002.01031.x](https://doi.org/10.1046/j.1365-2818.2002.01031.x)
- Geusens B, Van Gele M, Braat S et al (2010) Flexible nanosomes (SECosomes) enable efficient siRNA delivery in cultured primary skin cells and in the viable epidermis of ex vivo human skin. *Adv Funct Mater* 20:4077–4090. doi:[10.1002/adfm.201000484](https://doi.org/10.1002/adfm.201000484)
- Ghukasyan VV, Kao F (2009) Monitoring cellular metabolism with fluorescence lifetime of reduced nicotinamide adenine dinucleotide. *J Phys Chem C* 113:11532–11540. doi:[10.1021/jp810931u](https://doi.org/10.1021/jp810931u)
- Gratton E, Barbieri BB (1986) Multifrequency phase fluorometry using pulsed sources: theory and applications. *Spectroscopy* 1:28–36

- Hanson K, Behne M, Barry N, Mauro T (2002) Two-photon fluorescence lifetime imaging of the skin stratum corneum pH gradient. *Biophys J* 83(3):1682–1690
- Hanzon V (1952) Liver cell secretion under normal and pathologic conditions studied by fluorescence microscopy on living rats. *Acta Physiol Scand Suppl* 28:1–268
- Heikal AA (2010) Intracellular coenzymes as natural biomarkers for metabolic activities and mitochondrial anomalies. *Biomark Med* 4:241–263. doi:[10.2217/bmm.10.1](https://doi.org/10.2217/bmm.10.1)
- Höhn A, Grune T (2013) Lipofuscin: formation, effects and role of macroautophagy. *Redox Biol* 1:140–144. doi:[10.1016/j.redox.2013.01.006](https://doi.org/10.1016/j.redox.2013.01.006)
- Huang S, Heikal AA, Webb WW (2002) Two-photon fluorescence spectroscopy and microscopy of NAD(P)H and flavoprotein. *Biophys J* 82:2811–2825. doi:[10.1016/S0006-3495\(02\)75621-X](https://doi.org/10.1016/S0006-3495(02)75621-X)
- Ishikawa-Ankerhold HC, Ankerhold R, Drummen GP. Advanced fluorescence microscopy techniques—FRAP, FLIP, FLAP, FRET and FLIM. *Molecules*. 2012;17(4):4047–4132.
- Islam M, Honma M, Nakabayashi T et al (2013) pH dependence of the fluorescence lifetime of FAD in solution and in cells. *Int J Mol Sci* 14:1952–1963
- Jo JA, Fang Q, Marcu L (2005) Ultrafast method for the analysis of fluorescence lifetime imaging microscopy data based on the Laguerre expansion technique. *IEEE J Quantum Electron* 11:835–845. doi:[10.1109/JSTQE.2005.857685](https://doi.org/10.1109/JSTQE.2005.857685)
- Jung T, Höhn A, Grune T (2010) Lipofuscin: detection and quantification by microscopic techniques. *Methods Mol Biol* 594:173–193. doi:[10.1007/978-1-60761-411-1\\_13](https://doi.org/10.1007/978-1-60761-411-1_13)
- Kao Y-T, Saxena C, He T-F et al (2008) Ultrafast dynamics of flavins in five redox states. *J Am Chem Soc* 130:13132–13139. doi:[10.1021/ja8045469](https://doi.org/10.1021/ja8045469)
- Koehler M, Speicher M, Lange-Asschenfeldt S et al (2011) Clinical application of multiphoton tomography in combination with confocal laser scanning microscopy for in vivo evaluation of skin diseases. *Exp Dermatol* 20:589–594
- Köllner M, Wolfrum J (1992) How many photons are necessary for fluorescence-lifetime measurements? *Chem Phys Lett* 200:199–204
- König K (2008) Clinical multiphoton tomography. *J Biophotonics* 1:13–23. doi:[10.1002/jbio.200710022](https://doi.org/10.1002/jbio.200710022)
- König K (2012) Hybrid multiphoton multimodal tomography of in vivo human skin. *IntraVital* 1:11–26. doi:[10.4161/intv.21938](https://doi.org/10.4161/intv.21938)
- König K, Riemann I (2003) High-resolution multiphoton tomography of human skin with subcellular spatial resolution and picosecond time resolution. *J Biomed Opt* 8:432–439. doi:[10.1117/1.1577349](https://doi.org/10.1117/1.1577349)
- König K, So PT, Mantulin WW et al (1996) Two-photon excited lifetime imaging of autofluorescence in cells during UVA and NIR photostress. *J Microsc* 183:197–204
- König K, Schneckenburger H, Hibst R (1999) Time-gated in vivo autofluorescence imaging of dental caries. *Cell Mol Biol (Noisy-le-Grand)* 45:233–239
- König K, Uchugonova A, Gorjup E (2011) Multiphoton fluorescence lifetime imaging of 3D-stem cell spheroids during differentiation. *Microsc Res Tech* 74:9–17. doi:[10.1002/jemt.20866](https://doi.org/10.1002/jemt.20866)
- Labouta HI, Liu DC, Lin LL et al (2011) Gold nanoparticle penetration and reduced metabolism in human skin by toluene. *Pharm Res* 28:2931–2944. doi:[10.1007/s11095-011-0561-z](https://doi.org/10.1007/s11095-011-0561-z)
- Lakowicz JR, Berndt KW (1991) Lifetime-selective fluorescence imaging using an rf phase-sensitive camera. *Rev Sci Instrum* 62:1727. doi:[10.1063/1.1142413](https://doi.org/10.1063/1.1142413)
- Lakowicz J, Szmajnski H, Nowaczyk K, Johnson M (1992) Fluorescence lifetime imaging of free and protein-bound NADH. *Proc Natl Acad Sci* 89:1271–1275
- Leite-Silva VR, Le Lamer M, Sanchez WY et al (2013) The effect of formulation on the penetration of coated and uncoated zinc oxide nanoparticles into the viable epidermis of human skin in vivo. *Eur J Pharm Biopharm* 84:297–308. doi:[10.1016/j.ejpb.2013.01.020](https://doi.org/10.1016/j.ejpb.2013.01.020)
- Liebert A, Wabnitz H, Grosenick D et al (2003) Evaluation of optical properties of highly scattering media by moments of distributions of times of flight of photons. *Appl Opt* 42:5785. doi:[10.1364/AO.42.005785](https://doi.org/10.1364/AO.42.005785)
- Lin LL, Grice JE, Butler MK et al (2011) Time-correlated single photon counting for simultaneous monitoring of zinc oxide nanoparticles and NAD(P)H in intact and barrier-disrupted volunteer skin. *Pharm Res* 28:2920–2930. doi:[10.1007/s11095-011-0515-5](https://doi.org/10.1007/s11095-011-0515-5)



- McGinty J, Galletly NP, Dunsby C et al (2010) Wide-field fluorescence lifetime imaging of cancer. *Biomed Opt Express* 1:627–640. doi:[10.1364/BOE.1.000627](https://doi.org/10.1364/BOE.1.000627)
- Meredith P, Riesz J (2007) Radiative relaxation quantum yields for synthetic eumelanin. *Photochem Photobiol* 79:211–216. doi:[10.1111/j.1751-1097.2004.tb00012.x](https://doi.org/10.1111/j.1751-1097.2004.tb00012.x)
- Mizeret J, Wagnières G, Stepinac T, Van Den Bergh H (1997) Endoscopic tissue characterization by frequency-domain fluorescence lifetime imaging (FD-FLIM). *Lasers Med Sci* 12:209–217. doi:[10.1007/BF02765101](https://doi.org/10.1007/BF02765101)
- Munro I, McGinty J, Galletly N et al (2005) Toward the clinical application of time-domain fluorescence lifetime imaging. *J Biomed Opt* 10:051403. doi:[10.1117/1.2102807](https://doi.org/10.1117/1.2102807)
- Nakajima EC, Van Houten B (2013) Metabolic symbiosis in cancer: refocusing the Warburg lens. *Mol Carcinog* 52:329–337. doi:[10.1002/mc.21863](https://doi.org/10.1002/mc.21863)
- Nakashima N, Yoshihara K, Tanaka F, Yagi K (1980) Picosecond fluorescence lifetime of the coenzyme of D-amino acid oxidase. *J Biol Chem* 255:5261–5263
- Niesner R, Peker B, Schlüsche P, Gericke K-H (2004) Noniterative biexponential fluorescence lifetime imaging in the investigation of cellular metabolism by means of NAD(P)H autofluorescence. *Chemphyschem* 5:1141–1149. doi:[10.1002/cphc.200400066](https://doi.org/10.1002/cphc.200400066)
- Nobis M, McGhee EJ, Morton JP et al (2013) Intravital FLIM-FRET imaging reveals dasatinib-induced spatial control of src in pancreatic cancer. *Cancer Res* 73:4674–4686. doi:[10.1158/0008-5472.CAN-12-4545](https://doi.org/10.1158/0008-5472.CAN-12-4545)
- O'Connor D (1984) Time-correlated single photon counting. Academic Press, London
- Ogikubo S, Nakabayashi T, Adachi T et al (2011) Intracellular pH sensing using autofluorescence lifetime microscopy. *J Phys Chem B* 115:10385–10390. doi:[10.1021/jp2058904](https://doi.org/10.1021/jp2058904)
- Pan X, Hobbs RP, Coulombe PA (2013) The expanding significance of keratin intermediate filaments in normal and diseased epithelia. *Curr Opin Cell Biol* 25:47–56. doi:[10.1016/j.ceb.2012.10.018](https://doi.org/10.1016/j.ceb.2012.10.018)
- Pena A-M, Strupler M, Boulesteix T, Schanne-Klein M-C (2005) Spectroscopic analysis of keratin endogenous signal for skin multiphoton microscopy. *Opt Express* 13:6268. doi:[10.1364/OPEX.13.006268](https://doi.org/10.1364/OPEX.13.006268)
- Perrin F (1929) La fluorescence des solutions. Induction moléculaire – polarisation et durée d'émission, photochimie. *Photochimie Ann Phys* 12:169–275
- Philip J, Carlsson K (2003) Theoretical investigation of the signal-to-noise ratio in fluorescence lifetime imaging. *J Opt Soc Am A* 20:368. doi:[10.1364/JOSAA.20.000368](https://doi.org/10.1364/JOSAA.20.000368)
- Pollok BA, Heim R (1999) Using GFP in FRET-based applications. *Trends Cell Biol* 9:57–60
- Prevo B, Peterman EJG (2014) Förster resonance energy transfer and kinesin motor proteins. *Chem Soc Rev* 43:1144–1155. doi:[10.1039/c3cs60292c](https://doi.org/10.1039/c3cs60292c)
- Prow TW, Monteiro-Riviere NA, Inman AO et al (2012) Quantum dot penetration into viable human skin. *Nanotoxicology* 6:173–185. doi:[10.3109/17435390.2011.569092](https://doi.org/10.3109/17435390.2011.569092)
- Qu X, Wang J, Zhang Z et al (2008) Imaging of cancer cells by multiphoton microscopy using gold nanoparticles and fluorescent dyes. *J Biomed Opt* 13:031217. doi:[10.1117/1.2942373](https://doi.org/10.1117/1.2942373)
- Requejo-Isidro J, McGinty J, Munro I et al (2004) High-speed wide-field time-gated endoscopic fluorescence-lifetime imaging. *Opt Lett* 29:2249–2251
- Ribou A-C, Vigo J, Salmon J-M (2007) Lifetime of fluorescent pyrene butyric acid probe in single living cells for measurement of oxygen fluctuation. *Photochem Photobiol* 80:274–280. doi:[10.1111/j.1751-1097.2004.tb00083.x](https://doi.org/10.1111/j.1751-1097.2004.tb00083.x)
- Roberts MS, Roberts MJ, Robertson TA et al (2008) In vitro and in vivo imaging of xenobiotic transport in human skin and in the rat liver. *J Biophotonics* 1:478–493. doi:[10.1002/jbio.200810058](https://doi.org/10.1002/jbio.200810058)
- Roberts MS, Dancik Y, Prow TW et al (2011) Non-invasive imaging of skin physiology and percutaneous penetration using fluorescence spectral and lifetime imaging with multiphoton and confocal microscopy. *Eur J Pharm Biopharm* 77:469–488. doi:[10.1016/j.ejpb.2010.12.023](https://doi.org/10.1016/j.ejpb.2010.12.023)
- Robertson T, Sanchez W, Roberts M (2010) Are commercially available nanoparticles safe when applied to the skin? *J Biomed Nanotechnol* 6:452–468
- Romero G, Qiu Y, Murray RA, Moya SE (2013) Study of intracellular delivery of doxorubicin from poly(lactide-co-glycolide) nanoparticles by means of fluorescence lifetime imaging and confocal Raman microscopy. *Macromol Biosci* 13:234–241. doi:[10.1002/mabi.201200235](https://doi.org/10.1002/mabi.201200235)

- Sanchez W (2013) Changes in the redox state and endogenous fluorescence of in vivo human skin due to intrinsic and photo-aging, measured by multiphoton tomography with fluorescence lifetime imaging. *J Biomed Opt* 18:61217
- Sanchez WY, Prow TW, Sanchez WH et al (2010) Analysis of the metabolic deterioration of ex vivo skin from ischemic necrosis through the imaging of intracellular NAD(P)H by multiphoton tomography and fluorescence lifetime imaging microscopy. *J Biomed Opt* 15:046008
- Schneckenburger H, König K, Kunzi-Rapp K et al (1993) Time-resolved in-vivo fluorescence of photosensitizing porphyrins. *J Photochem Photobiol B* 21:143–147
- Seidenari S, Arginelli F, Dunsby C et al (2013) Multiphoton laser tomography and fluorescence lifetime imaging of melanoma: morphologic features and quantitative data for sensitive and specific non-invasive diagnostics. *PLoS One* 8:e70682. doi:[10.1371/journal.pone.0070682](https://doi.org/10.1371/journal.pone.0070682)
- Siegel J, Elson DS, Webb SED et al (2003) Studying biological tissue with fluorescence lifetime imaging: microscopy, endoscopy, and complex decay profiles. *Appl Opt* 42:2995–3004
- Skala MC, Riching KM, Bird DK et al (2007a) In vivo multiphoton fluorescence lifetime imaging of protein-bound and free nicotinamide adenine dinucleotide in normal and precancerous epithelia. *J Biomed Opt* 12:024014. doi:[10.1117/1.2717503](https://doi.org/10.1117/1.2717503)
- Skala MC, Riching KM, Gendron-Fitzpatrick A et al (2007b) In vivo multiphoton microscopy of NADH and FAD redox states, fluorescence lifetimes, and cellular morphology in precancerous epithelia. *Proc Natl Acad Sci U S A* 104:19494–19499. doi:[10.1073/pnas.0708425104](https://doi.org/10.1073/pnas.0708425104)
- So PT, König K, Berland K et al (1998) New time-resolved techniques in two-photon microscopy. *Cell Mol Biol (Noisy-le-Grand)* 44:771–793
- Speicher M, Köhler M, König K et al (2010) Clinical application of multiphoton tomography in combination with high-frequency ultrasound for evaluation of skin diseases. *J Biophotonics* 3:759–773
- Spitz J-A, Yasukuni R, Sandeau N et al (2008) Scanning-less wide-field single-photon counting device for fluorescence intensity, lifetime and time-resolved anisotropy imaging microscopy. *J Microsc* 229:104–114. doi:[10.1111/j.1365-2818.2007.01873.x](https://doi.org/10.1111/j.1365-2818.2007.01873.x)
- Straub M, Hell SW (1998) Fluorescence lifetime three-dimensional microscopy with picosecond precision using a multifocal multiphoton microscope. *Appl Phys Lett* 73:1769. doi:[10.1063/1.122276](https://doi.org/10.1063/1.122276)
- Stringari C, Sierra R, Donovan PJ, Gratton E (2012) Label-free separation of human embryonic stem cells and their differentiating progenies by phasor fluorescence lifetime microscopy. *J Biomed Opt* 17:046012. doi:[10.1117/1.JBO.17.4.046012](https://doi.org/10.1117/1.JBO.17.4.046012)
- Sun Y, Hatami N, Yee M et al (2010) Fluorescence lifetime imaging microscopy for brain tumor image-guided surgery. *J Biomed Opt* 15:056022. doi:[10.1117/1.3486612](https://doi.org/10.1117/1.3486612)
- Sun Y, Phipps JE, Meier J et al (2013) Endoscopic fluorescence lifetime imaging for in vivo intraoperative diagnosis of oral carcinoma. *Microsc Microanal* 19:791–798. doi:[10.1017/S1431927613001530](https://doi.org/10.1017/S1431927613001530)
- Tadrous PJ, Siegel J, French PMW et al (2003) Fluorescence lifetime imaging of unstained tissues: early results in human breast cancer. *J Pathol* 199:309–317. doi:[10.1002/path.1286](https://doi.org/10.1002/path.1286)
- Thorling CA, Dancik Y, Hupple CW et al (2011a) Multiphoton microscopy and fluorescence lifetime imaging provide a novel method in studying drug distribution and metabolism in the rat liver in vivo. *J Biomed Opt* 16:086013. doi:[10.1117/1.3614473](https://doi.org/10.1117/1.3614473)
- Thorling CA, Liu X, Burczynski FJ et al (2011b) Multiphoton microscopy can visualize zonal damage and decreased cellular metabolic activity in hepatic ischemia-reperfusion injury in rats. *J Biomed Opt* 16:116011. doi:[10.1117/1.3647597](https://doi.org/10.1117/1.3647597)
- Thorling CA, Liu X, Burczynski FJ et al (2013) Intravital multiphoton microscopy can model uptake and excretion of fluorescein in hepatic ischemia-reperfusion injury. *J Biomed Opt* 18:101306. doi:[10.1117/1.JBO.18.10.101306](https://doi.org/10.1117/1.JBO.18.10.101306)
- van Munster E, Gadella T (2005) Fluorescence lifetime imaging microscopy (FLIM). *Microsc Tech* 95:143–175. doi:[10.1007/b102213](https://doi.org/10.1007/b102213)
- Vergen J, Hecht C, Zholudeva LV et al (2012) Metabolic imaging using two-photon excited NADH intensity and fluorescence lifetime imaging. *Microsc Microanal* 18:761–770. doi:[10.1017/S1431927612000529](https://doi.org/10.1017/S1431927612000529)

- Vishwasrao HD, Heikal AA, Kasischke KA, Webb WW (2005) Conformational dependence of intracellular NADH on metabolic state revealed by associated fluorescence anisotropy. *J Biol Chem* 280:25119–25126. doi:[10.1074/jbc.M502475200](https://doi.org/10.1074/jbc.M502475200)
- Wakita M, Nishimura G, Tamura M (1995) Some characteristics of the fluorescence lifetime of reduced pyridine nucleotides in isolated mitochondria, isolated hepatocytes, and perfused rat liver in situ. *J Biochem* 118:1151–1160
- Wang H-W, Gukassyan V, Chen C et al (2008) Differentiation of apoptosis from necrosis by dynamic changes of reduced nicotinamide adenine dinucleotide fluorescence lifetime in live cells. *J Biomed Opt* 13:054011. doi:[10.1117/1.2975831](https://doi.org/10.1117/1.2975831)
- Wang B-G, König K, Halbhuer K-J (2010) Two-photon microscopy of deep intravital tissues and its merits in clinical research. *J Microsc* 238:1–20. doi:[10.1111/j.1365-2818.2009.03330.x](https://doi.org/10.1111/j.1365-2818.2009.03330.x)
- Watt RM, Voss EW (1979) Solvent perturbation of the fluorescence of fluorescein bound to specific antibody. Fluorescence quenching of the bound fluorophore by iodide. *J Biol Chem* 254:1684–1690
- Weber G (1948) The quenching of fluorescence in liquids by complex formation. Determination of the mean life of the complex. *Trans Faraday Soc* 44:185. doi:[10.1039/tf9484400185](https://doi.org/10.1039/tf9484400185)
- Weber P, Wagner M, Schneckenburger H (2013) Cholesterol dependent uptake and interaction of Doxorubicin in mcf-7 breast cancer cells. *Int J Mol Sci* 14:8358–8366. doi:[10.3390/ijms14048358](https://doi.org/10.3390/ijms14048358)
- Weidtkamp-Peters S, Felekyan S, Bleckmann A et al (2009) Multiparameter fluorescence image spectroscopy to study molecular interactions. *Photochem Photobiol Sci* 8:470–480. doi:[10.1039/b903245m](https://doi.org/10.1039/b903245m)
- Yu J-S, Guo H-W, Wang C-H et al (2011) Increase of reduced nicotinamide adenine dinucleotide fluorescence lifetime precedes mitochondrial dysfunction in staurosporine-induced apoptosis of HeLa cells. *J Biomed Opt* 16:036008. doi:[10.1117/1.3560513](https://doi.org/10.1117/1.3560513)
- Yu Y, Lee AMD, Wang H et al (2012) Imaging-guided two-photon excitation-emission-matrix measurements of human skin tissues. *J Biomed Opt* 17:077004. doi:[10.1117/1.JBO.17.7.077004](https://doi.org/10.1117/1.JBO.17.7.077004)
- Zhong W, Urayama P, Mycek M-A (2003) Imaging fluorescence lifetime modulation of a ruthenium-based dye in living cells: the potential for oxygen sensing. *J Phys D Appl Phys* 36:1689–1695. doi:[10.1088/0022-3727/36/14/306](https://doi.org/10.1088/0022-3727/36/14/306)
- Zipfel WR, Williams RM, Christie R et al (2003) Live tissue intrinsic emission microscopy using multiphoton-excited native fluorescence and second harmonic generation. *Proc Natl Acad Sci U S A* 100:7075–7080. doi:[10.1073/pnas.0832308100](https://doi.org/10.1073/pnas.0832308100)
- Zvyagin AV, Zhao X, Gierden A et al (2008) Imaging of zinc oxide nanoparticle penetration in human skin in vitro and in vivo. *J Biomed Opt* 13:064031. doi:[10.1117/1.3041492](https://doi.org/10.1117/1.3041492)

## Index

### A

Abe, K., 163–179  
 AD. *See* Alzheimer's disease (AD)  
 ALS. *See* Amyotrophic lateral sclerosis (ALS)  
 Alzheimer's disease (AD), 11, 47–50, 55–58, 62–64  
 Amyotrophic lateral sclerosis (ALS), 47, 50–51, 57–59  
 Angiogenesis, 106, 126, 131, 135, 172, 189, 238, 243  
 Antigen presentation, 84–85  
 Arbel-Ornath, M., 45–65  
 Arfors, K.E., 205  
 Awake mice, 25–39  
 Axonal bouton, 8–11

### B

Bacskai, B.J., 45–65  
 Bao, H., 312, 313  
 Becker, W., 371–412  
 Bewersdorf, J., 312  
 Bhattacharya, J., 224  
 Bird, D.K., 376  
 Blinder, P., 26  
 Bone marrow, 143–158, 250, 251  
 Both, M., 308  
 Brand, L., 376  
 Breast cancer, 107, 113, 114, 119, 254, 282, 300, 402, 404  
 Brooks, D.J., 60  
 Brown, C.M., 305–365  
 Brown, E., 241  
 Brown, M.B., 221–232

### C

Cahalan, M.D., 81–100  
 Calcium imaging, 3, 12–16, 62–64  
 Campagnola, P.J., 301, 308  
 Cancer, 125–138, 158, 166, 168, 169, 267, 269, 271, 273–275, 282, 361, 372, 390–392, 407  
     imaging, 54, 55, 105–121, 126, 128, 130–134, 233–256, 297–301, 306–307, 309, 364, 401–404  
 Cao, L., 163–179  
 Cell labeling, 85, 147, 148, 150, 245, 250, 251  
 Cell metabolism, 394–395, 397–398  
 Cell tracking, 147, 148, 153, 249–252, 271, 276  
 Celso, C.L., 143–158  
 Cervical imaging, 296–297  
 Chalfie, M., 2  
 Chieppa, M., 90  
 Chronic *in vivo* imaging, 6, 9, 15  
 Clinical imaging, 234, 315, 323  
 Collini, M., 376  
 Conklin, M.W., 403  
 Coppieters, K., 90, 178, 241  
 Cortical vessels, 29–31  
 Cranial window, 6, 7, 27, 28, 31, 35, 39, 61, 133, 173  
 Cunningham, V.J., 125–138

### D

Damayanti, N.P., 376  
 Dancik, Y., 376  
 Daniel, R., 125–138

Débarre, D., 308  
 Deep tissue imaging, 15–16, 61, 179, 190,  
 239, 256, 364  
 Dendritic spine, 8–11, 62, 63, 173  
 Denk, W., 2, 312, 313  
 Dewhirst, M.W., 136  
 Dextrans, 12, 87, 168, 176, 205–217  
 Digman, M.A., 388  
 Ding, L., 147  
 Dombek, D.A., 91, 308  
 Dorsal skin fold chamber (DSFC), 126, 128,  
 132, 133, 137, 172, 238, 241, 248,  
 254, 272  
 Drew, P.J., 32  
 Driscoll, J.D., 30  
 Drug delivery, 45, 106, 127, 157, 247, 249,  
 255, 282, 404–408  
 Drug response, 106, 108, 173, 235, 242, 249,  
 253, 255, 256  
 DSFC. *See* Dorsal skin fold chamber (DSFC)  
 Duma, V.-F., 294  
 Dunn, K.W., 178

## E

Earley, S., 268  
 Egeblad, M., 105–121  
 Ehlers, A., 376  
 Endocytosis, 176, 178, 200, 201, 206  
 Endogenous fluorescence, 84, 85, 87, 93, 154,  
 168–170, 189, 197, 198, 201, 211, 240,  
 253, 329, 332  
 Endogenous fluorophores, 165, 169–170, 336  
 Engelbrecht, C.J., 312

## F

Farrar, M.J., 6, 308  
 Fein, M.R., 105–121  
 Fenrich, K., 6  
 Ferrer, M., 90  
 FLAP. *See* Fluorescence localization after  
 photobleaching (FLAP)  
 FLIM. *See* Fluorescence-lifetime imaging  
 microscopy (FLIM)  
 Fluorescence-lifetime imaging microscopy  
 (FLIM), 237, 253, 372, 374, 377, 379,  
 381–408, 411, 412  
 Fluorescence localization after photobleaching  
 (FLAP), 269  
 Fluorescence resonance energy transfer  
 (FRET), 87, 120, 168, 234, 236, 239,  
 246, 253, 255, 269, 377, 386, 388,  
 407–412

Fluorescent proteins, 7, 8, 15, 82, 83, 85–87,  
 106, 107, 113, 151, 167–168, 187–201,  
 217, 251, 252, 267–269, 274  
 Fluorescent reporters, 179, 201, 250, 251,  
 267–270  
 Fluorochromes, 2, 137, 265, 266, 275  
 Fluorophore, 2–4, 7, 8, 15, 61, 65, 82, 84, 107,  
 116, 117, 120, 165, 166, 169–171, 179,  
 193, 205, 206, 209–210, 217, 235, 239,  
 245, 266, 275, 284, 311, 329, 333, 336,  
 372, 375–377, 379, 381, 387, 388,  
 394–396, 401, 409–411  
 Frequency domain, 383–385, 387–390, 412  
 Friedenstein, A.J., 144  
 Friedl, P., 308

## G

Gafni, A., 376  
 Gaillard, E.R., 376  
 Galletly, N.P., 391  
 Gambhir, S.S., 233–256  
 Genetically-encoded calcium indicators  
 (GECIs), 13, 16, 17, 269  
 GFR. *See* Glomerular filtration rate (GFR)  
 Giedt, R., 263–278  
 Glia, 8, 11, 36, 37, 49, 52, 57–59, 164, 173  
 Glomerular filtration rate (GFR), 210–213  
 Glomeruli filtration, 206, 210–214, 216  
 Goetz, M., 178  
 Gonçalves, J.T., 1–17  
 Green fluorescent protein (GFP), 2, 63, 136,  
 156, 168, 189, 234  
 GRIN lenses, 288, 289, 319, 321, 329–331,  
 338–342, 347–349, 351, 389, 390  
 Grinvald, A., 241

## H

Haematopoietic stem cells (HSC), 144–147,  
 150, 151, 153–158  
 Hall, A.M., 178  
 Hall, G., 281–301  
 Harvey, W., 222  
 HD. *See* Huntington's disease (HD)  
 Heikal, A.A., 395  
 Helmchen, F., 282, 289, 312  
 Helmlinger, G., 136  
 Hint, H., 205  
 Hoshida, T., 241  
 Hoy, C.L., 312  
 Huang, S., 308  
 Hughes, E., 11  
 Huland, D.M., 305–365

Huntington's disease (HD), 47, 51–53, 56, 59–60  
 Huo, L., 291  
 Hypoxia, 88, 126, 130, 131, 135, 136, 155, 209, 223, 231, 243–245, 247, 251, 401

## I

Imaging agents, 234–246, 250, 252, 253, 255, 256, 265  
 Imanishi, Y., 241  
 Intaglietta, M., 130  
 Intravital, 1–17, 83, 85, 107, 173, 176, 191, 195–200, 207, 229, 372, 373  
 Intravital imaging, 6, 7, 14–15, 45–65, 81–100, 105–121, 131, 136, 150, 153, 158, 164, 166, 167, 172–178, 187–201, 217, 231, 233–256, 264, 269–271, 273–277, 305–365, 371–412  
 Intravital microscopy, 5, 106–108, 116, 126, 128, 130–134, 136–138, 148, 151–158, 164, 167–168, 172, 190, 200, 221–256, 265, 271, 274–277, 371–412  
*In vivo* imaging, 4, 5, 11, 14, 27, 36, 56, 61, 63, 82, 85, 86, 88, 91–92, 143–158, 173, 176, 177, 215, 235, 239, 267, 276, 313, 323–328, 358–363  
*In vivo* physiology, 45, 48, 54, 62, 65  
 Ishii, M., 91  
 Islam, M., 376  
 Ito, K., 241

## J

Janssen, A., 255  
 Ji, N., 16  
 Jia, H., 13  
 Johnson, K.A., 49  
 Jung, T., 376

## K

Kang, J.J., 178  
 Kang, S.S., 91  
 Kastanenka, K.V., 45–65  
 Kedrin, D., 241  
 Keenan, T.W., 188  
 Kelly, K.J., 178  
 Kidney, 108, 164, 168, 169, 173, 174, 176–178, 200, 206–215, 217, 273, 276, 325–327, 344, 345, 354, 355, 361, 362  
 Kim, J.V., 90  
 Klinger, A., 178

Kobat, D., 15  
 Koenig, K., 371–412  
 Kohler, A., 91  
 Komatsu, N., 269  
 König, K., 376, 389  
 Kotsuma, M., 241  
 Kreisel, D., 90  
 Kuhn, B., 12

## L

Lactation, 192, 194, 195, 201  
 Lakowicz, J., 376  
 Le Harzic, R., 312, 313  
 Lee, S., 241  
 Lehr, H.A., 241  
 Leite-Silva, V.R., 406  
 Leu, A.J., 241  
 Leukocyte trafficking, 229, 230  
 Li, W., 91  
 Li, X., 281–301  
 Li, Z., 241  
 Liang, W., 281–301  
 Lin, C.P., 143–158  
 Liou, H.L., 90  
 Liu, X., 178  
 Liu, Y., 295  
 Liver, 97, 108, 117, 144, 164, 168–170, 173, 174, 177, 178, 241, 310, 325, 327, 344, 345, 374, 379–381, 396, 400, 408  
 Llewellyn, M.E., 90  
 Looney, M.R., 90, 241  
 Lung, 84, 85, 88, 90, 95, 97–99, 114–116, 119, 126, 137, 170, 176, 221–232, 297–300, 306, 325, 329, 331, 332, 346, 347, 354, 355, 358–361  
     cancer, 297–300  
     imaging, 85, 89, 95, 97–99, 114–116, 119, 356  
 Lunt, S.J., 125–138  
 Lymph node, 82, 94–97, 165, 241, 250  
 Lymphocyte dynamics, 83

## M

Magnetic resonance imaging (MRI), 46–54, 128, 138, 147, 148, 234–237, 240, 306  
 Mammary gland, 108, 109, 111–113, 126, 187–201  
 Mammary imaging, 111–114, 173  
 Marchiando, A.M., 178  
 Masedunskas, A., 187–201  
 Mather, I.H., 187–201



- Matheu, M.P., 81–100  
 Maxfield, F.R., 209  
 Mazo, I.B., 150, 158  
 McDole, J.R., 90  
 McGavern, D.B., 91  
 McGinty, J., 393  
 Mempel, T.R., 90  
 MEMS scanners, 292, 313, 315  
 Mendez-Ferrer, S., 158  
 Mesenchymal stem cells, 144, 150, 156–157  
 Microendoscopy, 281–301, 360, 364  
 Microenvironment, 107, 108, 120, 121, 126,  
 144–148, 150, 153, 173, 237, 242–245,  
 255, 258, 377, 394, 411  
 Micropores, 172  
 Milk lipids and proteins, 188, 197–200  
 Milk secretion, 188–190  
 Miller, M.J., 90  
 Miniaturized optics, 164, 172, 179, 311,  
 314–316, 318, 328–331, 334, 337, 339,  
 355  
 Molecular imaging, 62, 63, 165, 233–256  
 Molitoris, B.A., 178, 205–217  
 Montro, 390  
 Morrison, S.J., 147  
 Mortensen, L.J., 143–158  
 Mostany, R., 1–17  
 MRI. *See* Magnetic resonance imaging (MRI)  
 Multiphoton, 2–4, 15, 62, 281–283, 305–365,  
 372–381, 385, 394, 399, 402, 403,  
 405, 407  
 Multiphoton microscopy, 46, 134, 148, 178,  
 190, 237, 283, 285, 297, 300, 301,  
 309–311, 314., 322, 324, 329, 333,  
 339–341, 349, 360, 372, 374, 375, 377,  
 383, 389, 394, 397, 403, 404, 406  
 Myaing, M.T., 289, 312  
 Myiung, 282
- N**  
 NADH. *See* Nicotinamide adenine  
 dinucleotide (NADH)  
 Nadiarnykh, O., 282  
 Nakashima, N., 376  
 Nakasone, E.S., 254  
 Near-infrared (NIR), 63–65, 149, 165, 167,  
 234, 239, 240, 242, 245, 253, 256, 283,  
 375, 394, 398, 404  
 Neurodegeneration, 49, 62  
 Nicotinamide adenine dinucleotide (NADH),  
 169, 234, 240, 253, 284, 309, 310, 333,  
 376, 387, 394, 397, 398, 400, 401  
 Niesner, R., 376
- NIR. *See* Near-infrared (NIR)  
 Nobis, M., 407  
 Non-linear microscopy, 148, 282–285, 365  
 Nordberg, A., 56
- O**  
 Odoardi, F., 90  
 Ogg, S.L., 188  
 Optogenetics, 16–17, 120, 121  
 Orth, J.D., 268  
 Ouzounov, D.G., 305–365  
 Oxygenation, 48, 108, 125–138, 176, 247  
 Oye, K.S., 131
- P**  
 Pai, S., 91  
 Palmer, G.M., 241  
 Pancreas, 84, 88, 90, 97, 108, 117, 168, 169,  
 173, 174, 177, 178, 200, 241, 276, 306  
 Parker, I., 81–100  
 Parkinson's disease (PD), 47, 53–54, 57,  
 60–61, 144, 264, 265, 267–277  
 Patlak, C.S., 134  
 Pavese, N., 60  
 Paxian, M., 178  
 PD. *See* Parkinson's disease (PD)  
 Pena, A.M., 376  
 Perry, S.W., 301  
 PET. *See* Positron emission tomography (PET)  
 Peterman, E.J.G., 409  
 Peters, N.C., 90  
 Petersen, C., 12  
 Petrache, I., 221–232  
 Pharmacodynamics, 58, 127, 131, 263  
 Pharmacokinetics, 174, 235, 245, 249, 263,  
 265, 274  
 Piyawattanametha, W., 312  
 Positron emission tomography (PET), 46,  
 54–61, 63, 65, 128, 138, 234–237, 240,  
 244, 256  
 Pre-clinical imaging, 106–116  
 Pre-clinical research, 37, 46, 48, 57, 106–116,  
 145, 147  
 Presson, R.G., 221–232  
 Prevo, B., 409  
 Pyramidal neuron, 8, 9, 11
- R**  
 Red blood cell (RBC) velocity, 30–35, 39,  
 128–131, 207, 227  
 Rehberg, M., 308

Reyes-Aldasoro, C.C., 125–138  
 Riemann, I., 376  
 Ritsma, L., 178, 241  
 Rivera, D.R., 300, 305–365  
 Roberts, M.S., 371–412  
 Rothstein, E.C., 90

## S

Sackstein R., 156  
 Sanchez, W.Y., 371–412  
 Sandoval, R.M., 178, 205–217  
 Sawinski, J., 312, 313  
 Schneckenburger, H., 376  
 Secretion kinetics, 189, 193, 200  
 Seidenari, S., 405  
 Sen, D., 90  
 Shcherbakova, D.M., 15  
 Shih, A.Y., 25–39  
 Shimomura, O., 2  
 Single cell imaging, 263–278  
 Single photon emission computed tomography (SPECT), 46, 54–61, 65, 234, 235, 237  
 Skala, M.C., 282, 376, 402  
 Skin, 90, 92–94, 98, 99, 112, 113, 127, 150, 153, 164, 172, 173, 189, 192, 372, 374–377, 379, 381, 382, 389, 391, 396, 399, 404–407  
 Skin flap, 84, 91, 92, 95–97, 107–111, 113, 116, 118, 120, 126, 191, 192, 238  
 Smith, B.R., 241  
 Song, Z., 371–412  
 Sorg, B.S., 136  
 SPECT. *See* Single photon emission computed tomography (SPECT)  
 Spinal cord, 6, 7, 11, 50, 51, 90, 95, 97, 99–100, 173  
 Spleen, 84, 90, 92, 97, 108, 168, 173, 176, 178, 250  
 Stem cell niche, 145–147, 158  
 Steven, P., 241  
 Stroke, 9, 11, 12, 27, 36–38, 46  
 Subcellular imaging, 46, 55, 61, 163–179, 190, 231, 235, 237, 239, 240, 242, 249–255, 270, 274  
 Summers, P.M., 25–39  
 Sun, C.K., 308  
 Swirski, F.K., 178

## T

Tanaka, K., 241  
 Taylor, Z.J., 25–39

Thiberge, S., 178  
 Thinned-skull, 6, 7, 25, 27, 28, 38, 61  
 Thorling, C.A., 400  
 Thornton, E.E., 90  
 Thurber, G.M., 267, 277  
 Time-domain, 286, 383–390, 392, 397, 401, 404, 411, 412  
 Toma, I., 178  
 Tozer, G.M., 125–138  
 Transgenic mouse strains, 149, 195–198, 201  
 Tsien, R., 2  
 Tumor biology, 179, 272  
 Tumor blood supply, 108, 127–131, 244, 247  
 Tumor cell heterogeneity, 106, 119, 131, 249, 251, 255, 264, 271, 277  
 Tumor circulation, 243, 247  
 Tumor extracellular matrix (ECM), 107, 108, 234, 242, 243, 245–249, 251, 255, 282  
 Tumor-mediated angiogenesis, 126, 131, 135, 189, 238, 243  
 Tumor microenvironment, 107, 108, 120, 126, 173, 237, 242–245, 255  
 Tumor pH, 137, 243–245, 247  
 Tumor PO<sub>2</sub>, 135, 137, 244, 245  
 Tumor stroma, 108, 120, 254, 401  
 Two-photon laser scanning microscopy (TPLSM), 25–27, 38, 39

## V

Vascular permeability, 127, 130–134, 213, 214, 217, 229–230, 247  
 Vasculopathies, 36–37  
 Vasodynamics, 25–39  
 Vasoreactivity, 230–231  
 Vergen, J., 376  
 von Andrian, U.H., 150, 158

## W

Wagner, W.W. Jr., 222, 223  
 Wakita, M., 376  
 Wang, B.-G., 376  
 Wang, C.C., 297  
 Wang, H.-W., 399  
 Wang, X., 45–65  
 Watson, A.J., 178  
 WBCs dynamics, 208, 209  
 Webb, W., 2  
 Wegmann, S.K., 45–65  
 Weigert, R., 187–201  
 Weissleder, R., 263–278  
 Witte, S., 308

Wu, Y., 312  
Wysocki, R.W., 105–121

Yu, H., 233–256  
Yu, Y., 376

**X**

Xu, C., 305–365

**Y**

Yang, K., 263–278  
Yizhar, O., 16

**Z**

Zaher, W., 143–158  
Zhang, Y., 282, 296–299  
Zhong, Z., 178  
Zinselmeyer, B.H., 90  
Zipfel, W.R., 308, 376  
Zvyagin, A.V., 374